Gevorg Kocharyan
Andrey Lyakhov   *Editors*

Trigger Effects in Geosystems

The 5th International Conference,
Sadovsky Institute of Geospheres
Dynamics of Russian Academy
of Sciences

EXTRAS ONLINE

Springer

Springer Proceedings in Earth and Environmental Sciences

Series Editor

Natalia S. Bezaeva, The Moscow Area, Russia

The series Springer Proceedings in Earth and Environmental Sciences publishes proceedings from scholarly meetings and workshops on all topics related to Environmental and Earth Sciences and related sciences. This series constitutes a comprehensive up-to-date source of reference on a field or subfield of relevance in Earth and Environmental Sciences. In addition to an overall evaluation of the interest, scientific quality, and timeliness of each proposal at the hands of the publisher, individual contributions are all refereed to the high quality standards of leading journals in the field. Thus, this series provides the research community with well-edited, authoritative reports on developments in the most exciting areas of environmental sciences, earth sciences and related fields.

More information about this series at http://www.springer.com/series/16067

Gevorg Kocharyan · Andrey Lyakhov
Editors

Trigger Effects in Geosystems

The 5th International Conference,
Sadovsky Institute of Geospheres
Dynamics of Russian Academy
of Sciences

Springer

Editors
Gevorg Kocharyan
Sadovsky Institute of Geospheres
Dynamics RAS
Moscow, Russia

Andrey Lyakhov
Sadovsky Institute of Geospheres
Dynamics RAS
Moscow, Russia

Introduction

The Fifth International Conference "Trigger Effects in Geosystems" was organized by the Sadovsky Institute of Geospheres Dynamics of Russian Academy of Sciences, and was held on June 4–7, 2019 in Moscow, Russia.

The understanding of how the processes of nucleating instabilities in geosystems are triggered by external effects is extremely important in terms of elaborating new approaches to the problem of prediction and prevention of natural and anthropogenic catastrophes. Investigating trigger processes is very attractive, because these phenomena are one of the rare possibilities to detect the cause-and-effect relations in studying the dynamics of large-scale natural objects. Activities in this direction can suggest new ways in developing the strategy of forecasting and preventing geocatastrophes or, at least, lowering the damage. More than 250 scientific specialists, students, and postgraduates from institutes of the Russian Academy of Sciences, universities, and other Russian and foreign organizations took part in the Conference.

The Conference considered the following scientific problems:

- Exogenous triggering of deformation processes in the Earth's crust. Monitoring and forecasting trigger effects. Trigger effects in geology.
- Structure and properties of fault zones. Different sliding regimes on faults. Links to seismicity.
- Safety of mining operations. Deformation processes in mining activities. Fault-slip rock bursts. Mining seismicity. Stability of engineering constructions.
- Seismicity in developing hydrocarbon deposits and hydrocarbon recovery. Geomechanics and fluid dynamics of rock massifs.
- Geophysical fields. Their variations and interactions.
- Active disturbances of ionosphere and magnetosphere of the Earth. Experimental results, numerical and theoretical models.
- The global current circuit, electrical and optical processes in the atmosphere, in equilibrium plasma chemistry of atmospheric phenomena.
- Experimental data and theoretical models of the response of ionosphere to catastrophic natural events (fall of cosmic objects, earthquakes, tsunamis, volcanic eruptions, powerful cyclones).

Conference proceedings are published in two books. The reports presented in English are published in this book. For convenience, all the articles are structured into parts. The first part deals with trigger effects in the solid Earth. The second part is devoted to dynamic processes that emerge in the course of mining activities. The final part combines articles that consider dynamic effects in the upper geospheres.

The organizing committee thanks the Russian Foundation for Basic Research and the Ministry of Science and Higher Education for financial support.

<div align="right">Prof. Gevorg Kocharyan
Dr. Andrey Lyakhov</div>

Contents

Fluidodynamic Processes and Seismicity

Dynamic Processes in Mining

Dynamic Effects in Upper Geospheres

Part I
Trigger Effects in Solid Earth

Modeling Modern Geotectonic Processes of the Siberian Platform and Its Margins

Ayan Akhmetov, Pavel Makarov, Igor Smolin and Alexey Peryshkin

Abstract

This article presents the numerical modeling of modern tectonic flows in the Siberian Craton. It is based on global geotectonic processes in the Asian continent as well as its geological structure. The margins of Siberian Craton are unstable geological structures where local active geotectonic processes such as collision, shear stretching and metamorphisms are observed. We selected the region of the Yenisei Ridge because of its geological and geophysical specifics. The type of state of stress and strain in this area was estimated on the base of calculations of global tectonic flows in Central Asia. To get more details on the type of state of stress and strain in the Yenisei Ridge, calculations were carried out for the geological cross sections of Batolit 1982 and Shpat. The results show the presence of regions of localized inelastic deformation in the overstep region of the Yenisei shear zone. Also, in both sections, the bands of localized inelastic strain propagate to the surface of the mountain group exactly in the regions of the location of the large Siberian rivers of Yenisei and Velmo.

Keywords

Tectonic flow · Geological cross-section · State of stress and strain

A. Akhmetov (✉) · P. Makarov · I. Smolin
Tomsk State University, 634050 Tomsk, Russian Federation
e-mail: ayan.akhmetov93@gmail.com

A. Akhmetov · P. Makarov · I. Smolin · A. Peryshkin
Institute of Strength Physics and Materials Science SB RAS, 634055 Tomsk, Russian Federation

3

1 Introduction

The fundamental geodynamic processes such as collision, subduction, and spreading are natural phenomena that often studied based on the concept of plate tectonics originating from the theory of continental drift [1]. Geophysical community has demonstrated great interest in investigating the tectonics of large Eurasian Plate and, particularly, its most dynamic parts in the Central and Southeastern Asia. The whole spectrum of tectonic processes can be observed in these regions. The Asian continent has seismically active intracontinental rifts, for instance, the Red River Rift (China) and the Baikal Rift Zone (Russian Federation). The Indian subduction resulting from collision of the Eurasian and Indian plates plays the main role in formation of tectonic flows in Central and Southeastern Asia [2]. These geotectonic processes lead to formation of the Tibetan Plateau and the Himalayan mountains (Asian mountain system). Collision of the American and Eurasian plates in the North-East also influenced the geodynamic situation of the Asian continent with formation of the Verkhoyansk Range and the Kolyma Mountains [3]. Geotectonic transformations in the Asian continent, from separation of Pangea into Gondwana and Laurasia to evolution of modern Asian mountain systems, have been in progress for about 300 million years. This overall mechanism of plate movement plays a minimal role in the research of regional tectonic flow. It is only accepted to evaluate initial and boundary conditions in the studied area.

Siberian Craton is one of the largest Archean-Proterozoic regions, which is a major part of Northern Eurasia. It is adjoined by geological objects with different structural properties [4, 5]. Particularly, the Yenisei Ridge is one of the interesting regions of the Siberian Craton with regard to research of the Asian continent. It is the major structural feature of the western margin between the Siberian Craton and the Central Asian fold belt and located along the Yenisei River. The geological composition of Yenisei Ridge comprises various terranes separated by faults [6, 7]. For this reason, interpreting its geotectonic structure and formation conditions is essentially used for regional and global geodynamic reconstruction of the Eurasian lithosphere.

Introduction and development of calculational technologies have made possible to simulate global and regional tectonic flows of the Earth's crust. Müller et al. developed a computer program that simulates the global geological phenomena using experimental and theoretical data from geophysics, geochemistry, and plate tectonics [8]. Actually, difficulties emerge when we research the regional tectonic flows. To investigate both global and regional tectonic flows in the Asian continent, a modern concept was suggested to analyze the plate tectonics. This concept can help to permit investigating the tectonic flow pattern and stress field as characteristics of the evolutionary process which is inhomogeneous in space and time [9, 10]. Nevertheless, specifics of upright movements and volumetric stress state in the Earth's crust can't be treated within this approach.

The purpose of this paper is to interpret the numerical investigations of regional geotectonic pattern in the Yenisei Ridge in terms of evolution of stress state and tectonic flows in Central Asia resulting from collision of the Eurasian Plate with Hindustan and Arabia in the South and with North America in the North-East. To achieve this goal, we have simulated the tectonic flow pattern in the Asian continent and the regional geotectonic state of the Siberian Craton. Finally, we have analyzed the collision state in the deep structure of the Yenisei Ridge using the data from Batolit-1982 and Shpat geological profiles.

2 Problem Statement

To investigate tectonic movement in Central and Southeast Asia (predominantly in the Siberian Craton), we made use of the Seminskii's scheme—a zone-block lithospheric structure of Eastern and Central Asia that is used here as a general structural model. The developed model contains also boundary blocks which aim to mimic real geodynamic effects from neighboring regions [11]. This model is shown in Fig. 1.

This structural model is two-dimensional and can provide only a two-dimensional picture of geotectonic movements, yet the boundary condition for analysis of deep structures of the Yenisei Ridge can be obtained from it.

The computer models of vertical cross-sections of the Earth's crust are evolved for analyzing the state of stress and strain using the Batolit-1982 and Shpat geological profiles obtained from deep seismic sounding method. Their orientation are shown in Fig. 2.

Two computer models of the Yenisei Ridge cross sections produced by using the corresponding geophysical data are shown in Fig. 3. The dimensions of the computer models for Batolit profile is 341×60 km and for Shpat profile is 288×60 km.
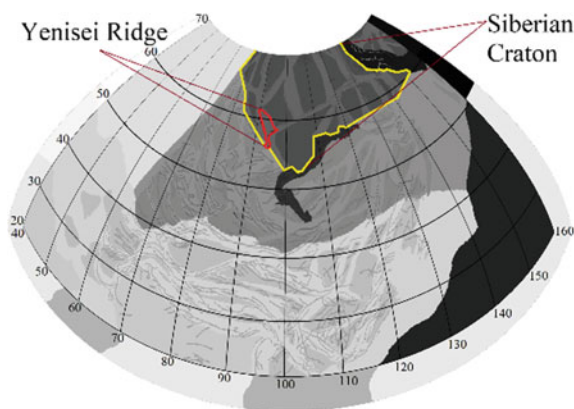
Fig. 1 Map of the numerical domain with the three groups of zone-block regions and boundary elastic blocks

Fig. 2 Orientation of Batolit-1982 (1) and Shpat (2) geological profiles crossing the Yenisei Ridge

The lens colored in red in Fig. 3 is revealed up to depth of 10–12 km in these cross-sections. Other crust layers are also revealed by the difference in geological, physical and mechanical properties of the media. The profiles include different types of faults. They were simulated in the form of weakened zones at the edges of these faults. The P- and S-wave velocities determined during deep seismic sounding were used to estimate the elastic properties of each layer of the structural models.

The elements of the Earth's crust and upper mantle are poorly studied because of lack of direct experimental constraints on physical and mechanical properties of geomaterials that comprise the layers of the Earth's crust. For this reason, we adopted the fundamental models describing depth variation of geomaterial strength presented elsewhere [12–15]. Since, as known, pressure increases almost linearly with depth, it is possible to accept strength models for pressure sensitive materials. The popular Drucker–Prager strength criterion on the base of linear pressure dependence is introduced as
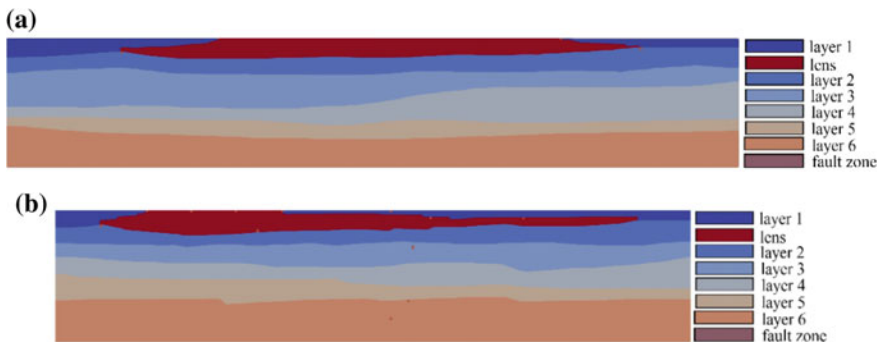
Fig. 3 Computer models of the Yenisei Ridge based on the Batolit-1982 (**a**) and Shpat (**b**) geological profiles
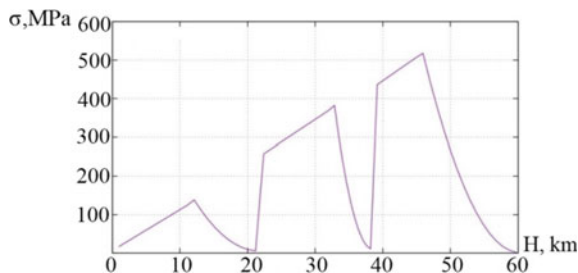
Fig. 4 Strength of the layers as a function of depth

$$\sigma = Y + \alpha \cdot P \tag{1}$$

where Y is the shear strength at zero pressure (cohesion), α is the friction coefficient, P is the pressure.

In fact, the depth dependence of strength is not monotonic, it has descending parts, and is often specified for continental plates in the form shown in Fig. 4 [12–16]. To meet such kind of relationship, the values of shear strength and friction coefficient are adopted as specific depth functions to get the strength-depth dependence with consideration for Eq. (1).

3 Mathematical Model

The fundamental equations of solid mechanics are included in the mathematical model that consists of the conservation laws and constitutive relations. The latter are formulated in rates. So, hypoelasticity equations characterize the elastic response of media. To describe the plastic response, the model of Drucker–Prager–Nikolaevskiy with non-associated flow rule is taken as a basis allowing for independent descriptions of dilatation and internal friction. In this case the equations read

$$f(\sigma_{ij}) = \frac{\alpha}{3}J_1 + J_2^{1/2} - Y = 0, \tag{2}$$

where $f(\sigma_{ij})$ is the yield surface and J_1, J_2 are the first and the second invariants of the stress tensor, Y is the current strength. In the case of non-associated flow rule, the plastic potential $g(\sigma_{ij})$ does not coincide with function of plasticity and according to Nikolaevskiy is written as follows [17]:

$$g(\sigma_{ij}) = J_2 + \frac{\Lambda}{3}J_1\left(2Y - \frac{\alpha}{3}J_1\right) + const. \tag{3}$$

Here Λ is the dilatancy coefficient.

Components of rates of inelastic strains will be defined as follows:

$$\dot{\varepsilon}_{ij}^{p} = \dot{\lambda}\frac{\partial g(\sigma_{ij})}{\partial \sigma_{ij}} = \dot{\lambda}\left(s_{ij} + \frac{2}{3}\Lambda\left(Y - \frac{\alpha}{3}J_1\right)\delta_{ij}\right), \tag{4}$$

where $\dot{\lambda}$ is the plasticity multiplier in the theory of plasticity.

Peculiarities of the boundary value problem statement in the case of tectonic flow modeling are presented in [9, 10]. The numerical implementation is performed using the Wilkins finite-difference method [18].

4   Results and Discussion

Specific features of deformation and loading of the adopted geological areas that govern the stress state type in them are defined from the computation of tectonic flows in Central and Southeastern Asia. We made these calculations only for collision related processes between the Eurasian, Indian and Arabian plates. The results are illustrated in Fig. 5. They indicate that compression predominates in the Yenisei Ridge.

Calculations of tectonic flows also show that the compression direction in the Yenisei Ridge is perpendicular to the Yenisei regional shear zone [4], and the Batolit-1982 and Shpat geological cross-sections lie in the compression direction. Consequently, we can calculate strains and stresses in the cross sections along the Batolit-1982 and Shpat profiles under loading by compression lengthwise of the profiles. The distributions of plastic strains and horizontal stress obtained in the simulation are given in Figs. 6 and 7.
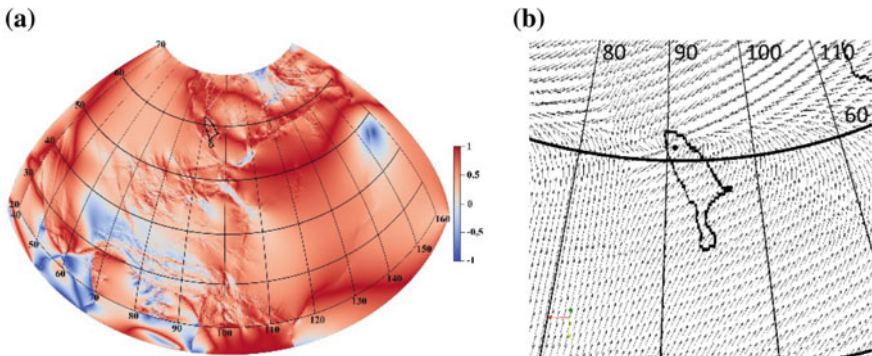
Fig. 5 Simulation results of tectonic flows in the Yenisei Ridge: **a** stress state type in Central and Southeastern Asia by the Lode parameter, **b** displacement fields determined in reference to the marked point
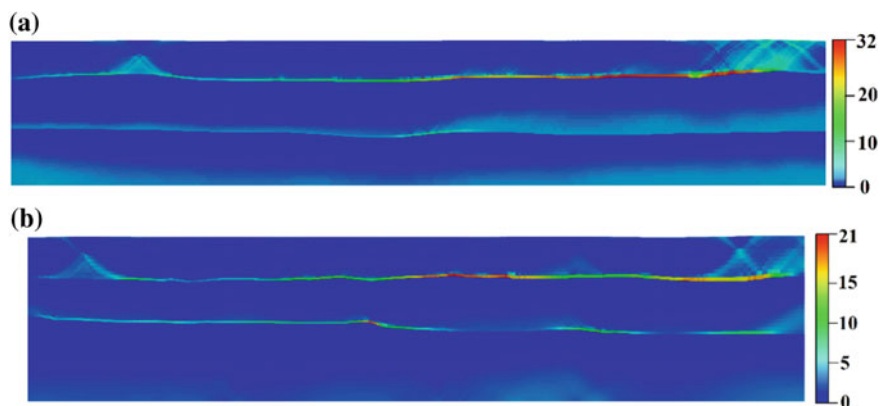
Fig. 6 Plastic strain (%) distributions in the Yenisei Ridge along the **a** Batolit-1982 and **b** Shpat profiles
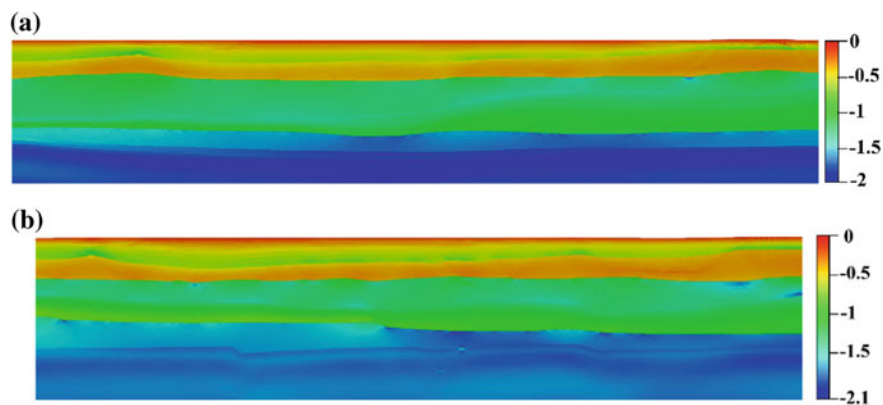
Fig. 7 Horizontal stress (GPa) distributions in the Yenisei Ridge along the **a** Batolit-1982 and **b** Shpat profiles

Analysis of the presented results yields the following. Fault zones are the places where plastic deformation and further evolution of localized strain originate from. The curvature of interfaces between the layers also affects localization of plastic strain. The internal friction and dilatancy that enter the Drucker–Prager–Niko-laevskiy plasticity law have an impact on the orientation of localized deformation bands. From the geological point of view, Fig. 6 evidences that in both cases deformation localizes in the Yenisei shear zone, which is located in the upper left part of the figures. In the right part of these figures, we can see another strain localization, which is consistent with the opposite side of the lens in the computer

models where the Velmo river is located. The stress field distribution is inhomogeneous and non-monotonously increase with depth due to the presence of physical and mechanical heterogeneities and curvature of interfaces between layers.

5 Conclusions

We solved the problem of computation of tectonic flows and the related stress state type in Central and Southeastern Asia caused by collision with the Indian and Arabian plates (in the South) and the North American Plate in the North-East. A special interest was to evaluate the stress state type in the Yenisei Ridge located to the South-West of the Siberian Craton. These calculations determined displacements of the Siberian Craton and allowed plotting the deformation pattern of Yenisei Ridge. The calculations also show that compression predominates in the Yenisei Ridge, the direction of compression being perpendicular to the Yenisei regional shear zone.

Calculations of depth distributions of stress and strain in the Yenisei Ridge along the Shpat and Batolit-1982 geological profiles show that the main factors determining nucleation sites of inelastic deformation and propagation of localized deformation bands are fault zones and curvature of interfaces between the layers. For both profiles, the plastic deformation distribution reveals deformation localization in the Yenisei shear zone and locations of the Velmo river. Variation in physical and mechanical properties and curvature of interfaces between layers result in heterogeneous and non-monotonous character of horizontal stress distribution.

References

1. Wegener, A.: The Origin of Continents and Oceans. Dover, New York (1966)
2. Replumaz, A., Capitanio, F.A., Guillot, S., Negredo, A.M., Villasenor, A.: The coupling of Indian subduction and Asian continental tectonics. Gondwana Res. **26**, 608–626 (2014). https://doi.org/10.1016/j.gr.2014.04.003
3. Lobkovsky, L.I.: Deformable plate tectonics and regional geodynamic model of the Arctic region and Northeastern Asia. Russ. Geol. Geophys. **57**, 371–386 (2016). https://doi.org/10.1016/j.rgg.2016.03.002
4. Likhanov, I.I., Regnier, J.-L., Santosh, M.: Blueschist facies fault tectonites from the western margin of the Siberian Craton: implications for subduction and exhumation associated with early stages of the Paleo-Asian Ocean. Lithos **304–307**, 468–488 (2018). https://doi.org/10.1016/j.lithos.2018.02.021

5. Cherepanova, Y., Artemieva, I.M., Thybo, H., Chemia, Z.: Crustal structure of the Siberian craton and the West Siberian basin: an appraisal of existing seismic data. Tectonophysics **609**, 154–183 (2013). https://doi.org/10.1016/j.tecto.2013.05.004
6. Domeier, M.: Early Paleozoic tectonics of Asia: towards a full-plate model. Geosci. Front. **9**, 789–862 (2018). https://doi.org/10.1016/j.gsf.2017.11.012
7. Vernikovsky, V.A., Metelkin, D.V., Vernikovskaya, A.E., Matushkin, N.Y., Kazansky, A.Y., Kadilnikov, P.I., Romanova, I.V., Wingate, M.T.D., Larionov, A.N., Rodionov, N.V.: Neoproterozoic tectonic structure of the Yenisei Ridge and formation of the western margin of the Siberian craton based on new geological, paleomagnetic, and geochronological data. Russ. Geol. Geophys. **52**, 24–39 (2016). https://doi.org/10.1016/j.rgg.2010.12.003
8. Müller, R.D., Qin, X., Sandwell, D.T., Dutkiewicz, A., Williams, S.E., Flament, N., Maus, S., Seton, M.: The GPlates portal: cloud-based interactive 3D visualization of global geophysical and geological data in a web browser. PLoS ONE **11**(3), 1–17 (2016). https://doi.org/10.1371/journal.pone.015088
9. Peryshkin, A.Y., Makarov, P.V., Eremin, M.O.: Numerical simulation of tectonic plates motion and seismic process in Central Asia. AIP Conf. Proc. **1623**, 487–490 (2014). https://doi.org/10.1063/1.4898988
10. Makarov, P.V., Peryshkin, A.Y.: Mathematical model and numerical simulation of slow deformation in the earth's crust structural elements. AIP Conf. Proc. **1783**, 020146 (2016). https://doi.org/10.1063/1.4966439
11. Seminskii, K.Z.: Hierarchy in the zone-block lithospheric structure of Central and Eastern Asia. Russ. Geol. Geophys. **49**, 771–779 (2008). https://doi.org/10.1016/j.rgg.2007.11.017
12. Goetze, C., Events, B.: Stress and temperature in bending lithosphere as constrained by experimental rock mechanics. Geophys. J. R. Astr. Soc. **59**, 463–478 (1979). https://doi.org/10.1111/j.1365-246X.1979.tb02567.x
13. Burov, E.B.: Rheology and strength of the lithosphere. Mar. Petrol Geol. **28**, 1402–1443 (2011). https://doi.org/10.1016/j.marpetgeo.2011.05.008
14. Stefanov, Y.P.: Some nonlinear rock behavior effects. Phys. Mesomech. **21**(4), 234–241 (2018). https://doi.org/10.1134/S1029959918030074
15. Smolin, I.Y., Makarov, P.V., Kulkov, A.S., Eremin, M.O., Bakeev, R.A.: Blow-up modes in fracture of rock samples and earth's crust elements. Phys. Mesomech. **21**(4), 297–304 (2018). https://doi.org/10.1134/S1029959918040033
16. Kozlovsky, Y.A.: The Superdeep Well of the Kola Peninsula. Springer, Berlin (1987)
17. Nikolaevskiy, V.N.: Geomechanics and Fluidodynamics with Applications to Reservoir Engineering. Kluwer, Dordrecht (1996)
18. Wilkins, M.L.: Computer Simulation of Dynamic Phenomena. Springer, Berlin (1999)

Formalized Forecast of the Gutenberg-Richter Law Parameters by Geodynamic and Seismotectonic Data

Eugeny Bugaev and Svetlana Kishkina

Abstract

Earthquake recurrence intervals have been compared with their estimated forecasting limits. The estimation was made taking into account the main fractal dimensions of the site, deformation conditions and destruction nature. The selected model demonstrated that the nonlinear recurrence intervals are determined by geological and geomechanical factors. It is proved that the estimation of forecasting recurrence interval limits can be possible on the basis of geodynamic data and limit seismotectonic relations that reflect the dependence of the maximum magnitude on the earthquake focus dimensions and destruction nature. The estimations are based on the example of the Calaveras fault area (California, USA), where it is possible to distinguish between the segments characterized by different creep rates. The analysis of the obtained results shows that the earthquake recurrence graph parameters of the investigated area significantly depend on its typical geological and geotechnical factors as area maximum structure size, similarity coefficient, conditions and deformation rate, destruction nature.

Keywords

Seismotectonic · Recurrence graph · Deformation · Fractal dimension

E. Bugaev
Scientific and Engineering Center for Nuclear and Radiation Safety,
Malaya Krasnoselskaya Street, 2/8, bld. 5, 107140 Moscow, Russia
e-mail: bugaev@secnrs.ru

S. Kishkina (✉)
Sadovsky Institute of Geospheres Dynamics RAS,
Leninsky prosp. 38, k.1, 119296 Moscow, Russia
e-mail: kishkinas@idg.chph.ras.ru

1 Introduce

According Based on regional and local assessments of earthquake recurrence intervals, variations b from 0.3 to 2.5 [5] were established, as well as the level change of several magnitude recurrences during the transition from the quiescence to seismic activation period. The nature of the earthquake nonlinear recurrence intervals (hereinafter recurrence graphs) has not been clearly defined to date. The left and right bends of the recurrence graph can be explained by incomplete catalogs or computation methods [9]. The physical sources of these variations have been attributed to changes in strain condition [11, 17], loading rate [2, 18], and structural and compositional properties [17]. Low b-values are thought to be associated with high strain [12], low loading rate [13], low heterogeneity [10] and small fractal dimensions of the fault seismogenic surface [1, 8]. However, there are no specific accounting methods to analyze the effects of these multiple factors on the seismic regime parameters as slope and activity. Therefore, it is important to determine geological factors and their qualitative characteristics, which control the changes of earthquake recurrence graph.

The article proposes a method to assess the forecasting recurrence intervals based on the model that reflects discrete characteristics of the Earth crust and earthquake foci, as well as the natural dependence of the maximum magnitude on the focus size and the nature of its destruction. The model is characterized by the size of its maximum element corresponding to the length of the potential focus zone (hereinafter PFZ) related to the investigated area, and the similarity coefficient k_s equal to the square root of ten. This model allows taking into account the maximum period T_{max} related to accumulation of ultimate deformations in the maximum PFZ when the ultimate deformations reach the effective elastic limit $\varepsilon_{eff} = 3.2 \cdot 10^{-5}$ for the Earth as a whole and the maximum PFZ is fractured. The flow rate of formation for various activated structures n is determined by the ratio of T_{max} to the number of rank structures n and up to the maximum element (n = 1) inclusive. Fractal curves are used to estimate the forecasting limits of the earthquake recurrence (hereinafter forecasting limits) taking into account the natural dependence of the maximum magnitude on the deformation conditions and the nature of the destruction [3].

The adopted method has been applied to geodynamic and seismic conditions of the Calaveras (California, USA) fault segment including the focus zone of the 1984 M 6.2 Morgan Hill earthquake (Fig. 1).

2 Seismic and Geodynamic Conditions and Model Parameters

Seismic conditions of the investigated area are listed in the Earthquake Catalog [15, 16], which is valid for M 3.5 and higher magnitude events for the observation period of 17 years, as well as for M 0.6 events for the observation period of about three years. The peculiarity of this catalog is that it includes data on the parameters
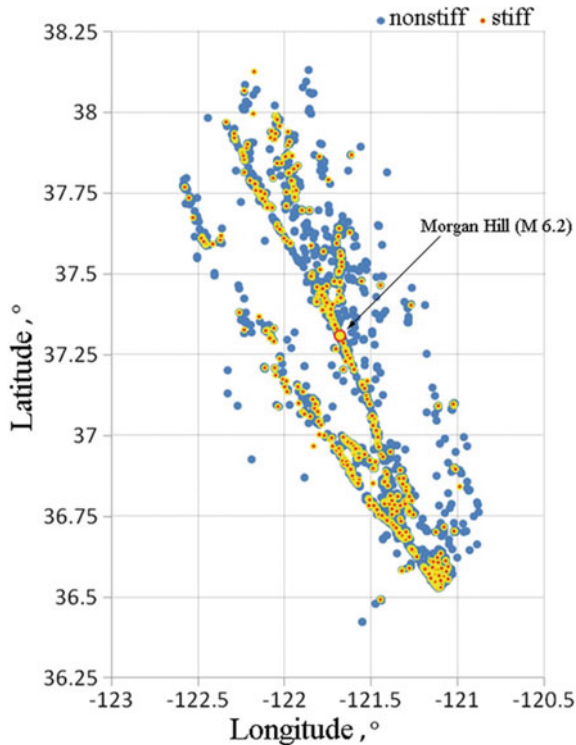
Fig. 1 Distribution of nonstiff (blue circles) and stiff (red circles) earthquake foci in the focal zone of the M 6.2 Morgan Hill earthquake (1984)

of the uncertainty ellipse related to the earthquake focus position. Taking into account high accuracy of determining foci to evaluate their deformation, the focus dimension was assumed as the maximum horizontal uncertainty ellipse axis [4]. The focus elastic limit ε is determined with account of the magnitude and focus size. The earthquake foci are divided into nonstiff $\varepsilon \leq \varepsilon_{eff}$ and stiff $\varepsilon_{eff} < \varepsilon \leq \varepsilon_{br\text{-}pl}$ taking into consideration the relation between ε and ε_{eff}, where ε is elastic limit, ε_{eff}—effective elastic limit equal to $\sim 3.2 \cdot 10^{-5}$. The brittle-plastic limit $\varepsilon_{br\text{-}pl}$ depends on the focus size and its impact (PFZ) and is determined as follows:

$$\log(\varepsilon_{br-pl}) = -0.5\log(L_0) + 0.5\log(L_{zone}) + \log \varepsilon_{eff} \tag{1}$$

where L_o—focus size, km; L_{zone}—focus effect zone length, km. The value of $\varepsilon_{br\text{-}pl}$ is a top physical elastic limit accumulated on the asperity. The relation (1) is obtained on the basis of empirical data on the dependence of the maximum deformation in the focus zone as well as on its size and on the ratio of the PFZ length to the maximum size of the PFZ's earthquake focus [6].

Nonstiff earthquakes are characterized by low seismic efficiency, whereas stiff earthquakes—by high seismic efficiency [6].

Calaveras fault is located in the zone of interaction between the Pacific plate and the North American platform constituting a right-hand shift. A specific feature of geodynamic conditions related to the Calaveras fault is its heterogeneity.

In terms of the investigated area, it is established that its North–Western segment is characterized by a low creep rate (less than 5 mm/year up to the locked sections), whereas for the South–Eastern segment, the creep rate reaches 25 mm/year and more [14]. Taking into account the area structure and geodynamic conditions, the main model characteristics have been adopted to allow a formalized assessment of the effective dimensions and the total number of constituent elements of the model rank n: size of the maximum model element equal to the maximum potential focus zone size L1 $\sim$ 320 (km); similarity coefficient k_s equal to the square root of ten; minimum ($Gmin \sim 1.8 \cdot 10^{-9}$ per year) and maximum ($Gmax \sim 4.1 \cdot 10^{-7}$ per year) deformation rate in the potential focus zone; $Gmin$ characterizes the conditions of comprehensive deformation for the investigated area in general, and $Gmax$ defines the conditions of uniaxial deformation for the fault central part.

The model type is determined by the deformation conditions, i.e. uniaxial deformation is relevant to the linear model with the fractal coefficient D equal to 1. Comprehensive deformation is relevant to the flat model where $D = 2$. According to the theoretical relationship between the fractal coefficient D and the slope b ($D/b = 2$), the effective value of the slope b is equal to 0.5 for uniaxial deformation, and 1—for comprehensive deformation, respectively. At the same time, for the strongest earthquakes, where the size of the foci tends to 1000 km, the slope b tends to 2 or more, which does not contradict to the data provided by Z. El-Isa and D.W. Eaton [5]. However, this above study [5] does not take into consideration the impact of deformation conditions and the nature of fracture related to b-value.

3   Diffusion of Earthquake Foci and Magnitude Recurrence Intervals

The analysis of earthquake foci diffusion in the impact zone of the Calaveras fault and the investigated area at different creep rates (Fig. 1) allowed to conclude that most stiff and nonstiff focis are into the principle zone of the Calaveras fault wich width is 0.6 km and less [7]; part of the nonstiff foci and single stiff events are manifested in the zone of the Calaveras fault dynamic impact with the width of about 20 km.

The Calaveras fault dynamic impact zone was also marked as the asymmetrical distribution of nonstiff foci: a smaller number of events are observed to the South–West of the locked section of the main rupture and to the North–East of the section with a high creep rate; while the North–East and South–West parts of the dynamic impact zone showed a larger number of events.

The conditions of uniaxial compression at the fault with a right-hand shift in its North–Western and South–Eastern regions of dynamic impact should indicate prevailing compression strains, while tensile strains should be present in the
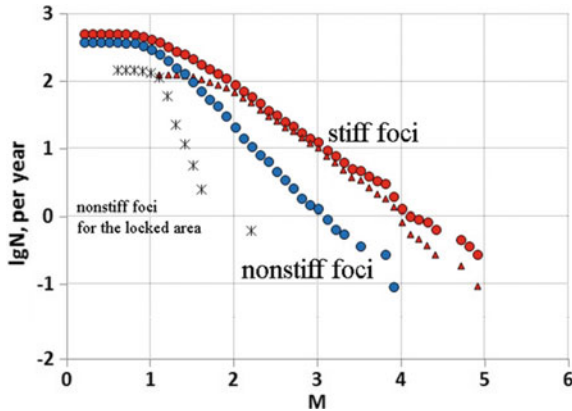
Fig. 2 Earthquake magnitude of both nonstiff and stiff earthquake recurrence graphs for Morgan Hill earthquake focal area. For comparison, graphs for regional (circles) and detailed (triangles) data and nonstiff foci for the locked area (asterisks) are shown

North–Eastern and South–Western. Compressive strains prevent the rearrangement of the structural plan while tensile strains contribute to it.

To analyze the creep effect on seismic regime parameters, recurrence intervals for the Morgan Hill earthquake focal area were estimated (Fig. 2). In Fig. 2, recurrence intervals of nonstiff foci are highlighted as blue and recurrence of stiff foci are highlighted as red. For comparison, graphs for regional and detailed data are shown.

The joint analysis of both nonstiff and stiff earthquake recurrence intervals allows to conclude the following: nonstiff foci events show a steeper slope compared to the stiff foci of the recurrence graph; slope b is more than in case with the creep events for the earthquakes in the locked part of the fault; nonstiff foci earthquakes associated with the creep section manifest clearly expressed nonlinearity of the recurrence graph; nonstiff foci earthquakes associated with the Morgan Hill earthquake zone also manifest nonlinearity and graph trend to bend downwards to the right; stiff foci earthquakes evidence less pronounced trend to nonlinearity for different observation conditions.

4   Comparison of Forecasting Limits with Recurrence Intervals

To identify the geological factors affecting the parameters of the recurrence, we compared them with the predicted limits (Fig. 3) estimated on the basis of the adopted model and geodynamic conditions of the investigated area. Zone "I" is the forecasting limits: line ($\varepsilon \leq 10^{-6}$) and line ($\varepsilon \leq \varepsilon_{eff}$) estimated for comprehensive
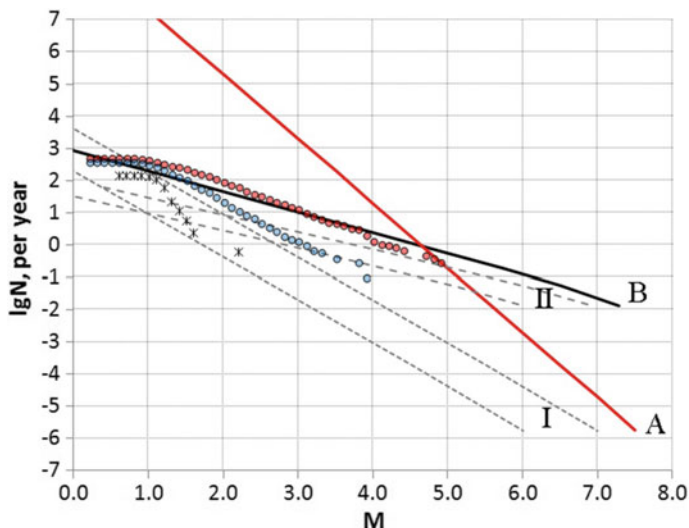
Fig. 3 A Comparison of the observed recurrent magnitude for nonstiff and stiff foci with the predicted limits estimated for different geodynamic conditions of deformation and destruction nature: zone "I"—forecasting limits of magnitude recurrent graphs for conditions of comprehensive deformation (up $\varepsilon \leq 10^{-6}$ to $\varepsilon \leq 3.2 \cdot 10^{-5}$); line "A"—most likely magnitudes of stiff foci ($\varepsilon > 3.2 \cdot 10^{-5}$); line "B"—forecasting limit for stiff foci under conditions of brittle-plastic destruction in case of uniaxial deformation ($\varepsilon > 3.2 \cdot 10^{-5}$); zone "II"—forecasting limits for weak foci in case of uniaxial deformation under conditions of brittle-plastic destruction ($\varepsilon \leq 10^{-6}$ and $\varepsilon > 3.2 \cdot 10^{-5}$ respectively)

deformation. Zone controls the recurrence graphs of nonstiff sources for the locked and for the creeping sections.

The recurrence diagrams of the Morgan Hill earthquake focal zone (blue circles in Fig. 3) slightly exceed one of the forecast limits (line 4 in Fig. 3), which may be due to a higher deformation rate or lower elastic limit in the focal zone than estimated. A higher deformation rate or a decrease in the elastic limit can be caused by the consolidation of the medium and an increase in its stiffness as a result of prolonged deformation and the preparation of a strong earthquake.

The recurrence graph position for stiff foci under different observation conditions is controlled by the top forecast limit of line "B" estimated for the conditions of uniaxial deformation and brittle-plastic fracture, and by bottom predicted limits for nonstiff sources (zone "II" from $\varepsilon \leq 10^{-6}$ to $\varepsilon \leq \varepsilon_{eff}$), estimated for the conditions of uniaxial deformation. It is likely that the recurrence graph bend on the right is physically stipulated by the impact of the brittle-plastic limit (1), the value of which decreases with the increase in the focus size.

5 Discussion

The analysis of the observed recurrence graphs for different geodynamic conditions and their comparison with the predicted limits of the recurrence graphs estimated for different deformation conditions and fracture nature allowed to establish main factors affecting the recurrence graph parameters.

Slope b is determined by deformation conditions and fracture nature: b = 1.33—at comprehensive deformation and brittle-plastic fracture; b = 0.64—at uniaxial deformation and brittle-plastic fracture; b = 1.07—at comprehensive deformation and brittle fracture; b = 0.55—at uniaxial deformation and brittle fracture.

Recurrence graph level (or seismic activity) is determined by the scale of the focus zone, elastic limit (or seismic impedance), and deformation rate. An increase in the process scale, a decrease in the elastic limit and medium consolidation, as well as an increase in the deformation rate during the activation of the seismic and geodynamic process can lead to a significant (by several orders of magnitude) increase in seismic activity. This was repeatedly observed in the last stage of catastrophic earthquake preparation; for example, the 1976 Tangshan earthquake in the North–Eastern area of the Chinese platform and the 2011 Tohoku earthquake in Japan.

Individual recurrence fragments are determined by the predicted limits estimated for different deformation conditions and fracture nature, so it is important to estimate the focus size and the amplitude of the adjustment movement in the focus.

Seismic process parameters are determined by a large number of geological, structural, geodynamic and geotechnical factors; lack of seismic statistical data complicates or makes it impossible to assess the seismic hazard on the basis of the probabilistic approach without taking into consideration a number of assumptions related to the Getenberg-Richter law linearity, constant value b = 1 (or close to it), and Mmax artificial limitation.

For low-activity and platform areas, it is recommended to perform seismic hazard assessment on the basis of geodynamic and seismotectonic data for different deformation conditions and fracture nature. The assessment validity of the forecasting limits is recommended to monitor by recurrent graph fragments estimated for different magnitude ranges with account of the limited but reliable historical and instrumental earthquake data, including paleoquakes and micro-earthquakes.

6 Conclusion

The analysis of the obtained results shows that the earthquake recurrence graph parameters of the investigated area significantly depend on its typical geological and geotechnical factors (area maximum structure size, similarity coefficient, conditions and deformation rate, destruction nature). The adopted method allows the following: assess seismic hazard on the basis of structural parameters of the investigated area, process scale, deformation conditions and destruction nature even

if representative earthquake statistical data are not available; assess the location, strength and frequency of the maximum earthquake in the investigated area, which is especially important for platform and low-activity areas with rare strong earthquakes; predict possible changes of seismic hazard in case of potential variations in geodynamic, seismic or geotechnical conditions during the construction or operation of particularly hazardous facilities.

References

1. Aki, K.: A probabilistic synthesis of precursory phenomena. In: Simpson, D., Richards, P. (eds) Earthquake Prediction. An International Review Manrice Ewing Ser, pp. 566–574 (1981)
2. Amelung, F., King, G.: Earthquake scaling laws for creeping and non-creeping faults. Geophys. Res. Lett. **24**, 507–510 (1997). https://doi.org/10.1029/97GL00287
3. Bugaev, E., Kishkina, S.: Assessment long-term and current seismic hazard of NPP site on basis of materials of engineering researches. Nucl. Radiat. Saf. **3**(80), 10–22 (2018). (in Russian)
4. Bugaev, E.G.: On structured and diffuse seismicity, stiffness of earthquake foci, and nonlinearity of magnitude recurrence. Geodyn. Tectonophys. **2**(3) (2011). (in Russian)
5. El-Isa, Z., Eaton, D.W.: Spatio temporal variations in the b-value of earthquake magnitude-frequency distributions: classification and causes. Tectonophysics **615**, 1–11 (2014)
6. Kocharyan, G.G.: Scale effect in seismotectonics. Geodyn. Tectonophys. **5**(2), 353–385 (2014). https://doi.org/10.5800/GT2014520133
7. Kocharyan, G., Kishkina, S., Ostapchuk, A.: Seismic picture of a fault zone. What can be gained from the analysis of fine patterns of spatial distribution of weak earthquake centers? Geodyn. Tectonophys. **1**(4), 419–440 (2010)
8. Legrand, D.: Fractal dimensions of small, intermediate, and large earthquakes. Bull. Seismol. Soc. Am. **92**, 3318–3320 (2002)
9. Mignan, A., Woessner, J.: Estimating the magnitude of completeness for earthquake catalogs. Commun. Online Resour. Stat. Seismic. Anal. 45 (2012) https://doi.org/10.5078/corssa-00180805
10. Mogi, K.: Magnitude-frequency relationship for elastic shocks accompanying fractures of various materials and some related problems in earthquakes. Bull. Earthquake Res. **40**, 831–883 (1962)
11. Scholz, C.H.: The Mechanics of Earthquakes and Faulting. Cambridge University Press, Cambridge (2002)
12. Schorlemmer, D., Wiemer, S., Wyss, M.: Variations in earthquake-size distribution across different strain regimes. Nature **437**(7058), 539–542 (2005)
13. Tormann, T., Wiemer, S., Mignan, A.: Systematic survey of high-resolution b value imaging along Californian faults: inference on asperities. J. Geophys. Res. Solid Earth. **119**, 2029–2054 (2014). https://doi.org/10.1002/2013JB010867
14. Vorobieva, I., Shebalin, P., Narteau, C.: Break of slope in earthquake size distribution and creep rate along the San Andreas Fault system. Geophys. Res. Lett. **43**, 6869–6875 (2016). https://doi.org/10.1002/2016GL069636

15. Waldhauser, F.: Near-real-time double-difference event location using long-term seismic archives, with application to Northern California. Bull. Seismol. Soc. Am. **99**, 2736–2848 (2009). https://doi.org/10.1785/0120080294
16. Waldhauser, F., Schaff, D.: Large-scale relocation of two decades of Northern California seismicity using cross-correlation and double-difference methods. J. Geophys. Res. **113**, B08311 (2008). https://doi.org/10.1029/2007JB005479
17. Wyss, M., Sammis, C., Nadeau, R., Wiemer, S.: Fractal dimension and b-value on creeping and locked patches of the San Andreas Fault near Parkfield, California. Bull. Seismol. Soc. Am. **94**, 410–421 (2004)
18. Wiemer, S., Wyss, M.: Mapping the frequency-magnitude distribution in asperities: an improved technique to calculate recurrence times? J. Geophys. Res. **102**(15), 115–128 (1997). https://doi.org/10.1029/97JB00726

Statistical Regularities of a Main Crack Formation in Rocks. Acoustic Emission and X-Ray Computed Microtomography

Ekaterina Damaskinskaya ⓘ, Vladimir Hilarov ⓘ, Ivan Panteleev ⓘ, Dmitry Korost ⓘ and Dmitry Frolov ⓘ

Abstract

Peculiarities of a main crack formation in Westerly granite and metasandstone under quasistatic uniaxial compression without any lateral upthrust have been studied using the acoustic emission (AE) data and X-ray computed microto-mography (CT). Multifractal analysis of intervals between AE signals and the energy distribution analysis of these signals have been performed. Two most important parameters—Hürst coefficient and singularity spectrum width were plotted versus time. Following peculiarities were found: while approaching the destruction time the Hürst coefficient becomes larger and the spectrum width narrower. It has been concluded from these facts that fractal self-organized state is formed before the destruction, i.e. process nature changes from more complicated multifractal to more simple monofractal one. Despite the spatially localized character of defect accumulation revealed by X-ray microtomography, the analysis of the energy distributions of acoustic emission signals allowed us in this work to separate principally different stages of the main crack growth. The first stage is characterized by an exponential energy distribution of AE signals and the second one by a power-low distribution.

E. Damaskinskaya (✉) · V. Hilarov · D. Frolov
Ioffe Institute, 26 Politekhnicheskaya, 194021 St Petersburg, Russian Federation
e-mail: Kat.Dama@mail.ioffe.ru

I. Panteleev
Institute of Continuous Media Mechanics of the Ural Branch of Russian Academy of Science, Academician Korolev Street, 614013 Perm, Russian Federation

D. Korost
Lomonosov Moscow State University, GSP-1, Leninskie Gory, 119991 Moscow, Russian Federation

23

1 Introduction

Numerous experiments on deformation of brittle heterogeneous materials (such as
rock, composite materials and ceramics) [1–4] showed that defect accumulation
under uniaxial quasi-static compression with a confining pressure occurs in several
stages. In the beginning of the loading process defects are formed randomly
throughout the entire volume of the deformed material. After that defects start to
localize in a certain spatial region where a main crack will form later. The first stage
of disperse defect accumulation is almost absent in the case when the lateral surface
of material is stress free [5]. Nevertheless, defect accumulation and formation of a
main crack remains to be a nonstationary process with nonlinear regularities.

The goal of our studies is to seek statistic peculiarities of a main crack formation
during the deformation of Westerly granite and metasandstone samples without
lateral upthrust. The specific feature of these studies is the application of two
non-destructive control methods, i.e.: acoustic emission and X-ray computed
microtomography.

2 Experimental

The X-ray tomography study of rock samples defect structure before and after
mechanical tests was carried out by using a ScyScan 1172 tomograph (Bruker,
Belgium) equipped with a Hamamatsu 100/250 microfocus X-ray tube and 11
Megapixels detector panel. Scanning parameters were: voltage 70 kV, current
129 μA, distance from the source to the camera (detector) = 213.580 mm, distance
from the source to the object = 75.030 mm. The rotation step was 0.200°, the
exposure time was 3770 ms, and the scan duration was about 24 h.

Shapes and dimensions of the samples optimal for both mechanical tests and
tomography were found. They were cylinders with a diameter of 10 mm and a
height of 20 mm. The spatial resolution of tomographic images with this sample
geometry was ∼3 μm. This resolution was the best possible for the samples of this
size [6], taking into account physical principles and engineering features of the
X-ray tube and tomograph chamber.

A tomographic survey of all samples was carried out before the mechanical tests.
We selected the samples without structural anomalies which could behave as stress
concentrators and sources of damage accumulation.

The quasi-static testing of samples was carried out under uniaxial compression by using a AGX-Plus (Shimadzu, Japan) electromechanical machine with a maximum force of 30 tons. To implement a real-time monitoring of acoustic emission during deformation, an Amsy-5 (Vallen, Germany) apparatus was used. Two AE105A wideband piezotransducers with a bandwidth of 450–1150 kHz were attached to the sample ends. Each acoustic emission signal was characterized by the emission time, coordinate, and energy. The source Su-Nielsen was used to verify accuracy of the location (approximately 2 mm).

To study statistical regularities of main crack formation, each of the samples was subjected to a uniaxial quasi-static compression at a constant rate of plunger displacement of 10 μm/min. Sandstone specimens were loaded in stepwise. Figure 1 shows the time dependence of stress during the deformation. The deformation process has been stopped when the acoustic emission activity increased as an avalanche (more than 100 AE pulses/second); the sample was unloaded, and its tomographic survey has been carried out. The above criterion of stopping the deformation process combined with the low deformation rate allowed us, on one hand, to form the main crack and, on the other hand, to conserve sample integrity.

Peculiarity of these experiments was that, the load has been removed a short time before the sample macroscopic fracture (Fig. 1a, b) occured; thereafter, acoustic emission continued to be recorded. This loading algorithm allowed us to study the process of stress relaxations in a material with a developed defect subsystem (with a main crack formed actually completely). We have tested two sample series. The first series was the Westerly granite one (denoted "W" sample, 7 samples) and the second series contained metasandstone samples (denoted "S" samples, 5 samples). Mineral composition of materials is given in the Tables 1, 2.
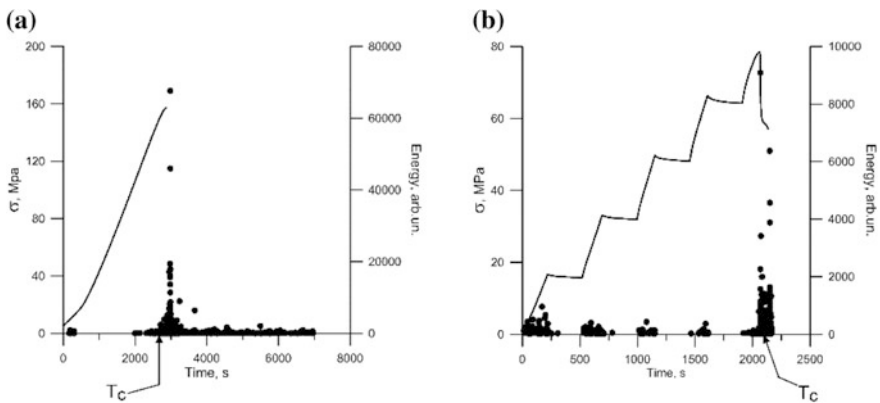
Fig. 1 Time dependences of the stress (the solid line) and the energy of individual AE signals (dots): **a** sample W and **b** sample S

Table 1 Mineral composition of the Westerly granite [7, 8]

Mineral	Quartz	Plagioglase	K-feldspar	Biotite	Muscovite
	28%	33%	33%	3.5%	1.9%

Table 2 Mineral composition of the metasandstone

Mineral	Quartz	Biotite	Muscovite	Garnet	Ore mineral
	40–50%	20–25%	20%	15%	15%

3 Results and Discussion

We used two different methods of analyzing AE data in order to study the stages of main crack formation process: the multifractal analysis of pauses between the acoustic emission successive signals and the analysis of the functional form of the acoustic emission signals energy distribution.

3.1 Multifractal Analysis of Pauses Between AE Signals Successive in Time

It has been noted [9] that time intervals between acoustic emission pulses are related to the intensity of the damage accumulation process in a material and, finally, to the dissipation rate of mechanical energy supplied to a sample. Statistical regularities in the behavior of time intervals between successive AE pulses contain much information [9–11] about the process, and allow one to characterize stages of the damage accumulation in a deformed material together with the laws of amplitudes (energies) variations [11, 12].

Because the pause flow is known to be nonstationary, traditional statistical methods (spectral analysis, correlation function method, etc.) are inapplicable here. Indeed, in the case of the nonstationary processes the two-time correlation function does not depend on the time difference (lag), but on each of the times separately, and the power spectrum cannot be calculated using the convolution theorem. However, multifractal techniques based on the wavelet transform do not have this disadvantage.

It was repeatedly shown before that various fractal characteristics undergo changes during the fracture process. The changes in the singularity spectra were observed [13] when studying the transformation of the lateral surface profile of amorphous alloys under an action of mechanical load. It was found for granite samples [14, 15] that the correlation fractal dimension (d-value) of a set of points corresponding to the forming and growing cracks decreases when approaching the fracture moment. In this work, we calculate the time dependences of the singularity spectra $D(h)$ parameters.

Singularity spectra were calculated using the method of wavelet leaders [16, 17]. Wavelet leader $L(j, k)$ is the largest coefficient of discrete wavelet transformation d(j′, k′) calculated in the narrow time interval (k−1) × 2j ≤ k′ × 2j′ ≤ (k + 1) × 2j on all scales smaller than given scale 2j′ ≤ 2j. Wavelet leaders describe the local Hölder coefficients that can be calculated using the method standard for the multifractal analysis: first build the generalized distribution function $Z(j, q) \propto \sum_k L(j, k)^q \propto 2^{j \cdot \tau(q)}$, next obtain scaling exponents τ(q), and finally use them to calculate singularity spectra D(h) using the Legendre transformation. Thus, the wavelet-leader method can be considered as a further development of the wavelet transform maximum module method [18].

For multifractal analysis of the time intervals between successive AE signals, we chose the time series of acoustic events: one Westerly granite sample (sample W) and one metasandstone sample (sample S). These time series contained 7815 and 2850 events, respectively. Time intervals between nearest events were calculated from the initial data. They were divided into partially overlapping sequences of 1024 elements each and the multifractal analysis was performed for them by means of the wavelet-leader method. The sequences were shifted with respect to previous ones by 16 events in order to obtain smoother time dependences. The singularity spectra D(h) were calculated for each of the sequences. Two main parameters, namely, H = h(Dmax) (corresponds to the global Hürst coefficient) and the spectrum width are plotted in Fig. 2 as a function of time.

Figure 2a shows time dependences of the parameters of spectral singularities for sample W. At the initial stage we see the tendency of an increase in *H* and decrease in *w*, but, then, this tendency disappears up to the burst at the moment $t \approx 2992$ s. It is good to bear in mind that the mechanical loading was removed at the moment $t = 2861$ s (it is indicated by the dash–dot line in Fig. 2a) and, then, the acoustic emission process proceeds due to the internal stress relaxation. The rapid increase of *H* at $t = 2992$ s can be explained by the fact that the crack observed by the tomography grows almost at this time. Then, the process continues in the persistent phase $H > 0.5$ for some time; thereafter, it takes the Brownian character and, lastly decreases; thus in this case, the main crack expansion is accompanied by a change in the process character from more complex multifractal to a simpler monofractal, i.e. a fractal self-organization.

Figure 2b displays the dependence on time of the Hürst coefficient and the width of the singularity spectrum of time intervals between successive acoustic events for the sample S. One can note that monofractalization and changing into persistent phase occur almost unevenly, however monofractalization starts earlier. This might be due to the fact that the main crack grows in homogeneous fraction of sandstone. It has been shown [19] that in homogeneous media preferably one crack grows while in heterogeneous media multiple fracture takes place. And indeed CT scan confirms this hypothesis.

Fig. 2 Time dependences of
the global Hürst coefficient
and the singularity spectrum
width for **a** sample W and
b sample S. The horizontal
dashed straight line
corresponds to $H = 0.5$; the
vertical dash-dot straight line
corresponds to the moment of
mechanical load removal
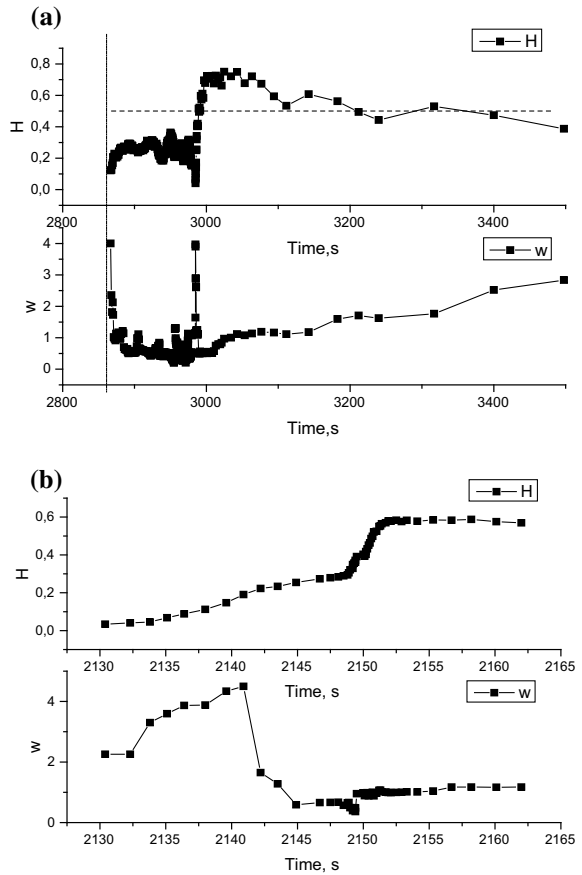
3.2 Energy Distribution of AE Signals

In [20–22], we found that energy distribution functional form of the AE signals can
be used as an indicator of the current state of a deformed material. Exponential
energy distribution of the AE signals indicates a noncritical (stable) state of
deformed material. Power-law distribution indicates that defect accumulation pro-
cess had passed to the critical ("dangerous") stage.

We carried out a detailed analysis of the AE signals energy distribution forms.
Using the successive approximations method, we succeeded in the determination of
T_c moment (Fig. 1), after which the energy distribution becomes a power-law one
for all our experiments.

Figure 3 shows the energy distribution of the AE signal recorded before T_c. The
distribution was plotted in the double logarithmic (Fig. 3a) and semilogarithmic
(Fig. 3b) coordinates. It is seen that in both cases the data is approximated by a
straight line with nearly equal determination coefficients R^2. This implies that this

(a)

$Ln\left(\frac{\Delta N}{\Delta E}\right)$ 6

$R^2 = 0.939$

Ln(E)

(b)

$Ln\left(\frac{\Delta N}{\Delta E}\right)$ 6

$R^2 = 0.936$

E, arb.un.
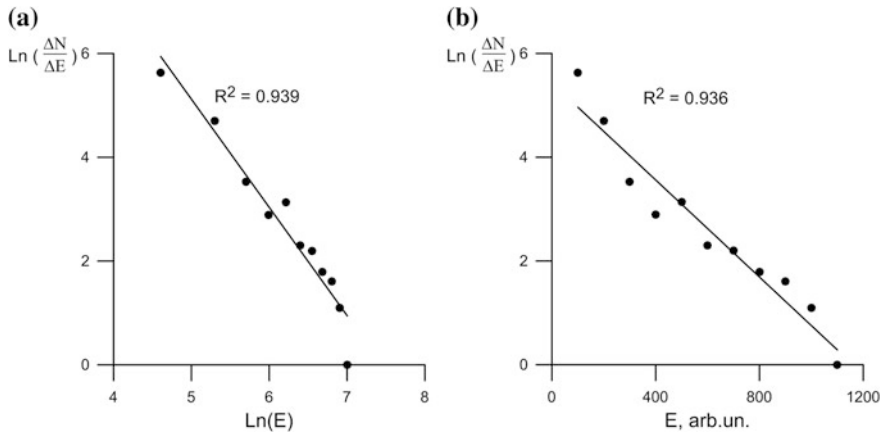
Fig. 3 Energy distribution of the AE signals recorded before the T_c moment

distribution can be approximated both with an exponential and power law functions. We obtained the similar result while analyzing other experiments on granite samples deformation [22]. According to the hypothesis proposed in [21], such a picture indicates that this region of the sample is not at a dangerous stage of defect accumulation.

Figure 4 shows the energy distribution of AE signals recorded after T_c moment. It is seen that the distribution is approximated with a power law function. This distribution function form indicates that the defect system in the sample has passed into the self-organized critical state [23]. This can lead to a catastrophic fracture, i.e., the loss of the sample integrity.

(a)

$Ln\left(\frac{\Delta N}{\Delta E}\right)$ 6

$R^2 = 0.92$

Ln(E)

(b)

$Ln\left(\frac{\Delta N}{\Delta E}\right)$ 6

$R^2 = 0.71$

E, arb.un.
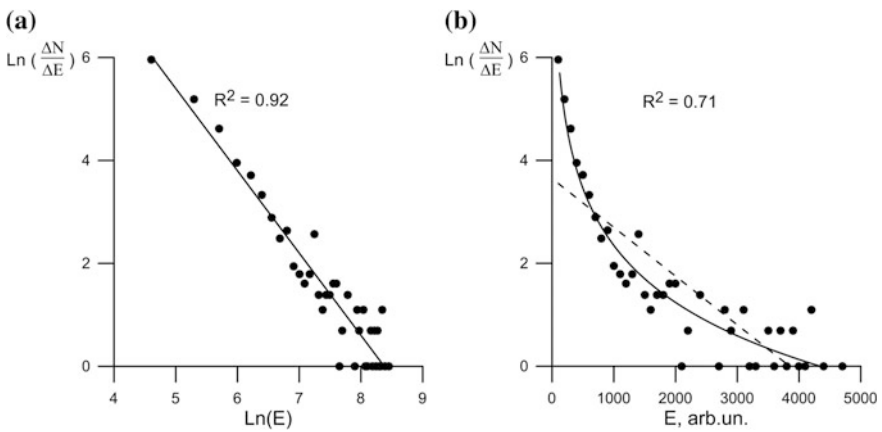
Fig. 4 Energy distribution of the AE signals recorded after the T_c moment
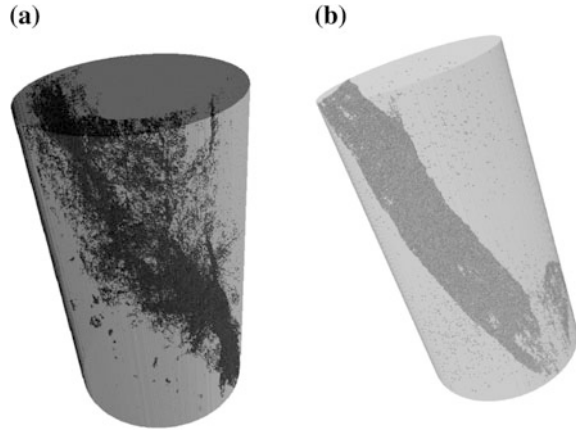
However, as already mentioned above, samples conserved their integrity, which allowed us to carry out tomographic dissection. Based on the analysis of the tomographic slices performed using the CTan and CTvol special software, we constructed the three dimensional visualization of the defect structure (Fig. 5).

The three-dimensional region of microcracks localization (main crack) in samples W and S has a complex shape (Fig. 5), and it is inclined with respect to the deformation axis at some angle, which is typical for uniaxial compression with stress free lateral surface of material.

Analysis of acoustic emission signals energy allowed us to separate principally different stages of main crack propagation. This fact demonstrates the universality of the approach used and the regularities revealed.

4   Conclusions

We have discovered the peculiarities of defect accumulation while deforming the samples with the quasi-static compression without lateral upthrust. Two stages of the main crack formation were observed: the first stage is characterized by the AE signals energy distribution that can be approximated both with an exponential and a power laws; the second stage is characterized by a power law energy distribution of the AE signals. This result enables us to assume that the main crack formation is a multistage process with the change from stable evolution stage to unstable crack propagation. This conclusion was confirmed by the results of the multifractal analysis of intervals between the successive AE signals. According to this analysis both series demonstrated the tendency in changing multifractal dynamics of acoustic emission time intervals to monofractal one when approaching the destruction moment.

References

1. Lockner, D.A., Byerlee, J.D., Kuksenko, V., Ponomarev, A., Sidorin, A.: Observations of quasistatic fault growth from acoustic emissions. In: Evans, B., Wong, T.-F. (eds.) Fault Mechanics and Transport Properties of Rocks, pp. 3–31. Academic, London (1992). https://doi.org/10.1016/S0074-6142(08)62813-2
2. Ben-Zion, Y., Lyakhovsky, V.: Accelerating seismic release and related aspects of seismicity patterns on earthquake faults. Pure. appl. Geophys. **159**, 2385–2412 (2002). https://doi.org/10.1007/s00024-002-8740-9
3. Hamie, Y., Katz, O., Lyakhovsky, V., Reches, Z., Fialko, Yu.: Stable and unstable damage evolution in rocks with implications to fracturing of granite. Geophys. J. Int. **167**, 1005–1016 (2006). https://doi.org/10.1111/j.1365-246X.2006.03126.x
4. Goebel, T.H.W., Becker, T.W., Schorlemmer, D., Stanchits, S., Sammis, C., Rybacki, E., Dresen, G.: Identifying fault heterogeneity through mapping, spatial anomalies in acoustic emission statistics. J. Geophys. Res. **117**, B03310 (2012). https://doi.org/10.1029/2011JB008763
5. Petružalek, M., Vilhelm, J., Rudajev, V., Lokajiček, T., Svitek, T.: Determination of the anisotropy of elastic waves monitored by a sparse sensor network. Int. J. Rock Mech. Mining Sci. **60**, 208–216 (2013). https://doi.org/10.1016/j.ijrmms.2012.12.020
6. Toth, T., Hudak, R.: Computed tomography—its development, principle and image artifacts. Acta Mech. Slov. **17**, 40–47 (2013). https://doi.org/10.21496/ams.2013.044
7. Chayes, F.: Composition of the granites of Westerly and Bradford. Rhode Island. Am. J. Sci. **248**, 378–407 (1950). https://doi.org/10.2475/ajs.248.6.378
8. Stesky, R.M.: Mechanisms of high temperature frictional sliding in Westerly granite. Can. J. Earth Sci. **15**, 361–375 (1978)
9. Panteleev, I.A., Bayandin, YuV, Naimark, O.B.: Spatio-temporal patterns of damage development during deformation of fiberglass woven laminate according to acoustic emission data. Fiz. Mezomekh. **19**(4), 64–73 (2016). (in Russian)
10. Tomilin, N.G., Damaskinskaya, E.E., Pavlov, P.I.: Fracture of rocks as a multilevel process. Izv. Phys. Solid Earth **41**(8), 660–669 (2005)
11. Krasil'nikov, A.Z.: Statistical kinetics of delocalized destruction. Extended Abstract of Cand. Sci. Dissertation 18 pp. (1991). (in Russian)
12. Builo, S.I.: Diagnostics of the predestruction state based on amplitude and time invariants of the flow of acoustic-emission acts. Russ. J. Nondestr. Test. **40**, 561–564 (2004). https://doi.org/10.1007/s11181-005-0097-6
13. Hilarov, V.L., Korsukov, V.E., Butenko, P.N., Svetlov, V.N.: Wavelet transform as a method for studying the fractal properties of the surface of amorphous metals under mechanical load. Phys. Solid State **46**(10), 1868–1872 (2004). https://doi.org/10.1134/1.1809422
14. Hilarov, V.L.: Self-similar crack-generation affects in the fracture process in brittle materials. Modelling Simul. Mater. Sci. Eng. **6**, 337–342 (1998)
15. Smirnov, V.B., Ponomarev, A.V., Zav'yalov, A.D.: Structure of the acoustic mode in rock samples and seismic process. Fiz. Zemli. (1), 38–58 (1995). (in Russian)
16. Wendt, H., Abry, P., Jaffard, S.: Bootstrap for empirical multifractal analysis. IEEE Signal Proc. **24**(4), 38–48 (2007). https://doi.org/10.1109/msp.2007.4286563. Source: IEEE Xplore
17. Wendt, H., Roux, S.G., Jaffard, S., Abry, P.: Wavelet leaders and bootstrap for multifractal analysis of images. Signal Proc. **89**(6), 1100–1114 (2009). https://doi.org/10.1016/j.sigpro.2008.12.015. Source: OAI

18. Muzy, J.F., Bacry, E., Arneodo, A.: Multifractal formalism for fractal signals: the structure-function approach versus the wavelet-transform modulus-maxima method. Phys. Rev. E **47**, 875–884 (1993). https://doi.org/10.1103/PhysRevE.47.875
19. Hilarov, V.: Simulation of crack growth during fracture of heterogeneous materials. Phys. Solid State **53**, 758–762 (2011). https://doi.org/10.1134/S1063783411040160
20. Damaskinskaya, E., Hilarov, V., Frolov, D.: Revealing the spatial region of a future fracture nucleation in heterogeneous materials at the initial deformation stage. In: AIP Conference Proceedings, vol. 1783, p. 020033 (2016). https://doi.org/10.1063/1.4966326
21. Damaskinskaya, E., Frolov, D., Gafurova, D., Korost, D., Panteleev, I.: Criterion for fracture transition to critical stage. Interpretation **5**(4), SP1 (2017). https://doi.org/10.1190/int-2016-0222.1
22. Damaskinskaya, E.E., Kadomtsev, A.G.: Locating the spatial region of a future fracture nucleation based on analyzing energy distributions of acoustic emission signals. Izvestiya Phys. Solid Earth **51**(3), 392–398 (2015). https://doi.org/10.1134/S1069351315030027
23. Bak, P.: How Nature Works: The Science of Self-Organized Criticality. Springer, New York (1996)

Numerical Modelling of Formation of Chuya-Kuray Fault Zone, Gorni Altai

Mikhail Eremin and Yurii Stefanov

Abstract Numerical modeling of fault zone evolution can elucidate the process of formation of a complicated fault system. Here we develop a numerical model of stress-strain state evolution in and around the Chuya-Kuray fault zone of Gorni Altay, Russia, to understand the fault zone evolution. The model's structure is constructed on the basis of seismotectonic and paleoseismological studies as well as high-resolution Space-Radar-Topography-Mission data. A mathematical model is described by a set of partial differential equations of solid mechanics. Constitutive equations for inelastic strains were derived earlier and are implemented in this work. Inelastic behavior is described by the modified Drucker-Prager plasticity model with non-associated plastic flow rule. An initial stress state of the model is a result of gravity forces, and the model is activated by a slip of a buried dextral strike-slip fault located in the basement of the model. The results of modelling illustrate the stages of fault development, the development of fault brunches and the structure of the modeled fault zone.

M. Eremin (✉) · Y. Stefanov
Institute of Strength Physics and Materials Science of Siberian Branch of Russian Academy of Sciences, Tomsk 634055, Russia
e-mail: eremin@ispms.tsc.ru

Y. Stefanov
Trofimuk Institute of Petroleum Geology and Geophysics of Siberian Branch of Russian Academy of Sciences, Novosibirsk 630090, Russia

33

1   Introduction

Continuous motions of crust blocks of the Earth cause activations of existing faults which in some cases are buried under the bed of sedimentary rocks. The strike-slip displacements in the basement of the fault cause the formation of a hierarchically organized fault zone. At the surface, lineaments of different types are observed. They are, basically, R-, R′-, P-, Y-shears, T-fractures, etc. [1]. Some authors also highlight the existence of F-fold axial trace [2, 3] and X-shears [3]. It was found that the emergence of different types of ruptures is connected with different stages of fault zone formation.

Generally, the formation of Riedel-type shear zones draws much attention: many works are dedicated to the instrumental investigation and physical modeling [1, 3–5]. At the same time, the works on numerical simulation began to appear [6–9]. The following questions were investigated: morphology and kinematics of structures, conditions of formation, trajectories of main stresses, mechanisms of shear accommodation, etc. However, the number of three-dimensional investigations of this difficult problem is still not large.

2   Input Data for Modelling

2.1   Some Data on the Chuya Earthquake

Analysis of the general morphological-and-tectonic pattern of Gorni Altay carried out on the system of neotectonic faults shows that majority of faults represent dextral strike-slip faults of NW–SE orientation [10]. We used the scheme of faults renewed in Neogene from [10] as input data, but we only took the main fault for simplicity of analysis and assumed the displacement occurred on the main fault. It is located between North and South Chuya ridges and Chuya and Kuray depressions.

The Chuya earthquake with $M = 7.5$ on the 27th of September 2003, Gorni Altay, is one of the strongest earthquakes for the whole period of instrumental observations. Field studies carried out during 2003–2005 in the epicentral zone of the mainshock and aftershock decay [10–15] gave comprehensive information about the kinematics, stages, depths, focal mechanisms, reconstruction of natural stresses, etc. Lunina et al. [12] reported that zone of seismotectonic fractures represents the fault zone in conformity with Riedel model, with a maximum width of about 4 km and is extended in North–West direction. The dextral strike-slip fault occurred in the Paleozoic basement and comes to the surface as 70 km system of lineaments of mostly R- and R′ shears in the bed of Cenozoic sediments.

2.2   The Use of SRTM-Data for Simulation

A Space-Radar-Topography-Mission data (SRTM) give information about absolute heights of surface relief with different accuracy. Figure 1 illustrates the shaded relief of the region under consideration with an accuracy of 90 m/pixel. We took these data to account for sharp changes of the surface relief when passing from ridges to depressions, but we coarsen the accuracy and use 180 m/pixel due to computing power limitations. Using Qgis 3.0 software it is easy to extract the surface relief and insert it into the model (Fig. 2).

3   Boundary Value Problem Formulation

3.1   Mathematical Model

Field observations referenced in Sect. 2.1 give good and comprehensive insight into the process of seismotectonic deformations of the Earth's crust of Gorni Altay. Numerical modelling can elucidate the process of fault activation, seismotectonic deformations, redistribution of stresses, and fracturing of crust elements. The system of equations can be found elsewhere [8]. Here we only provide the values of physical-and-mechanical properties used in our modelling. Properties of blocks are given in Table 1.

We utilized the Finite-difference method (FDM) [16] to solve the Boundary Value Problem (BVP). The number of cells in mesh along the Z-axis is 570, along the Y-axis is 425, along the X-axis is 50. The shape of an elementary cell is rectangular and the mesh step is 180 m. The initial state of stress in the whole computational domain is the result of gravity forces.
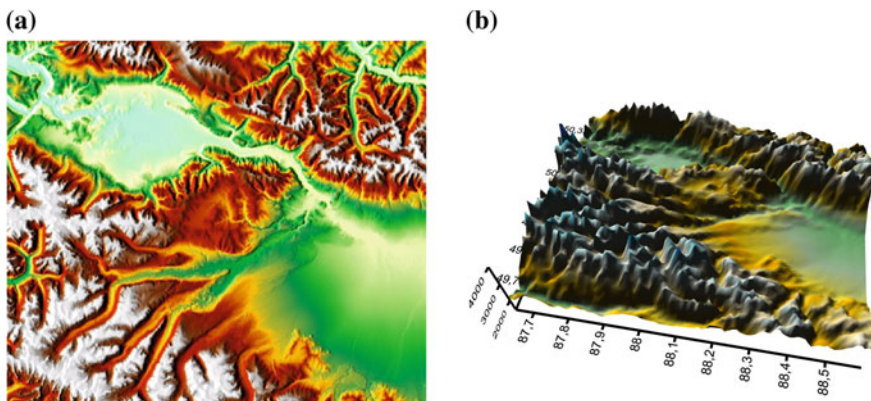
Fig. 1   The SRTM shaded pattern of absolute heights of the Chuya-Kuray zone (**a**), relief (**b**), the axis figures are related to geographic net and scale of absolute heights

Table 1 Physical-and-mechanical properties

Block no.	ρ, g/cm^3	K, GPa	μ, GPa	Y, MPa	α	Λ	γ_c	h
Block 1	2.5	12.28	5.34	15.0	0.55	0.1	0.005	0.15
Block 2	1.75	6.7	4.0	7.5	0.6	0.12	0.002	0.1
Block 3	2.5	12.28	5.34	24.0	0.5	0.1	0.005	0.15
Block 4	2.5	24.46	10.68	24.0	0.5	0.16	0.01	0.3
Block 5	2.5	12.28	5.34	–	–	–	–	–

3.2 Boundary Conditions

The structural model is given in Fig. 2a, b. In the basement of the model we put an elastic 1 km thick off-fault layer (indicated as block 5 in Table 1) containing an initial main fault (yellow curve in the Fig. 2b) according to [10]. The fault is simulated as an initial very thin zone with low density and elastic moduli. The next layer (5 km thick) represents a relatively rigid crystalline basement (indicated as block 4 in Table 1). The last floor is 4 km thick layer of sedimentary rocks, which consists also from several blocks (marked with corresponding numbers in Fig. 2a). We also added elastic blocks at the lateral boundaries of the model in order to avoid sufficient influence of boundary conditions, which is a common computational expedient applied in the case of sophisticated boundary conditions. Properties of the blocks are the same as for the elastic off-fault material.

Figure 2b schematically illustrates the boundary conditions applied to the model. We simulate the activation of the main fault by means of gradual strike-slip displacement in the basement of the model.

It is quite difficult to determine the depth structure of the crust. For example, the sedimentary rocks of Chuya and Kuray depressions are well studied [17, 18]. It was found that rocks in depressions are loose (mostly clays). However, there is a lack of data for depths greater than 1 km. Thus, by a large number of direct simulations, we tried to define the structure and properties of blocks in the model. Finally, we obtained the structure and properties of blocks in the model which give a satisfactory agreement with observational data.

In the next section, we provide the results of numerical modeling and discussion.

4 Results and Discussion

4.1 Stages of Fault Zone Formation

It is obvious that stages of fault zone formation depend on accumulated strike-slip displacement in the basement of the buried fault. The higher the value of accumulated displacement, the later stage of fault zone formation is observed and the higher the accumulated inelastic strains are. In applied model, the maximum value
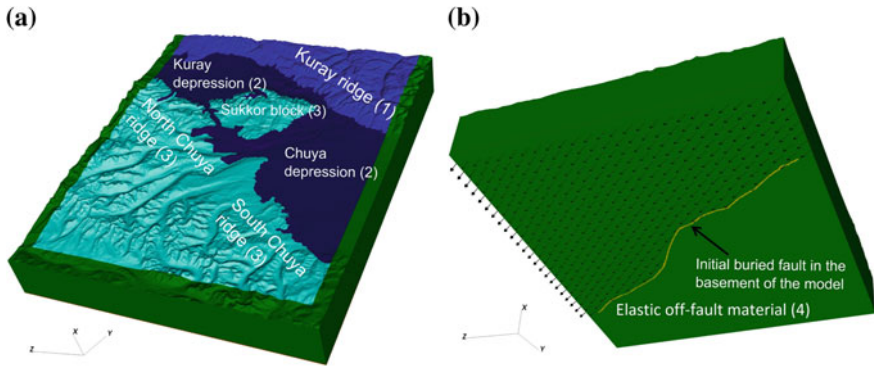
Fig. 2 Structural model of Chuya-Kuray zone (**a**), the numbers in brackets refer to the numbers of blocks in Table 1. Scheme of the boundary conditions and the structure of the model in the basement (**b**)

of $\gamma_c = 0.01$ is related to the crystalline basement. This value refers to the accumulated intensity of inelastic strain when the rock strength turns to residual strength, which is further controlled by the confinement pressure at the corresponding depth and frictional parameters of rocks. Stress concentration which occurred on the main fault at initial stages of deformation gradually moves towards the daylight surface while surrounding rocks lose stability. The change in depth obviously changes the confinement pressure and the trajectories of main stresses. It results in a change of shear direction and thus the surfaces of localized inelastic strains appear to be non-planar. We can trace the evolution of the fault zone in Chuya-Kyray zone in Fig. 3. It represents the contour of inelastic strain that shows the distribution in the volume of geomedium. The contour of inelastic strain might be interpreted as the surface limiting the dilatant (damaged) rocks that lost stability.

The stages of fault zone formation exhibit another peculiarity: the more soft layer (intermediate block (4)) of sedimentary rocks reacts on shear in the basement earlier before the propagating zone of localized strain from basement fault reaches it. At later stages, the coalescence of fractures occurs and forms the final morphology of the fault zone.

The numerical simulation data show that the average width of the fault zone is approximately 4 km if we account for newly formed lineaments of the second order. In these lineaments, the accumulated intensity of inelastic strain doesn't exceed the values of $\gamma^P \approx 0.002$. We re-scaled the distribution exactly on this threshold in Fig. 3. However, if we increase the threshold by a factor of 10 ($\gamma^P \approx 0.02$), then we will see the lineaments of the first order (Fig. 4) which occupy the much thinner region.
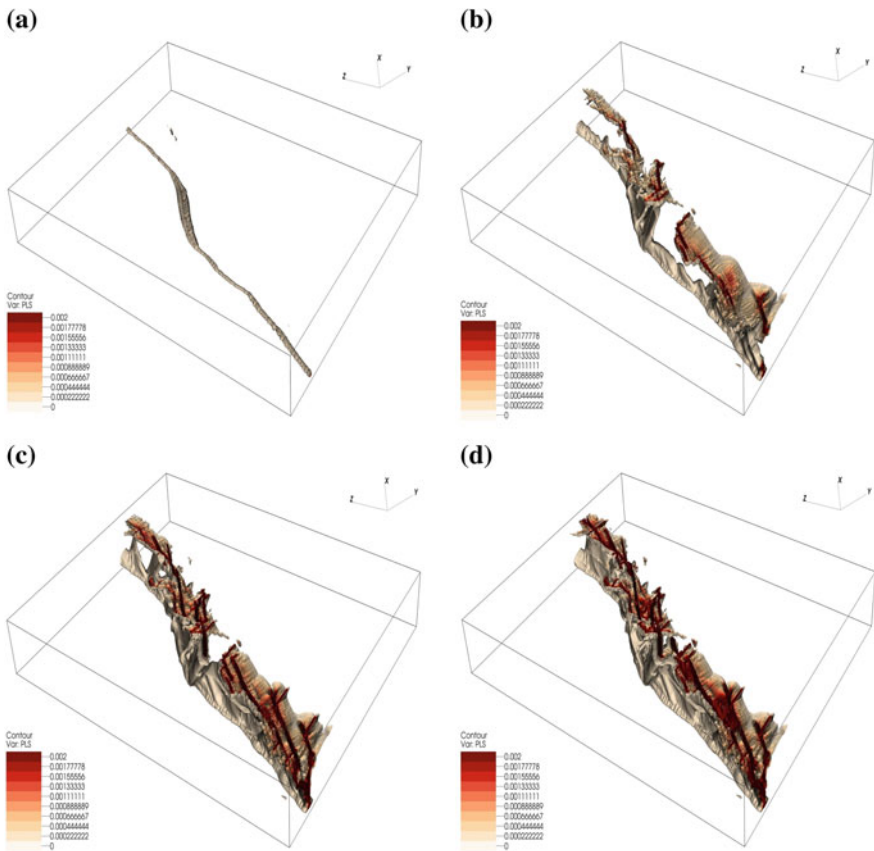
Fig. 3 Stages of Chuya-Kuray fault zone formation at different accumulated strike-slip displacement along the main fault in the basement of the model

One can see the surface ruptures in Fig. 5a drawn when the fault reached the surface. For clarity, the surface ruptures are combined with 5 × scaled relief of Chuya-Kuray zone. We have also made a classification scheme of lineaments of different types which is given in Fig. 5b. We can see that typical R-, R′-shears are frequently presented in the array of surface ruptures, while Y-shears and T-fractures more rarely. However, the X-shears are also observed at slightly different angles. It is, first of all, due to the non-linear shape of the initial fault and, secondary, due to the change of the stress state type. Usually, it indicates that in some sectors of the fault zone the transition from purely strike-slip to transtension occurs.
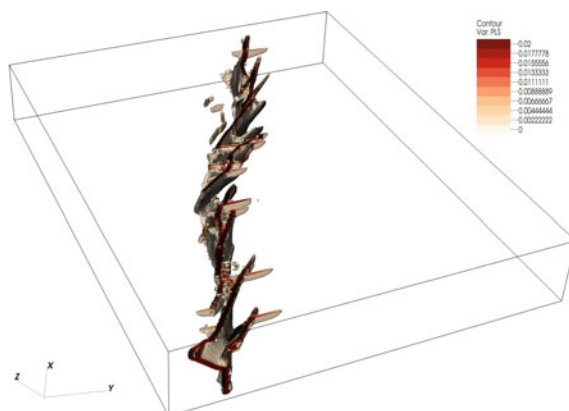
Fig. 4 The first order lineaments of the Chuya-Kuray fault zone, an accumulated strike-slip displacement correspond to the state shown in Fig. 3d
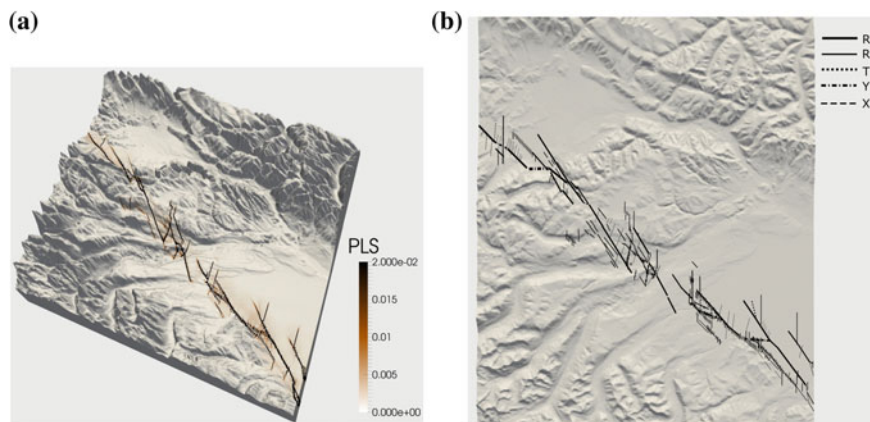
Fig. 5 The surface ruptures combined with 5x scaled digital elevation map (**a**) and the scheme of lineaments of different types (**b**) after the formation of the fault zone

5   Conclusions

In this work, we considered a possible scenario of formation of Chuya-Kuray fault zone. We took seismotectonic and paleoseismogeological data, as well as SRTM-data, to build a structural model and understand the boundary conditions.

Stages of formation, structure, and kinematics of fault zone are in satisfactory agreement with results obtained elsewhere [7–9] as well as with data of field observations if the boundary conditions and properties are taken in the model as aforementioned.

Fault zone represents an en-echelon system of dextral strike-slip according to the Riedel model. The system of surface lineaments is represented with R-, R′-shear bands, X- and Y-shears, T-fractures which is typical for slip-fault zones [1, 3, 4, 5].

References

1. Davis, G.H., et al.: Conjugate Riedel deformation band shear zones. J. Struct. Geol. **22**, 169–190 (2000)
2. Rebetsky, Y.L., Mikhailova, A.V.: Deep heterogeneity of the stress state in the horizontal shear zones. Izvestiya Phys. Solid Earth **50**(6), 824–838 (2014). https://doi.org/10.1134/S1069351314060068
3. Sengor, A.M.C., et al.: The geometry of the North Anatolian transform fault in the Sea of Marmara and its temporal evolution: implications for the development of intracontinental transform faults. Can. J. Earth Sci. **51**, 222–242 (2014). https://doi.org/10.1139/cjes-2013-0160
4. Ghosh, N., Chattopadhyay, A.: The initiation and linkage of surface fractures above a buried strike-slip fault: an experimental approach. J. Earth Syst. Sci. **117**, 23–32 (2008). https://doi.org/10.1007/s12040-008-0009-y
5. Mawer, C.K.: Kinematic indicators in shear zones. In: Bartholomew, M.J., Hyndman, D.W., Mogk, D.W., Mason, R. (eds.) Proceedings of the International Conferences on Basement Tectonics 8. Springer, Dordrecht (1992)
6. Taniyama, H.: Numerical analysis of overburden soil subjected to strike-slip fault: distinct element analysis of Nojima fault. Eng. Geol. **123**(3), 194–203 (2011). https://doi.org/10.1016/j.enggeo.2011.08.003
7. Stefanov, Y.P., et al.: Structure and formation stages of a fault zone in a geomedium layer in strike-slip displacement of the basement. Phys. Mesomech. **17**, 204–215 (2014). https://doi.org/10.1134/S1029959914030059
8. Stefanov, Y.P., Bakeev, R.A.: Deformation and fracture structures in strike-slip faulting. Eng. Fract. Mech. **129**, 102–111 (2014). https://doi.org/10.1016/j.engfracmech.2014.05.019
9. Chemenda, A.I., et al.: Numerical model of formation of a 3-D strike-slip fault system. Comptes Rendus Geosci. **348**(1), 61–69 (2016). https://doi.org/10.1016/j.crte.2015.09.008
10. Novikov, I.S., et al.: The system of neotectonic faults in southeastern Altai: orientations and geometry of motion. Rus. Geol. Geop. **49**(11), 859–867 (2008). https://doi.org/10.1016/j.rgg.2008.04.005
11. Rogozhin, E.A., et al.: Tectonic setting and geological manifestations of the 2003 Altai earthquake. Geotectonics **41**(2), 87–104 (2007). https://doi.org/10.1134/S00168521070 2001X
12. Lunina, O.V., et al.: Seismotectonic deformations and stress fields in the fault zone of the 2003 Chuya earthquake, Ms = 7.5, Gorni Altai. Geotectonics **40**(3), 208–224 (2006). https://doi.org/10.1134/s0016852106030058
13. Lunina, O.V., et al.: Geometry of the fault zone of the 2003 Ms = 7.5 Chuya earthquake and associated stress fields, Gorni Altai. Tectonophysics **453**(1–4), 276–294 (2008). https://doi.org/10.1016/j.tecto.2007.10.010
14. Leskova, E.V., Emanov, A.A.: Some properties of the hierarchical model reproducing the stress state of the epicentral area of the 2003 Chuya earthquake. Izvestiya, Phys. Sol. Earth **50**(3), 393–402 (2014). https://doi.org/10.1134/S1069351314030057

15. Nissen, E., et al.: Combining InSAR and seismology to study the 2003 Siberian Altai earthquakes-dextral strike-slip and anticlockwise rotations in the northern India-Eurasia collision zone. Geoph. J. Int. **169**(1), 216–232 (2007). https://doi.org/10.1111/j.1365-246X.2006.03286.x
16. Wilkins, M.L.: Computer Simulation of Dynamic Phenomena. Springer, Berlin-Heidelberg-New York (1999)
17. Dobretsov, N.L., et al.: Cenozoic history of topography in southeastern Gorny Altai: thermochronology and resistivity and gravity records. Russ. Geol. Geophys. **57**(11), 1525–1534 (2016). https://doi.org/10.1016/j.rgg.2016.10.001
18. Vetrov, E.V., Buslov, M.M., De Grave, J.: Evolution of tectonic events and topography in southeastern Gorny Altai in the Late Mesozoic-Cenozoic (data from apatite fission track thermochronology). Russ. Geol. Geophys. **57**(1), 95–110 (2016). https://doi.org/10.1016/j.rgg.2016.01.007

Indicators of Changes in the Stress-Strain State of the Geoenvironment in the Preparation and Realization of Strong Tectonic Earthquakes According to Long-Term Measurements with Underground Electric Antennas

Valery Gavrilov, Alexey Deshcherevskii, Yuliya Buss,
Yuliya Morozova, Ivan Panteleev, Yuriy Vlasov, Oleg Fedoristov
and Vladimir Denisenko

Abstract

We present the main results of the first stage of the study aimed at revealing the indicators of the changes in the stress-strain state (SSS) of the geoenvironment from the data of the long-term electromagnetic measurements with underground electric antenna in the Petropavlovsk-Kamchatskii geodynamic test site (PGS). Indicators are the most informative parameters. Their changes are associated with the preparation of nearby strong tectonic earthquakes. The physical basis of the method is the relationship between changes in the moisture content of a large volume of rock and tectonic stresses affecting the geoenvironment. We assume that such package of SSS indicators will be formed for the PGS on the basis of long-term complex borehole measurement data including measurements with underground electric antennas. We demonstrate the results of a comparison of

V. Gavrilov (✉) · Y. Buss · Y. Morozova · Y. Vlasov · O. Fedoristov · V. Denisenko
Institute of Volcanology and Seismology, Far Eastern Branch, Russian Academy of Sciences,
683006 Petropavlovsk-Kamchatskii, Russia
e-mail: vgavr@kscnet.ru

A. Deshcherevskii
Institute of Physics of the Earth, Russian Academy of Sciences, 123995 Moscow, Russia

I. Panteleev
Institute of Continuous Media Mechanics, Ural Branch, Russian Academy of Sciences,
614013 Perm, Russia
e-mail: pia@icmm.ru

the data on monitoring variations of the resistivity of rock to the results of other types of measurements carried out at the PGS.

1 Introduction

The Petropavlovsk-Kamchatskii geodynamic site (PGS) is an area with a radius of approximately 100 km centered at the city of Petropavlovsk-Kamchatskii. Among the main research directions currently under way here is to develop methods for continuous monitoring the stress–strain state (SSS) of the geological environment suitable for real-time identifying the final stages of preparation of strong earthquakes in Kamchatka. One of the key tasks in this direction is to form the set of indicators of the changes in the SSS of the geoenvironment. These indicators are the most informative parameters whose changes are related to the preparation of strong tectonic earthquakes. We assume that such package of SSS indicators for the PGS will be formed on the basis of data of long-term complex borehole measurements including the measurements with underground electric antennas. The purpose of this paper is to present the results of the first stage of the research on revealing the indications of changes in SSS of the geoenvironment based on the data of continuous monitoring of variation in the electrical resistivity of rock in the PGS zone.

2 Methods, Data, Results

The data presented in this paper were obtained by electromagnetic measurements with an underground electric antenna at the G-1 borehole of the network of integrated borehole measurements at the PGS. The G-1 borehole is located within the city of Petropavlovsk-Kamchatskii at a distance of 15 km from the coastline of the Avacha Bay. The depth of the borehole is 2540 m. The borehole is water filled and cased throughout its entire length. The rate of outflow of water to the surface is at most 0.00003 l/s in the last 10 years. The geological structure of the region is made up of loose Quaternary deposits which occupy the depth interval from 0 to 108 km and the Upper Cretaceous rocks represented by the alternating metamorphosed siltstones, mudstones, and schists. The main inflow of water to the borehole is provided from the depth interval of 1700–1800 m where the G-1 borehole intersects the zone of a deep fault.

The continuous monitoring methods for revealing changes in SSS of the geoenvironment that are currently used to forecast the earthquake hazard for Petropavlovsk-Kamchatskii include the method based on the measurements with underground electrical antennas which was developed in the Institute of Volcanology and Seismology of the Far Eastern Branch of the Russian Academy of Sciences. This method allows to monitor the changes of water content of the geological environment in the vicinity of the borehole.

The physical basis of the method is the relationship between changes in the humidity of the geoenvironment and the output signal of the underground antenna.

The changes of the intensity of the vertical component of the field of the geoenvironment are determined by the changes of the electrical resistivity of the geoenvironment in the measurement zone [3]. Thus, on a qualitative level, changes of the underground antenna signal reflect changes of the electrical resistivity of the geoenvironment. Under natural conditions, electrical resistivity of rock depends weakly on the resistivity of the mineral skeleton and is primarily determined by the amount of fluid in the pores and fractures of the rock [7, 10]. This fact makes it possible to monitor the changes of the electrical resistivity of the geological environment caused by variations of humidity of the rock in the time vicinities of strong close seismic events using measurements with the underground electric antenna.

The underground vertical electric antenna of an original design is used for electromagnetic measurements at the G-1 borehole. The main structural element of the antenna is the casing pipe of the borehole [4]. Measurements are carried out in the range of 25–1200 Hz by four frequency channels. A block diagram of the telemetry system currently in operation is given in [13]. The developed method uses continuous background electromagnetic radiation (EMR) as a sounding signal, either natural or artificial. The role of this radiation in the measurements at the G-1 borehole is played by the industrial EMR at the frequencies of ~ 50 and ~ 150 Hz. The calculated depths of monitoring resistivity in the zone of the G-1 borehole are 2250 m for the 30 Hz frequency channel, 950 m for the 160 Hz channel, and 400 m for the 560 Hz channel.

Figure 1 shows Petropavlovsk-Kamchatskii root mean square (RMS) intensity of the vertical electric field E_{gz} in geoenvironment in three frequency bands in the zone of the G-1 borehole in comparison to the moments of earthquakes with S $\geq$ 18%. S = L/R$_h$ * 100%, where L = $10^{0.44M-1.29}$ is the length (in km) of the earthquake source approximated by ellipse [11]; M is the magnitude of the event calculated from seismic moment; and R$_h$ is the hypocentral distance in km.

These time series were obtained by extracting the minimum time series' values from the initial RMS EMR time series and subsequent averaging in a moving 30-day window. The data on the occurred earthquakes are for the earthquakes with source depths of H $\leq$ 160 km. The exception is made for two deep earthquakes. The first event is the strongest (M$_W$ = 8.3) deep (H = 630 km) Okhotsk earthquake that occurred on May 24, 2013 in the Sea of Okhotsk at an epicentral distance of about 360 km from the city of Petropavlovsk-Kamchatskii. The second event is the strongest (M$_w$ = 7.7) deep (H = 626 km) earthquake with the epicenter in the Sea
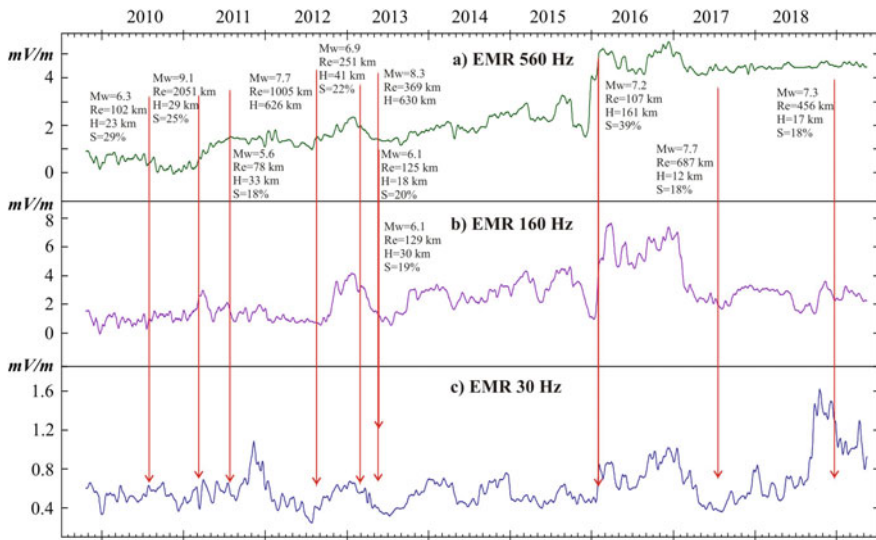
Fig. 1 Time variations of RMS intensity of the vertical electric field E_{gz} in geoenvironment in frequency bands **a** 560 ± 70 Hz, **b** 160 ± 20 Hz, and **c** 30 ± 4 Hz in the zone of the G-1 borehole in comparison to the moments of earthquakes with $S \geq 18\%$

of Okhotsk that occurred on August 14, 2012 at an epicentral distance of about 1000 km from the G-1 borehole.

The first of the noted earthquakes is the strongest seismic event recorded in the Kamchatka region since 1962 so far and the world strongest seismic event of comparable depth [1]. The second event is remarkable by the fact that the transition from the compression stage to the stage of relative extension began in the zone of the Petropavlovsk-Kamchatskii geodynamic site immediately after it.

By analyzing the data presented in Fig. 1 we may evaluate the degree of influence of earthquakes' parameters on the character of changes of the SSS of geoenvironment at the final stage of earthquake preparation. The general physical considerations suggest that the degree of influence on the character of changes in SSS of geoenvironment is determined by the magnitude of the earthquake and by the distance to its source. This assumption is supported by the results of long-term continuous electromagnetic measurements with underground antenna in the area of the G-1 borehole shown in Fig. 1. From these data it can be seen that all the strong earthquakes with $S \geq 18\%$ that took place from April 2005–May 2018 were preceded and accompanied by significant changes in electrical resistivity of geoenvironment.

The strongest changes in the intensity of electric field E_{gz} (and, correspondingly, in electrical resistivity of the geoenvironment) in the zone of the G-1 borehole were associated with seismic events that had highest S values. These events are the Zhupanovskoe earthquake (January 2016, S = 39%) and the strongest seismic events of 2013 including the deep strongest Okhotsk earthquake ($M_W = 8.3$) for

which the S value was not determined because of the large source depth (Fig. 1). The most significant changes in RMS intensity of the electric field (about the order of 17 dB for the 160 Hz frequency channel) were detected a few days prior to the Zhupanovskoe earthquake (Fig. 1). As it is noted above, variations of the underground electric antenna signal reflect the changes of electrical resistivity of the geoenvironment associated with the changes of its water content. Thus, the results of electromagnetic measurements with underground electric antenna presented in Fig. 1 indicate the activation of filtration processes at the final stage of the preparation of the Zhupanovskoe earthquake and at the final stages of the preparation of the other strong earthquakes with S $\geq$ 18% that occurred from September 2009–May 2018.

By its physical sense, intensification of filtration processes is, primarily, a response to the redistribution of the pore pressure caused by the changes of the field of mechanical stresses acting on the geological medium. The results obtained to date show that the final stages of the preparation of the close strong earthquakes are characteristically marked with a significantly increased flow rates of fluids [2]. So, currently we focus on revealing the indicators of the changes of the SSS of the geoenvironment associated with the changes of the fluid flow rate. The main obtained results are presented below.

Figure 2 displays the daily average velocity of variations in RMS intensity of the vertical electric field E_{gz} in the geoenvironment estimated by processing the data shown in Fig. 1. The displayed time series were obtained by differentiating the time series shown in Fig. 1 and subsequent averaging in the moving 30-day window.
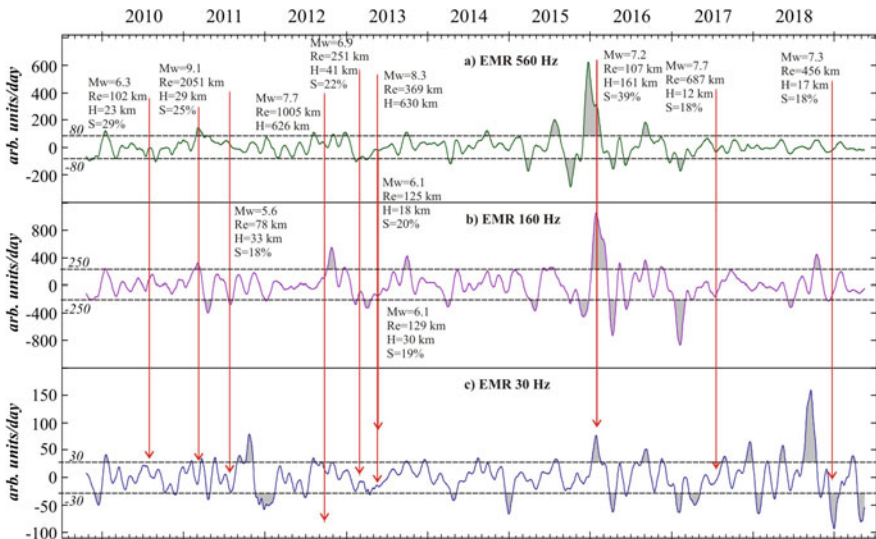
Fig. 2 Daily average velocity of changes in RMS intensity of the vertical electric field E_{gz} in the geoenvironment in the frequency ranges **a** 560 $\pm$ 70 Hz, **b** 160 $\pm$ 20 Hz, and **c** 30 $\pm$ 4 Hz in the zone of the G-1 borehole in comparison to the moments of earthquakes with S $\geq$ 18%

Dashed horizontal lines in each figure show threshold amplitudes of the variations of daily average velocity of changes in RMS intensity of the external electromagnetic radiation. These threshold values were selected individually for each frequency channel.

3   Discussion

The data presented in Fig. 2 demonstrate significant distinctions in the character of the time series obtained in different frequency channels. The presented data show that the lowest sensitivity to the changes of SSS in time vicinities of the earthquakes is observed in the measurements in the frequency channel with central frequency of 560 Hz. We note that the penetration depth of resistivity monitoring in rock in the 560 Hz frequency channel is about 400 m. With this taken into account, the observed result can probably be explained by the very weak hydraulic connection between the upper part of the section (shallower than 590 m) and the deeper horizons. This follows from the geological structure of the medium in the zone of the G-1 borehole where the depth interval from 589 to 734 m accommodates the intrusion of diorites from the peripheral zone of the extrusive rock mass of the nearby Mt. Mishennaya. Therefore, the upper part of the zone of the G-1 borehole has a lower sensitivity to the earthquake preparation processes in contrast to the measurements below 700 m [5]. At the same time, as the data in Fig. 2 show, in the time vicinity of the Zhupanovskoe earthquake, abnormally high velocities of variations in RMS intensity of the vertical electric field E_{gz} were recorded by the 560 Hz channel. It was explained above, that it means that rapid and significant changes occurred in the electrical resistivity of the geoenvironment at the depths down to 400 m due to the changes rock humidity.

This result can be explained in the context of the dilatancy–diffusion (DD) model of earthquake preparation [8, 12]. Below, it is shown that the pattern of the data of electromagnetic measurements for frequency channels of 560 and 160 Hz (the monitoring depths in the zone of the G-1 borehole are down to 400 m and down to 950 m, respectively) in the time interval from August 2012–July 2017 corresponds to the DD model. This model also fits the data of geoacoustic measurements in the G-1 borehole (Fig. 3).

In relation to the geoacoustic measurements we note that Fig. 3c illustrates the variations in the amplitude of geoacoustic emission (GAE) response to the action of the external alternating electromagnetic field in the zone of the G-1 borehole in the frequency band of 160 ± 20 Hz. The geophone was installed in the G-1 borehole at the depth of 1012 m. As shown in [6], in the case when the external alternating electric field has constant amplitude, the variations in the amplitude of GAE response are determined by the changes of water content of the geoenvironment in the zone of measurements. When a geological medium has fairly high water content, an external harmonic electric field with slowly varying amplitude acting on this medium will cause corresponding changes of GAE amplitudes. In this case, for
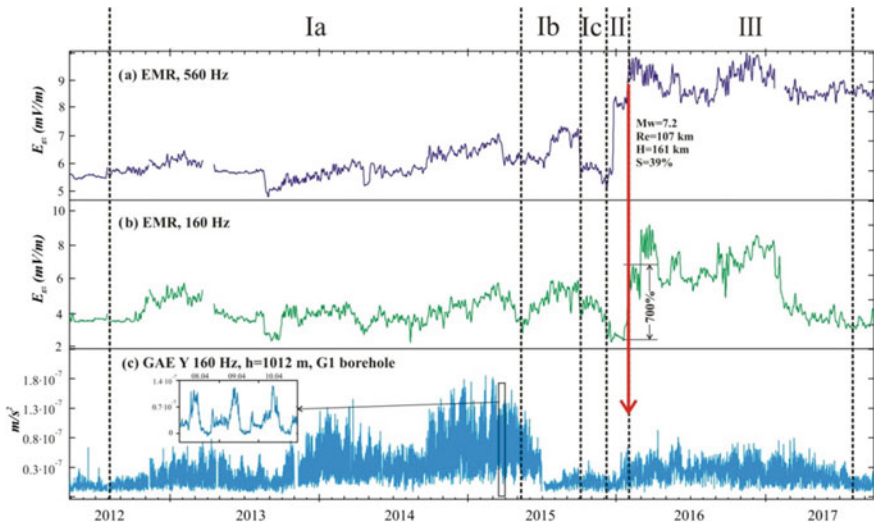
Fig. 3 The results of electromagnetic and geoacoustic measurements in the zone of the G-1 borehole in the time vicinity of the Zhupanovskoe earthquake: **a** changes in RMS intensity of the electric field E_{gz} in the frequency range of 560 ± 70 Hz (monitoring depth is ~ 400 m); **b** changes in RMS intensity of the vertical component of the electric field E_{gz} in the frequency range of 160 ± 20 Hz (monitoring depth is ~ 950 m; **c** changes in the amplitudes of GAE responses for a depth of 1012 m (160 Hz channel). Explanations are in the text

example, the diurnal variations in the amplitude of the external electric field acting on this environment will induce a corresponding diurnal variations in RMS GAE intensities. These diurnal variations in RMS GAE can be seen in the inset of Fig. 3c. It is established that given a sufficient water content of geoenvironment, the final stages of preparation of strong (in terms of S value) earthquakes are characteristically marked by significant variations in the amplitudes of GAE responses in the borehole zone due to the changes of the water content in rock [6, 9]. These processes are clearly expressed in the changes of amplitudes of GAE responses illustrated in Fig. 3c.

The data displayed in Fig. 3c show that the final stage of preparation of the Zhupanovskoe earthquake started to manifest itself in joint electromagnetic and geoacoustic measurements in the G-1 borehole from August 2012, i.e. almost 3.5 years prior to the earthquake. At the stage Ia (Fig. 1), the electromagnetic and geoacoustic data reflect the development of dilatancy processes in the region of the future earthquake source and beyond it, including the zones of electromagnetic and geoacoustic measurements. The beginning of the next stage (Ib, late May to early October 2015) is characterized by a drastic fall of the amplitudes of GAE responses presumably associated with the sharp growth of the volume of pore-fracture space of the geoenvironment in the zone of the G-1 borehole due to the enhancing dilatancy processes in the future source area of the earthquake. The electrical resistivity of the geoenvironment in the zone of the G-1 borehole begins to decrease

gradually (the stage Ic) probably due to the inflow of fluid into this zone. The stage II which directly precedes the earthquake is marked with a sharp jump of the electrical resistivity in the zone of G-1 borehole. In accordance with the DD-model, this can be related to the outflow of fluid from the zone of the G-1 borehole into the zone of the future earthquake source. The large (longer than one year) duration of the postseismic stage III testifies global changes that occurred in the flow regime at the distances significantly exceeding the source size of the Zhupanovskoe earthquake.

4 Conclusions

In this paper, we present the main results of the first stage of the study aimed at revealing the indicators of changes in the SSS of the geoenvironment from long-term electromagnetic measurements with an underground electric antenna at the G-1 borehole. The main attention was focused on revealing the indicators of changes in the SSS of the geoenvironment associated with the changes in the fluid flow rate. We analyzed the data of the electromagnetic measurements with underground electric antenna in the different frequency bands. On the whole, this approach proved to be efficient. The results of the study suggest the following conclusions.

(1) The most significant changes in electrical resistivity of the geoenvironment in the zone of the G-1 borehole turned out to be related to the strongest, in terms of the S value, seismic events (S = L/R_h * 100%, where L is the source length of an earthquake and R_h is hypocentral distance).

(2) The data of electromagnetic measurements in the frequency channel of 160 Hz (the monitoring depth is 950 m) turned out to be most informative. The measurements in the channel with central frequency of 560 Hz (the monitoring depth is about 400 m) are least sensitive to the changes in SSS in the time vicinities of the earthquakes. These peculiarities are largely follow from the geological structure of the region of the G-1 borehole.

(3) Revealing the indicators of the changes in the SSS of geoenvironment should be based on combined measurements. The composition of these measurements should allow the analysis of the obtained results from the positions of physically substantiated earthquake preparation models that gained acceptance in the scientific community.

(4) The most important results were obtained in the joint analysis of the data of electromagnetic measurements with the underground electric antenna and geoacoustic measurements in the G-1 borehole of the Petropavlovsk-Kamchatskii geodynamic site. It is shown that the character of these data in the time vicinity (August 2012–July 2017) of the strongest (M_W = 7.2) Zhupanovskoe earthquake

that occurred on January 30, 2016 at the epicentral distance of 107 km from the town of Petropavlovsk-Kamchatskii corresponds to the dilatancy–diffusion model of earthquake preparation.

References

1. Chebrov, V.N., et al.: Strong Kamchatka Earthquakes in 2013. Holding Company "Novaya kniga", Petropavlovsk-Kamchatskii (2014). (in Russian)
2. Dobrovolsky, I.P.: Mathematical theory of preparation and forecast of tectonic earthquakes. FIZMATLIT, Moscow (2009). (In Russian)
3. Dolukhanov, M.P.: Propagation of radio waves. Svyaz, Moscow (1972). (in Russian)
4. Gavrilov, V.A.: Method for continuous monitoring of electrical rock resistivity. Seism. Instrum. **50**(3), 196–205 (2014)
5. Gavrilov, V.A., Panteleev, I.A., Ryabinin, G.V., Morozova, Yu.V: Modulating impact of electromagnetic radiation on geoacoustic emission of rocks. Russ. J. Earth Sci. (2013). https://doi.org/10.2205/2013ES000527
6. Gavrilov, V.A., Naumov, A.V.: Modulation of geoacoustic emission intensity by time-varying electric field. Russ. J. Earth Sci. (2017). https://doi.org/10.2205/2017ES000591
7. King, R.W.P., Smith, G.S.: Antennas in Matters: Fundamentals, Theory and Applications. MIT Press, Cambridge, MA (1981)
8. Nur, A.: Dilatancy, pore fluids and premonitory variations of t_s/t_p travel times. Bull. Seism. Soc. Am. **62**(5) (1972)
9. Panteleev, I.A., Gavrilov, V.A.: Implications of electrokinetic processes for the intensity of geoacoustic emission in the time vicinity of a tectonic earthquake: a theoretical study. Russ. J. Earth Sci. (2015). https://doi.org/10.2205/2015ES000557
10. Parkhomenko, E.I.: Electric Properties of Rocks. Nauka, Moscow (1965). (in Russian)
11. Riznichenko, Yu.V.: Size of crustal earthquake's source and seismic moment. In: Research in Earthquake Physics, pp. 9–26. Nauka, Moscow (1976). (in Russian)
12. Sholz, C.H., Sykes, L.R., Aggarval, Y.P.: Earthquake prediction: a physical basis. Science **181**(4102), 803 (1973)
13. Vlasov, Yu.A, Gavrilov, V.A., Denisenko, V.P., Fedoristov, O.V.: Telemetry system of multidisciplinary geophysical monitoring network. Seism. Instrum. **45**, 14–18 (2009)

Earth's Natural Pulsed Electromagnetic Field (ENPEMF) Temporal Variation Anomalies as Earthquake Precursors

Vasiliy Gordeev, Sergey Malyshkov, Vitaly Polivach and Sergey Shtalin

Abstract

Natural and man-made disasters continue to shock mankind with their abruptness and tragic consequences. We are still unable to prevent, mitigate, or even predict such natural disasters as earthquakes, rock bursts, or landslides. In order to reduce the fallout from such events, we need efficient methods to predict their location, time, and energy. The authors suggest an integrated hardware/software solution to monitor the Earth's natural pulsed electromagnetic field (ENPEMF) pulse flow intensity temporal variations. A prototype station network is tested for monitoring different scale geodynamic processes in the lithosphere using the ENPEMF method. Its capability of early detection of seismic events and location of the earthquake epicenter bearing is discussed. This work aims to demonstrate experimentally that the analysis of the ENPEMF intensity parameter temporal variations is eligible for short-term prediction of the time and bearing of an upcoming earthquake at a distance of up to 500 km. For the first time, three stages of upcoming earthquake preparation are registered for the earthquake that took place on September 5, 2018, in the Chelyabinsk region. The earthquake precursor has manifested itself not only in the ENPEMF pulse flow intensity, but also in the incoming signal bearing estimation.

V. Gordeev (✉) · S. Malyshkov · V. Polivach
Institute of Monitoring of Climatic and Ecological Systems SB RAS, 634055 Tomsk, Russia
e-mail: gordeev@imces.ru

S. Shtalin
Tomsk State University of Control Systems and Radioelectronics, 634050 Tomsk, Russia

1 Introduction

Natural and man-made disasters continue to shock mankind with their abruptness and tragic consequences. We are still unable to prevent, mitigate, or even predict such natural disasters as earthquakes, rock bursts, or landslides. In order to reduce the fallout from such events, we need efficient methods to predict their location, time, and energy.

The initial step in classic approach to earthquake prediction sets the problem of statistically significant early detection of upcoming events. This problem can be solved using temporal variation data of VLF monitoring performed by the integrated hardware/software solution of the automated control system for geodynamic processes.

This work aims to demonstrate experimentally that the analysis of the Earth's natural pulsed electromagnetic field (ENPEMF) intensity parameter temporal variations is eligible for short-term prediction of the time and bearing of an upcoming earthquake at a distance of up to 500 km.

2 Results Obtained

In the night of September 5, 2018, at 3:58 local time (September 4, 23:58 GMT), an earthquake occurred in the Chelyabinsk region. Its seismic focus was located 7 km northeast of the town of Katav-Ivanovsk in the Chelyabinsk region. The nearest populated site to the focus, Orlovka, is within 1.5 km of the event location.

According to the European Mediterranean Seismological Centre, the magnitude reached 5.5 at the depth of 10 km. That means the shock was quite strongly felt.

Based on the materials of invention patent No. 2238575 "Earthquake prediction method" (patent holder IMCES SB RAS), an earthquake of that class should manifest in the form of precursors on ENPEMF pulse flow intensity temporal variations, recorded by "MGR-01" recorders located within 500 km of the upcoming event focus. The precursor duration time should be 20–30 h [1]. A jump decrease in the pulse flow intensity of ENPEMF diurnal variations serves as a precursor. Its duration gives a measure of the magnitude for an earthquake expected in the next (20–30) h and the intensity reduction value indicates the distance to the epicenter.

The ENPEMF is a consequence of dynamoelectric conversions in the solids of a faulted structure and is a signal in the very low frequency band (3–30 kHz).

In the landslide area of the Urengoy-Pomary-Uzhgorod gas pipeline, there is a functioning field observation site for the analysis of the stress-strain state of the rocks based on the ENPEMF parameters. The field observation site was established based on the fundamental research performed in IMCES SB RAS (Tomsk, Russia) in cooperation with the industry partner OOO "GEOTEK" (Moscow, Russia). The observation site allocates 12 multichannel geophysical "MGR-01" recorders, 11 of which are installed on a landslide slope at geodynamic anomaly locations and one

reference recorder is installed outside the area of active geological processes to estimate regional temporal variations. The basic idea of the method is to determine relative changes in the ENPEMF intensity between the landslide recorders and the reference recorder to forecast geodynamic events of the rocks [2].

The field observation site is located near the town of Sarapul at a distance of 235 km from the seismic focus, and the bearing from the site to the earthquake epicenter is around 120°.

According to invention patent No. 2238575 "Earthquake prediction method", a precursor of a geodynamic event can be detected as a sharp change in the signal intensity as compared to diurnal ENPEMF variations recorded previously or in previous years on the same calendar days during the periods when the seismic activity was relatively calm.

Recording of ENPEMF temporal variations allows tracking the process of preparation of a strong tectonic earthquake at the earliest stages of deformation and stress field changes (the stress-strain state of the rocks) as compared to the background fields of natural oscillations and can forewarn of seismic hazards [3, 4].

For that, we compare the times of anomaly manifestation at each of the stations and the level of ENPEMF intensity reduction during the anomaly (ΔN). Δt (in hours) is the precursor duration.

The level of intensity reduction is defined as

$\Delta N = Nav.prev. - Nav.cur.$, where

- Nav.prev. is the average ENPEMF intensity values 5–7 days before the anomaly.
- Nav.cur. is the average ENPEMF intensity during the anomaly.

It is worth noting that an earthquake can emerge without any magnetic bays in the signal intensity. Therefore, after the detection of a precursor in the form of a decrease in the ENPEMF signal intensity, it is necessary to alert the public about a possible event, and the longer the precursor duration, the more likely is the event with a high magnitude.

Figure 1 shows temporal variations of the ENPEMF pulse flow intensity for the period from August 1 to September 8, 2018, by the North-South signal reception direction. The horizontal axis represents the date in the day.month format.

We can distinguish three areas (a, c, and d) in the graph, where an anomalous decrease in the signal intensity appears:

(a) August 22–29; however, diurnal variations are weakly manifested in this period.
(c) September 3–5, with a weak diurnal variation on September 3.
(d) September 4, a very weak signal with no diurnal variation.
(b) August 29–September 3, a signal in 2018 corresponds, in shape, to the average values of that in 2014–2017, and the absolute values are even higher, which may indicate a bay increase in the signal intensity.
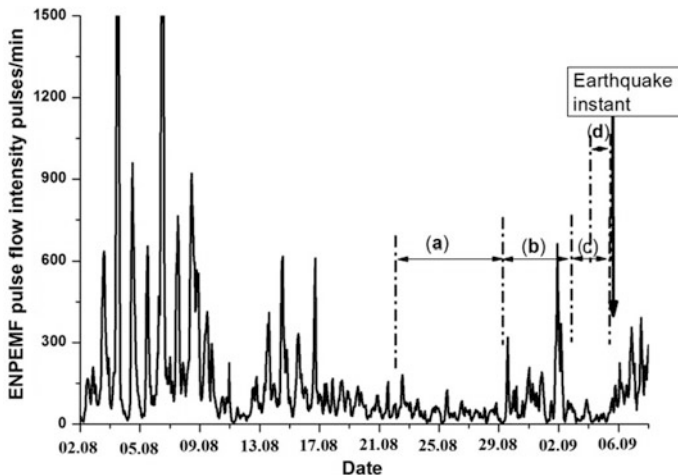
Fig. 1 Temporal variations of the ENPEMF pulse flow intensity

Hence, we can ascertain that the precursor of the geodynamic event started to manifest weakly 7 days before it, from August 22 to 29, and expressed obviously on September 4, when the diurnal variation of the ENPEMF intensity was completely absent.

For a more detailed study of the results, Fig. 2 demonstrates the ENPEMF pulse flow intensity variations for the period from September 1 to September 8 averaged for the previous four years and for the year 2018. As it can be clearly seen from the Figure, no diurnal variation in the ENPEMF pulse flow intensity was observed throughout September 4, and that was presumably related to the upcoming earthquake moment on September 5, 2018, near the town of Katav-Ivanovsk, the Chelyabinsk region.

Figure 3 shows measurement results for the ENPEMF pulse flow intensity between September 1 and September 8, 2018, with the signal reception directions North-South (N-S) and West-East (W-E) dominating. The figure shows that, during the entire period, there was a diurnal variation for the West-East direction, even when in the North-South direction on September 4 the signal intensity decreased more than 10 times as compared to the average values in the previous four years and there was no diurnal variation.

Applying the standard bearing measurement formula to a signal received by two mutually orthogonal ferrite antennas, we can calculate the angle of an incoming signal:

$$\alpha = \sin^{-1}\left(Nh2/\sqrt{Nh1^2 + Nh2^2}\right),\tag{1}$$

where $Nh1$ and $Nh2$ are the signal intensity values for the North-South and West-East channels, respectively [5].

Fig. 2 Temporal variations in the ENPEMF pulse flow intensity from 01.09 to 08.09 average for 2014–2017 (**a**), from 01.09 to 08.09 2018 (**b**)
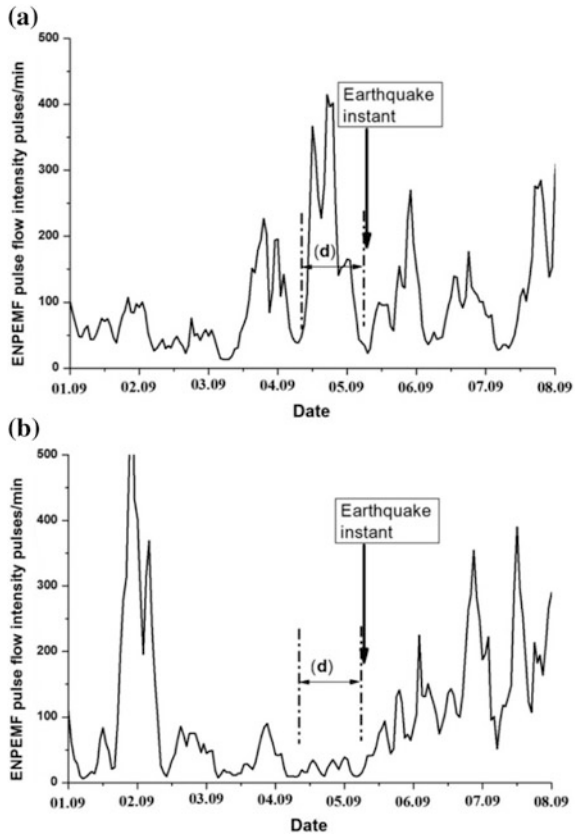
Let's review some specifics of the "MGR-01" recorder functionality regarding the determination of the incoming signal bearing. Figure 4 shows how it is determined by the "MGR-01" recorder.

To find the bearing, we need to know not only a signal's absolute value, but also its sign. It's worth noting that the "MGR-01" recorder has a threshold system of positive values only, so bearing calculation can only vary in the range of 0–90° and the signal source location will have four imaginary points as indicated by stars in Fig. 4.

Since the recorder cannot determine negative values, the source of a signal can be located in any quadrant of the polar coordinate system. The polar angle of one of them aligns with the actual direction to the earthquake epicenter and has a bearing of 100–110°. The problem of unambiguous determination of the coordinates of an upcoming earthquake's epicenter can be solved with a network of spatially distributed ENPEMF recorders, given that an earthquake is preparing to strike within the territory covered by that network.
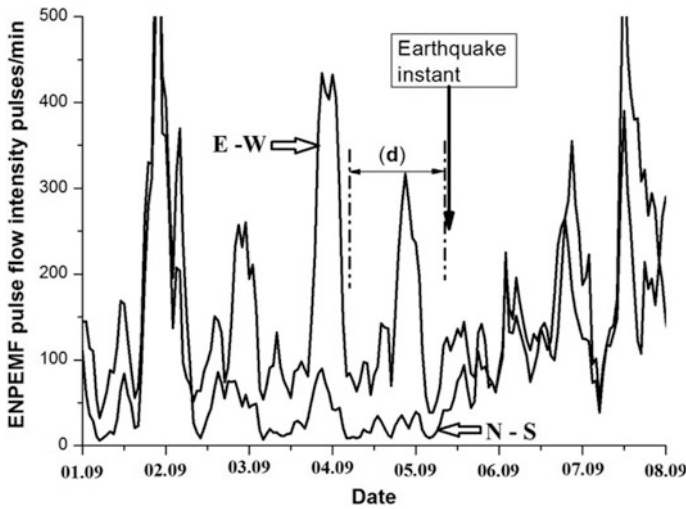
Fig. 3 Temporal variations in the ENPEMF pulse flow intensity from September 1 to September 8, 2018, in two mutually orthogonal directions of signal reception

Fig. 4 Determining the bearing of an incoming signal with two mutually orthogonal ferrite antennas
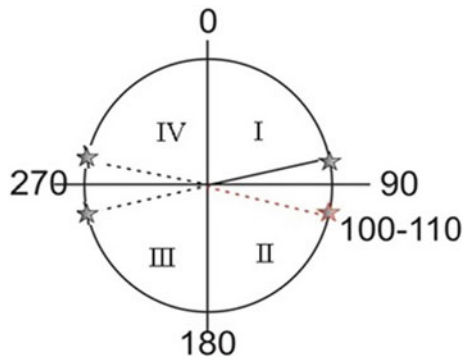
3   Conclusions

1. A scientific basis was developed for the monitoring of different scale lithospheric geodynamic processes based on the Earth's natural pulsed electromagnetic field temporal variations with the capability of source signal direction finding.
2. For the first time, three stages of upcoming earthquake generation were registered for the earthquake that took place on September 5, 2018, in the

Chelyabinsk region. The earthquake precursor manifested not only in the ENPEMF pulse flow intensity, but also in the incoming signal bearing estimation.

References

1. Malyshkov, Yu.P., et al.: RF patent N 2238575 Earthquake prediction method, Issued 20 Oct 2004
2. Malyshkov, Yu.P., et al.: Earth's natural electromagnetic noises in a very-low frequency band. In: Electromagnetic Fields: Principles, Engineering Applications and Biophysical Effects, pp. 1–86. Nova Science Publishers, Inc. (2013). ISBN: 978-1-62417-063-8
3. Vorobiev, A.A.: Geologia i Geophysika. **12**, pp.3–13 (1970) (in Russian)
4. Sadovsky, M.A.: Nauka, p 88, (1982) (in Russian)
5. Gordeev, V.F., Malyshkov, S.Yu., Krutikov, V.A., Polivach, V.I., Shtalin, S.G.: Lightning discharges bearing using dangerous geological processes monitoring system based on Earth's natural pulsed electromagnetic field parameters. In: IOP Conference Series: Earth and Environmental Science, vol. 211 (2018). https://doi.org/10.1088/1755-1315/211/1/012073
6. Gordeev, V.F., Kabanov, M.M., Kapustin, S.N.: Algorithm and software for landslide slopes stability estimation with online very low frequency monitoring. In: IOP Conference Series: Materials Science and Engineering, vol. 189(1) (2017). https://doi.org/10.1088/1757-899x/189/1/012015

Formalized Lineament Analysis as a Basis for Seismic Monitoring of Platform Areas

Galina Ivanchenko◯ and Svetlana Kishkina◯

Abstract

The research is devoted to one of the natural hazards of safety of nuclear power plants on the example of the Kursk Nuclear Power Plant (NPP). The analysis of recent geodynamic activity in the area of the Kursk NPP was performed on the basis of digital processing of space images in order to detect active fault zones for optimal organization of seismic monitoring. A formalized lineament analysis was applied (LESSA program) and stable statistical characteristics of the spatial distribution of small and extensive lineaments were obtained and analyzed. The expression of the post-Turonian regional flexure of the sedimentary cover in lineament forms is shown. An estimation of the existence of recent reactivation of Precambrian fracture zones has been made Kursk NPP area and in the adjacent region. The tectonic stability of the territory adjacent to the NPP has been confirmed. Weak seismic events recorded during seismic monitoring were classified as man-made.

Keywords

Lineament · LESSA program · Seismic monitoring · NPP site

G. Ivanchenko (✉) · S. Kishkina
Sadovsky Institute of Geospheres Dynamics RAS,
Leninsky prosp. 38, k.1, 119334 Moscow, Russia
e-mail: ivanchenko@idg.chph.ras.ru

S. Kishkina
e-mail: kishkinas@idg.chph.ras.ru

1 Introduce

According a modern approach to earthquake mechanics, seismic monitoring should be targeted at fault zones within controlled areas, as the most likely location of seismic events. For example, it should be done for areas around NPP sites. Regulatory documents provide for control of a radius of 300 km around a NPP. It seems problematic to cover such an area with uniformly highly sensitive measurements. It is necessary to select equipment installation sites and areas of the highest sensitivity of the seismic monitoring system. That implies an assessment of the current geodynamic conditions of the monitoring area. We use automated lineament analysis of digital images to describe the modern geodynamic conditions of the area. The assumption that active faults are expressed in the landscape as lineaments and lineament zones lies at the core of the analysis of remote sensing data.

A formalized lineament analysis of space images of various resolution and coverage was carried out for the territory of the Kursk NPP. That allows to identify zones of tectonic disturbances and to detail their internal structure.

Digital image processing by LESSA program give a chance together with other methods, to detect reactivated faults of the basement, which under the geodynamic conditions of the East European Platform (EEP) represent the main type of neotectonic (recent) activity manifestation. These methods significantly reduce the dependence on the expert's subjective view. In this case, the individuality of the expert assessment does not disappear, but is formalized, which leads to greater stability of the results. All work on the seismic monitoring of NPP sites conducted by our Institute (SIDG RAS) begins with the stage of a formalized lineament analysis of the geodynamic conditions. An analysis activity of recent tectonics of the Kursk NPP area is considered here as example.

2 Methods of Formalized Lineament Analysis

Fault zones active on the recent (neotectonic) and present stage (RAFZ) can be identified by the methods of formalized lineament analysis if they can be detected in the relief and landscape. Digital detection and interpretation of short ("strips") and rather long photolineaments with the interpretation of the most stable statistical characteristics of their spatial distribution has been done for this purpose. We used the software package LESSA [6, 7] for the digital processing of satellite images. It is proposed to analyze the primary digital images and automatically detect their orientation characteristics. The technology is based on the detection and selection of oriented elements of the image texture. Then the Hough transform is applied to these very numerous strips or small lineaments to make possible to construct compound extended lineaments.

The field of small lineaments is characterized by the means of statistics of directional data. Distribution of strips position and orientation are indicated by rose-diagrams and vector of their elongation. That allows to evaluate the reliability

of the results obtained [5]. First of all, these are the parameters reflecting the degree of R and the direction of elongation of the rose φ_R, its difference from the uniform rose D, as well as the degree of expression of a certain direction $h(\alpha_i)$ and size of the rose

$$H = \sum_{i=1}^{N} h(\alpha_i). \tag{1}$$

The size and direction of elongation can be estimated as: $R = \frac{1}{H} \sqrt{C_1^2 + C_2^2}$, $\varphi_R = arctg \frac{C_1}{C_2}$, where $C_1 = \sum_{i=1}^{N} h(\alpha_i) \sin 2\alpha_i$, $C_2 = \sum_{i=1}^{N} h(\alpha_i) \cos 2\alpha_i$, the ratio of the vector sum of the rose vectors to their scalar sum (basic concept of angular statistics). The angles are doubled in order to keep the uniform rose-diagram R = 0 when $0 \le \alpha_i \le 180°$. The maximum value of R = 1 for a rose consisting of one ray. We used the criteria for the statistical hypotheses separation between a uniform circular distribution and a von Mises distribution (circular normal distribution) to assess the reliability of the rose-diagrams properties. The degree of difference of a rose from a uniform is estimated by the value

$$D = \frac{1}{H} \sum_{i=1}^{N} \left| h(\alpha_i) - \frac{H}{N} \right|. \tag{2}$$

The algorithms LESSA contain a number of variable parameters to investigate the properties of fault networks of various ranks according to their appearance on raster images. LESSA lineament is any linear element of a raster image, the properties of which are described by the procedure of their detection in the image, while the image itself may have a diverse nature, such as a space image, a digital elevation model or some geophysical fields. We used space images of various scales.

The problem of identifying natural lineaments from technogenic "noise" is important for processing space images of the EEP territory. Therefore, only the most statistically stable characteristics of the lineament field should be used to study tectonic activity and to select RAFZ under these conditions. The global rose-diagram constructed for the large domain or entire analyzed image, and so-called lineament forms or "streamlines of R-vector field" are most statistically stable. Lineament forms are the lines of elongation of the reliable vectors R of rose-diagrams of small lineaments built in a sliding window. These lines are grouped into rectilinear or smoothly curved zones of different widths and lengths. A similar concept is the lineament zone having a certain width and internal structure [2].

3 General Geodynamic Conditions of the Kursk NPP Area

The research area is located in the Kursk region of the Russian Federation in the Seim river basin. In tectonic terms, the area belongs to the Kursk megablock of the Voronezh crystalline massif (VKM). The structure of the Precambrian basement is of great importance, since all the faults of the Phanerozoic within the VKM are differently activated basement faults. Study of the degree and style of ancient faults reactivation in the structures of the sedimentary cover, first of all Cenozoic age, is the main method of estimation their possible recent activity. For Cenozoic sediments of the region, gentle deformations expressed in extremely insignificant deviations beds from horizontal are typical over large areas. Such structure is characteristic of the peripheral parts of the Late Cretaceous-Paleogene regions of weak subsidence, in particular, the northern slope of the Donetsk Paleorift, to which the southern part of the territory under consideration belongs.

The main issue in conducting seismic monitoring is the allocation of RAFZ. Their activity at the present stage may be reflected in seismicity. Earlier, in the near zone of the Kursk NPP, the Zheleznogorsky, Nameless, Sublatitudinal and Rylsky faults were classified [4]. Our task was to study the signs of the latest tectonic activity of precisely these zones, as potential zones of earthquake foci.

4 Formalized Lineament Analysis of Kursk NPP Area

The largest and longest the Precambrian Zheleznogorsk regional fault of the NNW strike is not detected by the majority of experts in space images. However, on the structural map, a fragment of this zone is noted on the base of the Turonian deposits [1]. A field survey of fault zones near Kursk NPP site showed that some activity of the Sublatitudinal fault crossing the Zheleznogorsk disjunctive zone 15–20 km south-east of the NPP site is possible by indirect geological and geomorphological features. Activity at the present stage can be assumed for the Zheleznogorsk fault zone itself only for its eastern part. Indirect signs of activation are also noted at a distance of 15–20 km to the north of the site. The fault zones is not expressed in the relief near the site. The Zheleznogorsk fault zone is fragmentary clearly fixed in a geological section only. At present, traces of the activity of the Zheleznogorsk zone, including its secondary faults, such as the Nameless fault, are noted in emanations of radon. This suggests the effect of fault zones on the hydrogeological regime with a possible intensification of exogenous phenomena possibly reflected in landscape and small lineaments. Existence some signs of recent activity along the Nameless and Sublatitudinal faults and the disagreement of experts make to check the recent activity of these faults using automated lineament analysis methods. LESSA program allow detecting long lineaments expressed in modern landscapes (Fig. 1). The flexure-type structure and faults of post-Turonian time obtained as a result of the geological survey [1] are also shown in the Fig. 1.
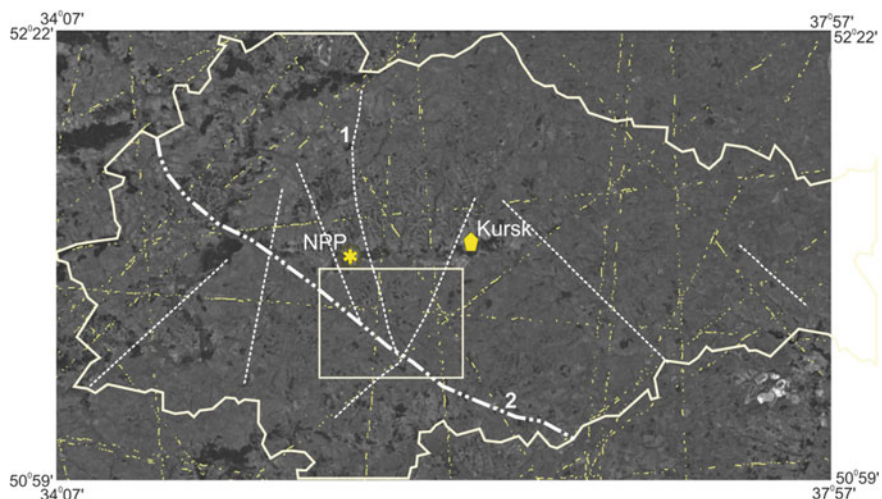
Fig. 1 Lineament analysis of the Kursk region. White box is the area of detailed research. Long lineaments highlighted by LESSA are shown by yellow. The active Late Cretaceous faults are shown by white broken lines. The Zheleznogorsk Fault is marked as "1", the Late Cretaceous flexure is marked as "2"

Figure 1 shows that submeridional strikes prevail among the selected extended lineaments. These lineaments probably reflect the structural pattern of the Archean-Proterozoic basement. The lineament zone of the NNE strike, highlighted in the west of the Kursk block, defines its border with the Bryansk Precambrian megablock. The Zheleznogorsk Fault is a complexly disjunctive structure, practically not expressed in lineaments. It should be noted that none of the lineaments selected according to the LESSA method passes near the NPP. This result, in our opinion, may be interpreted as the lack of reactivation of Mesozoic and older faults near NPP at the present stage and absence their manifestations in the landscape and relief. However, computer-assisted detection of long lineaments by space images is not very informative for technogenic landscapes of Kursk region, and one should rely more on stable statistical characteristics of a small lineaments of low hierarchical levels over large domain and also "lineament forms", which are interpreted as possible zones of localizations of tectonic deformations.

Let us compare the rose-diagrams for the Kursk block as a whole and for the test area of the alleged activation of faults. Distribution areas of small lineaments by direction (LESSA program) for the global (entire image) and local (for the test section) rose diagrams are shown in the figure. For sidebar analysis was performed on the image of a better raster resolution than for the entire image. The estimated neotectonic activity of the test site is determined by the fact that it is the area of intersection of the main faults identified during the geological survey, and the junction of the Cretaceous disjunctive and folded structures are localized here. When comparing rose diagrams constructed from space images of different scales

of detail, we can note the practical identity of rose diagrams (Fig. 2), which can be interpreted as a statistical criterion for the absence of local deformations.

Indeed, if the faults, for which some authors noted any signs of recent activity (the Nameless, Sublatitudional, and Zheleznogorsk fault zones) were active, then they and their secondary faults around could be reflected in the landscape lineaments and, thus, provide at least small difference of the regional and local directional statistics. However, this is not observed reliably.

The rose-diagrams have two maxima of the strike of small photolineaments: sublatitudinal and submeridional. The sublatitudinal direction is associated mainly with the strike of sedimentary strata of the Mesozoic and, partly, of the Cenozoic age, which have a slope in the southern direction to the Dnieper Paleorift. Modern erosional forms of the Seim river valley also have a sublatitudinal strike. Thus, a certain advantage of this trend, which can be seen at all scale levels, is quite natural.

The second predominant direction of the elongation of rose diagrams is submeridional one. This direction of the lineaments is associated with the main strikes of the deep basement faults. It is possible that the submeridional linear elements of the modern relief may reflect some elements of the deep crustal structure associated with the submeridional faults of the Precambrian crystalline basement. This determines the predominance of the meridional beam for both global and local rose diagrams of small lineaments.

Figure 3 presents the results of a lineament analysis of a space image for a detailed area to the south-east of the Kursk NPP site (Fig. 1).

The Late Cretaceous flexure installed according the base of the Turonian deposits [1] is well expressed in lineament forms and in the Cretaceous section throughout the Kursk region. This Mesozoic flexure divides Kursk region into two structural blocks. These are Schigrovsky uplift in the northeast and the northern slope of the Dnieper paleorift in the southwest. The pattern of lineament forms is different in these blocks (Fig. 3). Lineament forms within detailed area are subparallel to the flexure strike, marking it from the southeast to northwest. Lineament forms have a closed ring character to the northeast of the flexure and that corresponds to the deep plan of the uplift. The Sublatitudinal fault crossing this block is expressed in lineament forms that mark the zone of its dynamic influence. Lineament forms mainly have a WSW strike to south-west of flexure. This direction is
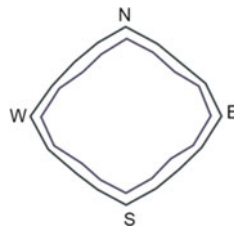
Fig. 2 Comparison of the regional rose-diagram (external contour) and rose-diagram of the detailed area (internal contour)
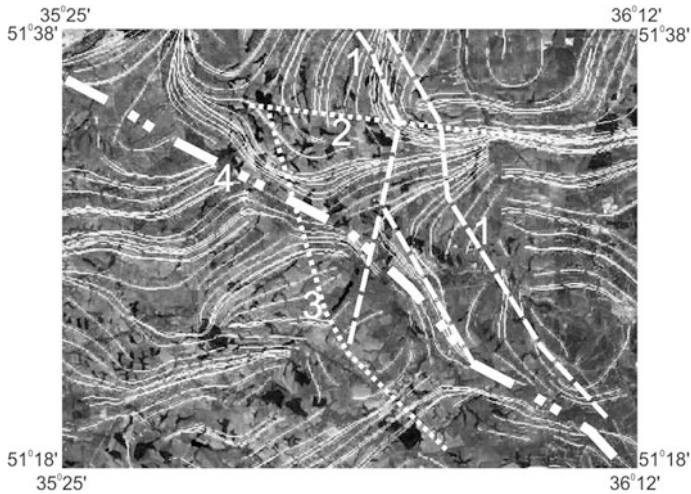
Fig. 3 Results of a lineament analysis of a space image for a fragment south-east of the Kursk NPP site. Zheleznogorsky (1), Sublatitudinal (2) and Nameless (3) faults (according geological survey) as well as Late Cretaceous flexure (4) and their relationship with lineament forms

orthogonal to the main Dnieper paleorift structures. The branches of the Zheleznogorsk fault are practically nowhere confirmed by the lineament forms, with the exception of a small area where the fragment of the Zheleznogorsk fault coincides with the flexure of the Mesozoic sedimentary cover. Therefore, we believe that exactly flexure is expressed in Fig. 3, and that it is not the fragment of the Zheleznogorsk fault coinciding with flexure in a small area.

The region of the location of the Kursk NPP is characterized by extremely small amplitudes (first tens of meters) of vertical movements during the Late Cenozoic [3], established by the stratigraphic method. Even the largest Precambrian faults of the crystalline base are not expressed in the sedimentary cover as faults or are manifested in it as very low-gradient flexural dislocations. The configuration of lineament forms obtained as a result of computer interpretation (Fig. 3) confirms the existence above-mentioned flexure, essentially the main Mesozoic fold structure of the region, in the modern field of lineaments. Based on the analysis of lineament forms, it can be said that only a fragment of the Sublatitudinal fault east of its intersection with the Zheleznogorsk fault is well expressed and thus possibly, has some resent activity. This conclusion corresponds with the results of field engineering and geological observations.

5 Seismic Data Analysis

Identification of the active tectonic structures within the low-activity platform area of the EEP is impossible without tracking changes that may be caused by human activities. The estimation of the seismic and geodynamic stability of the territory can be ensured by the registration of weak and micro earthquakes, reflecting the possible manifestations of both geodynamic and man-made processes. According to the catalog of the International Seismological Centre ISC (www.isc.ac.uk), from the beginning of 2000 to the end of 2018, about 1000 seismic events were recorded in the area of 400 km around the Kursk NPP site (gray dots on the Fig. 4).

Events do not contain an accurate assessment of the nature of their sources. Retrospectively, the division into man-made and tectonic nature for these events is quite difficult to carry out. Most of the events have highly likely explosive sources, because the time of their registration clearly fits into narrow intervals around 9–10 and 12 o'clock local time.

Since 2012, in the area where the Kursk NPP site is located, several organizations regularly conduct local seismic observations. As a rule, it is a network of seismic stations (from four to nine observation points at different times at different observation points). A small-aperture seismic array of IDG RAS twice (three
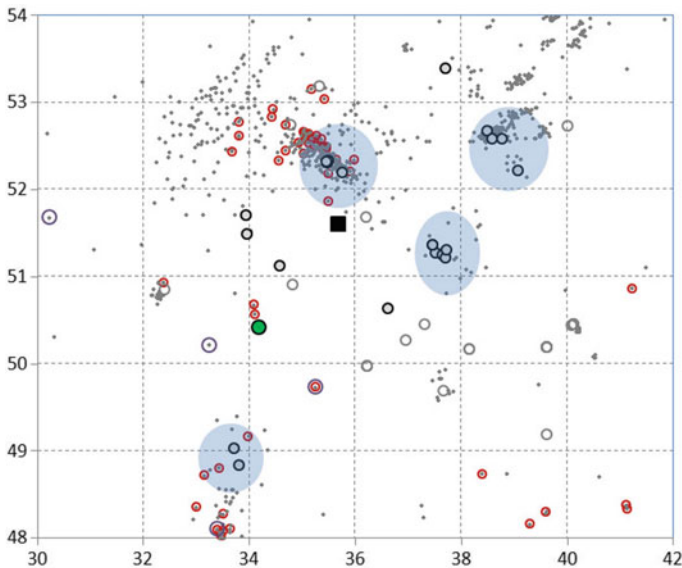
Fig. 4 Map of different seismic sources (earthquakes, quarry signals) epicenters of the Kursk NPP region. The black rectangle is the site of the Kursk NPP. The source of the Poltava event on 03.02.2015 (M 4.6) is highlighted in green; gray dots are the events appearing in the ISC catalog of seismic data from 01/01/2000 to 11/31/2018. Night events are circled in red. Gray circles with a black contour mark signals from explosions in quarries, registered by our small-aperture array. Gray highlighted areas are located around main well-known quarries

months in 2015 and four months in 2018) worked here. It was with its help that five very weak (with magnitudes M ∼ 0) seismic events were recorded and it was possible to locate their sources. This is certainly not enough to analyze the existing seismic situation. Local networks have not registered a single local seismic event of a tectonic nature for all this time. Existing data show that the maximum sensitivity of local observations was provided by a small-aperture array. It allowed in the study area to confidently record seismic events with magnitudes higher than 2.2–2.6. The sensitivity of seismic networks is even lower. However one should mention the seismic event M 3.8–4.0 that occurred in February 2015 in the Poltava region (Fig. 4). According to the ISC catalog, its parameters are M 3.8/4.6, depth is 3/10.0 km. According to the catalog of Geophysical Survey of RAS (www.ceme. gsras.ru) its depth is 10 km, mb 4.5/5. Unfortunately, the local observing system did not function at that moment, so the debate about its nature as for most platform events continues.

6   Discussion

The methods of computer lineament analysis have not established reliably signs of recent fault activity near the Kursk NPP site. An insignificant exception is the eastern fragment of the Sublatitudinal fault, which is marked by lineament forms expressed in the landscape. Comparing rose diagrams constructed from space images of different scales (10 and 30 m resolution), it can be noted that they are almost identical. This is interpreted as a statistical criterion for the absence of local deformations.

Weak fold deformations of the post-Turonian and post-Oligocene time are best expressed in lineament forms. That probably indicates their long development. The same weak fold deformations of the post-Oligocene time were established and estimated by the stratigraphic method according to the Poltava Miocene horizon taken as a stratigraphic frame. Post-Oligocene vertical movements of the Kursk NPP area range from −20 to +30 m and are slightly differentiated in space. The amplitude of movements is slightly different from the accuracy of the stratigraphic method (about 10 m) and the region can be classified as undoubtedly stable by these parameters. This result corresponds to most of the evaluations in previous works.

Thus: (a) the vertical deformations accumulated during the Cenozoic are relatively small (first tens of meters), not localized along any faults or protrusions of the basement; (b) the angular statistics of small photo-lineaments near the known large faults of the basement does not confirm their current activity; (c) analysis of geological sections based on drilling during geological surveys of various scales does not record displacements along faults, starting from the Late Cretaceous.

7   Conclusion

The results of automated interpretation of space images in combination with a stratigraphic method for evaluating Neogene-Quaternary vertical movements showed that the geodynamic setting of the Kursk NPP area is typical of stable platform regions with a tendency to slow and poorly differentiated uplift in conditions of regional compression not exceeding the strength limits of the main fault zones of the region. This situation does not imply any noticeable local seismicity, which is confirmed by the results of seismological observations. The advantages of automated lineament analysis lie in the greater objectivity of the method, the repeatability of the results and obtaining additional information about the structural features of the earth's crust which is inaccessible when examined by other methods due to a significant increase in statistical sampling.

Zheleznogorsk and Nameless faults closest to the Kursk NPP site do not exhibit tectonic activity in the Cenozoic The tectonic stability of the territory adjacent to the NPP and the stability of the Kursk megablock as a whole have been confirmed.

Despite the stability of the territory, permanent sensitive seismic monitoring is necessary for confident safety of the NPP site.

References

1. Drutskaya, S.V., Kononov, N.D.: Explanatory note to the geological maps of the Quaternary and sub-Quaternary sediments of the Kursk region. Scale 1: 500,000. Ministry Natural Resources RF. Moscow (2001) (in Russian)
2. Ivanchenko, G.N., Gorbunova, E.M.: Application of the remote sensing data of the area of the earth crust for analysis of the geodynamic situation. GEOS, Moscow (2015) (in Russian)
3. Ivanchenko, G.N., Malkin, B.V.: Evaluation of neotectonic deformations in the area of the Kursk NPP. Dyn. Process. Geosph. **9**, 32–41 (2017). (in Russian)
4. Makeev, V.M.: Structural and geodynamic conditions of stability of especially dangerous and technically complex objects on Precambrian platforms. Thesis for the degree of doctor of geol-min.sciences, Moscow (2014) (in Russian).
5. Mardia, K.V.: Statistics of Directional Data. Academic press, London (1972)
6. Zlatopolsky, A.: Program LESSA (Lineament extraction and stripe statistical analysis) Automated linear image features analysis—experimental results. Comput. Geosci. **18**(9), 1121–1126 (1992)
7. Zlatopolsky, A.A.: New Lessa technology resources and terrain map analysis. Methodology. Modern problems of remote sensing of the Earth from space **8**(3), 38–46 (2011) (in Russian)

Migration of Earth Surface Deformation as a Large Earthquake Trigger

Vladimir Kaftan and Andrey Melnikov

Abstract

The evolution of the horizontal deformations of the Earth's surface in the San Francisco region on a ten-year interval with a daily time resolution is investigated. The deformations of the total shear obtained from the data of permanent GPS observations are analyzed. The initial data are the time series of coordinate changes published by the Nevada Geodetic Laboratory of the University of Nevada, Reno. The evolution of the Earth's surface deformations is tracked using kinematic visualizations that demonstrate the change of the deformation field over time. The created animations make it possible to monitor the qualitative nature of the deformation in connection with the seismic process evolvement and fault tectonics. The region under study in recent years has been the subject of special attention due to possible occurrence of a strong earthquake. The visualization of the deformation process demonstrated the zones of activation and the propagation path of the deformation fronts. It is shown that the propagation of shear deformation, initiated from the epicenters of duplicate moderate earthquakes, migrates to the Napa Fault and provokes a major

V. Kaftan (✉)
The Geophysical Center of the Russian Academy of Sciences, Molodezhnaya St. 3, 119296 Moscow, Russia
e-mail: v.kaftan@gcras.ru

A. Melnikov
Peoples' Friendship University of Russia, Miklukho-Maklaya St. 6, 117198 Moscow, Russia
e-mail: acornum@mail.ru

earthquake. This phenomenon is regarded by the authors as a trigger for a seismic event. It is concluded that the Hayward Fault Zone is currently less seismically active as the most mobile one.

1 Introduction

Methods of observation of the Earth's surface movements and deformations using global navigation satellite systems are now being used more and more widely and efficiently. This is especially true for regions of high seismic activity, such as the US West Coast or the Japanese archipelago islands. Dense networks of continuous GNSS observations have been functioning for more than a decade in these regions. They contribute to the accumulation of significant amounts of data on the evolution of the Earth's surface deformations years before strong earthquakes at their occurrence places. In this regard, there is a special interest in the analysis of long-term changes in the deformation process in order to register possible deformation precursors and estimate the amount of the accumulated deformation before strong earthquakes.

1.1 Expecting a Strong Earthquake in the San Francisco Bay Area

The San Francisco Bay region is highly seismic, populous, and economically highly developed. It is prone to the strongest seismic events, the most destructive of which was the San Francisco earthquake of 1906 (M = 7.8). Today the region attracts special attention of scientists and representatives of the US government. The US Geological Survey (USGS) is leading a coalition to develop a HayWired strategic scenario and take appropriate measures [4, 5]. The probable consequences of a strong earthquake in the San Francisco Bay area of California are investigated. The name of the HayWired script refers to the Hayward Fault and is associated with possible blackout of numerous wired and wireless communications. The scenario predicts the consequences of a hypothetical earthquake M = 7+ (mainshock) and its aftershocks, confined to the Hayward Fault. The fault is located along the eastern water area of San Francisco Bay and is one of the most dangerous, as it passes through an urbanized region of developed wired communication system with a population of over seven million people. The HayWired theme is especially relevant for the region, where Silicon Valley and company leaders in high technology and digital communications are located.

2 Primary Data and Processing Results

In order to study the spatiotemporal evolution of the deformation of the Earth's surface in the studied region, a network of 52 continuously operating GPS (Fig. 1, left panel) stations from The California Real Time Network (CRTN) [http://sopac.ucsd.edu/crtn.shtml] is sampled. The data on the fault tectonics of the region obtained from the digital map of the geoportal of the US Geological Survey were used for tectonophysical interpretation [http://usgs.maps.arcgis.com/home/webmap/viewer.html?webmap=df1603b2bdd54615b6aa7c8d2b3f96ab]. Regional seismic data were obtained from the archive of the National Earthquake Information Center (NEIC) [https://earthquake.usgs.gov/contactus/golden/neic.php]. The deformations of the Earth's surface has been calculated using time series of daily solutions of GPS station coordinates, obtained from the open archive of the Nevada Geodetic Laboratory [1]. The observation interval is 4056 days, starting from January 16, 2006 to January 11, 2017. The coordinates were obtained by the Nevada Geodetic Laboratory from daily GPS solutions using the PPP (Precise Point Positioning) method with application of final GPS ephemeris by GIPSY OASIS II software, developed by the Jet Propulsion Laboratory (JPL). The standard errors of determining the coordinates obtained from internal convergence do not exceed the first millimeters. The coordinates of the stations are presented in the global reference frame IGS08.

Horizontal deformations were calculated for triangles of the Delaunay triangulation (Fig. 1, left panel). The strain tensor was used to calculate the finite element strain

$$T_\varepsilon = \begin{pmatrix} \varepsilon_n & \varepsilon_{ne} \\ \varepsilon_{en} & \varepsilon_e \end{pmatrix} \tag{1}$$

elements of which were $\varepsilon_n = \frac{\partial u_n}{\partial n}$, $\varepsilon_e = \frac{\partial u_e}{\partial e}$, and $\varepsilon_{en} = \varepsilon_{ne} = \frac{1}{2}\left(\frac{\partial u_n}{\partial e} + \frac{\partial u_e}{\partial n}\right)$, respectively, where $\frac{\partial u_n}{\partial e} + \frac{\partial u_e}{\partial n} = \gamma_{ne} = \gamma_{en}$ is shear deformation; u_n and u_e are displacements along coordinate axes n and e.

The following invariant characteristics were used to investigate the space–time distribution of horizontal deformations.

Principal strains ε_1 and ε_2.

$$\varepsilon_{1,2} = \frac{1}{2}\left[\varepsilon_n + \varepsilon_e \pm \sqrt{(\varepsilon_n - \varepsilon_e)^2 + \gamma_{ne}^2}\right] \tag{2}$$

Total sear strain $\gamma = ((\varepsilon_n - \varepsilon_e)^2 + \gamma_{ne}^2)^{1/2}$.

Dilatation $\Delta = \varepsilon_1 + \varepsilon_2$.

Maps of horizontal deformation fields were obtained for each day. Due to the substantial inequality of Delone triangles, the deformations are reduced to the average area of the triangle. The obtained frames were combined into a video film —kinematic animation of spatiotemporal changes of deformations [6]. The visual
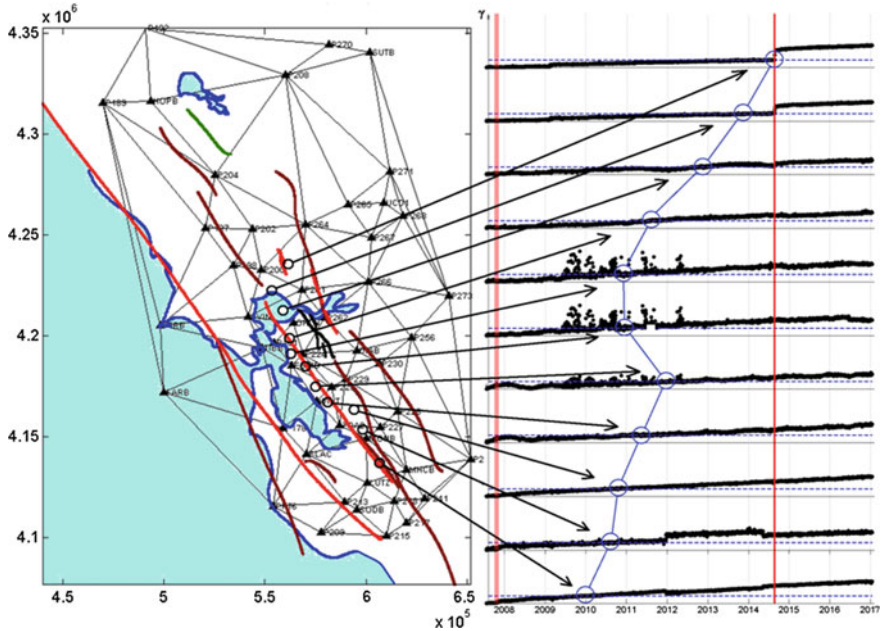
Fig. 1 Left panel: A network of permanent GPS stations in the study area. The vertices of the triangles of the Delaunay triangulation are the permanently operating GPS stations. Historical faults (<150 years) are red lines. Latest quaternary (<15,000 years), late quaternary (<130,000 years), and undifferentiated quaternary (<1.6 million years) faults are brown, green, and black lines. Blue color indicates the water areas. Map border coordinates are presented in UTM projection. Right panel: The time series of changes in deformation of the total shear in the corresponding triangles of the control network. The arrows indicate the correspondence of the triangles to the time series. The red vertical lines are the moments of moderate (left) and large (right) earthquakes. Blue circles and dashed lines indicate the level of accumulated deformation of the trigger $\gamma_c = 0.27 \cdot 10^{-5}$. The blue broken line shows the migration of critical strain from south to north along fault zones

analysis of such animations makes it possible to track the features and patterns of the evolution of deformations simultaneously with the evolvement of the seismic process and in relation to the fault tectonics.

A kinematic analysis of horizontal and vertical displacements, as well as dilatation deformations within the western coast of North America, is presented in [6, 7].

Below, we consider the evolution of the deformation of the total shear as the most indicative characteristic during the observations from July 20, 2007 to January 14, 2017.

3   Interpretation of the Results

The sparse sequence of frames of obtained kinematic animation is presented in Fig. 2. Observing the development of deformations, we can single out the following features.

The position of the source of the development of deformations (upper row in Fig. 2) practically coincides with the epicenters of duplicate moderate earthquakes near the Hayward Fault. Before the formation of the front of the accumulated deformation of the total shear, in one place and almost simultaneously one after another, two moderate earthquakes M = 5.45 and M = 5.6 occurred in the northern section of the Calaveras Fault (southeast of the territory in Fig. 2). The question then arises whether they have any genetic connection with the Napa earthquake.

Up until the Napa earthquake (2014 M = 6.02), the deformation front forms an elon-gated narrow zone. It spreads mainly along the Hayward Fault, reaching as a result the future epicenter of the Napa earthquake (Fig. 2, the 4th row from the top). The northern end of the front moved to the area of the future epicenter, reaching $0.27 \cdot 10^{-5}$ a day before the main shock.

The approximate speed of propagation of the deformation front was ~ 20 km/year.

After the Napa earthquake, the deformation front advanced more than 100 km to the northwest and southeast, passing the Hayward Fault continuation zone, but expanding to the west and east, encompassing the neighboring faults. At the beginning of 2017, the inelastic shear deformation in the region of the expected destructive earthquake [4, 5] reached a maximum value of $1.5 \cdot 10^{-5}$.

The recorded deformations are localized by fault lines. The most mobile was the Hayward Fault. Note that large (Napa M = 6.02) and moderate earthquakes were distributed east of the Hayward Fault. Weak events are distributed both along this "potentially dangerous" zone [5] and east of it. But four weak events also occurred on the locked San Andreas Fault exactly near the epicenter of the catastrophic earthquake of 1906.

4   Discussion and Conclusions

The first experimental evidence of the existence of surface deformation waves migrating from fault to fault is presented in the publications of Sidorov and Kuzmin. This phenomenon is explained by the autowave process. An estimate of their propagation velocity ranging from 1 to 100 km/year is given in [8]. Extensive reviews of theoretical and experimental studies of deformation waves, as well as their own results, are presented in Bykov and Trofimenko's works [2, 3, 11]. The authors estimated the speed of migration of various geophysical anomalies ranging from 100 to 1000 km/year [3]. The deformation trigger mechanism of seismic activity was considered in [10].

The results of a spatiotemporal analysis of shear deformations in the San Francisco region, obtained in our study, allow us to draw the following conclusions and assumptions.

Fig. 2 Spatiotemporal distribution of total shear deformation. Isolines are drawn through $0.25 \cdot 10^{-5}$. The big red star is the Napa earthquake M = 6.0. Small white stars are the strongest historical earthquakes. A small orange star is an expected catastrophic earthquake [4, 5]. Red circles are moderate earthquakes M = 5.4–5.6. Black dots are small earthquakes 3 < M < 5. For the legend of faults, see Fig. 1

The Earth's surface deformations are actively developing in the zone of expected future catastrophic earthquake [5] at the Hayward Fault. Total shear deformations have reached a significant magnitude of $1.5 \cdot 10^{-5}$ over the past 11 years. This maximum is located near the place of the expected destructive event [5].

The character of the propagation of the deformation front demonstrates the likely existence of a corresponding trigger mechanism. The deformation provokes the earthquake moving along the mobile fault, going over neighboring faults, avoiding the consolidated locked zones and reaching the mature source (area of critical elastic stress accumulation [5]) in the center of the study area (Fig. 3, left panel). In this case, the deformation wave triggered the 2014 Napa earthquake as visualizations show (Fig. 3, right panel).

The expected place of a future catastrophic event is the most mobile for ~ 10 years. This does not give a good reason for precise prediction of a strong earthquake for the next years-decades therein. Most likely, a strong earthquake can occur in places where there is no high recent mobility, similar to the Napa earthquake case [9]. For example, the San Andreas Fault zone affected by the deformation front for the past 40 years has been locked [12].

The region of maximum deformations in the zone of the expectation [4, 5] of the destructive event may indicate fluid circulation in the interblock space of this section of the Hayward Fault, contributing to the accelerated movement of the flanks in the directions of the main tectonic motions on the border of the North American and Pacific plates. Another explanation for this phenomenon may be a small coefficient of friction at the point of contact between the fault flanks. At the
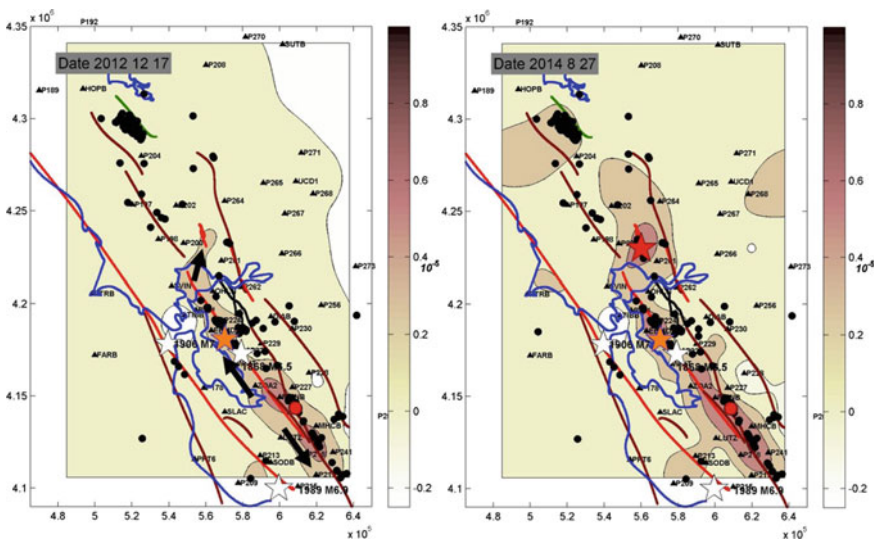
Fig. 3 Areal distribution of deformations of the total shear before (left panel) and on the third day after the large Napa earthquake (right panel). Black bold arrows indicate the direction of migration of the deformation front. For the rest of the figure captions, see Figs. 1 and 2

same time, the high mobility of the Hayward Fault, even in the absence of a strong earthquake, may have an undesirable effect on wired telecommunications in this area due to the relatively fast and continuous creep of its borders.

References

1. Blewitt, G., Hammond, W.C., Kreemer C.: Harnessing the GPS data explosion for interdisciplinary science. Eos **99** (2018). https://doi.org/10.1029/2018EO104623
2. Bykov, V.: Prediction and observation of strain waves in the earth. Geodyn. Tectonophys. **9** (3), 721–754 (2018). https://doi.org/10.5800/GT-2018-9-3-0369
3. Bykov, V., Trofimenko, S.: Slow strain waves in blocky geological media from GPS and seismological observations on the amurian plate. Nonlinear Process. Geophys. **23**, 467–475 (2016). https://doi.org/10.5194/npg-23-467-2016
4. Detweiler, S.T., Wein, A.M. (eds.): The HayWired Earthquake Scenario—Earthquake Hazards (Ver. 1.1, March 2018). U.S. Geological Survey Scientific Investigations Report 2017-5013-A-H, p. 126. https://doi.org/10.3133/sir20175013v1
5. Hudnut, K.W., Wein, A.M., Cox, D.A., Porter, K.A., Johnson, L.A., Perry, S.C., Bruce, J.L., LaPointe D.: The HayWired Earthquake Scenario—We Can Outsmart Disaster, vol. 3016, p. 6. U.S. Geological Survey, Fact Sheet 2018–3016 (2018). https://doi.org/10.3133/fs20183016
6. Kaftan, V., Melnikov, A.: Local deformation precursors of large earthquakes derived from GNSS observation data. In: IOP Conference Series Earth and Environmental Science, vol. 95, No. 3, p. 032030 (2017). https://doi.org/10.3133/fs20183016
7. Kaftan, V., Melnikov, A.: Revealing the deformation anomalies based on GNSS data in relation to the preparation and stress release of large earthquakes. Izvesti. Phys. Solid. Earth **54**(1), 22–32 (2018). https://doi.org/10.1134/S1069351318010093
8. Kuz'min, Yu.: Deformation autowaves in fault zones. Izvesti. Phys. Solid. Earth **48**(1), 1–16 (2012). https://doi.org/10.1134/s1069351312010089
9. Morozov, V., Kaftan, V., Tatarinov, V., Kolesnikov, I., Manevich, A., Melnikov, A.: Numerical modeling of the stress-strain state and results of GPS monitoring of the epicentral area of the August 24, 2014 earthquake (Napa, California, USA). Geotectonics **52**(5), 578–588 (2018). https://doi.org/10.1134/S0016852118040064
10. Sherman, S.I.: Deformation waves as a trigger mechanism of seismic activity in seismic zones of the continental lithosphere. Geodyn. Tectonophys. **4**(2), 83–117 (2013) (in Russian). https://doi.org/10.5800/GT-2013-4-2-0093
11. Trofimenko, S.V., Bykov, V.G., Grib, N.N.: Slow deformation waves in the seismic regime and geophysical fields at the northern margin of the Amur plate. Geodyn. Tectonophys. **9**(2), 413–426 (2018). https://doi.org/10.5800/GT-2018-9-2-0353
12. Wei, M., Kaneko, Y., Liu, Y., McGuire, J.J.: Episodic fault creep events in California controlled by shallow frictional heterogeneity. Nat. Geosci. **6**, 566–570 (2013). https://doi.org/10.1038/ngeo1835

Development of Geomechanical Model of the South Segment of Central Sakhalin Fault Zone

Pavel Kamenev, Leonid Bogomolov and Andrey Zabolotin

Abstract The geomechanical model has been developed. It describes the spatial distribution of stresses and strains and their temporal evolution for the southern part of the Central Sakhalin Fault. The boundaries of the model are the faces of a parallelepiped with sides of 150 km in the meridional direction, 60 km in the sublatitudinal direction and a depth of 30 km. Geographically, the model is confined to coordinates within 46.4°–47.4°N and 142.2°–142.8°E, the paper describes the main stages of creating a geomechanical model. The initial field data for the model are taken from the results of the deep seismic sounding, well logging, measurements with the GPS/GLONASS positioning, and seismological data. The model is divided into 8 layers in depth with different densities from 1.9 to 2.78 g/cm^3, Young's modulus from 1.2 to 44.9 GPa, and Poisson's ratio from 0.27 to 0.28. To estimate the details of deformation of the selected block of Central Sakhalin fault zone, the surface has been divided into 9 blocks with different strain rates from 0.5 to 2.3 mm/year. Stress values change with increasing depth in the range of 50 to 1500 MPa for σ_1, 30 to 1000 MPa for σ_2, and from 20 to 600 MPa for σ_3. The first results on the distribution of the stress-strain state in the fault area have been obtained.

P. Kamenev (✉) · L. Bogomolov · A. Zabolotin
Institute of Marine Geology and Geophysics FEB RAS, Nauki 1B, 693022
Yuzhno-Sakhalinsk, Russia
e-mail: p.kamenev@imgg.ru

79

1 Introduction

Sakhalin region is one of the most seismically active regions of Russia. Recently, as a result of earthquakes, the settlement of Neftegorsk and the city of Nevelsk were completely destroyed. Most of the population of the Sakhalin region lives in close proximity to the Central Sakhalin Fault (CSF), or rather the southern part of it (Fig. 1). Thus, observation of seismic activity, stresses and strains associated with it, as well as a possible seismic prediction, is a very keen task. A prerequisite for the creation of a geomechanical model of the active fault region was the results of a medium-term earthquake prediction using the LURR and self-developing process methods, which indicated the presence of a potential danger in the area of the southern CSF segment [1]. In addition to developing methods for medium-term forecasting, the team of the IMGG FEB RAS, together with other structural sub-divisions of the Russian Academy of Sciences and universities of the country, organized points of complex geophysical monitoring [2]. Nevertheless, it is an interesting task to study the distribution of strain and stress in the process of preparing a strong seismic event and after its occurrence. So, the authors attempted to create a geomechanical model of the southern part of the CSF, to simulate the distribution of the stress-strain state of the selected fault segment.

2 Main Data

The parallelepiped with the sides of 150 km in the meridional direction, 60 km in the sublatitudinal direction and a depth of 30 km gave the initial dimensions of the model. Geographically, the model is confined to coordinates within 46.4°–47.4°N and 142.2°–142.8°E. The Central-Sakhalin fault is represented by two branches—the western one (Tym-Poronaysky), the eastern one—Aprelovsky (Troitsky), which in some sources is considered as the feathering Tym-Poronaysky thrust [3]. The planes of displacers of both branches of the fault are inclined to the west at angles of 60–80°, when reaching the day surface with a gradual flattening to 20–30° at depths of 10–15 km. The western branch of the fault (Tym-Poronaysky) is expressed in relief in the form of a ledge up to 50–80 m high; shifts the pliocene-early quaternary and mid-quaternary leveling surface; along the fault plane, there is a plastic grease in the form of Bykovskaya formation, presented by claystone. The Aprelovskiy Fault (includes two contiguous discontinuities—Aprelovskaya and Klyuchevskaya) is well expressed in relief in the form of a tectonic ledge up to 20–40 m, the fault plane falls to the west at an angle of 75–85°. The rift separates the eastern foothills of the West Sakhalin Mountains from the Susunai Depression. Information about it is presented in [3]. It represents a clear boundary between the foothills zone and alluvial lake accumulative plain.
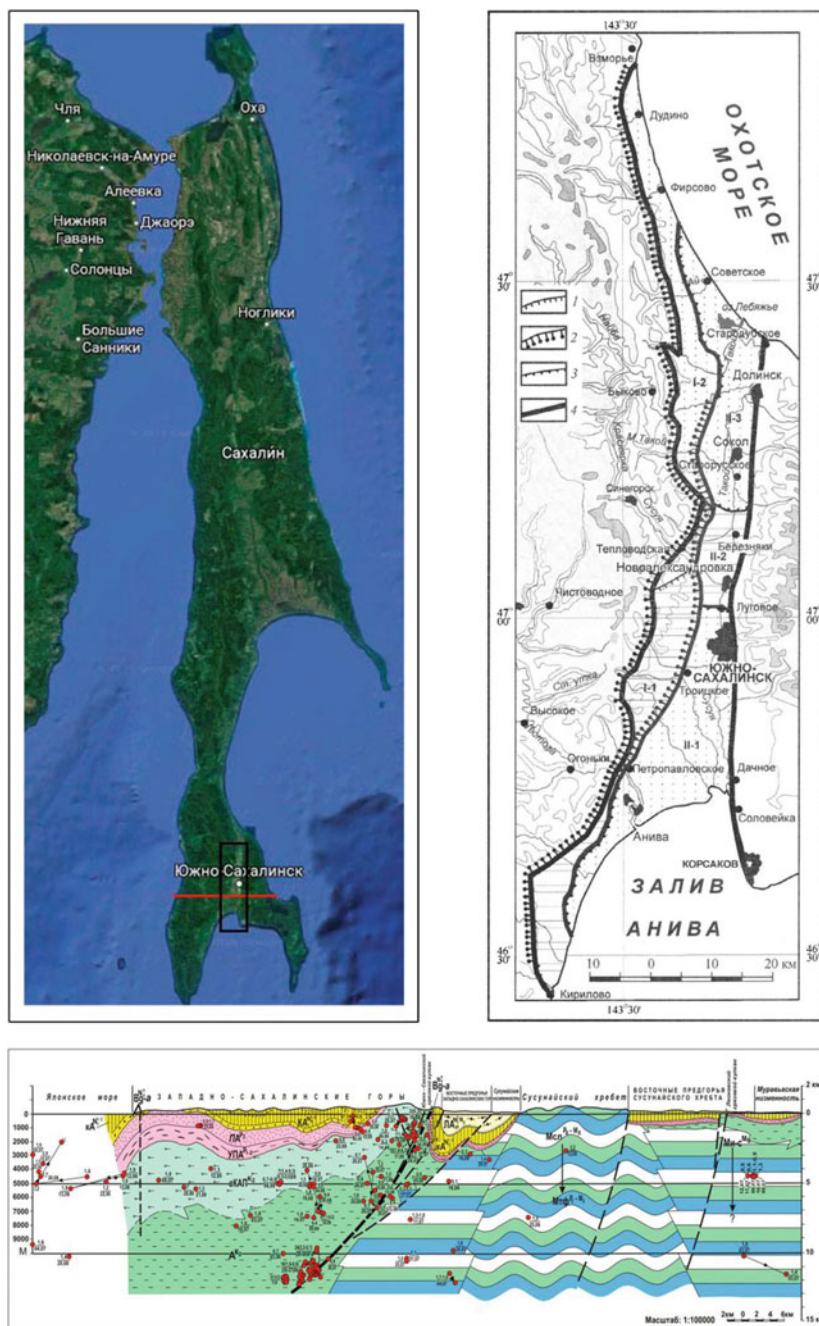
Fig. 1 The frames of the studied area in the Sakhalin (left), the layout of the faults (right) according to [8], a vertical cross-section of this zone (bottom) from [9]

The trenching of the Aprelovsky fault allowed to establish the western fall of the fault and to assume that earlier (about 1000 years ago) there could be shifts on the segments of this fault comparable in magnitude to the Neftegorsk and Uglegorsk-Ain earthquakes [4].

The strongest seismic events in the fault zone are as follows (from south to north): Krilonskie 1911, 1912, 1921. (M = 4.7–5.1); Anivskie 1951 (M = 5.5) and 1964 (M = 5.0); Perevalsko-Sinegorskie 1923 and 1924 (M = 4.5–4.8); Pereval-skoye, 1949 (M = 5.2) and Naybinskoye, 1928 (M = 4.9), Takoiskoye, 2001 (M = 5.2).

The initial field data for the model were taken from deep seismic sounding, well logging, measurements with the GPS/GLONASS positioning systems, and seismological data [5–7]. The model is divided into 8 layers to depth (H), with different densities ρ from 1.9 to 2.78 g/cm^3, Young's moduli E from 1.2 to 44.9 GPa, Poisson's coefficients μ from 0.27 to 0.28. Densities and geomechanical parameters were calculated basing on the data of the velocity model from [7]. The calculation of densities was performed using the ratio from [10].

The geomechanical parameters were calculated based on the phenomenological dependences of the corresponding parameters on the velocities V_p. [11, 12].

To estimate the deformation behavior of the selected CSF part, the surface was divided into 9 blocks with different strain rates from 0.5 to 2.3 mm/year. The source of the deformation data is the field measurements obtained in [6].

The selection of stresses acting in the area of the fault is made on the basis of systematization and synthesis of works [13–16]. Studies of the stress-strain state using instrumental methods have not been conducted in Sakhalin. The closest measurements were performed at the Nikolaevsky deposit of polymetallic ores in the Eastern Priamurye [14]. An excess of horizontal stresses over vertical ones was noted, with anisotropy of horizontal stresses. Maximum compressive stresses at a depth of down to 850 m are oriented along the azimuth of 340° and do not exceed 40 MPa. The deposit area is characterized by an increased seismic activity and a high velocity gradient of the latest vertical movements. The results of the work [11] based on the data on drilling deep wells were taken as a basis. Other data were obtained by extrapolating the stresses calculated in the upper intervals. The minimum horizontal stress was taken as the average value between the maximum horizontal and lithostatic stress taking into account the local geodynamics.

The lithostatic pressure in the geodynamic setting of the majority of Sakhalin territory, corresponds to the lowest of the main stresses defining the normal and shear components. This assumption is based on geodynamic conditions that determine the predominance of sublatitudinal compression as a result of the interaction of the Okhotsk Sea and Amur plates. The work on the World Stress Map project [16] on the stress map for the northeastern region of Eurasia shows a predominance of the horizontal compression mode, which manifests in mainly uplift movements in earthquake sources determined by solutions for focal mechanisms. The caliper data from the Piltun-Astokhskoye field [15], located in the north of Sakhalin, also show a predominance of horizontal stress (sublatitudinal compression) over the vertical one in the depth interval of 1800–2000 m. According to

[15], the walls of the well under study had pronounced collapses in two diametrically opposite angular sectors (ovalization), indicating the direction of the maximum compression—tension. All this confirms the relation of the main stresses $\sigma_1 > \sigma_2 > \sigma_3$, where σ_1—is the maximum horizontal stress (compression), σ_2 is the minimum of the two components of the horizontal stress and σ_3 is the vertical stress.

For the model being developed, the stress values change with increasing depth in the range of σ_1 from 50 to 1500 MPa, σ_2 from 30 to 1000 MPa, and σ_3 from 20 to 600 MPa. The summary characteristics of the distribution of geomechanical parameters and stresses with increasing depth in the southern part of the Central-Sakhalin fault are presented in Table 1.

For the model being developed, the stress values change with increasing depth in the range of 50 to 1500 MPa for σ_1, 30 to 1000 MPa for σ_2, and 20 to 600 MPa for σ_3. The summary characteristics of the distribution of geomechanical parameters and stresses with increasing depth in the southern part of the Central-Sakhalin fault are presented in Table 1.

The obtained values of horizontal and vertical stresses were compared to the results of studies of stresses in the superdeep wells Kolskaya SG-3 and KTB, and satisfactory agreement was observed. It should be noted that this paper does not take into account the effect of pore pressures.

The graphic model was created in the program COMSOL Multiphysics. The main work on modeling the stress-strain state of the selected CSF segment will also be carried out using this software package. The combined use of the geomechanical model, geophysical methods for monitoring the active fault area and the medium-term forecast using various methods allows identifying "problem" fracture areas, making optimal use of geophysical instrumentation for observations and significantly improving the accuracy of the medium-term forecast.

Table 1 Summary characteristics of the distribution of geomechanical parameters and stresses with increasing depth in the southern part of the Central-Sakhalin fault

H, km	E, GPa	μ	ρ, g/sm^3	σ_1, MPa	σ_2, MPa	σ_3, MPa
1	1.20	0.28	1.90	50	30	20
2	2.43	0.28	2.00	100	70	40
3	4.00	0.28	2.12	150	110	60
4	6.16	0.28	2.29	200	140	80
5	12.67	0.28	2.46	250	180	100
6	12.67	0.28	2.60	300	210	120
7	12.67	0.28	2.66	350	250	140
8	12.67	0.28	2.72	400	280	160
9	12.67	0.28	2.73	450	310	180
10	12.67	0.28	2.75	500	350	200
20	26.73	0.27	2.76	1000	700	400
30	44.95	0.27	2.78	1500	1000	600

3   Results and Discussions

The following assumptions were made in calculations of the intensity of shear stresses for a 10 year period for the initial model of the region under consideration, shown in Fig. 2:

1. Since the purpose of the work is a general assessment of the stress state of the medium, and in particular, determination of stresses at the fault, all geological layers are considered horizontal, and faults are treated according to the vertical cross—section of the medium from [9].
2. When calculating the stresses, we did not exclude the movement of the medium as a whole. Therefore free boundary conditions are set in the work at all external boundaries of the studied region.
3. Nine separate vertical areas with different horizontal velocities are distinguished according to [6]. These data are taken as the initial conditions for numerical implementation of the dependence on time (Fig. 2).
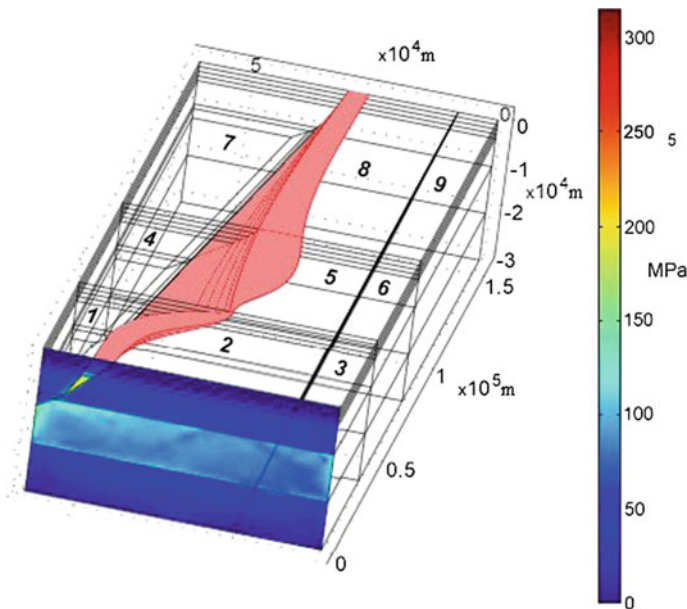
Fig. 2 The intensity of shear stress that formed in the 10th year according to the model of the region under consideration. The active fracture region is highlighted in red according to [8]. Numbers denote vertical areas with different horizontal velocities according to [6]. The following regions are distinguished: (1) Ve = 6 mm/a, Vn = 0.5 mm/a; (2) Ve = 8.3 mm/a, Vn = −0.4 mm/a; (3) Ve = 8.7 mm/a, Vn = −0.8 mm/a; (4) Ve = 6.9 mm/a, Vn = −0.4 mm/a; (5) Ve = 7.8 mm/a, Vn = −0.45 mm/a; (6) Ve = 8.5 mm/a, Vn = −0.5 mm/a; (7) Ve = 5.9 mm/a, Vn = 0.4 mm/a; (8) Ve = 8 mm/a, Vn = −0.4 mm/a; (9) Ve = 9 mm/a, Vn = −0.5 mm/a

4. Values of the principal stresses just inside the fault zone are assumed to be lower than in the enclosing massif over the entire fault depth (Fig. 2). Values of the main stresses were taken for the depth of 1 km, according to Table 1. This assumption is partially confirmed in [17], where it is shown that there is a linear dependence of the values of main stresses on depth.

Calculations of the excess tangential stresses arising in the considered area have shown that their maximum magnitude 'max' is concentrated in the fault zone. So, the maximum indicator is 289 MPa and it corresponds to the depth of 9 km and gradually decreases to the minimum indicator 'min' at the free surface.

4   Conclusion

The selection of boundary conditions, similarity conditions of the geological model, geomechanical parameters, of course, can distort the valid picture of the stress-strain state in the zone of the Central Sakhalin Fault and around it. Nevertheless, the obtained distributions of the intensity of shear stress correspond to the local geodynamic conditions, expressed in increased seismicity in the fault zone. The fact is that the majority of seismic events occur in the fault zone in the depth interval of the first ten kilometers. The combined use of the geomechanical model and geophysical methods for monitoring the active fault area allowed recognition of a fraction zone and significantly increased the accuracy of the medium-term predictions. This work reflects only the first stage of development of the geomechanical model of the Central-Sakhalin Fault as well as the first results obtained. The model adjustment (debugging and refinement) is to be continued in future.

References

1. Zakupin, A.S., Kamenev, P.A., Voronina, T.E., Boginskaya, N.V.: The estimation of seismic hazard in south part of Sakhalin for 2018 year (based on preliminary catalog). Geosystems Transit. Zones. **2**(1), 52–56 (2018). https://doi.org/10.30730/2541-8912.2018.2.1.052-056. (in Russian)
2. Makarov, E.O., Firstov, P.P., Kostylev, D.V., Rylov, E.S., Dudchenko, I.P.: First results of subsurface radon monitoring by network of points, operating in the test mode on the south of Sakhalin island. Vestnik KRAUNC. Fiz.-Mat. Nauki. **25**(5), 99–114 (2018). https://doi.org/10.18454/2079-6641-2018-25-5-99-114. (in Russian)
3. Kuchai, V.K.: The modern orogeny structure south part of Sakhalin Island. Russ. J. Pac. Geol. **6**(1), 50–57 (1987). (in Russian)
4. Bulgakov, R.F., Ivaschenko, A.I., Kim, Ch.U., Sergeev, K.F., Strel'tsov, M.I., Kozhurin, A.I., Besstrashnov, V.M., Strom, A.L., Suzuki, Y., Tsutsumi, H., Watanabe, M., Ueki, T., Shimamoto, T., Okumura, K., Goto, H., Kariya, Y.: Active faults in northeastern Sakhalin. Geotectonics **36**(3), 227 (2002)
5. Kamenev, P.A., Bogomolov, L.M., Valetov, S.A.: On estimatioin in situ of geomechanic parameters of sedimentary rocks from logging. Russ. J. Pac. Geol. **31**(6), 109–114 (2012). (in Russian)

6. Prytkov, A.S., Vasilenko, N.F.: Earth surface deformation of the Sakhalin Island from GPS data. Geodyn. Tectonophysi. **9**, 503–514 (2018). https://doi.org/10.5800/GT-2018-9-2-0358

7. Livshits, M.H.: Deep structure of Sakhalin based on geophysical data. Geophys. Dig. **24**, 16–25 (1972). (in Russian)

8. Voeikova, O.A., Nesmeyanov, S.A., Serebryakova, L.I.: Neotectonics and Active Faults of Sakhalin. Nauka, Moscow, 187 p. (2007). (in Russian)

9. The 2 August, 2007 Nevelsk Earthquake and Tsunami, Sakhalin Island. In: Levin, B.W., Tikhonov, I.N. (eds.), Yanus-K, Moscow (2009). (in Russian)

10. Gardner, G.H., Gardner, L.W., Gregory, A.R.: Formation velocity and density—The diagnostic basis for stratigraphic traps. Geophysics **39**(6), 2085–2095 (1974)

11. Kamenev, P.A., Usoltseva, O.M., Tsoi, P.A., Semenov, V.N., Sivolap, B.B.: Laboratory research of geomechanical parameters of sedimentary rocks massifs in the South Sakhalin. Geosystems Transit. Zones **1**(1), 30–36 (2017). https://doi.org/10.30730/2541-8912.2017.1.1. 030-036. (in Russian)

12. Kamenev, P.A., Zlobin, T.K.: Distribution of stress in lithosphere of Okhotsk sea area. In: Tectonics, Deep Structure and Geodinamics of East Asia, pp. 232–237. ITG, Khabarovsk (2003). (in Russian)

13. Kamenev, P.A., Bogomolov, L.M., Zakupin, A.S.: On the stress state of the Sakhalin crust according to the data of drilling deep boreholes. Russ. J. Pac. Geol. **11**(1), 25–33 (2017). https://doi.org/10.1134/S1819714017010043

14. Baryshnikov, V.D., Kurlenya, M.V., Leont'ev, A.V., Pirlya, K.V.: Stress-strain state of the Nikolaev deposit. J. Min. Sci. **18**(2), 3–12 (1982). (in Russian)

15. Ali, A.H.A., Marty, S., Esa, R., Ramamurty, R., Braun, T., Stuffer, T.: Advanced Hydraulic Fracturing Using Geomechanical Modeling and Rock Mechanics—An Engineered Integrated Approach. Oilfield Review Autumn (2002). https://www.slb.com/resources/oilfield_review/ ru/2002/or2002_ru_aut.aspx (in Russian)

16. Heidbach, O., Rajabi, M., Cui, X., Fuchs, K., Müller, K., Reinecker, B., Reiter, J., Tingay, K. M., Wenzel, F., Xie, F., Ziegler, M.O., Zoback, M.L., Zoback, M.D.: The world stress map database release 2016: crustal stress pattern across scales. Tectonophysics **744**, 484-498 (2018). https://doi.org/10.5880/wsm.2016.001

17. Pijush, P., Zoback, M.: Wellbore-stability study for the SAFOD borehole through the San Andreas fault. SPE Drill. Complet. **12**, 394–408 (2008)

Mathematical Modeling of Dynamic Processes in Seismic Activity Zones

Alexandr Kim 🄳, Yuriy Shpadi 🄳 and Yuriy Litvinov 🄳

Abstract Mathematical modeling of wave processes in a tense medium in the event of a sudden rupture with contacting banks was carried out using an analytical solution by Kim A.S. for a dynamic problem simulating the process of an earthquake. The displacement field in the zone of final rupture with viscous contact of the banks is obtained. The results of numerical analysis confirm the theoretical conclusions about the presence of a time interval during which the influence of the ends of the rupture on the movement of its banks can be neglected, and this time interval increases with increasing viscosity at the rupture. A computer visualization of the development in time of the total field of displacements in the focal zone was carried out, taking into account the field of repeated cylindrical waves, when a complete release of stresses occurs at the final rupture. It has been established that on the trunk rupture, reverse displacements of the banks of the rupture can occur, and the total displacement field in the rupture zone tends to its static state.

A. Kim (✉) · Y. Litvinov
Institute of Ionosphere, 050020 Almaty, Kazakhstan
e-mail: kim.as@mail.ru

Y. Shpadi
Institute of Space Techniques and Technologies, 050061 Almaty, Kazakhstan

1 Introduction

The article addresses to mathematical and computer modeling of dynamic processes in the focal zone of an earthquake simulated by a stressed medium with a rupture.

In the geospheres of the Earth, including its hard shell, complex dynamic and quasistatic processes occur. The processes currently attract much attention, because it is necessary to predict natural phenomena on our planet. Among such studies, an important place is taken by studies of non-stationary processes in the focal zones of earthquakes, calculations of vertical and horizontal movements of the Earth's surface, the studies of dynamics of block structures and faults [1, 2], which control the migration of seismic activity, filtration of fluids and rock destruction. These studies are also relevant for the analysis of lithospheric–ionospheric interactions, which are manifested in the response of the ionosphere to dynamic and quasistatic processes in the focal zones of the Earth's crust [3, 4], that precede and accompany destructive earthquakes.

Centers of tectonic earthquakes are located at great depths and are not accessible to direct observations, and therefore they play an important role in the research methods of mathematical and computer modeling of processes in the focal zones. Theoretical studies of non-stationary processes in a stressed environment, accompanying the occurrence of the rupture, were carried out in [5–8]. The dynamic problem of the rupture in a prestressed elastic medium is solved for the far zone or under the assumption of absence of interaction of its banks [7, 8]. Experiments [9–12] indicate the need to take into account the contact interaction of the rupture banks. In this article, we study the dynamic processes in the near focal zone of an earthquake using mathematical and computer modeling and visualization.

2 The Problem of Dynamic Processes in a Prestressed Environment with Sudden Appearance of a Semi-infinite Rupture

Suppose that in an elastic isotropic pre-stressed space with a uniformly distributed tangential stress $\tau_{yz}^p = q_p$, at instant $t_p = 0$, there is an instantaneous rupture of the continuity of the medium along the half-plane $y_p = 0$, $x_p < 0$, when contact conditions change instantaneously at a discontinuity. We assume that in the plane of the rupture at $t_p > 0$, viscous contact conditions suddenly appear [5, 13]:

$$
\left.
\begin{aligned}
\tau_{yz}^p &= q_p, && \text{при} \quad t_p < 0 \\
\tau_{yz}^p &= \eta_p \frac{\partial a_p}{\partial t_p}, && \text{при} \quad t_p > 0 \\
a_p &= 0, && \text{при} \quad t_p = 0
\end{aligned}
\right\}, \quad y_p = 0, \quad x_p < 0
\tag{1}
$$

$$a_p = w_p(x_p, +0, t_p) - w_p(x_p, -0, t_p) = \left[w_p(x_p, y_p, t_p) \right]_{y_p=0}. \tag{2}$$

Here: w_p is a non-zero displacement component; η_p is the coefficient of effective viscosity at the rupture; a_p is the value of mutual displacements of the rupture coasts; x_p, y_p—coordinates; t_p—time.

This problem was solved analytically by Kim [13, 14]. The solution is obtained for the second derivative of time displacements and is a superposition of plane and cylindrical waves. In the dimensionless form, the solution has the form [13]:

$$\frac{\partial^2 w(r,\theta,t;\eta)}{\partial t^2} = \Delta_\text{ц}(r,\theta,t;\eta) + \Delta_\text{пл}(r,\theta,t;\eta), \tag{3}$$

$$\Delta_\text{ц}(r,\theta,t;\eta) = \frac{1}{\pi} \frac{q}{1+2\eta} \frac{H(t-r)}{\sqrt{t^2-r^2}} \text{Re}\left\{ \text{tg}\, \zeta_0 e^{-g(\zeta_0)} \right\}, \tag{4}$$

$$\Delta_\text{пл}(r,\theta,t;\eta) = \frac{q}{1+2\eta} \delta(t-r\sin\theta) H\left(\theta - \frac{\pi}{2} \right), \tag{5}$$

$$g(\zeta_0) = \frac{1}{\pi} \int_{\frac{\pi}{2}}^{\zeta_0} \frac{\eta\zeta - \frac{1}{2}\arccos(-v)\sin\zeta}{v+\cos\zeta} - \frac{1}{\pi} \int_{\frac{\pi}{2}}^{\zeta_0} \frac{\eta\zeta - \frac{1}{2}\arccos v \sin\zeta}{v-\cos\zeta}, \tag{6}$$

$$\zeta_0 = \theta + i\xi_0, \quad \xi_0 = \ln\frac{t+\sqrt{t^2-r^2}}{r}, \quad H(\xi) = \begin{cases} 1, & \xi > 0 \\ \frac{1}{2}, & \xi = 0, \\ 0. & \xi < 0 \end{cases}$$

$$i = \sqrt{-1}, \quad v = \sqrt{1-4\eta^2}, \quad d = \sqrt{4\eta^2-1}, \quad v = -id, \tag{7}$$

$$0 < r < \infty, \quad 0 < \theta < \pi, \quad -\infty < t < \infty, \quad 0 < \eta < \infty,$$

$\delta(\xi)$—Dirac delta function.

Formulas (3)–(7) represent the solution of the problem of nonstationary processes in a stressed medium with the sudden appearance of a semi-infinite rupture. Dimensional quantities are related to the dimensionless ones by the following ratios:

$$w_p = w_s^p + w_d^p; \quad w_s^p = \frac{q_p y_p}{\mu}; \quad q_p = \mu q, \quad \eta_p = \frac{\mu\eta}{b}; \quad t_p = \frac{Lt}{b},$$

$$(x_p, y_p, w_d^p) = L(x, y, w); \quad x = r\cos\theta, \quad x = r\sin\theta, \tag{8}$$

where: μ—shear modulus, b—velocity of transverse waves, L—scale factor.

3   Dynamic Processes in the Focal Zone in Case of a Sudden Rupture with a Viscous Contact of the Coasts

The general case of the study of non-stationary processes occurring in a stressed medium in the event of a sudden rupture with a viscous contact of the coasts is based on the analytical solution (3)–(7). All calculations were carried out in dimensionless form.

At time $0 < t < 1$ the total displacement field consists of three terms: a cylindrical wave from the left edge of the gap $w^1(-x-1, y, t)$, a cylindrical wave from the right edge of the rupture $w^1(x, y, t)$ and a plane wave $w_0(x, y, t)$ extending from the plane of rupture $y = 0$, $-1 < x < 0$ at the moment of its occurrence. The cylindrical wave $w^1(x, y, t)$ is given by the formula (3).

$$w(x, y, t) = w^1(x, y, t) + w^1(-x - 1, y, t) + w_0(x, y, t), \tag{9}$$

$$w_0 = \frac{q}{1 + 2\eta}(t - y)H(t - y)H(-x)H(1 + x). \tag{10}$$

The following are the results of a numerical experiment when first-order cylindrical waves from both ends of the rupture with a viscous contact of the banks are taken into account. All calculations were carried out in dimensionless form. Dimensional quantities are linearly related to dimensionless parameters [13].

Figure 1 shows the displacements at the rupture and in its vicinity at the time $t = 1$ with the contact interaction coefficient at the rupture $\eta = 1$.

Fig. 1 Discontinuous displacement at the fault $-2 \le x \le 1$, $0 \le y \le 1$ for $\eta = 1$, $t = 1.0$
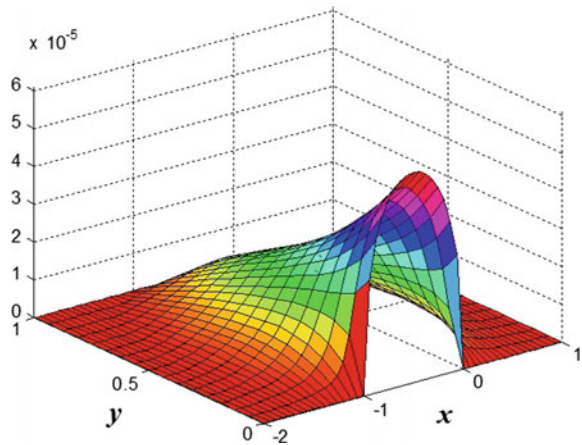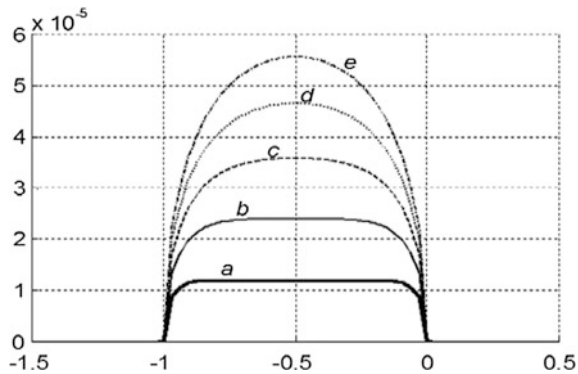
Fig. 2 Discontinuous displacements on the line $y = 0$ for $\eta = 1$ at time points: **a** $t = 0.2$, **b** $t = 0.4$, **c** $t = 0.6$, **d** $t = 0.8$, **e** $t = 1.0$

Figure 2 shows the displacements at the rupture at different points in time, where the displacement plots are given vertically, and the location of the rupture is horizontal.

As follows from the results of the numerical analysis presented in Figs. 1 and 2, the influence of the ends of the rupture on the displacements of its coasts occurs with some delay, during which the influence of the ends of the rupture on the movement of the coasts can be neglected.

4 The Field of Displacements in the Focal Zone with a Complete Discharge of Stresses at the Rupture with a Superposition with a Field of Displacements in a Third-Order Wave

Nonstationary processes in the focal zones of the Earth's crust have been studied using mathematical and computer modeling methods. An analytical solution has been constructed for the dynamic problem of non-stationary processes in a stressed medium with a sudden appearance of a finite discontinuity with complete discharge of stresses at the rupture. The analytical solution is expressed in terms of elementary and special functions. When obtaining an analytical solution, spectral methods were used. The initial problem was reduced to a problem with homogeneous boundary conditions at the boundaries, for which eigenvalues and eigenfunctions were obtained, and the solution was written in the form of the corresponding series. Using the Fourier–Bessel transform and identities for the Bessel functions, calculated formulas are obtained and invoked for numerical analysis.

As a result of numerical-analytical calculations, we obtained the displacement field at the rupture and in the focal zone. The patterns of seismic wave propagation are determined. The field of secondary cylindrical waves was determined and there

was obtained a computer-generated visualization of the development in time of the total field of displacements in the focal zone in the event of a sudden appearance of a finite rupture with a complete discharge of stresses at the rupture (with due consideration of field of secondary cylindrical waves). As a result of numerical calculations and computer visualization, it has been established that reverse banks of the banks may occur on the trunk rupture.

At time $0 < t < 1$, the total displacement field consists of three terms: a cylindrical wave from the left edge of the rupture, a cylindrical wave from the right edge of the rupture, and a plane wave extending from the plane of the rupture $y = 0$, $-1 < x < 0$—at its moment occurrence. When $1 < t < 2$, it is necessary to take into account the displacement field in second-order cylindrical waves, the total displacement field in this case consists of five terms: a cylindrical wave from the left edge of the rupture, a cylindrical wave from the right edge of the rupture, a plane wave, a cylindrical wave of the second order from the left and a cylindrical wave of the right edge of the rupture.

Figure 3 shows the disturbed zone at $2 < t < 3$, when third-order repeated reflected waves occur. Solid lines indicate cylindrical wave fronts from the right edge, and dashed lines indicate wave fronts from the left edge of the break. Line (a) indicates the front of a cylindrical wave of the first order, line (b)—the front of a cylindrical wave of the second order, (c)—the front of a wave of the third order, segment MN denotes the front of a plane wave; $0 < t_1 < 1$, $t_2 = 1 + t_1$, $t_3 = 1 + t_2$.

An initial boundary value was posed and the problem was solved for the field of displacements of repeated cylindrical waves. An nth order cylindrical wave for the right edge of the rupture is obtained as

$$u_n(r, \theta, t) = \sum_{k=0}^{\infty} u_k^n(r, t) \sin \frac{2(k+1)\theta}{2} \tag{11}$$

$$u_k^n(r, t) = \frac{2\lambda_k}{\pi} \int_0^t d\tau \int_0^\infty \frac{g_n(\xi, \tau)}{\xi} d\xi \int_0^\infty J_{\lambda_k}(rs) J_{\lambda_k}(\xi s) \sin s(t - \tau) ds. \tag{12}$$
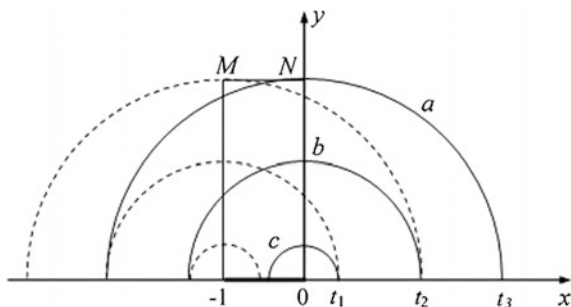
Fig. 3 Perturbed near-fault zone at $2 < t < 3$
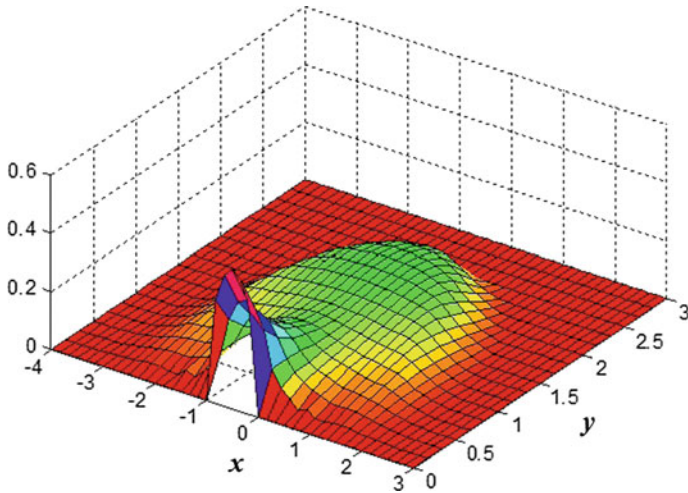
Fig. 4 The displacement field in the vicinity of the discontinuity at $t = 2.5$

The function $g_n(\xi, \tau)$ is determined recurrently through $g_{n-1}(\xi, \tau)$ for a cylindrical wave of the previous order $(n = 1, 2, 3, \ldots)$. For the left edge of the rupture, a cylindrical wave is obtained by mirror reflection about the middle of the rupture. On the basis of analytical formulas for displacements (11), under condition (12), the process of seismic wave propagation from the source was visualized, taking into account the displacement field in repeated waves up to the third order. The visualization of dynamic processes shows that the displacement of the coasts of the rupture first increases, reaching a certain maximum, then they begin to decline indicating their inverse movement of the rupture coasts.

Figure 4 shows the displacement field with regard to third-order repeated cylindrical waves at time $t = 2.5$.

The animation of the displacement field in the rupture zone is presented in the video KimAS_Video.mp4.

5 Conclusion

An analytical solution and numerical calculations of displacements in the source zone for primary and secondary seismic waves for the case of a suddenly occurring limited rupture with a viscous contact of the coasts are presented.

Numerical calculations and computer visualization of displacements in the focal zone were carried out under the condition of complete relief of stresses at the rupture, taking into account repeated cylindrical waves of the first, second and third order. The results of computer visualization of the dynamic process with due

consideration of second and third order waves evidence that reverse displacements of the rupture coasts can occur at the rupture, and the total displacement field in the rupture zone tends to its static state.

References

1. Adushkin, V.: Actual problems of geomechanics crust. Electron. Sci. Inf. J. **1**(16), 1–33 (2001) (in Russian), Bulletin of the OGGGGN RAS
2. Kocharyan, G., Ostapchuk, A., Markov, V., Pavlov, D.: Some problems of geomechanics of the continental crust faults. Fiz. Earth **3**, 51–64 (2014) (in Russian)
3. Hayakawa, M.: On the fluctuation spectra of seismo-electromagnetic phenomena. Nat. Hazards Earth Syst. Sci. **301**(11), 301–308 (2011). https://doi.org/10.5194/nhess-11-301-2011
4. Namgaladze, A., Klimenko, M., Klimenko, V., Zakharenkova, I.: Physical mechanism and mathematical modeling of earthquake ionospheric precursors registered in total electron content. Geomagn. Aeron. **49**(2), 252–262 (2009). https://doi.org/10.1134/s0016793209020169
5. Kim, A.: Mechanics of Non-stationary Processes in the Focal Zones of the Earth's Crust. Publisher Gylym Ordasy, Almaty (2017) (in Russian)
6. Martynyuk, P.: On the Dynamic Loading of a Half-Plane with a Crack Under Conditions of Antiplane Deformation, vol. 22, pp. 216–230. Continuum Dynamics, Novosibirsk (1975) (in Russian)
7. Fleetman, L.: Waves caused by the instantaneous discontinuity of the elastic medium. J.: Appl. Math. Mech. **27**(4), 618–628 (1963) (in Russian)
8. Richards, P.: Dynamic motions near an earthquake fault a three-dimensional solution. Bull. Seismol. Soc. Am. **66**(1), 1–32 (1976)
9. Dragoni, M., Santini, S.: A two-asperity fault model with wave radiation. Phys. Earth Planet. Inter. **248**, 83–89 (2015)
10. Wu, F., Thomson, K., Kuenzler, H.: Stick-slip propagation velocity and seismic source mechanism. Bull. Seismol. Soc. Am. **62**(6), 1621–1628 (1972)
11. Chang, K., Segall, P.: Injection-induced seismicity on basement faults including poroelastic stressing. J. Gephys. Res. **121**(4), 2708–2726 (2016). https://doi.org/10.1002/2015JB012561
12. Zhang, H., Ge, Z.: Rupture pattern of the Oct 23, 2011 Van-Merke Eastern Turkey earthquake. Earthq. Sci. **27**(3), 257–264 (2014)
13. Kim, A.: On shear waves in the focal zone in case of a sudden rupture. In: Proceedings of the Scientific and Technical Society KAHAK, vol. 2, pp. 4–31 (2015) (in Russian)
14. Kim, A.: Non-stationary processes in nidal zone at sudden appearance of break. In: The 24th International Congress of Theoretical and Applied Mechanics (ICTAM-2016), Book of Papers, pp. 2263–2264. Montréal, Canada (2016)

Effect of Multiple Weak Impacts on Evolution of Stresses and Strains in Geo-materials

Vladimir Kosykh

Abstract

The paper describes experimental findings on stresses and strains in specimens made of an equivalent geo-material and subjected to static compression and multiple weak impacts. Against the background of gradual increase in the total compressional strain, the specimen area adjacent to the impact point is first compressed and then stretches. The temporal variations in strains are non-monotonous but fluctuate relative to the general trend. Weak impacts initiate a slow deformation wave at a rate of 8.8 mm/h in the specimen. The initial compression stress decreases non-monotonously with time, too. There are areas of both rise and drop of the stress. On the whole, the specimen periodically accumulates and releases elastic energy in the course of the whole loading experiment. The aforementioned behavior has the following qualitative explanation. Weak impacts, which act on the background of pre-limited static stress, lead to irreversible micro-strain between structural elements (grains) of the sample. This effect is accumulated in the form of sample macrostrain with time.

Keywords

Geomaterial · Loading experiment · Weak impacts · Inhomogeneous behavior · Energy accumulation · Slow deformation wave

V. Kosykh (✉)
Chinakal Institute of Mining, Siberian Branch, Russian Academy of Sciences, 630091 Novosibirsk, Russia
e-mail: v-kosykh@yandex.ru

1   Introduction

A real rock mass experiences cyclical dynamic loading against the background of static stresses. Such loading may be represented by the effects of tides, atmospheric pressure, seismicity, mining, etc. The strength and deformation characteristics of rocks depend on their chemical composition and internal structure, as well as on the external environment: temperature, type of stress state, duration of loading, number of loading cycles, etc.

Under long-term static loading, rocks display their rheological properties—creep and stress relief [1, 2]. Cycling of long-term stresses results in fatigue failure of rocks [3]. A strong dynamic impact (explosion) provokes an alternating response in the form of the sign change of stresses after each blast [4]. Weak vibrations have influence on the behavior of plastic strains and initiate failure-governing effects— concentration or relief of stresses at discontinuities [5, 6]. Microseismic vibrations trigger seismic activity [7, 8]. Under certain loading conditions, rocks can accumulate and release elastic energy, which is governed by their internal block–grain structure, elasticity of the blocks and their relative slip [9–11]. Weak but long-term dynamic impacts can invoke irreversible strains in fractured rocks. The internal structure facilitates energy accumulation, the external impacts liberate this energy, or, vice versa, the energy of these impacts accumulates in rock mass [12, 13]. The medium evolves between equilibrium states.

This study focuses on accumulation and release of elastic energy from specimens made of equivalent geomaterials with cohesion, subjected to loading with static compressive stresses and periodic weak impacts.

2   Experimental Procedure

The tests were carried out on tube specimens made of a mixture of acrylic gypsum (ecoresin), sized quartz sand particles of 0.3 mm and water at a ratio of: 100 : 100 : 28.

The sample presents a solid body made in the form of a hollow tube, which was caused by the design of the stand clamps, providing, along with axial compression, the loading of the sample by the torque. In the present work, we restricted ourselves to compression loading.

Ecoresin was placed in water with continuous stirring to make a uniform blend, then, keeping stirring, sand was gradually added. The ready mix was formed, and air bubbles were removed from it using a vacuum pump. The solidified specimen was dried under room temperature for a day and, after that, under 180 °C for 2 h.

The specimen had a tube shape with the overall length of 120 mm, including the operating length of 95 mm. The outer and inner diameters were 37 and 15.4 mm.

In order to measure longitudinal static deformation, 4 foil strain gages BF100-3AA with active gage length of 3 mm and resistance of 100 Ω were pasted in line on the side surface along specimen axis by glue BFR-2 K. The gages were arranged at equal spacing of 24 mm relative to each other. After drying for 3 h, the specimens were heated up to 160 °C and held under that temperature within 3 h and, then, under 190–200 °C within 7 h.

The prepared specimens had the ultimate compression strength of 12–14 MPa and elasticity modulus of 5.8–6.2 GPa.

The test bench enabled tracing the evolution of strength and deformation characteristics in geomaterials under weak impact against the background of the preset static load.

Figure 1 shows the loading assembly of the test bench. The geomaterial specimen 3 is fixed in the grippers 1 and 4. The left-hand gripper 1 is fastened on the vertical plate using the membrane 2 and is centered by a fluoroplastic sleeve. The right-hand gripper 4 is also centered by means of a fluoroplastic sleeve and transmits compression from the screw 5, via a ball, to the specimen. The vertical plates are dead placed on the solid basis 6. The dynamic effect on the specimen during the tests can be exerted by delivering certain energy blows to the tail of the gripper 1. The measurement facility of the test bench is represented by the crate system LTR-EU-8-2 of L-Card for the continuous gathering of data from the strain gages. The detailed description of the test bench is given in [12, 13].

A specimen was immobilized in the grippers using the same ecoresin and quartz sand mixture. The test bench with the specimen was placed in a thermostatic oven and held for two days at the temperature of 24 ± 0.1 °C. Then, after the specimen was screw-loaded by the compressive stress of 6 MPa (∼0.5 of the ultimate strength), the impact device was activated. The blow energy was 0.08 J, and the blow frequency was 2 Hz. During the experiment lasting for more than 700 h static strains and compressive stresses were continuously recorded.
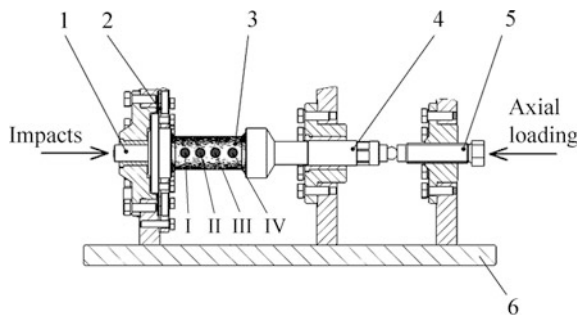
Fig. 1 Test bench: 1—mobile gripper; 2—membrane; 3—specimen; 4—immobile gripper; 5—loading screw; 6—basis

3   Experimental Results

The experiments produce the strain curves of specimens subjected to concurrent compression and weak impacting. The total strain is a sum of the initial strain ε_0 of static loading and the slowly increasing strain ε_t. In the tests, the average $\bar{\varepsilon}_0$ from the readings of 4 sensors glued on the specimen (Fig. 1) makes 1.68×10^{-3}. The curves of the average $\bar{\varepsilon}_t$ and time are presented in Fig. 2. The compressional strains are assumed to be positive.

As is seen in Fig. 2a, $\bar{\varepsilon}_t$ grows during the experiment (~ 700 h) up to 2.5×10^{-5}. The growth is non-monotonous. The curve has sections of opposite increment in the strain, such as the line between 500 and 600 h, i.e. the specimen draws up in these sections. The behavior of the stress conforms with the change in $\bar{\varepsilon}_t$: against the background of the general decrease in the stresses, there are sections of their local increase (Fig. 2b).

The variation in the strain along the length of specimens with time is illustrated in Fig. 3. The ordinate axis shows the current values of ε_t with the deducted initial strains ε_0; the abscissa axis is the time. The Roman numerals are the numbers of the strain gages with regard to their distance from the impact source (Fig. 1).

It is apparent in Fig. 3 that the local longitudinal strains change non-uniformly along the length of specimens. For example, the compressional strain velocities measured by strain gages II–IV disagree (the strain curves part). Moreover, the increase in the local strains with time is non-monotonous. The curves are undulating though similar. Deformation of the specimen nearby the strain gage I is of different nature. After compression for 180 h, the strain increment changes sign, i.e. compression in this part of the specimen reduces with time.
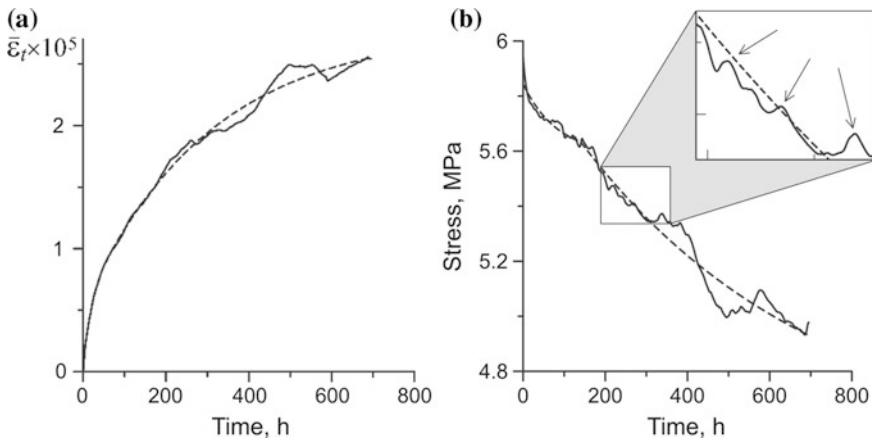
Fig. 2 Time dependences of **a** average strain ε_t and **b** stress of specimen

Fig. 3 Variation in strains with a distance from the impacted side of the specimen with respect to time
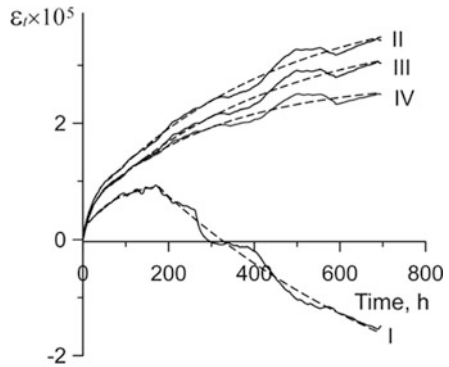
Under initial loading of specimens, the test bench accumulates the elastic energy as well. During impacts, the energy is spent for deformation of a specimen. The deformation power W per unit volume of a specimen can be given by $W = \sigma \cdot \dot{\varepsilon}_t$, where $\dot{\varepsilon}_t$ is the rate of increment in the longitudinal strains of specimens.

Figure 4 shows the plots of W in the vicinity of strain gages I–IV on the specimen surface.

The deformation power curve plotted from the readings of gage I mostly lies in the area of negative values (Fig. 4, curve I). This means that the specimen vicinity of this gage releases energy. The specimen areas in the vicinity of gages II–IV absorb energy in the most of time (Fig. 4, curves II–IV). The deformation power is positive.

Thus, the specimen releases the accumulated elastic energy on the side of impacts and accumulates energy on the opposite side. During the test time, the specimen dissipates the elastic energy accumulated in the specimen–test bench system under initial loading, which results in the increase of the average strain and in the drop of the stresses in the specimen.
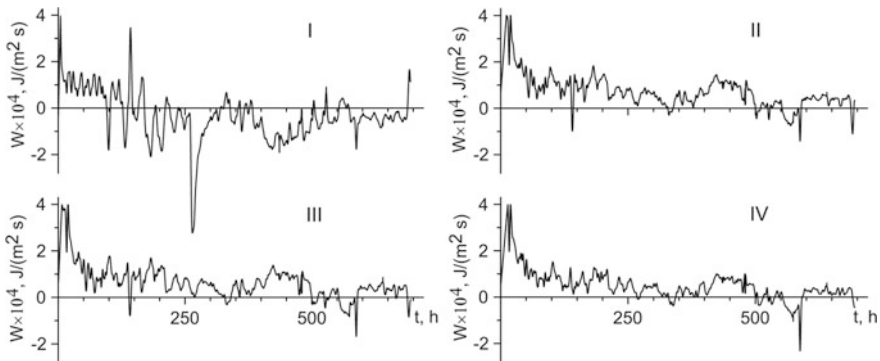
Fig. 4 Change in deformation power along specimen with time
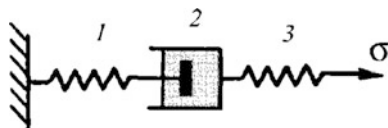
Fig. 5 Rheological model of the specimen–test bench system

The non-uniformity of strain variation in time may be explained using the Maxwell model of viscoelasticity [14]. The model, shown in Fig. 5, consists of elastic 1 and viscous 2 elements. Additionally, the model is given an elastic element 3 to characterize the elastic strains (Fig. 5).

Under constant deformation in the specimen–test bench system, the stress σ affecting the specimen decreases with time t in conformity with the formula:

$$\sigma = \sigma_0 e^{-t/n}, \tag{1}$$

while the strain ε_{smp} changes according to the relation below:

$$\varepsilon_{smp} = \frac{n}{\eta}\sigma_0 + \left(\frac{1}{E} - \frac{n}{\eta}\right)\sigma_0 e^{-t/n}, \tag{2}$$

where σ_0 are the initial stresses; E and η are the elasticity modulus and viscosity coefficient of the specimen; l and S are the length and cross-section area of the specimen, respectively; c is the test bench stiffness; $H = \frac{c \cdot l}{S}$; $E_1 = \frac{EH}{E+H}$; $n = \frac{\eta}{E_1}$.

The formulas (1) and (2) were used to approximate the experimental curves of stresses and strains. The initial sections of the curves (to 180 h) were approximated separately. The result is demonstrated in Figs. 2 and 3 by the dashed lines. The derived relations describe well the experimental trends. After the trends were removed from the experimental data, "fast" components of strains were found (Fig. 6).

Fig. 6 Variable components of strains
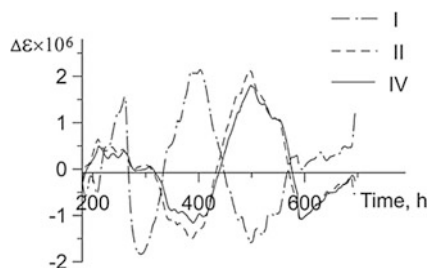
It is seen in Fig. 6 that the "fast" strains alternate after 180 h of the tests. Cures II and IV have similar shapes but disagree with respect to phase. Curve II lags behind curve IV by 5.2 h on average. This means that a slow deformation wave propagates along the specimen from gage IV to gage II, i.e. toward the impact source. The velocity of this wave is ${\sim}1.2 \times 10^{-6}$ m per impact (8.8 mm/h).

In a certain area of the specimen from the side of the impact source, the strains behave oppositely. Curve I has the opposite phase relative to curves II and IV. This implies that the specimen portion at one of the grippers is compressed while the rest part of the specimen stretches.

Thus, as a result of the impact energy absorption, the specimen undergoes compression (at long times) but the process runs non-monotonously. At short times, the periods of higher and lower compressive strains alternate. In the specimen–test bench system, energy flows between the specimen and the test bench to and from periodically. The elastic energy, at the background of a general dissipation accumulates and releases at times. This process is non-uniform along the length of the specimen. The part of the specimen at the side of the impact source releases energy for the most time of the experiment duration, while the more distant specimen's parts absorbs (dissipates) energy. By the way, a slow deformation wave travels along the specimen toward the impact source.

The experimentally found behavior of the equivalent geo-material can be explained by the initial heterogeneity of its mechanical properties and by different energy accumulation rate of energy along the specimen length, which could be governed by increased amplitude of the impact impulse upon reflection from the immobile gripper.

Qualitatively, the mechanism of strain accumulation in the sample can be explained as follows. Initially, the sample is loaded with a longitudinal static compressive load, which is 50% of the breaking load. In this state, weak impact loads additionally influence on the sample. When striking the clamp, an elastic impulse propagates at the speed of sound and damped oscillations occur in the "stand sample" system. In this case, the cross-sections of the sample are consistently subjected to additional dynamic compression and tension. The maximum value of dynamic local deformation under the pulse was 3×10^{-5}. Since the sample has a non-uniform structure, additional stresses appear in some microregions (for example, at the contacts of particles). These stresses can exceed the tensile strength and cause rearrangement of particles with appearing of microplastic deformations or the formation of micro-cracks. As the number of impacts increases, a gradual accumulation of plastic deformations and micro-cracks occurs, which results in a gradual change in the overall stress-strain state of the sample. It should be noted, that the samples tested for compression have brittle fracture, while their viscous properties appear slightly. Compression diagrams are qualitatively look like as similar diagrams of testing fragile rocks. Therefore, the results obtained, in our opinion, can be qualitatively applicable to natural geomaterials.

4 Conclusions

- A specimen of equivalent material subjected to static compression and repeated weak impacts gets compressed with time. Compression takes place nonuniformly with respect to time and length of the specimen. At the background of gradual increase in the total compressive strain, the specimen area near the point of impacts is first compressed and, then, stretched. The compression of the rest part of the specimen increases in this case.
- The temporal behavior of deformation is nonmonotonous, and strains fluctuate relative to the general trend. The comparison of the compression wave phases at different points of the specimen shows that weak impacts initiate a slow deformation wave at a rate of $\sim 1.2 \times 10^{-6}$ m per impact.
- The initial compression decreased nonmonotonously with time. There are areas of the stress increase and decrease. The specimen periodically accumulates and releases elastic energy in the course of the whole experiment.

References

1. Erzhanov, Z.S., Saginov, A.S., Gumenyuk, G.N., et al.: Creep of Rocks. Theory and Practice. Nauka, Alma-Ata (1970) (in Russian)
2. Svalov, A.M.: Deformation characteristics of rocks in oil and gas reservoir development. Monit. Nauka Tekhnolog. **3**(8), 84–90 (2011) (in Russian)
3. Mokhnachev, M.P.: Fatigue of Rocks. Nauka, Moscow (1979) (in Russian)
4. Kurlenya, M.V., Adushkin, V.V., Garnov, V.V., et al.: Alternating response of rocks to dynamic impacts. Doklady Akad. Nauk SSSR **323**(2), 263–265 (1993) (in Russian)
5. Trapeznikov, Y.A., Manzhikov, B.T., Bogomolov, L.M.: Effect of small weak vibrations on strain in rocks at constant load. Volcanol. Seism. **22**(1), 22–106 (2000)
6. Kuksenko, V.S., Manzhikov, B.T., Tilegenov, K., et al.: Trigger effect of weak vibrations in solids (rocks). Phys. Solid State **45**(12), 2287–2291 (2003)
7. Kocharyan, G.G., Kulyukin, A.A., Pavlov, D.V.: Role of nonlinear effects in the mechanics of accumulation of small perturbations. Fiz. Mezomekh. **9**(1) 5–14 (2006) (in Russian)
8. Deshcherevskii, A.V., Lukk, A.A., Mirzoev, K.M., Sidorin, A.Y.: Potentiality of trigger effect of daily variations in microseismic vibrations on seismic process. Nauka Tekhnol. Razrab. **94** (4) 16–29 (2015) (in Russian)
9. Stavrogin, A.N., Shirkes, O.A.: Aftereffect in rocks caused by preexisting irreversible deformations. J. Min. Sci. **22**(4), 235–244 (1986)
10. Moroz, A.I.: Self-Stress State of Rocks. MGGU, Moscow (2004) (in Russian)
11. Lavrikov, S.V., Revuzhenko, A.F.: Modeling deformation processes in self-stressed rock specimens. J. Min. Sci. **53**(1), 12–20 (2017)
12. Kosykh, V.P., Kosykh, P.V.: Fluctuations of stresses in geomaterials during long-term weak dynamic impacts. In: IV All-Russian Conference with International Participation on Trigger Effects in GeoSystems, pp. 176–182. GEOS, Moscow (2017) (in Russian)

13. Kosykh, V.P., Kosykh, P.V., Revuzhenko, A.F.: Test bench to study complex stress evolution in geomaterials under weak dynamic loads. J. Min. Sci. **53**(6), 1147–1151 (2017)
14. Rzhanitsyn, A.F.: Theory of Creep. Stroyizdat, Moscow (1968) (in Russian)

Modeling Accumulation and Release of Energy in a Geo-medium Under the Influence of Tidal Forces

Sergey Lavrikov and Alexander Revuzhenko

Abstract

Using the discrete element method, the authors model numerically the process of accumulation and release of energy in a geo-medium subjected to long-term periodical impacts. The medium consists of particles grouped into clusters. Within the cluster, all particles are elastically connected between each other. Periodical loading is implemented through setting of kinematic boundary conditions to simulate tidal deformation. It was shown that under a high tidal compression, fluctuations of the accumulated elastic energy have two pronounced maximums and minimums within a deformation cycle (one turn of tidal wave). It means such system lacks the ability of long-term accumulation of elastic energy. With the decrease in tidal compression, the part of elastic energy accumulated within one cycle is preserved in the form of internal self-balancing stresses for next cycles. In this case, the system has an ability to accumulate the energy for a long period of time, but to release dynamically in the mode of a catastrophe.

S. Lavrikov (✉) · A. Revuzhenko
Chinakal Institute of Mining, Siberian Branch, Russian Academy of Sciences, 630091 Novosibirsk, Russian Federation
e-mail: lvk64@mail.ru

1   Introduction

It is commonly recognized in our days that a rock mass is a complex and hierarchically structured heterogeneous geo-medium [1–6]. The block structure defines basic properties of a rock mass such as dilatancy, internal friction, cohesion, nonlinear behavior and anisotropy. At the same time, the block structure allows infinite number of equilibrium conditions in a rock mass. Some areas of such rock mass can be "charged" with energy in the form of self-balancing stresses, i.e. such areas can act as potential energy sources [7–11].

It is well known that short but strong impacts, for example, blasts, can result in internal restructuring of a medium and, as a consequence, in accumulation of the impact energy in the form of self-balancing stresses. In the meanwhile, one of the critical properties of a block-structure rock mass is its ability to accumulate energy of both strong and relatively weak impacts when they act on a timely basis within a long period. Such impacts may be repetitive blasts far from a study area, various anthropogenic effects, tidal deformations, etc. under certain conditions, the elastic energy being accumulated for a long period of time can be released, and this liberation process may proceed as a stable relaxation or as an unstable disaster in the form of shocks, rock bursts and earthquakes [12–16].

This study aims at numerical modeling of elastic energy accumulation and release in a structurally heterogeneous geo-medium under the influence of relatively periodic forces of the tidal wave style.

2   Mathematical Description of Structurally Heterogeneous Medium

Numerical modeling uses the discrete element method (DEM) including additional interaction potentials of particles composing the medium.

DEM is originally developed to describe flow of crushed rocks [17]. The medium is replaced by a set of spherical (in space case) or disc (in plane case) particles. In general case the particle sizes (radii) are assumed to be different. The particles are assumed as non-deformable, and, therefore, when the particles displace, overlapping areas appear. Using the basic interaction potentials of particles and the values of their overlaps, the normal and shear forces between the contacting particles are calculated. The normal repulsive force is determined from the Hertz contact problem [18], and friction between particles—using the Mindlin–Deresiewicz model [19]. Aiming to stabilize oscillatory processes, the viscous mechanism of energy dissipation is introduced by setting the recovery factor for velocity (ratio of scatter velocity of particles after collision to their approach velocity before collision). Modeling of deformation in the medium reduces to integration of the motion equations and finding the velocity vector and coordinates of each discrete particle based on the calculated forces and moments of forces applied by the neighbor particles.

Fig. 1 A cluster of five
interconnected particles
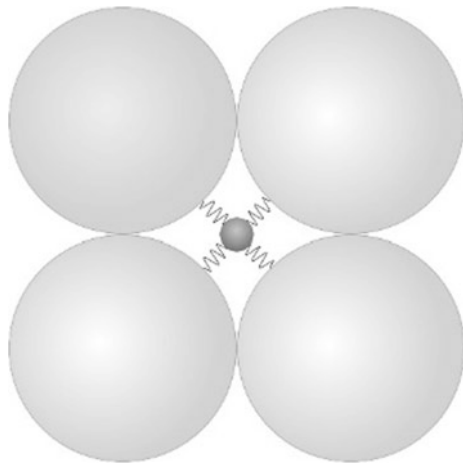
In this study, alongside with the basic interaction potentials of particles, an indirect elastic potential is additionally introduced to describe the property of a geo-medium to accumulate and release elastic energy [20]. Generally, this potential can be introduced for any particle ensembles (description of blocks, grains of different scales, boundaries, which provides body connectedness etc.). Here we will limit ourselves by the case when all particles of the medium are distributed between separate clusters in the form as shown in Fig. 1.

Here is presented a plane model of the cluster consisted of five particles connected by elastic springs between each other. The cluster consists of one central particle with small radius, which connected by elastic springs with other particles of the cluster. It is quite possible to avoid using central particle and to connect surrounding particles crosswise to each other. It is enough to describe the medium feature to accumulate and release elastic energy. The role of central particle is only to prevent the cluster from breaking up into separate pairs of connected particles during deformation.

In the cluster under deformation, some elastic elements stretch, the others constrict, and the cluster as a whole can self-jam. The cluster in this case accumulates some elastic energy from compression and tension of its elements.

The motion equations of particles appear as:

$$m_i \frac{d\mathbf{v}_i}{dt} = \sum_{j=1}^{n_b} \mathbf{F}_{ij} + m_i \mathbf{g}, \quad J_i \frac{d\boldsymbol{\omega}_i}{dt} = \sum_{j=1}^{n_b} \mathbf{M}_{ij}, \quad i = \overline{1, n}. \tag{1}$$

Here, $\mathbf{v}_i, \boldsymbol{\omega}_i$ are the vectors of linear and angular velocity, respectively; m_i is the mass; J_i is the moment of inertia of an i-th particle; $\mathbf{g}$ is the gravitational vector; $\mathbf{F}_{ij}, \mathbf{M}_{ij}$ are, respectively, the principle vector and principle moment of forces applied on the i-th particle by a j-th particle; n_b is the number of neighbor particles in contact with the i-th particle at the current moment of time; n is the total number

of particles. Alongside with the described basic interaction, an additional potential of indirect elastic interaction between particles integrated in a cluster is introduced. The elastic interaction of the same cluster particles is described using Hook's linear law. The equations for calculating forces on the i-th particle from the j-th particle are given by:

$$\mathbf{F}_{ij} = F_{n,ij} \cdot \mathbf{n}_{ij} + F_{t,ij} \cdot \mathbf{t}_{ij}$$
$$F_{n,ij} = k_{n,ij} \cdot d_{n,ij} - \gamma_{n,ij} \cdot v_{n,ij} + k_{s,ij} \cdot l_{ij} ,$$
$$F_{t,ij} = k_{t,ij} \cdot d_{t,ij} - \gamma_{t,ij} \cdot v_{t,ij}$$

(2)

where $\mathbf{n}_{ij}, \mathbf{t}_{ij}$ are the normal and shear unit vectors for the contact plane of the i-th and j-th particles; $v_{n,ij}, v_{t,ij}$ are the normal and tangential projections of the relative velocity vector at the contact point; $d_{n,ij}, d_{t,ij}$ are the normal overlap and the shear slip of particles; $k_{s,ij}$ is the stiffness of the elastic connection between the i-th and j-th particles; l_{ij} is the distance between the centers of the i-th and j-th particles. No constraint is imposed on the value of l_{ij}, i.e. elastic forces arise even between non-contacting particles. The elastic $k_{n,ij}$, $k_{t,ij}$ and viscous $\gamma_{n,ij}$, $\gamma_{t,ij}$ moduli in (2) are taken in accordance with the works [21, 22]:

$$k_{n,ij} = \frac{4}{3}E^* \cdot \sqrt{R^* \cdot d_{n,ij}},\ k_{t,ij} = 8G^* \cdot \sqrt{R^* \cdot d_{n,ij}},$$
$$\gamma_{n,ij} = -2\sqrt{\frac{5}{6}} \cdot \beta \cdot \sqrt{S_{n,ij} \cdot m^*},\ \gamma_{t,ij} = -2\sqrt{\frac{5}{6}} \cdot \beta \cdot \sqrt{S_{t,ij} \cdot m^*},$$
$$S_{n,ij} = 2E^* \cdot \sqrt{R^* \cdot d_{n,ij}},\ S_{t,ij} = 8G^* \cdot \sqrt{R^* \cdot d_{n,ij}},\ \beta = \frac{\ln(c_r)}{\sqrt{\ln^2(c_r) + \pi^2}} < 0,$$

(3)

where $0 \le c_r \le 1$ is the recovery factor of velocity. The generalized radius R^*, mass m^*, Young's modulus E^* and shear modulus G^* are calculated from the formulas:

$$\frac{1}{R^*} = \frac{1}{R_i} + \frac{1}{R_j},\ \frac{1}{m^*} = \frac{1}{m_i} + \frac{1}{m_j},\ \frac{1}{E^*} = \frac{(1-\mu_i)^2}{E_i} + \frac{(1-\mu_j)^2}{E_j},$$
$$\frac{1}{G^*} = \frac{2(2-\mu_i)(1+\mu_i)}{E_i} + \frac{2(2-\mu_j)(1+\mu_j)}{E_j},$$

(4)

where R_i, m_i, E_i, μ_i are, respectively, the radius, mass, Young's modulus and Poisson's ratio of the i-th particle. The tangential force $F_{t,ij}$ is evaluated by (2) up to a certain moment until $F_{t,ij} < tg\phi \cdot F_{n,ij}$ (developing friction stage); otherwise, it is assumed that $F_{t,ij} = tg\phi \cdot F_{n,ij}$ (developed friction stage), where $tg\phi$ is the dry friction coefficient of particles.

3 Problem Formulation

We discuss a problem on deformation of a structurally heterogeneous medium under the action of periodic tidal-style waves. As is known, the tidal forces reduce to the mass forces that stretch the body towards and away from the disturbing mass. The body rotates relative to these directions so that it experiences complex loading at continuous rotation of axes of stress tensor. The kinematic method of modeling such deformation is proposed in [23]. In the simplest variant of plane strain, the boundary of the deformation domain is subjected to the velocities:

$$\frac{dx_1}{dt} = kx_1 - \omega x_2, \quad \frac{dx_2}{dt} = -kx_2 + \omega x_1. \tag{5}$$

When $k/\omega < 1$ the respective boundary displacements are:

$$
\begin{aligned}
x_1(t) &= \left(\frac{k}{\lambda} \cdot x_1(0) - \frac{\omega}{\lambda} \cdot x_2(0)\right) \cdot \sin(\lambda t) + x_1(0) \cdot \cos(\lambda t), \\
x_2(t) &= \left(-\frac{k}{\lambda} \cdot x_2(0) + \frac{\omega}{\lambda} \cdot x_1(0)\right) \cdot \sin(\lambda t) + x_2(0) \cdot \cos(\lambda t),
\end{aligned}
\tag{6}
$$

where $\lambda = \sqrt{\omega^2 - k^2}$. Here, k is the mean rate of extension of the body toward the disturbing mass; $-k$ is the rate of compression in the orthogonal direction; ω is the rotation velocity of the body relative to the compression and tension directions.

We will solve the problem in 2D-formulation. The representative unit volume of the medium is selected as a square domain filled with particles grouped in clusters (Fig. 2a). In the figure, for better visualization of deformation, particles in the middle layer of the square domain are colored darker. Deformation is implemented through displacement of the domain boundary points by the law (6). Because of the loading periodicity, the original configuration of the domain boundary will transform to a series of parallelograms with the course of time and then, after one half-period of the tidal wave circulation relative to the body, will reset. Thus, in the complete turn of the tidal wave relative to the body (one cycle of loading), the body boundary recovers two times.

4 Numerical Modeling

The parameters of particles and their interaction potentials are chosen to be: $\phi = 25°$, $c_r = 0.7$, $E = 1.2 \times 10^4$ MPa, $\mu = 0.25$, $k_s = 3.0$ kN, $R = 5$ mm. The number of particles is $n = 10^4$, their weight is disregarded. The external boundaries are assumed as perfectly smooth and free from friction. The calculations are performed by the described scheme of loading based on the model (1)–(4).
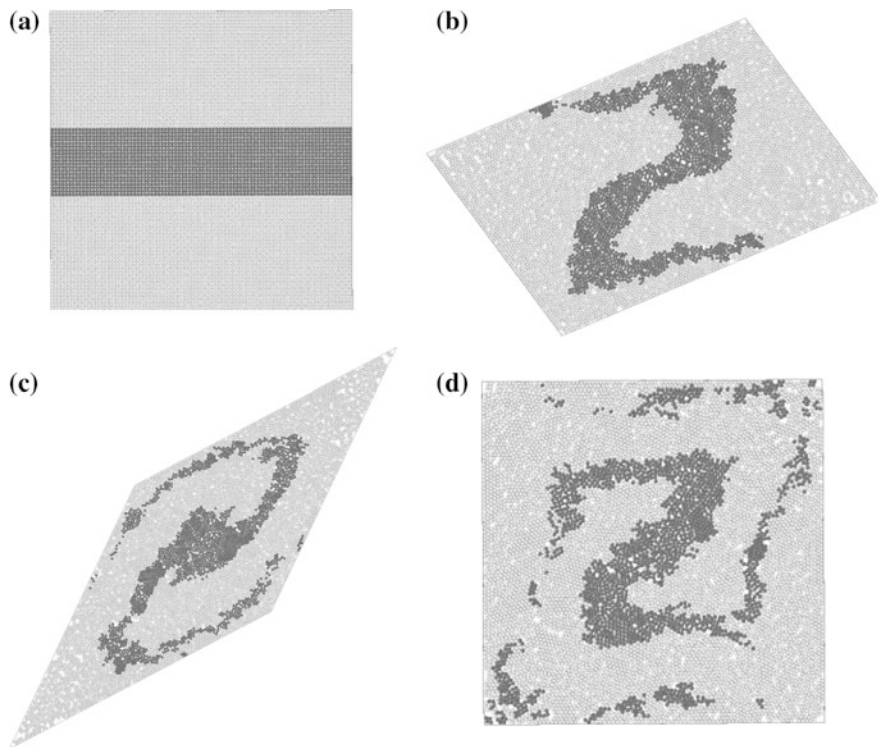
Fig. 2 Sequential reconfiguration of the body and the effect of directional mass transfer under influence of tidal wave: **a** initial position; and after **b** 3.65, **c** 6.25 and **d** 10 cycles of loading

One of the essential model parameter is ratio k/ω. As is well known, the natural tidal deformations of the solid surface of the Earth are about $\sim 10^{-8}$. However, in the framework of numerical simulation, there is no necessity to consider so small deformations and to wait the effect from their influence during very big number of loading cycles (may be, millions and more). The advantage of numerical simulation is the ability to consider significantly larger compression ratios and try to reveal the qualitative deformation effects already in the first tens of loading cycles.

Figure 2a–d demonstrate sequential kinematics of particles during deformation of the medium at $k/\omega = 0.5$. It is seen that the particles in the middle layer of the unit volume form a spiral line during deformation, and the line spirals infinitely with time. This means that the medium undergoes directional transfer of internal masses, which has earlier been experimentally found in granular and viscous media by kinematic modeling of tidal deformation [24].

The numerical experiments investigate the total energy of the constricted and stretched elastic connections between particles in a cluster. It appears that loading first goes with a relatively short (to 2 loading cycles) period of stabilization, and then deformation reduces to fluctuations of the total elastic energy value at definite
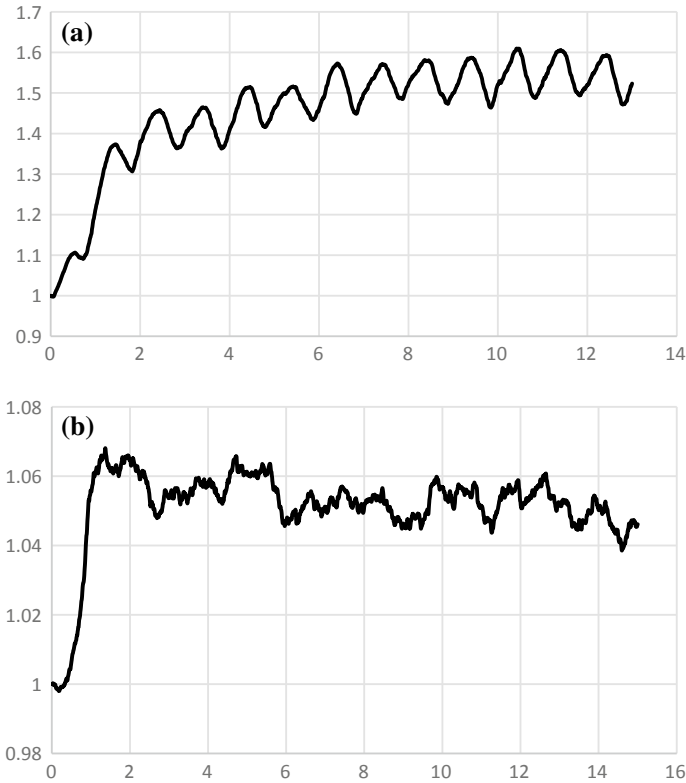
Fig. 3 Reduced elastic energy depending on the number of loading half-cycles at: **a** $k/\omega = 0.5$ and **b** $k/\omega = 0.01$

mean governed by the value of k/ω. Figure 3 describes these fluctuations of the total elastic energy related with its value at the initial time.

Of interest are mainly the fluctuations depending on the cycle of loading by the tidal wave and on the number of the loading cycles. At values of $k/\omega \sim 0.5$, the energy fluctuations have two pronounced maximums and two minimums in one deformation cycle (Fig. 3a). Here, the tidal deformations are such high that all elastic energy accumulated during one cycle releases in full. Thus, the system lacks the ability of long-term accumulation of elastic energy, and the process of deformation acquires a periodic nature. The decrease in k/ω down to $k/\omega \sim 0.01$ and below makes the fluctuations less deterministic but stochastic (Fig. 3b). In the latter case, the maximums and minimums of the energy fluctuations get "smeared", and the energy accumulated inside a cycle is preserved in the form of internal self-balancing stresses of the deformed cluster in the next cycles of deformation. As a consequence, it becomes possible that energy accumulates for a few cycles of loading while releases by jumps.

5 Conclusions

- The periodic deformations of the tidal wave style, because of their long-term effect, can result in irreversible internal re-structuring of geo-medium and, consequently, in long-term accumulation of elastic energy in the form of internal self-balancing stresses.
- The release of the accumulated energy may proceed in the mode of a catastrophe.

References

1. Sadovsky, M.A.: Natural lumpiness of rocks. Doklady Akad. Nauk SSSR **247**(4), 829–831 (1979) (in Russian)
2. Kocharyan, G.G.: Mechanics of Faults. Geos, Moscow (2016) (in Russian)
3. Melnikov, N.N. (ed.): The Earth's Crust Destruction and Self-organization in the Zones of Strong Anthropogenic Impact. SO RAN, Novosibirsk (2012) (in Russian)
4. Sobolev, G.A., Ponomarev, A.V.: Physics of Earthquakes and Prerequisites. Nauka, Moscow (2003) (in Russian)
5. Kolymbas, D.: Tunneling and Tunnel Mechanics. A Rational Approach to Tunneling. Springer, Berlin (2005)
6. Lavrikov, S.V., Revuzhenko, A.F.: Deformation of a blocky medium around a working. J. Min. Sci. **26**(6), 485–492 (1990)
7. Moroz, A.I.: Self-stress State of Rocks. MGU, Moscow (204) (in Russian)
8. Ponomarev, V.S.: Problems of studying an energetically active geologic medium. Geotectonics **45**(2), 157–165 (2011)
9. Stavrogin, A.N., Shirkes, O.A.: Aftereffect in rocks caused by pre-existing irreversible deformations. J. Min. Sci. **22**(4), 235–244 (1986)
10. Vlokh, N.P., Lipin, Y.I., Sashurin, A.D.: Residual stresses in hard rocks. In: Modern Problems of Rock Mechanics, pp. 186–189. Nauka, Leningrad (1972) (in Russian)
11. Lavrikov, S.V., Revuzhenko, A.F.: One experimental rock model. J. Min. Sci. **27**(4), 288–293 (1991)
12. Kurlenya, M.V., Adushkin, V.V., Garnov, V.V., Oparin, V.N., Revuzhenko, A.F., Spivak, A.A.: Alternating response of rocks to dynamic impact. Doklady Akad. Nauk RF **323**(2), 263–265 (1992) (in Russian)
13. Goryainov, P.M., Davidenko, I.V.: Tectonic–decompression effect in rocks and ore bodies—critical geodynamic phenomenon. Doklady Akad. Nauk SSSR **247**(5), 1212–1215 (1979) (in Russian)
14. Sibiryakov, B.P., Podberezhnyi, M.Y.: Instability of porous and cracked solids and catastrophe scenarios. Geolog. Geofiz. **47**(5), 648–654 (2006) (in Russian)
15. Lavrikov, S.V., Revuzhenko, A.F.: Modeling deformation processes in self-stressed rock specimens. J. Min. Sci. **53**(1), 12–20 (2017)
16. Lavrikov, S.V., Revuzhenko, A.F.: DEM code-based modeling of energy accumulation and release in structurally heterogeneous rock masses. AIP Conf. Proc. **1683**, 020121 (2015)
17. Cundall, P.A., Strack, O.D.L.: A distinct element model for granular assemblies. Geotechnique **29**, 47–65 (1979)
18. Johnson, K.L.: Contact Mechanics. Cambridge University Press, Cambridge (1985)
19. Mindlin, R.D., Deresiewicz, H.: Elastic spheres in contact under varying oblique forces. J. Appl. Mech., Trans. ASME **20**, 327–344 (1953)

20. Lavrikov, S.V., Revuzhenko, A.F.: Numerical modeling of elastic energy accumulation and release in structurally heterogeneous geomaterials. J. Min. Sci. **52**(4), 632–637 (2016)
21. Klishin, S.V., Klishin, V.I., Opruk, G.Y.: Discrete element modeling of gravity flow of broken rocks in the technology of longwall top coal caving. IOP Conf. Ser.: Earth Environ. Sci. **206**, 012007(2018)
22. Klishin, S.V., Revuzhenko, A.F.: Spatial discrete element analysis of problem on floor buckling in underground openings. IOP Conf. Ser.: Earth Environ. Sci. **53**, 012012 (2017)
23. Revuzhenko, A.F.: Tidal Waves and Directional Mass Transport in the Earth System. Nauka, Novosibirsk (2013) (in Russian)
24. Bobryakov, A.P., Revuzhenko, A.F., Shemyakin, E.I.: Possible mechanism of transfer of the Earth's masses. Doklady Akad. Nauk SSSR **272**(5), 1097–1099 (1983) (in Russian)

Optimal Methods and Parameters of Electromagnetic Monitoring in Seismically Active Areas

Nina Nevedrova and Aleksandr Shalaginov

Abstract

The article describes the methods of observation and data interpretation of electromagnetic methods with a controlled source for seismically active regions of Siberia. The approach proposed by the laboratory of electromagnetic Fields of IPGG SB RAS is being developed to estimate the variations of geoelectric parameters by determining them by solving an inverse problem. An analysis the results of the interpretation of VES monitoring data using the integral electrical conductivity parameter presented for the site in the Selenginskaya depression of the Baikal rift zone. For the territory of Gorny Altai, a measurement technique demonstrated with several modifications of the TEM method for determining variations of electrical resistivity and anisotropy coefficient in the aftershock period of the 2003 Chuya earthquake. Attracting the electrical anisotropy coefficient expands the informativeness of the study, as it allows monitoring variations associated with changes in the seismic regime and allows assess the degree of activity of fault zones.

N. Nevedrova · A. Shalaginov (✉)
Trofimuk Institute of Petroleum Geology and Geophysics, 630090 Novosibirsk, Russia
e-mail: ShalaginovAE@ipgg.sbras.ru

N. Nevedrova
e-mail: NevedrovaNN@ipgg.sbras.ru

1 Introduction

Electromagnetic methods with a controlled source are widely used for monitoring the electrophysical characteristics of the geological massif of rocks, which are subject to the influence of natural or man-made geodynamic processes. Earthquakes, landslides, rock bursts, karst processes in the areas of residential and industrial infrastructure, in areas of mineral deposits development can be attributed to the dangerous phenomena that need to be monitored. In regions with high seismic activity, an increased interest in the study of fault zones is associated with the fact that they can be seismic, therefore, the determination of the degree of their activity using geoelectrics methods is an urgent task.

It is known that active electromagnetic methods are numerous, classified according to a number of characteristics, differ in the ways of excitation and registration of the field. Each of the methods has its advantages and disadvantages, different depth of research. For successful monitoring, it is important to choose a specific research method. For regular observations, modifications of non-stationary electromagnetic sounding (TEM) and methods of resistance, such as vertical electrical sounding (VES), electrotomography (ERT), are most often attracted. Given the characteristics of the methods, the choice should focus on the required depth. However, the information content of the study increased using a set of methods. Monitoring on several sites of the Chui depression of the Gorny Altai carried out using several modifications of TEM soundings and resistance methods, which made it possible to observe variations of several electromagnetic parameters.

Based on the existing experience of monitoring in the Baikal rift zone and Gorny Altai, on the geoelectric features of the research site, it is important to choose the optimal geoelectric parameters. For example, the VES data of long-term monitoring in the Selenginskaya depression revealed the optimal parameter for this area—the integrated conductivity of the section, the variations of which increased with depth and correlated well with the seismic events that are taking place. The flooded section of the coast of Lake Baikal characterized by monotonous interlaying of clays and sandstones with rather low values of electrical resistivity. The integral conductivity parameter in this case is effective for observations.

The presence of sub-vertical cracks system with a predominant orientation in any direction will generate effective anisotropy, which manifested in electromagnetic fields. Therefore, when organizing regular measurements within fracture fractured structures, variations in the electrical anisotropy coefficient are considered. To determine this parameter in the epicentral zone of the Chuya earthquake of 2003 in Gorny Altai, the method of measurement and interpretation developed and tested using the TEM method. Thus, the choice of the parameter depends on the geoelectric conditions of the study sites.

For a complete analysis of regular observations, information about the structure of the site, fault zones, their extent, width, inclination of the displacer needed, and so fieldwork conducted in parallel with monitoring aimed at refining the geoelectric structure. Monitoring performed in the zone of influence of the fault makes it

possible to assess the degree of its activity. Certainly, an important issue is the method of interpretation. All field data obtained in seismically active areas were interpreted using modeling and inversion software systems in order to obtain quantitative estimates of the parameters of the section and their variations. The article presents examples of the application of the developed methods of electromagnetic monitoring, the parameters used, and their effectiveness is considered.

2 Electromagnetic Monitoring in the Chui Depression of the Gorny Altai

Investigations in Gorny Altai started by the electromagnetic monitoring group of the Institute of Petroleum Geology and Geophysics in the aftershock period of the Chuya earthquake of 2003 in the central part of the Chuya depression in the village Mukhor-Tarkhata, since 2007. Regular long-term observations carried out by the TEM method using induction (Q, q), combined (AB-q) and galvanic (AB-MN) installations.

It is known that the signal of the galvanic installation substantially depends on the anisotropy of conductivity, the components of the electric dipole field are a combination of galvanic and induction modes. Consequently, when measuring the electric components of the field with galvanic excitation and signal detection, it is possible to investigate the electrical anisotropy of the rock mass [1]. However, measurements with galvanic installations (AB-MN) are more susceptible to the influence of various distorting factors, such as the influence of the inhomogeneities of the section and the induced polarization (IP) of rocks.

During induction excitation of a field and signal detection, local near-surface inhomogeneities, which are geoelectric interferences, have little effect, since the distortions generated by them are mainly galvanic in nature. The combined use of induction and galvanic installations, when measured at one point, leads to a decrease in the operation of the principle of equivalence, which makes it possible reliably determine both the isotropic and anisotropic parameters of the model. According to the data of a coaxial induction installation, the geoelectric model determined and the isotropic parameters of all horizons of the geoelectric profile estimated, and the anisotropy coefficient (λ) is determined from the data of the galvanic installation. The chosen measurement technique is due to the minimal influence of distorting factors on the installation of "coaxial loops", and the AB-MN installation is the most technologically advanced in field work [2].

When measuring by galvanic installation, it is necessary to select the parameters of the receiving-generator set so that the measured signal was minimally distorted. At the preparatory work stage, measurements performed with an AB-MN installation with different placement of the receiving line MN relative to the AB line, the azimuth angle ϕ and the angle ψ between the MN line and AB were changing (Fig. 1a). The measurements performed in 9 points with the MN line with several azimuth angles ϕ and angles $\psi = 0, 45, 90°$ (Fig. 1b).
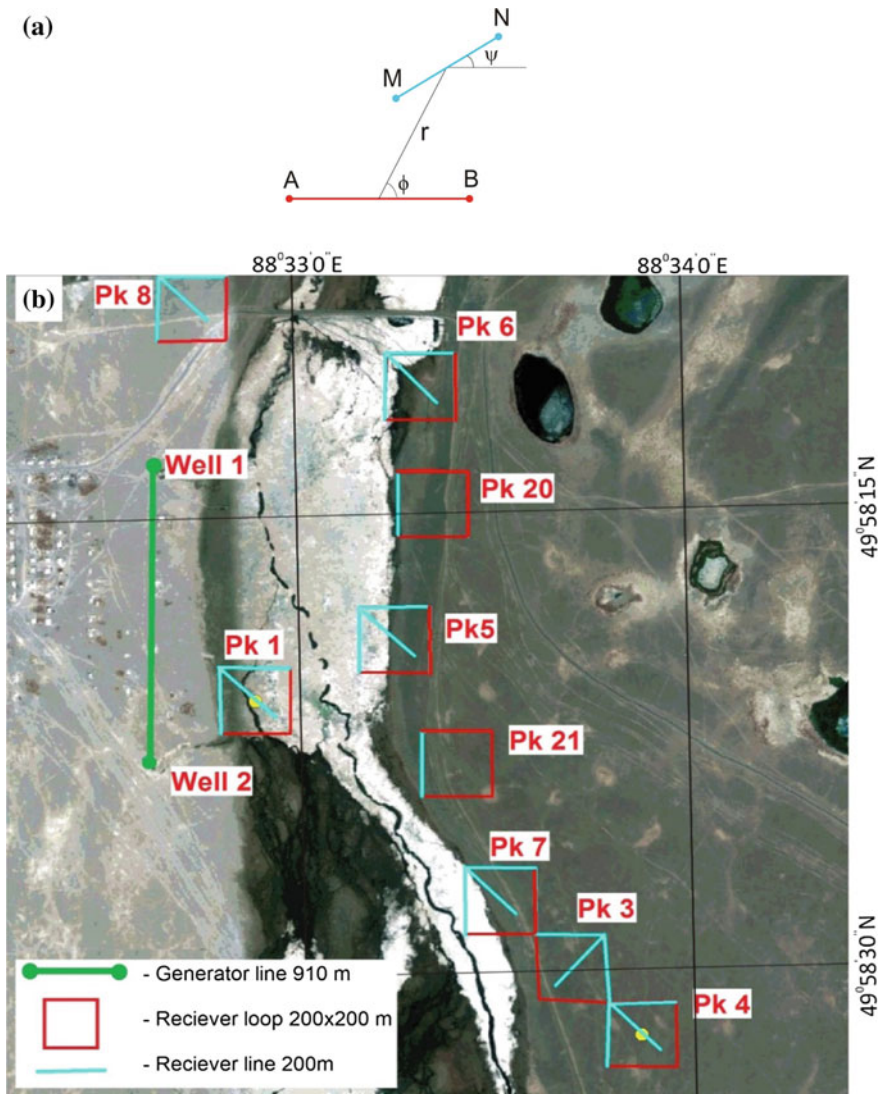
Fig. 1 **a** Layout of the MN line relative to the AB; **b** Layout of the measurement points during the experiment in Mukhor-Tarkhata

From the comparison of the EMF curves for measurements at different azimuthal angles (ϕ) with a parallel installation, it is found that according to TEM points 5, 20 and 21 (azimuth angles 70–85°), a distortion of the EMF curve observed at late times, possibly due to inconsistencies in the section or caused by polarization. For the remaining TEM points (azimuth angles of 40–50°), there are no distortions on the EMF curve at late times. For example, comparison of the data interpretation

results for TEM point 5 and 6 (Fig. 2), shown that, according to TEM point 5 data, with an azimuthal angle of 84°, a characteristic distortion of the field curve is observed in late times. According to TEM point 6 data with an azimuth angle of 46°, the selection error is minimal and the geoelectric model corresponds to a horizontally layered one. Thus, concluded that placing the MN line at angles of 40–50°, the data obtained are the least distorted and the error in selecting the theoretical curve is minimal.

This is justified by the studies conducted by E. Yu. Antonov and A. N. Shein. In their work, they revealed a high sensitivity of the galvanic installation to the relative position of the lines [3]. For a parallel azimuthal setup, they found that on the isoline map for the late field formation times there are always two regions corresponding to positive and negative values of the signals. Also shown that the boundary, separating these regions, passes through the points of the day surface, where the effect of the induced polarization is weakened. The position of the boundary depends on the size of the installation and on the parameters of the medium. In the section Mukhor-Tarkhata for the installation AB-MN with dimensions AB = 910 m, MN = 200 m and the corresponding geoelectric parameters of the medium, the data are the least distorted when measured at an azimuthal angle of 40–50°.

Then, the field and theoretical curves compared for measurements at different angles ψ of the MN line relative to the AB line. Comparison of data for the TEM point 2 (Fig. 3), shown that the field curve obtained by measuring with the MN line at an angle $\psi = 0°$ best matches the theoretical curve calculated for the geoelectric model of this section. The same is according to other TEM points.

Thus, on the Mukhor-Tarkhata section, for regular observations of electrical anisotropy changes, a measurement technique was chosen and justified. The field data measured by a parallel galvanic installation with azimuth angles of 40–50° are the least distorted, and the geoelectric model corresponds to a model with a coaxial installation.

No less important is the issue of further processing and interpretation of the field data. All field data obtained in Gorny Altai were interpreted using modeling and inversion software systems and the degree of current seismic events influence on
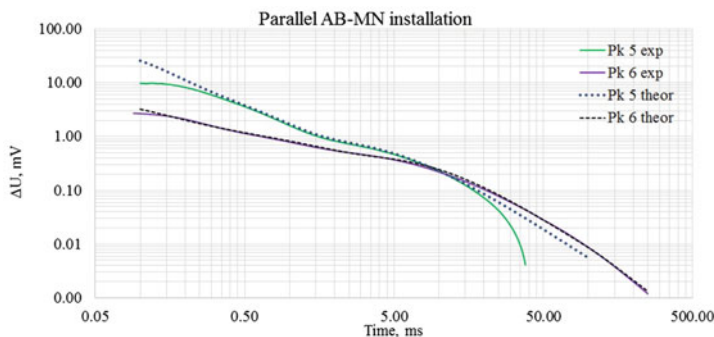
Fig. 2 Comparison of EMF curves of TEM points 5 and 6 with theoretical curves
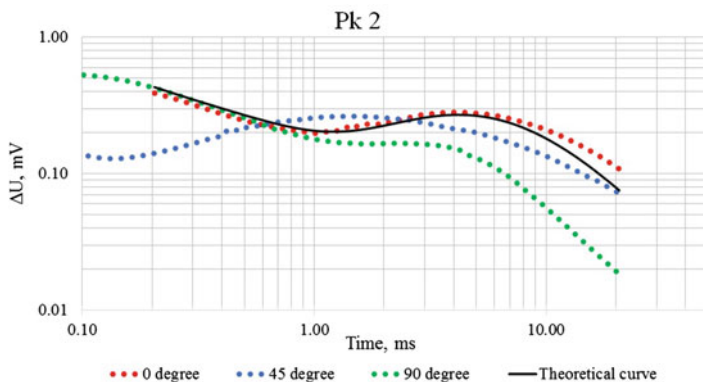
Fig. 3 Comparison of field and theoretical curves of TEM point 2 with the MN line with angles $\psi = 0, 45, 90°$

the geoelectric characteristics was based on quantitative estimates of variations in resistivity and λ. In addition, the interpretation carried out with the involvement of a large amount of a priori materials. The starting model formed according to the lithologic stratigraphic data of the existing wells. Geological and structural studies, tectonic schemes, satellite images were used to verify faults. The data interpretation method corresponds to the proposed measurement method—according to the data of the induction installation, the geoelectric model was determined at the research site, which was further considered as the initial model for interpreting the data of the AB-MN installation.

According to the results of processing monitoring TEM data for 2007–2019 the time series of values of electrical resistivity, electrical anisotropy coefficient and variations of these parameters for different layers of the geoelectric section were obtained. Involving, apart from the traditionally used electrical resistivity, the coefficient of electrical anisotropy certainly expands the informativeness of the study, as it allows not only to monitor variations associated with seismic activity, but also effectively investigate fractured fault zones in order to clarify their location and degree of activity [4]. In particular, according to the results of observations in the Chuay depression, after the devastating earthquake of 2003, a whole series of internal faulting structures activated and the most significant variations of electrophysical parameters were obtained in the zone of influence of faults.

3 The Results of Monitoring According to VES Data in the Selenginskaya Depression of the Baikal Rift Zone

The modern look of the research site was formed because of multistage neotectonic processes. The largest geological and tectonic elements include the South Baikal Basin Lake Baikal, as well as such continental structures as the Selenga depression

and the narrow coastal depression adjacent to it from the village of Oymour to village Suhaya, elongated along the coast of the lake from south-west to northeast. According to seismological data, this territory belongs to the most seismically active central part of the Baikal rift zone. High seismicity is due to the modern development of these neotectonic structures.

Regular observations by the VES method of a Schlumberger four-electrode symmetric installation using a 3 km generator line carried out daily from 1990 to 1996 with some technological interruptions. The recording equipment provided a measurement error in the range of 2–3%.

When processing long-term observations, the inversion was solved for each daily VES measurement. As a result, the parameters of the section for the entire time interval of observations were obtained. Integral geoelectric parameters chosen as the interpretational characteristic. The medium model simultaneously characterized by longitudinal conductivity (S) and transverse resistance (T), which were calculated for several depth ranges using the conductivity values obtained. It is known that the integral parameters in solving the inverse problem are determined more stably compared with electrical conductivity. A joint analysis of the relative variations of the true electrical parameters and the seismic regime of the region showed their good correlation. In Fig. 4 showed the variations of apparent resistivity (ρk) and integral conductivity (ST) at different depths for 1992. Variations are related to seismic events. Earthquakes shown by arrows at the bottom of the figure. The magnitude of the arrow depends on the class of the earthquake; the corresponding scale bar shown (the distance from the epicenter of the seismic event to the observation point).
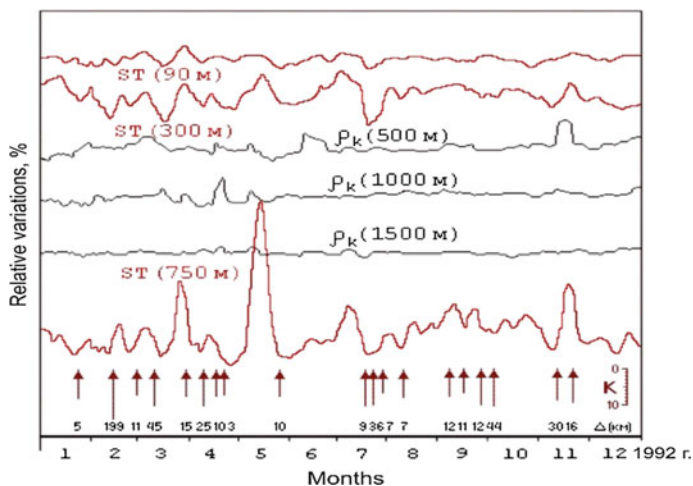
Fig. 4 Variations of the integral longitudinal conductivity in comparison with ρ_k variations and seismic events at the VES monitoring station for 1994–1995 in the area of the Selenginskaya depression of the Baikal rift zone

Variations of ρ_k reflect seismic processes, but in comparison with the integral conductivity parameter, they are less significant. The most expressive time series of integrated conductivity are obtained for a depth of 750 m. As a rule, the seismic event (or group of events) preceded by an anomalous maximum of conductivity, which corresponds to a decrease in electrical resistivity before an earthquake. Analysis of ST variations over the entire observation period allowed us to establish different sensitivity to seismic events of the stationary field observation system. The amplitude of variations of the integral parameters of the section substantially depends on the azimuthal direction to the epicenter of the earthquake. Comparison of the monitoring results and features of the geoelectric structure showed that electrical conductivity variations with maximum amplitudes are associated with seismic events occurring in the coastal fault structures of Proval Bay, the Selenginskaya depression [5].

4   Conclusions

The article considers two seismically active regions of Russia, in each of which the tense state of the earth's crust caused by different reasons. In the Baikal rift system, transverse stretching prevails in the upper part of the lithosphere and earthquakes with different types of displacements are observed. For the Altai-Sayan mountain region, shear type foci prevail and there are completely different hydrogeological conditions. On the coast of lake Baikal with small tectonic movements, significant volumes of water solutions begins to move and significant amplitudes of variations are observed on the monitoring time series, anticipating earthquakes of even a small energy class, although there is certainly a relationship between electrical conductivity variations, epicentral distance, earthquake magnitude. For the Baikal rift zone, the capabilities of the DC method for monitoring seismotectonic processes are shown.

For Gorny Altai, measuring by TEM method using three receiving-generator sets and an appropriate method for processing and interpreting data have been proposed. This technique allows determine the parameters of the geoelectric model (resistivity, layer thickness and electrical anisotropy coefficient) most reliably and accurately, which then used to calculate variations, their evaluation and comparison with changes in the seismic regime. Variations of the electric anisotropy parameter characterize the seismic activity of the territory, and allows to effectively investigate fractured fault zones in order to determine the degree of their activity.

References

1. Mogilatov, V.S.: Poorly studied phenomena in geoelectrics. J. Min. Inst. **222**, 783–788 (2016) (in Russian)
2. Nevedrova, N.N., Shalaginov, A.E.: Monitoring of electromagnetic parameters in the seismic activity zone of Gorny Altai. Russ. Geophys. **1**, 31–40 (2015) (in Russian)
3. Antonov, E.Y., Shein, A.N.: Improving inversion quality for IP-affected TDEM data. Russ. Geol. Geophys. **49**(10), 1046–1062 (2008) (in Russian)
4. Shalaginov, A.E., Nevedrova, N.N., Shaparenko, I.O.: Variations in electrophysical parameters estimated from electromagnetic monitoring data as an indicator of fault activity. Geodyn. Tectonophys. **9**(1), 93–107 (2018) (in Russian)
5. Nevedrova, N.N., Epov, M.I.: Electromagnetic monitoring in seismically active regions of Siberia. Geophys. J. **34**(4), 209–223 (2012) (in Russian)

Fault Block Structure of Gorny Altai Intermountain Areas According to Geoelectrical Data

Nina Nevedrova , Aydisa Sanchaa , Ilya Shaparenko
and Sergey Babushkin

Abstract

The article presents the results of studies of the deep structure of the largest intermountain depressions of Gorny Altai (Chuya, Kuray, Uimon areas) using a suite of electromagnetic methods that includes transient electromagnetic method, vertical electrical sounding and electrical resistivity tomography. Investigation of their internal structure is important in the study of seismic activity of the region, the patterns of formation of the neotectonic structure, and mineral deposits. Interpretation of the obtained results with consideration of a priori geological and seismological information, enables to reveal the fault block structure of these basins. The common features of the structure of all three basins are fault boundaries with mountain ridges framing them, as well as the presence of numerous within the depressive disjunctive disorders. The study identified the locations of faults overlapped by Cenozoic sediments and thrusts of Paleozoic rocks of the northeastern mountain ranges to sedimentary depressions, which were verified by three-dimensional numerical modeling.

N. Nevedrova · A. Sanchaa (✉) · I. Shaparenko
Trofimuk Institute of Petroleum Geology and Geophysics, Siberian Branch,
Russian Academy of Sciences, Koptug ave. 3, 630090 Novosibirsk, Russia
e-mail: SanchaaAM@ipgg.sbras.ru

N. Nevedrova
e-mail: NevedrovaNN@ipgg.sbras.ru

S. Babushkin
Seismological Branch, Geophysical Survey, Russian Academy of Sciences,
Koptug ave. 3, 630090 Novosibirsk, Russia

1 Introduction

Gorny Altai is in the western part of the Altai-Sayan folded region. Its modern morpho-structural plan is not inferior to high sizes in intermountain depressions. The largest of them—Chuya, Kuray, and Uimon relate to the Cenozoic structure and have a similar history of neotectonic development. Continental sediments yield high thickness, but there are not many sections available to study. Important structural features of all three depressions are heterogeneous borders with framing of their mountain ranges, as well as the presence of numerous interdigital disjunctive disorders. They are also objects for studying their patterns of formation, neotectonic evolution and modern relief of the Altay mountain.

Controlled source geoelectrical methods are successfully used to study the deep structure of depressions in different mountain areas [1]. A modern suite of electromagnetic methods allows us to construct models of a sedimentary cover, the upper part of the basement, existing fault structures. Information about the structure of depressions is necessary for prospecting and exploration of mineral resources, problems of safety of population in the territories with high level of seismic danger, for identifying possible seismogenic faults, as well as for a number of geological disciplines.

The epicentral zone of the destructive Chuya earthquake of 2003 with M = 7.3 includes the territory of Chuya and Kuray basins. In connection with the study of consequences of this event, in 2004, IPGG SB RAS began a new phase of work using the electrical survey methods, first in the Chuya and Kuray depressions, and then in Uimon. During the period of instrumental seismological observations in the Uimon depression, no significant earthquakes were recorded, but paleoseismological data indicate repeated events with magnitudes 7 and above that occurred in the Holocene [2].

A survey map of the area under study is shown in Fig. 1.
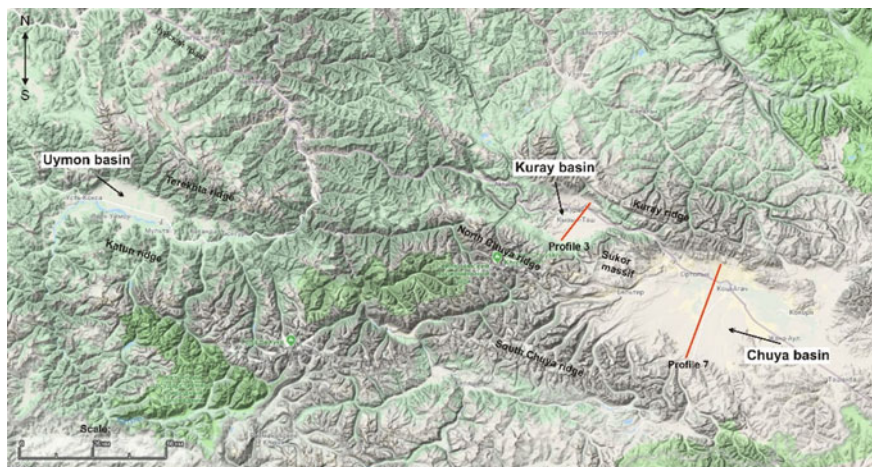
Fig. 1 Disposition of Chuya, Kuray and Uimon depressions of Gorny Altai

For complex measurements, DC and AC methods were involved. In addition to basic deep-seated methods such as transient electromagnetic method (TEM), vertical electrical sensing (VES), also electrical resistivity tomography (ERT) was used to build detailed models of the upper part of the section to depths of 50–100 m. Archival electrical survey materials of TEM and VES dated 60–80s last century along the Chuya and Kuray basins were included in the total field data. For the purposes of interpretation, geological, hydrological and other materials were used. Before 2011, no geophysical (electromagnetic) measurements were carried out on the territory of the Uimon depression, so the age, thickness and lithological characteristics of the compounding rocks were unknown. Shallow prospecting and hydrogeological wells drilled core sampling on average up to 100 m. Geological specialists only assumed the presence of Neogene sediments in it on the base of a set of formal features.

Thus, the tasks were to clarify the structure of the Chuya and Kuray basins after a major seismic event and clarify the structure of the Uimon intermountain basin.

2 Methods, Instrumental and Methodical Means, Interpretation of Electromagnetic Research Data

The combined use of a suite of multi-depth methods of electrical exploration, as is shown by practice, makes it possible to obtain geoelectrical characteristics of the section in a wide range of depths from the surface to the basement. The works by the TEM method are aimed at building deep models of the sedimentary cover and the upper part of the basement. The depth of the TEM in the geoelectrical conditions of the Altai depression reaches several kilometers. Using the VES method to depths of 200–300 m, more detailed geoelectrical characteristics of the upper sedimentary layers were obtained, which in the range from 50 to 100 m are in good agreement with the data of electro-tomography. The ERT revealed tectonic ledges and thrusts at the transitions from sediments of depressions to mountain framing, and the zones of rupture faults in the near-surface sediments. Let us consider in more detail each of the methods.

2.1 TEM Method

Measurements in 2004–2017 were performed by digital telemetry equipment of the «BAIKAL MERS» series [3]. To build deep models of the Chuya depression, data of 2004–2017s and a large amount of archival TEM data were used (more than 2000 soundings from the 80s last century). All field work was carried out with the inductive installations of "coaxial square loops" with sides of the generator loop of 500 and 400 m. The average distance between the profiles was 2 km, and between TEM points—400–500 m. The average relative measurement error was estimated

at about 5%, but for archival data could increase to 10–15% due to a weak signal in late times.

Taking into account the results of preliminary processing of archival data in the field work on the territory of the Kuray Basin in 2008–2017, the same installation was chosen—"coaxial loops" with sizes of the generating loop 200×200 m, and the receiving one 100×100 m. The points were located as evenly as possible across the depression territory.

In the Uimon depression, the TEM measurements were carried out in two modifications: coaxial and spaced loops. Since the thickness of the sedimentary deposits was unknown in advance, in order to achieve the required depth at the first stage of work in 2011, the side of the generator and measuring loops was 500 m and 200 m, respectively, and the spacing for the boundary observations varied from 600 to 1000 m. Further work was carried out with smaller sizes of coaxial arrays (200×200 m, 100×100 m).

2.2 VES Method

Measurements in 2004–2017 in all three depressions were performed by a symmetric four-electrode Schlumberger installation with half-spacing of the generator line (AB/2) from 1.5 to 1000 m, along with the ANCh-3 and Medusa equipment. The largest volume of archive VES in the 60–70s of the last century was obtained in the Kuray depression and used for interpretation. According to the results of repeated VES, the relative error of the measurements did not exceed 5%.

2.3 Electrical Resistivity Tomography

The investigation was carried out with the Scala 48 electrical prospecting station developed at IPGG SB RAS [4]. Two 24-electrode cables with spacing between electrodes of 5 m are connected to the station, which makes it possible to obtain a geoelectrical section along a profile 235 m long. Using the Schlumberger four-electrode installation, the depth of measurements was about 50–60 m. To increase the depth of investigation to 100–120 m, measurements were carried out with the three-electrode installation AMN∞, with an external supply electrode.

2.4 Interpretation

Interpretation includes the stage of preliminary processing, analysis and evaluation of the quality of field data. For the ES method, we consider the curves of the emf and those of apparent resistivity. Consideration of the material in all three depressions showed that most of the apparent resistivity curves have a pronounced minimum and at least a few points after it, which form the right ascending branch allowing us to determine high-resistivity horizon (basement) depth with large

confidence. Some parts of the curves, mainly corresponding to late stage of the transition process, are distorted by influence of three-dimensional inhomogeneities, and most of them are obtained at the points located near the fault zones.

At the next stage, quantitative interpretation is performed using software systems for modeling and inversion (Era, EMS, developed at IPGG SB RAS, and Zond-TEM) [5, 6]. Due to high spatial locality of the inductive coaxial loops, the interpretation is based on a horizontally layered model. Distortions were analyzed using three-dimensional numerical modeling programs [7].

For the VES method, the apparent resistivity curves characterizing the quality of the field data were considered directly in the field. Preliminary analysis of the archived VES curves along the Kuray basin showed that not all curves went to the right asymptote, which is related to insufficient size of the installation for achieving the required depth. According to VES data, it was impossible to determine the depth of the basement roof in a number of sites, especially in the southern part of the depression in the zone of deep foothill deflections. According to data obtained in the Uimon basin, only a part of the VES curves can be used to determine depth parameters of the section, hence, using TEM method is advisable.

At the second stage of quantitative interpretation, a one-two-dimensional inversion was performed; the results were visualized using the Zond software [8].

Preliminary processing of ERT field data was performed using the SiBER Tools software, which is intended for creating and editing files with arrays settings, primary data processing, filtering, layout, and export to interpretation programs. ERT data have been processed using the software packages RES2D [9], ERTLab [10], ZondRes2d [8]. The resulting geoelectrical sections clearly reflect the two-dimensional distribution of electrical resistivity, from which it is possible to estimate the size of inhomogeneities, the width of the fault zone and, if necessary, you can extend or shift the profile. In the course of further processing, various methods of inversion and visualization of data were tested for construction of final sections and models. After these, the results of electro-tomography were used in the construction of initial models of three-dimensional numerical modeling.

3 Discussion of the Results

The Chuya depression is the largest intermountain structure of the Altai Mountains (Paleogene). The fault boundaries of the depression are well defined by the change of Cenozoic sediments to the rocks of mountain ranges. From the South-West one can see the faults of the South Chuya ridge, and from the North-East—the Kuray fault zone. The thickness of the sedimentary cover in the northern and western parts of the depression according to electromagnetic sounding data reaches 1000 m or more [11]. Figure 2 shows geoelectrical section constructed from the archival data of the TEM method (the location of the profile is shown in Fig. 1). The section cuts the main structural elements of the basin from North to South. The greatest thickness of sediment is observed in the deep northern trough and in the central part
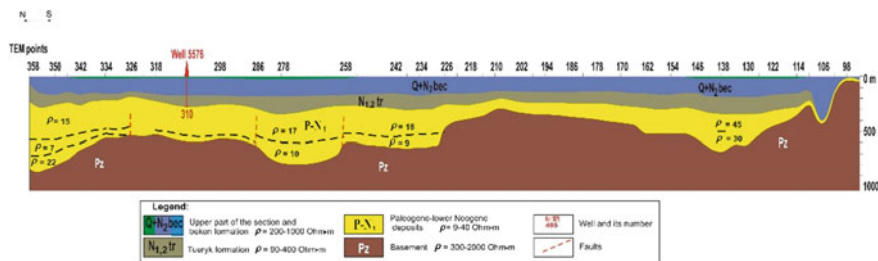
Fig. 2 Geoelectrical section along the profile 7 in Chuya basin according to TEM data

of the profile. Further in the South direction one can recognize a lengthy raised basement block (points 226–170) and two local deflections, piedmont of which is filled with higher-resistive deposits (point 106). Considering the remaining meridional sections, it can be noted that the northern side of the depression is the most complicated. Along it there are oversteps of Paleozoic rocks to later tertiary deposits and almost everywhere there are maximum basement depths.

New information about the structure of the western part of the Chuya Depression (valley of the Chagan river) was obtained according to the suit of electromagnetic methods after the Chuya earthquake, which significantly changed the shape of the valley. The epicenter of the main shock is located in the Chagan-Uzun block dividing the Chuya and Kuray depressions, and the valley of the Chagan river is in the zone of the devastating effects of the event. In its territory there are numerous primary and secondary seismic dislocations in the form of landslides, landslides, cracks, griffins. In the result of interpretation of deep-seated methods, geoelectrical models of the sedimentary sequence and the upper part of the basement were constructed, fault structures were identified, and a general increase in the thickness of the Cenozoic sediments towards the port side was revealed [12].

In order to confirm continuation of faults covered by sediments to the upper part of the section and to obtain more detailed characteristics in the near-surface part, then ERT measurements were performed in local areas.

The results of different methods are in good agreement in the depth range within the first few hundred meters, and an integrated approach improves the overall informational content of the study. The model of the reference horizon (basement) clearly shows the presence of a raised block in the northeast valley with a Cenozoic sediment thickness not exceeding 120 m relative to the southwestern block, where the depth to the base is about 300 m. These blocks are separated by a fault structure. To clarify their parameters several ET profiles were made. The data obtained confirm continuation of the fault in the Quaternary deposits. The ERT profiles in the southwestern part of the Chagan river valley are crossed by primary seismogenic fractures of the Chuya earthquake. On the constructed sections, there are subvertical and inclined zones with a low value of resistivity and different depths, corresponding to gaps on the surface.

The smaller Kuray depression developed simultaneously with the Chuya basin, but differs significantly from it in structural features. According to results of interpretation of ground-based electrical prospecting data (VES, TEM, ERT), it features a complicated fault-block structure. The greatest depths to the basement, exceeding 1000 m, in contrast to Chuya, are located along the southern and southeastern sides. The thickness of sediments in the Aktash Trough along the northern side is substantially less and is approximately 600 m [13]. We also note the complicated structure of the southern part of the depression in the junction zone of the Eshtykel and South–West troughs, where not only latitudinal but also sub-meridional faults are observed. Submeridional structures are confirmed by collation of geoelectrical and seismological data. Distribution of earthquake epicenters shows that they are mainly located within the fault zones identified by analysis of electromagnetic data [14]. Figure 3 shows a geoelectrical section built on the base of TEM and VES (see the profile location in Fig. 1). It cuts almost the entire Kuray depression from South to North,. It is clearly seen that the depression in the North and South is limited by deep foothill troughs, and the southern trough is much deeper. The smallest depths to the basement are observed in the area of the Salganduy block covered by sediments 200 m thick, and in the Central Kuray depression with a sediment thickness of about 400 m. Geoelectrical models confirm the fact that the Kuray ridge is thrust over the depression. According to TEM data, there is a forberg in the southeastern part of the depression. This is consistent with geological materials.

Electro-tomography measurements in the Kuray depression were performed in its marginal and central parts. In the central part of the depression, a series of parallel profiles intersects a fault nicely seen in the relief. The results of measurements over the course of several years show a significant change in the electrical resistivity of the inclined low-resistivity zone (fault zone), which is presumably associated with increased seismicity in the southern part of the depression. In the selvedge parts of the depression, the results of measurements by ERT method reflect the complicated structure of the basement with presence of ledges.
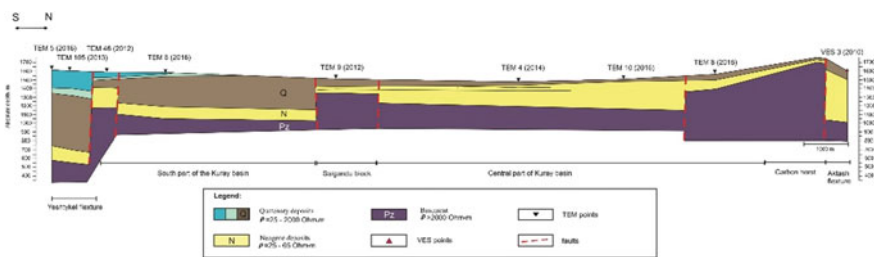
Fig. 3 Geoelectrical section along the profile 3 in Kuray intermountain area according to TEM and VES data
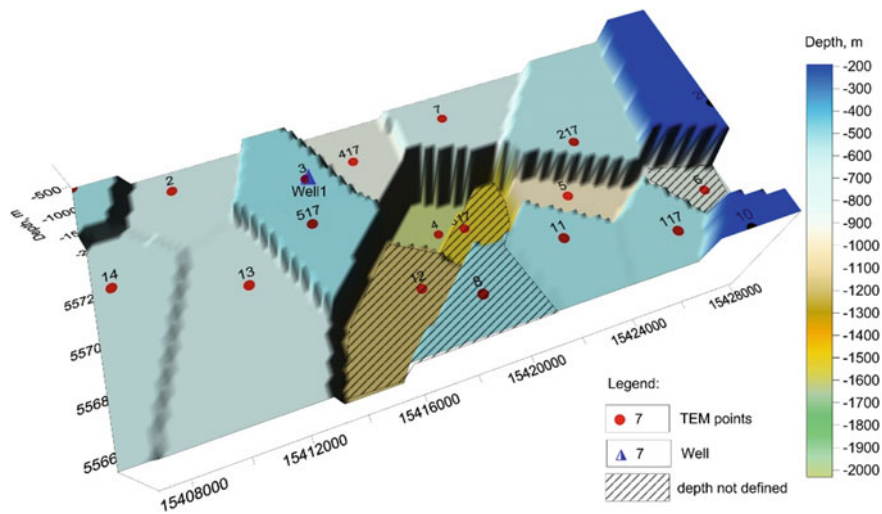
Fig. 4 Fault block model of basement surface in Uimon depression according to TEM data

Although electromagnetic measurements were previously performed in the Uimon depression, at present time it remains poorly studied. For the first time in 2011, there were invoked a suite of multiple-depth electromagnetic methods (ERT, VES, TEM) to study the internal structure of the Uimon depression. And in 2013 specialists of Gorny Altai Expedition drilled a well in the central part on the base of analysis of our materials on the structure of the basin that presented a section of Neogene-Quaternary sediments [15]. Comparison of borehole and geoelectrical data indicates their good agreement.

In general, interpretation of electromagnetic data for 2011, 2012 and 2017 yields near-surface and deep geoelectrical characteristics of sedimentary filling and the reference horizon of the depression. Figure 4 shows the fault-block model of the foundation according to the data of TEM. The greatest depths are shifted to the southern and southeastern sides of the depression, where the thickness of the sedimentary filling reaches 2500 m. Distortions of some TEM curves evidence the influence of three-dimensional inhomogeneities.

Electrical resistivity tomography profiles are made in the zones of transition from sediments to mountain framing. These profiles intersect tectonic ledges observed in relief. On the 2D sections in the northern part of the depression, one can distinguish high-resistivity sloping zones corresponding to the ledges; according to a priori data, low-resistivity sections are associated with fault fractures flooded with a series of small sources. The sections show the approach of a mountain frame in the zone of the South Terekhta fault to the Uimon depression.

4   Conclusions

The geological and geophysical interpretation of data obtained by a suite of electromagnetic methods presents the structure of three tectonic depressions of Gorny Altai, and, despite the common features of their formation and development, the structure is significantly different. The common feature is the fault block structure of the considered depressions. It can be seen in the models of sedimentary sequence and the upper part of the basement built on the base of data from geoelectrical studies. Important results include localization of faults overlapped by Cenozoic sediments and thrusts of the Paleozoic rocks of the northeastern mountain ranges to the sedimentary depressions. The assumed faults are first identified on the base of interpretation of electromagnetic data using geological, seismological, and other a priori information. On cross sections, the fault structures are characterized by sharp change in the thickness of sediments as well as lower values of electrical resistivity relative to the host medium. Then, the selected faults were verified by three-dimensional numerical modeling using the programs developed at IPGG SB RAS.

The Chuya and Kuray basins actually form a single system, but each of them has its own characteristics, described in the article. The greatest structural differences are observed in the Uimon depression. It is located far enough from the Chuya and Kuray depressions. At present, this depression is aseismic, but multiple traces of ancient earthquakes indicate its high seismic potential. Sedimentary rocks making the Uimon basin are characterized by higher values of resistivity, in addition, maximum basement depths are observed (up to 2500 m), and the most submerged blocks are located in the central and eastern parts, while in the Kuray and Chuya basins there are deep troughs stretching along the northern and southern mountain framing.

Future studies will be carried out in order to clarify the most difficult constructed areas of the depressions with the assistance of three-dimensional programs.

References

1. Lunina, O., Nevedrova, N., Gladkov, A.: Tectonic and geoelectric structures of rift basins in the Baikal region. C.R. Geosci. **344**, 149–158 (2012)
2. Deev, E.V., Zolnikov, I.D., Turova, I.V., Rusanov, G.G., Ryapolova, Y.M., Nevedrova, N.N., Kotler, S.A.: Paleoearthquakes in the Uimon basin (Gorny Altai). Russ. Geol. Geophys. **4** (59), 351–362 (2018)
3. Babushkin, S.M., Nevedrova, N.N.: Instrumental and methodical means in the search for ore deposits by the method of nonstationary electromagnetic sounding. In: 13th International Scientific Conference on GEO-Siberia 2017, vol. 2, pp. 271–275. Novosibirsk (2017) (in Russian)

4. Balkov, E.V., Panin, G.L., Manstein, Y.A., Manstein, A.K., Beloborodov, V.A.: Experience of using electrotomography in geophysics. Geofizika **6**, 54–63 (2012) (in Russian)
5. Khabinov, O.G., Chalov, I.A., Vlasov, A.A., Antonov, E.Y.: The system for interpretation of EMS transient electromagnetic sounding data. In: GEO-Siberia—2009: The V International Scientific Congress, Siberian State University of Geosystems and Technologies, pp. 108–113. Novosibirsk (2009) (in Russian)
6. Kaminsky, A.E. Programma ZondTEM1D. http://zond-geo.ru. Accessed 18 May 2018
7. Sanchaa, A.M., Nevedrova, N.N., Stabel, N.V.: Three-dimensional modeling of fault structures in the Chuya depression according to the method of formation of the electromagnetic field. In: International Conference "Computational Mathematics and Mathematical Geophysics", dedicated, 90th Anniversary of the Birth of Academy, pp. 106–107. A. S. Alekseeva, Novosibirsk (2018) (in Russian)
8. Kaminsky, A.E.: Zond Software. http://www.zond-geo.com. Accessed 18 May 2018
9. Loke, M.H.: Geotomo Software Pvt Ltd. http://www.geotomosoft.com. Accessed 18 May 2018
10. Geostudi sAtier s.r.l. http://www.geostudisrl.com/. Accessed 18 May 2018
11. Nevedrova, N.N., Epov, M.I., Antonov, EYu., Dashevsky, Y., Duchkov, A.D.: Reconstruction of the deep structure of the Chuya depression of the Gorny Altai according to the data of electromagnetic soundings. Geol. Geophys. **42**(9), 1399–1416 (2001)
12. Nevedrova, N.N., Deev, E.V., Ponomarev, P.V.: Fault structures and their geoelectric parameters in the epicentral zone of the 27 September 2003 Chuyaa earthquake (Gorny Altai) from resistivity data. Russ. Geol. Geophys. **58**(1), 123–132 (2017). https://doi.org/10.1016/j.rgg.2016.01.021
13. Nevedrova, N.N., Deev, E.V., Sanchaa, A.M.: Deep composition and characteristics of the marginal structures of the Kuray basin (Gorny Altai), from data of geoelectric studies with a controlled source. Russ. Geol. Geophys. **55**(1), 98–107 (2014). https://doi.org/10.1016/j.rgg.2013.12.008
14. Sanchaa, A.M., Nevedrova, N.N., Ponomarev, P.V.: Block structure of the southern Kuray Basin of Gorny Altai according to geoelectric data compared to the distribution of earthquake epicenters. Geodyn. Tectonophys. **10**(1), 167–180 (2019). https://doi.org/10.5800/GT-2019-10-1-0409
15. Rusanov, G.G., Deev, E.V., Zolnikov, I.D., Khazin, L.B., Khazina, I.V., Kuzmina, O.B.: Reference section of Neogene-Quarternary deposits in the Uimon Basin (Gorny Altai). Russ. Geol. Geophys. **58**(8), 973–983 (2017)

Geoelectrical Models of Fault Zones in the Gorny Altai Region

Nina Nevedrova⬤, Sergey Babushkin⬤, Aydisa Sanchaa⬤,
Ilya Shaparenko⬤ and Alexander Shalaginov⬤

Abstract

The article reviews structurally-complex areas with presence of fault zones in the territory of large depressions (Chuya and Kuray) of the Gorny Altai. The research was carried out in the aftershock period of the destructive Chuya earthquake in 2003, in an area with high seismic activity. Determining the structure and location of zones of fracture disturbances, concealed by loose sediments, causes certain difficulties. In such case, it is necessary to involve several electromagnetic methods. A measurement and interpretation method is proposed for designing geoelectrical models of faults, including those concealed by loose sediments. A complex of methods of different depth is involved (transient electromagnetic method, vertical electrical sounding, electrical resistivity tomography) for measurements. Interpretation is carried out by means of modelling software and inversion systems, 2D and 3D software. Depth and near-surface models of fault zones are designed. The characteristics of these models are relevant for identifying seismogenic faults, geodynamic and predictive problems.

N. Nevedrova (✉) · A. Sanchaa · I. Shaparenko (✉) · A. Shalaginov
Trofimuk Institute of Petroleum Geology and Geophysics, Siberian Branch,
Russian Academy of Sciences, Koptug ave. 3, 630090 Novosibirsk, Russia
e-mail: NevedrovaNN@ipgg.sbras.ru

I. Shaparenko
e-mail: ShaparenkoIO@ipgg.sbras.ru

S. Babushkin
Seismological Branch, Geophysical Survey, Russian Academy of Sciences,
Koptug ave. 3, 630090 Novosibirsk, Russia

1 Introduction

Regular observations by means of electrical and non-stationary electromagnetic sounding methods i.e. vertical electrical soundings (VES), electrical resistivity tomography (ERT) and transient electromagnetic method (TEM) are concentrated in several parts of the epicentral zone of the destructive Chuya earthquake of 2003, on the territory of Gorny Altai. The observations have been carried out since 2004. In addition, new measurements are carried out by these methods to clarify the structure in each surveying season.

A significant amount of VES and TEM data is used for research works, which was obtained on the territory of Altai depressions (Chuya, Kuray) in the second half of the last century before the Chuya earthquake Data of the contemporary measurements that have been carried out after the event is also used for research works. A survey map of the area under study is shown in Fig. 1.

Modifications of sounding method with grounded and combined installations were tested for non-stationary electromagnetic sounding, in addition to installations with inductive excitation. According to the data of grounded installations, it is possible to determine not only the electrical conductivity of the section, but also the
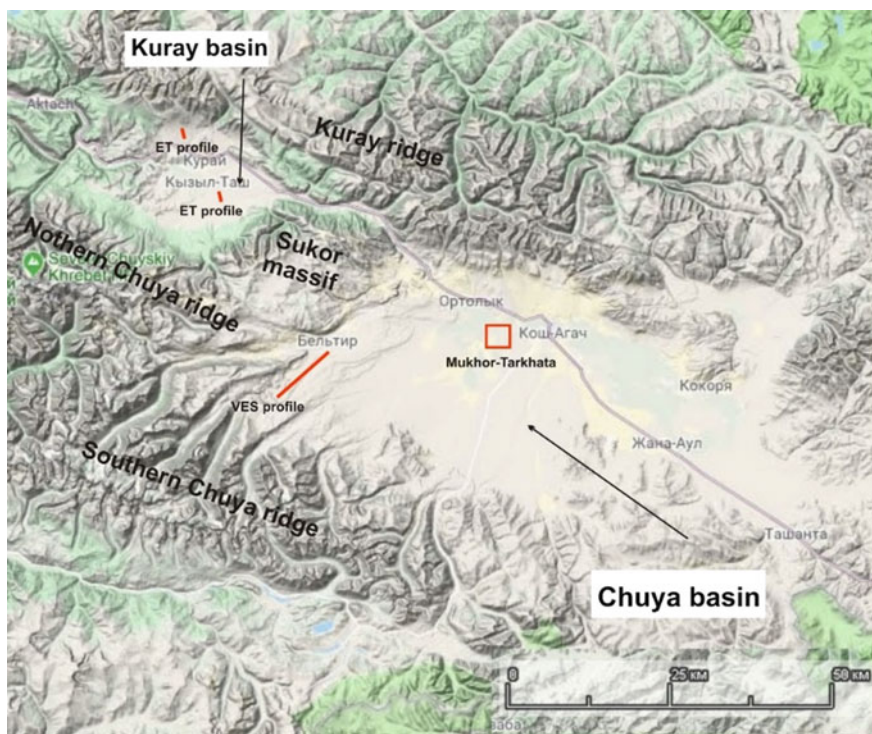
Fig. 1 Survey map of the area under study

electrical anisotropy parameter (λ). The anisotropy coefficient was also obtained from the direct current geoelectrical survey data. At present, it has been experimentally proven for Altai depressions that both the parameters i.e. electrical resistivity and anisotropy coefficient can be effectively applied for electromagnetic monitoring in seismically active areas to assess the impact of geodynamic processes on the geological environment.

The experience of processing and analysing electromagnetic monitoring data in different seismically active regions of Siberia has shown that detailed knowledge is required on the structure of the area under study i.e. its tectonic features and fracture faults, in order to understand and assess the impact severity of seismotectonic processes on the physical parameters of the geological rock massif.

Determining the structure and location of fracture disturbance zones, concealed under loose sediments, causes certain difficulties. In this case, it is necessary to involve several electromagnetic methods. The measurement technique for designing geoelectrical fault models implies application of two methods of different depth: TEM, ERT or VES, depending on the sedimentary sequence thickness. Initially, the fault is separated out according to VES TEM data and ERT method is applied to confirm the fault structure continuation in the upper part of the section and to determine its characteristics in details. In the case of small thickness of sediments i.e. approximately 100 m, only ERT method can be applied. Such areas, for example, transition zones from depressions to mountain framing are observed.

The complexity of using the proposed set of methods is to obtain multi-scale models. Therefore, in the course of interpretation, the depth model at first and then the near-surface model is sequentially taken into account and the technique for interpreting the field data of each method is somewhat different. On the other hand, the approach is common. At first, simpler 1–2D modelling and inversion software tools are used and then three-dimensional software is used to verify and refine the models.

Structurally-complex areas with presence of fault zones in the territory of large basins of the Gorny Altai were selected for this study (Fig. 1). The faults can be seismogenic and their detailed characteristics are important for a number of geological disciplines, geodynamic and forecasting tasks.

2 Fault Structure Delineation in Western Part of the Chuya Basin

2.1 Chagan River Valley

The epicentre of the Chuya earthquake is located approximately 20 km west of the valley. Tectonic rupture of an event of up to 70 km long can be traced on the Earth's surface in the form of a discontinuous strip of cracks, landslides and soil displacements. The tectonic rupture occurrences are observed on the slopes of the mountain ranges bordering the Chuya basin, and covering its western

part. Numerous seismic dislocations indicate the complex fault structure of the epicentral zone in pleistoseist region.

The most severe consequences of the Chuya earthquake are observed in the Chagan River valley and Beltir village is located in the north of the valley. This territory is historically a place of settlement and economic activity of indigenous people of Altai. Previous geoelectrical studies have shown that the thickness of sediments in the valley reaches up to approximately 300 m. Therefore, application of direct current methods is optimal. The complex included vertical electrical sounding and electrical resistivity tomography (ERT). ERT method allows creating a dense observation network and to significantly increase the detail of the study of near-surface sediments up to first hundred meters, depending on the installation. VES method is used at the first stage and according to the VES data, depth models of sedimentary thickness and the upper part basement have been constructed by separating out the predicted faults. ERT measurements are performed at the second stage at the sites of selected dislocations. The fault structure is reflected by a lowering resistivity zone on the sections of ERT with respect to the enclosing sediments. The results of the two methods are in good agreement in the depth range of electrical resistivity tomography.

Let us consider two sections with the presence of a fault zone in the north of the depression (Fig. 2). The VES profile intersects the section from the southwest to the northeast and the ERT profile of 800 m long is performed in the area of VES point 34 across the assumed fault structure.

According to the VES data, the section reflects block structure of the site, as well as the presence of permafrost sediments at depths of up to 100 m. Fault is determined by a sharp change in absolute elevations of the basement roof and the thickness of low-resistivity horizon. The total thickness of cenozoic deposits in the south-western block reaches 300 m and the north-eastern one is only 120 m. According to the VES data with an average distance of 500 m between points, it is impossible to determine a detailed characteristics of the fault zone, such as width, specific resistivity range and possible fault plane inclination. Measurements were performed on a series of ERT profiles in order to obtain the above-mentioned parameters and determine the fundamental possibility of fault continuation in the upper part of the section. One of the profiles (Fig. 2b) was performed with a three-electrode installation and the section was structured to a depth of approximately 80 m, based on the results of a two-dimensional interpretation data. A sub-vertical zone with reduced rock mass resistivity, separating the two higher resistivity blocks, clearly stands out almost in the centre of the section. The width of the conductive zone is 120–130 m. The zone is concealed under significantly more high-resistivity rock mass up to a depth of 30–40 m and most likely by permafrost. Thus, it is possible to continue the fault in quaternary deposits by taking into account the ERT data. The presence of disturbance is confirmed by the geological work performed after the Chuya earthquake and numerous frost heaves were formed on the strike of identified fault zone [1].
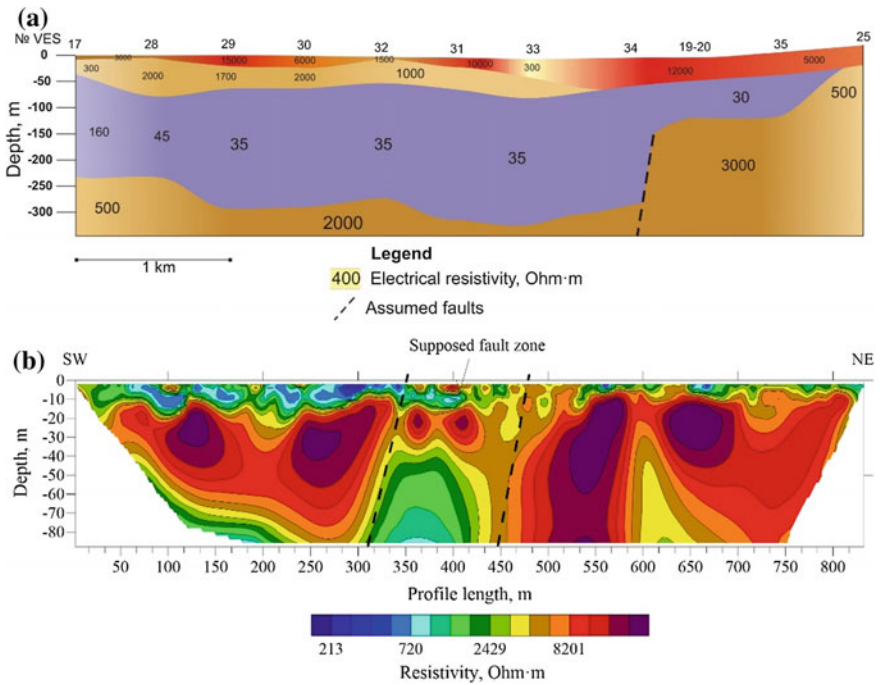
Fig. 2 Fault zone structure in the Chagan river valley (Chuya basin); **a** section according to VES data, **b** section according to ERT data

2.2 The Muhor-Tarkhata Site

The Mukhor-Tarkhata site is located in the western part of the Chuya basin, near Mukhor-Tarkhata village. A team of electromagnetic monitoring of the Institute of Petroleum Geology and Geophysics, Siberian Branch of the Russian Academy of Sciences (IPGG SB RAS) has been carrying out structural and monitoring observations by means of three modifications of the transient electromagnetic method (TEM) since 2007. Surface measurements by means of TEM method with uniaxial installations were performed to determine the depth structure. A map of the depths to the surface of the foundation was drawn out. According to the TEM data, the fault is separated out by a submerged basement block, practically in the central part of the site, extended from south to north and correlated with the flow of the Mukhor river (Fig. 3a). This rift was based on the geological data. A renowned geologist Zolnikov I.D. divided the territory of Chuya basin into several large geomorphological segments, based on the analysis of the digital terrain model from the radar mapping (SRTM) data and satellite images LANDSAT. The border between two of these segments passes directly through Mukhor-Tarkhata section along the Mukhor river and indicates the presence of interblock fault [2].
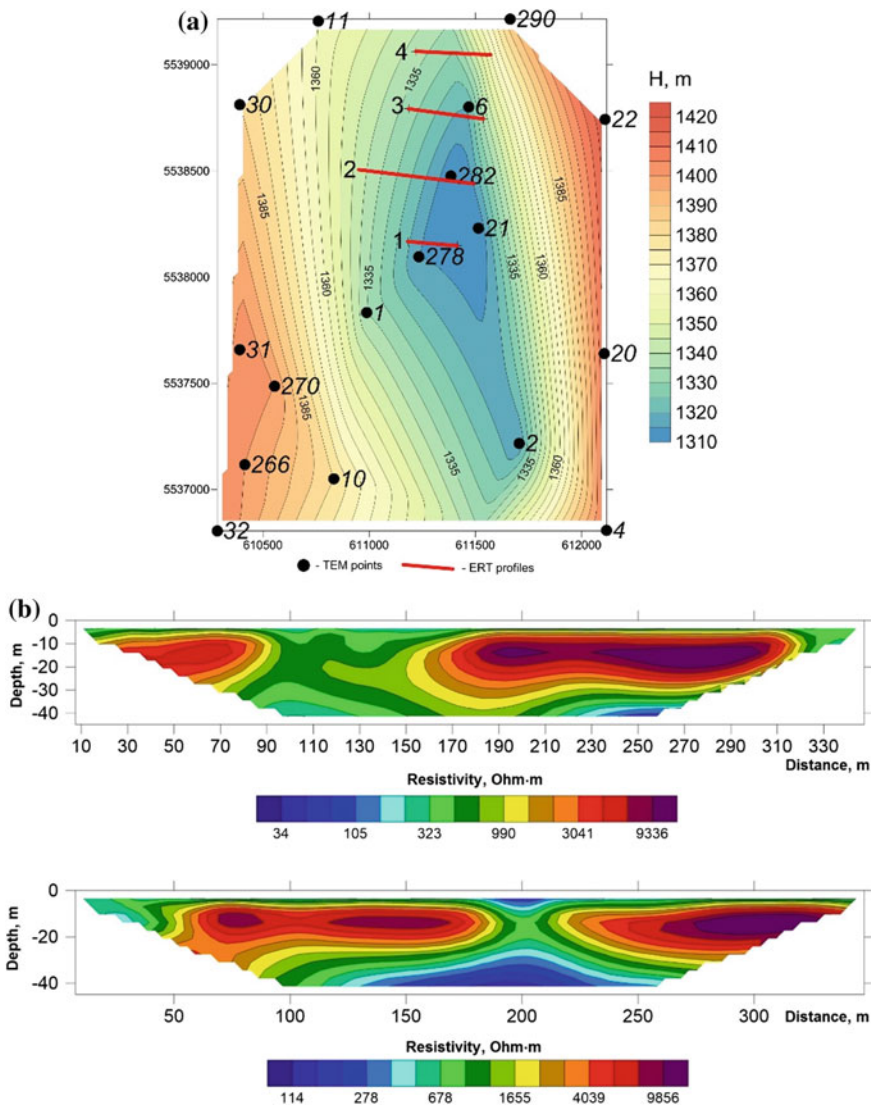
Fig. 3 Geoelectrical structure of Mukhor-Tarkhata area; **a** depth map to the basement, **b** ERT sections through the fault zone

The electro-tomography method was involved in order to determine the near-surface structure of the fault structure and to confirm its continuation into quaternary loose sediments. The measurements were carried out by means of Schlumberger installation for several profiles of different lengths due to specificities of the site as it was heavily marshy in some places. The Res2DInv software package [3] was applied for interpretation. As a result of two-dimensional inversion of the

ERT field data, it is possible to estimate the geoelectrical characteristics of the upper part of the fault zone, its size and specific electrical resistivity intervals (Fig. 3b).

Zones with lowered electrical resistivity values in respect to the containing medium are well traced in sections along the ERT profiles, starting from the day surface to a depth of approximately 40 m. These zones can be interpreted as a manifestation of a fault disturbance. It can be noted that a significant decrease in the electrical resistivity values in respect to the surrounding medium is most often observed for zones of active faults. In addition, they can differ in their anisotropic electrical properties, which is confirmed by a number of field experiments and theoretical calculations.

3 Faults in Kuray Basin

Faults are often expressed in relief, for example, in form of steps (ledges). Such structures were revealed at several sites in the Kuray basin. The ERT method is applied at a small thickness of sediments or in cases of reliable separation of a fault according to several geological and geophysical features and a priori data.

Let us consider a few examples. The rift that passes at the foot of the ledge in the northern part of Kuray basin (Aktash graben) was verified according to ERT data. Initially, this fault was justified by geological structural work and confirmed by the results of interpretation of VES data. Geoelectrical models in points located at the top of the ledge (VES 1301) and at its foot (VES 1302) differ (Table 1). According to the comparison of the models obtained, it follows that the thickness of the sedimentary layer in the VES 1302 area reaches 350 m and the thickness for VES 1301 is 250 m. The thickness of the conducting 6th horizon of VES 1301 is equal to 150 m whereas, the thickness for VES 1302 is 300 m Such a drastic change in thickness may indicate the presence of a fault zone here.

Table 1 Geoelectrical models according to VES data in the Aktash graben region of the Kuray Basin

Layer	VES 1301		VES 1302	
	Resistivity ($\Omega \cdot$ m)	Thickness (m)	Resistivity ($\Omega \cdot$ m)	Thickness (m)
1	150	0.4	150	2
2	3000	2	3000	1
3	300	13	300	8
4	1000	35	800	13
5	300	50	200	50
6	100	150	60	300
7	2000		500	500
8			2000	

Therefore, ERT measurements were later performed through these VES points and they were carried out initially with a single profile. An analysis of results of the interpretation of ERT and VES data has shown their congruity. A high-resistivity rock mass (up to 3000 $\Omega \cdot$ m) with a thickness of approximately 30 m is observed, lying at a depth of 15 m in the western part of the ERT section and which corresponds to the fourth layer of the geoelectrical model for VES 1301. A similar area has less resistivity (approximately 860 $\Omega \cdot$ m) and lower thickness (no more than 20 m) at a depth of 10 m in the eastern part of the section and which also corresponds to the fourth horizon in the geoelectrical model VES 1302.

Further, areal ERT measurements were performed using a system of parallel profiles. Vertical sections of a three-dimensional model of the area is presented as a result of 3D inversion and visualization using the ERTLab software package [4]. Fault disturbance is distinguished by the zone of resistivity decrease of up to 170 $\Omega \cdot$ m in respect to higher-resistive host sediments (Fig. 4).

A ledge, having an amplitude of several meters, is also well distinguished in the relief of the central part of Kuray basin. The ledge is traced along the strike of the basin parallel to the Chuya river, as if limiting its raised central part. 4 ERT profiles were laid across the strike of the assumed fault structure in order to design a model of the area. As a result of three-dimensional inversion of areal ERT data, a geoelectrical model was constructed. The model is characterized by a high-resistivity upper part with a resistivity in the range of 800–10,000 $\Omega \cdot$ m and a well-defined inclined conducting zone with a lowering resistivity of 200 $\Omega \cdot$ m, which most likely corresponds to the fault structure (Fig. 5).

ERT measurements have repeatedly been performed in this site annually since 2015. Comparison of geoelectrical parameters of the fault zone has illustrated significant variations in resistivity. These variations can be attributed to seismic
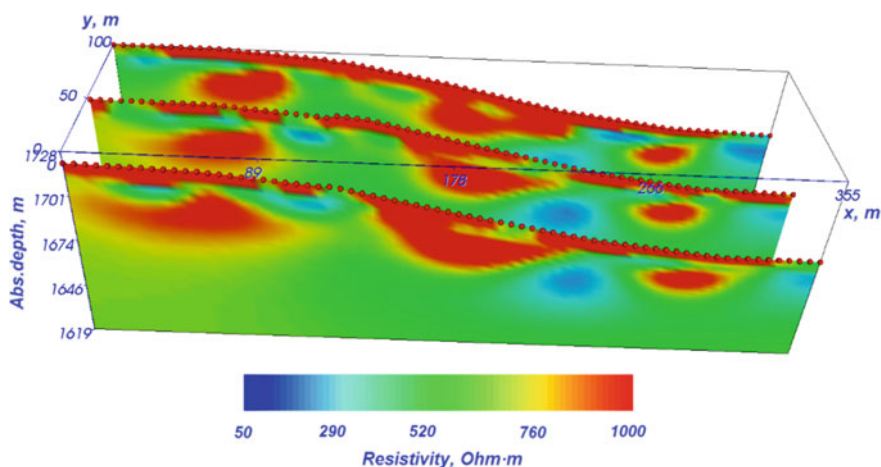
Fig. 4 The result of a three-dimensional inversion of areal ERT data in the Aktash graben of Kuray Basin
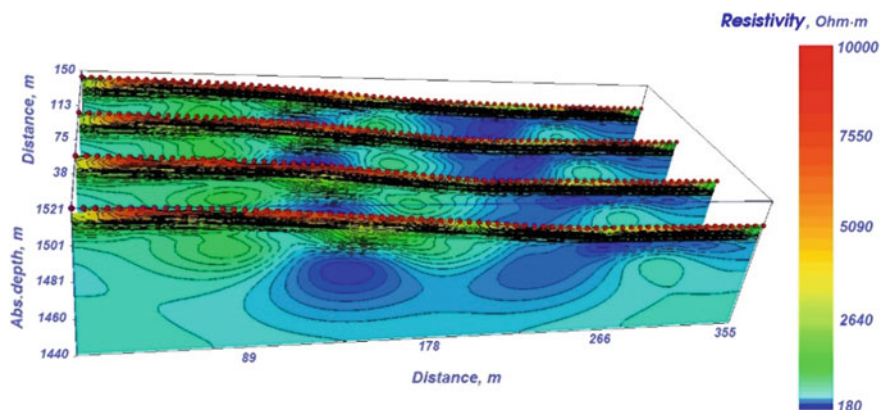
Fig. 5 The result of a three-dimensional inversion of ERT data for 2018 in the central part of Kuray basin

activity due to incomplete aftershock period of the Chuya earthquake and periodic activations and calm periods are observed during the aftershock. In addition, the fault activity can be estimated in terms of magnitude of variations of geoelectrical parameters in the fault zone.

4 Conclusion

The system of electromagnetic methods with a controlled source is used to solve two important tasks i.e. constructing geoelectrical models of intermountain depressions and monitoring the electrophysical characteristics of rock mass. These tasks are undoubtedly related, since the structure specificities, information on the existing fault zones and geoelectrical parameters of the zones are important for selecting the optimal location of regular observation points and further for a comprehensive analysis of the obtained data. In addition, it was revealed that monitoring observations in the fault impact zone determine the extent of fault activity and as a result, highlight the probable seismogenic faults.

The involvement of electrical resistivity tomography in the study in recent years makes it possible to construct detailed models of fault zones in the intermountain depressions of Gorny Altai. Based on the analysis of ERT results, it is concluded that these zones are characterized by lower values of resistivity in respect to the bedrock. In addition, different intervals of decreasing resistivity from 70–100 to 400–500 $\Omega \cdot$ m were obtained depending on fracturing, the presence of permafrost and the extent of fault activity.

References

1. Nevedrova, N.N., Deev, E.V., Ponomarev, P.V.: Fault structures and their geoelectric parameters in the epicentral zone of the 27 September 2003 Chuya earthquake (Gorny Altai) from resistivity data. Russ. Geol. Geophys. **58**(1), 123–132 (2017). https://doi.org/10.1016/j.rgg.2016.01.021
2. Zol'nikov I.D., Lyamina V.A., Deev E.V.: New data on Quaternary morpholithogenesis in the Chuya basin (Gorny Altai). Russ. Geol. Geophys. **51**, 339–348 (2010) (in Russian)
3. Loke, M.H.: Geotomo Software Pvt Ltd. http://www.geotomosoft.com. Accessed 18 May 2018
4. Geostudi sAtier s.r.l. http://www.geostudisrl.com/. Accessed 18 May 2018

Rotation Factor: Dynamics and Interaction of the Earth's Core and Mantle

Vladimir Ovtchinnikov and Dmitry Krasnoshchekov

Abstract

The crystalline solid inner core is the most distant and enigmatic part of our planet, and along with the Earth's crust is the smallest one. The inner core was discovered in 1936 and to date there have been observed a number of its anomalous and puzzling features —low rigidity and viscosity (comparing to other solids), high seismic attenuation, strong anisotropy and differential rotation. The inner core is isolated from the upper solid Earth shells by the liquid outer core with low viscosity, and hence it can rotate, oscillate, precess, vibrate and move out along the spin axis. About 25 years ago studies of generation, evolution and sustainment of the Earth's magnetic field launched active investigations of the crystalline core. Estimate of IC differential rotation velocity with respect to mantle is important for explaining a number of geodynamical patterns and effects—e.g. the observed global distribution of seismicity spatially coordinated with critical latitudes. One of the hypotheses associates the distribution with variation in the Earth's rotation velocity. In this report we analyse information published thus far on differential rotation of the Earth's inner core and acknowledge multiple controversies. The differential rotation velocity estimated by body waves is between 0° and 3° per year; the Earth's normal mode data yield the velocities between –2.5° and –0.8° per year, whereas the most probable estimates are from –0.2° to 0.2° per year. The inner core stationary rotation envisaged by geodynamo simulations is unlikely; it is rather non-stationary—with accelerations/decelerations induced by the Earth's mantle.

V. Ovtchinnikov (✉) · D. Krasnoshchekov
Institute of Dynamics of Geospheres, Russian Academy of Sciences,
Leninsky pr. 38 korp. 1, 119334 Moscow, Russia
e-mail: ovtch@idg.chph.ras.ru

D. Krasnoshchekov
e-mail: krasnd@idg.chph.ras.ru

145

1   Introduction

The inner core (IC) is the deepest and volumetrically smallest shell of the Earth. Since its discovery [1] there have been observed a number of its anomalous and puzzling features—low rigidity and viscosity (comparing to other solids), high seismic attenuation, strong anisotropy and differential rotation. IC is related to lots of problems—the ones of geophysics, geochemistry, magnetic field generation etc. It is affected by various external factors including changes in orbital and rotation parameters, tides, mantle gravity, outer core (OC) viscosity and electro-magnetic forces. Variation in thermal and chemical parameters may lead to IC internal strains resulting in differential rotation, convection in solid, deformations and anisotropy. IC is isolated from mantle by low viscosity liquid of the OC, so it can rotate, oscillate, precess and even move out from equilibrium [2–5]. Seismologists became interested in IC differential rotation due to geodynamo simulations [6], where its predicted strength and direction were determined by inner core boundary (ICB) conditions [7] and the balance between the gravitational and electromagnetic torques [8]. The IC rotation velocity was estimated as 1.6° per year, but later it turned out its precise value could be also important when explaining other geophysical processes that were not previously associated with the core. For example, distribution of seismicity around the critical latitudes—the region where the sign of deformations caused by rotation of the Earth inverts. This feature can be related to variation in rotation velocity of the Earth [9, 10]. Furthermore, Khain [11] suggests full accounting for the rotation factor in global geodynamics, not only for the purposes of explaining local configuration of crustal features like faults, cracks or lineaments.

Here we address studies of IC differential rotation to collate their outputs and constrain the range of possible IC rotation velocities with due consideration of mechanical models of such rotation.

2   IC Rotation by Seismic Body Waves

Seismological observations evidence faster propagation of seismic waves through the IC in quasi-meridional plane than in quasi-equatorial one by 3–4% [12]. It was also shown that the outer 2/3 of the IC feature cylindrical symmetry (anisotropy with transverse isotropy) [13]. Anisotropy of body wave propagation velocity (dependence of seismic velocity on the angle with the Earth's rotation axis) is an important feature of core dynamics, that enables estimates of IC differential rotation (Fig. 1).

Song and Richards [3] estimated it as 1.1° per year on the base of dependence of differential travel time residuals $ddt = (t_{bc} - t_{df})_{mea} - (t_{bc} - t_{df})_{ref}$ on calendar time. Specifically there were used PKPdf and PKPbc waveforms recorded after events at South Sandwich Islands (SSI) by the Alaskan station of COL 151° away (Fig. 2). They assumed the fast IC anisotropy axis was tilted with respect to the Earth's spin
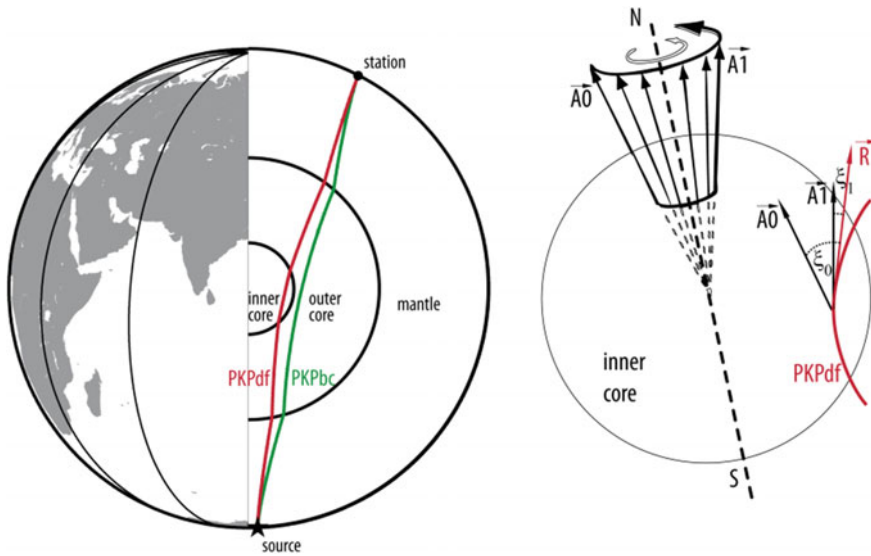
Fig. 1 Left: example ray diagram for PKPdf and PKPbc ray paths for the case of quasi-meridional (or quasi-polar) propagation in the IC. Right: schematic representation of rotating IC. R—PKPdf ray vector in bottom refraction point, A0 … A1—consecutive directions of fast anisotropy axis in eastward rotating IC, ξ—angle between PKPdf ray and fast anisotropy axis

axis, hence, if IC rotates, the angle (ξ) between PKPdf ray and the anisotropy axis should be dependent on time. It was found the dependence of *ddt* on calendar time makes 0.3 s each 30 years or 0.01 s per year. Using this value and the relation [14]:

$$\alpha = \frac{k}{(2b\cos\xi + 4c\cos^3\xi)(-R_xA0_x + -R_yA0_y)}$$

the IC rotation velocity can be estimated between 0.4° and 1.8° per year (considering uncertainty)—here R_x, R_y and $A0_x$, $A0_y$, respectively, the directional cosines of vectors R (PKPdf ray direction in the bottom refraction point) and *A0* (initial direction of fast anisotropy axis), *k*—regression slope of the experimental data, α—rotation velocity.

This estimate initiated a lot of criticism [15–18] mostly based on lack of evidence that the fast anisotropy axis did not coincide with spin axis. Besides, the observed trend of 0.3 s can result from source location error capable of making more than 50 km—it was shown the epicentral distance reduction procedure in such dataset can yield the bias of about the same value of 0.3 s. It was also noted that magnitude of the analyzed events systematically decreased in time, which encouraged positive trend in measured residuals. Finally, seismic paths to the Alaskan station of COL involve the subduction zone with its significant azimuthal heterogeneity, and IC anisotropy is not necessarily homogeneous, which may also
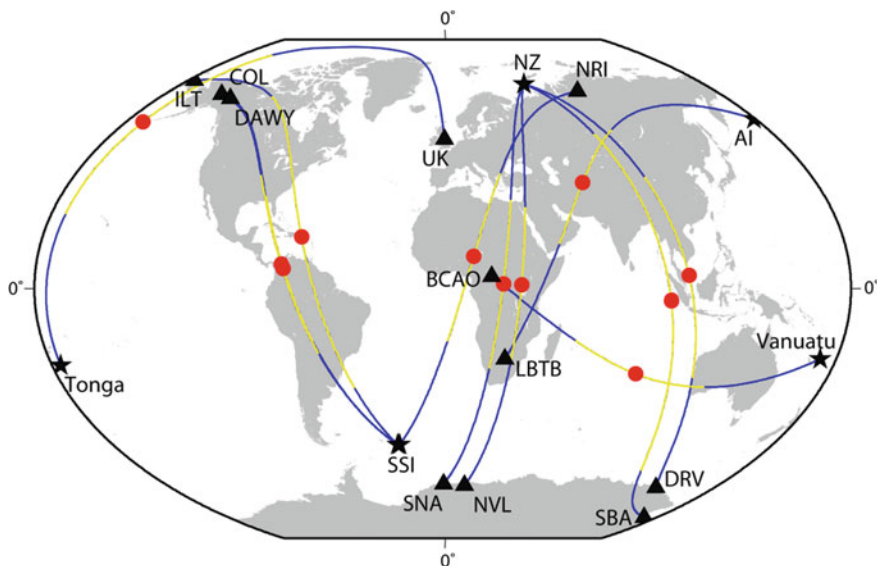
Fig. 2 Examples of referenced daylight projections of PKPdf great circle paths scanning the IC (blue); yellow—their portions in the IC; red—turn points. Stars—sources; triangles—seismic stations

contribute into the observed trend (though the latter factor in a lesser degree since the analyzed PKPdf propagation paths were scanning a restricted IC volume for which the assumption of anisotropic homogeneity was rather valid than not).

The IC rotation velocity of about 3° per year was also derived from spherical harmonics expansion of PKPdf–PKPbc differential measurements of ISC [4]:

$$\delta v(\lambda, \vartheta, \tau) = \sum_{l,m} \{A_{lm} Cos[m(\lambda - \omega\tau)] + B_{lm} Sin[m(\lambda - \omega\tau)]\} p_{lm}(Cos\vartheta).$$

It should be noted, that the analyzed ISC data featured high scatter and high-frequency variation. Creager [19] used linear parametric model to account for lateral velocity gradient in the IC:

$$\Delta v(\xi, \Delta) = \delta v_0 + \frac{\partial v}{\partial \xi}(\xi - \xi_0 - \alpha\gamma T_i) + \frac{\partial v}{\partial \Delta}(\Delta - \Delta_0)$$

where T_i—origin time, ξ—azimuth, Δ—epicentral distance, α—IC differential rotation rate, γ—coefficient of the linear model. For the data from [3] his estimate made 0.2°–0.3° per year with uncertainty of 0.05°–0.31° per year. Similar approach was invoked by Collier and Helffrich [20] who analyzed British records of Tonga events and obtained 0.47°–0.77° per year over 10 years long time period. Authors of the last referenced paper also admitted possible oscillations of the IC with period

of about 280 days, whereas the initial westward rotation changes for the eastward one.

Ovtchinnikov et al. [21] showed that the jump in differential travel time residuals of about 0.3 s in Antarctic records of Novaya Zemlya explosions carried out between 1976 and 1979 was due to localized IC heterogeneity that rotated at 0.4°– 1.8° per year. Table 1 lists some other estimates for events at SSI and in Eastern Siberia recorded at Alaska (FYU, COLA, SCM), Chukchi Peninsula (ILT) and in Antarctica (NVL, SBA, DRV, SNA), respectively. According to Table 1, the coefficient k that characterizes the change rate of IC differential rotation takes both signs. It can be explained by different configuration of seismic paths with respect to anisotropy axis. Joint interpretation of these data yields the IC rotation rate estimate of about 0.05° per year [22], which is comparable with lower bound by Creager [19]. We note, that the obtained values of slope k support IC rotation in the same direction including estimates at the Chukchi station of ILT, and the Alaskan stations of COLA, FYU and SCM that reside on the opposite sides of the subduction zone located beneath them (Fig. 2).

To scrutinize IC rotation, studies after the year of 2000 frequently invoked earthquake doublets—the events from essentially the same location, with same mechanism and energy (magnitude). Use of records of such events enables discarding the influence of near-source heterogeneities, whereas the PKPbc waveforms are not influenced by IC heterogeneities and exhibit extremely high correlation. If PKPdf arrivals correlate much worse, the IC fabric may undergo changes during the lapse time between the doublets, so the dislocation (and rotation) rate can be estimated by comparison of the waveforms.

Early studies of doublets estimated IC differential rotation rate by differential PKPbc–PKPdf travel time measurements treated as a result of dislocation of a restricted IC volume with lateral velocity gradient in it [23, 24]. The latter of the last referenced papers yields the rotation velocity of 0.27°–0.35° per year, and the former $0 \pm 1°$ per year.

Unfortunately, the above results are not backed by normal mode studies that show the IC is rotating either as not rigid body, or at an insignificant rate of $0.11° \pm 0.13°$ per year (e.g. [25]). These data however can be reconciled by the idea from [26], where differential travel times after doublets observed at COL were interpreted on the base of Bayesian statistic approach. They infer the IC rotation rate is time dependent, exhibits accelerations and decelerations, and, specifically, after the year of 2007 we'd expect westward, not eastward rotation. On the other hand, their outputs still contradict to slow (about 0.05°–0.1° per year) eastward rotation of scatterers in the IC observed by Vidale and Earle [27].

Another study [28] that produces results similar to the ones by normal modes invokes linear models of differential travel time dependency on calendar time (T) and the spatial coordinate of longitude (λ): $ddt_i = a + b(T_i - T_0)$ and $ddt_i = c + d(\lambda_i - \lambda_0)$. Table 2 shows some results. They show that except for station DAWY, measurements at all Alaskan stations do not contradict to early estimates of IC rotation rate based on anisotropy. On the other hand, measurements at the

Table 1 Parameters of seismic sources and arrays/networks

Stations	Number of measurements	k, %/year	σ_k	Distance range, degrees	Time interval	Sources
COLA	54	0.013	0.00117	150.2–152.3	1951–1995	[14]
FYU	15	0.014	0.00226	149.5–151.1	1974–1995	[14]
FYU	26	0.0115	0.00249	149.9–152	1974–1998	[14]
SCM	14	0.0115	0.00197	148.9–150.4	1975–1998	[14]
NVL	21	–0.018	0.00747	146.4–146.52	1966–1990	[22]
SNA	9	–0.0051	0.01	147.94–148	1966–1988	[22]
NRIL	83	–0.0115	0.0041	148.41–151.87	1966–2002	[22]
ILT	47	0.01324	0.0093	161.52–163.6	1965–1993	[22]
DRV	13	–0.0018	0.002	150.3–150.39	1966–1988	[22]
SBA	19	–0.0037	0.0022	163.38–163.49	1966–1984	[22]

Table 2 A few results from [28]

Source region	Station (region)	IC rotation velocity, degrees per year
SSI	COL (Alaska)	–0.13 ± 0.05
SSI	INK (Alaska)	–0.38 ± 0.19
SSI	DAWY (Alaska)	No rotation
Vanuatu	BCAO, BGCA (Africa)	0.14 ± 0.04
Aleutian Isl.	LBTB (Africa)	–0.1 ± 0.3

African station of BCAO (BGCA) yield the opposite sign of IC differential rotation velocity, and, consequently, do not support rotation (at least as a rigid body).

3   Mechanical Models of IC Differential Rotation

Here we address only two papers in the first of which [8] IC differential rotation is examined considering the combined effects of gravitational and electromagnetic torques, and friction caused by movements of the IC in the viscous OC. The moment of electromagnetic forces was estimated to 10^{18}–10^{20} N m, and of gravitational ones to 10^{19}–10^{21} N m. The retarding torque of rotating IC in the viscous turbulent medium of the OC makes about 10^{15} N m. If gravitational torque dominates, IC oscillates with periods between 1 and 10 years; if electromagnetic torque dominates, IC rotates with imposed rotation rate of the nearby OC fluids. When electromagnetic torques are only marginally stronger than the gravitational torques, the IC slowly rotates prograde by 90° relative to the mantle, escaping a gravitational well in roughly 100 years, then falls into the next gravitational well, rotating through 90° in just 4 years. Finite IC viscosity is modeled using a relaxation time

for the IC topography. With relaxation, the gravitational torque reduces but does not eliminate the anomalous IC rotation.

Another model [29] does not account for electromagnetic torque but focuses on retarding crust and mantle rotation due to the tidal torque of the Moon and the Sun. Mathematically the problem is reduced to the classical problem of a nonlinear oscillator exposed to a constant torque. It was shown the IC can rotate either at the same angular velocity as mantle, or at a larger velocity (i.e. the model does not support slower IC rotation with respect to mantle). Fitting model parameters to account for the observed variation in Earth's rotation velocity between 1955 and 2003 yields the gravitational torque is to exceed the tidal one by a factor of 5.9. It was also shown that ellipsoidality of the gravitationally interacting bodies provides a periodic interchange of kinetic angular momentum between mantle and solid core that results in either acceleration or deceleration of the IC.

4 Conclusions

It is obvious the rate of IC differential rotation is a topic to debate. Short-period body waves mostly predict eastward rotation at the rate of not more than 3° per year. Normal modes limit the rotation velocity by values an order of magnitude as small, and in both directions (eastward and westward). Simple eastward stationary rotation of the IC predicted by geodynamo simulations hardly exists, so the process is rather non–stationary, with accelerations and decelerations possibly induced by interaction with the Earth's mantle.

References

1. Lehmann, I.: P'. Periodical: Publications du Bureau Central Séismologique International Series: A **14**(3), 87–115 (1936)
2. Avsyuk, Y.N.: Possible explanation for latitude variation. Doklady Akademii Nauk SSSR **254**(4), 834–838 (1980) (in Russian)
3. Song, X.D., Richards, P.G.: Seismological evidence for differential rotation of the earth's inner core. Nature **382**(6588), 221–224 (1996)
4. Su, W.-J., Dziewonski, A.M., Jeanloz, R.: Planet within a planet: rotation of the inner core of the Earth. Science **274**(5294), 1883–1887 (1996)
5. Avsyuk, Y., Adushkin, V.V., Ovchinnikov, V.M.: Multidisciplinary study of the mobility of the Earth's inner core. Izvestia Phys. Solid Earth **37**(8), 673–683 (2001)
6. Gubbins, D.: Rotation of the inner core. J. Geophys. Res. **86**(12), 11695–11699 (1981)
7. Glatzmaier, G.A., Roberts, P.H.: A three-dimensional convective dynamo solution with rotating and finitely conducting inner core and mantle. Phys. Earth Planet. Inter. **91**(1–3), 63–75 (1995)
8. Aurnou, J., Olson, P.: Control of inner core rotation by electromagnetic, gravitational and mechanical torques. Phys. Earth Planet. Inter. **117**, 111–121 (2000)

9. Levin, B.V.: Role of movements of the Earth's inner core in tectonic processes. In: Fundamental Problems in General Tectonics, pp. 444—460. Nauchnyi Mir, Moscow (2001) (in Russian)

10. Levin, B.V., Sasorova, A.V., Domansky, V.A.: Features of "critical latitudes", variations of rotation and seismicity of the earth. In: Vestnik of the Far East Branch of the Russian Academy of Sciences, vol. 3, pp. 3–8 (2013) (in Russian)

11. Khain, V.E.: Constructing a truly global model of Earth's dynamics: basic principles. Russ. Geol. Geophys. **51**(6), 587–591 (2010)

12. Poupinet, G., Pillet, R., Souriau, A.: Possible heterogeneity in the Earth's core deduced from PKIKP travel times. Nature **305**, 204–206 (1983)

13. Morelli, A., Dziewonski, A., Woodhouse, J.: Anisotropy of the core inferred from PKIKP travel times. Geophys. Res. Lett. **13**, 1545–1548 (1986)

14. Song, X.D., Li, A.Y.: Support for differential inner core super-rotation from earthquakes in Alaska recorded at South Pole station. J. Geophys. Res.: Solid Earth **105**(1), 623–630 (2000)

15. Souriau, A., Roudil, P., Moynot, B.: Inner core differential rotation: facts and artefacts. Geophys. Res. Lett. **24**, 2103–2106 (1997)

16. Souriau, A.: New seismological constraints on differential rotation of the inner core from Novaya Zemlya events recorded at DRV, Antarctica. Geophys. J. Int. **134**(2), F1–F5 (1998)

17. Poupinet, G., Souriau, A., Coutant, O.: The existence of an inner core super-rotation questioned by teleseismic doublets. Phys. Earth Planet. Inter. **118**, 77–88 (2000)

18. Souriau, A., Poupinet, G.: Inner core rotation: a critical appraisal. In: Geodynamics Series, vol. 31. AGU, Washington (2003)

19. Creager, K.C.: Inner core rotation rate from small-scale heterogeneity and time-varying travel times. Science **278**(5341), 1284–1288 (1997)

20. Collier, J.D., Helffrich, G.: Estimate of inner core rotation rate from United Kingdom regional seismic network data and consequences for inner core dynamical behavior. Earth Planet. Sci. Lett. **193**(3–4), 523–537 (2001)

21. Ovtchinnikov, V.M., Adushkin, V.V., An, V.A.: The relative rotational velocity of the Earth's inner core. Doklady Earth Sci. **363**(8), 1117—1119 (1998)

22. Ovtchinnikov, V.M., Kaazik, P.B.: Station travel time residuals in calendar time and differential rotation of the inner core. In: Dynamic Processes in Geospheres. Collected Works of IDG RAS, pp. 10—19, Moscow (2011) (in Russian)

23. Zhang, J., Song, X., Li, Y., Richards, P.C., Sun, X., Waldhauser, F.: Inner core differential motion confirmed by earthquake waveform doublets. Science **309**(5739), 1357–1360 (2005)

24. Song, X.D., Poupinet, G.: Inner core rotation from event-pair analysis. Earth Planet. Sci. Lett. **261**, 259–266 (2007)

25. Laske, G., Masters G.: The Earth's free oscillations and differential rotation of the inner core. In: Earth's Core: Dynamics, Structure, Rotation. Geodynamic Series, vol. 31, Washington (2003)

26. Tkalčić, H., Young, M., Bodin, T., Ngo, S., Sambridge, S.: The shuffling rotation of the Earth's inner core revealed by earthquake doublets. Nat. Geosci. **6**(6), 497–502 (2013)

27. Vidale, J., Earle, P.: Evidence for inner core rotation from possible changes with time in PKP coda. Geophys. Res. Lett. **32**, L01309 (2005). https://doi.org/10.1029/2004GL021240

28. Makinen, A., Deuss, A.: Global seismic body-wave observations of temporal variations in the Earth's inner core, and implications for its differential rotation. Geophys. J. Int. **187**(1), 355–370 (2011)

29. Denisov, G., Novikov, V., Fedorov, A.: Gravitational interactions of the solid core and the Earth's mantle and variations in the length of the day. Astron. Rep. **52**(12), 1027–1034 (2008)

Fault Complexity and Interaction: Evidence of Static Earthquake Triggering

Eleftheria Papadimitriou and Vasileios Karakostas

Abstract

Fault interaction investigation was performed in several cases on a regional scale by evaluating stress patterns for different configurations based on specific natural fault arrays. Coseismic Coulomb stress changes that are induced on the surrounding receiver faults by the earthquake on the source fault and in several cases the accumulated stress changes that included the long-term tectonic loading have revealed. Triggering occurs as a redistribution of stress induced by an earthquake. One of the primary reasons to study earthquake triggering is to work toward being able to predict where the next seismic event will occur. Triggered event can happen very fast, after several years, or after decades. Research results that successfully highlighted triggering effects are accumulated from several cases from Greece and other areas and for different faulting types.

Keywords

Fault population · Interaction and triggering · Coulomb stress changes

E. Papadimitriou (✉) · V. Karakostas
Geophysics Department, School of Geology, Aristotle University of Thessaloniki, GR54124 Thessaloniki, Greece
e-mail: ritsa@geo.auth.gr

V. Karakostas
e-mail: vkarak@geo.auth.gr

1   Introduction

Despite substantial advances in our understanding in the last decades on mechanical properties of the faults and their interaction through the stress field, there is still a long way to achieve reliable estimates of the recurrence times of the stronger earthquakes associated with the major faults in a given area. This highlights the requisiteness for intensifying our efforts towards identification of the location and occurrence time of the anticipated strong earthquakes. Substantial progress has been made in identifying the source regions of future earthquakes by stress interaction modeling, which led to the assessment that stress changes caused by the coseismic slip of an earthquake increased the likelihood for the occurrence of nearby earthquakes.

Calculations of static Coulomb stress changes associated with the coseismic slip of strong earthquakes on specific fault segments in a fault population were confirmed ample to explain many seismic observations, including aftershock locations, the spatial evolution of earthquake sequences, and the lack of anticipated earthquakes in active regions following strong earthquakes. Although static stress changes may be an important trigger for near field aftershocks, the influence of static stress changes has remarkable impact in distances of two or three fault lengths from the source, even though they are negligible even compared to tidal stresses. Remote triggering at great distances (from several fault lengths to hundreds of km, depending upon the magnitude of the causative earthquake) has been observed, however, after a strong earthquake and best explained by the transient (dynamic) passage of seismic waves, which either immediately induce Coulomb–type failure or initiate a secondary mechanism that induces delayed triggering. The passage of seismic waves may also play a significant role in the triggering of near–field earthquakes.

Triggering does not mean that the coseismic stress change associated with one earthquake is enough to generate another earthquake in an originally stress-free location. It means, of course, that the stress at the location of the second earthquake is already close enough to failure that the first earthquake can "trigger" the second one by introducing a positive increase in ΔCFF to move it into the failure regime. Various rupture lengths may be attributed to the role of stress shadow in rupture termination. It appears that a large earthquake starting in a region of static stress increase may have terminated when it encountered a region of static stress decrease [1]. The quiescence periods following the excitations are consistent with a model in which triggered earthquakes are events that are clock advanced by static stress changes on a finite set of available faults or by stress transients on any fault population [2], since an increased earthquake rate leaves fewer faults available for failure and thus quiescence follows a seismicity increase.

2 Coulomb Stress Changes

Coulomb stress changes caused by the coseismic slip of strong earthquakes mainly (i.e. M $\geq$ 6.0) are computed on the target fault planes, namely on the fault segments whose triggering is inspected. Planar rectangular models are assumed for both causative and receiver faults, and homogeneous slip models may adequately provide reliable results since the resulted stress field changes are only affected in close distances from the causative fault when detailed slip model is considered. Changes in stress associated with large earthquakes are calculated by putting coseismic displacements on ruptured fault segments in the elastic half–space and adding the changes in the components of the stress tensor together as they occur in time. The displacement field, u_k (kth component of u) in a semi-infinite elastic medium for an arbitrary uniform dislocation, U, across a surface, Σ, can be determined from

$$u_k = \frac{U_i}{8\pi\mu} \iint_{\Sigma} w_{ij}^k v_j d\Sigma, \tag{1}$$

where μ is the shear modulus, v_j are the direction cosines of the normal to the dislocation surface, U_i is the ith component of U, and w_{ij}^k are six sets of Green's functions [3]. The elastic stress s_{ij} is calculated from strain e_{ij} using Hooke's law for an isotropic medium

$$s_{ij} = \frac{2\mu v}{1 - 2v} \delta_{ij} e_{kk} + 2\mu e_{ij}, \tag{2}$$

where v is Poisson's ratio, and δ_{ij} is the Kronecker delta.

Earthquakes occur when the stress exceeds the strength of the fault. The closeness to failure was quantified using the change in Coulomb failure function (ΔCFF) (modified from [4]; Harris [5] and references therein):

$$\Delta CFF = \Delta\tau + \mu(\Delta\sigma + \Delta p), \tag{3}$$

where $\Delta\tau$ is the onto fault shear stress change, $\Delta\sigma$ is the fault–normal stress change and Δp is the pore pressure change in the rupture area. A positive value of ΔCFF for a particular fault denotes movement of that fault toward failure (that is, the likelihood that it will rupture in an earthquake is increased). This may happen when the shear stress is increased or the effective normal stress, $\mu(\Delta\sigma + \Delta p)$ is decreased.

Both $\Delta\tau$ and $\Delta\sigma$ are calculated from the stress tensor shown in (2) for a fault plane at the observing (field) point. Shear stress change, $\Delta\tau$, is positive for increasing shear stress in the slip direction on the observing fault; $\Delta\sigma$ is positive for increasing tensional normal stress. Decrease of compressional normal stress is associated with decrease of the static friction across the fault plane. Both positive $\Delta\tau$ and $\Delta\sigma$ move a fault toward failure; negative $\Delta\tau$ and $\Delta\sigma$ move it away from failure. During the coseismic phase, the porous medium is considered still under undrained conditions and the pore pressure change is given by [6]:

$$\Delta p = -B \frac{\Delta \sigma_{kk}}{3}. \tag{4}$$

where B is the Skempton's coefficient ($0 \leq B < 1$) depending on the bulk moduli of the material and the fraction of volume that the fluid occupies and $\Delta \sigma_{kk}$ is the trace of the induced stress tensor. Rock experiments suggest typical values of B ranging between 0.5 and 0.9 [7]. The undrained case is usually considered [8] where Δp depends upon the normal stress change on the observational fault plane.

A more—complex assumption is that the fault zone materials are more ductile than the surrounding materials, as in the model of Rice, so that $\sigma_{xx} = \sigma_{yy} = \sigma_{zz}$ in the fault zone, and therefore $\Delta \sigma_{kk}/3 = \Delta \sigma$. In this case, with the assumptions that the medium is homogeneous and isotropic outside the fault zone inside the more–ductile fault zone, one can obtain

$$\Delta CFF = \Delta \tau + \mu' \Delta \sigma. \tag{5}$$

The parameter μ' is often called the apparent coefficient of friction comprising the effects of pore fluids as well as the material properties of the fault zone. For the homogeneous isotropic poroelastic model, μ' is a function of $\Delta \sigma_{kk}$ and $\Delta \sigma$, where β' for rock is similar to Skempton's coefficient B:

$$\mu' = \mu \left(1 - \frac{\beta'}{3} \frac{\Delta \sigma_{kk}}{\Delta \sigma} \right). \tag{6}$$

The selection of an appropriate value for the coefficient of friction, μ, is of importance for the model application, and in coseismic stress changes investigations has varied from 0.0 to 0.75, with the most widely accepted equal to 0.4 [1]. A change in the friction coefficient primarily affects the magnitude of the Coulomb stress changes and only to a lesser extent their spatial distribution. A lower friction coefficient leads to lower Coulomb stress changes because the resistance to coseismic slip is reduced. Therefore, the coseismic stress drop on the source fault is lower, which implies that also the Coulomb stress changes on the receiver faults are smaller.

When the evolutionary stress model is considered, it is assumed that stress changes can be modeled as those caused by elastic strain accumulation and release during the earthquake cycle [9]. The basic assumption is that the static stress change at the time of a large earthquake is completely recovered during the period of strain accumulation; i.e., the net change in stress over the earthquake cycle is zero. This assumption is equivalent to the time–predictable model of earthquake occurrence.

3 Stress Changes as a Tool to Explore Interaction and Triggering

Earthquakes in a sequence generally are not independent [4]. Each one is affected by both tectonic loading and stress changes caused by prior events, especially by either great earthquakes or other shocks that occur nearby. Earthquake interaction is a fundamental feature of seismicity, leading to earthquake sequences, clustering, or aftershocks. From this point of view, the state of stress and its variation with time are studied. One interaction criterion that promises a deeper understanding of earthquake occurrence is Coulomb stress transfer [10]. Harris [5] in a thorough review elucidated the influence of even small stress changes generated by a nearby earthquake.

The data that can be used to study earthquake recurrence are quite limited because recurrence times are generally large—a hundred years or more, while information exists for shorter time intervals. In many tectonically active regions, reliable historical records cannot be obtained for periods earlier than about a hundred years before instrumental era. Consequently, for many areas of the world, one complete seismic cycle has not been documented yet, and for others only one is known, which does not carry any information about periodicity. Lack of periodicity in the occurrence of even large events may result from stress transfer between fault segments.

Observations on strong earthquake clustering alternating with relative quiescence periods, as well as impressive epicentral migration of strong earthquakes in a certain fault zone, are perfectly explained by stress transfer and triggering. Coulomb stress calculation and investigation of the possible triggering in a sequence of earthquakes is briefed in this section, with examples not confined in the territory of Greece alone. The most spectacular examples were presented for strike slip faulting type regimes, like the San Andreas Fault in California [1, 9]. In the area of Northern Aegean, Greece, dominated by dextral strike-slip faulting, calculation of the evolutionary stress field during the twentieth century, including both the coseismic slip in large (M ≥ 7.0) earthquakes and the slow tectonic stress buildup along the major fault segments, revealed that all large events occurred in regions of increased positive Coulomb stress changes, alike the majority of moderate events [11]. In the Kefalonia Transform Fault Zone (KTFZ), the second major dextral strike slip zone in the Greek territory, the occurrence of large events during short time intervals comparing with the periods of relative quiescence were explained by static stress triggering [12]. The temporal history of strong (M ≥ 6.3) earthquake occurrence showed that the two main fault branches of the KTFZ failed almost contemporarily, three times in the last 130 years. During each seismic excitation one or more earthquakes occurred in each fault, in a short time interval (two up to five years), followed by much longer quiet periods (30 up to 43 years). If this pattern will be proven consistent with past earthquake occurrence, then it will provide a tool to assess if a future event may signify the initiation of a new cluster of large earthquakes, contributing to the mitigation of the seismic hazard in the study area.

The more recent clustering took place during 2003–2015 (Fig. 1), when adjacent fault segments along the KTFZ were failed, for each one of them high positive ΔCFF values were calculated just before each strong (M ≥ 6.0) main shock [13].

Strong earthquake epicentral migration was observed along the Xianshuihe fault, Sichuan Province, one of the major strike-slip faults in the world because of its relatively high slip rate and the frequent occurrence of large (M ~ 7) earthquakes. The fault zone has relatively simple geometry and structure, with several distinctive stepovers that control rupture termination and enable reliable definition of consecutive segments. The observed adjoining or overlap between the rupture zones and the relatively short time intervals between them lead to the hypothesis that the earthquakes might be linked through stress interaction. The epicentral migration was more evident by resolving ΔCFF associated solely with coseismic displacements of previous events [14]. Since strike-slip earthquakes cause an increase in Coulomb stress along strike, the contiguous fault segments were put in stress enhanced areas and thus earthquake occurrence along strike is encouraged.

Calculations of Coulomb stress changes on dip-slip faults carried out in specific fault zone of the back-arc Aegean region and revealed similar triggering effects as for the strike-slip faults. One remarkable example concerns the episodic occurrence of M ≥ 6.2 earthquakes in Thessalia fault zone between 1954 and 1957, when three seismic sequences took place and where no such events have occurred for about two centuries [15]. Relative clustering in strong earthquake occurrence alternating with relatively quiescent periods, was satisfactorily interpreted by stress transfer
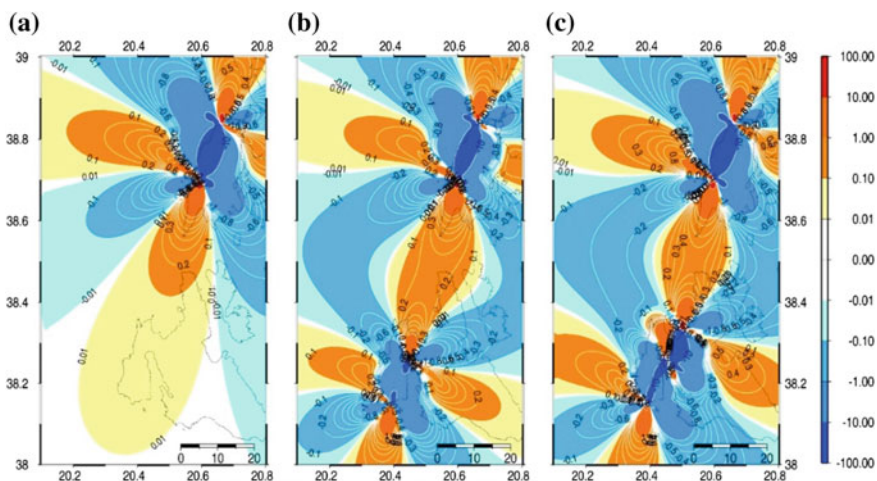
Fig. 1 Coulomb stress changes due to the coseismic slips of the M ≥ 6.0 main shocks that occurred in central Ionian Islands since 2003, calculated at a depth of 8 km. Changes are according to the scale to the right (in bars) and by the numbers in the contour lines. The stress field is calculated according to the faulting type of the 2015 main shock and is due to the coseismic slip of **a** the 2003 main shock, **b** the 2003 and the first 2014 main shock, and **c** the 2003 and both 2014 main shocks (after [13])

among the fault segments comprising in a fault population, like in the southern Aegean [16] and Northern Greece and Bulgaria [17].

Aftershock triggering is frequently inspected given that aftershocks occur either due to the slip residuals onto the main rupture plane or by stress redistribution and transfer. The positive Coulomb stress changes are not only located at the tips of the causative faults, but they also form off-fault lobes where the aftershock activity is expected to be triggered. An explanation of why off-fault aftershocks were observed is firstly given by Das and Scholz [18] who pointed out that the aftershocks have occurred in specific locations where crack models predict an increase in stress resulting from the main shock rupture. Large stress increases were noticed near the crack tip, but in addition there were small stress increases on either side of the crack or about one crack away. These were the regions in which off-fault aftershocks were often seen, alike in the case of the M_w = 6.4 July 26, 2001 Skyros (North Aegean, Greece) earthquake that struck the submarine western end of Northern Aegean Sea [19].

Combination of the variation of the values of the parameters μ and B, and the resulted percentage of aftershocks being located in stress enhanced areas may provide indications about the fault frictional properties. The 2013 aftershock sequence was investigated for this purpose, evidencing high fault friction [20]. In a first step the influence of the μ-value variation alone is examined, keeping the same value for B and equal to 0.0 (Fig. 2a). When the percentage of aftershock foci being located inside areas of positive Coulomb stress changes is plotted against the μ-value, an abrupt increase is observed for values of the friction coefficient ranging between 0.5 and 0.9.
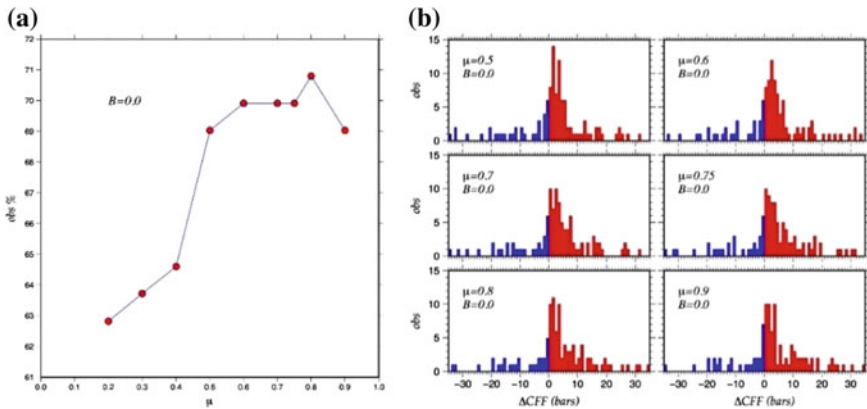
Fig. 2 **a** Percentage of aftershocks of the 2013 North Aegean main shock, originated in areas of positive static stress changes, as a function of the friction coefficient, μ, keeping constant the value of Skempton's coefficient ($B = 0.0$). **b** Histograms of the Coulomb stress changes at the foci of the aftershocks for values of friction coefficient, μ, between 0.5 and 0.9 and fixed value for the Skempton's coefficient ($B = 0.0$) (after [20])

It is noteworthy that for $\mu > 0.5$, this percentage kept its high score and is more or less "stabilized", keeping the high score invariant. We show in the histograms of Fig. 2b this distribution of ΔCFF and for this range of μ-values, which provides information on both the values and the competition between positive (red bars) and negative (blue bars) calculated static stress changes.

4 Conclusions

A review of Coulomb stress changes application and their role to earthquake triggering is presented, along with the parameters of the Coulomb Failure Function, namely the geometry and kinematics of both the source fault and the target fault, the friction coefficient and Skempton's coefficient. It has been shown that the spatial patterns of Coulomb stress changes vary for the different source fault slip models. The tectonic loading on the major regional fault segments play decisive role in the calculations and consequently to any forecasting model. Strong earthquake epicentral migration along major fault zones and clustering, alternating with periods of relative quiescence, are well explained by stress transfer among the activated fault segments. When measuring the spatial correlation between the positive Coulomb stress changes and the aftershock foci the triggering effect was robustly evidenced when the stress field was resolved for the focal mechanism of each aftershock. This implies that the stress triggered aftershock zones should be considered with caution when forecasting models are to be applied, for avoiding artificial static stress changes values.

References

1. King, G.C.P., Stein, R.S., Lin, J.: Static stress changes and the triggering of earthquakes. Bull. Seism. Soc. Am. **84**, 935–953 (1994)
2. Gomberg, J., Beeler, N.M., Blanpied, M.L., Bodin, P.: Earthquake triggering by transient and static deformations. J. Geophys. Res. **103**, 24411–24426 (1998)
3. Okada, Y.: Internal deformation due to shear and tensile faults in a half-space. Bull. Seism. Soc. Am. **82**, 1018–1040 (1992)
4. Scholz, C.: The Mechanics of Earthquakes and Faulting. Cambridge University Press (1990)
5. Harris, R.A.: Introduction to special session: stress triggers, stress shadows, and implications for seismic hazard. J. Geophys. Res. **103**, 24347–24358 (1998)
6. Rice, J., Cleary, M.: Some basic stress diffusion solutions for fluid saturated elastic porous media with compressible constituents. Rev. Geophys. **14**, 227–241 (1976)
7. Roeloffs, E.: Poroelastic techniques in the study of earthquake–related hydrologic phenomena. Adv. Geophys. **37**, 135–195 (1996)
8. Beeler, N.M., Simpson, R.W., Hickman, S.H., Lockner, D.A.: Pore fluid pressure, apparent friction and Coulomb failure. J. Geophys. Res. **105**, 25533–25542 (2000)
9. Deng, J., Sykes, L.: Evolution of the stress field in Southern California and triggering of moderate size earthquakes: A 200-year perspective. J. Geophys. Res. **102**, 9859–9886 (1997)
10. Stein, R.: The role of stress transfer in earthquake occurrence. Nature **402**, 605–609 (1999)

11. Papadimitriou, E.E., Sykes, L.R.: Evolution of the stress field in the Northern Aegean Sea (Greece). Geophys. J. Int. **146**, 747–759 (2001)
12. Papadimitriou, E.E.: Mode of strong earthquake occurrence in central Ionian Islands (Greece). Possible triggering due to Coulomb stress changes generated by the occurrence of previous strong shocks. Bull. Seismol. Soc. Am. **92**, 3293–3308 (2002)
13. Papadimitriou, E., Karakostas, V., Mesimeri, M., Chouliaras, G., Kourouklas, C.: The Mw6.7 17 November 2015 Lefkada (Greece) earthquake: structural interpretation by means of aftershock analysis. Pure Appl. Geophys (2017). https://doi.org/10.1007/s00024-017-1601-3
14. Papadimitriou, E.E., Wen, X., Karakostas, V.G., Xueshen, J.: Earthquake triggering along the Xianshuihe fault zone of western Sichuan. Pure Appl. Geophys. **161**, 1683–1707 (2004)
15. Papadimitriou, E.E., Karakostas, V.G.: Episodic occurrence of strong (Mw ≥ 6.2) earthquakes in Thessalia area (central Greece). Earth Planet. Sci. Lett. **215**, 395–409 (2003)
16. Papadimitriou, E.E., Sourlas, G., Karakostas, V.G.: Seismicity variations in southern Aegean, Greece, before and after the large (M7.7) 1956 Amorgos earthquake due to the evolving stress. Pure Appl. Geophys. **162**, 783–804 (2005)
17. Papadimitriou, E., Karakostas, V., Tranos, M., Ranguelov, B., Gospodinov, D.: Static stress changes associated with normal faulting earthquakes in South Balkan area. Intern. J. Earth Sci. (2007). https://doi.org/10.1007/s00531-006-0139-x
18. Das, S., Scholz, C.H.: Off-fault aftershock clusters caused by shear stress increase? Bull. Seis. Soc. Am. **71**, 1669–1675 (1981)
19. Karakostas, V.G., Papadimitriou, E.E., Karakaisis, G.F., Papazachos, C.B., Scordilis, E.M., Vargemezis, G., Aidona, E.: The 2001 Skyros, northern Aegean, Greece, earthquake sequence: off fault aftershocks, tectonic implications and seismicity triggering. Geophys. Res. Lett. **30**(1), 1012 (2003). https://doi.org/10.1029/2002GL015814
20. Karakostas, V.G., Papadimitriou, E.E., Gospodinov, D.: Modeling the 2013 North Aegean (Greece) seismic sequence: geometrical and frictional constraints, and aftershock probabilities. Geophys. J. Intern. (2014). https://doi.org/10.1093/gji/ggt523

On the Results of Studying Deep Paleo Seismic Dislocations (at the Example of the Marginal Suture of the Siberian Craton)

Valery Ruzhich ⓘ, Alexey Ostapchuk ⓘ and Dmitry Pavlov ⓘ

Abstract

The results are discussed of using a complex geological-geophysical approach directed towards detecting and studying deep paleo seismic dislocations (PSD), i.e., ancient coseismic ruptures, at the example of investigations performed at exhumed segments of a marginal suture of the Siberian craton in the Western Baikal region. The obtained data testify that there is a possibility to reconstruct the P–T conditions and regimes of fluid activity in PSDs that had developed in powerful earthquakes in previous seismically and tectonically active eras at focal depths of about 10–25 km. The possibility of absolute dating over syn-metamorphic newly formed minerals, "geo-barometers", using the Ar^{40}/Ar^{39} method, have also been demonstrated. Studying deep P–T conditions of PSD emergence using the above approach has a key importance for the cognition of geological factors and petrophysical mechanisms that promote triggering coseismic displacements in faults during seismic source nucleation. The information obtained in studying deep PSDs is actual for developing geomechanical models of seismogenic faults and elaborating methods of their relaxation using preemptive complex anthropogenic actions on potentially dangerous segments of active faults.

V. Ruzhich (✉)
Institute of Earth's Crust of Siberian Branch of Russian Academy of Sciences, 664033 Irkutsk, Russia
e-mail: ruzhich@crust.irk.ru

A. Ostapchuk · D. Pavlov
Sadovsky Institute of Geospheres Dynamics RAS, 119334 Moscow, Russia

1 Introduction

Reliable geological, geophysical and tectonophysical information is required for development of geomechanical models of faults and sources of powerful earthquakes corresponding to natural conditions of their preparation in deep fault segments. To some extent, it is possible to obtain this information in laboratory modeling and in drilling deep wells in seismogenic faults. However, the obtained results do not allow to overcome the limits in duration of deep petrophysical processes and scaling of fracturing in multilevel systems of rock mass destruction. New approaches to studying tectonophysical and frictional conditions of powerful earthquake nucleation and stage-by-stage development are being developed for this purpose. PSDs emerged in the sources of powerful earthquakes at the Earth's lithosphere envelope, which is considered to be inaccessible, as deep as 10–25 km. Due to the lack of information, the prevalent notion about deep structure and conditions of earthquake source nucleation is based mainly on the results of numerical and laboratory physical modeling, which turns to be too simplified and ambiguous. This circumstance complicates a lot elaboration of adequate source models, more reliable methods of earthquake prediction and development of new techniques of lowering seismic risk, in particular, in unintended triggering of rock bursts in drifting deep tunnels in stressed rocks containing active faults.

2 Region Under Investigation

Geological and geomechanical investigations were held at several deeply exhumed segments of the Early—Proterozoic zone of the marginal suture of the Siberian craton, where the processes of seismic and tectonic activation had been taking place in the core of the Baikal Rift Zone and the Primorskiy seismogenic fault during tens of millions years in the Cainozoic age. PSDs of the ages of about several thousand years observed at the free surface, for example, in the outfall of the river of Sarma testify that powerful earthquakes had occurred there. In order to detect deep PSDs the main emphasis in investigations was made on application of petrochemical signs detected in studying the collected rock samples of pseudo-tachylites and fault mirrors, which are regarded by specialists as reliable evidences of high-speed displacements in fault zones [1, 2].

The results of geological and geophysical studies of the detected deep paleo seismic dislocations that emerged in ancient ages of tectonic activations at one of the exhumed segments of the marginal suture of the Siberian plate are considered below. The considered segments of the marginal suture, including the zone of the Primorskiy fault, which formed during the Cainozoic age of seismic and tectonic activation of the rift, are located at the north–western side of the Baikal rift depression, between the Pre-Cambrian exhumed prominence of the foundation of the southern part of the Siberian craton and the Caledonian Central-Asian folded

belt. A complex approach was used, which combined traditional geological and structural methods of classical geology and geophysics with methods of experimental physics, mechanics, physical and numerical modeling, isotope dating.

3   Results

Samples for petrographic studies and dating of the neogenic mineralization in discontinuities of different ages were collected mainly in the outfall parts of the rivers of Bugulgeika and Talovka (see Fig. 1). Rocky outcrops contain dislocated series of hornblende-biotite-wise plagiogniesses of the Neo-Proterozoic that had undergone multistage physical and chemical transformations while being exposed to stress-metamorphism, specific for the amphibolite and greenshale facies of regional metamorphism. Petrographic studies of samples collected in rock discontinuities, which once had been located in the midst of the Earth's crust, have revealed the presence of pseudo-tachylites and multiple fault mirrors with signs of brittle, elasto-plastic and visco-plastic deformations of mineral grains. The grains had also undergone granulation, fine attrition and recrystallization. In particular, studying the samples from the segment of the marginal suture have detected manifestations of stress-metamorphic transformations in the form of inclusions of black tourmaline (schorl), pseudo-tachylites, muscovite, quartz, chlorite, sericite, epidote, calcite, barroisite and other minerals. Pseudo-tachylites, which are considered to be the products of frictional heating caused by fast sliding [3], have been detected in ancient intensively mylonitized granites and granodiorites of the Primorskiy complex. As a rule, pseudo-tachylites in this region form layers 1–2 mm thick inside the mylonitized mass [4]. Estimations of temperatures and pressures, at which ancient coseismic displacements took place in rock discontinuities, have been made on the collected rock samples from the zones of coseismic ruptures by detecting the characteristic mineral associations, including the "geotermometer" and "geobarometer" minerals. It has been established that crystallization of calcium tschermakite and hornblende in the samples from the right side of the Buguldeika river had occurred at the temperature of ~ 880 °C and the pressure of 3kbars. It has been concluded that the level of erosion shear in the segment of the marginal suture under investigation is currently about 10 km. The temperature of hornblende crystallization, at the moments when pseudo-tachylites were emerging in coseismic ruptures, was about 850–950 °C, and the pressure, when the magnesia hornblende was being formed, reached the value of 5.0–5.5 kbars. At the moments of fast coseismic displacements the pressure in the contact zones instantly increased up to the value of 2.0–2.5 kbars, and the temperature "jump" from frictional heating to melting during fast displacements at the velocities of about 1–10 m/s reached the value of about 500 °C, while the initial background temperature level was about 400 °C. Detection of the barroisite mineral in pseudo-tachylites testifies that coseismic displacements had occurred under high pressure.
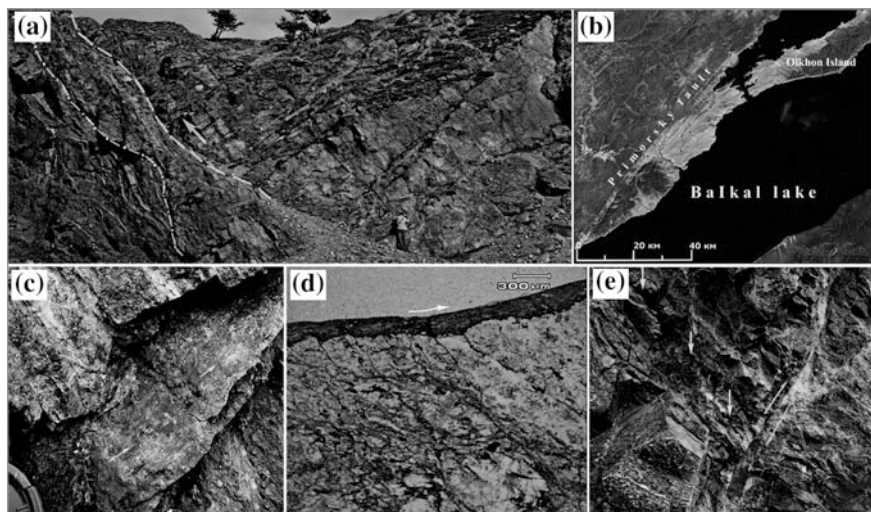
Fig. 1 Quartz-tourmaline mineralization in a PSD of the exhumed segment of the marginal suture of the Siberian craton near the outfall of the Buguldeika river: **a** two fault zones of different ages with coseismic ruptures: dashed line corresponds to the Middle-Paleozoic thrust dislocation, dash-and-dot line—to a more ancient Neo-Proterozoic zone; **b** space photo of the region under investigation in the zone of the Primorskiy riftogenic thrust in the limits of the marginal suture; **c** polished section of a fault morror with a tourmaline covering, arrows point to the direction of sliding strokes; **d** polished section of a fault mirror along tourmaline, the fledging cracks are seen that displace the lower part of visco-plastic tourmaline layer; **e** two generations of coseismic cracks of different ages with fault mirrors: short vertical arrows mark the places of tourmalinization of coseismic rupture of the Neo-Proterozoic age, long inclined arrows mark a younger Paleozoic coseismic rupture, which displaces the ancient rupture with tourmaline

A rare mineral—the black tourmaline—that was detected in fault mirrors, was used for estimating the absolute ages of PSDs. This mineral is highly tolerant to thermal effects because of its unique petrochemical and physical properties, and dating accuracy is comparable to that of muscovite and hornblende. Studies of fault mirrors with tourmaline mineralization have shown that fast displacements had occurred in visco-plastic flows. Such a rheologic behavior was possible under previously existing P–T conditions that corresponded to the amphibolite facies of the regional metamorphism. Thus, we have every reason to date the coseismic displacement close to the established age of the tourmaline mineralization— 673 ± 5 million years. This dating based on tourmaline doesn't contradict the estimates of the age of protoliths of the Olkhon region established by zircons from the blasto-mylonite metamorphic complex of Orso (844 and 792 million years) and by the age of basalt protolith in the neighboring Chernorudskaya zone (624 ± 4.1 million years) [5]. It is supposed in the frames of the geodynamic reconstruction that the obtained age of displacement of about 673 ± 5 million years is better be considered as an evidence of a seismogenic activation of deep coseismic ruptures in one of the segments of the marginal suture of the Siberian craton in

Neo-Proterozoic. One more dating have been made of a later PSD of the age of 415.4 ± 4.1 million years. The age was established by the muscovite collected from a tensile fracture of the "pull-apart" type, typical to a shear seismic dislocation, which most likely had emerged in the limits of the collision suture [4].

Another remarkable result of studying deep PSDs is the ascending flows, which are widely spread inside the PSDs. These flows had left traces in the form of various neogenic minerals on the slickensides. Similar phenomena are specific for, for example, floating-up of foreshocks [6]. The nature of such metasomatic transformations of the matter of dislocated rocks is attributed to the accelerated lowering of resistance to shear in shear cracks, increasing velocity of sliding and emergence of pseudo-tachylites, which is specific for deep PSDs [7, 8].

4 Conclusion

Studying deep PSDs using the above approach has a key sense for detecting the reasons of instant coseismic displacements to occur at the moments of generation of earthquakes at deep fault segments. The proposition has been substantiated that it is the active intrusion of highly mobile fluids into stressed segments of contact interaction inside faults in a series of events that could have triggered coseismic displacements in faults at seismic focal depths. It is difficult to control such a mechanism with modern observation techniques, and this explains difficulties in solving the problems of short-term forecast of earthquakes. Nevertheless, the suggested explanation along with the other frictional mechanisms can expand our knowledge of tectonic and physical processes in the sources of powerful earthquakes. Information retrieved in the above methodical approach can also be needed in developing methods of regulating the seismic regime by injecting mortars into wells drilled in the detected potentially dangerous segments of active faults [9, 10]. A multidisciplinary systematic study of deep PSDs allows to broaden the possibilities of the well-known paleo-seismo-geological method of studying PSDs at the free surface.

References

1. Sobolev, G.A., Vettegren', V.I., Mamalimov, R.I., Shcherbakov, I.P., Ruzhich, V.V., Ivanova L.A.: A study of nanocrystals and the glide-plane mechanism. J. Volcanol. Seismol. **9**(3), 151–161 (2015)
2. Sobolev, G.A., Vettegren, V.I., Kireenkova, S.M., Kulik, V.B., Mamalimov, R.I., Morozov, Yu.A, Smulskaya, A.I., Scherbakov, I.P.: Nanocrystals in Rocks. GEOS, Moscow (2016). (in Russian)

3. Rice, J.R.: Heating and weakening of faults during earthquake slip. J. Geophys. Res. **111**(B5), B05311 (2006)
4. Ruzhich, V.V., Savel'eva, V.B., Rasskazov, S.V., Yasnygina, T.A., Kocharyan, G.G., Ostapchuk, A.A., Travin, A.V., Yudin, D.S.: Determination of the PT conditions that accompanied a seismogenic slip along a deep segment of the marginal suture of the Siberian craton. Dokl. Earth Sci. **481**(2), 1017–1020 (2018)
5. Fedorovskiy, V.S., Sklyarov, E.V., Izokh, A.E., Kotov, A.B., Lavrenchuk, A.V., Mazuk-bazov, F.M.: Strike-slip tectonics and subalkaline mafic magmatism in the early Paleozoic collisional system of the western Baikal region. Russ. Geol. Geophys. **51**(5), 534–547 (2010)
6. Rodkin, M.V., Rundquist, D.V.: Geofluidogeodynamics. Application to Seismology, Tectonics, and Processes of Ore and Oil Genesis. Publishing House "Intellect", Dolgoprudny (2017)
7. Sibson, R.H.: Interactions between temperature and pore fluid pressure during an earthquake faulting and a mechanism for partial or total stress relief. Nat. Phys. Sci. **243**(126), 66–68 (1973)
8. Kocharyan, G.G.: Geomechanics of Faults. GEOS, Moscow (2016)
9. Savage, H.M., Kirkpatrick, J.D., Mori, J.J., Brodsky, E.E., Ellsworth, W.L., Carpenter, B.M., Chen, X., Cappa, F., Kano, Y.: Scientific exploration of induced seismicity and stress (SEISMS). Sci. Dril. **23**, 57–63 (2017)
10. Ruzhich, V.V., Psakhie, S.G., Shilko, E.V., Vakhromeev, A.G., Levina, E.A.: On the possibility of development of the technology for managing seismotectonic displacements in fault zones. In: AIP Conference Proceedings, vol. 2051, no. 1, p. 020261 (2018)

Effect of Changing Basal Friction on the Formation of Thrust

Antonina Tataurova [ORCID], Yurii Stefanov [ORCID] and Vladimir Suvorov [ORCID]

Abstract

The deformation problem of a wedge lying on a rigid base is considered. The effect of basal friction on the formation of thrusts is studied numerically. A model with a decreasing value of basal friction is proposed. The effect of clustering of areas with differently reduced friction was found. As a result, the friction coefficient changes periodically and it correlates with the formation of localized shear bands and stressed state. Zones with reduced friction correspond to areas with higher irreversible deformation and lower values of the ratio of τ/p. Thrust differences are shown in the case of constant and decreasing friction. In the first case, the faults are linear, and the topographic slope is consistent with the critical wedge theory. The faults have a list form when friction decreases during the deformation process. The greatest slope of the topographic surface is in the frontal zone, where shear deformation bands are formed. The slope of the topography becomes much less in the zones, where the slip occurs with low friction.

Keywords

Basal friction $\cdot$ Thrust $\cdot$ Plastic deformation $\cdot$ Shear band $\cdot$ Numerical modeling

A. Tataurova ($\boxtimes$) $\cdot$ Y. Stefanov $\cdot$ V. Suvorov
Institute of Petroleum Geology and Geophysics SB RAS, Novosibirsk 630090, Russia
e-mail: TataurovaAA@ipgg.sbras.ru; anttat2@gmail.com

Y. Stefanov
Institute of Strength Physics and Materials Science SB RAS, Tomsk 634055, Russia
e-mail: yu_st@mail.ru

1 Introduction

Fold-thrust belts are composed of sedimentary rocks that were contorted as a result of two plates' convergence [1]. The stress state in such conditions is determined by gravitational forces and the load applied to the inner border of the fold-thrust belt [2, 3]. The degree of rock deformation increases from the outer zone of the orogen to the inner one. Deformation structures on the periphery of the fold-thrust belts are the youngest ones.

Thrust faults are typical of fold-thrust belts, direction of dip is usually towards the orogens (Fig. 1). They are connected at some depth by a detachment separating the sedimentary strata and the foundation. The thrust geometry is represented as sliding zones parallel to the bedding of sediments and ramps—faults intersecting layers (Fig. 1a). Often ramps have a listric form, and the angle of dip is steep when approaching the surface. Thrust systems are imbricate fans, which can be divided into two types: dependent (Fig. 1b) and independent (Fig. 1c). In the first case, the thrust plates influence each other. In the second case, they do not affect each other, as they are separated by a sufficient distance.

According to kinematic ideas, each thrust fracture is generated on the front of the forming detachment and is distributed up along the section, crossing deforming layers. At the same time, the analysis of field and seismic data provides the opportunity to make an alternative suggestion that thrusts can be generated in deforming layers above the detachment [4, 5]. Similar data are obtained using physical modeling [6]. The results of computer simulation suggest that the formation of ramps can occur near the surface [7, 8] or near the detachment [9] (see Fig. 1).

There is no consensus about the parameters that determine the distance between the thrusts, it can be constant, or it can decrease when approaching the front border. There is an assumption that this is due to the topography of the basement [10], but seismic data do not always confirm this [11]. Also, the results of geophysical studies do not confirm that the distance between thrusts is proportional to the depth
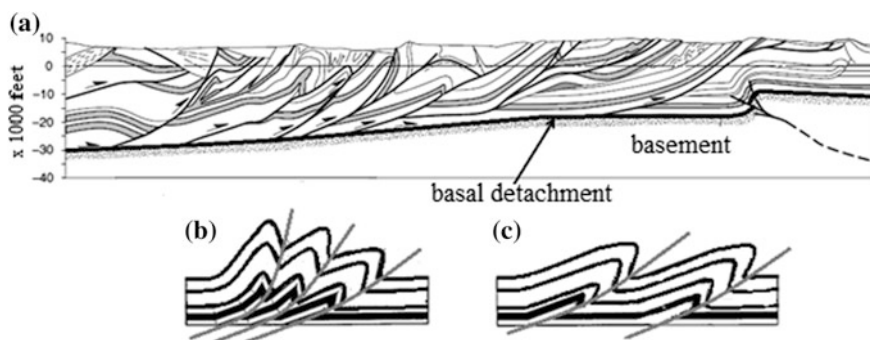
Fig. 1 Thrusts at the example of the Wyoming fold-thrust belt (**a**) [16]. Types of thrust systems that represent imbricate fans: dependent system (**b**); independent system (**c**) [17]

up to the detachment [12]. One of the main models describing the mechanical behavior of the fold-thrust belt is the critical wedge theory [2].

It is believed that variations in basal friction play an important role in the management of wedge geometries and kinematics. The greater the value of basal friction is, the more numerous are the thrusts and the smaller is the distance between them [13]. There are estimates of basal friction [2, 14], but they do not provide an answer to the question of how the basal friction changes in the process of the medium deformation. It can be assumed that in the process of destruction the magnitude of basal friction will change [15], this may determine additional features in the stressed state of the medium and deformation structures. The deformation structures of the fold-thrust belts are closely associated with the study of the processes occurring in the Earth's crust, as well as the study of the conditions and parameters that determine their structure. In this paper, we try to answer a series of questions about the conditions of nucleation and distribution of thrusts by numerical modeling.

2 Problem Formulation and Constitutive Equation

A homogeneous wedge model is used in calculations (Fig. 2). It is assumed that the surface of basal friction separates the sedimentary layer from the basement, therefore, the upper part of the medium can be deformed. The law of dry friction acts between the upper part of the model and the rigid basement:

$$|\sigma_\tau| \leq -\mu_b \sigma_n \tag{1}$$

σ_τ, σ_n are the shear and normal stress components; μ_b is the friction coefficient. When $|\sigma_\tau| < -\mu_b \sigma_n$, parts of the model do not move relative to each other: $u_\tau = 0$. When $|\sigma_\tau| = -\mu_b \sigma_n$, a shift along the base is possible.

The slope angle of wedge base is equal to 1.5°. The size of the study area is 10.5°km along the y axis and 100 km along the x axis. The upper surface of the wedge is considered to be stress free.

At the first stage, the initial stress state was calculated taking into account the effect of gravity $\sigma_{x0}(y), \sigma_{y0}(y)$. The lateral surfaces do not move in the horizontal direction: $u_x|_{A,B} = 0$.
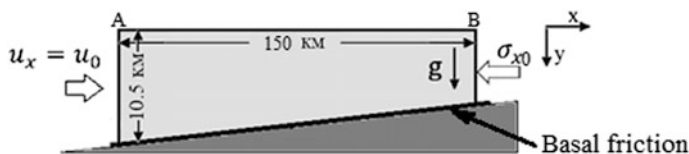
Fig. 2 Model of the fold-thrust belt's fragment with boundary condition

At the second stage of the calculation, the loading of the medium was carried out due to the displacement of the left boundary of the wedge (Fig. 2): $u_x|_{A,B} = u(t)$. The stresses on the right border remain constant: $\sigma_x|_B = \sigma_x^0$. Modeling of the deformation process was carried out using a numerical solution of equations of mechanics. The behavior of the medium was described using the model of elastoplastic deformation, taking into account hardening and softening due to the accumulation of damage with the Drucker-Prager limit surface [18–20]:

$$f = \tau - \alpha p + Y \tag{2}$$

where τ is the intensity of shear stresses; p is the pressure; α and Y are the strength parameters of the medium expressed through the coefficient of internal friction and cohesion. The increment of plastic deformation is determined by the equation:

$$d\varepsilon_{ij}^p = d\lambda \frac{\partial g}{\partial \sigma_{ij}} \tag{3}$$

where $d\lambda$ is the parameter determined during the solution, ε_{ij}^p is the component of the strain tensor, σ_{ij} is the component of the stress tensor, $g\left(\sigma_{ij}, d\varepsilon_{ij}^p\right) = \tau - \beta p$ is the plastic potential, β is the dilatancy. Models of this type describe the irreversible deformation of rocks in the modes of brittle and viscous shear fracture.

The system of equations was solved using an explicit finite-difference scheme [21] in a 2D plane strain.

Different values of the strength parameters and basal friction were considered in order to establish their connection with the peculiarities of the formation of thrust structures (Table 1). It was previously established that for values less than 0.05, the entire wedge is displaced, and for values greater than 0.5, an extended system of faults is not formed.

It is believed that the behavior of the upper crust is controlled by the Byerlee law [22]. However, there are no standard rheological profiles and modern models are built on the basis of regional structural and material features. It is also noted that deformations associated with geological processes develop with smaller values of parameters than the ones represented in the Beyrlee law. It is related to the action of the fluid or the change of properties in the friction zones which is caused by grinding of the material and physical and-chemical transformations. In addition, basal friction can vary in the process of the medium deformation as a result of

Table 1 Elastic and strength parameters

ρ, g/cm	K, GPa (Compression modulus)	G, GPa (Shear modulus)	Y, MPa	α	Dilatancy factor	μ_b
2.34	20.8	11.7	5	0.1–0.3	0.3α	0.05–0.6

fracture, changes in fluid pressure, etc. A number of numerical experiments were conducted in which the friction value decreased when a certain value of plastic deformation was reached. Friction varies according to the equation:

$$\mu_b(\gamma_{pl}) = \mu_0(1 - (\gamma_{pl} - \gamma_1)/\gamma_2) \tag{4}$$

for $\gamma_1 \leq \gamma_{pl} \leq \gamma_2$, where γ_{pl}, γ_1 and γ_2 are the equivalent plastic shear strain, the strain value of the onset and completion of friction reduction due to rock crushing, μ_0 is the initial basal friction, $\mu_0 \geq \mu_1$, μ_1 is the minimal friction coefficient [8].

3 Results and Discussion

3.1 Constant Basal Friction

According to the model of the critical wedge, in the case of dry running material with $\varphi = 6°(\alpha = 0.1)$ and friction at the base $\mu_b = 0.1$, the slope of the day surface should be $\angle a = 3.4°$. As a result of numerical simulation with the specified parameters, the slope of the topography is from 1° to 3° (Fig. 3). The slight difference in the results is probably due to the incomplete correspondence of the parameters of the model, as well as the fact that the medium is not flowing. The surface rises by 2 km due to the thickening of the sedimentary layer that occurred when the left border shifted by 4.8 km.

Ramp structures or shear bands with constant basal friction have an almost straight line form and it is typical of adjacent reverse thrusts; they probably do not occur as faults (Fig. 3). The slope angle of inclination of ramp structures varied in the range of 38°–40°. The principal stress axes deviate from the vertical and horizontal directions, and the deviation increases with depth, but it does not exceed 15°. The maximum principal stress σ_1 lies in a subvertical direction (Fig. 4a). The zone of plastic deformation exceeds the area where the ramps are formed. The formation of a ramp is preceded by a change in the slope of the displacement vector inside the thrust sheet, while the adjacent outer medium is almost stationary (Fig. 4b). After the formation of the next shear band, the direction of displacement of the medium changes nearly to horizontal, and an area with an inclined displacement appears in front of it (Fig. 4b). In this case, the displacements in the
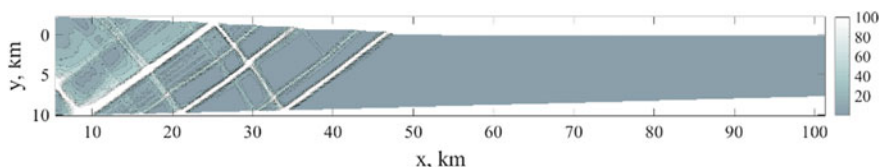
Fig. 3 Distribution of inelastic equivalent shear strain γ_{pl} (%)

extreme frontal plate, which are separated by faults, rotate and increase the amplitude even before the fracture zone appears. Thus, the two extreme shear bands separate the directions of displacements. The appearance of a strip of localization on the surface contributes to the formation of steps in the relief.

It was noted that with constant basal friction, the place of the fault structure's formation is determined by internal friction α [8]. Zones of localization grow bottom-up from the detachment at values less than 0.2. They form from the upper surface and often do not reach the basement in the case of α greater than 0.5. The intermediate range is characterized by the fact that the formation of a fault occurs simultaneously at the upper and lower surfaces.

3.2 Decreasing Basal Friction

Simulation results with decreasing basal friction differ from those with constant friction. Friction decreases (4) because the plastic deformation develops in the adjacent layer. For calculations, we took: $\mu_0 = 0.3; \mu_1 = 0.01; \gamma_1 = 0.2; \gamma_2 = 0.8$. The main difference is a closer location of ramp structures, which have a listric form in the frontal part (Fig. 5). The listric form is most clearly seen in the last fault, where the upper section is steeper, and its angle of incidence is 40°. The lower part falls at an angle of less than 30°. The system of faults is an imbricate fan. The intensity of irreversible shear strain in the associated localization zones is less than in the main faults under these conditions. Fault structures form and develop from bottom to top, and adjacent bands form on the upper surface, which becomes stepped.

There is a noticeable slope of the day surface only in the front part, where the faults do not have adjacent shear bands. The angle of inclination of the surface ($\sim 5.5°$) and the forming ramp depend on the initial basal friction in the range of 0.1–0.3 when the internal friction coefficient $\alpha = 0.1$. Outside this zone, the relief becomes nearly horizontal. Theoretically, when a basal friction is 0.3, the critical angle should be equal to 11.3°. Thus, the displacement of the wedge is easier than its internal deformation due to the detachment. The left part of the sediment layer became thicker by 2°km because of the displacement of the boundary by 2.6°km. In contrast to the case of constant friction, the main stress axes are significantly rotated relatively to the coordinate axes by approximately 45° (Fig. 6a). In the lower part of the front low-deformed zone, where plastic deformation is small, and the basal
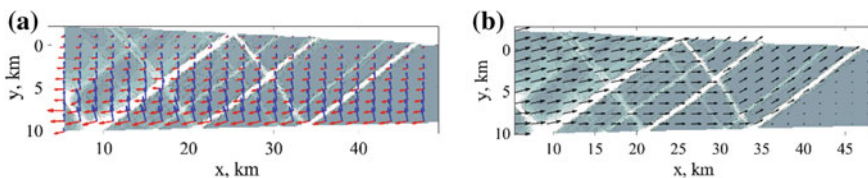
Fig. 4 Principal stress axes (**a**) and velocity vectors (**b**) near localization zones
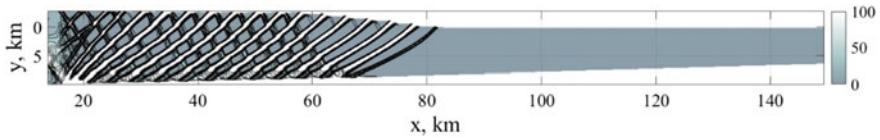
Fig. 5 Distribution of inelastic equivalent shear strain γ_{pl} (%)
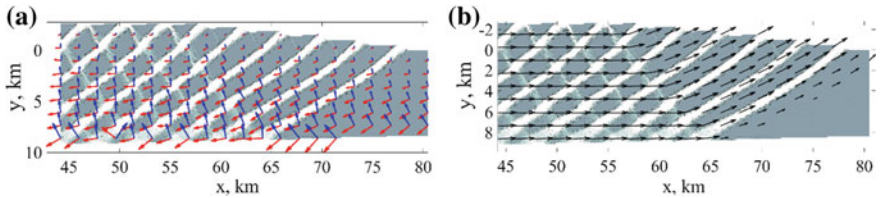
Fig. 6 Principal stress axes (**a**) and velocity vectors (**b**) near localization zones

friction is large, the orientation of the main axes differs by 90° from the orientation in the zone of intense deformation.

Displacement vectors have a slope only in the front part (Fig. 6b). Displacements are practically absent before the faults, and they occur at the moment of localization zones' formation. In the zone where the adjacent shear bands have formed, the direction of the displacements becomes horizontal. Thus, the active process of deformation develops only in the front part, the rest of the sedimentary layer slides easily along the base.

Friction decreases at the base due to plastic deformation and does not change evenly. Areas are formed where friction remains substantially higher than on most part of the sliding surface. The zones of low and high friction are clustered. As a result, the distribution of the friction coefficient at the base becomes periodic (Fig. 7a). In zones with increased friction shear plastic deformation takes the smallest values. The largest deformation values occur in the central part of the areas where the friction is low.

The stress distribution is also periodic. Coulomb stresses and their variants corresponding to the Drucker-Prager model do not provide information about the process in a plastic medium. This parameter is convenient for estimating the possible formation of plastic deformation zones while the medium is elastic. For analysis, we used the ratio of the equivalent shear stress to pressure: τ/p. In Fig. 7b it can be seen that the largest values of this parameter correspond to the smallest strain. Zones of shear deformation correspond to areas with a reduced ratio.
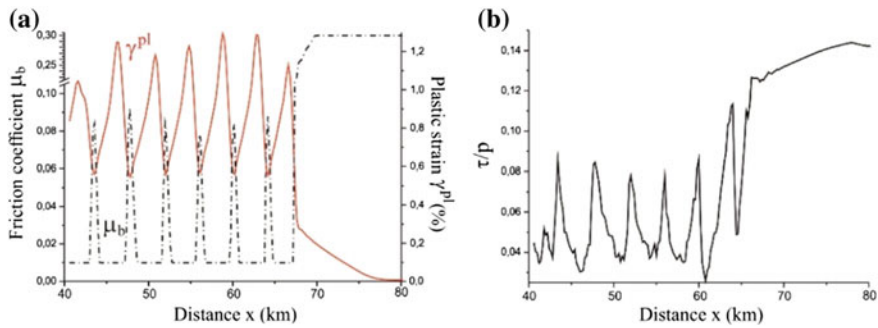
Fig. 7 The formation of a periodic distribution of the coefficient of friction $\mu_b(\gamma_{pl})$ and equivalent shear strain γ_{pl} (**a**), the distribution of τ/p in the adjacent layer of the medium (**b**)

4 Conclusion

The processes occurring in the zone of detachment determine the thrust structure. Linear ramps are formed with constant basal friction. The faults obtain close to listric forms while friction decreases in the deformation process. At low strength of the medium, the topography obtained in the simulation is consistent with the critical wedge theory. The greatest slope of the topography in the process of deformation is in the front zone when friction decreases. In the zone where slip occurs with low friction, the inclination of the surface becomes much smaller.

A relationship was found between the friction coefficient and the accumulated plastic strain. It contributes to the clustering of zones with reduced and increased friction. As a result, the friction coefficient and localized shear zones form a periodic distribution.

References

1. Dahlstrom, C.D.A.: Balanced cross section. Can. J. Earth Sci. **6**, 743–757 (1969)
2. Davies, D., Suppe, J., Dahlen, F.: Mechanics of fold-and-thrust belt and accretionary wedges. J. Geophys. Res. **88**(B2), 1153–1172 (1983)
3. Dahlen, F.A.: Noncohesive critical Coulomb wedges: an exact solution. J. Geophys. Res. **89**, 10125–10133 (1984)
4. Chapman, T.J., Williams, G.D.: Displacement-distance methods in the analysis of fold-thrust structures and linked fault systems. J. Geol. Soc. Lond. **141**, 121–128 (1984)
5. Ferrill, D.A., Morris, A.P., Wigginton, S.S., Smart, K.J., McGinnis, R.N., Lehrmann, D.: Deciphering thrust fault nucleation and propagation and the importance of footwall synclines. J. Struct. Geol. **85**, 1–11 (2016)

6. Marshak, S., Haq, S.S.B., Sen, P.: Ramp initiation in fold-thrust belt: insight from PIV analysis of sandbox models. J. Struct. Geol. **118**, 308–323 (2019)
7. Goff, D., Wiltschko, D.V.: Stresses beneath a ramping thrust sheet. J. Struct. Geol. **14**, 437–449 (1992)
8. Stefanov, Yu.P., Tataurova, A.A.: Effect of friction and strength properties of the medium on the formation of strain localization zones in thrust structures. Phys. Mesomech. **22**(6), (2019) (in Press)
9. Panian, J., Pilant, W.: A possible explanation for foreland thrust propagation. J. Gephys. Res. Sol. Earth **95**(B6), 8607–8615 (1990)
10. Knipe, R.J.: Footwall geometry and the reology of thrust sheets. J. Struct. Geol. **7**, 1–10 (1985)
11. Harris, L.D., Milici, R.C.: Characteristics of Thin-Skinned Style of Deformation in the Southern Appalachians and Potential Hydrocarbon Traps. U.S. Geological Survey Professional Paper, Washington (1977)
12. Dixon, J.S.: Regional structural synthesis, Wyoming salient of western overthrust belt. AAPG Bull. **66**, 1560–1580 (1982)
13. Bose, S., Mandal, N., Mukhopadhyay, D.K., Mishra, P.: An unstable kinematic state of the Himalayan tectonic wedge: envidence from experimental thrust-spacing patterns. J. Struct. Geol. **31**, 83–91 (2009)
14. Schott, B., Koyi, H.A.: Estimating basal friction in accretionary wedge from the geometry and spacing of frontal faults. Earth Planet Sci. Lett. **194**(1–2), 221–227 (2001)
15. Kocharyan, G.G., Markov, V.K., Ostapchuk, A.A., Pavlov, D.V.: Mesomechanics of shear resistance along a filled crack. Phys. Mesomech. **16**(5), 5–15 (2013)
16. Pluijm, B.A., Marshak, S.: Earth Structure. An Introduction to Structural Geology and Tectonics. W. W. Norton & Company, New York (2004)
17. Haiduk, V.V., Prokopiev, A.V.: Metody izucheniya skladchato-nadvigovykh poyasov. Nauka, Novosibirsk (1999)
18. Drucker, D.C., Prager, W.: Soil mechanics and plasticity analysis or limit design. Quart. Appl. Math. **10**(2), 157–165 (1952)
19. Nikolaevskii, V.N.: Governing equations of plastic deformation of a granular medium. J. Appl. Math. Mech. **35**(6), 1017–1029 (1971)
20. Stefanov, Yu.P: Localization of deformation and fracture in geomaterials. Numer. Simul. Phys. Mesomech. **5**(5–6), 67–77 (2002)
21. Wilkins, M.L.: Computer Simulation of Dynamic Phenomena. Springer, Berlin (1999)
22. Byerlee, J.D.: Friction of rocks. Pure. Appl. Geophys. **92**, 3681–3682 (1978)

Calculation of Filtration Properties of the Antey Uranium Deposit Rock Massif at the Deformation Phases: Microstructural Approach

Stepan Ustinov , Vladislav Petrov , Valery Poluektov and Vasily Minaev

Abstract

The spatial and geometric parameters of various types and systems of microstructures were established, basing on the special technique of microstructural analysis, implemented by using the authors' GIS module, in oriented rock samples of the Antey molybdenum-uranium deposit (Southeastern Transbaikalia, Russia). The sequence of activation of these microstructures was reconstructed by using additional methods for analysis of mineral substances. We investigated the fluid inclusion planes, which are microcracks that captured secondary fluid inclusions in the hydrothermal activity process, as reliable indicators of changing parameters of the stress-strain field and the identification of rock deformation phases. Thus, three successive structural phases in the history of the formation of the Antey deposit, were established. The established phases reflect the impacts of different stress-strain fields, which led to the formation of a specific set of microstructures generations that behaved as fluid-conducting channels within the hydrothermal process. The values of porosity and permeability were calculated for each identified structural phase of the deposit formation associated with certain deformations that directly influence the migration process of ore-bearing fluids.

S. Ustinov (✉) · V. Petrov · V. Poluektov · V. Minaev
Institute of Geology of Ore Deposits, Petrography, Mineralogy and Geochemistry
of the Russian Academy of Sciences, Staromonetny per. 35, 119017 Moscow, Russia
e-mail: stevesa@mail.ru

179

1   Introduction

The filtration properties of rocks are among the most important, having a significant impact on the process of fluid migration and on the nature of the ore-magmatic system evolution. The process of cracks, microcracks and pores formation, even despite their relatively small volume, significantly contributes to increase of the filtration characteristics of rocks, thereby accelerating the chemical processes. The reconstruction of the fluid migration phases and the quantitative calculation of the porosity and permeability values of rocks in the paleo-conditions are quite complex and not entirely unambiguous.

The most important physical factors determining the evolution of a hydrothermal system are magmatic thermal power and permeable structures. Permeability of host rocks determines whether the heat transfer around a cooling-down intrusion will be predominantly convective (low permeability) or advective (moderate and high permeability). As the work of researchers has shown, it is most likely that the boundary between the two regimes is close the permeability values of 10^{-16} m^2 (0.1 mDarcy) [1–3].

Cracks and microcracks form mainly in the zone of brittle deformations, as a response to the external stress effect. But, at the same time, geological bodies characterized by brittle properties can acquire plastic characteristics at drastic in temperature growth by hundreds of degrees. The results of studies of modern geothermal systems in granites [4], as well as the mechanisms of fluid migration in hydrothermal systems from plastic to brittle rocks, has allowed us to establish that the brittle-plastic transition is usually in the temperature range of 370–400 °C [5].

The results of numerical simulation and research of microcracks under an optical and electron microscope [6] confirms that the forecast of changing the permeability in low-porous crystalline rocks should be based on the analysis of the fractured space permeability.

The rock microstructures are usually classified by open microcracks not filled with mineral material, as well as mineralized microcracks, filled with secondary minerals or secondary fluid inclusions (FI),. Microstructures capture the secondary FIs under influence of some later, for example hydrothermal, process when the crystallization of the host mineral has already been completed [7].

The secondary fluid inclusions are usually captured by microcracks formed against the background of oriented stress and therefore have a predetermined orientation direction. These microcracks during the structural studies are called fluid inclusion planes (FIPs) [8, 9].

The spatial orientation of each generation of FIPs directly depends on the parameters of the stress-strain field (SSF) that was in effect at the time of its formation. Therefore, studying such FIPs systems as structural markers and the comprehensive study of other types of microstructure systems can be used for restoring the deformation phases and rock permeability, reconstruction of the geometry of fluid migration pathways, establishment of the dynamics of
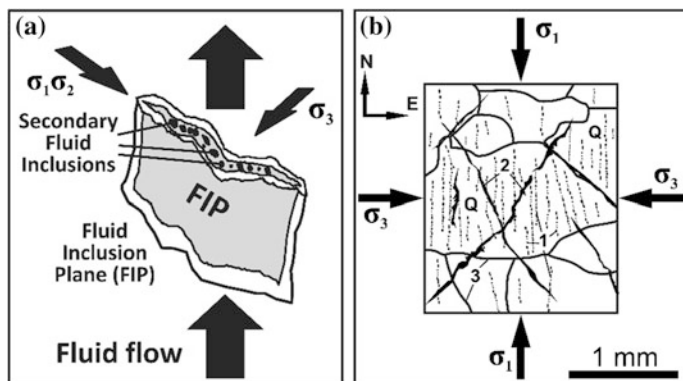
Fig. 1 The orientation of the stress-strain field axes in relation with the fluid inclusion plane (FIP) orientation; **a**—in three-dimensional space; **b**—in the plane of the oriented thin section: 1—FIPs, 2—open or mineralized microcracks, 3—borders of mineral grains, Q—quartz grains. σ_1 is the axis of maximum compression, σ_3 is the axis of least compression, $\sigma_1\sigma_2$ is the plane of the intermediate axis and the axis of maximum compression

temperature-and-pressure changes, the physical and chemical conditions associated with certain deformation phases of geological bodies [10, 11] (Fig. 1).

FIPs can be detected in many rock-forming minerals, regardless of their crystallographic properties. At the same time, the quartz grains provide for the best preservation. The experiments prove that the feldspar and carbonate crystals are less resistant to hydrothermal-metasomatic transformations, leaching and weathering processes, respectively, the preservation of FIPs and the possibility of their studying in these minerals are unlikely.

Considering the above, the main goal of the work was to develop an approach for the spatial analysis of various microstructures, including FIPs, as indicators of the heterogeneous SSF. On the basis of the obtained results, the calculation of the filtration characteristics of rocks at different deformation phases was carried out.

2 The Special Technique of Microstructural Analysis

Basing on the accumulated experience of the complex study of microstructures in oriented rock samples, the authors have developed the specialized technique of microstructural analysis (STMA) and have formulated the theoretical grounds for its application [12]. The authors' approach to the STMA implementation, in addition to establishing the orientations of the FIPs, includes reconstruction of the spatial parameters and the nature of the mineral filling of mineralized and other types of microstructures.

An important requirement for the implementation of STMA is the selection of oriented samples. Then, oriented thin sections are made from the selected samples. The spatial parameters of various generations of microstructures and the nature of their relationships can be studied by using the optical microscope. But, in this case, measurement of the geometric characteristics of microstructures reaching several thousands in a thin oriented section takes quite a time. All this determines the need to create a specialized tool for speeding up the collection, processing and analysis of spatial microstructural data. Some researchers [13, 14] have already taken attempts to create such a tool based on the development of original software. But these developments are not open to a wide range of researchers and available only to the scientists who develop them, even without the possibility of acquisition by other researchers on a commercial basis. This state of affairs has forced the authors to develop their proprietary GIS module for implementing STMA, which allows studying structural heterogeneity of rocks, establishing the geometry of various types and systems of microstructures, their spatial relationships, reconstruction of the activation sequence and calculation of filtration parameters [15].

The papers [13, 16, 17] were used to evaluate the filtration parameters of rocks at different deformation phases, various formulas for calculation of the microcrack porosity and permeability. These formulas were adjusted to reflect the specific geometry of the fractured-pore space formed at a certain deformation phase s. The formulas can be used to calculate both general and directive values of porosity and permeability.

3   The Antey Uranium Deposit

The work carried out by authors at the Antey uranium deposit can be the case example of how to calculate the filtration characteristics of rocks for different deformation phases. The Antey deposit is the most deep-seated object of the Streltsovsky ore field (Southeastern Transbaikalia) and is unique in its reserves and quality of uranium ores. This vein-stockwork deposit is located in the eastern part of Streltsovskaya caldera and localized in the basement at a depth of 400–1400 m from the surface. The host rocks are represented by the Late Paleozoic (~ 250 Ma) granitoids. The two facies of granitoids are distinguished: coarse-grained porphyritic and medium-grained leucocratic granites [18]. Granitoids underwent multi-phase hydrothermal-metasomatic transformations, including the high-temperature K-feldspatization, low-temperature hydromication, hematite-albitization, silicification and post-ore metasomatic transformations [19].

The main role in the localization of uranium mineralization belongs to the north–northeast strike faults (25–30°), which cut off the sublatitudinal elements of the prototectonics [20]. These structures are mostly developed in the eastern part of the deposit and are represented by large faults of 13, 161 and 160. At the upper levels of the deposit (in granites), the faults have a fall to the northwest at an angle of 70–80°. The fall changes to nearly vertical as the depth increases [18].

4 Results and Discussion

Earlier works, such as the spatial study of various microcrack systems, implemented on the basis of STMA and modular software, microthermometric studies of FIPs and analysis of mineralized generations of microstructures with use of the SEM method, have established three structural phases in the history of the Antey deposit formation (Table 1). The filtration characteristics of rocks can be calculated for each of these phases characterized by a specific set of microstructures and reflecting the impacts of different SSFs against the background of hydrothermal activity and fluid migration.

The first structural phase of the deposit formation is characterized by elasto-plastic and minor brittle deformations, which led to the formation of a small amount of microcracks of sublatitudinal orientation. During the first structural phase, microcracks practically did not play any role in the fluid migration process. Therefore, the calculated values of microcrack porosity and permeability are insignificant.

The second structural phase is also characterized by the uneven impact of SSF in the upper part of the deposit. As the brittle deformations manifested, the clear-cut systems of numerous microcracks began to form, thus significantly increasing the filtration capacity. At the 14th horizon, unlike the upper horizons, the second

Table 1 Structural phases at 9th, 11th and 14th horizons of the Antey deposit according to the STMA data and microthermometric studies of the FIPs secondary fluid inclusions

9th and 11th horizons (550 and 670 m from the surface)			
Parameter	Stage I	Stage II	Stage III
FIPs orientations	Sublatitudinal	Northwest (1st generation), northeast	Sublatitudinal, northwest (2nd generation), submeridional
Fluid inclusion homogenization temperatures °C	380–300	300–220	220–150
Type of deformations	Elastic and plastic	Brittle	
Hydrothermal metasomatic transformations	K-feldspatization, albitization	Greisenization	Argillization, chloritization, hematitization
14th horizon (850 m from the surface)			
Parameter	Stage I	Stage II	Stage III
FIPs orientations	FI not detected	Submeridional	Northwest, northeast
Fluid inclusion homogenization temperatures °C	–	290–205	205–150
Type of deformations	Elastic and plastic	Brittle	
Hydrothermal metasomatic transformations	K-feldspatization, albitization	Greisenization	Argillization, chloritization, hematitization
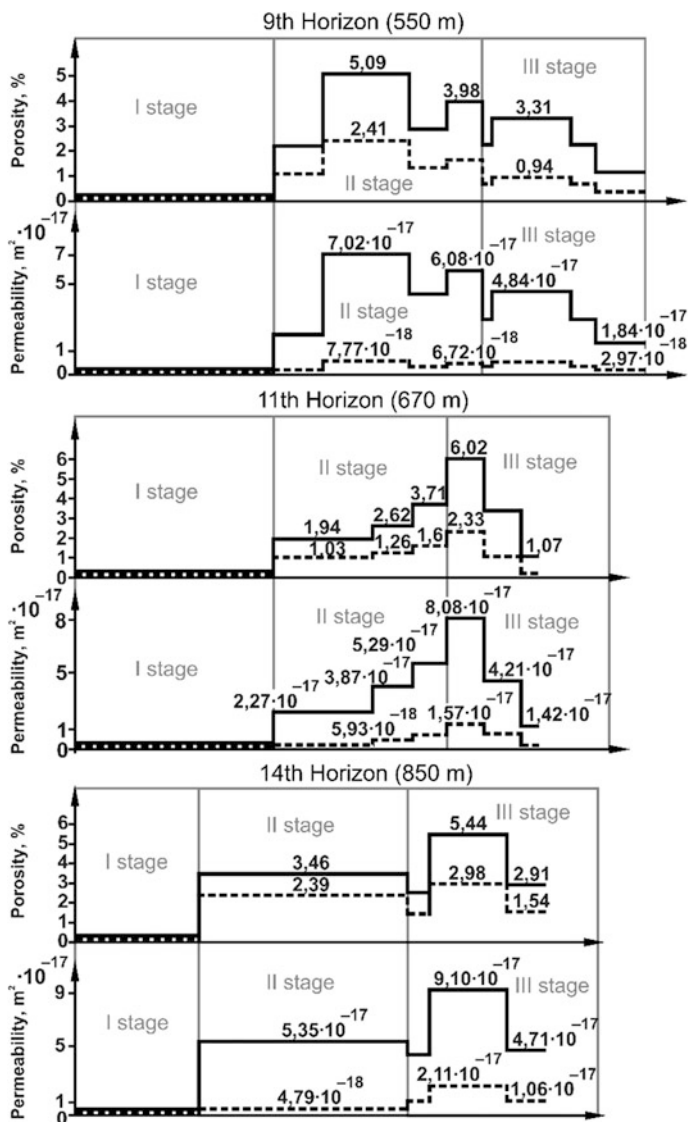
Fig. 2 Dynamics of changing the filtration parameters at horizons of the Antey deposit rock massif within the deformation phases. The e-Evolution of the filtration properties in the fault core is shown by the solid line, and the same in the host rocks—by the dotted line

structural stage dominated by the generation of submeridional microstructures, apparently, formed under the conditions of homogeneous SSF. These microstructures ensured a rather stable migration of fluids, which is related to a significant increase of the rocks filtration characteristics. At transition to the upper horizons,

the flow rate of the solutions could slow down due to dissimilar structural conditions, which also influenced the decrease of the rocks filtration parameters.

The third structural stage manifested itself at the final phases of hydrothermal activity and ore genesis. The NW–SE sublatitudinal and submeridional microcracks formed at the upper parts of the deposit (9th and 11th horizons) and they ensured the close values of filtration characteristics. The structural differences between the upper and lower parts of the field continue to remain. The NW–SE and NE–SW microstructures formed further along the section (14th horizon). The rocks porosity and permeability of this deeper part is significantly increased as compared to the upper parts.

The proposed table is supplemented with the diagrams of changing the porosity and permeability values of microcracks of various generations formed within the three established successive structural evolution phases of the Antey deposit rock massif (Fig. 2). The diagrams feature the evolution of the filtration properties in the fault core shown by the solid line, and the same in the host rocks—by the dotted line. At building the diagrams, we have accounted the individual and joint impact of generations of microstructures on the rock properties in the areas in which they overlap.

5   Conclusion

The calculation of the filtration characteristics of rocks with account of the sequence of microstructures formation and specific fracture-pore geometry indicating a structural phase of the Antey deposit formation is done with use of the specific technique of microstructural analysis and software for its implementation, the microthermometric measurements, scanning electronic microscopy. Now it is possible to do the mapping of any individual microstructure in the sample and study its geometrical parameters. In addition to the geometrical parameters for microcracks, the nature and properties of the mineral filling can be studied. The sequence of the formation of microstructures can be restored and clearly indicated. This approach has made it possible to calculate the porosity and permeability values for each specific structural phase of the deposit formation associated with the deformations that directly influence the migration of ore-bearing fluids.

References

1. Cathles, L.M.: An analysis of the cooling of intrusives by ground water convection which includes boiling. Econ. Geol. **72**(5), 804–826 (1977)
2. Cathles, L.M.: Scales and effects of fluid-flow in the upper crust. Science **248**, 323–329 (1990)

3. Hayba, D.O., Ingebritsen, S.E.: Multiphase groundwater flow near cooling plutons. J. Geophys. Res. **102**, 12235–12252 (1997)
4. Tamanyu, S., Fujimoto, K.: On the models for the deep-seated geothermal system in the kakkonda field. Rept. Geol. Surv. Jpn. **284**, 133–164 (2000)
5. Fournier, R.O.: Hydrothermal processes related to movement of fluid from plastic into brittle rock in the magmatic-epithermal environment. Econ. Geol. **94**, 1193–1211 (1999)
6. Shmonov, V.M., Vitovtova, V.M., Zharikov, A.V.: Fluid Permeability of the Earth's Crust Rocks. Nauchnii Mir, Moscow (2002). (in Russian)
7. Roedder, E.: Fluid inclusions. Rev. Mineral. **12**, 644 (1984)
8. Tuttle, O.F.: Structural petrology of planes of liquid inclusions. J. Geol. **57**, 331–356 (1949)
9. Lespinasse, M.: Are fluid inclusion planes useful in structural geology? J. Struct. Geol. **21**, 1237–1243 (1999)
10. Boullier, A.M.: Fluid inclusions: tectonic indicators. J. Struct. Geol. **21**, 1229–1235 (1999)
11. Petrov, V.A., Ustinov, S.A., Poluektov, V.V., Prokofiev, V.Yu.: Reconstruction of the paths and conditions of ore-bearing hydrothermal solutions migration: the structural-geological and thermobarogeochemical approach. Vestnik RFBR **1**, 27–33 (2013). (in Russian)
12. Ustinov, S.A., Petrov, V.A.: Theoretical basics and opportunities of the special technique of microstructural analysis application. Uspekhi Sovrem yestestvoznaniya **10**, 125–131 (2018). (in Russian)
13. Lespinasse, M., Désindes, L., Fratczak, P., Petrov, V.: Microfissural mapping of natural cracks in rocks: implications for fluid transfers quantification in the crust. J. Chem. Geol. **223**, 170–178 (2005)
14. Xu, J., Zhao, X., Liu, B.: Digital image analysis of fluid inclusions. Int. J. Rock Mech. Min. Sci. **44**(6), 942–947 (2007)
15. Ustinov, S.A., Petrov, V.A.: Using of GIS-technology for microstructural analysis in geology. Geoinformatika **2**, 33–46 (2015). (in Russian)
16. Gueguen, Y., Dienes, J.: Transport properties of rocks from statistics and percolation. Math. Geol. **21**, 1–13 (1989)
17. Sausse, J., Jacquot, E., Fritz, B., Leroy, J., Lespinasse, M.: Evolution of crack permeability during fluid-rock interaction. Example of the Brézouard granite (Vosges, France). Tectonophysics **336**(4), 199–214 (2001)
18. Ischukova, L.P., Modnikov, I.S., Sychev, I.V., Naumov, G.B., Melnikov, I.V., Kandinov, M.N.: Uranium Deposits of the Streltsovsky Ore Field in Transbaikalia. Glazovskaya Printing House, Irkutsk (2007). (in Russian)
19. Andreeva, O.V., Aleshin, A.P., Golovin, V.A.: Vertical zoning of near-ore transformations at the uranium deposit Antey-Streltsovskoe (Eastern Transbaikalia, Russia). In: Geologiya Rudnykh Mestorozhdeniy, vol. 38, no. 5, pp. 396–411 (1996). (in Russian)
20. Petrov, V.A., Poluektov, V.V., Rebetsky, Y.L., Burmistrov, A.A.: Tectonophysics of hydrothermal ore formation: an example of the Antei Mo–U deposit. Transbaikalia. Geol. Ore Depos. **57**(4), 292–312 (2015)

Trigger Effect of a Heat Flow on Distribution of Critical Level of Deformations in Focal Zones

Andrey Vilayev

Abstract

This article describes the impact of changes of the Earth's crust deep temperatures in a seismically active region of the Northern Tien-Shan on the formation of thermal deformations in earthquake focal zones. The research method is based on numerical modelling of temperatures using data of seismic velocity up to a depth of 100 km and experimental dependencies of thermal parameters: heat flow, thermal conductivity, radiogenic heat generation. Comparative analysis of the geothermal model parameters and distribution of earthquakes in the area has been performed. The crucial factor influencing the formation of critical deformations is the existence of high-temperature areas with excessive temperatures $100 \div 250$ °C above solidus at depths of $20 \div 45$ km. The distribution of earthquake hypocenters is controlled by the values of thermoelastic stresses with an isobaric border of 0.35 GPa and anomalous temperature values over the isotherm of 230 °C.

Keywords

Crustal temperature · Heat flow · Thermal stress · Earthquake

A. Vilayev (✉)
Institute of Ionosphere, National Center of Space Research and Technology, 050020 Almaty, Republic of Kazakhstan
e-mail: vilayev@gmail.com

1 Introduction

The impact of thermodynamic energy on the stress-strain state of the Earth's crust and related geodynamic processes is considered in monographs [1–7] etc. The effect of temperature and pressure in geological time determines the mechanisms of rock destruction. Velocity of seismic waves is the main source of information about the structure of the Earth's crust, because depends on lithological composition, physical properties and mechanical state of rocks. In situ rock properties can be determined from functional relationships of seismic wave velocity. The heat flow density on the surface reflects the release of thermal energy from the Earth's crust.

This paper presents research results of geothermal structure of the Northern Tien-Shan crust.

2 Initial Data and Equations

2.1 Initial Data

Information about the deep structure of the Earth's crust can be obtained from seismic wave measurements of earthquakes or from special geophysical studies. We used the published materials of deep seismic soundings on four sublatitudinal and six submeridional profiles [8–10] (Fig. 1, left). A 3D modeling of seismic compression waves was performed with absolute values on a cross section of 0.2 km/s in a detailed study area $N42^{\circ} \div N45^{\circ}$, $E75^{\circ} \div E80^{\circ}$ and 100 km in depth. An important feature of the velocity model is the existence of a waveguide at depths of $30 \div 45$ km. The relative decrease in velocity in the waveguide is $0.1 \div 0.2$ km/s.
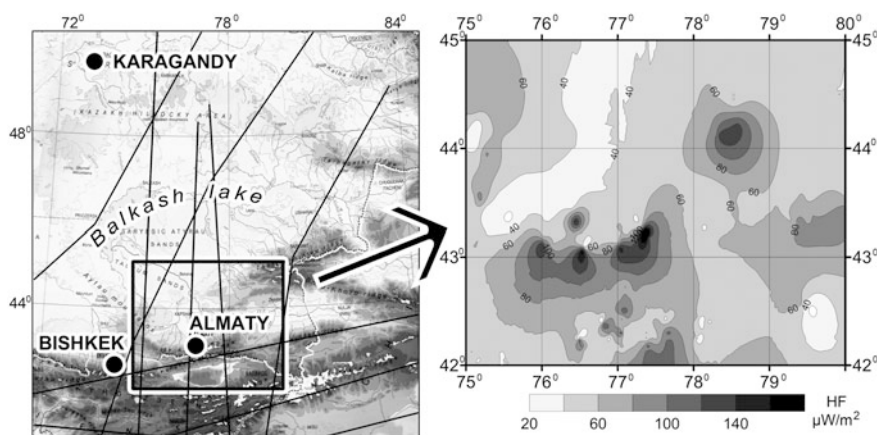
Fig. 1 Geotraverse system of P-waves velocity modeling (left) and heat flow density (right)

The initial data for temperature modeling is based on the distribution of the Earth's surface heat flow. We used our direct geothermal gradient measurement data in wells. The coefficient of thermal conductivity of rocks from the core of these wells was determined in the laboratory at normal PT (pressure, temperature). The heat flow was calculated by multiplying the geothermal gradient by the coefficient of thermal conductivity. Worldwide data on the distribution of heat flow published in [11, 12] were also used (Fig. 1, right).

2.2 Temperature Equations

The temperature (T) can be calculated at any depth using a stationary conductive heat transfer Eq. (1) and depends on the thermal conductivity λ of the rocks at the point with coordinates (x, y, z) and the radioactive heat generation in a unit volume A(x, y, z) [1, 2].

$$\nabla \lambda \nabla T + \lambda \nabla^2 T + A(x, y, z) = 0 \tag{1}$$

Equation (1) corresponds to a heterogeneous anisotropic medium without convection. The time factor is not taken into account for stationary long-time geological processes.

Currently available data from numerous studies establish a functional relationship of thermal conductivity with seismic waves velocity and the temperature of rocks, in general as: $\lambda = \lambda_0 \times f(V_p, T)$, where λ_0 is heat conduction coefficient measured at normal temperature and pressure ($T_0 = 20\ °C$, $P_0 = 1$ bar).

We used a correlation relationship for λ (x, y, z) with regard to temperature:

$$\lambda(x, y, z) = \lambda_0 \times \left(\frac{V_p(x, y, z)}{V_0} \right)^3 \times \frac{1}{(-0.9 + 0.00246T + 343T^{-1})} \tag{2}$$

where Vp − P wave seismic velocity (km/s), T—temperature in °K, $\lambda_0 = 2.6$ W/m · K, $V_0 = 6.0$ km/s (for granite layer).

Radiogenic heat generation A(x, y, z) in the Earth's crust due to decay of radioactive elements ^{40}K, ^{238}U and ^{232}Th (Eq. (1)) was considered in view of relation with seismic velocities in rock formation [13–15]. The correlation relation is calculated as:

$$A(x, y, z) = 0.03125 \times \exp(1.61 V_p(x, y, z)) \tag{3}$$

where A—heat generation in ($\mu W/m^3$) and Vp is P wave seismic velocity (km/s).

2.3   Boundary Conditions

Equation (1) with allowance for (2), (3) was solved using the numerical finite difference method on a grid with a 10 × 10 × 5 km cell with a variable direction scheme with boundary conditions [16]. The distribution of the Earth's heat flow was taken as a first boundary condition for heat transfer on the surface. The average annual temperature is 10 °C at the depth of 1 m was taken as a second boundary condition. The initial temperature distribution with depth was assumed to correspond to a linear geothermal gradient of 12 °C/km. The lateral boundary conditions are equal to zero heat flow through vertical boundaries. At the lower boundary (100 km), the mantle heat flow was determined as the difference between the heat flow on the surface and the radiogenic component according to the Gordienko method [15]. A constant temperature of 1140 °C is assumed at a modeling depth of 100 km assuming a solidus temperature of 1370 °C at a depth of 120 km.

2.4   Thermotension Equations

Nonlinear temperature distribution causes deformation and creates thermoelastic stresses [2–4] etc.

In our work we consider the isothermal type of deformation. It is assumed that the values determined for solving thermoelastic equations are statistically averaged by their actual distribution. Defects of the geological environment and tectonic faults were not considered as separate objects in the volume of the Earth's crust. Stresses and strains were taken as continuous. For the initial conditions, the stresses are zero and the temperature T_0 is constant for the entire volume. When a change in $T > T_0$ occurs, the rock expands, causing deformations described by the equation $\varepsilon = -\beta\,(T-T_0)$, where β is the coefficient of thermal expansion. If deformation is negative, then there is an increase in volume. On the surface, shear deformations are zero, and the main direction of the existing deformations is vertical (lithostatic pressure).

To calculate the effective thermal stresses in the Earth's crust, we applied the equation [2]:

$$\tau_{zz} = \rho g z + 3\beta K(T - T_0) \tag{4}$$

where—3β is the volume coefficient of thermal expansion of the rocks, K is the bulk modulus, ρ is the density, g is acceleration of gravity, and $(T - T_0)$ is temperature deviation from the initial linear distribution. The result $3\beta K(T - T_0)$ denotes thermal stresses caused by a combination of nonlinear temperature change. The bulk modulus K is calculated from the ratio of the P-waves and S-waves velocities in the conditions of natural rock-bedding:

$$K = \rho \left(V_p^2 - \frac{4}{3} V_s^2 \right) \tag{5}$$

where Vp/Vs = 2.04 stands for the rocks of the Northern Tien-Shan.

Density of rocks $\rho(x,\ y,\ z)$ is defined according to the law of linear approximation:

$$\rho(x,y,z) = \left(0.315 V_p(x,y,z) + 0.74 \right) \times 10^3 \tag{6}$$

It should be noted that application of linear theory of elasticity to the crust gives approximate characteristics, since its structure is a heterogeneous multiphase system. We calculated the correlation coefficients and empirical numerical constants in (2), (3),(6) using the least squares method compared with the published data to take into account the change of high thermodynamic parameters [17]. Currently, there are no other more accurate methods for calculating thermoelastic parameters of the Earth's crust.

3   Results and Discussion

3.1   Geothermal Model

Taking into account the total error limit for determining heat flow, heat conductivity and heat generation for rock formations, the accuracy of calculated geothermal model is around ±70 °C.

In accordance with the Hooke's law linear distribution of temperature doesn't result in thermal stress in homogeneous area. From this point of view, the structure of the thermal field was studied by dividing temperatures into stationary (linear) and anomalous ones. The anomalous (excess) temperatures are determined by subtracting the stationary component corresponding to a linear geothermal gradient of 12 °C/km from the calculated field (Figs. 2, 3).

According to petrological research data [18] in the presence of 0.5–1.0% of water partial melting of granite occurs at temperature 650 ÷ 750 °C, diorite—950 ÷ 1000 °C, basalt—1100 ÷ 1150 °C. Temperature of rocks located in the anomaly area exceeds their solidus on average by 50 ÷ 150 °C (in maximum by 270 °C). Level of material's partial melting in such conditions reaches 3 ÷ 5%. Thus, there is temperature heterogeneity in the lower part of the crust, which contributes to the partial melting of the layers. Under high temperature conditions over 650 °C [18] partial melting occurs and phase transformations of granulite and eclogite environment into basalt occur. With an increase in melting the rock volume grows and density decreases and therefore vertical movements of the Earth's crust surface occur (dome formation) above the melting zone [19].
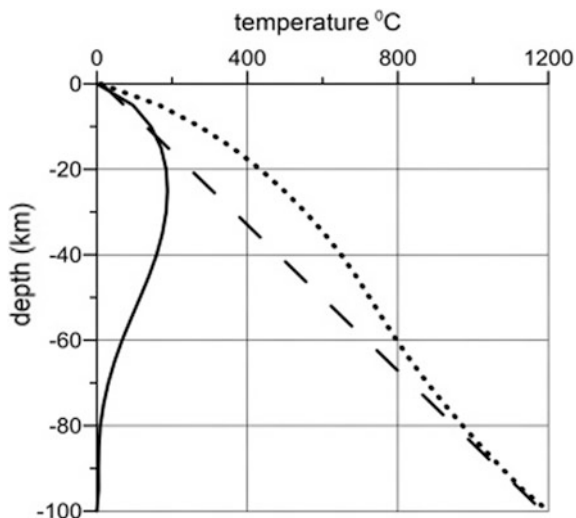
Fig. 2 Full temperature (dotted) and temperature deviating from the linear (solid)
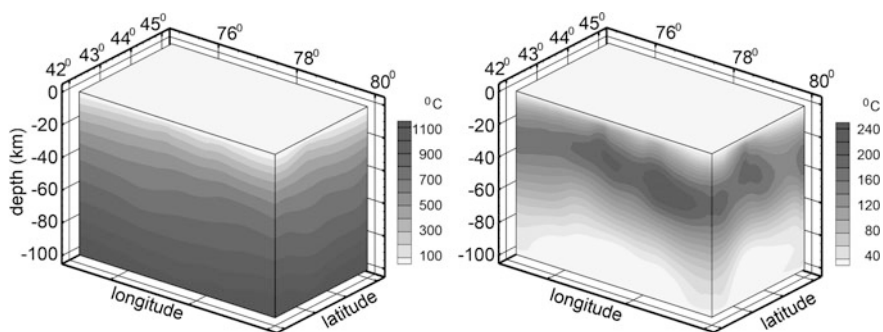
Fig. 3 Results of temperature distribution modelling. Left—integrated temperature field (°C), right—anomalous (excess) temperatures (°C)

About 6% of molten mass is formed in accordance with this model and density decrease can be up to 15% from the initial amount. This amount of molten mass is sufficient to explain the observed decrease of seismic velocities in the lower part of a basalt layer. Per every 100 °C of temperature exceeding solidus in the partial melting zone velocity of seismic waves reduces by 0.075 km/s, density—by 0.01 g/cm^3. Temperature anomalies in space coincide with the zone of reduced seismic waves velocities (waveguide). Local reduction of seismic waves velocity in depth and at 50 km in the Northern Tien-Shan megablock is 0.1 ÷ 0.2 km/s. Anomaly heating range (comparing to rock solidus temperature) reaches ≈150

250°. Such temperature increase provides seismic waves velocity reduction of 0.11–0.18 km/s.

3.2 Thermoelastic Stresses

Working pressure is calculated as the sum of lithostatic pressure and thermoelastic stresses caused by non-linear heating and heterogeneity of physical and mechanical properties.

At depths of 30 ÷ 50 km, temperature stresses are 12 ÷ 27% of lithostatic pressure and reach absolute values of up to 0.45 GPa. The ratio of total pressure (taking into account thermobaric pressure) to lithostatic pressure in the region of abnormal temperatures is 1.3 ÷ 1.4 (Table 1).

The calculations are in the range of experimental data of mineral equilibrium, which evidences that tectonic pressure can reach up to 100% of the lithostatic pressure and values of a few gigopascals [20]. Intensity of thermal stress decreases with depth almost to zero. This can be explained by the temperature field smoothing and transfer into stationary mode of heating lithosphere by mantle heat transfer with linear temperature gradient.

Table 1 Thermophysical model of the Tien-Shan Earth crust in latitude E770. z is depth, Vp compressional wave velocity, VS shear wave velocity, A radiogenic heat generation, λ thermal conductivity coefficient, ρ density, HF heat flow, T temperature, K bulk modulus, PL lithostatic pressure, PT thermal stresses (bold text data from Pasquale et al. [1], Chapter 1, Table 1.1, p. 4)

z (km)	V_p (km/s)	V_S (km/s)	A ($\mu W/m^3$)	λ (W/m·K)	ρ (kg/m³)	HF ($\mu W/m^2$)	T (°C)	K (GPa)	P_L (GPa)	P_T (GPa)
0	5.3	2.6	0.21	1.70	2404	58.04	10.00	45.6	0.00	0.00
0	**5.6**	**3.2**			**2600**			**46.0**	**0.00**	
−5	5.7	2.8	0.71	2.22	2522	57.51	184.68	54.9	0.14	0.12
−15	6.2	3.1	1.32	2.88	2706	51.52	360.52	71.6	0.39	0.28
−15	**6.4**	**3.6**			**2750**			**65.1**	**0.34**	
−20	6.4	3.1	1.10	2.90	2753	48.23	423.07	76.4	0.52	0.30
−35	6.8	3.3	0.64	2.73	2869	41.12	573.87	89.1	0.94	0.29
−35	**7.6**	**4.4**			**2900**			**97.1**	**0.60**	
−40	7.0	3.4	0.48	2.75	2931	39.53	616.07	96.4	1.08	0.27
−50	7.4	3.6	0.28	2.86	3071	37.46	694.10	114.2	1.38	0.21
−60	7.6	3.7	0.18	2.72	3144	36.24	772.94	124.5	1.69	0.11
−70	7.7	3.8	0.15	2.44	3161	35.39	861.68	126.9	2.00	0.04
−80	7.8	3.8	0.12	2.27	3200	34.71	960.74	132.6	2.31	0.00
−80	**8.1**	**4.5**			**3375**			**130.3**	**2.45**	
−90	8.0	3.9	0.09	2.17	3251	34.18	1065.94	140.5	2.63	0.00
−100	8.2	4.0	0.06	2.12	3312	33.79	1200.00	150.1	2.95	0.00
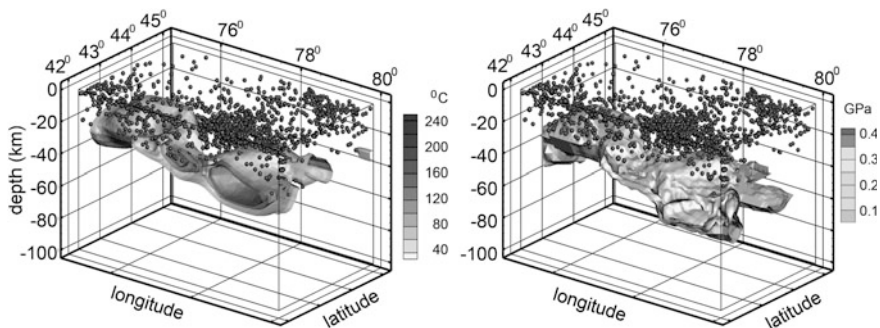
Fig. 4 The isothermal surface of anomalous temperatures (230 °C, left) and the isobaric surface of thermoelastic stresses (0.35 GPa, right). Earthquake hypocenters are shown as black dots

Earthquake hypocenters are located on the border of the regional abnormal (excess) temperatures with an isotherm of 230 °C. The isobar of thermoelastic stresses of 0.35 GPa is also highlighted by us as a criterion controlling the distribution of the hypocenters (Fig. 4).

Comparison of the heat flow distribution and earthquakes of the average energy class (9.0 ÷ 10.5) shows that the epicenters are concentrated mainly in the areas with low HF values (Fig. 5). Here, the increased density of epicenters is probably associated with increased fragility of rocks and lower viscosity of the Earth's crust. It can be assumed that the fragile mechanism of the earthquake formation is due to a decrease in the plasticity limit of the material.

However, the catastrophic earthquakes of the last century (Vernenskoye, Ms = 7.1, 1887; Chilik, Ms = 8.1, 1889; Keminskoye, Ms = 8.0, 1911) occurred in the

Fig. 5 Depth heat flow model with earthquake hypocenters
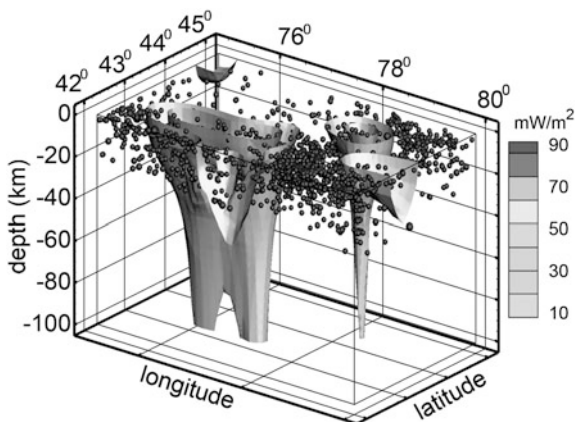
areas of increased heat flow values. We assume that at the depths of 35–60 km, eclogite-basalt phase transformations with partial melting can occur. In the area of melting, the volume of rocks increases, and their density decreases, and as a result, vertical movements inside the crust are activated above the melting zone. The mountains are growing up due to the increase in the volume and the growth of the mountains "roots" down through the melting of basalts. Thus conditions for catastrophic earthquakes are being formed.

4 Conclusions

Geothermal modelling allows us to conclude that temperature regime has the prevailing influence on the development of seismic processes in continental conditions. One of the crucial aspects is determining the high-temperature regions with excess temperatures of $100 \div 250$ °C above the solidus, which can lead to partial melting of rocks.

The accumulation of thermoelastic stresses in the Earth's crust can be considered as one of the criteria for seismic activity observed in the area of the Northern Tien-Shan. The distribution of hypocenters of the average energy class earthquakes is controlled by the area of excess temperatures of 230 °C and the isobar of thermal stresses of 0.35 GPa.

The trigger effect of heat flow on the distribution of the critical level of deformations in the Earth's crust determines seismic processes in focal zones. This information is important for understanding the physical mechanisms and parameters of seismically active medium.

References

1. Pasquale, V., Verdoya, M., Chiozzi, P.: Geothermics: Heat Flow in the Lithosphere, University of Genova. Springer (2014)
2. Jaeger, C., Cook, N.G.W., Zimmerman, R.W.: Fundamentals of Rock Mechanics. 4th edn (2007)
3. Burov, E.: Thermo-mechanical models for coupled lithosphere-surface processes: applications to continental convergence and mountain building processes. In: New Frontiers in Integrated Solid Earth Sciences. Springer-Business Media (2010)
4. Zang, A., Stephansson, O.: Stress Field of the Earth's Crust. Springer Science-Business Media (2010)
5. Gordienko, V.V.: Glubinnye protcessy i seismichnost. Geofizicheskii zhurnal **36**(1) (2014). (in Russian)
6. Regenauer, L.K., Weinberg, R.F., Rosenbaumd, G.: The role of elastic stored energy in controlling the long term rheological behaviour of the lithosphere. J. Geodyn. **55**, 6–75 (2012)
7. Afonso, J.A., Ranalli, G., Fernandez, M.: Thermal expansivity and elastic properties of the lithospheric mantle: results from mineral physics of composites. Phys. Earth Plane. Inter. **149**, 279–306 (2005)
8. Nusipov, E.N., Ospanov, A.B., Shatcilov, V.I.: Skorostnye modeli litosfery Vysokoi Azii po sisteme geotraversov. Vestneyk NIATC RK. **2**, 109–121 (2005). (in Russian)

9. Xu, Y., Liu, F., Liu, J., Sun, R.: Seismic Tomography of the Nortwestern Chinese Continent and Deep Tectonics of Orogenic Belts. In: 99 International Symposium on Tianshan Earthquakes, Abstracts, pp. 182–183. Urumqi (1999)

10. Shatcilov, V.I., Saipbekova, A.V.: Profilnaia tomografiia litosfery Tian-Shania po materialam regionalnoi seismologii. Doclady NAN RK **6**, 47–52 (1994). (in Russian)

11. Davies, J.: Global map of solid Earth surface heat flow. Geochem. Geophys. Geosystems https://doi.org/10.1002/ggge.20271 (2013)

12. Gosnold, W., Panda, B.: The Global Heat Flow Database of The International Heat Flow Commission (2011) https://engineering.und.edu/research/global-heat-flow-database/data.html

13. Rybach, L., Bantebarth, G.: Relationships between the petrophysical properties, density, seismic velocity, heat generation and mineralogical constitution. Earth Planet Sci. lett. **57**, 367–376 (1982)

14. Smyslov, A., Moiseenko, U., Chadovich T.: Teplovoy rezhym i radioaktivnost Zemli (1979). (in Russian)

15. Gordienko, V., Zavgorodniaia, O., Iakobi, N.: Teplovoy potok kontinentov (1982). (in Russian)

16. Samarskii, A., Gulin, A.: Chislennye metody (1989). (in Russian)

17. Baiuk, E.I., Tomashevskaia I.O., Dobrynin, V.M. i dr.: Fizicheskie svoistva mineralov i gornykh porod pri vysokikh termodinamicheskikh parametrakh. Spravochnik. red. Volarovich M.P. M. Nedra (1988)

18. Beselov, O.V., Gordienko, V.V., Sokolova, L.S.: O temperature chastichnogo plavleniia porod verkhnei mantii. Geofizicheskii zhurnal. **9**(6), 44–47 (1987). (in Russian)

19. Kurskeev, A.K.: Geotermicheskaia model i sovremennoe koroobrazovanie v Tian-Shanskom segmente. Rezultaty kompleksnykh issledovanii v seismoaktivnykh raionakh Kazakhstana. Alma-Ata. Nauka, 27–40 (1984). (in Russian)

20. Pleuger, J., Podladchikov, Y.Y.: A purely structural restoration of the NFP20-East cross section and potential tectonic overpressure in the Adula nappe (central Alps). Tectonics **33**, 656–685 (2014). (in Russian)

Properties and Type of Latitudinal Dependence of Statistical Distribution of Geomagnetic Field Variations

Andrei Vorobev [ORCID] and Gulnara Vorobeva [ORCID]

Abstract

Understanding the nature of latitudinal dependence of geomagnetic field (GMF) variations is of quite definite interest in tasks, which are related to assessment of geomagnetic activity. Partly it is related to the fact that according to the type of function, approximating the probability density distribution of geomagnetic variation (GMV) values, it is possible to define the physical mechanism which is determined by geomagnetic variations. Therefore, for example, as a result of observing the sum effect of many random and weakly interdependent values, each of which provides a small contribution to the total sum, a normal distribution is formed; in a closed system, the energy of the system components is distributed according to the exponential law or the Laplace law (i.e., double exponential distribution); a random multiplicative set of several parameters leads to log-normal distribution and etc. In such case, analysis of heavy-tailed distributions is a separate task since the variance of the studied values is predominantly determined by rare intense deviations rather than frequent minor deviations in distributions of such type. Although a number of leading research works provide some data regarding the dependence of GMV parameter values on geographic latitude, but nevertheless it remains unclear when neither an analytical (graphical) form has the dependence, nor the manner in which the probability density function values of GMV change at movement, e.g., from the Poles to Equator. Moreover, it is a common practice for the majority of leading research works to deal with only the mean values of amplitude of GMV, which are specific for the latitudinal range. Relying on these values without understanding the general nature of the distribution can lead to

A. Vorobev
Geophysical Center of the Russian Academy of Sciences, 119296 Moscow, Russia

A. Vorobev · G. Vorobeva (✉)
Ufa State Aviation Technical University, 450008 Ufa, Russia
e-mail: geomagnet@list.ru; gulnara.vorobeva@gmail.com

improper conclusions and unauthentic results. Thus, the latitudinal dependence of statistical parameters is studied, the nature of the change of probability density function and distribution law for the northern and eastern components of geomagnetic field vector variations is analysed on the basis of the data obtained from magnetic observatories of the INTREMAGNET network. The observed functional dependencies are approximated, analysed and are illustrated in graphical and analytical form.

1   Introduction

The knowledge, conception and interpretation of the pattern of latitudinal dependence of distribution parameters and statistical characteristics of geomagnetic field (GMF) variation values is of a specific interest in many contemporary tasks of both applied and fundamental nature, which are directly or indirectly related to geomagnetic activity (GMA) assessment.

First of all, it is related to the fact that according to the type of function, which approximates the probability density distribution of geomagnetic variation (GMV) values, it is possible to define the physical mechanism which is determined by geomagnetic variations. Thus, for example, as a result of observing the sum effect of many random, weakly interdependent values, each of which makes a small contribution with respect to the total sum, a normal distribution is formed; in a closed system, the energy of the system components is distributed according to the exponential law or the Laplace law (i.e., double exponential distribution); a random multiplicative set of several parameters leads to a lognormal distribution and etc. In such case, analysis of heavy-tailed distributions is a separate task since the variance of the studied values is predominantly determined by rare intense deviations rather than frequent minor deviations in distributions of this type.

A number of leading research works (e.g., [1–3]) are concerned with some general information regarding GMV parameters dependence on geographic latitude. However, it is still not studied, what the analytical (graphical) form of the dependence is and the manner in which the probability density function of GMV values changes, e.g., from the Poles to the Equator. Moreover, it is a common practice for the majority of scientific works to deal with only the mean values of amplitude of GMV, which are specific for the latitudinal range. Relying on these values without understanding the general nature of the distribution can lead to improper conclusions and unauthentic results.

2 Preliminary Process of Source Data

The minute time series of "definitive" type was used as the data source in the research work [4]. INTERMAGNET magnetic observatories network (i.e., http://www.intermagnet.org/) [5] publishes the minute time series and the time series also represents the variations of the northern (X) and eastern (Y) components of GMF vector.

The research result can be influenced by some third-party factors, such as geomagnetic data source distribution by longitude, effects of seasonal variations [6, 7] including the magnetosphere asymmetry, which is observed due to the change in the angle of inclination of the Earth's rotation axis with respect to the Earth-Sun line. Therefore, for the purpose of minimizing the impact of the factors on the research result, only the source data is used, which is recorded by the observatories located along the $19.1 \pm 1.75°E$ meridian (i.e., ABK, LYC, UPS, HLP, BEL, HRB, THY, GCK, HER, KMH, TSU) in the period of vernal equinox for several years.

The array of values is formed by excluding the data for the day, in the course of which the relative information efficiency [8] of at least one magnetic observatory was less than 99.9% with an average system recovery time of 1 min. The array of values corresponds to the periods of the vernal equinox from 2011 to 2016 for all 11 observatories. Sporadic omissions of values of the INTERMAGNET Magnetic Observatory (IMO) "Grocka", observed on 2014-03-20 at 5:35 and 6:25 UT, were recovered by means of linear interpolation method. In this respect, the calculated value of recovery accuracy does not exceed the allowable value, which is set for the INTERMAGNET observatories [9]. The result is represented by 22 time series (i.e., X- and Y-components for 11 observatories) of 8,640 values (i.e., 6 days $\times$ 1440 min/day $\times$ 1 value/min) in each one of them.

Further, the samples $|\Delta BX|$ and $|\Delta BY|$, representing variations of the corresponding components of the GMF vector with respect to the annual variation and which is represented here by the median value of the daily sample, are formed for each IMO in accordance with the expressions (1) [10]:

$$|\Delta BX_i| = |BX_i - md_{BX}|, |\Delta BY_i| = |BY_i - md_{BY}|, \tag{1}$$

where BX_i and BY_i are values of i measurement of GMF induction of X- of Y-components respectively on a specific observatory for one day (where $i = 1, 2, …,$ 1440); md_{BX} and md_{BY} are median values of X- and Y-component of the induction vector of GMF respectively in the daily sample, which BX_i and BY_i belong to.

Expression in (1) has the provision to use the mean values of the sample instead of the median values. However, due to the reason that the median is more resistant to outliers [11, 12], relying especially on the parameter under the conditions of the task, is more preferable.

3   Research on Latitudinal Dependence of Statistical Parameters and Values of Distribution Parameters

The generalized normal distribution law (2) or more precisely, its right-hand side is proposed in the research work as a function, approximating the normalized histograms of samples $|\Delta BX|$ and $|\Delta BY|$ since according to the expression (1), it refers to absolute values.

It should be noted that for the majority of high-latitude stations, the log-normal distribution (3) is more specific (Figs. 1a, 2a). However, in spite of that, the selection of the generalized normal law is first of all, related with the fact that this type of distribution includes all normal and Laplace distributions, and in extreme cases, at limited intervals of valid straight also includes continuous uniform distributions. As a result, such universality allows to successfully apply the generalized normal law to all the data sets considered here, as well as to conduct a comparative analysis of the results obtained.

The calculation and assessment of Kolmogorov's criterion [13] illustrated that the compliance hypothesis of distribution values $|\Delta BX|$ and $|\Delta BY|$ with the generalized normal law can't be rejected with reasonable probability.

$$\text{PDF}(x) = \frac{\beta}{\gamma(1/\beta)} \exp\left(-|x|^{\beta}\right), \tag{2}$$

where PDF(x) is the probability density function; β is a shape variable: at $\beta = 2$, distribution corresponds to normal law and at $\beta = 1$, corresponds to Laplace distribution law (thus, the distribution tails are heavier than normal laws when $\beta < 2$ and lighter than normal laws when $\beta > 2$).

$$\text{PDF}(x, \sigma) = \frac{1}{x\sigma\sqrt{2\sigma}} \exp\left(-\frac{\log^2(x)}{2\sigma^2}\right), \tag{3}$$

where σ is a shape variable.

Figures 1 and 2 represent empirical probability density distributions (i.e., normalized histogram) and survival functions (4) for the northern and eastern components of GMF, and also approximation functions formed on the basis of generalized normal distribution law (where, the number of intervals of normalized histogram is selected in accordance with the Sturges Rule [12]). The approximation functions are specific for high-latitude (e.g. IMO ABK), mid-latitude (e.g. IMO GCK) and near-equatorial (e.g. IMO TSU) magnetic observatories.

$$\text{SF}(x) = 1 - \text{CF}(x), \tag{4}$$

where SF(x) is survival function; CF(x) is cumulative distribution function.

A further analysis on statistical parameters of probability density distribution demonstrated that the shape variable β for the values of X-component increases in the direction from the Pole to the Equator, whence it follows that the statistical
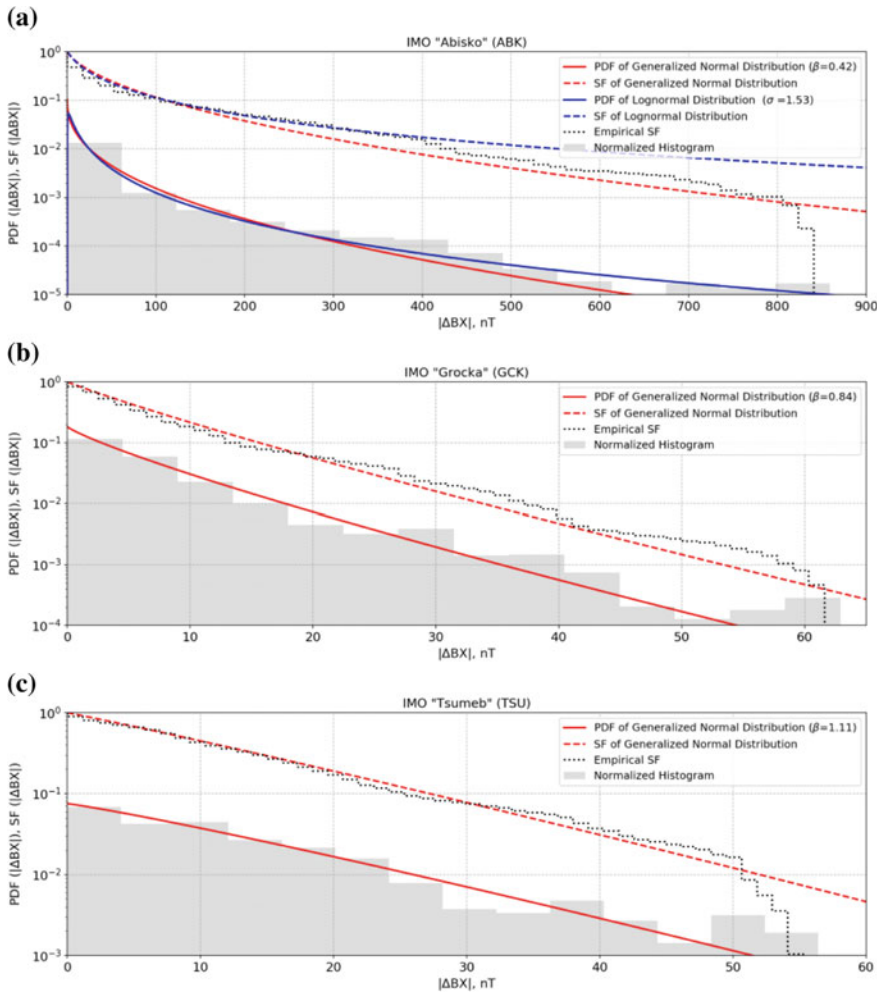
Fig. 1 Distribution of *X*-component values at polar (**a**), mid-latitude (**b**) and equatorial (**c**) IMOs

nature of GMV *X*-component values is transformed from a form that has patterns of Gaussian distribution at the Equator (Fig. 1c) to exponential form and further due to weighting of tails, it transforms to log-normal form on the Poles (Fig. 1a).

Similar studies on the *Y*-component demonstrated that β has a maximum value at middle latitudes (Fig. 2b) and decreases in the direction of both the Poles (Fig. 2a) and the Equator (Fig. 2c). In other words, the distribution form at middle latitudes best corresponds to the normal law and is transformed through the exponential to log-normal form while moving both towards the Poles and the Equator.
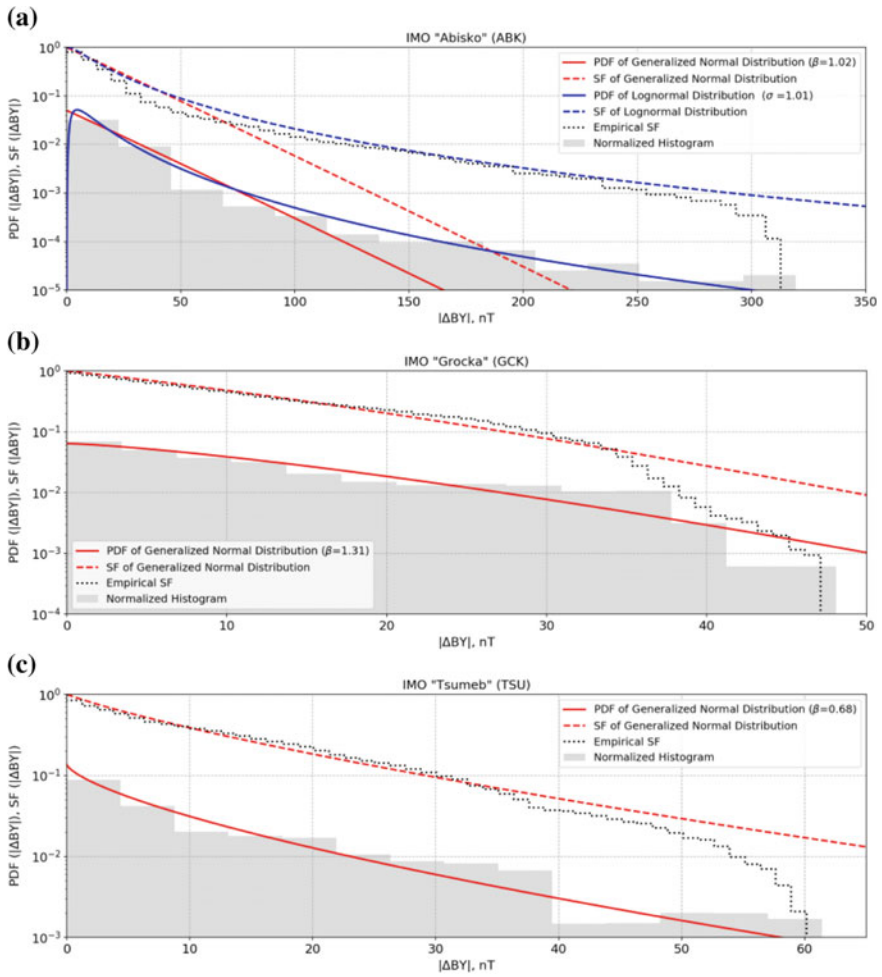
Fig. 2 Distribution of *Y*-component values at polar (**a**), mid-latitude (**b**) and equatorial (**c**) IMOs

Research on the latitudinal dependence of range limit values and the probability of being within the range values is 90% demonstrated that in the case of both northern and eastern components, the minimum of the upper boundary of the range falls on the 45th circle of latitude. The upper range limit of probable values increases monotonously at advancing from mid-latitudes towards the Poles or the Equator.

4 Synthesis and Analysis of Approximating Functions

According to empirical values of distribution parameters, it is permissible to assume that analytically the latitudinal dependence of these parameters on the latitude interval from 45 to 90° can be represented by an exponential function $f(x) = ab^x + c$, and the dependence on latitudes from 0 to 90° can be represented by a parabola, which is defined by a quadratic function.

$$\begin{cases} P_d(\text{Lat}) = a|\text{Lat}|^2 + b|\text{Lat}| + c, \text{ when } 0 < |\text{Lat}| < 45, \\ \quad P_d(\text{Lat}) = ab^{|\text{Lat}|} + c, \text{ when } 45 \leq |\text{Lat}| \leq 90, \end{cases} \tag{5}$$

where P_d is a parameter of distribution (mean value, median value, standard deviation i.e., root-mean-square deviation or upper limit of probable values range); Lat is geographical latitude, in degrees; a, b and c are coefficients.

The values of coefficients a, b, and c for expressions (5) are presented in Table 1. The values are obtained as a result of solving the least-squares problem by means of Levenberg-Marquardt algorithm [14]. The result of latitudinal dependence approximation of the main parameters of GMV X- and Y-components distribution is illustrated in Fig. 3.

According to the data from Table 1, it is possible to provide a qualitative assessment of latitudinal dependence of the studied parameters (Table 2).

Table 1 Coefficients of approximating functions

Coef.	Param.							
	$|\Delta BX|$				$|\Delta BY|$			
	mn	md	std	max	mn	md	std	max
$0 < |Lat| < 45°$								
a	1.56e+3	−1.69e-3	4.29e-3	7.88e-3	−1.85e-3	−8.37e-4	−2.74e-3	−1.47e-2
b	−3.09e-1	−8.59e-2	−4.19e-1	−1.044	1.38e-1	1.59e-1	9.31e-2	6.83e-1
c	1.73e+1	1.14e+1	1.78e+1	5.18e+1	9.913	3.709	1.21e+1	3.3e+1
$45 \leq |Lat| \leq 90°$								
a	3.27e-8	1.13e-6	6.44e-7	1.93e-8	1.01e-7	3.88e-8	7.09e-8	5.0e-9
b	1.358	1.267	1.314	1.352	1.302	1.314	1.320	1.392
c	6.994	4.527	6.641	20.941	12.674	9.567	10.795	34.64

Note mn—mean; md—median; std—standard deviation; max—upper bound of the range of probable values

(a)

(b)

(c)

(d)
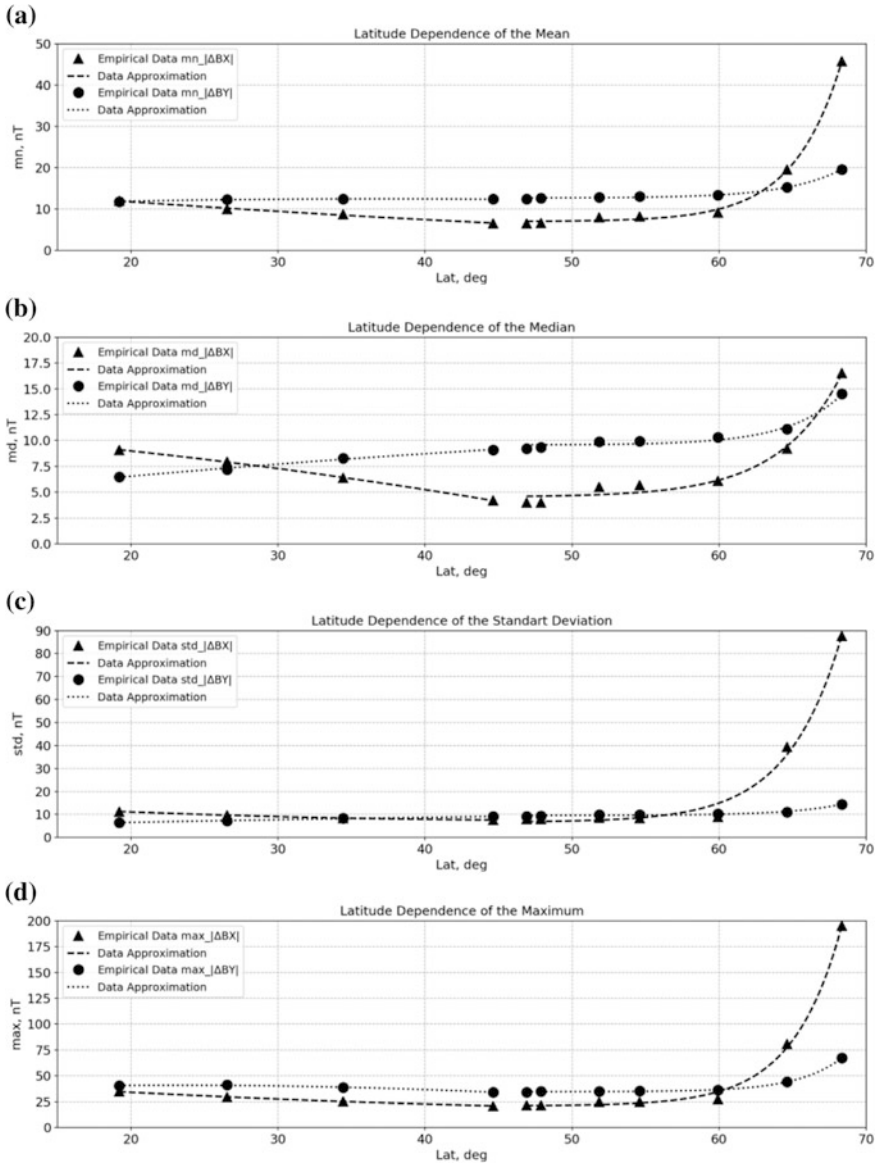
Fig. 3 Latitudinal dependence of *X*- and *Y*-components distribution parameters

Table 2 Latitudinal distribution of parameters of distribution of GMF X and Y-components

Domain	Param.			
	mn (Lat)	md (Lat)	std (Lat)	max (Lat)
The north component of the magnetic field vector (X)				
$0 < |Lat| < 45$	Type 1	Type 2	Type 1	Type 1
$45 \leq |Lat| \leq 90$	Type 3	Type 3	Type 3	Type 3
The east component of the magnetic field vector (Y)				
$0 < |Lat| < 45$	Type 4	Type 4	Type 4	Type 4
$45 \leq |Lat| \leq 90$	Type 3	Type 3	Type 3	Type 3

Note Type 1: Decreases as $f(x) = ax^2 + bx + c$; Type 2: Decreases as $f(x) = -ax^2 + bx + c$
Type 3: Increases as $f(x) = ab^x + c$; Type 4: Increases as $f(x) = -ax^2 + bx + c$

5 Conclusion

The statistical distribution of GMV northern component values is transformed from a form, having patterns of Gaussian distribution at the Equator, to exponential form and further due to weighting of the tails, it transforms into a log-normal form at the Poles. At the same time, the form of GMF eastern component distribution at middle latitudes shows the best correlation with the normal law and transforms through the exponential to log-normal when moving both towards the Poles and the Equator (Figs. 1 and 2).

It follows from the above-stated that all factors provide a comparable contribution to GMV X-component formation on middle latitudes. However, at approaching the Poles and in the case of Y-component approaching both to the Poles and the Equator, contribution of some dominant factors, such as ring current at the Equator and substorm in polar regions, becomes defining factors. The latitudinal dependence of distribution parameters for GMV northern and eastern components on the interval of latitudes from 45 to 90° is well approximated by an exponential function $f(x) = ab^x + c$ and on latitudes from 0 to 90° is well approximated by a parabola, defined by a quadratic function.

Thus, based on the latitudinal dependence characteristics, it is possible to conclude that the intensity of GMF vector X-component variations decreases at advancing towards middle latitudes and reaches a minimum at the 45th circle of latitude, while the minimum intensity of GMF vector Y-component variations are observed at the Equator. Maximum values of the distribution parameters for both the northern and eastern components of GMF vector variations are observed in the polar regions of the planet. In other words, a probability of extremely large values of GMV X-component occurrence is always minimal at the Equator and the Y-component occurrence is always minimal at the 45th circle. The obtained observation results can be useful at estimating geomagnetic activity indices and the calculation methodology of the indices depend on geographical coordinates, e.g., K-index.

References

1. Vorobev, A.V., Pilipenko, V.A., Sakharov, Ya.A., Selivanov, V.N.: Statistical relationships between variations of the geomagnetic field, auroral electrojet, and geomagnetically induced currents. Solar-Terr. Phys. **5**(1), 35–42 (2019). (in Russian)
2. Zabolotnaya, N.A.: Geomagnetic Activity Indices. LKI Publishing House, Moscow (2007). (in Russian)
3. Yanovsky, B.M.: Terrestrial Magnetism. Publishing House of the Leningrad State University, Leningrad (1978). (in Russian)
4. Intermagnet technical reference manual. http://intermagnet.org/publications/intermag_4-6.pdf. Accessed 05 Feb 2019
5. Love, J.: An international network of magnetic observatories. EOS Trans. Am. Geophys. Union **94**(42), 373–384 (2013)
6. Nusinov, A.A., Rudneva, N.M., Ginzburg, E.A., et al.: Seasonal variations in statistical distributions of geomagnetic activity indices. Geomag. Aeron. **55**(4), 493–498 (2015)
7. Russel, C.T., McPherron, R.L.: Semiannual variation of geomagnetic activity. J. Geophys. Res. **78**(1), 92 (1973)
8. Vorobev, A.V., Vorobeva, G.R.: Approach to assessment of the relative informational efficiency of intermagnet magnetic observatories. Geomag. Aeron. **58**(5), 625–628 (2018)
9. Magnetic Observatories (IMOs). http://intermagnet.org/imos/magobs-eng.php. Accessed 05 Feb 2019
10. Newell, P.T., Gjerloev, J.W.: Evaluation of SuperMAG auroral electrojet indices as indicators of substorms and auroral power. Magnetos. Phys. **116**, A12 (2011)
11. Hinkle, D.E., Wiersma, W., Jurs, S.G.: Applied Statistics for the Behavioral Sciences. Houghton Mifflin, Boston (2003)
12. Sturges, H.: The choice of a class-interval. J. Am. Statist. Assoc. **21**, 65–66 (1926)
13. Bolshev, L.N., Smirnov, N.V.: Tables of Mathematical Statistics. Nauka, Moscow (1983). (in Russian)
14. Gill, P.E., Murray, W., Wright, M.H.: Practical Optimization, Academic Press Inc. (London) Limited (1981)

Destruction of Artificial Sandstone Samples in a State Close to Unstable with Electrical Pulses

Vladimir Zeigarnik, Vadim Kliuchkin and Vladimir Okunev

Abstract An attempt was made to bring the sample that was in a near-critical state (that is, in the state close to losing mechanical stability) to failure by electrical current. An analysis was performed of the cracking process peculiarities. The results of experiments with three identical samples of artificial sandstone saturated with 1% of NaCl solution are described. The experiments were conducted on a lever press under step-wise loading conditions: DC pulses were applied during the quasi-stationary loading stage. The electrical impact resulted in an increase of acoustic emission in samples at loads close to failure indicating intensification of the process of fracturing with its transition to the stage of avalanche-like cracking. According to experimental data, the amount of energy supplied to the sample within each loading cycle by electrical action, on the one hand, and due to mechanical compression, on the other hand, and the one that can be spent on cracking are close in magnitude; so the suggestion on the trigger role of electrical impact becomes questionable.

Keywords

Laboratory simulation · Trigger effect · Electrical impact · Avalanche-like fracture

V. Zeigarnik (✉) · V. Kliuchkin · V. Okunev
Joint Institute for High Temperatures, RAS, Izhorskaya Str. 13, Bd.2, 125412 Moscow, Russia
e-mail: zeigarnik@ihed.ras.ru

207

1 Introduction

The results obtained at the Garm and the Bishkek test-sites, indicating the effect of high-power current pulses on the seismic regime [1–4], initiated a series of laboratory experiments in which the effect of electrical pulses of various shapes on the temporal and spatial dynamics of acoustic emission was investigated. In this case, the task was in trying to find the nature of the influence of sufficiently weak electromagnetic fields and currents on the processes of fracturing and destruction of samples loaded closely to the threshold of losing the mechanical stability.

Of course, physical modeling cannot fully reproduce mechanical, structural, and thermodynamic conditions typical to real earthquake focal zones and the ambient medium. Nevertheless, many experimental facts indicate the similarity of fracture patterns at different scales and for tested samples under different conditions including primarily the development of destruction, characterized by certain stages, grouping (clustering) of cracks at different scale levels, reactions to changes of fluid content, etc. In [5], the process of earthquake preparation is also considered as the process of emerging cracks with their transition to a next hierarchical level in size and with gradual approach to their critical concentration. So the formation of the main fault takes place and the earthquake focus emerges in the volume of the geological medium. The work [6] develops this approach.

Since the 90th years of the last century, quite a lot of work was done to study the processes of crack formation in rock samples and their destruction. Here, the works performed at the Ioffe Physikotechnical Institute [7, 8] and the US Geological Survey [9, 10] are undoubtedly highlighted. As for the works concerning the influence of the electric current pulses or the effect of electromagnetic field on behavior of solid samples, there are only few works available. Most of them are made at the O. Yu. Schmidt Institute of Physics of the Earth, the Joint Institute for High Temperatures and the Research Station in Bishkek [11–18]. In these works, the main attention is paid to the influence of the electrical impact on the intensity and the spatial distribution of acoustic emission. In these works, the acoustic emission was considered as a manifestation of the process of cracking in the sample. One of the main conclusions made here is that with increasing load, when its value approaches the elastic strain limit, the influence of electrical impact becomes more pronounced. As we have already noted [18], above works lacked the reproducibility of result, some of the measured parameters showed a non-monotonic behavior, and those facts did not find a satisfactory explanation in the authors' comments. And the most important point: the authors did not develop a generally accepted physical model describing the processes accompanying the electrical impact.

In the present work, we make an attempt to bring the sample staying in a near-critical state (that is, in a state close to instability) to failure by applying an electrical impact, and we present the analysis of the cracking process dynamics.

2   Experimental Results

The experiments were carried out on the facility described in detail in [18]. It is a lever press providing uniaxial compression of the sample making it possible to realize both a continuous loading mode (the loading rate could vary from 0.23 to 2.5 kN/min) and a step-wise loading mode with a quasi-static loading stage between steps. Within this stage, at the first interval, after the completion of the load increase a pause of at least 30 min was maintained, then electrical impact was exposed for at least 30 min and then a pause of approximately the same duration came on again. In fact, the duration of each of the three sub-steps was determined by how close the acoustic emission activity had reached the background level. We call the stage of load increase combined with the stage of quasi-static load a cycle. The indicated algorithm makes it possible to study the behavior of the sample at a fixed level of compression strength in dynamics. If the duration of the quasi-static load stage was significantly greater than the above specified values, the loading force somewhat decreased (by 0.3–0.5 kN at a load level of 100–150 kN) due to relaxation processes in the sample. In this cases manual adjusting of the loading stress was performed to keep the conditions of its invariability more accurately. During the experiment the following parameters were continuously recorded: the applied compression force, the longitudinal and the transverse displacements, the acoustic signals in three points of the sample at different heights, the temperature on the surface of the sample and the current through it. The electric current was fed to the upper and the lower end faces of the sample through the plane electrodes, the size of which exceeded a little the area of those end faces. The frequency range of the acoustic emission sensors was 20–200 kHz. The sensitivity of vertical and horizontal displacement sensors was about 2 μ. The functional block diagram of the generator and the measuring equipment as well as their characteristics are given in [18] in more details.

In our experiments, electrical impact was applied by using the direct current whose magnitude within a pulse gradually decreased due to both electrochemical processes on the electrodes and smooth increase in sample temperature. Such pulse shape was chosen on the base of preliminary experiments which showed that there is no unambiguous connection between the type of electrical pulse and the sample response to it [18]. The results of these preliminary tests are also described in that work in detail. In this situation it seemed reasonable to carry out experiments with the simplest electrical pulse type: the quasi-direct current.

For the experiments we took three artificial sandstone samples with dimensions of $80 \times 95 \times 195$ mm and effective porosity of 12–12.5%. The samples were saturated with 1% of NaCl solution. This provided a sufficient level of sample conductivity: the full conductance of a sample was $(0.3–0.7) \cdot 10^{-3}$ Sm. The analysis of the sample structure and their material composition was performed at a high-resolution electron microscope NovaNanoSem 650. It showed a rather wide range of particle size distribution: 0.1–4.5 mm, SiO_2, CaO, and $CaCO_3$ being the predominant chemical compounds.

In [18], the results of experiments performed with two samples (No. 6 and No. 7) similar to the ones described above are presented. The main results of those experiments are as follows:

1) For most cycles (9 cycles of 10 for the sample No. 6 and 9 cycles of 12 for the sample No. 7), there is a pronounced effect of the electrical impact. It consists in an increase of both the acoustic pulses quantity and their intensity in the energy terms. These experiments also showed that for other cycles, after the beginning of electrical impact, even at high compression strength level ($k_p > 0.8$, where k_p is the ratio of the current strength to the destruction one), the response of the sample in the form of acoustic emission was somewhat controversial. The number of acoustic pulses per time unit either decreased or remained without significant changes.

2) The temperature on the sample surface began to rise almost immediately after switching on the current and continued to rise, although insignificantly, long enough after the current was turned off. Total temperature rise during an electrical impact as a rule slightly exceeded 2 °C.

3) The observed deviations of the strength curves, as well as the transverse and longitudinal displacements of the sample from the monotonous drift are suggested to be associated with the temperature rise. And although these deviations were only several hundred newtons for compression force (at the very value of about 165 kN) and about of the first microns for the sizes of samples, these features were clearly noticeable against the general drift.

The combination of factors observed allowed us [18] to suggest that the noticeable Joule heat release leads to a thermal expansion and respective restructuring of pore and crack structure transformation and to their size variation: its pattern is quite complicated since we are dealing with a heterogeneous energy-saturated medium.

With account to these results, the authors designed experiments to investigate the destruction of the samples in the critical state directly under the electrical pulse with approximately the same parameters as in the experiments described above with the samples No. 6 and No. 7. Thus, three experiments were conducted with the samples Nos.13, 15 and 16. It was found from the totality of the previous experiments that the samples are destroyed under the compression force of 170–190 kN, corresponding to the destruction stress of $22.4 \div 25$ MPa. On this base, the load on the sample was increased stepwise until a noticeably pronounced acoustic emission appeared, not only at the load increase stage, but immediately after it, at the beginning of the quasi-stationary loading stage. Then, only after the intensity of the acoustic emission had reached the background level, the electric current was applied. The sample response to the electrical impact gave a reason to make conclusion about how close the sample state is to the critical one and what duration of the electrical exposure should be chosen. Since the damage stress itself in different samples differed markedly and the behavior of the samples when approaching the critical state varied noticeably, it was impossible to create a formalized criterion to

choose the moment of electrical impact beginning basing on the parameters of acoustic emission or on the behavior of such measured quantities as the axial stress, the vertical displacement or others. Truth to be told that the decision on this matter was taken on an intuitive level, with account for the experience gained in preliminary experiments. Note that the current in different samples differed more than 2 times, even at the same applied voltage of 200 V. Most likely it was due to the different conditions at the electrode-sample contact surface and irregular desiccation of the samples during their pre-treatment and the experiment run.

The Table 1 presents data on the conditions of the experiments performed.

Figure 1 shows the results of experiments on the sample No. 13. It should be noted that a sufficiently intense acoustic emission began to manifest itself when the load of 150 kN was reached. Prior to this, the acoustic emission intensity both within the stages of the load increase and electrical impact was insignificant. At the load of 150 kN within sufficiently long time period (about 30 min) before electric exposure, the acoustic emission was also insignificant. About 6 min after switching on the current a noticeable acoustic emission appeared, its level remaining more or less stable both during the rest of the electric exposure interval and about 25 min after the current was turned off. Then, for 35 min, the acoustic emission gradually increased until this process became avalanche-like. An additional short electric pulse at this stage did not affect the blow up nature of the process and the sample destruction. The avalanche-like fracturing process was accompanied by a markedly more pronounced shortening of the sample and a growth of its transverse displacement: the most likely evidence on sample transition to the post-peak strength (overcritical) state.

Figure 2 presents the results of experiments for the sample No. 15. Before reaching the load of 120 kN, the sample No. 15 also showed a very weak acoustic activity. As the load further increased, the activity both at the load increase stage and at the electric impact stage became more pronounced. This pattern with some variations remained intact up to the load of 162 kN. Then the acoustic emission intensity decreased and recovered only when the load changed from 167 to 174 kN and during the subsequent electrical impact. However, the next step from 174 to 181 kN did not cause any significant emission. Only the subsequent load step up to 191 kN resulted in a pronounced acoustic emission at a level slightly exceeding the background one for the whole quasi-stationary strength stage (for about 30 min.). Then, with the beginning of the electrical impact, the acoustic emission noticeably intensified, actively continued after the completion of the electric exposure, and

Table 1 Data on the conditions of the experiments

Example number	Number of load increase cycles	Load value interval, kN	Load increase rate, kN/min,	Electrical current, mA
13	9	80–150	2.5	30
15	11	100–191	0.27	70
16	3	140–171	0.23	60
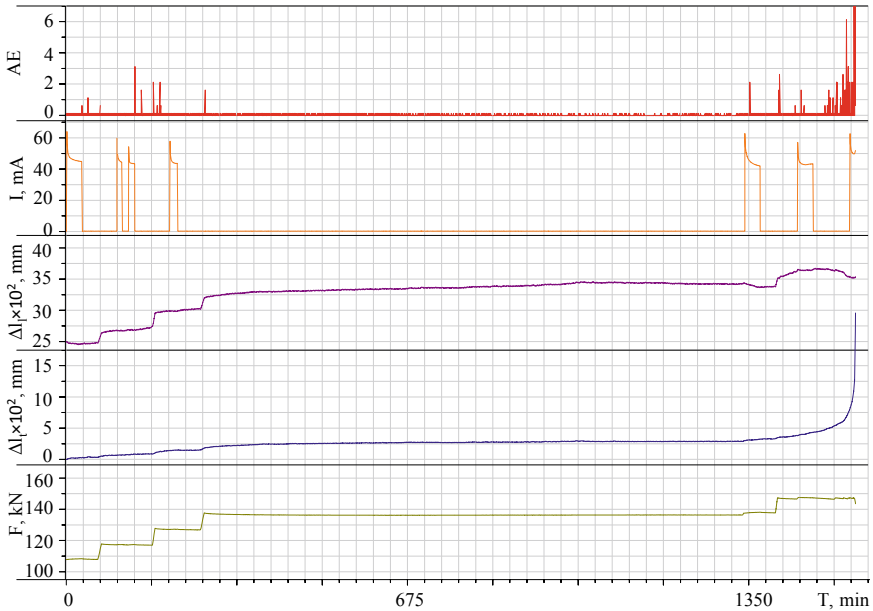
Fig. 1 Experimental results for the sample No. 13. The presented fragment is the final portion of the experimental data after 2676.45 min from the very beginning of the run. This time is pointed as zero time on the graph. Acoustic emission intensity (AE) is given in arbitrary units; I is the electric current; ΔL_l and ΔL_t are the longitudinal and transverse shifts (i.e. size changes) correspondingly. The same comments are applicable to Figs. 2 and 3

almost 20 min after its completion the process transformed into the avalanche-like stage with subsequent damage of the sample. At this point the sample most likely went over to the post-peak strength state, since at almost constant (until the transition to the avalanche-like stage) compression strength, the longitudinal size of the sample continued to decrease at the same rate as during the load stage, while the transverse displacement grew even at a higher rate than at the load stage.

Figure 3 shows the results of experiments for the sample No 16. The acoustic emission pattern of the sample No. 16 was somewhat similar to that of the sample No. 13: up to the load of 161.4 kN the acoustic emission intensity was expressed weakly both at the load stages and at the electrical impact stages. Within the interval between the completion of the load increase and the beginning of the electrical impact, the acoustic emission intensity differed a little from the background level. With the current supply, the acoustic emission became uniform for quite a long time (about 180 min). And only after that, spontaneously, without any additional external impact, the sample transited into the stage of avalanche-like fracturing with subsequent destruction. Here, the transition to the post-peak strength state occurred about at the middle of the electrical impact stage, but very gradually, not as sharply as for the sample No. 15.

Fig. 2 Experimental results for the sample No. 15. The presented fragment is the final portion of the experimental data after 3932.43 min from the very beginning of the run
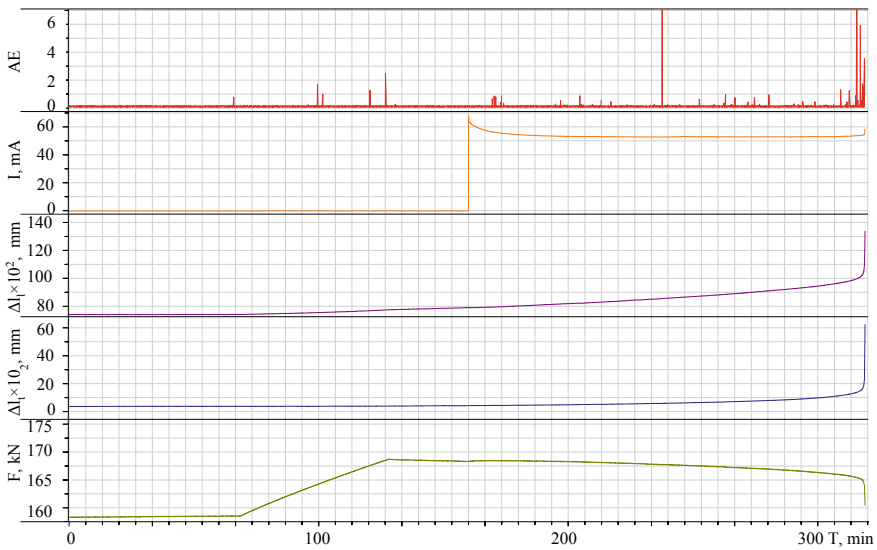

Fig. 3 Experimental results for the sample No. 16. The presented fragment is the final portion of the experimental data after 2873.95 min from the very beginning of the run

3 Discussion

First of all, note that despite certain pronounced common patterns many details in behaviors of samples differed markedly, particularly in the cycles more distant from the rupture occurrence ($k_p < 0.9$). This has been also observed in our previous experiments [18]. This is not surprising. Indeed, the tested samples, as is shown by the electron microscopy analysis, have an irregular structure with significant variations in sizes of the constituent agglomerates and grains. Thus, the conditions of the crack nucleation and interaction will be somewhat different. As a result, even the destructive loads of the samples were also essentially different (from 150 to 190 kN). In this regard, it is appropriate to refer again to [5]: its authors state that the development of the destruction process should be considered as an accumulation of cracks and their transition to the next hierarchical size level with a gradual approach to the critical crack concentration and to the formation of the main fault. Really, such seeing agrees with avalanche-like fracturing concept proposed in [19]. In the process of crack structure development and their interaction, the stresses acting in the sample vary and, accordingly, local strains redistribute.

It is also connected with the peculiarities of the material composition of the investigated samples. The behavioral features of heterogeneous materials in the post-peak stress state were showed in detail in [20]. In Figs. 1–3, one can see that the effect of electrical current results in sample heating. Usually the temperature increased by up to 2.5° as a result of a single electrical impact session, and only in the last cycle of the experiment on the sample No. 16 this value was as high as 6.5°. These values are consistent with estimates of expected heating based on energy balance. Note that the rise in the sample surface temperature did not stop with the electrical impact termination, which is a matter of course for the situation with a volumetric heat release. After the completion of electrical exposure the temperature decay rate is much less than the temperature rise rate after switching on the current due to the low heat transfer coefficient from the sample surface. It appears to be one of the possible reasons for the observed residual effect of an electric pulse, so often mentioned in a number of works cited above, including our work [18]. The deviations from the monotonous course of the curves for the compression strength, the vertical and the transverse displacements correlate with the temperature change. Although these deviations are rather small, they can be measured quite reliably.

Thus, the data obtained on the acoustic emission increasing for the samples at the loads close to destruction, as a result of electrical impact, indicate an intensification of the cracking process with its transition to the avalanche-like fracturing stage. This confirms the conclusion made in [16]: this phenomenon is caused by the pressure increase in the pores and the cracks due to the thermal effect.

If we analyze the effect of electrical impact in terms of energy input, it is necessary to compare the energy input due to the mechanical compression of the sample with the one due to Joule heat release caused by electric current. Despite a seemingly small current (30–70 mA), the typical energy input from a single exposure lies in the range of $(1–2) \cdot 10^4$ J. It was as high as $5 \cdot 10^4$ J in the last electrical impact session for the

sample No. 16 due to its nearly two hours duration. At the same time, the energy supplied to the sample by a single load increase is, on average, of about 10 J, while the total compression energy, supplied to the sample by the time of its damage, is of about 10^2 J. This means that even with account for the electromechanical conversion coefficient which was experimentally found to equal to $(2–3) \cdot 10^{-3}$ [21], the energies delivered to the sample within each loading cycle via either mechanical compression or electrical impact and the one that might be spent on cracking are close in magnitude. However, this ratio of electrical and mechanical energy supplied to the sample is sufficient to cause the avalanche-like fracturing only in the state close to the metastable one. At lower k_p, despite the fact that this energy ratio almost does not change, the transition to the avalanche-like fracturing does not occur. So it turns out that the mechanism of destruction of the sample by an electric current in experiments described above is more energy-consuming than that due to the mechanical compression, and therefore there is no reason to speak about the triggering role of the electrical impact. It may be quite possible that under other conditions, including sliding along a fault, this energy relation will be alternative and the conclusion made above should not be extended to such situation.

4   Conclusions

The results of electrical impact on three identical artificial sandstone samples under conditions close to the loss of mechanical stability (destruction) show that such an impact itself at constant mechanical strength might lead to the initiation of the avalanche-like fracturing process resulting in sample destruction. In the process of electrical impact, the sample transits to the post-peak strength (overcritical) state and loses mechanical stability. The results correlate with the conclusion made in [16]: this phenomenon is caused by the pressure increase in pores and cracks due to the thermal effect. According to the estimates, the energies applied to the sample in each loading cycle due to either mechanical compression or electrical impact and the one that might be spent on cracking are close in magnitude; this fact makes the assumption about the trigger mechanism of electrical impact questionable under conditions of the experiment described.

References

1. Tarasov, N.: Crustal seismicity variation under electric action. Dokl. Earth Sci. **353A**(3), 445–448 (1997)
2. Tarasov, N., Tarasova, N., Avagimov, A., Zeigarnik, V.: The effect of electromagnetic pulses on seismicity in the Bishkek geodynamic test ground. Russ. Geol. Geophys. **42**(10), 1558–1566 (2001)

3. Bogomolov, L., Sychev, V., Alad'ev, A., Avagimov, A., Bragin, V., Zeigarnik, V., Zakupin, A., Sycheva, N.: On manifestation of electrically induced seismisity on the Bishkek test ground (forward to active electromagnetic monitoring). In: II International Workshop on Active Geophysical Monitoring of the Earth Lithosphere, p. 112. Sib. Branch RAS Publisher, Novosibirsk (2005) (in Russian)

4. Matcharashvili, T., Chelidze, T., Zhukova, T.: Influence of high energy electromagnetic pulses on the dynamics of the seismic process around Bishkek test area (Central Asia). Pure Appl. Geophys. **172**(7), 961–975 (2014). https://doi.org/10.1007/s00024-014-0860-5

5. Kuksenko, V., Tomilin, N., Damaskinskaya, E., Lockner, D.: A two-stage model of fracture of rocks. Pure Appl. Geophys. **146**(2), 253–263 (1996)

6. Sobolev, G., Tyupkin, Yu.: Analysis of energy release process during main rupture formation in laboratory studies of rock fracture and before strong earthquakes. Izv. Phys. Earth **36**(2), 138–149 (2000)

7. Damaskinskaya, E., Tomilin, N.: Simulation modeling of the flux of destruction acts in geterogenuous materials. Solid State Phys. **33**(1), 278–285 (1991). (in Russian)

8. Damaskinskaya, E., Panteleev, I., Kadomtsev, A., Naimark, O.: Effect of the state of internal boundaries on granite fracture nature under quasi-static compression. Phys. Solid State **59**(5), 944–954 (2017). https://doi.org/10.21883/ftt.2017.05.44381.364

9. Thompson, B., Young, R., Lockner, D.: Fracture in Westerly granite under AE feedback and constant strain rate loading: nucleation, quisi-static propagation, and the transition to unstable fracture propagation. Pure Appl. Geophys. **163**, 995–1019 (2006). https://doi.org/10.1007/s00024-006-0054-x

10. Thompson, B., Young, R., Lockner, D.: Premonitory acoustic emission and stick-slip in natural and smooth-faulted Westerly granite. J. Geophys. Res. **114**, BO2205 (2009). https://doi.org/10.1029/2008jb005753

11. Sobolev, G., Ponomarev, A., Avagimov, A., Zeigarnik, V.: Initiating acoustic emission with electric actionIn, pp. 277–281. XXVII General Assembly of the European Seismological Commission, Lisbon University, Lisbon (2000)

12. Smirnov, V., Ponomarev, A.: Seismic regime relaxation properties from in situ and laboratory data. Izv. Phys. Earth **40**(10), 807–816 (2004)

13. Avagimov, A., Zeigarnik, V., Klyuchkin, V.: On the structure of acoustic emission of model samples in response to an external energy action. Izv. Phys. Earth **42**(10), 824–829 (2006). https://doi.org/10.1134/S1069351306100065

14. Borovskii, B., Bogomolov, L., Zakupin, A., Mubassarova, V.: On the stimulation of acoustic emission in rock samples by electromagnetic fields. Izv. Phys. Earth **47**(10), 926–936 (2011). https://doi.org/10.1134/S1069351311100028

15. Mubassarova, V., Bogomolov, L., Zakupin, A., Panteleev, I., Naimark, O.: Strain localization peculiarities and distribution of acoustic emission sources in rock samples tested by uniaxial compression and exposed to electric pulses. Geodyn. Tectonophys. **5**(4), 919–938 (2014). https://doi.org/10.5800/GT-2014-5-4-0163

16. Lapshin, V., Patonin, A., Ponomarev, A., Stroganova, S., Potanina, M., Smirnov, V.: Initiation of acoustic emission in fluid-saturated sandstone samples. Dokl. Phys. Earth **469**(1), 705–709 (2016). https://doi.org/10.1134/S1028334X16070047

17. Bogomolov, L., Mubassarova, V., Zakupin, A., Panteleev, I., Sychev, V.: To the question of the mechanisms of influence of electromagnetic fields on the micro-nonelasticity of deformed geomaterials and geo-media In: VII International. Symposium on Modern Problems of Geodynamics and Geoecology of Intercontinental Orogens, p. 220, Bishkek (2017) (in Russian)

18. Zeigarnik, V., Kliuchkin, V., Okunev, V.: Influence of an electrical current on acoustic response of stressed artificial sandstone samples. Uspekhi Prikl. Phys. **6**(3), 199–208 (2018). (in Russian)

19. Myachkin, V., Kostrov, B., Sobolev, G., Shamina, O.: Basis of earthquake source physics and earthquake precursors. In: Earthquake Source Physics, pp. 6–29. Nauka, Moscow (1976). (in Russian)
20. Goldin, S.: Dilatancy, repacking, and earthquakes. Izv. Phys. Earth **40**(10), 37–54 (2004)
21. Avagimov, A., Zeigarnik, V., Okunev, V.: Dynamics of energy exchange in model samples subjected to elastic and electromagnetic impact. Izv. Phys. Earth **47**(10), 918–925 (2011). https://doi.org/10.1134/s1069351311100016

Part II
Fluidodynamic Processes and Seismicity

Apparent Permeability Loss Over Time in Long-Term Measurements Using the Steady-State Method

Nikolay Baryshnikov⬤, Evgeniy Zenchenko⬤
and Sergey Turuntaev⬤

Abstract

The paper analyzes possible causes of time trends observed under constant net confining stresses in long-term measurements of low-permeable sample permeabilities. Experimental study of flow in a limestone core sample was conducted. During the experiment with duration of 40 days, the fluid pumping was carried out in several stages with different constant values of the confining pressure and the pore pressure gradient. As a result, the permeability of the sample decreased by 10 times. It was shown that such significant decrease in the permeability in time can be caused by clogging of the sample pore space. The additional experiment with sequential pumping of single-phase gas and liquid through the sample showed that the gas contained in the flow of liquid can act as a dispersed phase that clogs pores. The estimations show that even very low particle concentrations at large time periods lead to significant decrease in the permeability. The possibility of clogging of core sample pore space must be considered when conducting long-term experiments on study of the permeability by the steady-state method.

N. Baryshnikov (✉) · E. Zenchenko · S. Turuntaev
Sadovsky Institute of Geospheres Dynamics RAS, 119334 Moscow, Russia
e-mail: nabarysh@gmail.com

1   Introduction

In the last few years, tight oil production has increased significantly. This is why the study of the filtration properties of ultralow-permeable rocks has acquired particular significance. Such rocks can be subject to considerable compaction during development [1], which manifests itself in the permeability loss in time at constant net confining stress. In the laboratory, the compaction (or creep) of porous rock samples under constant stress conditions was observed by many researchers for experiment durations ranging from several hours [2, 3] to several weeks [4–6]. Conducting such lengthy flow experiments accompanies by a number of challenges. First of all, it is necessary to exclude factors not related to the deformation of the sample. In the paper, we attempted to analyze possible causes of time trends observed under constant net confining stresses in long-term measurements of low-permeable sample permeabilities.

2   Procedure

For experimental study of flow in cylindrical core samples, we use the laboratory setup, which diagram is shown in Fig. 1. The filtration properties of the sample are studied with the steady-state method in a flow of liquid or gas. The tested sample in a rubber sleeve is placed in the core holder and required confining pressure in its shell is created. Fluid flows under a constant pore pressure gradient. When studying the liquid flow, the pressure gradient is created by means of a hydroaccumulator. In case of gas flow, the pressure is supplied directly from a gas tank. Mass flow rate of liquids is measured using a laboratory balance by continuously weighing the fluid accumulated at the outlet of the core holder. To measure the gas flow rate, a thermal mass flow meter is used, which is also installed downstream the core holder. Apparent permeability of the sample is calculated according to the Darcy law in stationary flow based on the flow rate of the liquid or gas at a given pore pressure gradient.

When conducting long-lasting measurements, we face often the fact that the permeability of the sample decreases significantly over time. On the figure (Fig. 2a), it is shown how the permeability of the limestone sample taken from the aquifer well from a depth of 27 m decreases over time. Before the start of the experiment, the sample was placed in the core holder, evacuated and saturated. During the experiment, the fluid (distilled water) pumping was carried out in several stages with different constant values of the confining pressure P_c and the pore pressure P_{pore} gradient. The average duration of each stage was several hours. Between the stages, the sample was leaved under the constant external and pore pressures. The maximum confining pressure for the entire series was 150 Bar, the minimum—7 Bar. The average pore pressure throughout the experiment varied in the range of 0.5–1.5 Bar.
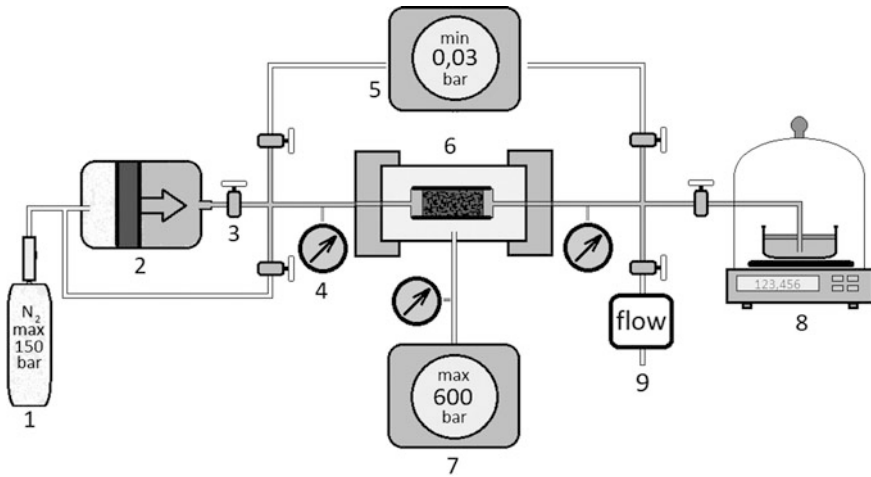
Fig. 1 Experimental setup. 1—buffer tank; 2—hydroaccumulator; 3—valves; 4—pressure sensors; 5—vacuum pump; 6—core holder; 7—high pressure pump; 8—balance with tank for accumulated fluid; 9—thermal mass flow meter

On the plot (Fig. 2a), each point corresponds to the average permeability measured during each stage of the experiment. It can be seen that the permeability of the sample dropped significantly with time, the main drop occurred at constant effective pressure $P_{eff} = P_c - P_{pore}$.

Figure 3 shows how the sample permeability changed during the injection of fluid at each stage of the experiment. After the initial drop, the permeability continues to decrease almost linearly with increase of volume of fluid pumped through the sample.

3 Colmatage of the Sample Pore Space

Such behavior of permeability, as on Fig. 3, is typical for process of the porous medium colmatage (or clogging) by particles contained in flow. At present, a number of experimental work [7] showed that the change in permeability k of a porous medium filtering thin suspension with a constant concentration of particles can be described by the equation

$$k = k_0 \frac{1}{1 + \beta\sigma}, \tag{1}$$

where k_0—initial permeability of the porous medium, σ—is the fraction of the porous medium volume occupied by the picked-up particles, β—is an empirical coefficient. Based on this equation and mass balance equations of particles and
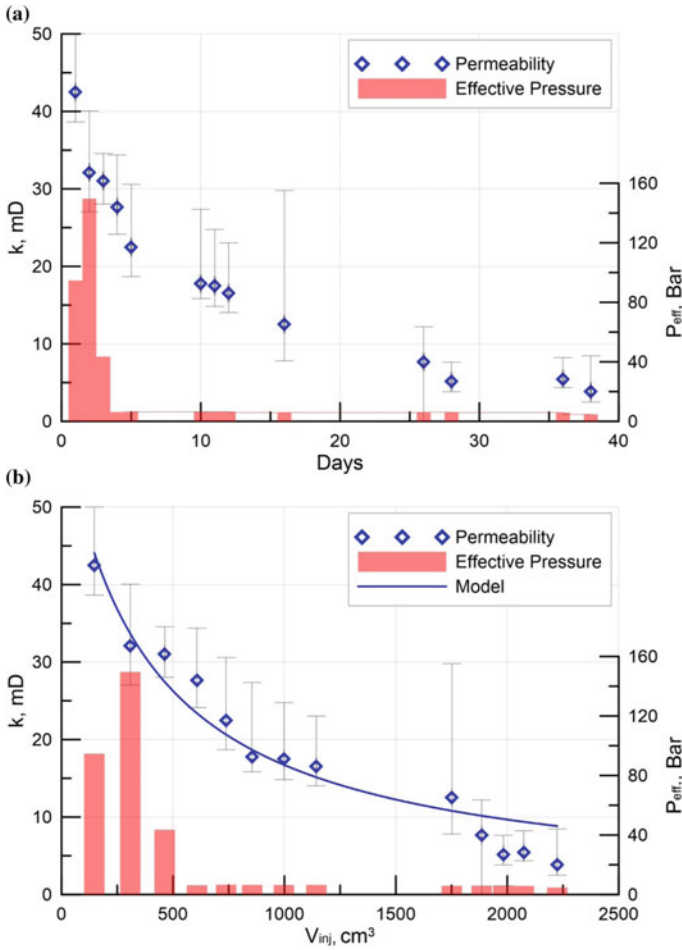
Fig. 2 Effective pressure and permeability of the sample during the entire experiment: **a** with time; **b** with the total volume of the liquid pumped. The solid line in figure **b** is plotted using Eq. (2)

liquid, and in case when the volume fraction of the particles in the flow is small, as well as the change in of the medium porosity due to the particle sedimentations, we can obtain the model dependence of the medium permeability on volume of pumped liquid [8]:

$$k = k_0 \frac{1}{1 + \beta C_0 V_{inj}(t)/V_{pore}} \approx 1 - \beta C_0 V_{inj}(t)/V_{pore}, \qquad (2)$$
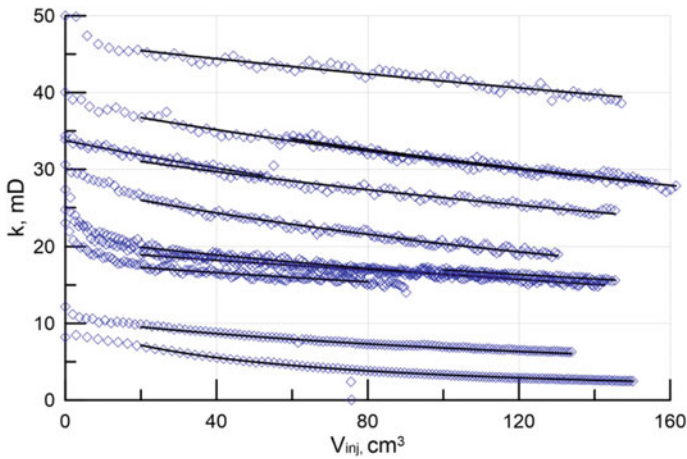
Fig. 3 Permeability of the sample during each stage of the experiment with total volume of liquid pumped. The solid lines are plotted using Eq. (2)

where $V_{inj}(t)$—volume of fluid pumped through the sample, V_{pore}—the sample pore volume, C_0—initial volume fraction of the suspension particles. This equation describes well the dependence of permeability on the pumped fluid volume both during the whole series of experiments (Fig. 2b), and at each stage (Fig. 3). Coefficients βC_0 obtained by approximating experimental data for each stage of the experiment are shown on the plot Fig. 4. The red line on the plot indicates the value of the corresponding coefficient obtained by approximating the data on permeability throughout the entire experiment.
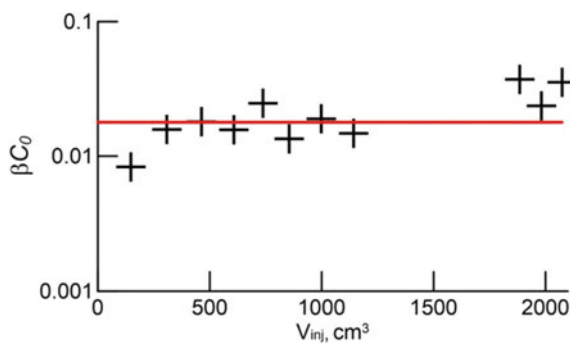
Fig. 4 βC_0 value for each stage of the experiment with the total volume of liquid pumped. The line shows the value of the coefficient for the entire experiment

4 Discussion

For now, we were not able to establish the nature of particles that clog the pore space of the sample in the experiment. According to [8, 9], the value of the coefficient β may be of the order of 10^3. This allows us to estimate the volume fraction of clogging particles in the flow as $C_0 \approx 10^{-5}$, which is quite small. The characteristic pore size of the sample with the permeability of 50 millidarcies and porosity of 0.25 can be estimated at 0.5 μm. At the same time, the characteristic size of particles that could penetrate into such pores should be at least 5 times smaller—about 0.1 μm [10]. Filtering the fluid from particles of such size requires use of special filtering techniques. We assume that the pore space of the sample was clogged by gas dissolved in water or contained in it in the form of bubbles. Partially, this is indicated by significant effect of a slight increase in the pore pressure on permeability of the sample (Fig. 5). Due to significant compressibility of gas bubbles unblocking of the pore channels occurs with increasing of pore pressure, which leads to the increase in the permeability being measured. To test this hypothesis, we carried out the additional experiment. Permeability of a ceramic sample under the same condition was consequently investigated in single-phase gas (nitrogen) and liquid (water) flows. For each case the fluid was pumped for about four hours. The confining pressure in both cases was 20 Bar, the average pore pressure was maintained at the value of less than 0.5 Bar. Before pumping the liquid, the sample was evacuated and saturated directly in the core holder without changing compression. The result of the experiment is shown in figure (Fig. 6). When pumping gas, the sample permeability remained almost constant most of the time. The permeability increase at the beginning can be associated with the evaporation of the residual liquid contained in the sample before the experiment start.
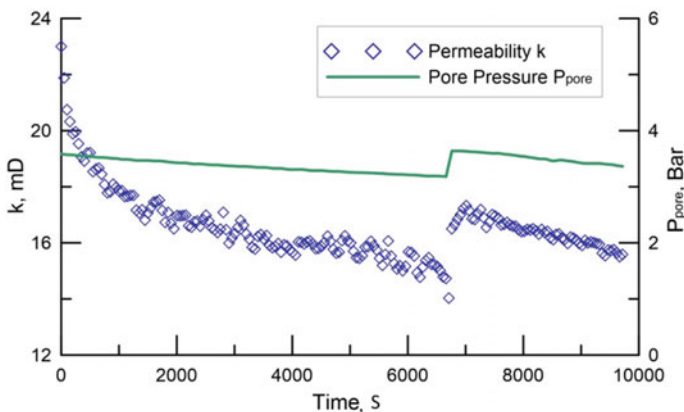
Fig. 5 The change in the permeability of the sample with a slight increase in the average pore pressure

Fig. 6 Permeability with
time when pumping gas
(curve 1) and water (curve 2)
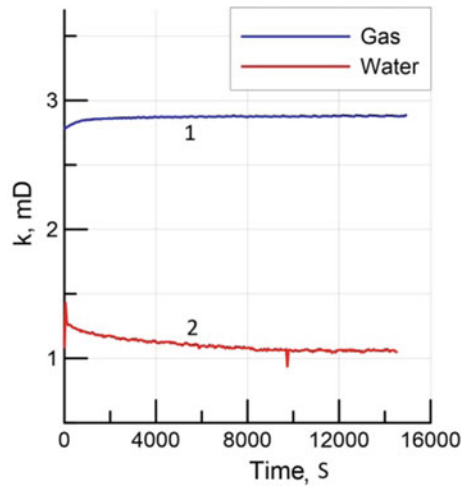
The permeability measured when pumping the liquid is much lower and decreases significantly with time. We believe that this may be evidence in favor of the version of the gas effect on measured sample permeability.

5 Conclusions

Decrease in measured permeability in time during the long-term filtration experiments can be caused by clogging of the pore space of the samples under study. The dispersed phase may be represented by the gas contained in the flow of the fluid pumped. The experiments and the estimations show that even very low particle concentrations at large time periods lead to significant decrease in the permeability. Reasons for the gas appearance in the injected fluid may be different. In our experiments, the gas could penetrate in minimal quantities through piston's sealing rings of the hydroaccumulator. It is also possible for the gas to penetrate with the liquid when the accumulator is refilled. The possibility of clogging of core sample pore space must be considered when conducting long-term experiments on study of the permeability by the steady-state method.

References

1. Kwon, O., Kronenberg, A.K., Gangi, A.F., Johnson, B.: Permeability of Wilcox shale and its effective pressure law. J. Geophys. Res. **106**(B9), 19339–19353 (2001). https://doi.org/10.1029/2001JB000273

2. Sone, H., Zoback, M.D.: Visco-plastic properties of shale gas reservoir rocks. American Rock Mechanics Association (2011)

3. Almasoodi, M.M., Abousleiman, Y.N., Hoang, S.K.: Viscoelastic Creep of Eagle Ford Shale: Investigating Fluid-Shale Interaction. Society of Petroleum Engineers (2014). https://doi.org/10.2118/171569-ms

4. Chhatre, S.S., Braun, E.M., Sinha, S., Determan, M.D., Passey, Q.R., Zirkle, T.E., … Kudva, R.A.: Steady-State Stress-Dependent Permeability Measurements of Tight Oil-Bearing Rocks. Society of Petrophysicists and Well-Log Analysts (2015)

5. Van Noort, R., Yarushina, V.: Water, CO2 and Argon permeabilities of intact and fractured shale cores under stress. Rock Mech. Rock Eng. **52**, 299 (2019). https://doi.org/10.1007/s00603-018-1609-8

6. Baryshnikov, N.A., Zenchenko, E.V., Turuntaev, S.B.: The change in the permeability of an ultra-low permeable limestone sample under the Influence of confining pressure during the loading-unloading cycle. In: Karev, V., Klimov, D., Pokazeev, K. (eds.) Physical and Mathematical Modeling of Earth and Environment Processes (2018). Springer Proceedings in Earth and Environmental Sciences. Springer, Cham (2019), https://doi.org/10.1007/978-3-030-11533-3_25

7. Herzig, J.P., Leclerc, D.M., Le, P.: Flow of Suspensions through porous media—application to deep filtration. Goff Ind. Eng. Chem. **62**(5), 8–35 (1970). https://doi.org/10.1021/ie50725a003

8. Mikhailov, D.N., Ryzhikov, N.I., Shako, V.V.: Experimental investigation of transport and accumulation of solid particle and clay suspensions in rock samples. Fluid Dyn. **50**(5), 691–704 (2015). https://doi.org/10.1134/s0015462815050117

9. Wong, R.C.K., Mettananda, D.C.A.: Permeability reduction in Qishn sandstone specimens due to Particle suspension injection. Transp. Porous Med. **81**, 105 (2010). https://doi.org/10.1007/s11242-009-9387-0

10. Abrams, A.: Mud design to minimize rock impairment due to particle invasion. J. Pet. Technol. **29**(May), 586–592 (1977)

Experimental Study of the Effect of Plastic Rock Properties on Hydraulic Fracturing

Igor Faskheev and Maria Trimonova

Abstract

Hydraulic fracturing is one of the most common technologies for stimulating oil and gas reservoirs. Due to the high cost and technical complexity of this operation, laboratory and numerical experiments on hydraulic fracturing using modern computational packages are becoming increasingly important. Laboratory experiments on hydraulic fracturing on model samples, carried out at the Sadovsky Institute of Geospheres Dynamics of the Russian Academy of Sciences (SIDG RAS), showed the impossibility of classic elastic models to accurately predict the fracture pressure values. At the same time, a considerable number of publications devoted both to deformation and the theory of cracks in rocks in general, and hydraulic fracturing technology, in particular, show that to accurately consider the complex properties of deformation and fracturing of rocks, it is necessary to take into account not only elastic, but also plastic properties. This article is devoted to the study of the possible influence of the plastic properties of the medium when conducting experiments on the modeling of hydraulic fracturing using the Abaqus Student Edition software package.

I. Faskheev (✉) · M. Trimonova
Sadovsky Institute of Geospheres Dynamics RAS, 119334 Moscow, Russia
e-mail: fiomsu@mail.ru

229

1   Introduction

The theory of the crack propagations in rocks is of great practical importance in modeling the processes occurring in reservoirs during oil production.

The most common enhancement technology used for the oil extraction from rock is hydraulic fracturing. The method allows to create a fracture with high conductivity in the reservoir to increase the flow of the produced hydrocarbon (oil or gas). The technology includes injection of a special fracturing fluid into the well at pressures higher than the fracturing pressure. To maintain the fracture in the open state, a special proppant is used to fill the fracture.

With the development of computer technology, the numerical simulation of the development of cracks based on the equations of continuum mechanics has become one of the main tools for predicting the behavior of rocks. The theory of hydraulic fracturing within the framework of the elastic deformation regime is well studied and described in scientific publications, but the complexity of the technology and design of real layers often requires more complex models that take into account the inelastic properties of rocks. The presented article is devoted to the study of the possible influence of inelastic (plastic) properties of the medium on the simulation of hydraulic fracturing.

Most of works on rock deformations under various stresses imply that the rock behaves like an elastic medium. The propagation of hydraulic fracture in elastic media is a well-studied problem, to which a large number of scientific works are devoted. However, in many real situations, the inelastic behavior of the rock has a significant effect on the basic parameters of the problem (strain, pressure, displacement). In contrast to the elastic mode of deformation, the elastic-plastic regime in fracturing conditions is incomparably less studied.

The article [1] discusses the influence of plasticity on the hydraulic fracture. The fluid flow in the fracture is modeled according to the theory of lubrication. Rock deformation is modeled based on the Coulomb-More plastic model. The crack propagation criterion is based on the softening behavior of the rocks. The related nonlinear problem is solved using a combined finite difference-finite elemental scheme. The results show that the plasticity (which occurs near the tip of the propagating fracture) significantly affects the values characterizing the rock fracturing. These studies are developed in articles [2, 3], in which the model was expanded to take into account the poro-elastic-plastic clutch in the process of hydraulic fracturing.

Classical models of plasticity were originally developed to describe the inelastic behavior of metals, which, generally speaking, have a more homogeneous and simple structure than the rocks with their complex internal geometry, pores and cracks. Therefore, for a more accurate description of the deformation properties of the rocks, the special plasticity models are required, taking into account the structural features of the rocks.

In [4] a Drucker-Prager model is proposed, that generalizes the Coulomb-Mohr model using the associated Mises-Schleicher form of the flow law, which includes the angle of internal friction and the coefficient taking into account the cohesion of the material.

In [5, 6] a variant of this model is proposed with an unassociated law of flow. This model allows to take a more accurate account of the deformation properties of rocks. The advantages of the non-associated law are detailed in the work of Vermeer and De Borst [7].

In [8], numerical experiments were carried out on the formation of cracks in geomaterials for various loading options. Cracks near the inclusion and inside the medium are considered. The calculations were carried out using the Prandtl-Reuss, Drucker-Prager and Nikolayevsky models. In the paper [9], the development of localized deformation zone and cracks are simulated numerically for elastic brittle-plastic materials for various types of loads. For numerical modeling, Nikolaevsky model and the new method of partitioning grid nodes are used. The results obtained are in good agreement with experimental data on the behavior of the geological medium under various stresses.

A numerical simulation of hydraulic fracturing in the porous rocks exhibiting plastic deformations was performed in [10]. Plastic deformation of porous rock is described by a non-associated plastic model based on the Drucker-Prager criteria. Plastic deformation in combination with the fluid pressure change was described by the theory of lubrication. The extended finite element method is used to model the crack propagation. The propagation criterion for fracturing is based on the J-integral. The proposed numerical model is compared to numerical and analytical results. This paper shows the effect of the friction angle and plastic deformation on the process of hydraulic fracturing.

Thus, the above works show the importance and relevance of taking into account the inelastic properties of the material in numerical and analytical models of hydraulic fracturing. The present article explores the laboratory experiment on hydraulic fracturing. Special attention is paid here to the dependence of the pressure on time in the well in which the hydraulic fracturing was carried out. In real conditions of the oil production, this curve is one of the main sources of the information about the reservoir. In particular, the authors were interested in the fracturing pressure, as an indicator of the influence of plastic properties of rocks on the propagation of the hydraulic fracture.

2 Laboratory Work

Given the high cost and technological complexity of the hydraulic fracturing in oil and gas reservoirs, the laboratory experiments play an important role in mathematical (analytical and numerical) modeling.

Several years ago a series of experiments on hydraulic fracturing on artificial samples was conducted at the Sadovsky Institute of Geospheres Dynamics (SIDG RAS) [11, 12].

The main objectives of this work were: the development of a general methodology for conducting such experiments, determining the similarity criterion between a laboratory setup and a real reservoir under conditions of fracture development, and comparing data for model material and rock based on this criterion. In the experiments, the special attention was paid to the study of the effect of the pore pressure and stress anisotropy on the fracture propagation direction.

Taking into account the obtained similarity criteria, gypsum with the addition of cement was chosen as the sample material. For this material, its strength and filtration properties were measured.

Figure 1 shows a photo of a fracturing unit with a prepared unsaturated sample. The samples are disk-shaped with a diameter of 43 cm and a height of 7 cm.

The laboratory setup allows:

1. to set the gradients of the reservoir pore pressure using holes in the bottom cover of the setup;
2. to maintain three-dimensional stress conditions using side and vertical chambers into which a liquid or gas is pumped under pressure;
3. to conduct the hydraulic fracturing under conditions of a constant fluid pressure or a constant flow rate;
4. to measure the pore pressure throughout the experiment using sensors mounted in the lower cover of the setup.

Fig. 1 Photo of a laboratory setup with a prepared saturated sample
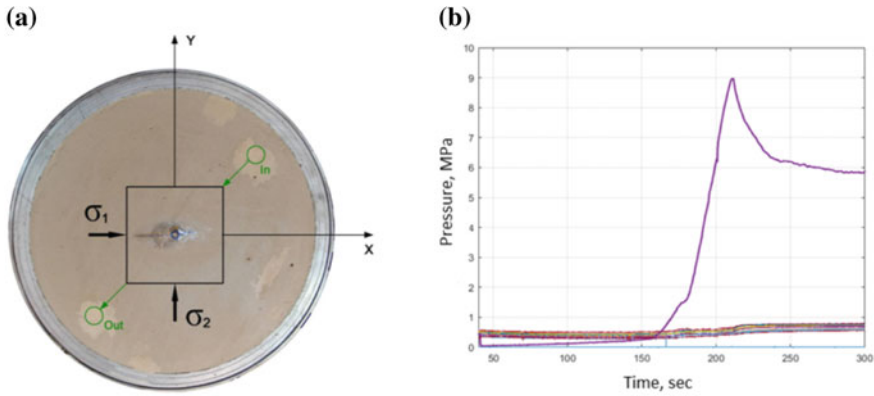
Fig. 2 **a** View of hydraulic fracture in experiment; **b** The dependence of the pressure in the central well on the time of the experiment

Figure 2a shows a sample with a fracture, obtained in one of the laboratory experiments on hydraulic fracturing. The graph (see Fig. 2b) shows a typical curve of the pressure dependence in the central well on the time of the experiment. Such a characteristic form of the curve was inherent in most experiments; in particular, this curve refers to the experiment in Fig. 2a. The authors of the experimental work have attracted attention to the fact, that the values of the fracturing pressure in the experiments significantly exceed the expected values.

That is, if we take the solution of the classical Kirsch problem for the stress concentration around a circular hole [13], for which biaxial compression is used as the boundary conditions (two perpendicular main stresses S_H, S_h, $S_H > S_h$) at infinitely distant boundaries and pressure on the hole P_{mud} (in this case, the medium is considered to be poroelastic), saturated with pressure P_{por} [14], the expression for the breakdown pressure will have the following form:

$$P_{mud} = 3\sigma_h - \sigma_H + P_{por} + UTS \tag{1}$$

$$\sigma_H = S_H - P_{por} \tag{2}$$

$$\sigma_h = S_h - P_{por} \tag{3}$$

According to the conditions of the considered experiment:

$$S_H = 1MPa, \quad S_h = 0.55MPa, \quad P_{por} = 0.5MPa, \quad UTS = 0.8MPa \tag{4}$$

Fracturing pressure must be equal to $P_{mud} = 0.95MPa$. According to the experimental results, the breakdown pressure was $P_{mud}^{exp} = 9MPa$, which is an order of magnitude higher than the pressure calculated theoretically.

This difference in the fracturing pressures, obtained experimentally and analytically (according to the elastic model), led us to study the possible influence of the inelastic behavior of the sample material on its strength properties.

3   Results

To solve the problems of rock deformations, it is necessary to describe their behavior during loading. Depending on the method of loading and the material properties, the deformation beyond the elastic limit is accompanied by various effects. In this mode of deformation, it is extremely important to separate the properties during shearing and stretching. While during stretching the fracture, as a rule, is brittle, the shear deformations are more complex, due to significant volumetric changes, and are highly dependent on the pressure. With increasing pressure, the rocks usually behave like elastoplastic bodies and collapse in a viscous manner with the development of inelastic deformations. The formation of large cracks is usually preceded by dilatancy, i.e. accumulation of microfractures with an increase in the effective volume.

As noted above, the mode of elastic deformation does not allow to take into account all the features of the development of processes occurring in the rocks during hydraulic fracturing. Experiments conducted in the Sadovsky Institute of Geospheres Dynamics (IDG RAS) showed the inability of standard elastic models to adequately predict the distribution of the fracture pressure.

To study the effect of plasticity on the main characteristics of the hydraulic fracturing, the present paper uses the educational version of Abaqus Student Edition software from Dassault Systems, which is designed to solve traditional problems of finite element analysis. In this program, a two-dimensional model of an experimental sample was created, which has a disk shape with a central hole (see Fig. 3a). The dimensions of the model and the applied loads corresponded to the experimental conditions.

It turned out that when taking into account the elastic-plastic properties of the material, a zone of plasticity is formed around the central notch (Fig. 3b).

The appearance of the plasticity zone in the near-critical zone suggests that at sufficiently large loads, irreversible deformations accumulate in the body, which can lead to an increased hydraulic fracture pressure, since in real bodies, the deformations beyond the elastic limit are usually accompanied by a displacement along the boundaries of existing and emerging microcracks with the destruction of intergranular contacts and grains.
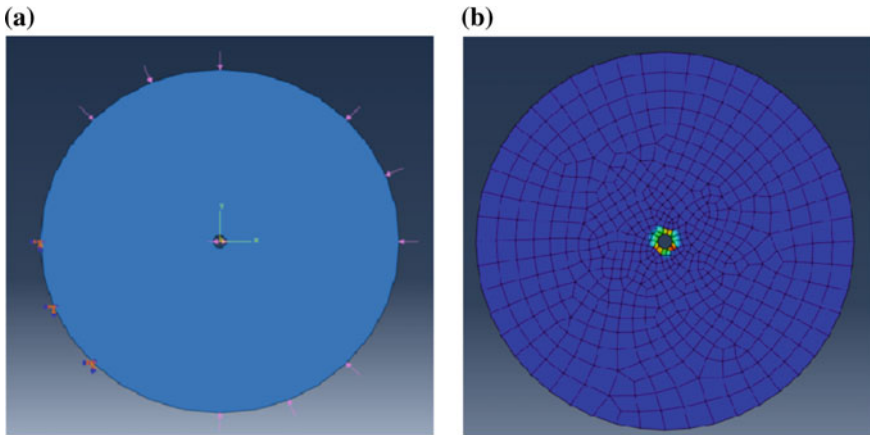
Fig. 3 a Two-dimensional model of an experimental sample in Abaqus; **b** Calculated plasticity zone in the sample

4   Conclusion

As a result of the conducted numerical experiment using the Abaqus Student Edition software package, it was shown that the model behaves plastically in the near-well zone. The geometry of the model and the system of loads were modeled in accordance with real samples, for which the hydraulic fracturing experiments were carried out in IDG RAS, which revealed the drawbacks of elastic models in the description of the fracture pressure values. Plastic behavior leads to a complication of the internal structure of bodies, which in turn can affect the fracture pressure of a hydraulic fracture.

Also, in accordance with the previous publications, the elastoplastic consideration seems to be more accurate for rocks under fracturing conditions.

References

1. Papanastasiou, P.: The influence of plasticity in hydraulic fracturing. Int. J. Fract. **84**, 61–79 (1997)
2. Sarris, E., Papanastasiou, P.: The influence of the cohesive process zone in hydraulic fracturing modelling. Int. J. Fract. **167**(1), 33–45 (2011). https://doi.org/10.1007/s10704-010-9515-4
3. Sarris, E., Papanastasiou, P.: Numerical modeling of fluiddriven fractures in cohesive poroelastoplastic continuum. Int. J. Numer. Anal. Meth. Geomech. **37**, 1822–1846 (2013)
4. Drucker, D.C., Prager, W.: Soil mechanics and plastic analysis or limit design. Q. Appl. Math. **10**(2), 157–165 (1952)

5. Nikolayevsky, V.N.: Mechanical properties of soils and theory of plasticity. Mech. Solid Deform. Bodies **6**, 5–85 (1972). The results of science and technology. Moscow: VINITI, USSR Academy of Sciences
6. Garagash, I.A., Nikolaevskiy, V.N.: Non–associated laws of plastic flow and localization of deformation. Adv. Mech. **12**(1), 131–183 (1989)
7. Vermeer, P.A., De Borst, R.: Non-associated plasticity for soils, concrete and rock. Heron **29** (3), (1984)
8. Stefanov, Y.P.: Deformation localization anf fracture in geomaterials. Numeri. Simul. Phys. Mesomech. **5**(5–6), 67–77 (2002)
9. Stefanov, Y.P.: Numerical investigation of deformation localization and crack formation in elastic brittle-plastic materials. Int. J. Fract. **128**(14), 345–352 (2004)
10. Zeng, Q., Yao, J., Shao, J.: Effect of plastic deformation on hydraulic fracturing with extended element method. Springer-Verlag GmbH Germany, part of Springer Nature (2018). https:// doi.org/10.1007/s11440-018-0748-0
11. Trimonova, M., Baryshnikov, N., et al.: Estimation of the hydraulic fracture propagation rate in the laboratory experiment. In: Karev, V., et al. (eds.) Physical and Mathematical Modeling of Earth and Environment Processes, pp. 259–268. Springer International Publishing, Moscow (2018)
12. Trimonova, M., Baryshnikov, N., Zenchenko, E., Zenchenko, P., Turuntaev, S.: The Study of the Unstable Fracure Propagation in the Injection Well: Numerical and Laboratory Modeling. SPE-187822-MS (2017)
13. Kirsch, E.G.: Die Theorie der Elastizitat und die Bedurfnisse der Festigkeitslehre, Zeitschrift des Verlines Deutscher Ingenieure. Z. Vereines Deutsch. Ing. **42**, 797–807 (1898)
14. Jaeger, J.C., Cook, N.G.W.: Fundamentals of Rock Mechanics, 2nd edn., p. 593. Chapman and Hall, New York (1979)

Features of Fluid-Dynamic Processes in a Seismically Active Region (Case Study of Kamchatka Peninsula, Russia)

Galina Kopylova and Svetlana Boldina

Abstract

The effects of 19 earthquakes ($M_w = 6.8-9.0$, epicentral distances 80–14600 km) are considered on data of long-term precision water level observations in the YuZ-5 well, Kamchatka Peninsula. Four types of water level variations were identified: I—oscillations, II—oscillations with short-term rise, III—short-term rises, IV—long-term decreases. Manifestations of the selected types of water level variations are determined by the intensity of seismic impact corresponding to the ratio of magnitude and earthquake's epicentral distance, the calculated values of specific density of energy in seismic wave, maximum velocity and amplitude-frequency composition of maximum phases in the earthquake record, obtained from broadband seismic waveforms at the nearest station. Dynamic deformation of water-bearing rocks during the passage of seismic waves is accompanied by different hydrogeodynamic processes in the "well—water-bearing rock" system including amplification of water pressure variations in the wellbore, short-term impulses of pressure near the wellbore, water pressure decrease at distances up to hundreds of meters from the well due to increased permeability of water-bearing rocks during intense shocks. Based on water level variations modelling, we show evaluation criteria for possibility of their occurrences. These criteria include the presence of certain frequencies in composition of seismic wave (oscillations), values of amplitudes and relaxation times of water pressure impulses (short-term level rises), presence of geological objects with variable permeability in the vicinity of the well.

G. Kopylova (✉) · S. Boldina
Kamchatka Branch of the Geophysical Survey of the Russian Academy of Sciences, Piip Boulevard 9, 683006 Petropavlovsk-Kamchatsky, Russia
e-mail: gala@emsd.ru

S. Boldina
e-mail: boldina@emsd.ru

1   Introduction

Generation of seismic waves is accompanied by different disruptions of the hydrodynamic regime of ground—and surface waters in the form of changes in discharges, pressure and water levels [12]. During the strongest earthquakes with magnitudes of 8–9, the effects of seismic waves are recorded at distances up to tens of thousands of km from the epicenter, reflecting the planetary scale of the impact of such earthquakes on the hydrodynamic regime of the Earth's hydrosphere. Below, the vibration effects of seismic waves in water level changes in wells are called hydrogeoseismic variations or HGSV. Different types of HGSV reflect aggregative changes of groundwater pressure due to dynamic deformation of water-bearing rocks and attendant filtration processes caused by changes in properties of water-bearing rocks, mainly their permeability [12]. Mechanisms of permeability change under vibration impact of seismic waves may include the development of fracture dilatancy in water-bearing rocks [2, 3, 6], the groundwater degassing [11], the decolmatisation of fracture-pore space [3], the effects of cumulative accumulation of interblock deformations [7].

This paper presents HGSV data of water level changes in the YuZ-5 well, Kamchatka Peninsula, recorded by digital equipment with a measurement interval of 5 min. Observations have been carried out by the Kamchatka Branch of the Geophysical Survey of the Russian Academy of Sciences (KB GS RAS) since 1997 for the purposes of studying hydrogeodynamic precursors of earthquakes and other seismicity effects in the water level changes [9]. In 1997–2017 19 HGSV caused by earthquakes with $M_w = 6.8$–9.1 at epicentral distances $d_e = 80$–14600 km were recorded in the well (Fig. 1, Table 1). These data allow dividing HGSV into four types (I–IV). The dependence of the selected type of HGSV manifestation on intensity of seismic impact and amplitude-frequency composition of maximum phases of the Earth's surface motions are considered in the records of the PET seismic station. For example, the processes of HGSV formation are discussed on the base of modelling.
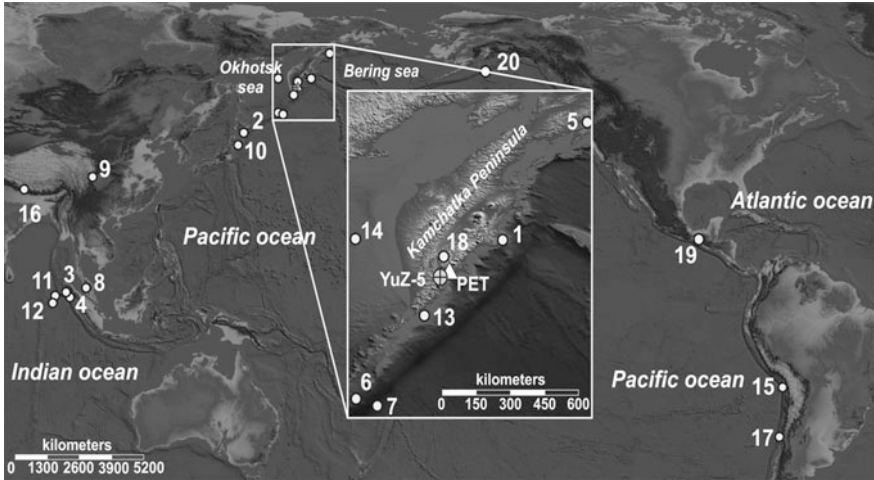
Fig. 1 The location Scheme of earthquake epicenters (Table 1), YuZ-5 well and the PET seismic station (inset)

2 HGSV Types and Their Dependence on the Intensity of Seismic Impact and Amplitude-Frequency Composition of Seismic Waves

Among the registered HGSV (Table 1) we distinguish four types based on the morphological characteristics and duration (Fig. 2): type I—forced and free oscillations within hours; type II—oscillations with short-term rises (minutes to hours); type III—short-term rises (hours); type IV—long-term (1.5–3 months) water level decreases.

To estimate seismic impact intensity in the well area, the values of specific energy density of the seismic wave e, J/m^3 [12] and maximum velocity of ground motion V_m, cm/s were used. The values of V_m were determined as average estimates from (1)–(2) [5]:

$$V_m = 81/(0.9 + d_e/D)^2, \tag{1}$$

$$V_m = 21/(d_e/D)^{1.5}, \tag{2}$$

where D is the maximum linear size of the earthquake source in km, calculated by the equation $lgD = 0.44M_w - 1.289$ [10], where M_w is the earthquake magnitude.

Figure 3 shows the distribution of the selected HGSV types depending on the ratio of M_w, d_e and e (Fig. 3a) and M_w, d_e and V_m (Fig. 3b). One can see there is a change in water level response to seismic waves, depending on the intensity of

Table 1 Earthquake data (https://earthquake.usgs.gov/earthquakes) and characteristics of HGSV according to observations in the YuZ-5 well in 1997–2017. Earthquake numbers correspond to numbers in Fig. 1

No	Date, dd. mm.yy	Time, hh:mm: ss	Coordinates, degrees Lat,°N	Lon,° E	M_W	H, km	Epicentral distance, d_e, km	Area	Character of water level variations	Type
1	05.12.97	11:26:54	54.84	162.04	7.8	33	200	Kamchatka	Decrease with an amplitude of 1 m for 3 months	IV
2	25.09.03	19:50:06	41.81	143.91	8.3	27	1670	Hokkaido Isl.	Oscillations for 1.5 h with an amplitude of $\geq$ 1.7 cm, rise for 1.5 h with an amplitude of 1 cm	II
3	26.12.04	00:58:53	3.30	95.98	9.0	30	8260	Sumatra Isl.	Oscillations for 12 h with an amplitude of 5 cm, rise for 8 h with an amplitude of 2 cm	II
4	28.03.05	16:09:36	2.09	97.11	8.6	30	8290	Sumatra Isl.	Oscillations for 5 h with an amplitude of at least 1 cm	I
5	20.04.06	23:25:02	60.95	167.09	7.6	22	1018	Koryakia	Rise for 6 h with an amplitude of 1.8 cm	III
6	15.11.06	11:14:13	46.59	153.27	8.3	10	812	Simushir Isl.	Rise during the day with an amplitude of 6.5 cm	III
7	13.01.07	04:23:21	46.24	154.52	8.2	10	810	Simushir Isl.	Oscillations for 3.5 h with an amplitude of $\geq$ 3 cm, rise for 3.5 h with an amplitude of 1 cm	II
8	12.09.07	11:10:26	4.44	101.37	8.5	34	7770	Sumatra Isl.	Oscillations within 3.5 h with an amplitude of $\geq$ 0.9 cm	I
9	12.05.08	06:28:00	31.08	103.27	7.9	10	5176	China	Rise for 3 h with an amplitude of 0.9 cm	III
10	11.03.11	05:46:24	38.8	142.37	9.1	29	2000	Japan	Oscillations for 18.5 h with an amplitude of $\geq$ 6.6 cm, rise for 20.5 h with an amplitude of 4 cm	II
11	11.04.12	08:38:38	2.35	93.07	8.7	33	8560	Sumatra Isl.	Oscillations for 24 h with an amplitude of $\geq$ 1.5 cm	I
12	11.04.12	10:43:09	0.77	92.45	8.2	16	8760	Sumatra Isl.	Oscillations for 22 h with an amplitude of $\geq$ 0.7 cm	I
13	28.02.13	14:05:51	50.93	157.34	6.8	45	260	Kamchatka	Decrease with an amplitude of 28 cm for 1.5 months	IV

(continued)

Table 1 (continued)

No	Date, dd. mm.yy	Time, hh:mm: ss	Coordinates, degrees		M_W	H, km	Epicentral distance, d_e, km	Area	Character of water level variations	Type
			Lat, °N	Lon, ° E						
14	24.05.13	05:44:48	54.89	153.22	8.3	611	348	Okhotsk Sea	Rise for 7 days with an amplitude of 9 cm	III
15	01.04.14	23:46:47	−19.61	−70.77	8.2	25	13300	Chile	Oscillations within 4.5 h with an amplitude of ≥ 0.4 cm	I
16	25.04.15	06:11:26	28.15	84.71	7.8	15	6810	Nepal	Oscillations for 4 h with an amplitude of ≥ 0.5 cm	I
17	16.09.15	22:54:33	−31.57	−71.65	8.3	25	14600	Chile	Oscillations within 6.5 h with an amplitude of ≥ 0.5 cm	I
18	30.01.16	03:25:10	54.01	158.51	7.2	180	80	Kamchatka	Decrease with an amplitude of 40 cm for 3 months	IV
19	08.09.17	04:49:21	15.07	93.72	8.1	70	7400	Mexico	Oscillations for 1–2 h with an amplitude of ≥ 2 cm	I

seismic impact on the "well—water-bearing rock" system. With increase in values of e and V_m, the type of HGSV changes from I to IV. Using filtered earthquake records in different frequency ranges, we can estimate maximum velocities of the Earth's surface motion and the corresponding center frequencies. Distribution of HGSV types (I–IV) depending on the amplitude-frequency composition of maximum phases in velocity records of BHN, BHE, BHZ channels at the PET seismic station are shown in Fig. 4. The position of types I–IV along the horizontal axis corresponds to the central frequencies in which the maximum velocities of ground motion were registered. In this case, low-frequency and low-amplitude seismic signals during the passage of surface waves are accompanied by oscillations in the water level (type I HGSV). With amplitude increase, water level short-term rises are superimposed on the oscillations (type II HGSV). Relatively high-frequency seismic signals of the surface waves are accompanied by short-term rises in the water level (type III HGSV). In cases of local strong earthquakes accompanied by tangible shakes with the intensity I_{msk-64} = 5–6 points, the long-term water level decreases are observed (type IV HGSV).

3 Assessment of Criteria for the Occurrence of Various HGSV Types

The study of HGSV types of I–IV was carried out by comparing the observed water level variations with its calculated behavior according to mathematical models [3, 4, 11] taking into account the parameters of water-bearing rocks and geometric dimensions of the well. This approach allows to obtain quantitative criteria for the emergence and development of various hydrogeodynamic processes cased by seismic impact and to construct phenomenological models for the HGSV of various types.

As shown [4], water level oscillations in the well (HGSV of I and II types (Fig. 2) are due to two factors including harmonic changes of water pressure in the "well—water-bearing rock" system and vertical displacements of the Earth's surface. The degree of water level response to seismic waves is determined by geometrical characteristics of the well, the value of transmissibility of water-bearing rocks and depends on the type and period of seismic waves. To describe water level oscillations in the YuZ-5 well, an analytical expression was used for the amplitude ratio between the water level variations x_0 and the head h_0, taking into account the effect of groundwater pressure amplification in the "well—water-bearing rock" system during the passage of surface seismic waves [4]. The example of the earthquake on December 26, 2004, M_w = 9.1 (№ 3, Table 1) describes the conditions for the occurrence of the water level oscillations in the YuZ-5 well, exceeding the vertical displacement of the Earth's surface ($x_0/h_0 > 1$), and it was shown that amplification of water level oscillations in the well occurs during the passage of surface waves with a period of ω = 44.6 s at the value of the parameter $T/r_w^2 \geq 1 \text{ s}^{-1}$ [8]. In this work, the parameters for the YuZ-5 well are presented.
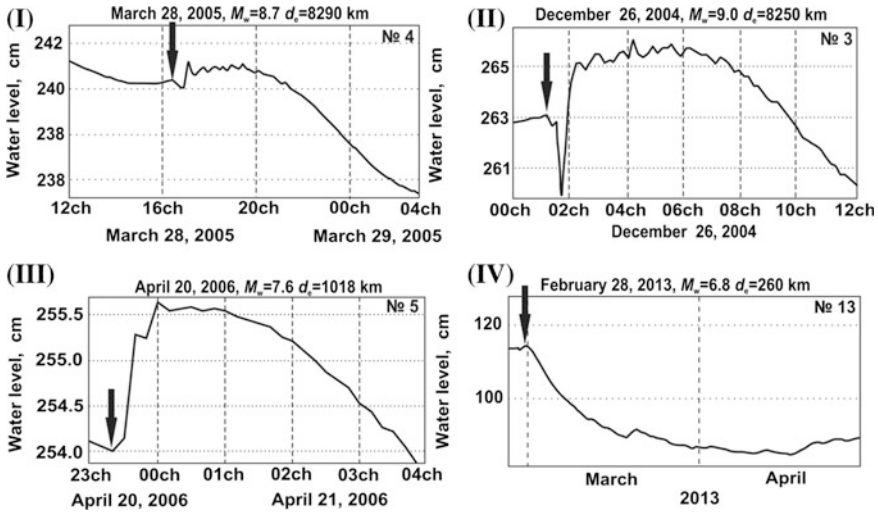
Fig. 2 Types I–IV HGSV in water level changes in the YuZ-5 well. The arrows show moments of earthquakes (numbers correspond to Fig. 1 and Table 1)

They determine the occurrence of water level oscillations: the transmissibility $T = 0.9 \cdot 10^{-4}$ m^2/s, the storage coefficient of water-bearing rocks $S = 18.7 \cdot 10^{-5}$ m^{-1}, the radius of the borehole in the area of its contact with water-bearing rocks $r_w = 0.084$ m, as well as the effective height of the water column in the well $H_e = 494$ m.

Short-term water level rises after the arrival of seismic waves (types II and III HGSV, Fig. 2) reflect the impulse increase of groundwater pressure when a non-linear filtration effect near the well is accompanied by water inflow into the wellbore. As shown in [7] the effects of non-linear filtration can occur in the presence of local inhomogeneities of the filtration properties of water-bearing rocks adjacent to the wellbore. To describe water level rise due to short-term pressure increase, a decaying exponential function was used. It characterizes the process of water flow without specifying spatial distribution of the pressure field causing water inflow into the well [11]: $u(t) = u_0(1 - exp(-t/t_r))$, where u_0 is the maximum amplitude of the groundwater pressure increase, t is the time, t_r is the time of pressure relaxation in the "well—water-bearing rock" system. The calculated results of the water level rise within two hours after arrival of seismic waves from the earthquake on April 20, 2006, $M_w = 7.6$ (№ 5, Table 1) are consistent with the observed data when the increase of water pressure is $u_0 = 1.6$ cm and the time of pressure relaxation is $t_r = 14$ min.

The long-term water level decrease as a result of strong local earthquakes (Type IV HGSV, Fig. 2) can be caused by a decrease of the groundwater pressure due to localized improvement of filtration properties of water-bearing rocks during seismic shocks with an intensity of $I_{msk-64} \geq 5$ points. Such water level decreases are
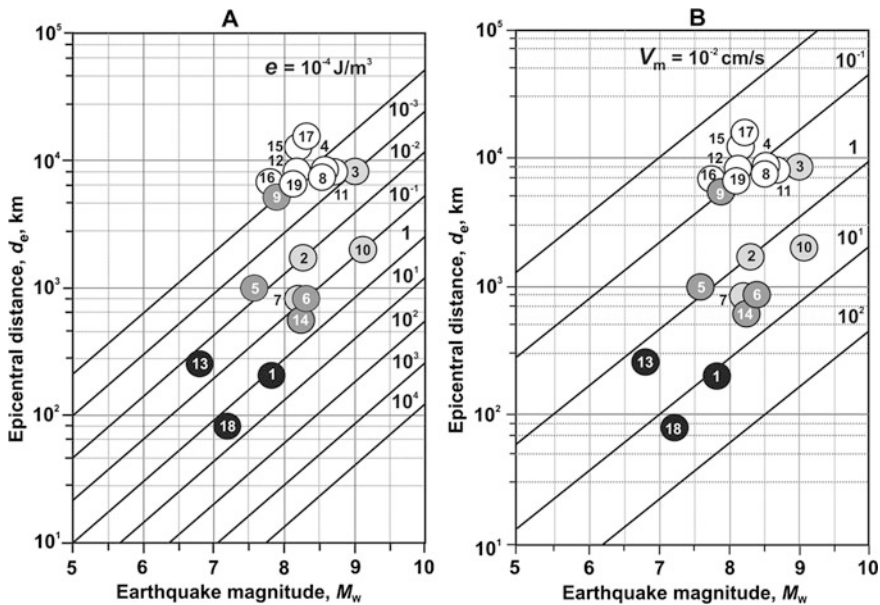
Fig. 3 Distribution of the selected HGSV types (type I— white circles, type II— grey, type III— dark grey, type IV— black) depending on the parameters of earthquakes. M_w and d_e correspond to the seismic energy density in wave e (**a**) and maximum velocity of wave V_m (**b**). Numbers correspond to the numbers of earthquakes in Table 1 and Fig. 1

described by a mathematical model of a distant point source of pressure disturbance in an aquifer [3]: $x = x_0 - \Delta h \cdot erfc(R/\sqrt{4ct})$, where x is water level in the well, x_0 is the initial water level in the well, R is the distance from the well to the source of head drop, c is the hydraulic diffusivity, t is the duration of level decrease, $erfc(x)$ is the addition of the $erf(x)$ error function to 1, i.e. $erfc(x) = 1 - erf(x) = \frac{2}{\sqrt{\pi}} \int_0^x exp(-u^2)du$. The calculated results of the water level decrease with the amplitude of $\Delta h = 0.40$ m within three months after the earthquake of January 30, 2016, $M_w = 7.2$ (№ 18, Table 1). It can occur when the hydraulic diffusivity is $c = 0.24$ m²/s and the distance between the well and pressure drop source is $R = 450$ m [1]. The calculated results of the water level decreases after the earthquakes of December 5, 1997, $M_w = 7.8$ (№ 1) and February 28, 2013, $M_w = 6.8$ (№ 13) are consistent with the above presented results in terms of hydraulic diffusivity of water-bearing rocks and the distance to the pressure drop source. In all three cases the distances to the pressure drop source were the same $R = 450$ m. This may indicate the presence of a geological object at a distance of about 450 m from the well, for example, a fault zone or another type of hydrogeological "window", where the permeability sharply increases during intense seismic shocks.
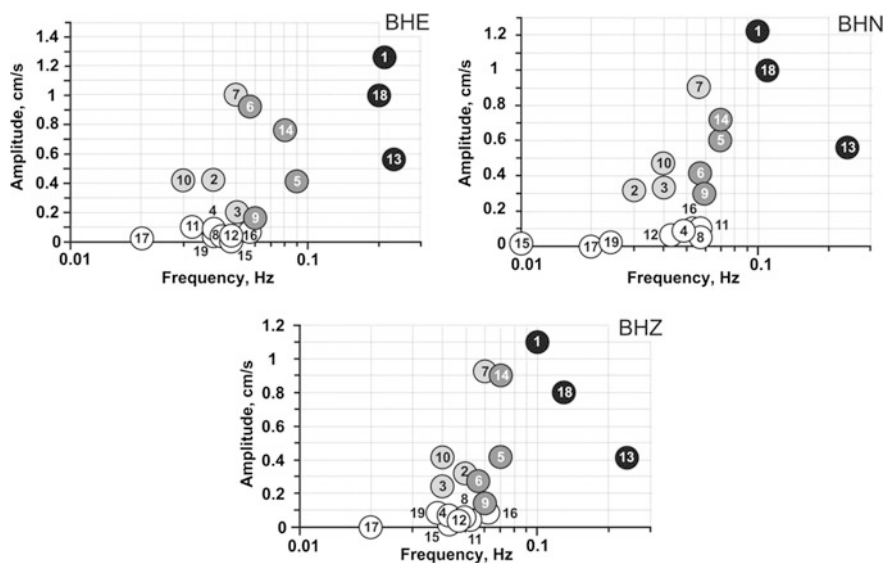
Fig. 4 Distribution of the selected HGSV types (type I— white circles, type II—grey, type III—dark grey, type IV—black) depending on the values of maximum velocity and central frequency in the records of BHE, BHN, BHZ channels at the PET station located 20 km away from the YuZ-5 well. Numbers correspond to the numbers of earthquakes in Table 1 and Fig. 1

The examples of HGSV modelling on the basis of known mathematical models and observation data with consideration of properties of water-bearing rocks and the structure of the well give evaluation of hydrogeodynamic processes interpreted in terms of different HGSV types in the observed well, and yield quantitative criteria for their initiation and development.

References

1. Boldina, S.V., Kopylova, G.N.: Effects of the January 30, 2016, Mw = 7.2 Zhupanovsky earthquake on the water level variations in wells YuZ-5 and E-1 in Kamchatka. Geodyn. Tectonophys. **8**(4), 863–880 (2017). (in Russian)
2. Bower, D., Heaton, K.: Response of an aquifer near Ottawa to tidal forcing and the Alaskan earthquake of 1964. Can. J. Earth Sci. **15**, 331–340 (1978)
3. Brodsky, E.E., Roeloffs, E., Woodcock, D., Gall, I., Manga, M.A.: A mechanism for sustained groundwater pressure changes induced by distant earthquakes. J. Geophys. Res. **108**, 2390–2400 (2003)
4. Cooper, H.H., Bredehoeft, J.D., Papadopulos, I.S., Bennet, R.R.: The response of well-aquifer system to seismic waves. J. Geophys. Res. **70**, 3915–3926 (1965)

5. Gomberg, J., Felzer, K., Brodsky, E.: Earthquake dynamic triggering and ground motion scaling. In: 4th International Workshop on Statistical Seismology on Proceedings, pp. 45–51. Kanagawa, Japan (2006)
6. Kanamori, H., Brodsky, E.E.: The physics of earthquakes. Rep. Prog. Phys. **67**, 1429–1496 (2004)
7. Kocharyan, G.G., Vinogradov, E.A., Gorbunova, E.M., Markov, V.K., Markov, D.V., Pernik, L.M.: Hydrologic response of underground reservoirs to seismic vibrations. Izvestiya Phys. Solid Earth **47**(12), 1071–1082 (2011)
8. Kopylova, G.N., Boldina, S.V.: The response of water level in the YuZ-5 well, Kamchatka to the magnitude 9.3, Sumatra–Andaman earthquake of december 26, 2004. J. Volcanol. Seismol. **1**(5), 319–327 (2007)
9. Kopylova, G.N., Boldina, S.V., Smirnov, A.A., Chubarova, E.G.: Experience in registration of variations caused by strong earthquakes in the level and physicochemical parameters of ground waters in the piezometric wells: the case of Kamchatka. Seism. Instrum. **53**(4), 286–295 (2017)
10. Riznichenko, YuV: The source dimensions of the crustal earthquakes and the seismic moment, in Issled po fizike zemletryasenii (Studies in Earthquake Physics). Nauka, Moscow (1976). (in Russian)
11. Roeloffs, E.A.: Persistent water level changes in a well near Parkfield, California, due to local and distant earthquakes. J. Geophys. Res. **103**(B1), 869–889 (1998)
12. Wang, C.-Y., Manga, M.: Earthquakes and Water. Lecture Notes in Earth Sciences 114. Springer, Berlin (2010)

Analysis of Crack Formation in Model Specimens During Hydraulic Fracturing in Holes

Arkady Leontiev and Ekaterina Rubtsova

Abstract This study relates to the technological aspect of hydraulic fracturing stress measurement technique widely applied currently for stress assessment in rock. The physical simulation data on hydraulic fracturing of the wall of a borehole are presented. The experiments were carried out in polymethacrylate cubes with edge length of 200 mm. In the specimens, either open-end or blind holes were drilled with a diameter of 12 mm at the center of one of the cube faces. In some specimens, longitudinal and transverse slots were cut to promote stress increase under critical pressure of hydraulic fracturing. The hydraulic fracturing tests were implemented using a prototype borehole survey tool designed to seal the assigned interval in the hole and feed it with fluid (glycerin) under pressure. The behavior of hydraulic fractures was studied at 12 model specimens. The experimental results are compiled in the table and contain some canonical information on the nature and features of initiation of hydraulic fractures in the vicinity of measurement holes under different stress conditions of the host medium. The physical simulation results can be used in formulation and solution of analytical problems in hydraulic fracturing stress measurement, or to advance in the technology of in situ directional hydraulic fracturing and stress measurement in underground mines.

A. Leontiev (✉) · E. Rubtsova
Chinakal Institute of Mining, Siberian Branch, Russian Academy of Sciences, 630091 Novosibirsk, Russian Federation
e-mail: leon@misd.ru

1 Introduction

Applied geomechanical researches in any country make important experimental measurements of effective stresses and tracing their variation in rock in the course of mining activities. About twenty methods of in situ stress estimation have been developed by now [1, 2]. The most popular methods include hydraulic fracturing in boreholes. This method is named the hydraulic fracturing stress measurement in contrast to the industrial application of this technology to stimulate oil and gas recovery [3–7]. The method of stress measurement by hydraulic fracturing is often combined with other techniques of stress estimation in rock, such as stress relief, microseismicity, acoustic techniques, etc. [8–10].

The hydraulic fracturing stress measurement can be implemented in three ways: hydraulic fracturing in intact (free from cracks) borehole (HF), hydraulic fracturing in a hole with natural fracture (HTPF), as well as directional hydrofracturing when initiation slots are deliberately made at a certain orientation in the borehole wall, including the borehole-jack fracturing technique [1, 11, 12]. Improvement of procedures and equipment engaged in the hydraulic fracturing stress measurement makes use of physical simulation of the fracturing process in small specimens placed in the specially designed testing facilities as well as numerical modeling [13–19]. Problems addressed in such tests have a wide range: optimizing fracturing fluid feed; hydraulic fracturing with fluids of different viscosities, including dynamic or impulsive destruction of specimens; hydrofracturing process control by the methods of microseismicity or acoustics; the effect of created fracture parameters and fracturing tool dimensions on the accuracy of stress measurement, etc.

Let us take, for example, model hydrofracturing in the organic glass [13]. Model blocks $250 \times 250 \times 250$ mm in size (free from external loads) were installed in a set-up, comprising equipment to feed fracturing fluid and measuring instrumentation. Fracturing was carried out in blind holes with a diameter of 13 mm, and the mouths of the holes were sealed. The created fractures were of disc shape, both axial and oblique relative to the hole axis, reaching the block boundaries or not. The experimental determination of influence exerted by deviatoric stress on the orientation of hydraulic fractures in mineral salt is described in [15]. The tests were carried out on prism-shaped blocks subjected to external loads at a ratio from 1 (hydrostatic) to 1.5. It was found that the shape of a fracture showed whether the effective stresses were hydrostatic or not. At a high stress ratio (more than 1.5), the created fractures were straight and had a distinct orientation; at the ratios around 1, the created fractures were poorly oriented and featured a pronounced branchiness. Cubic specimens with an edge of 150 mm and with a hole with 13 mm in diameter in face center were made of Fredeburg shale and subjected to uniaxial and triaxial compression at the Ruhr University Bochum (Germany) [18]. The tests were

implemented on a specific machine equipped with special systems for loading, hydraulic fracturing and measuring. It was found that inclusion of rock anisotropy considerably improves prediction of initiation and growth of cracks. Fracturing depends on the values of external stresses, orientation of principal stresses and on the anisotropy of rocks.

This paper describes physical simulation of hydraulic fracturing in open and blind holes in cubic specimens made of polymethyl methacrylate exposed to triaxial compression with various load distribution on a special set-up. The experiments were aimed at retrieving information on orientation and shape of created fractures under typical ways of borehole loading with fracturing pressure, including the scenario when initiation slots (cuts) were made beforehand in the hole wall.

2 Experimental Equipment and Instrumentation

It is important to determine the direction of a created fracture growth in the technology of hydraulic fracturing stress measurements. From the experience, the available devices for tracing a fracture on the surface of borehole wall are incapable to sense actual direction of crack propagation in rock. In this respect, it seems to be expedient to perform directional hydraulic fracturing, i.e. to create fractures in preset directions. Directional hydrofracturing tests in differently oriented holes will provide experimental data for estimation of values and directions of all actual stresses in rock.

Physical simulations of directional hydraulic fracturing used a pre-production prototype of the borehole survey tool. At the Mining Information Science Laboratory, Chinakal Institute of Mining, SB RAS, a testing machine has been designed that provides independent triaxial compression (Fig. 1). Specimen 1 (a polymethyl methacrylate cube $200 \times 200 \times 200$ mm in size) is placed on platform 2. A vertical hole of the diameter of 12 mm is preliminary made along the axis of the specimen for installation of a borehole survey tool. The specimen is held in clamp 3 composed of three interconnected levers. One lever is immovable, and the two others are fold-down. The power clamp is set horizontally using screws 4. The levers of the clamp accommodate hydraulic jacks 5 (DN10P10) with the capacity of 10 ton-forces for horizontal compression of the specimen along the orthogonal directions. The fifth jack 6 provides vertical compression of the specimen. The compression forces are transmitted to the specimen from the jacks through open-end support plates 7 with fluoroplastic gaskets (they are not shown in Fig. 1). Screw 8 serves to tighten the vertical jack. The welded structure of vertical plates 9 and lower platform 10 makes a rigid frame for handling and feeding the prototype borehole survey tool. The set-up is arranged inside the stiff frame 11.

Operation of the jacks when applying external forces to the sides of the specimens was controlled with manual pump NRG7035, delivery valves and distributors, manometer DM02-100-1 and flexible high-pressure lines. The pressure feed of
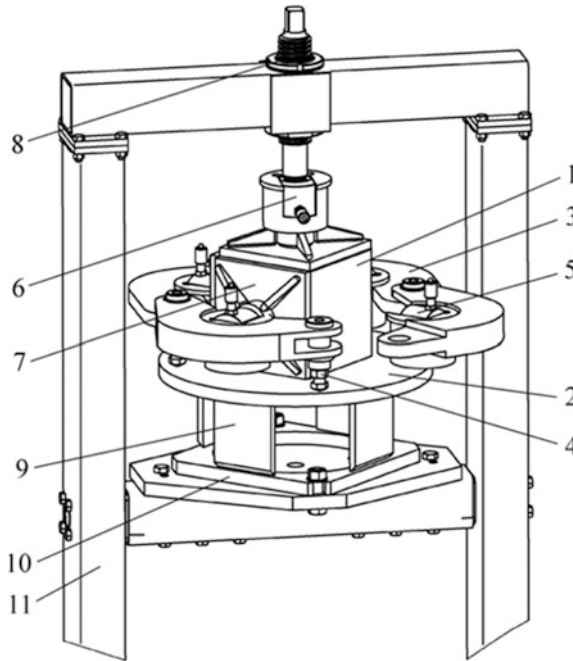
Fig. 1 Testing machine providing hydraulic fracturing stress measurements in laboratory: 1—specimen; 2—platform; 3—power clamp; 4—screw; 5 and 6—hydraulic jacks; 7—support plate; 8—screw; 9—plate; 10—lower platform; 11—frame
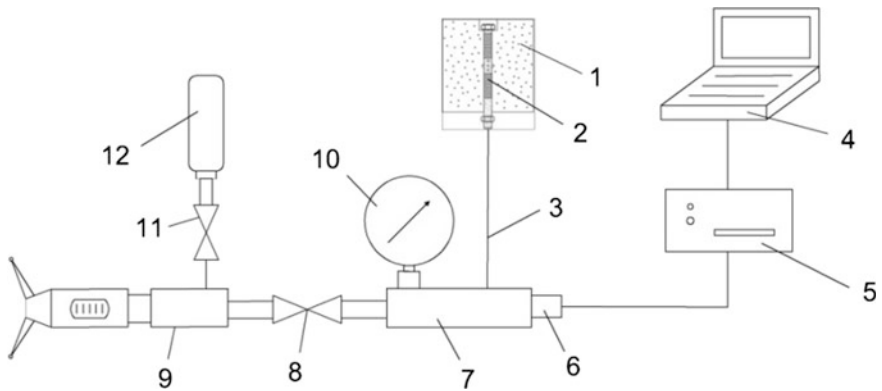
Fig. 2 Test control: 1—specimen; 2—prototype borehole survey tool; 4—portable computer; 5—data conversion and transmission device; 6—pressure sensor MIDA-PI-5.1; 7—adapter; 8, 11—stopcocks; 9—press-meter; 10—check manometer; 12—cell with glycerin
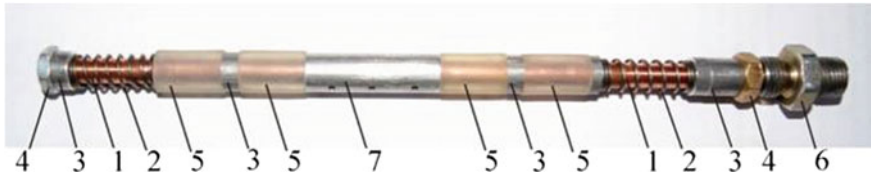
Fig. 3 Two-packer survey tool: 1—central hollow rod; 2—springs; 3—sleeves; 4—nuts; 5—polyurethane packers; 6—connector to inlet channel; 7—packer-to-packer interval sleeve with holes

fracturing fluid to the survey tool as well as the parametric monitoring was executed by the control system (Fig. 2). Hydraulic fracturing was carried out using the prototype borehole survey tools fitted with one packer and with two packers. The single-packer tool was employed to seal mouths of blind holes. The two-packer tool was installed in open holes.

Figure 3 depicts the two-packer tool. The fracture interval was sealed by polyurethane push packers 5. Uniform compression was maintained by identical springs 2. The tool design allowed adjusting the length of the packer-to-packer interval within a range from 1 to 3 diameters of the hole by using changeable bush sleeves 7.

Efficiency of the two-packer tool design was tested in hydraulic fracturing of a model specimen in an unbound state (Fig. 4). The tests resulted in creation of one-side directed rectangular fractures of arbitrary orientation within the length of the packer-to-packer interval.
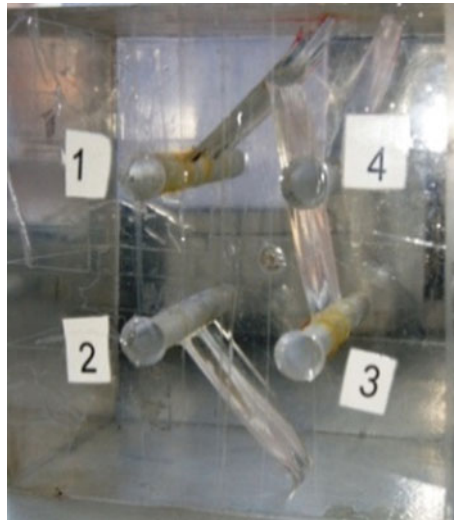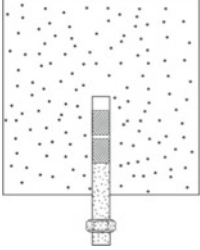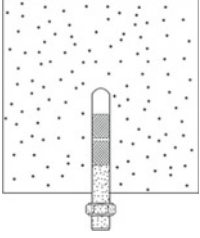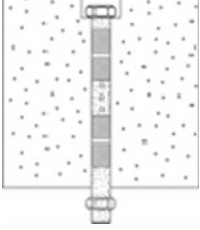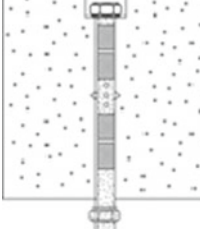
Fig. 4 The specimen with hydraulic fractures created using the two-packer survey tool: 1–4—numbers of boreholes

3   Physical Simulation Procedure and Results
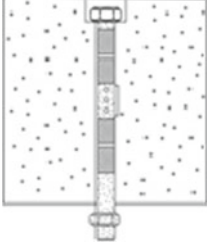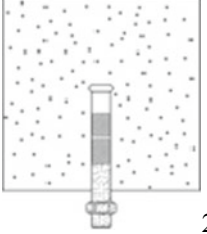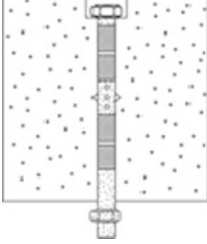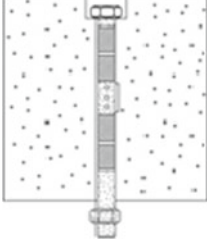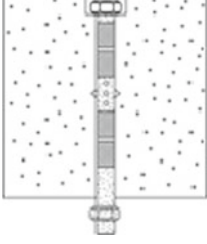
The experimental procedure included: manufacturing of a model specimen; making of a measurement hole oriented along the central axis of one of the specimen faces; cutting longitudinal (300 mm long) or transverse initiation slots of triangular shape with a vertex angle of 600 and 3 mm deep in the holes; placing the prototype survey tool in the measurement hole; connecting the tool to the test control systems; applying force to the specimen by pressure feed to hydraulic jacks; setting packers and hydraulic fracturing in the hole using the test control system.

   The experimental designs and description of the results are compiled in the table below.

Experimental design	Results and comments
1A	Blind hole with a flat bottom. The hydraulic fracturing pressure is 40.0 MPa. The created fracture is at the corners of the flat bottom. It has circular spherical configuration
1B	Blind hole with a spherical bottom. No fracture is created under the pressure of 53.0 MPa
1C	Open hole. Two-packer survey tool is used. One-side directed hydrofractures of arbitrary orientation and nearly rectangular shape are created. The fractures grow along the hole generatrix within the length of the packer-to-packer interval (**Fig.** 4)
2. Model specimens in unbounded state. Slots are cut in holes	
2A	Open hole with a transverse slot in the wall. The hydraulic fracturing pressure is 22.3 MPa. The created fracture is flat and circular. It has a diameter of 100 mm and falls short of free surface
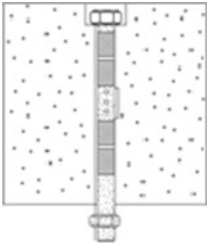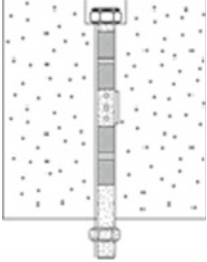
(continued)
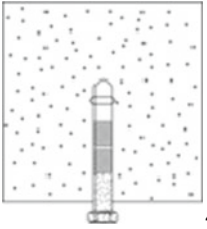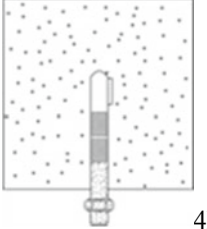
Experimental design	Results and comments
2B	Open hole with a longitudinal slot in the wall. The hydraulic fracturing pressure is 28.0 MPa. The created fracture is flat and one-side oriented in the direction preset by the initiation slot
2C	Blind hole with a flat bottom and a transverse slot nearby. The hydraulic fracturing pressure is 17.3 MPa. The created fracture is circular and slightly incurved towards the upper boundary

3. Model specimen is in a loaded state. Slots are pre-cut in holes

3A	Model specimen is subjected to the vertical force S_v = 6 tf and horizontal force $S_h = S_H$ = 4.5 tf. The hole is open and has a transverse slot. The hydraulic fracturing pressure is 17.0 MPa. The one-side directed hydrofracture grows in the plane of the hole approximately at an angle of 30^0 to the vertical axis; the initiation slot has no influence on the orientation of the created fracture
3B	Open hole with a longitudinal slot. The model specimen is subjected to the vertical force Sv = 6.5 tf and horizontal force Sh = SH = 3.0 tf. The hydraulic fracturing pressure is 15.0 MPa. The one-side created fracture grows in the plane of the hole in the direction set by the longitudinal slot
3C	Open hole with a transverse slot. The model specimen is subjected to the horizontal forces SH = 6.5 tf and Sh = 2.5 tf, as well as to the vertical force SV = 3.0 tf. The hydraulic fracturing pressure is 22.0 MPa The created circular fracture is directed by the initiation slot in the normal plane relative to the hole axis

(continued)

Experimental design	Results and comments
3D	Open hole with a longitudinal slot. The model specimen is subjected to the horizontal force SH = 6 tf directed towards the slot and to the forces Sh = SV = 4.0 tf along the other axes. The hydraulic fracturing pressure is 20.0 MPa. The created fracture grows in the plane of the longitudinal slot in the direction of the maximum applied force
3E	Open hole with a longitudinal slot. The model specimen is subjected to the force of 10 tf along the axis of the hole. The created fracture emerges in the domain of the longitudinal slot and then turns to the direction of the applied force

4. Hydraulic fracturing with viscous fluid (plasticine). Model specimens are in a loaded state. Slots are pre-cut in the holes

4A	Blind hole with a spherical bottom and a transverse slot cut in the middle of the sealed interval. The model specimen is subjected to the force of 10 tf along the hole axis and to the forces of 3 tf along the other axes. The two-side directed flat fracture is created along the hole generatrix at a random place and predominantly grows in the direction of the maximum force applied. The slot has no influence on the created fracture orientation
4B	Blind hole with a spherical bottom and a longitudinal slot in the sealed interval. The force of 6 tf is applied normally to the plane of the slot. The other faces are subjected to the force of 3 tf. The two-side directed hydrofracture is initiated by the longitudinal slot and tends to turn towards the maximum force applied

The hydraulic fracturing tests were carried out on 13 model specimens. Due to limited number of the tests and implemented scenarios, we regard the findings on the features of the created fracture formation as preliminary. It has been observed in the tests that: (1) the fracture behavior depends on the experimental conditions governed by the hole design (blind or open) and the method of sealing the fracturing interval; (2) preliminary weakening of the hole wall by cutting initiation slots allows to reduce the critical hydraulic fracturing pressure 2 times; (3) using the

two-packer borehole survey tool results, as a rule, in longitudinal fracturing of the hole wall while the initiation slots not always ensure the preset direction of the created fracture growth, which means that it is necessary to undertake studies into substantiation of geometrical parameters for longitudinal slots; (4) the ring (normal to axis) slots cut in the holes allow creation of disc hydrofractures in the preset direction.

4   Conclusion

The authors have developed a physical simulation procedure for hydraulic fracturing stress measurements and have tested it on cubic polymethyl methacrylate specimens using the prototype borehole survey tool. The specimens were subjected to hydraulic fracturing in unbounded state and under triaxial loading by unequal stresses on a special testing machine.

The experimental results contain the canonical series of data on the nature and specificity of hydrofracture formation in model specimens in varied stress conditions and with longitudinal or transverse initiation slots cut preliminary in the borehole wall. The results of physical simulations can be used to formulate and solve analytical problems on hydraulic fracturing stress measurements, and to improve the methods and equipment of this stress control technique in mines.

References

1. Haimson, B.C., Cornet, F.H.: ISRM suggested methods for rock stress estimation—part 3: hydraulic fracturing (HF) and/or hydraulic testing of pre-existing fractures (HTRF). Int. J. Rock Mech. Min. Sci. **40**, 1012–1020 (2003)
2. Leontiev, A.V., Popov, S.N.: Operational experience gained in application of hydraulic fracturing. Gornyi Zhurnal. **3**, 37–43 (2003). (in Russian)
3. Synn, J.H., Park, C., Jung, Y.B., Sunwoo, C., Kim, K.S., Choi, S.Y., Song, M.K., Shin, I.J., Rutqvist, J.: Integrated 3-D stress determination by hydraulic fracturing in multiple inclined boreholes beneath an underground cavern. Int. J. Rock Mech. Min. Sci. **75**, 44–55 (2015)
4. Zhang, C., Jiang, Q., He, X., Liu, G.: Applications of hydraulic fracturing method in measurement of in-situ railway tunnel stress. Electron. J. Geotech. Eng. **18**, 2851–2862 (2013)
5. Ratigan, J.L.: The use of the fracture reopening pressure in hydraulic fracturing stress measurements. Rock Mech. Rock Eng. **25**(4), 225–236 (1992)
6. Yokoyama, T., Sakaguchi, K., Ito, T.: Re-opening and shut-in behaviors under a large ratio of principal stresses in a hydraulic fracturing test. In: Symposium of the International Society for Rock Mechanics. Proc. Eng. **191**, 862–868 (2017)

7. Jalali, M.R., Gischig, V., Doetsch, J., Krietsch, H., Amann, F.: Mechanical, hydraulic and seismological of crystalline rock as a response to hydraulic fracturing at the grimsel test site. ARMA. In: 51st U.S. Rock Mechanics/Geomechanics Symposium. San Francisco, California, USA (2017)
8. Krietsch, H., Gischig, V., Evans, K., Doetsch, J., Dutler, N.O., Valley, B., Amann, F.: Stress measurements for an in situ stimulation experiment in crystalline rock: integration of induced seismicity, stress relief and hydraulic methods. Rock Mech. Rock Eng. **52**(2), 517–542 (2019)
9. Ask, D.: New developments in the integrated stress determination method and their application to rock stress data at the Äspö HRL, Sweden. Int. J. Rock Mech. Min. Sci. **43**, 107–126 (2016)
10. Bjarnason, B., Leijon, B., Stephansson, O.: The bolmen project: rock stress measurements using hydraulic fracturing and overcoring techniques. Tunn. Undergr. Sp. Technol. **3**, 305–316 (1988)
11. Yokoyama, T., Sano, O., Hirata, F., Ogawa, K., Nakayama, Y., Ishida, N., Mizuta, Y.: Development of borehole-jack fracturing technique for in situ stress measurement. Int. J. Rock Mech. Min. Sci. **67**, 9–19 (2014)
12. RF Patent No. 2641679. Directional fracture tool for rocks. (2018) (in Russian)
13. Serdyukov, S.V., Kurlenya, M.V., Patutin, A.V.: Hydraulic fracturing for in-situ stress measurement. J. Min. Sci. **52**(6), 1031–1038 (2016)
14. Bohloli, B., Pater, C.J.: Experimental study on hydraulic fracturing of soft rocks: influence of fluid rheology and confining stress. J. Pet. Sci. Eng. https://doi.org/10.1016/j.petrol.2006.01.009
15. Doe, T.W., Boyce, G.: Orientation of hydraulic fractures in salt under hydrostatic and non-hydrostatic stresses. Inter. J. Rock Mech. Min. Sci. Geomech. **26**(6), 605–611 (1989)
16. Guo, F., Morgenstern, N.R., Scott, J.D.: An experimental study of well communication by hydraulic fracturing. Int. J. Rock Mech. Min. Sci. Geomech. Abstr. **30**(3), 203–218 (1993)
17. Choi, S.O.: Interpretation of shut-in pressure in hydro fracturing pressure-time records using numerical modeling. Int. J. Rock Mech. Min. Sci. **67,** 29–37 (2012)
18. Stoeckhert, F., Molenda, M., Brenne, S., Alber, M.: Fracture propagation in sandstone and slate—laboratory experiments, acoustic emissions and fracture mechanics. J. Rock Mech. Geotech. Eng. **7**, 237–249 (2015)
19. Atroshenko, S.A., Krivosheev, S.I., Petrova, A.Y.: Crack propagation in dynamic failure of polymethyl methacrylate. Zhurnal tekhnicheskoi fiziki, **72**(2), 52–58 (2002) (in Russian)

Determination of Filtration Properties and Mass Transfer Coefficient for Fractured Porous Media by Laboratory Test Data

Larisa Nazarova and Leonid Nazarov

Abstract

The method for determination of mass transfer and filtration characteristics of fractured porous reservoir rocks, considered as dual porosity and dual permeability media is developed and implemented under laboratory conditions. The procedure for filtration tests consists in series of three measurements of the fluid flowrate in the same specimen: standard scheme (Q_0), fractures are tamped at one face (Q_1) and at another face (Q_2). The mathematical model of the experiment is developed; analytical solution is worked out to the problem on the stationary filtration in a dual permeability medium; the inversion relationships are derived based on the new solutions in view to calculate fracture k_1 and matrix k_2 permeability as well as mass transfer coefficient by using the measured flowrate values Q_0, Q_1 and Q_2. Numerical analysis revealed low stability of the inverse problem solution against input data, as this implies more rigorous requirements regarding measurement precision. The laboratory tests of the oil-bearing rock specimens of Bazhenov formation with well pronounced fracturing justifies that ratio k_2/k_1 lies within the range 0.04–0.055.

Keywords

Fractured porous reservoir rock · Dual permeability model · Filtration · Flowrate · Mass transfer coefficient · Lab experiment · Inverse problem

L. Nazarova (✉) · L. Nazarov
Chinakal Institute of Mining, Siberian Branch RAS, 630091 Novosibirsk, Russia
e-mail: lanazarova@ngs.ru; mining1957@mail.ru

257

1 Introduction

The present-day concept on the block structure of a rock mass at all the scale levels is employed as the base for development of geomechanical models of natural and anthropogenic objects [1, 2]. Generally, production strata of hydrocarbons deposits has the jointed-blocked structure [3, 4], this feature should be taken into account when modeling mass transfer processes.

Resolution capacity of advanced geophysical methods enables to identify the structure in the vicinity of a well, including structural elements up to few centimeters in size [5–7]. Nevertheless, it is impossible to estimate smaller-size blocks, as well as thickness of interblock gaps which are required to evaluate permeability. Owning to such imperfect resolution of the used instruments the accounting for the actual medium geometry envolves serious technical and computation problems [8–10].

The conceptual approach considering an elementary volume as a continuum with two permeabilities and porosities, intensity q of mass transfer between blocks and fractures depending on difference Δp between pressures in fractures p_1 and in porous blocks (matrix) p_2 [11] was proposed to model fractured porous media (FPM). This idea was developed in [12], where the author introduced concept "representative elementary volume". This approach was applied to describe a complex-structure medium [13] in investigation into mass transfer processes in oil- and gas-bearing beds [14–17], as well as in coal-rock masses [18–20].

FPM models, mainly concerning quantitative evaluation of porosity and permeability of fractures k_1 and a matrix k_2 were verified based on the data of laboratory [21, 22] and natural [23, 24] experiments, along with analytical and numerical calculations of effective parameters of the media specified with regular-block [25, 26] and stochastic [27–29] structure. It is hypothesized in [11] that empirical function $q(\Delta p)$ can be found exclusively in the case of a non-stationary filtration mode, viz., from the pressure-recovery curve under natural conditions [24].

In the present research the method is proposed for quantitative evaluation of permeability of the matrix and fractures as well as the factor of proportionality between fluid crossflow intensity q and pressures difference Δp, using the data on laboratory tests of the study specimens at a stationary filtration mode within the model [11] supposing linear relationship $q = q(\Delta p)$.

2 Statement of the Problem and a Set of Equations on Filtration in a Fractured Porous Rock Mass

2.1 System of Equations

Let consider a cylindrical specimen (length l, faces radius r_0) with isolated lateral surface (Fig. 1a), the constant pressure p_c is preset at one face; flowrate is measured at another face at atmosphere pressure p_a The system describing non-stationary filtration in FPM includes [11]:
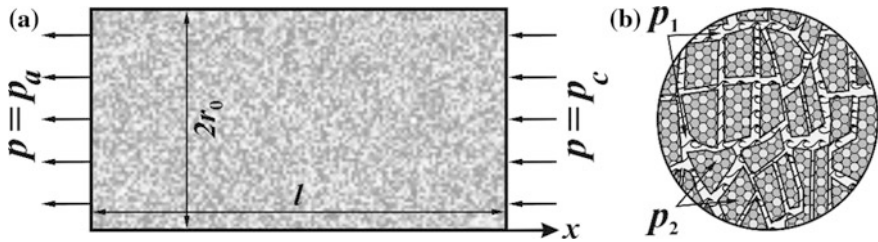
Fig. 1 Scheme of experiment (**a**) and fractured porous structure of specimen faces (**b**)

Mass conservation equation

$$\frac{\partial(m_i\rho)}{\partial t} + div(\rho\vec{V}_i) - (-1)^i q = 0;$$ (1)

Darcy law

$$\vec{V}_i = -k_i\nabla p_i/\eta;$$ (2)

Relationship of porosity m_i $(i = 1, 2)$ and fluid density ρ versus corresponding pressure

$$\rho = \rho_0[1 + \beta(p_i - p_a)];$$ (3)

$$m_i = m_{i0} + \beta_i(p_i - p_a),$$ (4)

where indices "1" and "2" refer to fractures and matrix, respectively; $\vec{V}_i$ is velocity; ρ_0 and m_{i0} are values of density and porosity at atmospheric pressure; β_1, β_2 and β are compressibility of fractures, matrix, and a fluid; η is fluid viscosity. Intensity of mass transfer between a matrix and fractures is a linear function versus pressures difference [30]

$$q = \rho_0 A(p_2 - p_1),$$ (5)

A—empirical coefficient.

Under assumption that a FPM and a fluid are weakly compressible media the system (1)–(5) is reduced to two equations

$$(\beta_i + m_{i0}\beta)\frac{\partial p_i}{\partial t} = \frac{k_i}{\eta}\Delta p_i + (-1)^i A(p_2 - p_1).$$ (6)

2.2 Stationary Mode

Given that pressures do not depend on time and under consideration is 1D filtration, it follows from (6):

$$k_1 \frac{\partial^2 p_1}{\partial x^2} - \alpha(p_2 - p_1) = 0;$$

$$k_2 \frac{\partial^2 p_2}{\partial x^2} + \alpha(p_2 - p_1) = 0,$$

(7)

$\alpha = A\eta$ is dimensionless mass transfer coefficient. The general solution of (7) is:

$$p_1(x) = C_1 + C_2 x + \xi f(x);$$
$$p_2(x) = C_1 + C_2 x - f(x),$$

(8)

where $f(x) = C_3 \sin \gamma x/l + C_4 \cos \gamma x/l$, $\xi = k_1/k_2$, $\gamma = l\sqrt{\alpha(1/k_1 + 1/k_2)}$.

We formulate the problem to work out a pattern of sequential filtration tests in order to obtain data for evaluation of permeabilities k_1, k_2 and coefficient A. It is obvious that at least three information units are required. It is feasible to obtain them by prescribing different conditions on the faces of the test specimen.

Assume that electronic microscopy method or high-resolution camera is used to take pictures of specimen faces (Fig. 1b). Areas of fractures S_1 and the matrix S_2 of the left face are determined from the photos. Let consider three types of filtration experiments conducted in series for the same specimen.

T0. Pressure p_c is preset at the right face and flowrate Q_0 is recorded at the left face.

T1. Fractures at the left face are tamped. The test is conducted similarly to T0 with recording flowrate Q_1.

T2. Fractures at the right face are tamped. The test runs similarly to T0 with recording Q_2.

Boundary conditions for tests T0, T1 and T2 are summarized in Table 1.

Determination of constants $C_1, \ldots, C_4$ in (8) for every type of boundary conditions enables to establish distribution of pressures in a matrix and fractures and to find a flowrate at the left face.

Type T0:

$$p_1(x) = p_2(x) = p_a + (p_c - p_a)x/l;$$

(9)

Table 1 Boundary conditions

Type	Boundary	
	$x = 0$	$x = l$
T0	$p_1 = p_2 = p_a$	$p_1 = p_2 = p_c$
T1	$\frac{\partial p_1}{\partial x} = 0, p_2 = p_a$	$p_1 = p_2 = p_c$
T2	$\frac{\partial p_1}{\partial x} = 0, p_2 = p_a$	$\frac{\partial p_1}{\partial x} = 0, p_2 = p_c$

$$Q_0 = \frac{1}{\eta}\left(S_1 k_1 \frac{\partial p_1}{\partial x} + S_2 k_2 \frac{\partial p_2}{\partial x}\right)\bigg|_{x=0} = \frac{(S_1 k_1 + S_2 k_2)(p_c - p_a)}{\eta l} \tag{10}$$

Type T1:

$$p_1(x) = p_c + (p_c - p_a)\frac{D(\gamma,x) + \xi \sin \gamma(1-x/l)}{D(\gamma,l)};$$

$$p_2(x) = p_c + (p_c - p_a)\frac{D(\gamma,x) - \sin \gamma(1-x/l)}{D(\gamma,l)}; \tag{11}$$

$$Q_1 = \frac{S_2 k_2}{\eta}\frac{\partial p_2}{\partial x}\bigg|_{x=0} = \frac{S_2 k_2(p_c - p_a)}{\eta l} G(\gamma, \xi). \tag{12}$$

Type T2:

$$p_1(x) = p_c + (p_c - p_a)\frac{D(\gamma/2,2x) + \xi \sin \gamma(0.5-x/l)}{2D(\gamma/2,l)};$$

$$p_2(x) = p_c + (p_c - p_a)\frac{D(\gamma/2,2x) - \sin \gamma(0.5-x/l)}{2D(\gamma/2,l)}; \tag{13}$$

$$Q_2 = \frac{S_2 k_2}{\eta}\frac{\partial p_2}{\partial x}\bigg|_{x=0} = \frac{S_2 k_2(p_c - p_a)}{\eta l} G(\gamma/2, \xi). \tag{14}$$

The designations introduced at this point are:

$$D(\gamma,x) = \sin \gamma + \frac{\gamma \xi x}{l}\cos \gamma \; ; \; G(\gamma, \xi) = \gamma(1+\xi)/(\tan \gamma + \gamma \xi).$$

2.3 Analysis of the Solution

Figure 2a and b demonstrate pressure p_2 distribution in the specimen under T1 and T2 conditions, respectively, at $p_c = 0.3$ MPa, $\xi = 0.023$ and different values of parameter γ. It is reasonable to turn attention to the following specific features:

– given that filtration tests are conducted under standard procedure T0, then pressure in fractures and matrix is the same and tends to vary according to the linear law, the flowrate is calculated from Dupuis formula (10);
– pressure in fractures and matrix are almost independent on permeabilities ratio ξ in steady-state regime of filtration;
– flowrate at T0 is obviously greater than at T1 and T2;
– when $\gamma \to 0$ (crossflow between fractures and the matrix is absent) or under $\xi \to \infty$ ($k_1 \to 0$—either fractures are impermeable, or $k_1 \ll k_2$) solutions according to T1 and T2 coincide with T0, in particular,
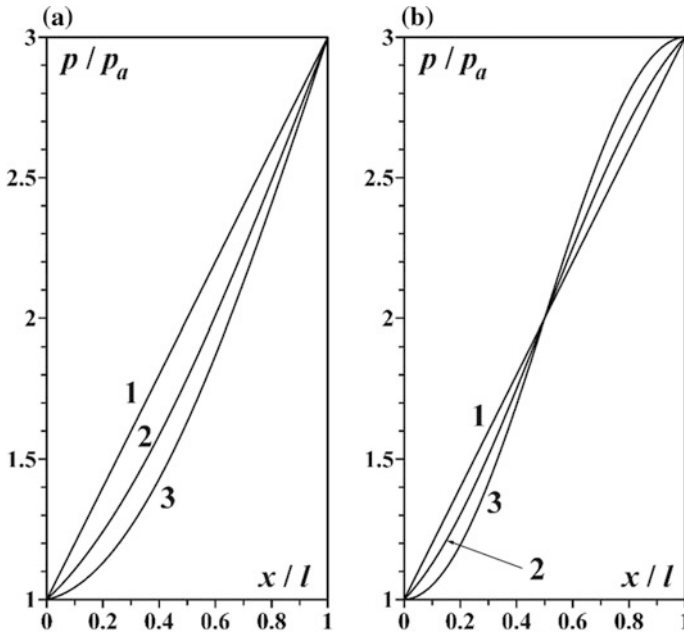
Fig. 2 Pressure distribution in a specimen at different test patterns: T1 (**a**); T2 (**b**). Lines 1, 2, and 3 correspond to values $\gamma = 0.7$, 1.2, and 1.55

$$\lim_{\gamma \to 0} G(\gamma, \xi) = 1, \ \lim_{\xi \to \infty} G(\gamma, \xi) = 1.$$

Figure 3 demonstrates isolines of functions $G(\gamma, \xi)$ and $G(\gamma/2, \xi)$ that illustrate their weak dependence on γ. This peculiarity presents some problems with interpretation of experimental data.

2.4 Experimental Data Inversion

Let T0, T1 and T2 tests are carried out for the same specimen with measurements of respective flowrates Q_0, Q_1 and Q_2. Dividing (12) and (14) by (10), we obtain a set of equations to determine γ and ξ

$$F(\gamma, \xi) = q_1, \ \ F(\gamma/2, \xi) = q_2, \tag{15}$$

where $F(\gamma, \xi) = \xi G(\gamma, \xi)/(\delta + \xi)$, $\delta = S_1/S_2$, $q_1 = Q_1/Q_0$, $q_2 = Q_2/Q_0$.

Now, we are to analyze stability of solution (15) against measurement error. With this aim in view we consider function
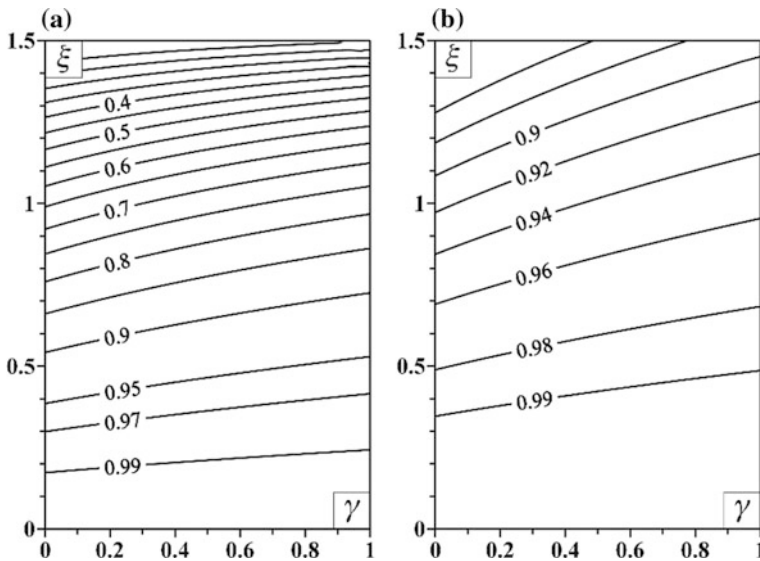
Fig. 3 Isolines of dimensionless flowrate at different test patterns: T1 (**a**); T2 (**b**)

$$B(\gamma, \xi) = \sqrt{[F(\gamma, \xi) - (1+\varepsilon)F(\gamma_0, \xi_0)]^2 + [F(\gamma/2, \xi) + (1+\varepsilon)F(\gamma_0/2, \xi_0)]^2}$$

which level lines are shown in Fig. 4 at $\gamma_0 = 0.17$, $\xi_0 = 0.12$, $\delta = 0.002$ and different values of relative error ε. Equivalence domain E (where $B < 0.002$) is toned. It is explicit that at $\varepsilon = 0.005$ point $(\gamma_0, \xi_0) \in E$ (Fig. 4a); while at $\varepsilon = 0.02$ the parameter evaluation error ξ can reach 40% (Fig. 4b). This implies more rigorous requirements for precision of flowrate measurements in the performance of an experiment.

Maclaurin expansion of tangents at small γ can reduce Eq. (15) to the system

$$\frac{\xi(1+\xi)}{(\delta+\xi)(1+\xi+\gamma^2/3)} = q_1, \frac{\xi(1+\xi)}{(\delta+\xi)(1+\xi+\gamma^2/12)} = q_2,$$

which has analytical solution

$$\xi = \frac{3q_1q_2\delta}{4q_1 - q_2 - 3q_1q_2}, \quad \gamma^2 = \frac{12(1+\xi)(q_2 - q_1)}{4q_1 - q_2}, \tag{16}$$
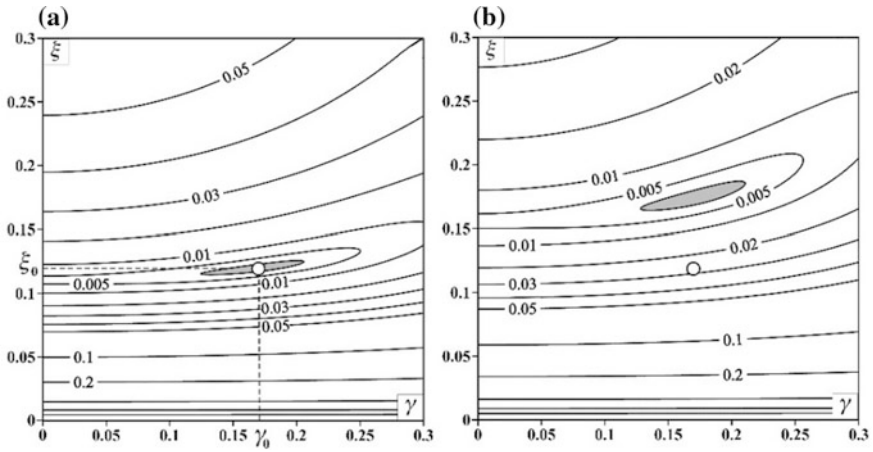
Fig. 4 Level lines of squared error function $B(\gamma, \xi)$: $\varepsilon = 0.005$ (**a**); $\varepsilon = 0.02$ (**b**)

3 Interpretation of Laboratory Test Results

The bituminous argillite specimen (Salym oil deposit, Bazhenov formation, West Siberia) specified with pronounced fracturing ($l = 76$ mm, $r_0 = 19$ mm) was selected as a study object (Fig. 5). The side surface of the test specimen was tightened and sealed with the help of a rubber sleeve. The gas (air, $\eta = 10^{-5}$ Pa s) pressure was built up at the right face $p_c = 0.40, 0.45, \ldots, 0.90$ MPa, the flowrate was recorded at the left face with relative measurement precision of 1%. The fractures at the left face and then at the right face were tamped with penetrant prior to filtration tests according to T1 and T2. The high-resolution photo of the left face was used to determine $\delta = 0.0014$.
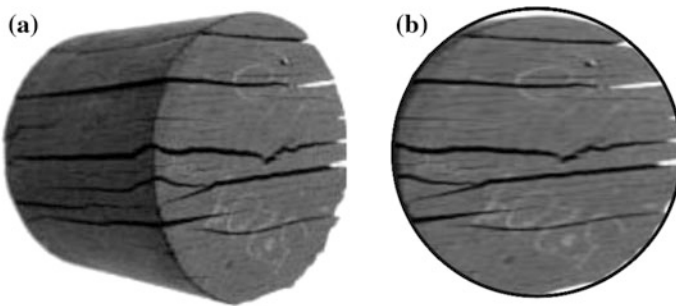
Fig. 5 The test specimen before it is placed into the sleeve: general view (**a**); the right face (**b**)

Table 2 Experimental data and results of their processing

p_c, bar	Q_0, l/min	Q_1, l/min	Q_2, l/min	ξ	γ	k_1, mD	θ_1, %	k_2, mD	θ_2, %	$10^7 A$, 1/(Pa s)	θ_A, %
1	2	3	4	5	6	7	8	9	10	11	12
4.0	4.69	4.48	4.54	0.0410	0.2292	4123.7	16.4	169.2	0.47	1.479	0.47
4.5	5.48	5.23	5.29	0.0434	0.2295	3905.4	10.3	169.5	0.29	1.481	0.34
5.0	6.26	5.98	6.05	0.0516	0.2304	3299.1	7.2	170.3	0.17	1.489	0.20
5.5	7.04	6.73	6.81	0.0498	0.2302	3420.4	3.5	170.2	0.12	1.487	0.07
6.0	7.82	7.47	7.57	0.0537	0.2306	3177.9	10.3	170.5	0.29	1.490	0.28
6.5	8.61	8.22	8.33	0.0558	0.2309	3056.6	13.7	170.7	0.41	1.492	0.42
7.0	9.39	8.97	9.08	0.0448	0.2297	3784.2	6.9	169.7	0.17	1.483	0.21
7.5	10.17	9.72	9.84	0.0435	0.2295	3893.3	9.9	169.5	0.29	1.481	0.35
8.0	10.95	10.46	10.59	0.0516	0.2304	3299.1	6.8	170.3	0.17	1.489	0.20
8.5	11.73	11.21	11.35	0.0558	0.2309	3056.6	13.4	170.7	0.41	1.492	0.42
9.0	12.52	11.96	12.11	0.0431	0.2295	3929.7	11.0	169.5	0.29	1.481	0.35

The flowrate measurement results at different input pressures p_c are summarized in Table 2 (columns 2–4). Values of γ and ξ (columns 5 and 6) were calculated for every value of p_c by using (16).

Permeability of fractures was assessed from (10) at known ξ

$$k_1 = \frac{\eta l (1 + \delta) Q_0}{(p_c - p_a)(\delta + \xi)\pi r_0^2},$$

then permeability of the matrix is $k_2 = \xi k_1$ and finally mass transfer coefficient is

$$A = \frac{\gamma^2 k_1}{\eta l^2 (1 + \xi)}.$$

The average values $\overline{k}_1 = 3541$ mD, $\overline{k}_2 = 170$ mD and $\overline{A} = 1.486 \times 10^{-7} 1/(\text{Pa s})$ are taken as target values (Table 2, columns 7, 9 and 11). The corresponding percentage errors $\theta_1 = |1 - k_1/\overline{k}_1|$, $\theta_2 = |1 - k_2/\overline{k}_2|$ and $\theta_A = |1 - A/\overline{A}|$ are listed in the Table 2 (columns 8, 10 and 12).

4 Conclusion

The research process for quantitative estimation of filtration properties and mass transfer coefficient A for fractured porous reservoir rocks was worked out and realized. Filtration tests were conducted on the specimen under three differing conditions at the faces of one and the same specimen. The solution to the problem

on stationary filtration is obtained within the model of the dual permeability continuum; the novel solution enabled to derive analytical expressions for estimation of A value, permeability of fractures and the matrix. Up to the present the mass transfer coefficient used to be determined exclusively under natural conditions by the curve for recovery of pressure in a shut in well. The new-proposed procedure allows the respective estimation under laboratory conditions.

References

1. Sadovsky, M.A.: Natural lumpiness of rock. DAN USSR **247**(4), 829–831 (1979)
2. Sadovsky, M.A., Bolkhovitinov, L.G., Pisarenko, V.F.: Medium Deformation and Seismic Process. Nauka, Moscow (1987). (in Russian)
3. Dorofeeva, T.V. (ed.): Bazhenov Oil Reservoir Formation in Western Siberia. Nedra, Leningrad (1983). (in Russian)
4. Lonergan, L., Jolly, R.J.H., Rawnsley, K., Sanderson, D.J. (eds.): Fractured Reservoirs. Special Publications 270. Geological Society, London (2007)
5. Kearey, P., Brooks, M., Hill, I.: An Introduction to Geophysical Exploration, 3rd edn. Blackwell Science Ltd., London (2002)
6. Prioul, R., Jocker, J.: Fracture characterization at multiple scales using borehole images, sonic logs, and walkaround vertical seismic profile. Am. Assoc. Pet. Geol. Bull. **98**, 1503–1516 (2009). https://doi.org/10.1306/08250909019
7. Rock fractures and fluid flow. In: Contemporary Understanding and Applications. The National Academies Press, Washington, DC (1996). https://doi.org/10.17226/2309
8. Bourbiaux, B.: Fractured reservoir simulation: A challenging and rewarding issue. Oil Gas Sci. Technol. **65**(2), 227–238 (2010). https://doi.org/10.2516/ogst/2009063
9. Hauge, V.L., Aarnes, J.E.: Modeling of two-phase flow in fractured porous media on unstructured non-uniformly coarsened grids. Transp. Porous Media **77**, 373–398 (2009). https://doi.org/10.1007/s11242-008-9284-y
10. Obeysekara, A., Lei, Q., Salinas, P., Pavlidis, D., Xiang, J., Latham, J.P., Pain, C.C.: Modelling stress-dependent single and multi-phase flows in fractured porous media based on an immersed-body method with mesh adaptivity. Comput. Geotech. **103**, 229–241 (2018). https://doi.org/10.1016/j.compgeo.2018.07.009
11. Barenblatt, G.I., Zheltov, YuP., Kochina, I.N.: Basic notions of seepage theory for fractured media. Prikl. Mat. Mekh. **24**(5), 852–864 (1960)
12. Hill, R.: Elastic properties of reinforced solids: some theoretical principles. J. Mech. Phys. Solids **11**(5), 357–372 (1963). https://doi.org/10.1016/0022-5096(63)90036-x
13. Coussy, O.: Mechanics and physics of porous solids. Wiley, United Kingdom (2010)
14. Douglas, J., Arbogast, T.: Dual-porosity models for flow in naturally fractured reservoirs. In: Cushman, J.H. (ed.) Dynamics of Fluids in Hierarchical Porous Media, pp. 177–221. Academic Press, London (1990)
15. Nie, R.-S., Meng, Y.-F., Jia, Y.-L., et al.: Dual porosity and dual permeability modeling of horizontal well in naturally fractured reservoir. Transp. Porous Media **92**(1), 213–235 (2012). https://doi.org/10.1007/s11242-011-9898-3
16. Wu, Y.-S.: Multiphase fluid flow in porous and fractured reservoirs. Elsevier, Amsterdam (2016). https://doi.org/10.1016/c2015-0-00766-3

17. Nazarova, L.A., Nazarov, L.A.: Evolution of stresses and permeability of fractured-and-porous rock mass around a production well. J. Min. Sci. **52**(3), 424–431 (2016). https://doi.org/10.1134/s106273911603061x

18. Espinoza, D.N., Vandamme, M., Dangla, P., Pereira, J.-M., Vidal-Gilbert, S.: A transverse isotropic model for microporous solids—application to coal matrix adsorption and swelling. J. Geophys. Res. Solid Earth **118**, 6113–6123 (2013). https://doi.org/10.1002/2013jb010337

19. Nazarova, L.A., Nazarov, L.A., Vandamme, M., Pereira, J.-M.: Direct and inverse problems of gas emission and the sorptive deformation of coal beds. J. Appl. Ind. Math. **11**(2), 236–243 (2017). https://doi.org/10.1134/s1990478917020090

20. Nazarova, L.A., Nazarov, L.A., Vandamme, M., Pereira, J.-M.: Estimation of the deformation and filtration properties of coal by adsorption test data based on solution of the inverse problem. Dokl. Phys. **62**(6), 323–327 (2017). https://doi.org/10.1134/s1028335817060076

21. Babadagli, T., Ren, X., Develi, K.: Effects of fractal surface roughness and lithology on single and multiphase flow in a single fracture: an experimental investigation. Int. J. Multiph. Flow **68**, 40–58 (2015). https://doi.org/10.1016/j.ijmultiphaseflow.2014.10.004

22. Jones, B., Brouwers, L., Dippenaar, M.: Partially to fully saturated flow through smooth, clean, open fractures: qualitative experimental studies. Hydrogeol. J. **26**(3), 945–961 (2018). https://doi.org/10.1007/s10040-017-1680-3

23. Dake, L.P.: The Practice of Reservoir Engineering. Elsevier, London (2001)

24. van Golf-Racht, T.: Fundamentals of Fractured Reservoir Engineering. Elsevier, London (1982)

25. Yang, X., Lu, T.J., Kim, T.: An analytical model for permeability of isotropic porous media. Phys. Lett. A **378**, 2308–2311 (2014). https://doi.org/10.1016/j.physleta.2014.06.002

26. Durlofsky, L.J.: Numerical calculation of equivalent grid block permeability tensors for heterogeneous porous media. Water Resour. Res. **27**(5), 699–708 (1991). https://doi.org/10.1029/91wr00107

27. Guerillot, D., King, P., Ravenne, C.: Reservoir characterization using expert knowledge. Data Stat. Oilfield Rev. **4**(1), 25–31 (1992)

28. Huang, Z., Yao, J., Li, Y., Wang, C., Lv, X.: Numerical calculation of equivalent permeability tensor for fractured vuggy porous media based on homogenization theory. Commun. Comput. Phys. **9**(1), 180–204 (2011). https://doi.org/10.1007/s11431-011-4480-3

29. Teimoori, A., Chen, Z., Rahman, S.S., Tran, T.: Effective permeability calculation using boundary element method in naturally fractured reservoirs. Pet. Sci. Technol. **23**(5–6), 693–709 (2005). https://doi.org/10.1081/lft-200033029

30. Pollard, P.: Evaluation of acid treatment from pressure build-up analysis. Trans. AIME **216**, 38–43 (1959)

Hydraulic Fracturing Pressure Curves as a Way for Determining Reservoir Parameters

Helen Novikova and Mariia Trimonova

Abstract

The paper describes the study of pressure drop curves in a fractured well, which were obtained in laboratory experiments on hydraulic fracturing. The aim of the study was to determine the fracture closure pressure, which is necessary for the correct numerical simulation of the hydraulic fracturing as well as for solving various geomechanical problems during oil field developments. The application of the G-function technique, which is based on plotting different graphs of dependence of the derivatives and logarithmic derivatives of the hydraulic fracture pressure on some time-dependent functions, is examined. This method is derived from analytical solutions of filtration problems for the system reservoir + well + fracture in various approximations. Applying this approach to experimental data, the fracture closure pressure is determined by the behavior of derivatives and semi-log derivatives of the fracture pressure. In the framework of the study, the plotting of various dependences of the pressure derivatives on G-function was carried out for two experimental pressure drop curves. The main results of the presented work include the determination of the fracture closure pressure in the experiments and comparison of the obtained values with the minimum horizontal stress created in the sample.

H. Novikova (✉) · M. Trimonova
Sadovsky Institute of Geospheres Dynamics RAS, 119334 Moscow, Russia
e-mail: helenvn97@gmail.com

1 Introduction

The paper presents a study of one of the main ways to intensify oil recovery—hydraulic fracturing. It has been in use for over 50 years [1]. Recently, due to the growth of the low-permeable reservoir developments, the interest in both numerical and experimental modeling of the hydraulic fracturing has grown. Besides the increase of oil production, the results of hydraulic fracturing are used to determine some important reservoir characteristics. Thus, the hydraulic fracturing is the main way to determine the minimum tectonic stress of the reservoir [2], which plays an important role in the field development: for example, the minimum stress knowledge is necessary constructions of geomechanical models of the field. In addition, there are techniques that allow use of the pressure curves to determine such important characteristics of the reservoir as the pressure of the fracture closure, a coefficient of fluid leakoff into the reservoir, permeability and an initial reservoir pressure [3, 4].

The basis of these techniques is the study of the pressure variations with time. Thus, Baree [4] gives three methods for studying the dependences of some transformed pressure functions versus time functions: G-function, square root of time and logarithm of time. The G-function method is based on the works of Nordgren [5] and Nolte [6], which considered the formation of a vertical fracture in the reservoir when the fluid is injected into a borehole, and the fluid flow inside the fracture. The technique is aimed at constructing the pressure dependence on dimensionless time-dependent function—G-function. Analysis of the pressure curves allows to determine the time of the fracture closure after the moment of stopping of the injection into the reservoir. The second method is described in Baree's paper [4], it is based on the construction of the pressure dependence on the square root of time and is used for verifying the correctness of the time of the fracture closure found by the first method. The third technique includes the study of the pressure curves versus time in the logarithmic scale. According to the typical behavior of the pressure decrease curve and its semi-logarithmic derivative, the flow regimes before and after the moment of the fracture closure can be determined.

Our paper presents the study of the pressure variations in time, which were obtained in two laboratory experiments. The curves of the pressure decrease in time were analyzed using the G-function technique in order to determine the time and the pressure of the fracture closure after stopping the injection of fluid into the formation.

2 Description of the Method

In accordance with the continuity equation for the injected fluid [5], the volume of the injected fluid is represented as the sum of the volume of the fluid leakoff into the reservoir and volume of the fluid in the cross section of the fracture. Nordgren wrote this equation in the form:

$$-\frac{\partial Q(z,t)}{\partial z} = \lambda(z,t) + \frac{\partial A(z,t)}{\partial t} \tag{1}$$

In the Eq. 1 the fluid loss per unit length and cross-sectional area are expressed by the corresponding formulas:

$$\lambda = \frac{2CH_p}{\sqrt{t - \tau(z)}} \tag{2}$$

$$A = \int_{-h/2}^{h/2} wdz = \frac{\pi}{4}Wh = \frac{\pi H^2}{2E'}p \tag{3}$$

where

Q	the rate of injection
C	the coefficient of the fluid loss
w	width of the fracture
H	the height of the fracture
H_p	the height over the fracture, where the leakoff into the formation emerges
τ	the time of the fraction growth to the point z
$E' = E/(1 - v^2),$	where E—Young modulus and v—Poisson coefficient.

Substituting the Eqs. (2) and (3) into the Eq. (1) and taking into account the boundary and the initial condition on the fluid flow in the fracture, it is possible to express the derivative of the pressure with respect to time.

By integrating the obtained expression over the entire length of the fracture, the pressure equation can be rewritten as in Nolte paper [6]:

$$\Delta P(\delta_0, \delta) = \frac{CH_pE'\sqrt{t_0}}{H^2\beta_s}G(\delta_0, \delta) \tag{4}$$

where

β_s the ratio of average pressure and wellbore pressure.

The Eq. 4 includes the dimensionless function (5), which is time-dependent and equal to the ratio of the difference between the current time and the injection stop time to the time of the injection stop, the pressure drop and the G-function, dimensionless time-dependent function:

$$\delta = \frac{\Delta t}{t_0} = \frac{t - t_0}{t_0} \tag{5}$$

$$\Delta P(\delta_0, \delta) = P(\delta_0) - P(\delta) \tag{6}$$

$$G(\delta_0, \delta) = \frac{16}{3\pi}[(1+\delta)^{3/2} - \delta^{3/2} - (1+\delta_0)^{3/2} + \delta_0^{3/2}] \tag{7}$$

where

t_0 the injection stop time
$\delta_0 - \delta$ function at the time of the injection stop.

After deducing the pressure dependence on the G-function, an important part of the considered technique is an observation of the behavior of the first derivative of the pressure with respect to G-function (G∂p/∂G), as well as semi-logarithmic derivative (∂p/(∂(ln(G))) = G∂p/∂G) of the pressure with respect to G-function. By considering the typical behavior of the curves, it is possible to determine the time of the fracture closure, and hence the pressure at the moment of the fracture closure. Castillo [7] in his work showed that if at the time of the fracture closure the fluid leakoff into the reservoir has a constant rate, the pressure dependence on the G-function, which is written by the formula (4), will look as a horizontal line expressed by the formula:

$$\frac{dP(\delta_0, \delta)}{dG(\delta_0, \delta)} = P_* \tag{8}$$

Accordingly, until the fracture closure, the plot of the semi-logarithmic pressure derivative versus G-function will be a straight line passing through the axis origin. Taking into consideration this typical behavior of the curves, the moment of the fracture closure is determined by the point of deviation of the semi-logarithmic curve of the pressure derivative versus G-function from the straight line passes through the axis origin. Moreover, this moment of time should correspond to the maximum on the curve of the first derivative of the pressure versus time.

3 Experiment Description

Hydraulic fracturing is a method of acting on a productive formation, which consists in creating a highly conductive fracture by pumping fluid into the well under high pressure.

Special experimental setup (Fig. 1) was constructed in order to model the hydraulic fracturing in the laboratory of the Sadovsky Institute of Geospheres Dynamics [8, 9]. Its construction includes upper and lower covers with thickness of 75 mm and an outer diameter of 600 mm, and a sidewall with a height of 75 mm, diameter of 430 mm and thickness of 25 mm. The covers are connected with each other by of sixteen studs. The working dimensions of the chamber: diameter—430 mm, height—66 mm. The rubber membrane separates the upper cover from
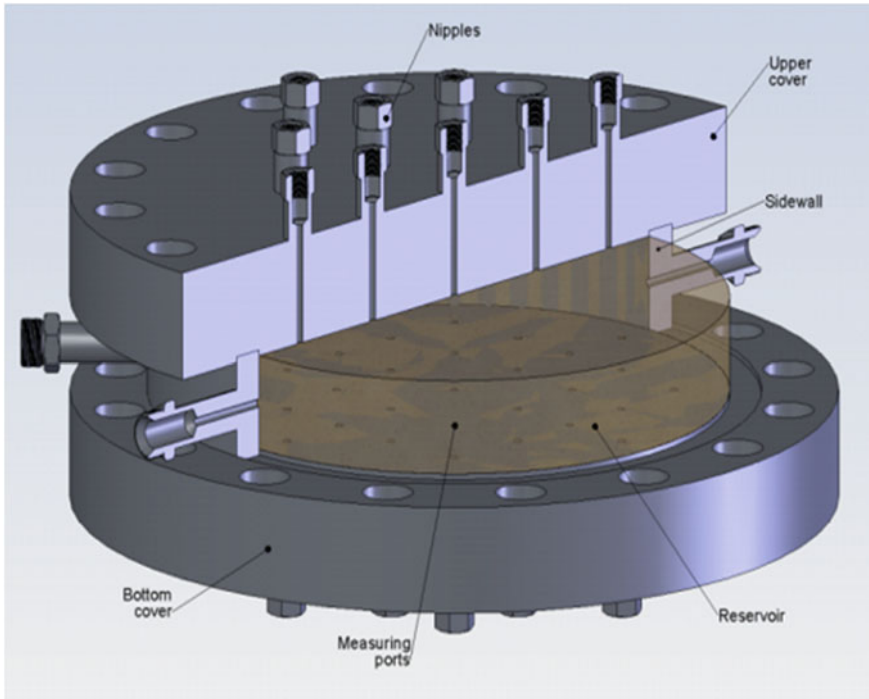
Fig. 1 Scheme of experimental setup

the model sample simulating the formation. A gap remains between the cover and the membrane, that gap is filled with water under pressure, which allows to simulate the lithostatic pressure to the formation model. The pressure above the membrane is provided and maintained by a separation cylinder, the upper part of which is filled with compressed nitrogen under the required pressure, and the lower part is filled with water. Horizontal stress is provided by sealed copper cameras located on the side walls of the chamber; the gas or liquid is pumped into that copper cameras.

The model formation is made from gypsum (calcium sulfate solution) with the addition of portland cement. The resulting substance has good initial fluidity and no shrinkage during solidification, which allows to get close contact with the walls of the experimental setup.

Hydraulic fracturing of the model reservoir is carried out by pumping vacuum oil into the central well with a constant flow rate through the hole in the lower cover. The time of fracturing was related with sharp decline in the fluid pressure measured in the well.

As a result of two experiments, the curves of the fluid pressure versus time were obtained and are presented in Figs. 2 and 3.
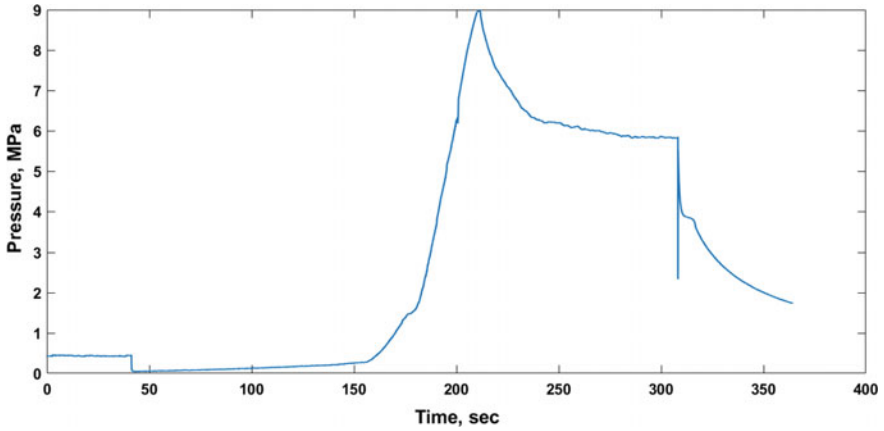
Fig. 2 Dependence of the fracturing fluid pressure with respect to time in the first experiment
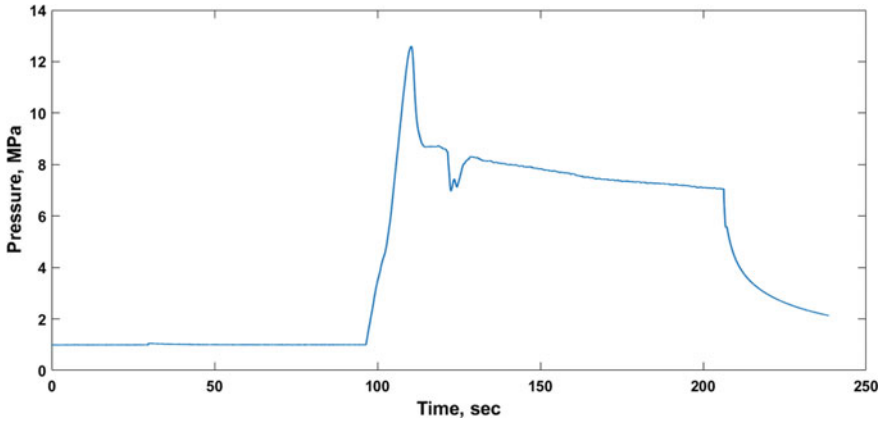
Fig. 3 Dependence of the fracturing fluid pressure with respect to time in the second experiment

4 Results of Application of the Methodology

The time-dependent pressure data, obtained during the experiment, were smoothed. After that the technique of the G-function was applied to the resulting curve.

4.1 The First Experiment

Firstly, the known time of the injection stopping was marked on the smoothed curve. Then the G-function is calculated according to the formula (7) at each
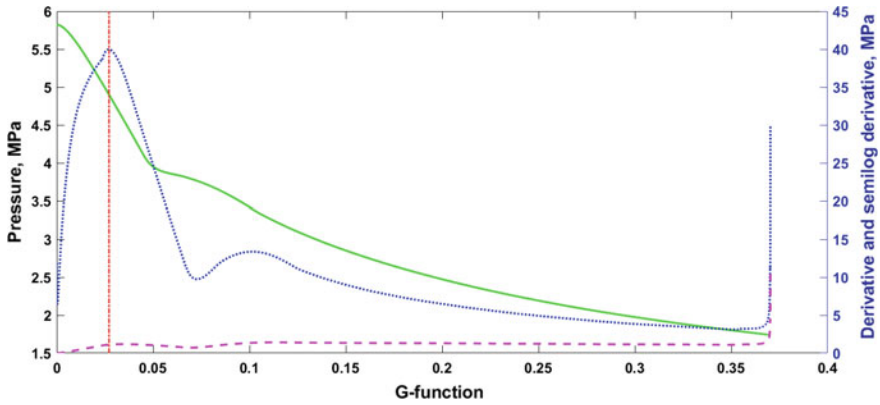
Fig. 4 Dependence of the pressure difference versus G-function is shown with solid green line. Values are marked on the left axis. Dependence of the pressure derivative versus G-function is shown with dotted blue line. Semi-logarithmic pressure derivative with respect to G-function is shown with dashed pink line. These values are marked on the right axis. The time of the fracture closure is shown with dash-dot vertical red line

moment of the time after stopping the fluid injection. Then the derivative and the logarithmic derivative of the pressure versus the G-function were calculated.

The Fig. 4 shows three dependencies: the pressure versus G-function, derivative of the pressure versus G-function, and semi-logarithmic pressure derivative versus G-function. The behavior of the semi-logarithmic derivative curve allows to observe, that at first it behaves almost like a straight line coming out of the axis origin. Then a more detailed examination of this curve revealed a point at which the curve ceased to behave as a straight line, which according to the G-function technique corresponds to the moment of the fracture closure. The correctness of this observation can be verified by the behavior of the first derivative of the pressure with respect to G-function, because the moment of the fracture closure must coincide with the maximum of the derivative, which can be seen in the Fig. 4. Thus, the closing time tc = 308.7 s was determined. Received time of the fracture closure corresponds to the pressure in the well, which is equal to 4.9 MPa.

There is an assumption in some papers, that the fracture closure pressure is approximately equal to the minimum tectonic stress. In considered experiments the minimum horizontal load on the sample was 0.6 MPa. The calculated fracture closure pressure turned out to be an order of magnitude higher. This discrepancy in the results does not allow us to make correct conclusions about the real value of the minimum tectonic stress based on the pressure of the hydraulic fracture closure, calculated as it was described above.
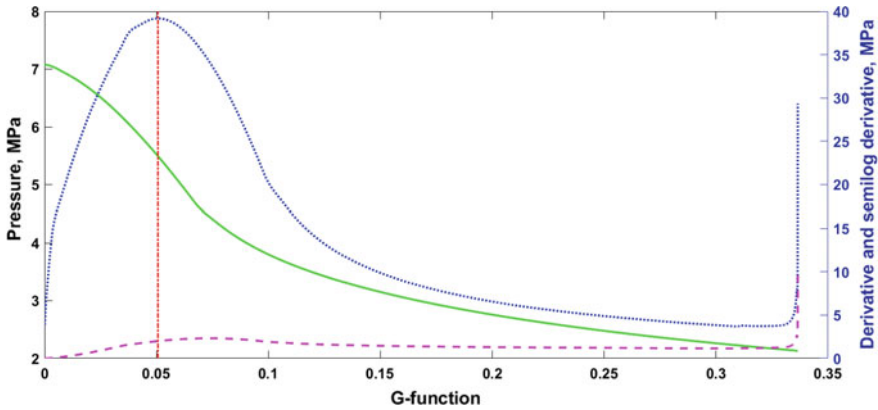
Fig. 5 Dependence of the pressure difference versus G-function is shown with solid green line. Values are marked on the left axis. Dependence of the pressure derivative versus G-function is shown with dotted blue line. Semi-logarithmic pressure derivative with respect to G-function is shown with dashed pink line. These values are marked on the right axis. The time of the fracture closure is shown with dash-dot vertical red line

4.2 The Second Experiment

The course of reasoning is similar to the description of the first experiment while applying the G-function technique to the data of the second experiment. The pressure dependence curves versus G-function, the pressure derivative versus the G-function, and the semi-logarithmic pressure derivative versus the G-function are also shown in Fig. 5.

The curve of the semi-logarithmic derivative behaves in the initial period of time as a straight line coming out of the axis origin, which allows with the more detailed examination to determine the inflection point, which in turn corresponds to the time of the fracture closure. As in the first experiment, there is a coincidence of the obtained time of the fracture closure with the maximum point of the first derivative of the pressure versus G-function. Thus, the time of the fracture closure is obtained as equal to tc = 207.8 s. Received time of the closing corresponds to the pressure in the well equal to 5.5 MPa, which also does not coincide with the horizontal load applied in the experiment.

5 Conclusions

In this paper, the analysis of the time-dependent pressure data obtained during the laboratory experiment on the hydraulic fracturing was carried out. The technique of G-function was studied in detail, which allows to determine the exact time of the fracture closure based on the observation of the characteristic behavior of the

pressure drop curves depending on a certain dimensionless function of time—G-function. Determination of the time of the fracture closure allows to determine the fracture closure pressure, which according to the presented results does not coincide with the minimum compressive stress in the experiment.

The reasons of that discrepancy should be studied in the further researches.

References

1. Turuntaev, S., Kocharyan, G.: Introduction to the geophysics of hydrocarbon deposits. MIPT (2007). (in Russian)
2. Koning, E.J.L., Niko, H.: Fractured water-injection wells: a pressure falloff test for determining fracture dimensions. Las Vegas (1985)
3. Soliman, M.Y.: Analysis of buildup tests with short producing time. New Orleans (1982)
4. Baree, R.D.: Holistic fracture diagnostic. USA (2007)
5. Nordgren, R.P.: Propagation of a vertical hydraulic fracture. Houston (1972)
6. Nolte, K.G.: Determination of fracture parameters from fracturing pressure decline. Las Vegas (1979)
7. Castillo, J.L.: Modified fracture pressure decline analysis including pressure-dependent leakoff. Denver (1987)
8. Trimonova, M., Baryshnikov, N., et al.: Estimation of the hydraulic fracture propagation rate in the laboratory experiment. In: Karev, V., et al. (eds.) Physical and Mathematical Modeling of Earth and Environment Processes, pp. 259–268. Springer International Publishing, Moscow (2018)
9. Trimonova, M., Baryshnikov, N., Zenchenko, E., Zenchenko, P., Turuntaev, S.: The Study of the Unstable Fracure Propagation in the Injection Well: Numerical and Laboratory Modeling (2017). SPE-187822-MS

Modeling of Fault Deformation Driven by Fluid Injection

Vasily Riga and Sergey Turuntaev

Abstract

A fault aseismic slip induced by fluid injection into the fault in homogeneous elastic low-permeable medium is considered numerically with the help of Embedded Discrete Fracture Model (EDFM). Modified two-parameter rate-and-state law was used to model the dynamics of the fault slip. The influence of the two-parametric friction law parameters and the rock filtration properties on the fault slip was considered. It was shown that the fault normal stiffness and remote shear stress resolved on the fault plane have the greatest impact on the fault deformation. It was found that the fault behavior is different for cases of impermeable and low-permeable matrix.

Keywords

EDFM · Fault deformation · Aseismic slip · Numerical modeling

V. Riga (✉) · S. Turuntaev
All-Russian Research Institute of Automatics, Moscow 127055, Russia
e-mail: rigavu92@gmail.com

S. Turuntaev
e-mail: s.turuntaev@gmail.com

S. Turuntaev
Sadovsky Institute of Geospheres Dynamics RAS, Moscow 119334, Russia

Moscow Institute of Physics and Technology, Moscow 141701, Russia

279

1 Introduction

Seismicity induced by underground fluid injection attracts a lot of attention of the society and scientific community. This is a result of an increase of the number of induced seismicity cases. To prevent the catastrophic seismic events, so-called "traffic light" principle is used [1]. But using of this principle is not enough. The modeling is required to take into account specific features of a site and main physical processes that take place there. Many of the existing models describe in detail the process of fluid filtration, poroelastic stress changes or stress changes due to slip of other faults.

In the presented paper, we are looking at the process of the fault weakening due to aseismic slip during fluid injection. We consider a single fault in infinite elastic homogeneous low-permeable medium as in [2] (Fig. 1). The fault is highly permeable and its permeability increases with growth of the fluid pressure inside it. To link the simulation and the real conditions, we take the bottom hole pressure history from [3] and elastic modulus and initial fault aperture from [2]. By numerical modeling we investigate what is an impact of the different parameters of the model like the fault normal stiffness, matrix permeability and the used friction law form on the fault deformation. Aseismic slip could lead to shear stress concentration at some areas, and this fact should be taken into account for future operations.

For the slip description, we use a bit more complicated form of the friction law than usually used "classical" one-parameter rate-and-state law, because we showed in earlier works [4] that it is the two-parameter form of the rate-and-state law, which allows to describe with great accuracy the fault motion observed in laboratory experiments. Here we investigate what is the degree of the friction law influence on behavior of the real-scale fault subjected to water injection.
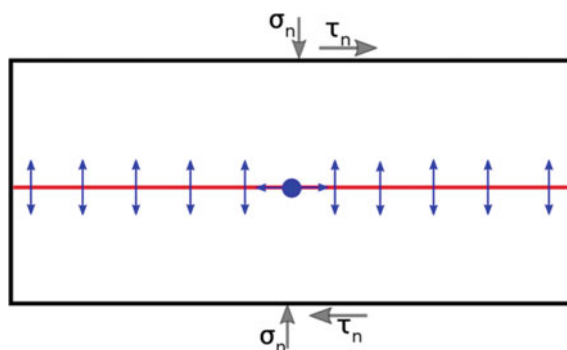
Fig. 1 Model geometry

2 Modeling of Fluid Injection and Induced Fault Slip

We consider simplified uncoupled model of the fluid filtration and stress change due to fluid injection into the fault. The fault permeability increase is caused only by the pressure change, the change of the normal stress due to the fault opening is neglected. So, there are consequent two steps of modeling. On the first one, the evolution of the fluid pressure inside the fault is calculated, on the second step the fault deformation is calculated.

2.1 Filtration Model

We use EDFM method to model the fluid filtration inside the fault. The main idea is that grids for matrix and for the fault are created separately, and so, the matrix grid could be structured without refinements. We have implemented EDFM in Matlab Simulation Toolbox (MRST) [5] with some modifications. The governing equations for the system are the single-phase continuity equation and Darcy's equation:

$$\frac{\partial}{\partial t}(\varphi\rho) + \nabla \cdot (\rho\vec{v}) = q \tag{1}$$

$$\vec{v} = -\frac{k}{\mu}\nabla \mathrm{p} \tag{2}$$

where φ is porosity, ρ is fluid density, $\vec{v}$ is Darcy velocity, q is source term, k is permeability, μ is fluid viscosity.

For the fault permeability we used cubic law [6]. The hydraulic aperture of the fault varies as a function of the change in effective normal stress or change in the fluid pressure, as we neglect the total normal stress change:

$$a_h = a_{h0} + \frac{\Delta p}{k_n} \tag{3}$$

where a_{h0} is initial aperture, k_n is the fault normal stiffness (Pa/m).

Matrix domain and the fault interact through the flux between them. We used two-point flux-approximation scheme (TPFA) where the flux between the two computational cells i and j is proportional to the pressure difference:

$$v_{ij} = \frac{T_{ij}}{\mu}(p_i - p_j) \tag{4}$$

where T_{ij} is transmissibility between the cells i and j, μ is the fluid viscosity.

The transmissibility for the two cells depends on type of these cells. For two matrix cells it is:
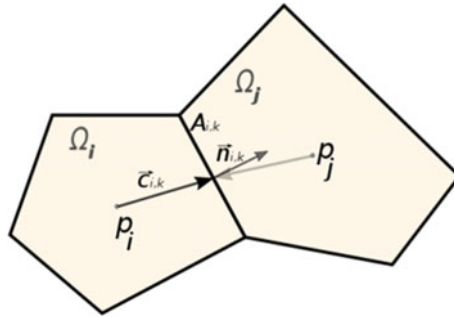
Fig. 2 Two cells used to define finite-volume discretization

$$T_{ik} = \frac{T_{i,k} + T_{k,i}}{T_{i,k} \cdot T_{k,i}} \tag{5}$$

$$T_{i,k} = A_{i,k} k_i \frac{\vec{c}_{i,k} \cdot \vec{n}_{i,k}}{|\vec{c}_{i,k}|^2} \tag{6}$$

where $T_{i,k}$ is one-sided transmissibility or half-transmissibility, $A_{i,k}$ is area (or length in 1D) of common boundary of the two cells, $\vec{c}_{i,k}$ is vector from center of the cell i to the center of the common boundary, $\vec{n}_{i,k}$—normal vector to the boundary (Fig. 2).

For the well and the fault element [7]:

$$T_{fk,w} = \frac{2he_k^3}{12a_k} \tag{7}$$

where e_k—is aperture of the kth element of the fracture connected with the well, a_k is the element length.

2.2 Geomechanical Modeling

To model the fault slip, we used displacement discontinuity method. We consider a horizontal fault in infinite homogeneous elastic media. The fault is represented as a set of elements. Displacement discontinuity over each element is constant. Here we neglect the stress changes due to the normal displacement and consider only the shear displacement. The displacement discontinuity of any element leads to change of the stress state of the system, specifically to change of the shear stress acting on the neighboring elements (Fig. 3). So, the change of the shear stress of ith element at some time is:

$$\Delta \tau_i(t) = K_{ij}^s \delta_j(t) \tag{8}$$
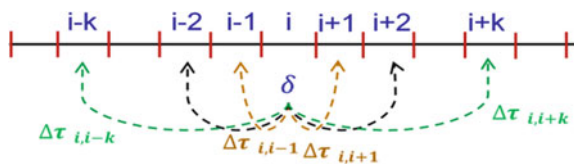
Fig. 3 Change of the shear stress acting on neighboring elements due to the displacement discontinuity on ith element

The corresponding expressions for the stiffness matrix K_{ij}^s are taken from [8]. For the fault divided into equal elements with length *2l*:

$$K_{i,i\pm k}^s = -\frac{G}{\pi(1-v)(2k^2-1)l} \tag{9}$$

where *G* is shear modulus.

For $k > 6$ the stiffness decreases more than 100 times, so it is possible to neglect these terms.

For every element, the slip velocity is defined as time derivative of the displacement discontinuity. Initially the fault doesn't slip, but numerically this situation is described as a slip with very slow rate (10^{-10} m/s). The element slip initiates in accordance with Mohr-Coulomb criterion. While the shear stress is less than the friction force, the element doesn't slip. Otherwise the slip rate is determined by equality of the shear stress and the friction force:

$$\tau = \mu_f \sigma_n' + S_0 \tag{10}$$

where μ_f is the friction coefficient, S_0 is cohesion, σ_n' is the effective normal stress acting on the fault, τ is the shear stress.

The two-parameter rate-and-state law can be written as [9]:

$$\mu_f = \mu_0 + a\ln\left(\frac{|v|}{v^*}\right) + \theta_1 + \theta_2$$
$$\dot{\theta}_i = -\frac{v}{L_i}\left[\theta_i + b_i\ln\left(\frac{v}{v_*}\right)\right] \tag{11}$$

This form was used because (as it was shown in [4]) it allows to describe the chaotic motion and complex regimes of sliding [10]. It should be noted that when $L_1 = L_2$ the two-parameter law become the one-parameter law with $b = b_1 + b_2$:

$$\mu_f = \mu_0 + a\ln\left(\frac{|v|}{v^*}\right) + \theta$$
$$\dot{\theta} = -\frac{v}{L}\left[\theta + b\ln\left(\frac{v}{v_*}\right)\right]$$

In our work, we consider the influence of the friction law form on the fault displacement during aseismic sliding. Corresponding system of equations was solved numerically by using explicit third-order Runge-Kutta method with adaptive time stepping [11].

3 Results

3.1 Model Setup

The size of the model was 800×200 m. Values of the basic variables were taken from [2]. In our model, the bottom hole pressure variations were taken from [3] (Fig. 4).

We considered several cases and changed the matrix permeability from 0 to 2 μD. The initial fault aperture was 9 μm, the shear modulus G was 9 GPa. The normal stiffness of the fault was varied from 8×10^{11} to 0.25×10^{11} Pa/m, that corresponds to the change of the fault maximum permeability from factor ~ 2 to ~ 270. The initial effective normal stress $\sigma'_{n,0}$ was 4.25 MPa, μ_0 was 0.6. We used three values of the initial shear stress τ_0 (1.65, 1.8 and MPa), different values of the friction law parameters: $b_1 + b_2 - a = 0.002$, $a = 0.015$, $\frac{b_2}{b_1} = 1 \div 10$, $\frac{L_2}{L_1} = 0.5 \div 10$. When we change b_2/b_1, we saved the difference $b_1 + b_2 - a$.

3.2 Results

Figures 5 and 6 show how the shear stress along the fault at $t = 1400$ s changes with change of the normal stiffness and permeability. The data indicates that for the
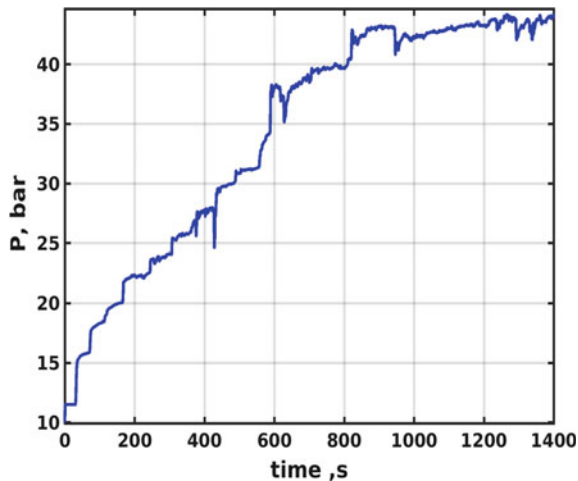
Fig. 4 Fluid pressure
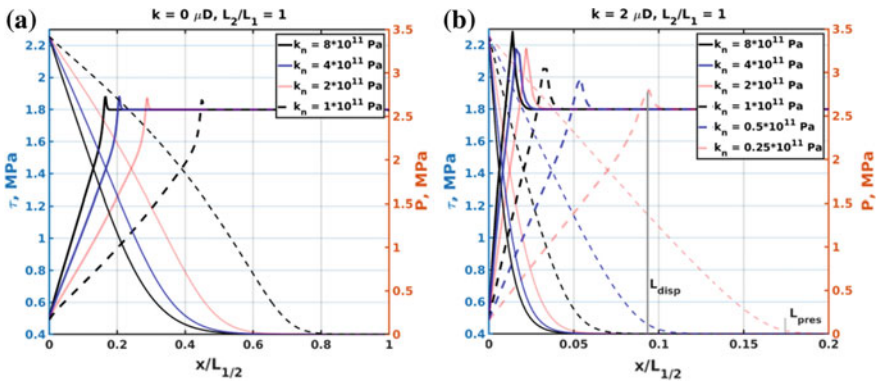
Fig. 5 Half-profiles of shear stress and pore pressure along the fault at the end of calculation for different values of normal stiffness and matrix permeability ($\tau_0 = 1.8$MPa): **a** impermeable matrix **b** low-permeable matrix, positions of the maximum shear stress (L_{disp}) and pressure front (L_{pres}) are shown by vertical gray lines
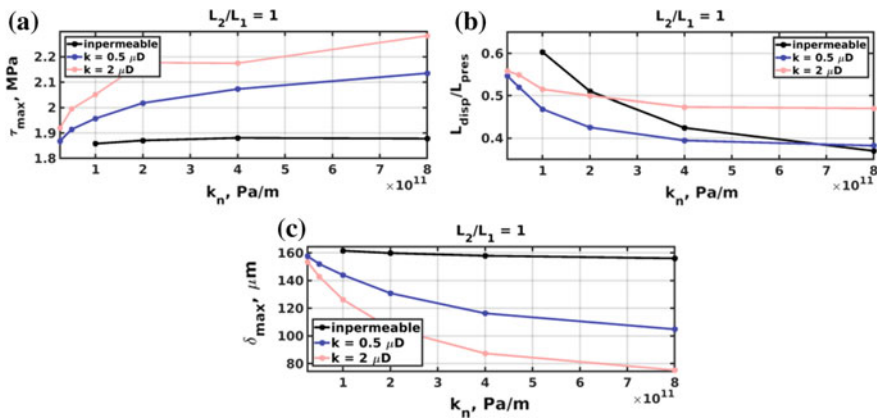
Fig. 6 Influence of the fault normal stiffness, matrix permeability ($\tau_0 = 1.8$ MPa) on: **a** maximum shear stress at the end of the calculations **b** relative position of the shear-stress (L_{disp}/L_{pres}) **c** displacement at the center of the fault

impermeable matrix case, the normal stiffness almost doesn't affect the maximum shear stress. For case of the low-permeable matrix, the growth of the normal stiffness leads to increase of the maximum shear stress and this dependency is more pronounced for larger values of the matrix permeability. The same behavior could be seen for slip at the center of the fault: for the case of impermeable matrix, the displacement doesn't depend on the normal stiffness, but there is strong dependence for the case of the low-permeable matrix. Relative location of maximum shear stress

depends on the normal stiffness for all cases and mostly for impermeable matrix. Overall dependence of this value on the matrix permeability isn't linear.

The parameters of the rate-and-state law have no so significant effect on the fracture deformation (Fig. 7). Considering the case of the one-parameter rate-and-state law as a base ($L_2/L_1 = 1$), the maximum change of the fault deformation parameters is no more than $\sim 2\%$. The most significant influence on the parameters of the fault deformation has the parameter L_2/L_1, but not B_2/B_1. With change of L_2/L_1 from 1 to lower or to larger values, the two-parameter rate-and-state law begin differ more and more from the one-parameter version, in particular, the parameters θ_1 and θ_2 changes on different spatial scales, that causes different response to the velocity change. The fact, that B_2/B_1 does not almost affect the system, indicates that the parameter $B_1 + B_2$ seems to be crucial.

Initial shear stress τ_0 influences on the fault displacement and on the slip length (characterized by the position of the shear stress maximum) are followings: the grater the initial shear is—the grater these characteristics are. But the difference $\tau_{max} - \tau_0$ is almost the same for all the values of τ_0. These results are expected, because with increase of τ_0 the fault becomes closer to the critical state. Also, it is worth to note that the increase of the fault displacement is greater ($\sim 32\%$) than the increase of τ_0 (21%), so when τ_0 approaches to critical value, the significant growth of the fault displacement should be expected.

4 Discussion and Conclusions

The problem of the influence of the matrix permeability, the fault normal stiffness and the parameters of the rate-and-state law on the fault deformation was studied by numerical simulation. Cases of the water injection in the single fault in homogeneous low-permeable or impermeable elastic media were considered. The model of the fluid filtration and the fault deformation was uncoupled.

It was shown, that the matrix permeability influences on the dependence of the fault deformation on the normal stiffness. The fault stiffness has greater impact on the position of the slip front relative to the pressure diffusion front for cases where the matrix is less permeable. If we consider the maximum displacement of the fault or maximum shear stress, the behavior is opposite. These differences could be explained by qualitatively different profile of the pore pressure for cases of impermeable and low-permeable matrix. These results could be used for assessment of risks of induced seismicity. For example it's relevant for heterogeneous fault where there are less stable parts of the fault in neighboring. We can conclude that for our model the slip is mainly driven by the fluid pressure change and the cases of impermeable and low-impermeable matrix should be studied separately and more closely in the future.

As for friction law, we see that use of the two-parameter law give some changes to the fault deformation. The ratio of L_2 and L_1 has greatest impact on the fault deformation. Ratio of B_2/B_1 at the fixed value of their sum has not such a matter.
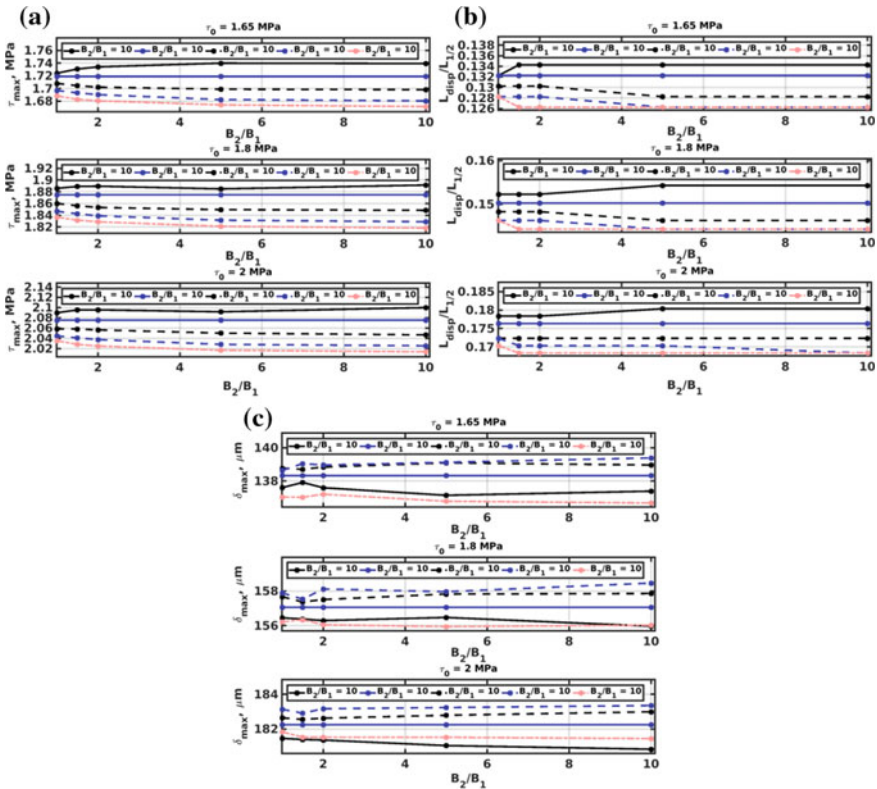
Fig. 7 Dependences of **a** maximum shear stress, **b** its position relative to the half-length and **c** displacement in the center of the fault on the parameters of the two-parameter rate-and-state law and initial shear stress ($k_m = 0.5 \, \mu D$, $k_n = 0.5 \cdot 10^{11}$ Pa/m)

We could expect that these changes would be more pronounced and crucial for cases of the seismic slip than for aseismic one.

Our model has potential for future study of the induced seismicity. Some improvement should be done. One of them is the coupled model, which could allow to estimate the dependence of the seismicity on volume of injected water for different cases. Also, we show that the friction law could matter, and further researches in this direction are needed.

References

1. Bommer, J.J., Oates, S., Cepeda, J.M., Lindholm, C., Bird, J.F., Torres, R., Marroquin, G., Rivas, J.: Control of hazard due to seismicity induced by a hot fractured rock geothermal project. Eng. Geol. **83**(4), 287–306 (2006). https://doi.org/10.1016/j.enggeo.2005.11.002

2. Cappa, F., Guglielmi, Y., Nussbaum, C., Birkholzer, J.: On the relationship between fault permeability increases, induced stress perturbation, and the growth of aseismic slip during fluid injection. Geophys. Res. Lett. **45**(20), 11–12 (2018). https://doi.org/10.1029/2018gl080233

3. Guglielmi, Y., Cappa, F., Avouac, J.-P., Henry, P., Elsworth, D.: Seismicity triggered by fluid injections induced aseismic slip. Science **348**(6240), 1224–1226 (2015). https://doi.org/10.1126/science.aab0476

4. Turuntaev, S.B., Riga, V.Y.: Rate-state based simulation of laboratory and natural-induced seismicity. In: SEG Technical Program Expanded Abstracts, pp. 5002–5006 (2018). https://doi.org/10.1190/segam2018-2998197.1

5. Lie, K.-A.: An Introduction to Reservoir Simulation Using MATLAB: User guide for the Matlab Reservoir Simulation Toolbox (MRST). SINTEF ICT (2016)

6. Jaeger, J.C., Cook, N.G.W., Zimmerman, R.W.: Fundamentals of Rock Mechanics, 4th edn. Blackwell Publishing, Malden (2007)

7. McClure, M.W., Horne, R.N.: Discrete Fracture Network Modeling of Hydraulic Stimulation: Coupling Flow and Geomechanics. Springer, Berlin (2013)

8. Shou, K.J., Crouch, S.L.: A higher order displacement discontinuity method for analysis of crack problems. Int. J. Rock Mech. Min. Sci. Geomech. Abstr. **32**(1), 49–55 (1995). https://doi.org/10.1016/0148-9062(94)00016-v

9. Hobbs, B.E.: Chaotic behaviour of frictional shear instabilities. In: Rockbursts and Seismicity in Mine, Mineapolis, pp. 87–91 (1990)

10. Budkov, A.M., Kocharyan, G.G.: Experimental study of different modes of block sliding along interface. Part 3. Numerical modeling. Phys. Mesomechan. **20**, 203–208 (2017). https://doi.org/10.1134/s1029959917020102

11. Noda, H., Dunham, E., Rice, J.R.: Earthquake ruptures with thermal weakening and the operation of major faults at low overall stress levels. J. Geophys. Res. **114**, B07302 (2009). https://doi.org/10.1029/2008JB006143

Measurement of Gas-Dynamic Parameters of Superheated Gas Flow in Slit, Applicable to the Bazhenov Formation

Aliya Tairova and Georgy Belyakov

Abstract

The paper describes the results of a laboratory study of the filtration of hot gas flows in a gap during the evaporation of its walls as applied to the Bazhenov formation. The slit imitated a crack in a shale layer, which was modeled by plexiglass plates that make up the cell. The slit was blown by heated gas flows. During the experiment, a change in the mass of the cell and a pressure differential was recorded, on the basis of which the flow rates were estimated. The evaporation rate and ablation of the mass of material from the surface of the slit were also measured. The flow measurement technique presented in the work allowed determining the coefficient of extraction of liquid and gas phases of hydrocarbons from shale.

Keywords

Exothermic reaction · Evaporation · Flow rate · Flow density

A. Tairova (✉) · G. Belyakov
Sadovsky Institute of Geospheres Dynamics RAS, Leninskiy Prospect, 38, K.1, 119334 Moscow, Russia
e-mail: moscouposte@gmail.com

A. Tairova
Moscow Institute of Physics and Technology (State University), 141701 Dolgoprudnyi, Russian Federation

1 Introduction

One of the key strategies of petroleum production development at present is related with the development of reserves of the Bazhenov Formation. The Bazhenov Formation is an unconventional reservoir, which is characterized by high oil saturation and where hydrocarbons can be present both in shale and highly productive lenses. However, the key potential of the Bazhenov Formation is predominantly related with kerogen, which is contained in oil shales. Two groups of technology exist at present for extracting oil from kerogen, contained in shales and they are ex situ and in situ shale oil mining technology. The first group of methods, i.e. ex situ technology involves shale rock extraction by open-pit or mined method with subsequent processing the shale rock on surface. The second group of methods, i.e. in situ technology involves oil extraction from kerogen without lifting the rock onto the surface. The latter methods provide the scope to carry out cost-effective oil production at significant depths in comparison to ex situ methods. According to experimental studies, hydrocarbon extraction from kerogen is practicable when subjected to temperatures above 100 °C. Therefore, one of the technologies being designed present day, is the thermal gas treatment method. The method principle lies in pumping air into the seam and transforming the seam into displacement agents. Several specific problems related with modelling the under-surface hydrodynamics exist in such case. It is necessary to be aware of the interaction processes between preheated agents and forming the layers of hydrocarbon phases in the seam, in order to optimize the technological effects. The nature of these processes is quite complex and multi-phase. It is assumed that heat generation or combustion wave zone advance, heating-up the surrounding layers of oil-source rock and kerogen, at pumping-in air mixture in the fissured interstratified layers. Filtration of re-formed gas agents and liquid hydrocarbons, extracted from kerogen, takes place simultaneously with the advance of heat-up front. The passage of heat-up front causes a change in filtration properties of the reservoir by changing the reservoir permeability. The process can lead to an increased inflow of air mixture, local acceleration of kerogen degradation process and stability loss of the heat-up front. Within a framework of the above-mentioned problem, it is intended to study the behaviour pattern of filtration flows, caused by changes in phase composition of the substances of porous reservoir matrix, i.e. reservoir melting, gasification and condensation, by means of laboratory modelling method.

It is necessary to be aware of the course of interaction processes between heated gas flows and hydrocarbon phases of the seam material in the fissure, in order to optimize the degradation process of seam material. An important task emerges in practical terms, being the subject of this work, i.e. to determine the hydrocarbon material flowrate, rarefied by the concurrent stream of hot gas and exerting influence on the flow.

2 Experiments

Experiments were carried out on original laboratory setup. Flat slit of the cell (Fig. 1) of length $l = 30$ cm and opening (aperture) $h = 0, 2$ cm, made of poly methyl metacrylat glass sheets, had an initial free-distance area of $S_0 = 1, 2$ cm^2. Three steel-armoured spokes with a diameter of 0.2 cm each, are inserted along the cell at an equal distance from each other in order to prevent the slit narrowing at heat-up. The differential air pressure value, measured by pressure gauge (6) at the length of the cell from the operation of the pump-turbine (8), was $\Delta p = p_0 - p = 50 \cdot 10^3$ g/(cm s^2). The gas stream, created by the pressure drop Δp proceeded along the slit and then exited to the vertical tube (3), without friction, connected to the tube by the cross-sectional area $S = 0.38$ sm^2 and exiting to the pump-turbine. The differential air pressure value, measured by pressure gauge (6) at the length of the cell from the operation of the pump-turbine (8), was $\Delta p = p_0 - p = 50 \cdot 10^3$ g/(cm s^2).

The gas stream, created by the pressure drop Δp proceeded along the slit and then exited to the vertical tube (3), without friction, connected to the tube by the cross-sectional area $S = 0.38$ sm^2 and exiting to the pump-turbine. Measurement of the vertical force of impact on the gas stream cell was carried out by scales (5) of Shinko AJH 4200 model, in the course of the experiment and the measurement accuracy of these scales was 0.01 g.
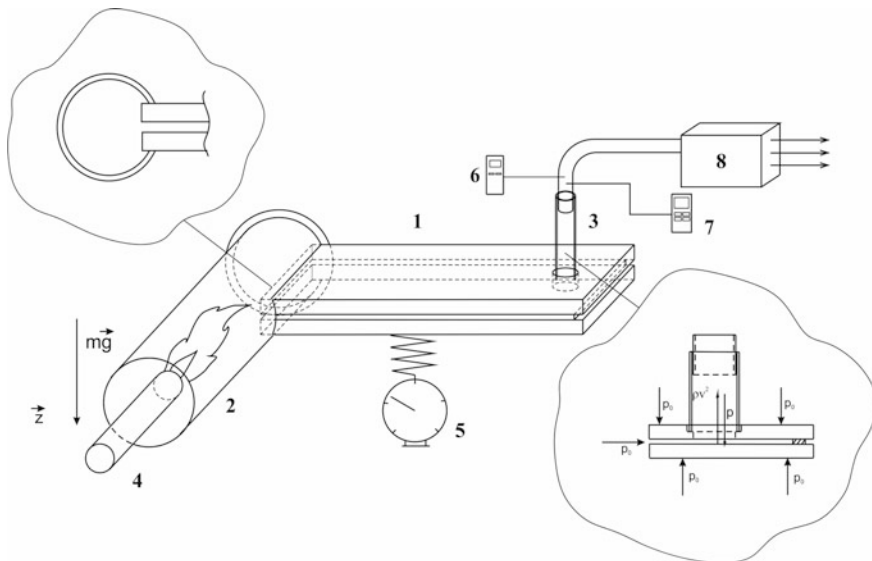
Fig. 1 The experimental setup scheme: 1—the cell, 2—combustion chamber, 3—vertical tube, 4—gas burner, 5—precision balance, 6—manometer, 7—thermometer, 8—turbopump

3   Results and Discussion

The velocity determination is only made possible by means of experiments. It is assumed that the front of constant average stream velocity is perpendicular to the slit surface for turbulent flow and the near-wall gas layer, moving at a speed different from the average speed, is thin and does not significantly affect the stream velocity value. According to the experiment flowchart (Fig. 1), the cell is placed horizontally on the scales. The sum of forces, acting on the cell in the direction of z axis, is balanced by the gas stream pulse through vertical tube outlet and which is connected friction-free along the z axis to the pipeline of the turbine-pump. At a considerably slow mass rarefaction from slit surfaces and for a steady-state flow, the equilibrium equation becomes (Table 1):

$$-N + \dot{m}gt = -(p_0 - p)S + \rho v^2 S \tag{1}$$

The pressure and temperature of the gas at the outlet of the cell are recorded by pressure gauge and thermocouple, respectively (Fig. 2). The pre-weighing result of the cell before switching on the turbine-pump is taken as the reference starting point of forces, acting in the direction of z axis. The maximum rarefaction from the turbine-pump operation at zero stream rate $p \simeq 100$ mbar. A record of the scale readings, pressure and temperature difference at the outlet of the cell is shown in Fig. 2. Instants of time, specific to the experiment in Fig. 2, are illustrated in figures. The range of digits from 0 to 7 corresponds to the total time of the experiment. A section of the record in Fig. 2 in a course of time corresponds to the initial readings of mass, pressure and temperature, recorded by measuring devices before switching on the turbine-pump. Subsequently, the turbine-pump operates from instant 1 to instant 2, which in the course of time of approximately 1 min (till instant 2) causes a constant air flow from pressure drop.

Based on the readings of the scales and pressure gauge at achieving equilibrium, the steady-state stream velocity at the outlet tube section is calculated according to Eq. (1):

Table 1   Equation (1) input parameters

Letter	Input parameters
S	Output section of the tube;
p_0, p	Pressure, respectively, at the inlet and outlet of the cell;
N	Support reaction along the z axis of the cell lying on the scales;
$\dot{m}$	Is weight loss of the cell at instant of time t as a result of wall material evaporation and rarefaction;
$\dot{m}gt$	Is mass evaporation rate of the cell surfaces;
$(p_0 - p)S$	"Lifting" force of the cell;
$\rho v^2 S$	Is "thrust" force along z axis
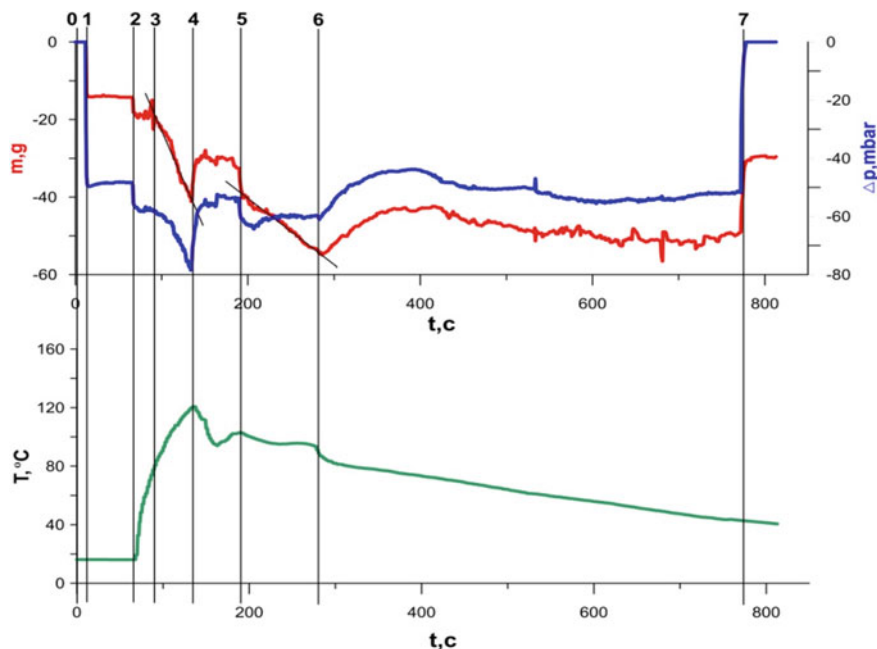
Fig. 2 Instrument readings: red is the balance, blue is the manometer, green is the thermometer. Stages of experiments: 1—pump start, 2—turn the burner, 3—the beginning of the material evaporation, 4—turn off the burner, 5—turn the burner, 6—stopping the burner, 7—switch the pump

$$v_t = \sqrt{\frac{\frac{-N}{S} + (p_0 - p)}{\rho}} = 52 \, \text{m/s} \tag{2}$$

where $\rho = \frac{p\mu}{RT}$, μ—is the molecular weight of air.

The corresponding cell flowrate in slit is equal to $v_c = \frac{S}{S_0 - S_{\text{eff}}} \cdot v_t = 33 \, \text{m/s}$, where S_{eff} is effective area of cross section of the cell.

In conformity with Fig. 2 at instant of time 2, the gas burner is switched on and the propane-butane mixture with specific combustion $Q = 4 \cdot 10^{11}$ erg/g is consumed here. Fuel consumption in the burner is constant and the value is $\bar{m} = 5 \cdot 10^{-2}$ g/s. This value is much less than the mass of the air stream ($\dot{m} = \rho v_t S \approx 3,6$ g/s), flowing through the cell i.e. v_t is the gas flow velocity in quartz tube 3 in Fig. 1. A streamtube of air-propane mixture is formed and burns out at the outlet of burner tube with a diameter of d = 2 cm. The burner tube is inserted at a depth of 2 cm in the quartz bucket of 4 cm diameter, thus forming a combustion chamber between the tube and the inlet to the cell. The side surface of the bucket has a notch to suit the cell end size (Fig. 1).

It is expected that the burner design (i.e. a welding torch) is worked out in such a way that combustion rate of the propane-air mixture corresponds to the stoichiometric reaction equation:

$$C_3H_8 + 5O_2 = 3CO_2 + 4H_2O + q^* \qquad (3)$$
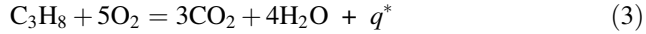
where $q*$ is the heat produced during combustion reaction of the propane-air mixture. According to the latter equation, it follows that the number of fuel moles, which are reacting at its nominal mass flowrate, should correspond to 5 times the number of oxygen moles that is contained in the air flow i.e.

$$\frac{\bar{m}}{\mu_1} = \frac{\frac{\pi d^2}{4} \cdot v_s \rho_0 \cdot 0.2}{5\mu_2},$$

where $\mu_1 = 44$ is molecular weight of propane; $\mu_2 = 32$ is molecular weight of oxygen; v_s is air stream velocity, $\rho_0 = 1,2 \cdot 10^{-3} \text{g/cm}^3$. Thus, the design speed of stoichiometric air flow from the burner nozzle is $v_s = 2.41$ m/s. The mass flowrate of the burner gas corresponds to the heat release rate and is equal to $q* = \frac{Q \cdot \bar{m}}{S_{eff}} = \frac{2 \cdot 10^{10}}{S_{eff}}$ erg/(s cm^2), where S_{eff} is the area of effective heat release. The flowrate increment in any place of the cell, which depends on both the amount of heat released in the combustion chamber $q*$ and the heat absorbed by the slit walls $q** q**$ can be difficult to evaluate. The flowrate increment can be determined by simultaneous solution of the equations of mass, momentum and energy flows through the reference surfaces of inlet and outlet of the combustion chamber [1, 2]:

$$\dot{m} = S\rho v = Sj = \text{const} \qquad (4)$$

$$\Delta(p + jv) = 0 \qquad (5)$$

$$\Delta[j(\frac{v^2}{2} + \frac{\gamma p}{(\gamma - 1)\rho})] = q* - q** \qquad (6)$$

and the simultaneous solution of the following equation determines the flowrate increment

$$\Delta v = \frac{(\gamma - 1) \cdot (q* - q**)}{\rho(c^2 - v^2)} \qquad (7)$$

where $c^2 = \gamma \frac{p}{\rho}$ is the sound speed ($\gamma = 1,4$). The value of mass ablation from the slit surface can be neglected for a short period of time and the flowrate at the end of the cell is determined from the Eq. (1): $v_q = 64$ m/s. The value of velocity increment from heating is $\Delta v = v_q - v_t \sim 12$ m/s.

A small end part of the cell, concaved inwardly the volume of the combustion chamber, is located near the flame from the burner nozzle, where the temperature is $T_{\mathrm{comb}} \simeq 700\,°C$ much higher than the boiling temperature of acrylic glass $T_{boil} \simeq 200\,°C$. This part quickly boils over volumetrically, turning into steam and liquid spray (Fig. 2). The boiling mass, mixing with the gas stream, slows its speed. A partial "blockage" of the stream exists at the inlet to the cell. Stream stagnation at a running turbine-pump leads to an increase in rarefaction in the cell of up to 80 millibars. After switching off the burner (i.e. time interval), the rarefaction is reduced to a value corresponding to the rarefaction from the operation of the turbine-pump, to absence of heat generation in the combustion chamber. An increase in rarefaction takes place when the burner is switched on again (Fig. 2). The rarefaction remains constant at 60 millibars level, which corresponds to the previous gas stream density.

4 Conclusion

As a result of the action of hot gas stream, the material of the slit surface evaporates and is rarefied by the flow. The value of rarefied mass, measured in steady-state mode ($\Delta t \sim 5 \div 6$), is approximately $m \simeq 15\,g$. The evaporation and rarefaction rate of the mass by the stream during the time interval remains constant: $\frac{dN}{gdt} = \mathrm{const} = \dot{m} = 0,16\,g/s$. During the operating time of the burner, the mass of the burnt propane-butane mixture $\hat{m}\Delta t = 0,05 \cdot 93 = 4,65\,g$. Presuming that the material of the cell walls "corresponds" to the oil shale material, the "production" efficiency at combustion of oil shale, or propane-butane mixture is equal. Thus, the proposed method can illustrate a high-scale extraction of hydrocarbons from shale deposits.

References

1. Landau, L.D., Levich, E.M.: Hydrodynamics, 3d edn. Nauka, Moscow (1986). (in Russian)
2. Sedov, L.I.: A Course in Continuum Mechanics, vol. 2, 4th edn. Nauka, Moscow (1984). (in Russian)

Structural Transformations of the Nanoconfined Water at High Pressures: A Potential Factor for Dynamic Rupture in the Subduction Zones

Alexey Tsukanov , Evgeny Shilko and Sergey Psakhie

Abstract Confined in porous oceanic minerals, the subducted water alters physical and mechanical properties of host rocks, induces their super-hydration and thereby plays an important role in geodynamics. Under the extremal conditions of subduction zones, water can be trapped inside nanoscale slit-shaped pores of hydrophilic minerals as layered oxides/hydroxides. The structure and mechanical properties of water in such nanopores are quite different from those in normal bulk conditions. To understand how the nanoconfined water affects the properties of water-saturated rocks at extreme pressure conditions corresponding to subducting slabs, we use the atomistic molecular dynamics simulations. Considering a water-filled layered mineral $Me^{II}(OH)_2$, in which Me^{II} is some divalent metal, we found two points of nanoconfined water phase transition in slit-shaped nanopore within pressure range 0.1–10 GPa: transformation from liquid phase to hexagonal close-packed (HCP) crystal at pressure 3.0 GPa and HCP to face-centered cubic (FCC) crystal transformation at 6.7 GPa. Moreover, the phase transformations of water in the nanopore of the mineral are accompanied by a stepwise reversible increase in the compressibility of water up to 1–1.5 orders of magnitude. Strong transient variations in the compressibility of confined water can cause significant difference in local values of compressive mean stress grow rate in heterogeneous subducting slab, thus contributing to localization of shear strain and initiation of dynamic rupture.

A. Tsukanov (✉) · E. Shilko · S. Psakhie
Institute of Strength Physics and Materials Science, Siberian Branch of Russian
Academy of Sciences (ISPMS SB RAS), 634055 Tomsk, Russia
e-mail: a.a.tsukanov@yandex.ru

1 Introduction

Water being a very common substance in the Earth crust is involved in a variety of geodynamic processes in a wide range of depths down to the deep mantle. During the subduction process, the water masses captured by porous minerals of oceanic sediments and oceanic plate can submerge under the continental crust into great depths, reaching the upper mantle and the transition zone [1, 2]. Under these conditions, water is one of the key factors of the subduction process, including the dynamics of lithospheric plates migration, as well as the geometry of the subducting plate and the elastic stress field [3, 4].

High pressures $\sim 10^9$–10^{10} Pa, which are typical for depths from tens to hundreds of kilometers, lead to minerals compaction with the significant decrease of their porosity. Only nanoscale pores can be persisted in minerals under such conditions. In addition, the counter-intuitive pressure-induced water insertion into hydrophilic layered minerals can take place at extreme gigapascal pressures [5]. In particular, it has been reported that under the influence of high pressure the water molecules intercalate into the interlayer region of clay minerals such as kaolinite (at ~ 2.7 GPa) [6] and sodium hectorite (at 1.7 GPa) [7], forming super-hydrated phases of these minerals. The subducted water can be released in a wide range of depths, depending on host mineral [8, 9], and completes its deep cycle by degassing through arc volcanoes [10].

Confined water, being a component of the hydrated mineral, affects its physical (mechanical) and chemical properties. A striking example is the "water-induced" decrease in strength and melting temperature of rocks, which largely determines the dynamics of the subduction process [11]. The behavior of contrast (porous fluid-saturated) systems, which include hydrophilic minerals with nanoconfined water, is complex and nonlinear when at extremely high pressures >1 GPa. To predict their effective mechanical characteristics under such conditions, it is necessary to understand the patterns of structural changes and mechanical properties of water in nanopores with an increase of the external pressure.

In specific thermodynamic conditions (pressure, temperature) the physical (mechanical) properties of water are determined by such atomic-scale parameters as the mutual arrangement of water molecules, as well as the concentration and topology of the network of hydrogen bonds between water molecules. In the case of (nano)confined water, the density and structure of the network of hydrogen bonds are also affected by the interactions within the "hard matter–soft matter" interface between the water and mineral surface, formed the nanopore [12, 13].

In the present work we study the structure of water nanoconfined in hydrophilic layered mineral and its physical properties as density, compressibility and self-diffusion at extremely high pressures. To obtain qualitative and quantitative estimates we used the atom-level molecular dynamics simulations, which is an effective tool for identifying nanoscale mechanisms of the "hard matter–soft matter" interaction in fluid-rich minerals at high pressures realized in the subduction zones

[14], phase transition of nanoconfined matter [15, 16] and even for studying the crystalline structure of the material under internal core conditions [17].

The model mineral $Me^{II}(OH)_2$, in which Me^{II} can be Mg ("brucite"), Fe ("white rust"), Ni, Co, Mn, Cd and Ca [18], was chosen here as the host mineral. These minerals have a typical brucite-like layered structure with hydrophilic interlayer galleries, which can potentially be hydrated. The unit cell parameters a and c of $Me^{II}(OH)_2$ minerals, where Me = {Mg, Zn, Co, Fe}, depending on substituted metal, are in ranges 3.147–3.262 Å and 4.596–4.769 Å, respectively [19], i.e. difference is less than 3.8%. Such minerals chosen can allow us to generalize in some extent the simulations' outcomes to understand the behavior of range of the hydrated hydrophilic minerals at high pressures.

2 Model and Method

To estimate the structure and physical properties of nanoconfined water in the mineral, we developed all-atom molecular dynamic model of a slit-shaped nanopore filled with water. The model system is hierarchical material with "host-guest" architecture having a chemical composition of $36[2Me^{II}(OH)_2 \cdot 7H_2O]$. The geometry of the model was a layer of water about 2 nm thick confined by two parallel mineral nanosheets of the metal layered hydroxide (each fragment contains 36 $Me^{II}(OH)_2$) oriented in the XY plane (Fig. 1). Along the X and Y axes, periodic boundary conditions are used. The periodic domain contained 252 water molecules. Three-sites model of water molecule TIP3P was used in simulations [20]. The structural model was prepared using experimental data obtained for deuterated layered hydroxide of divalent iron $Fe(OH)_2$ [21]. Partial atoms charges were set according to CLAYFF force field [22], where the divalent metal in hydroxides has a charge of +1.05e. The net charge of the system was zero.

Pairwise interactions of mineral atoms as well as the covalent bond of mineral OH-groups were parameterized according to the CLAYFF force field. Non-zero Lennard-Jones parameters of a hydroxyl proton $r_0 = 0.449$ Å and $\varepsilon = 0.1925$ kJ/mol were set for compatibility with the TIP3P water model, as it previously was used in Ref. [23].

The X and Y dimensions of the computational domain were 16.965 Å and 19.59 Å, respectively, and these values were fixed. Bottom mineral nanosheet played a role of an immovable substrate with all non-hydrogen atoms frozen (Fig. 1). Top nanosheet was used in a piston-like manner, undergoing a certain compressional loading along—Z. All non-hydrogen atoms of the top nanosheet were grouped into a single rigid body, while the hydroxyl protons remain movable freely. Compressive loading was uniformly distributed on non-hydrogen atoms of the top nanosheet by applying static external force f_z. The magnitude of applied force f_z was chosen to maintain the target pressure. According to CLAYFF force field formalism, the covalent bond with harmonic potential between H and O atoms of same OH-group on the mineral surface was explicitly included in the MD models.
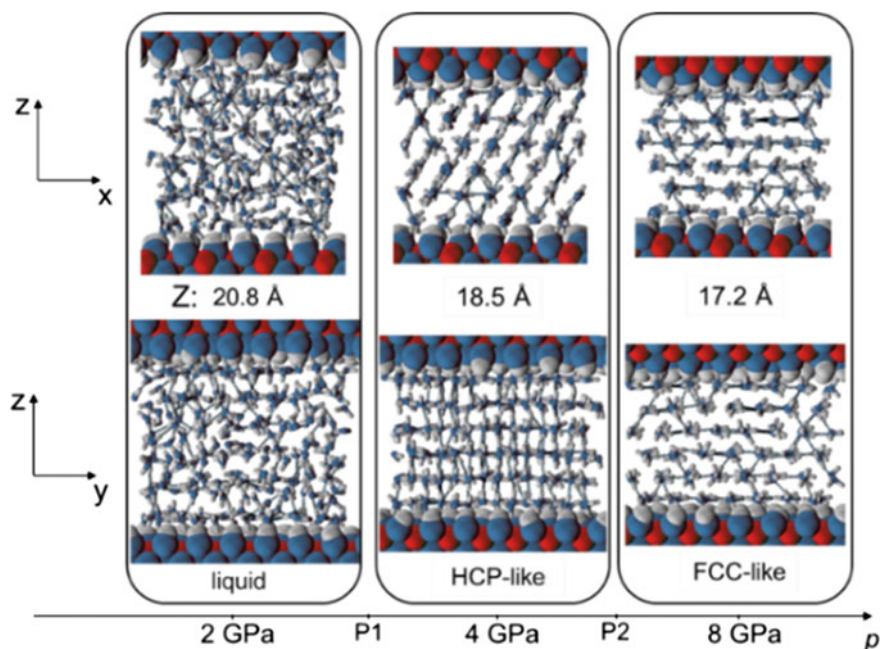
Fig. 1 Structure of the water confined in slit-shaped nanopore of the studied hydrophilic layered mineral at different pressures 2, 4 and 8 GPa. Color code: hydrogen—white, oxygen—blue, metal —red; mineral atoms are shown by van-der-Waals spheres, water molecules are depicted by balls-and-sticks for the clarity; hydrogen bonds are also shown (by the lines)

The isothermal conditions with the same temperature (310 K) were also applied to the systems, aiming to exclude temperature influence on the simulations results. Pairwise interactions were cut off at distance over 10 Å with smooth reducing to zero after 8 Å. "Long-range" electrostatic interaction was calculated with the particle-particle particle-mesh (PPPM) algorithm with a relative accuracy of 10^{-4}. An integration time step was $\tau = 1$ fs.

The described model of water in slit-shaped nanopore of host mineral has the following limitations:

1. The system is considered at a constant temperature (the same for all P);
2. Model rock contains only one type of mineral;
3. The number of water molecules per unit cell is fixed (trapped water);
4. The mineral walls Me–O are non-deformable and, therefore, neither the structural changes of the wall (stretching/contraction of Me–O bond length and the lattice constants etc.) nor the possible intercalation effects, cannot be caught by the simulation;
5. Triaxial compression is implemented by means of axial loading normal to pore walls (along Z axis) and applying periodic boundary conditions, which ensure

constant size of the box in XY plane; these conditions provide isotropic pressure equal to applied axial stress in the case of water in liquid phase; note that the value of pressure in water will differ from the value of applied axial stress after liquid-to-solid phase transformation of water, but this difference is not crucial;

6. We assume, that applied force fields are accurate enough at pressures up to 10 GPa.

Simulations were performed using LAMMPS package [24] and the "Lomonosov-2" supercomputer of Lomonosov Moscow State University [25].

3   Results and Discussion

To obtain the structural and physical properties of the water confined in the water-filled mineral the studied system was undergone compression along the Z direction (Fig. 1). The applied pressure P varied from 0.1 to 10 GPa that roughly corresponds to pressures in the Earth at depths of 3–300 km.

Simulation results revealed three phases of nanoconfined water in the considered pressure range (Figs. 1 and 2). The pressures at which phase transitions occur are denoted by P1 and P2. The values of P1 and P2 were defined as the pressures corresponding to the peaks on the compressibility curve. At pressures below P1 $\sim$ 3.0 GPa, the water confined between the $Me^{II}(OH)_2$ nanosheets is in the liquid state. This is evidenced by the high mobility and disordered position of the molecules (Fig. 1, at P < P1). The diffusion coefficient estimation of nanoconfined water D $\sim$ 10^{-9}–10^{-8} m^2/s (Fig. 2b), obtained on the basis of mean square displacement (MSD), corresponds in order of magnitude to diffusivity of the bulk water at normal pressure-temperature conditions D $\sim$ 2.299·10^{-9} m^2/s [26]. The density of nanoconfined liquid water rises from value of ρ = 1210 kg/m^3 (at 0.5 GPa) to ρ = 1540 kg/m^3 (at 3.0 GPa). The latter is 50% higher than the density of bulk water at normal conditions. The water compressibility, estimated from uniaxial compression (along Z), in the pressure interval of 0.5 – 3.0 GPa decreases from the value β = 2·10^{-10} Pa^{-1} to β = 6·10^{-11} Pa^{-1} (estimation of bulk water isothermal compressibility at normal conditions is β = 4.599·10^{-10} Pa^{-1} [27]). We note that the possibility of water existence in the liquid state at high pressures, at least up to 1.8 GPa, is shown experimentally in [28].

At the phase transition point P1 in which water in the slit-shaped nanopore crystallizes, an abrupt increase in density from ρ = 1540 kg/m^3 at P = 3.0 GPa to ρ = 1630 kg/m^3 at P = 3.2 GPa is observed. At the same time, the water diffusion coefficient falls by several orders of magnitude, showing that water losses its liquidity (Fig. 2b). The spatial arrangement of water molecules becomes ordered (Fig. 1, P = 4 GPa and P = 6 GPa). The lattice type, which was estimated using the adaptive common neighbour analysis [29] for water oxygen atoms, is hexagonal close-packed (HCP). The positions of hydrogen atoms of water were not included
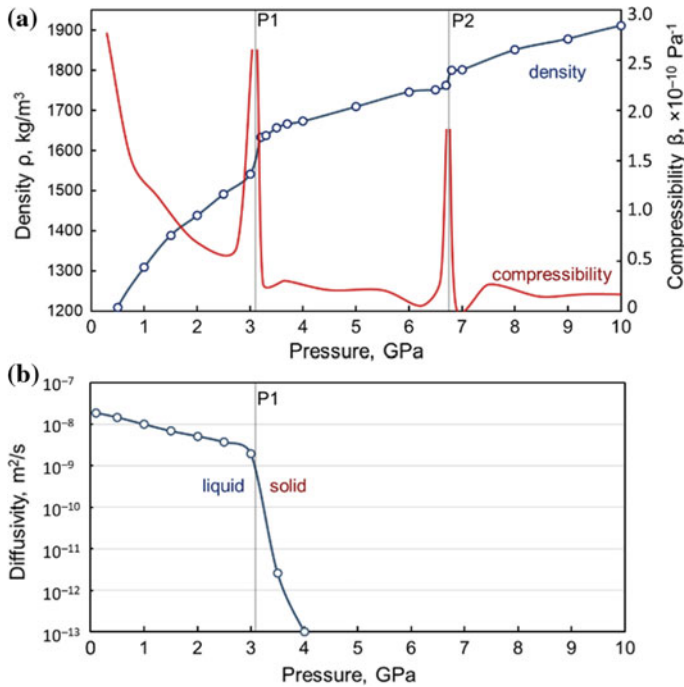
Fig. 2 Results of physical properties estimation using the MD simulations. Density, compressibility (**a**) and the self-diffusion coefficient (**b**) of nanoconfined water as a function of applied pressure

to the lattice type analysis, so this structure of nanoconfined water we will further call as HCP-like structure.

It's important to note that, according to the experimental results [6], at the pressure of 2.7 GPa (which is not far from the point P1) water insertion to kaolinite interlayer regions occurs with the formation of the super hydrated kaolinite phase $Al_2Si_2O_5(OH)4\cdot 3H_2O$. Our simulation results show that this relates to an abrupt (by 4–5 times) increase in the compressibility of nanoconfined water near the phase transition point P1, what can be seen in Fig. 2a.

We observed the nanoconfined water HCP-like phase in the pressure range from P1 to P2 (3.0–6.7 GPa). In this interval, the density of water gradually increases from $\rho = 1630$ to $\rho = 1760$ kg/m^3, and the compressibility along the Z-axis (in the direction normal to nanosheets) decreases several times from $\beta = 6\cdot 10^{-11}$ Pa^{-1} to $\beta = 2\cdot 10^{-11}$ Pa^{-1}.

The second phase transition of nanoconfined water occurs at the point $P2 \sim 6.7$ GPa. The analysis of the mutual arrangement of oxygen atoms shows that at this pressure, the HCP-like molecular "crystal lattice" transforms to the face-centered cubic type (FCC-like). This phase transition is accompanied by a

density jump (from $\rho = 1760$ kg/m^3 to $\rho = 1800$ kg/m^3, Fig. 2a). The face-centered cubic phase of water remains stable up to the upper limit of the investigated pressure range (P = 10 GPa), where the density of the confined water reaches the value of $\rho = 1910$ kg/m^3. The abrupt changes in the density and mechanical characteristics of water, including the compressibility in nanopores under the HCP-to-FCC phase transition (at P2), determine the corresponding abrupt changes in the effective mechanical properties and the stress-strain state of the host rock in subducting slab at the corresponding depth.

The physical meaning of abrupt change in compressibility of water trapped in slit-shaped nanopore of host mineral by an order of magnitude can be better clarified by analyzing the loading curve (stress-strain diagram) in Fig. 3. Note that under the considered condition of side mechanical constraint of water, this curve is directly related to "pressure–volume strain" diagram. One can see that liquid-to-HCP and HCP-to-FCC transformations of water confined in the mineral appear on stress-strain curve in the form of sub-horizontal segments: α and β, respectively (Fig. 3). At these segments, the compression of water occurs *almost* without increase in mechanical resistance to volume strain change.

The presence of sub-horizontal sections in the "pressure–volume strain" diagram, where the instantaneous bulk modulus (estimated as pressure derivative by volume strain) decreases by order of magnitude, can significantly affect the process of rock deformation at high ambient pressures. In particular, it can lead to corresponding abrupt fluctuations in the effective value of the bulk stiffness and compressibility of the whole water-filled nanoporous mineral and rock. The amplitude of these fluctuations is determined by the volume content of water in nanopores, the specific surface area of the slit-shaped nanopores and also their orientation.
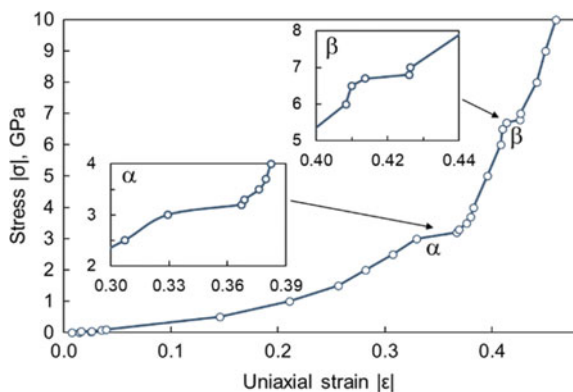
Fig. 3 Numerical prediction of stress-strain behavior (along Z) of the water confined in the studied nanoporous mineral. Inserts show enlarged views of sub-horizontal fragments α and β of σ(ε) curve

One of the possible consequences of this effect is different rate of increase of compressive mean stress (or different rate of volume contraction) in the adjacent regions of subducting slab with different water contents at the depth corresponding to one of above mentioned phase transformations in nanoconfined water (section α or β in Fig. 3). Under the condition of complex stress state (bulk compression and high shear stresses) the mentioned difference in the rate of means stress and/or volume change can promote strain localization at the boundary between these regions in the form of shear band or even dynamic rupture with accompanying seismic effects.

4 Conclusion Remarks

The revealed conditions and sequence of phase transitions of the water in water-filled $Me^{II}(OH)_2$ (Me^{II} = Mg, Zn, Co or Fe) mineral give a new understanding of complex nanoscale processes in rocks at depths from tens to hundreds of kilometers and must be taken into consideration when constructing large-scale models of subduction zones. Established pressure dependent effects in nanoconfined water can appear in different minerals and multicomponent rocks and can determine the number of behavioral features of subducting slabs. Among them is the effect of abrupt increase in compressibility of rocks at pressure conditions, which correspond to phase transformations in interstitial water. This effect can potentially promote the phenomenon of strain localization in heterogeneous subducting slab in different forms (aseismic deformation or dynamic intraplate or interfacial rupture). So, phase transformations in interstitial water are an essential factor of geodynamic processes at intermediate depths.

The next step in the theoretical investigation of this problem would be to improve the numerical model by the taking to the consideration the real temperature-depth dependence for a (cold) subduction zone and the use of fully deformable model of the host mineral. Furthermore, consideration of different host minerals, which are presented in oceanic sediments (e.g. kaolinite [30], smectite and other sheet silicates [31]), would have research significance.

References

1. Fujie, G., et al.: Controlling factor of incoming plate hydration at the north-western Pacific margin. Nat. Comm. **9**(1), 3844 (2018)
2. Ohtani, E., Zhao, D.: The role of water in the deep upper mantle and transition zone: dehydration of stagnant slabs and its effects on the big mantle wedge. Russ. Geol. Geophys. **50**, 1073–1078 (2009)

3. Kimura, J.I., Nakajima, J.: Behaviour of subducted water and its role in magma genesis in the NE Japan arc: a combined geophysical and geochemical approach. Geochim. Cosmochim. Acta **143**, 165–188 (2014)
4. Nakao, A., Iwamori, H., Nakakuki, T.: Effects of water transportation on subduction dynamics: roles of viscosity and density reduction. Earth Planet. Sci. Lett. **454**, 178–191 (2016)
5. Talyzin, A.V., et al.: Colossal pressure-induced lattice expansion of graphite oxide in the presence of water. Angew. Chem. Int. Ed. Engl. **47**, 8268–8271 (2008)
6. Hwang, H., et al.: A role for subducted super-hydrated kaolinite in Earth's deep water cycle. Nat. Geosci. **10**, 947–953 (2017)
7. You, S.J., et al.: Pressure-induced water insertion in synthetic clays. Angew. Chem. Int. Ed. Engl. **52**, 3891–3895 (2013)
8. Schmandt, B., Jacobsen, S.D., Becker, T.W., Liu, Z., Dueker, K.G.: Dehydration melting at the top of the lower mantle. Science **344**, 1265–1268 (2014)
9. Okazaki, K., Hirth, G.: Dehydration of lawsonite could directly trigger earthquakes in subducting oceanic crust. Nature **530**, 81–84 (2016)
10. Parai, R.I.T.A., Mukhopadhyay, S.U.J.O.Y.: How large is the subducted water flux? New constraints on mantle regassing rates. Earth Planet. Sci. Lett. **317**, 396–406 (2012)
11. Duarte, J.C., Schellart, W.P., Cruden, A.R.: How weak is the subduction zone interface? Geophys. Res. Lett. **42**, 2664–2673 (2015)
12. Bampoulis, P., Teernstra, V.J., Lohse, D., Zandvliet, H.J., Poelsema, B.: Hydrophobic ice confined between graphene and MoS_2. J. Phys. Chem. C **120**, 27079–27084 (2016)
13. Nomura, K., Kaneko, T., Bai, J., Francisco, J.S., Yasuoka, K., Zeng, X.C.: Evidence of low-density and high-density liquid phases and isochore end point for water confined to carbon nanotube. Proc. Natl. Acad. Sci. U. S. A. **114**, 4066–4071 (2017)
14. Plumper, O., et al.: Fluid-driven metamorphism of the continental crust governed by nanoscale fluid flow. Nat. Geosci. **10**, 685–690 (2017)
15. Zhilyaev, P., Iakovlev, E., Akhatov, I.: Liquid-gas phase transition of Ar inside graphene nanobubbles on the graphite substrate. Nanotechnology **30**(21), 5701 (2019)
16. Iakovlev, E., Zhilyaev, P., Akhatov, I.: Atomistic study of the solid state inside graphene nanobubbles. Sci. Reports **7**(1), 17906 (2017)
17. Belonoshko, A.B., et al.: Stabilization of body-centred cubic iron under inner-core conditions. Nat. Geosci. **10**, 312–316 (2017)
18. Brindley, G.W., Kao, C.C.: Structural and IR relations among brucite-like divalent metal hydroxides. Phys. Chem. Miner. **10**(4), 187–191 (1984)
19. Oswald, H.R., Asper, R.: Bivalent metal hydroxides. In: Lieth, R.M.A. (ed.) Preparation and Crystal Growth of Materials with Layered Structures, pp. 77–140. Reidel Pub Co, Holland (1977)
20. Jorgensen, W.L., et al.: Comparison of simple potential functions for simulating liquid water. J. Chem. Phys. **79**, 926–935 (1983)
21. Parise, J.B., Marshall, W.G., Smith, R.I., Lutz, H.D. Möller, H.: The nuclear and magnetic structure of "white rust"—$Fe(OH0.86D0.14)2$. Am. Miner. **85**, 189–193 (2000)
22. Cygan, R.T., Liang, J.J., Kalinichev, A.G.: Molecular models of hydroxide, oxyhydroxide, and clay phases and the development of a general force field. J. Phys. Chem. B **108**, 1255–1266 (2004)
23. Tsukanov, A.A., Psakhie, S.G.: Energy and structure of bonds in the interaction of organic anions with layered double hydroxide nanosheets: A molecular dynamics study. Sci. Rep. **6**, 19986 (2016)
24. Plimpton, S., Crozier, P., Thompson, A.: LAMMPS-large-scale atomic/molecular massively parallel simulator. Sandia Natl. Lab. **18**, 43 (2007)
25. Sadovnichy, V., Tikhonravov, A., Voevodin, Vl., Opanasenko, V.: "Lomonosov": Supercomputing at Moscow State University, Contemporary High Performance Computing: From Petascale toward Exascale, Chapman Hall/CRC Comput. Sci. Ser, pp. 283–307 (2013)

26. Holz, M., Heil, S.R., Sacco, A.: Temperature-dependent self-diffusion coefficients of water and six selected molecular liquids for calibration in accurate 1H NMR PFG measurements. Phys. Chem. Chem. Phys. **2**, 4740–4742 (2000)
27. Rodnikova, M.N.: A new approach to the mechanism of solvophobic interactions. J. Mol. Liq. **136**, 211–213 (2007)
28. Lee, G.W., Evans, W.J., Yoo, C.S.: Crystallization of water in a dynamic diamond-anvil cell: evidence for ice VII-like local order in supercompressed water. Phys. Rev. B **74**, 134112 (2006)
29. Stukowski, A.: Structure identification methods for atomistic simulations of crystalline materials. Modell. Simul. Mater. Sci. Eng. **20**, 045021 (2012)
30. Aoki, S., Kohyama, N., Oinuma, K.: Clay mineral distribution in surface sediments in the seas and ocean along the eastern Asian continent, with special reference to the relation to morphology and chemistry. Clay Sci. **11**(5), 431–449 (2001)
31. Melka, K., Fediuk, F., Langrova, A.: Mineral composition of the deep sea sediments in three sectors of Western Pacific Ocean. Acta Geodyn. Geromaterialia **6**(1), 77–87 (2009)

Part III
Dynamic Processes in Mining

Inrush of Ay River Water into Kurgazakskaya Mine Workings as Trigger of Tectonic Rock Burst

Andrian Batugin

Abstract

A hypothetical mechanism of one of the strongest rock bursts ever at Russian mines is considered in this paper. Kurgazakskaya mine is located in one of the geodynamically active areas of the southern Urals near the Ay river course. The mine field is intersected by major tectonic faults, which incidentally constitute boundaries of the crustal blocks that are active in the current stress field with a horizontally oriented axis of maximum compression. Mining operations created large gob areas supported by pillars. Over and over again karst voids used to be developed at the same place of the Ay river bed where it crosses the boundary of the active crustal blocks and it is there that river water ingressed into the mine workings through tectonic faults. This paper considers the case when the normal stresses at the major fault plane decreased due to hydrostatic expansion pressure after yet another inrush of river waters into tectonic faults which triggered a tectonic rock burst with sudden fault wall displacement towards the mined-out area. It is concluded that the inrush of the Ay river water into the mine workings through tectonic faults could be the trigger of the tectonic rock burst.

Keywords

Rock burst · Water inrush · Fault reactivation · Trigger effect

A. Batugin (✉)
National University of Science and Technology «MISiS», Leninsky Prospect, 4, 119049 Moscow, Russia
e-mail: as-bat@mail.ru

1   Introduction

In the Russian classification of rock bursts there are rock bursts of tectonic type manifested in the form of an Earth shock, causing brittle failure of mine workings and pillars. Hypocenter of such bursts is located deep in rock massif. A tectonic rock burst is accompanied by a strong Earth tremor, grating noise, the formation of dust and air waves [1]. The first tectonic rock bursts were described in the works of G. Gelashvili and I. Petukhov, when the Tkibuli-Shaorsky coal deposit was being developed in Georgia in the 1970s [1, 2]. It was believed that the tectonic rock burst was triggered by a seismic wave from the earthquake. When a seismic wave arrives at the critically stressed zone, the stressed rock is subject to dynamic fracture [1–3]. The more we learn about the stress-strain behaviour of the rock within the mine fields, the clearer it gets that the tectonic stress field available in the area of the deposit contributes to the manifestation of strong rock bursts. The concept of tectonic rock burst was transformed into the concept of rock burst trigerred by the tectonic stress field the hypocenter of which is located in rock massif [1–6]. In some cases strong tectonic rock bursts result in displacement of tectonic fault walls. Rock bursts of this type are globally known at a number of mine fields where they are called "Fault slip" [7].

Currently, strong rock bursts continue to occur at many mine fields of the world, and the problem of rock bursts is building up into the hazard of man-induced seismicity of mining areas [4–13]. Similar to other hazards of mining operations [14–19], this issue continues to arrest attention. Due to the limited statistics of strong rock bursts on the one hand, and the great importance of this issue on the other, there is always a tendency to generalize, reinterpret available information and search for predicted patterns [2, 5, 8, 20]. This article considers possible mechanism of one of the strongest tectonic rock bursts which occurred in the 1990 at the Kurgazakskaya bauxite mine in the southern Urals. The Investigation Commission which worked at the mine after the rock burst made general conclusions that the tectonic rock burst was associated with the tectonic stress field available in that segment of the earth's crust.

Recently, opinions were offered that the reason behind man-made earthquakes was flooding of mines [21–23], and the suggestion could be made that it is water inrush from the Ay river into the mine excavations that triggered the rock burst.

2   Rock Burst at the Kurgazakskaya Mine

Kurgazakskaya mine was developing a bauxite deposit of the same name located in the southern Urals near Mezhevoy Log village in Chelyabinsk region. Up to 4 m thick tabular ore body is deposited at a depth of 225–550 m stretching from NE to SW for 6 km dipping at 0–15°. The tectonic rock burst in 1990 was one of the strongest ones that ever occurred in the practice of developing Russian ore deposits [5, 24, 25]. Pillars collapsed and mine infrastructure was destroyed on an area of

about 45 hectares, the total size of this area reached 1.2 km along the strike of the ore deposit. Seismic energy is estimated at 10^{10}–10^{11} J. Cracks appeared on the surface, and new traces of displacements were recorded during the survey of fault planes in the focal zone. Earlier, rock bursts (spalling and dynamic failure of the stope roof) had been only manifested on the northeast wing of the ore deposit. The tectonic rock burst occurred in the central part of the deposit where only bumps had been recorded in the floor of stopes. The tectonic rock burst caused a rise of the floor which in turn triggered the typical failure of pillars, and cracks appeared on the Earth's surface. The expert Commission listed a number of causes of that tectonic rock burst, one of them being high concentration of tectonic stresses at the Kurgazakskaya mine field along the contour of unpayable ore zones, near ore pillars and geological faults stretching in latitudinal direction, yet the true mechanism of that rock burst remained unclear.

Following the tectonic rock burst, studies were conducted to analyse geodynamic condition of the deposit area, damaged sections and tectonic failures were examined in the focal zone. Over time, analyzing the mechanisms of tectonic rock bursts at other mine fields as well as cases of earthquakes related to mine closures, the author came to the conclusion that the tectonic rock burst at the Kurgazakskaya mine was accompanied by movement of rock blocks along the fault plane which, in turn, was caused by the inrush of the Ay river water from the karst cavity.

According to the tectonophysical model of tectonic rock bursts, the rock blocks move along large tectonic faults in the direction of the tangential stress created by the regional stress field [26]. Conditions contributing to the occurrence of tectonic rock burst are: high level of tectonic stresses in the ground and the stress field inheritance (i.e., if rock is 'prepared' for deformations in the current stress field by prior displacements along the already existing slackening surfaces); presence of considerable worked out areas; reduced normal compression of the fault wings due to anthropogenic impact. Evidently, all these conditions were in place shortly before the occurrence of the tectonic rock burst.

3 Field and Desktop Study

3.1 Investigation of Stress Fields

To assess the current stress fields in the area of deposits, it has been proposed to use methods of tectonophysics in which the input data are the data on the orientation of the active crustal block boundaries and their relative displacements [3]. It is believed that the currently ascending movements of the crustal blocks indicate the predominance of horizontal compression over vertical compression. In our case, current uplift of the terrain is characteristic for the entire area of the Southern Urals. For example, the Ay riverbed is downcut to the depth of 150–200 m whereas river terraces are located above the water line at heights of over 40 m. In the process of geodynamic zoning of the deposit area using the technique described in [3],
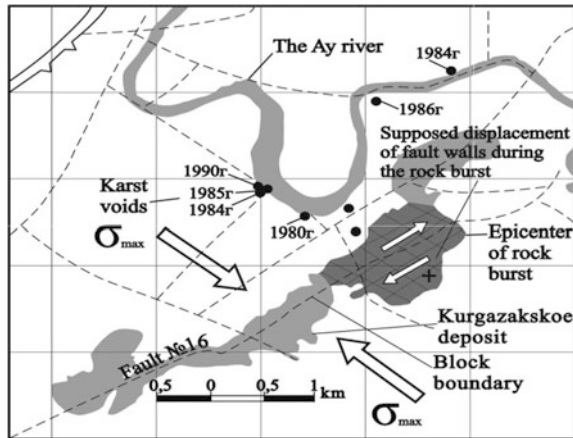
Fig. 1 Structural confinement of Ay River Karst Cavities to block boundaries

I–IV rank units were identified, Fig. 1. The block boundaries correlate both with tectonic and neotectonic elements. Part of the block boundaries inherits major reverse faults and shift faults. Reverse faults dip at 40–50° on the average whereas the shift faults have almost vertical fault plane (they dip vertically). The boundaries of the crustal blocks stretching to the north-west have the dextral slip component.

These data help to map out, with due limitations, approximate orientation of the displacement vector at the block boundaries, which can be used for tectonophysical analysis. Thus, maximum compression axis σ_{max} has a north-west trending, and the axis of intermediate stresses, σ_{min}, is oriented vertically (Fig. 2).

Most faults observed in underground workings are either reverse faults or shift faults. The vertical amplitude of reverse faults ranges from the 1 m to 20–28 m; vertical amplitude of shift faults is not recorded. Most reverse faults stretch out in the north-east direction whereas their fault planes dip to the north-west and south-east at 30–60°. The steeply dipping extended faults locally called "faults without displacement" are in fact dextral and sinistral slips. Fault planes are well polished, slickenlines are clearly visible on their slickensides. The tectonophysical analysis of the entire set of faults is presented in Fig. 2. The principal stress axes have following azimuth bearings and angles of dip:

$$\sigma_{max} = 115/10; \ \sigma_2 = 205/5; \ \sigma_{min}\text{---almost vertical.}$$

Therefore, consistency in the orientation of the principal stress axes is set up both for the regional stress field reconstructed based on active jointing data (boundaries of I–IV rank blocks), and for the stress field reconstructed on local disjunctive fault data. This indicates that there is an inheritance of stress fields, and this is one of the conditions that facilitate tectonic rock bursts.
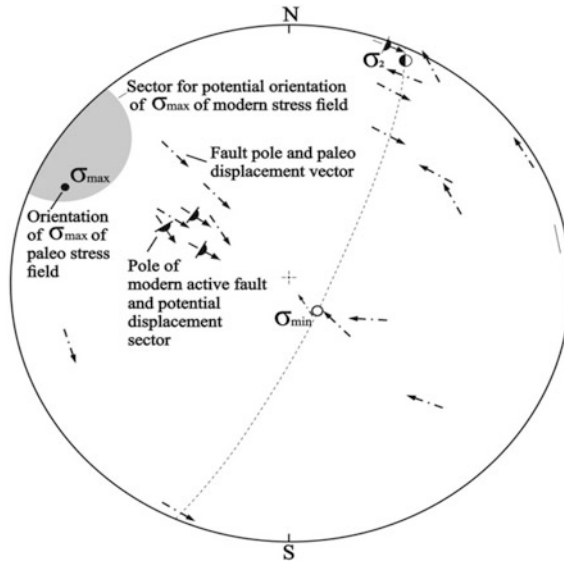
Fig. 2 Tectonophysical scheme of stress fields

3.2 Mining Operations at Kurgazakskaya Site

Mining practice shows that large mined out spaces contribute to strong rock bursts [2, 5, 8, 27]. Tectonic rock bursts result in displacement of fault walls towards the goaf. Mining operations at the Kurgazakskaya mine using room & pillar mining systems began in 1979. By 1990, the depth of mining exceeded 340 m, and the total area underground where the roof was supported by pillars, exceeded 100 hectares which is comparable to the size of the IVth rank crustal blocks.

3.3 Decrease of the Fault Wall Normal Compression Due to Man-Caused Impact

Formation of stress concentration zones due to stress redistribution caused by mining operations brings about strong rock bursts. However, not only zones of high stress concentration are formed due to mining operations, but also de-stressed zones, where the fault wall normal compression is reduced and conditions are created for their displacement in case of a tectonic rock burst. Another important factor that that is linked with the decrease of the normal compression in fault walls is hydrostatic pressure developed when mines are flooded and precipitation seeps from the surface [21–23, 28]. It is this factor that could become crucial and trigger the 1990 tectonic rock burst. Carbonate rock at the deposit is overlain by sandy-pebble and clayey sand quaternary formations. Presumably, it was at that

time that the local karst cavities were filled with coarser material [29]. Filtration properties of the aggregate material are usually negligible. However, they, together with carbonate rocks, provide a route for groundwater flow. The water bearing stratum of karst rocks at the site is traced to the depth of 480 m. Due to gross negligence of the filtration flow regime in carbonate rock in the process of field drainage, hydrogeological conditions were created that contributed to the formation of suffosion erosion of clayey sand material in karst cavities [29]. This mechanism was launched at the Kurgazakskaya mine field after mining operations began and the cone of depression developed. As soon as the cone of depression was formed water began to flow into the mine through interconnected tectonic faults, which resulted in gradual flushing of their fault planes from the bottom upward to the earth's surface with subsequent formation of karst holes.

Karst holes repeatedly appeared in the riverbed of the Ay River, on the borders of geodynamically active blocks (Fig. 1), which resulted in a sharp increase of the mine inflow to 10 000 m^{3}ph. For example, on July 15, 1984, a hole was spotted in the riverbed measuring 10 m across the river, 14 m along the river, and 21 m deep. This void was liquidated by September 1. On June 21, 1985, one more hole was found measuring 10 m across the river, 8 m along the river, 9 m deep. On August 29, 1985, yet another 20 m deep hole was spotted in the same place, measuring 5 m across the river and 4 m along the length of the river. The analysis of the spatial location of these holes shows that they are confined to the block boundaries (Fig. 1). Thus, prior to the tectonic rock burst, conditions could have been developed for the rapid filling of fault planes with water that might have resulted in hydrostatic expansion in case of formation of yet another hole.

4 Discussion (on Tectonic Rock Burst Mechanism)

The stress state of the mine site area is characterized by the following orientation of the main stress axes: the maximum compression axis σ_{max} trends at 115° in almost horizontal plane; the minimum compression axis σ_{min} trends at 205°, also in a nearly horizontal plane; the σ_2 axis is almost vertical. The mine field is intersected by a major fault with an amplitude of 22 m, its azimuth and angle of dip being, respectively, 130° and 60°. Simple calculations show that with $\sigma_{max}/\sigma_{min}$ ratio = 2.5 and friction factor at the fault plane k = tg10° (according special investigation of slickensided surface by Yu. A. Voronin), in this stress field the shear stresses at this fault plane exceed the frictional force by 2.3 times (net of adhesion). In May 1990 another major hole was formed in the riverbed of the Ay River, exactly where a number of cavities had been repeatedly developed earlier—Fig. 1. Obviously, the river water quickly filled fault planes of the preceding repeatedly washed faults stretching from the earth's surface to the area of mining. After the fault planes had been filled with water and hydraulic connection had been established along the fault, the normal compression of the fault walls might rapidly drop by several megapascals. This resulted in outbalancing their cohesion forces, whereby limit

state was attained and the fault hanging wall was abruptly displaced towards the goaf. At the time when the fault hanging wall slipped up, seismic energy was released, the floor of the stopes heaved, pillar footings collapsed and cracks appeared on the earth's surface.

It appears that the rate of hydraulic pressure build-up could be crucial for the trigger-type displacement of the fault walls, especially if we take into account the concept of the critical stress state of the top part of the Earth crust's [30]. In case the stress state of the rock formation changes abruptly due to river water break-through into the mine workings along the fault, the "natural vs. technical media" balance may be upset quicker than with a slow, gradual effect. Consequently, after the decision was taken in 2002 to flood the mine and the groundwater table in the abandoned mine gradually rose, no significant seismic events were observed in the area.

5   Conclusions

The genesis of a tectonic rock burst can be considered as a result of the interaction between the system of geodynamically active blocks and a technical system (mine). In our case, activation of suffosion-karst and geodynamic processes were realized due to incorporation of technical systems into the natural media, which led to the inrush of river water into the mine workings along the fault planes where the crustal active block boundaries cross the Ay river course. This process caused a drastic drop of the fault plane normal compression at one of the major faults within the deposit area and triggered sudden displacement of its wall toward the mined-out area whereby seismic energy was released and mine infrastructure was smashed.

References

1. Petukhov, I.: Rock Bursts in Coal Mines, 2nd edn. ISC VNIMI, Saint-Petersburg, (2004) (In Russian)
2. Petukhov, I., Batugina, I.: Bibliography of Rock Bursts. Balkema, Rotterdam (1991)
3. Batugina, I., Petukhov, I.: Geodynamic Zoning of Mineral Deposits for Planning and Exploitation of Mines. Oxford and IBH Publishing Co. Pvt. Ltd., New Delhi (1990)
4. Yakovlev, D., Lazarevich, T., Tsirel', S.: Natural and induced seismic activity in Kuzbass. J. Min. Sci. **49**(6), 862–872 (2013). https://doi.org/10.1134/S1062739149060038
5. Lovchikov, A.: Review of the strongest rockbursts and mining-induced earthquakes in Russia. J. Min. Sci. **49**(4), 572–575 (2013). https://doi.org/10.1134/S1062739149040072
6. Kozyrev, A., Semenova, I., Zhuravleva, O., Panteleev, A.: Hypothesis of strong seismic event origin in Rasvumchorr mine on January 9, 2018. Min. Inf. Anal. Bull. **2018**(12), 74–83 (2018) (In Russian)
7. Scott, D., Williams, T., Friedel, M.: Investigation of a Rockburst site. In: 4th International Symposium Rockbursts and Seismicity in Mines, Krakow, pp. 311–315. Balkema, Rotterdam (1997)
8. Keneti, A., Sainsbury, B.: Review of published rockburst events and their contributing factors. Eng. Geol. **246**, 361–373 (2018). https://doi.org/10.1016/j.enggeo.2018.10.005

9. Lan, T., Zhang, H., Han, J., Song, W., Wu, H., Cai, Z.: Study on rock burst mechanism based on geo-stress and energy principle. Caikuang Yu Anquan Gongcheng Xuebao/J. Min. Saf. Eng. **29**(6), 840–844+875 (2012)

10. Marcak, H., Mutke, G.: Seismic activation of tectonic stresses by mining. J. Seismolog. **17**(4), 1139–1148 (2013). https://doi.org/10.1007/s10950-013-9382-3

11. Rasskazov, I., Saksin, B., Usikov, V., Potapchuk, M.: Rock mass geodynamics and mining-induced rockbursting at Nikolaev complex deposit. Gornyi Zhurnal (12), 13–19 (2016). https://doi.org/10.17580/gzh.2016.12.03 (In Russian)

12. Adushkin, V.: Technogenic tectonic seismicity in Kuzbass. Russ. Geol. Geophys. **59**(5), 571–583 (2018). https://doi.org/10.1016/j.rgg.2018.04.010

13. Adushkin, V., Kishkina, S., Kocharyan, G.: New approach to monitoring induced earthquakes. J. Min. Sci. **53**(1) (2017). https://doi.org/10.1134/s1062739117011784

14. Odintsev, V., Miletenko, N.: Water inrush in mines as a consequence of spontaneous hydrofracture. J. Min. Sci. **51**(3), 423–434 (2015). https://doi.org/10.1134/S1062739115030011

15. Coli, M., Furesi, D., Cantini, C., Soldo, L.: Evaluation of the water-inflow in tunnelling on the base of geostructural studies. Rendiconti Della Societa Geologica Italiana **4**, 204–206 (2007)

16. Kaledina, N., Kobylkin, S., Kobylkin, A.: The calculation method to ensure safe parameters of ventilation conditions of goaf in coal mines. Eurasian Min. **1**, 41–44 (2016). https://doi.org/10.17580/em.2016.01.07

17. Tatarinov, V., Kaftan, V., Morozov, V., Kamnev, E., Tatarinova, T.: Reduction of the geodynamic risk in the disposal of radioactive waste in geological formations. In: 18th International Multidisciplinary Scientific GeoConference Surveying Geology and Mining Ecology Management (SGEM), vol. 18, no. 4.3, pp. 11–18, Albena, Bulgaria (2018). https://doi.org/10.5593/sgem2018v/4.3/s04.002

18. Balovtsev, S., Shevchuk, R.: Geomechanical monitoring of mine shafts in difficult ground conditions. Min. Inf. Anal. Bull. (8), 77–83 (2018). https://doi.org/10.25018/0236-1493-2018-8-0-77-83 (In Russian)

19. Slastunov, S., Kolikov, K., Ermak, G., Yutyaev, E.: Safety of coal mining in long-run development. Gornyi Zhurnal (4), 46–49 (2015). https://doi.org/10.17580/gzh.2015.04.08 (In Russian)

20. Batugin, A., Myaskov, A., Ignatov, Y., Khotchenkov, E., Krasnoshtanov, D.: Re-using of data on rockbursts for up-to-date research of the geodynamic safety problem. In: 3rd Multidisciplinary Earth Sciences Symposium (WMESS 2018). IOP Conference Series: Earth and Environmental Science, vol. 221, no. 1, Prague, Czech Republic (2019). https://doi.org/10.1088/1755-1315/221/1/012089

21. Batugin, A., Klimanova, V.: Assessment of the influence of the depth of flooding of the liquidated mines on the increase of the geodynamic hazard. In: Deformation and Destruction of Materials with Defects and Dynamic Phenomena in Workings, pp. 26–27, Simferopol (2000) (In Russian)

22. Srinivasan C., Benady S., Sivakumaz, C.: Fluid seismicity in Kolar mining region. In: Dam Safety, Including Instrumentation of Dams, Proceedings of Workshop, Thiruvananthapuram (2000)

23. Goldbach, O.D.: Seismic risks posed by mine flooding. In: Hard Rock Safe Safety Conference, pp. 149–174, Pretoria (2009)

24. Lomakin, V.: On the relationship between the volume of the focal destruction zone and the seismic energy of a rock burst. Russ. Geol. Geophys. **5**, 129–132 (1989). (In Russian)

25. Dyagilev, R.: Induced seismicity and seismic hazard in mining regions. In: 15th International Multidisciplinary Scientific GeoConference Surveying Geology and Mining Ecology Management, SGEM, vol. 3, no. 1, pp. 879–886, Albena, Bulgaria (2015). Code 153999

26. Batugin, A., Batugina, I., Lan, T.: Tectonophysical model of fault tectonic rock burst with wing sliding. Liaoning Gongcheng Jishu Daxue Xuebao (Ziran Kexue Ban)/J. Liaoning Tech. Univ. (Nat. Sci. Ed.) **35**(6), 561–565 (2016). https://doi.org/10.11956/j_issn. 1008-0562.2016.06.001

27. van Aswegen, G.: Forensic Rock mechanics, Ortlepp shears and other mining induced structures. In: 8th International Symposium Rockburst and Seismicity in Mines, Saint-Petersburg, Moscow (2013)
28. Zhukova, S., Samsonov, A.: Assessment of natural impact on the seismicity in Khibiny mountains. Gornyi Zhurnal **10**, 47–51 (2014). (In Russian)
29. Plotnikov, P.: Environmental Protection in the Development of Ore Deposits, Moscow (1985) (In Russian)
30. Batugin, A.: Critically Stressed areas of earth's crust as medium for man-caused hazards. In: 7th International Scientific Conference "Problems of Complex Development of Georesources" (PCDG 2018), vol. 56. E3S Web of Conferences, Khabarovsk, Russian Federation (2018). https://doi.org/10.1051/e3sconf/20185602007

Triggering Tectonic Earthquakes by Mining

Gevorg Kocharyan, Alexander Budkov and Svetlana Kishkina

Abstract

A phenomenological model of mining-induced earthquakes M > 3 has been proposed. The main reasons for initiation of a dynamic slip along fault during mining are: a quasi-static change of the stress field as a result of excavation and movement of rock; a change of the effective stiffness of the surrounding rock mass as a result of drifting; a change of the hydro-geological regime of fault zones; an accumulation of minor strains localized on breaks in the zones of active faults. The following geomechanical criteria must be met for a dynamic slip along a fault to occur: (i) tangential stresses at the local fault section must reach a level close to the current strength value (in most cases this is true for active faults); (ii) the fraction of the central part of the fault should have softening properties with increasing sliding velocity; (iii) a certain ratio of rock stiffness to fault stiffness should be met. At the same time, the level of stresses or the properties of material should change over a large fault segment, several times larger than the area of the nucleation zone of a future earthquake.

Keywords

Mining-induced earthquakes · Mining · Trigger effect · Fault stiffness · Coulomb stress

G. Kocharyan · A. Budkov · S. Kishkina (✉)
Sadovsky Institute of Geospheres Dynamics RAS, 119334 Moscow, Russia
e-mail: SvetlanK@gmail.com

G. Kocharyan
e-mail: Gevorgkidg@mail.ru

1 Introduction

Mining-triggered or mining-induced earthquakes are the oldest known ones that are associated with human activities. Probably, this class of phenomena (we will not distinguish these terms in the article) can be attributed to one of the first manifestations of induced seismicity. It was noticed a hundred years ago that as soon as humans began occupying more extensive and deeper ore zones, earthquakes took place more and more often. For example, strong earthquakes occurred at the turn of XIX–XXth centuries in the Witwatersrand gold mine in South Africa. Mining continues, so earthquakes occur there right up to now [5, 8].

As seismic equipment developed and arrived at mining enterprises widely, hundreds and thousands of weak seismic events have been recorded. Their occurrence is definitely associated with mining development. Much more questions arise about the connection of large induced/tectonic(?) earthquakes, that occur at a considerable distance from a mining plant or a quarry, to mining. Such events are not always related to mining directly [4, 14], etc.

It is well known that most mining areas around the world are in highly loaded conditions due to depth, tectonic stresses, or a combination of these two. So, arguments whether earthquakes occurring somewhere are caused by mining or occur independently of human activities are going on. Detailed studies in the Earth's interior, i.e. direct studies of the sources of such earthquakes showed that even under extremely high seismic loads, no destruction of rock occurs: the sources are slides along existing faults and tectonic cracks [8, 12, 16]. Criteria for triggering a dynamic movement.

Let's consider the conditions for a slip along a fault to occur.

The first necessary condition is the approach of the effective stresses tangential to the fault plane, to the local shear strength:

$$\tau \sim \tau_0 \tag{1}$$

In this case, slippage can occur under tangential stresses obviously lower than τ_p—the Coulomb strength. What slip mode will emerge and what proportion of deformation energy will go to seismic radiation is determined by the ratio between the stiffness of the rock massif K and the fault stiffness k_s $\psi = |k_s|/K$. The fault stiffness $|k_s| = \left|\frac{\partial \tau}{\partial D}\right|$ determines the rate of decreasing resistance to shear along the fault, and the stiffness of the massif $K = \eta \frac{G}{\hat{L}}$—is the rate of decreasing elastic stresses in the massif due to the shear along the fault. Here G is the shear modulus of the enclosing massif; $\eta \sim 1$ is the shape factor; $\hat{L}$ is the characteristic size associated with the earthquake magnitude [12]. If the condition

$$|k_s| = \left|\frac{\partial \tau}{\partial D}\right| \geq K = \eta \frac{G}{\hat{L}} \tag{2}$$

is satisfied, then the system radiates energy. Otherwise, there will be no dynamic slip and no seismic radiation. The value of this ratio determines not only the possibility of sliding, but also the slip mode [12]. When the fault stiffness is several times higher than the one of the rock massif, i.e. the rate of decreasing shear resistance is quite high—a discontinuous slip occurs on the fault. "Normal" or "fast" earthquakes occur. If the fault stiffness exceeds the one of the massif no more than twice, "slow" earthquakes occur [17, 12].

The stiffness of rock varies very slightly for different regions and different depths within the Earth's crust. The fault stiffness may vary several orders of magnitude due to the scale of the fault, P–T conditions, the degree of watering of the fault, and the composition of the fluid. But it is at most sensitive to the composition of the narrow principal slip zone of the fault [18, 12]. Laboratory experiments have convincingly demonstrated that, for example, the presence of watered clays in the central zone of a fault, makes the fault stiffness several times as small. The same effect is observed when a certain amount of talc is present in the fault central zone. Talc often replaces minerals of the serpentine group at fracture walls as a result of the chemical reaction of serpentine with silicon dioxide contained in thermal fluids. Thus, the following condition should be true for a failure on a fault to occur—a decrease of the frictional strength of the contact with an increase of the sliding velocity v and/or displacement D:

$$\frac{d\tau_{fr}}{dv} < 0, \quad \frac{d\tau_{fr}}{dD} < 0 \tag{3}$$

Obviously, it is the fault shear stiffness k_s, which is a very sensitive parameter, that can serve as a reliable marker of fault behavior. Characteristic values of stiffness of faults of different hierarchical levels are given in Kocharyan [12] (Fig. 1).

Summarizing, the occurrence of dynamic slip is realized only on those faults for which all three geomechanical criteria for the occurrence of instability are fulfilled. Namely: (i) shear stresses at a local fault segment should reach a level close to the current value of shear strength (it is true for active faults in most cases); (ii) a certain ratio of the rock stiffness to the fault stiffness should be satisfied; (iii) the material in the principal slip zone of the fault must demonstrate velocity weakening when sliding along the fault occurs.

2   Mining Operations as Earthquake Triggers

Let's consider which of the above parameters can critically change as a result of mining operations: alteration of frictional properties of sliding surface (the principal slip zone of the fault); alteration of tangential stresses at a local fault segment; alteration of the stiffnesses of the fault and the host rock mass.
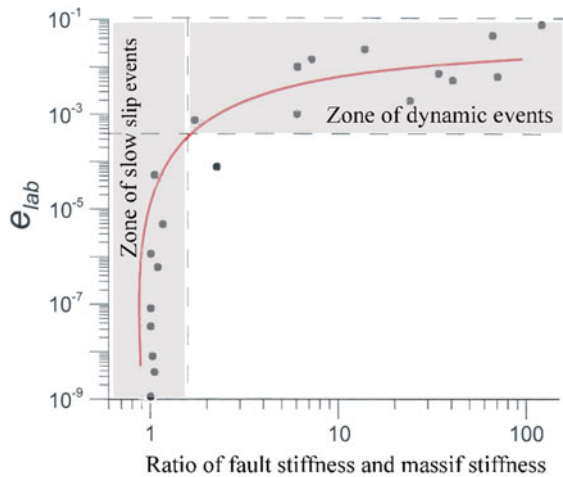
Fig. 1 Seismic energy versus the ratio of the stiffness of the fault to the stiffness of the massif. Dots are results of laboratory experiments. Above the horizontal dotted line is the zone of dynamic events. To the left of the vertical dotted line are slow slip events

Laboratory experiments [13] convincingly demonstrated the possibility for a fluid penetrating into the filler material of a laboratory fault to significantly change its frictional properties. Namely: in the course of loading a granite block, sliding on a thin layer of granular material, fluids with different properties were quickly injected into this layer. When the fluid spread over a large contact area, the rate of movement, the value of released stresses and the radiated energy [13] changed. At the same time, the authors note that the change in pore pressure, compared to the level of normal stress on the fault, was insignificant; the sliding mode changed just because of the alteration of the frictional properties of the contact. There is some evidence that injection (or pumping) of a fluid can change the characteristics of the geological material even in natural conditions [3, 7], etc. And again we are talking about such an insignificant change in hydrostatic pressure that it is hardly possible to speak of a change in pore or reservoir pressure and, accordingly, a decrease of the effective Coulomb strength of a fault or a fracture.

Thus, as a result of the anthropogenic impact—injection or pumping of fluid into/out of the rock massif—it is most likely that frictional properties of the sliding surface will change. Note, that currently the mechanism of such an impact is not clear, since the change of the fluid-dynamic regime should occur over a sufficiently large fault area. Although, hypothetically, this is perhaps the only possibility to change the frictional properties of a sliding surface by human activities.

Let us now consider whether it is possible for tangential stresses to change at a local fault section in the course of mining operations, and if so, what will be the scenario?

We will estimate stress-strain conditions of the massif in the area of a segment of a fault, which is located just below a large mining quarry. We may solve the Love problem of the stress field [15], which results from applying a load to a rectangle on the surface of an elastic half-space. One can find that in the vicinity of the fault (at a depth of 4–10 km) the main stresses change by less than two percent of the lithostatic stress. This calculation was carried out for a site 10 × 2 × 0.3 km in dimensions. Bearing in mind [6] that for an extended section excavation of rock of the depth of h can be replaced by a uniform removal of the load $\zeta_z = \rho g h$, the task corresponds to a large quarry located above the fault zone. Such small quasi-static stress changes, a few percent of the lithostatic one, most likely cannot be the direct cause of an earthquake. However, in terms of the Coulomb initiation theory, even such a small stress change $\Delta\sigma_c$ can be strong enough to initiate seismicity at a «prepared» fault [9], etc. Comparing results of calculating changes of the static stress field to occurrence of aftershocks is one of popular explanations that aftershocks of an earthquake occur not only within the fault zone, but also in neighboring areas [1]. Today it is the most vivid evidence of the possibility to initiate dynamic movements. It is possible to calculate changes of the Coulomb function without knowing absolute values of the stresses—no data on the stress-strain conditions in the region is required, and no need to consider stress-fields from other sources:

$$\Delta\sigma_c = \Delta\tau - \mu(\Delta\sigma_n - \Delta p) \tag{4}$$

At the stage of preparation of a dynamic failure $\sigma_c < 0$. If the shear stress τ increases or the effective normal stress $(\sigma_n - p)$ decreases, the fault approaches the critical state $\sigma_c = 0$. Basing on this approach, we can estimate variations of the Coulomb function on a site oriented in the fault plane:

$$\sigma_c = \tau - \mu(\sigma_n - p) \tag{5}$$

where σ_n—normal to the plane stress, τ—tangential to the plane stress, p—pore pressure and μ—friction coefficient.

A detailed description of all calculations is given in Kocharyan et al. [10, 11]. Variations of the Coulomb function at a fault plane with an angle of incidence of 30 degrees are shown in Fig. 2. The result of calculations along the central axis of the fault plane is shown (y = 0). It is seen that at the fault plane—i.e. at the depth of the supposed earthquake hypocenter location—the increment of the Coulomb stress is positive, i.e. it brings the fault closer to the critical state. The change of the Coulomb stress amounts to about 1 MPa for different calculated cases. The key point is that such a change of the Coulomb stress occurs over an extended section of the fault plane, which significantly exceeds the zone of nucleation of earthquakes $M \leq 6$.

Thus, a change in the stress state at the fault plane resulting from excavation and removal of rock during open pit mining cannot be the direct cause of a powerful earthquake, however, it can accelerate its occurrence at an already "prepared" fault.
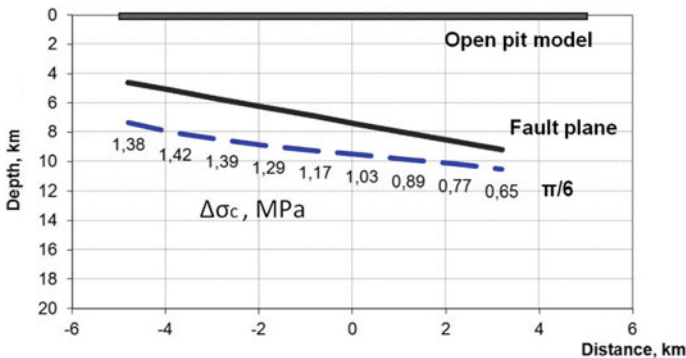
Fig. 2 Results of calculating the Coulomb stress increment at the fault plane under the quarry. The angle of incidence of the fault plane is 30°

Note that the chosen model corresponds to the parameters of the Bachatsky quarry (Kuzbass, Russia), where the earthquake with ML = 6.1 occurred on June 18, 2013. Debates about its nature continue. Taking into account that it is a seismically active region, the presented analysis can be a strong argument in favor of the fact that the earthquake was triggered by mining at an already "prepared" active fault.

The question as to the time when the stress state changes occurred remains ambiguous: it's a matter of years, if we are talking about quarry development, and seconds, if we mean dynamic movement during an earthquake. The difference of fault reactions in these two cases can be fundamental. To estimate this time, calculations were made through the "Rate & State" model [2]. That is, complex laws of friction, depending on velocity and displacement were introduced in the static calculation of the Coulomb stress.

A slider model of a rigid block, sliding on a rough surface under the action of a force applied through a spring of the stiffness of K when its free end slowly moves at velocity of $\dot{u}_0$, was used in the numerical simulation. The friction factor in the interaction of the block and the substrate is written as follows:

$$\mu = \mu_0 - a \ln\left(\frac{V_0}{V} + 1\right) + b \ln\left(\frac{V_0\theta}{D_c} + 1\right) \tag{6}$$

where μ_0 is the constant corresponding to constant slip, V is the running velocity, θ is the state variable, a, b, D_c are empirical constants. The value of θ varies according to the Dieterich law [2]:

$$\frac{d\theta}{dt} = 1 - \frac{V\theta}{D_c} \tag{7}$$

The equation describing the movement of the movable block of the model has the form:

$$m\ddot{x} = K(u_s t - x) - S \cdot \tau_s \tag{8}$$

where m is the mass of the block, S is the block contact area, K is the spring stiffness, u_s is the velocity at which the spring is being pulled, $F_s = S \cdot \tau$ is the force of resistance to shear in accordance to Eq. (6).

The parameters of dynamic failure in the reference variant were compared to the characteristics of the failure when the value of normal stress at the contact σ_n was changed by 1%. The results of calculations indicated (see Fig. 3) that the time of failure, the stress drop, and the maximum velocity of block displacement are approximately the same in the case of both dynamic and quasi-static decrease of the normal load [10].

Now let's consider the possibility of changing the stiffness of the massif due to rock excavation. It is clear that mining operations in a quarry can't affect noticeably the elastic characteristics of the massif at a depth of several kilometers.

Let us estimate whether underground mining is capable of producing such changes of the effective elastic properties of the rock massif.

Numerical modeling of the shearing process was carried out for a monolithic rock block and for a block with cells. Just as in the case of the open-quarry modeling, one of the key parameters here is the size. According to Kocharyan [12],
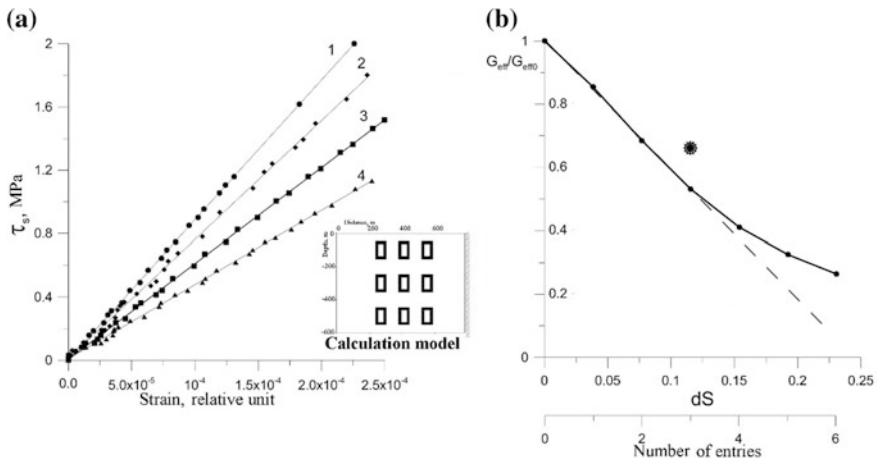
Fig. 3 Numerical modeling of the shearing process of a block with cells: **a** shear stress versus shear strain for the monolithic block (1) and for the block with 1, 2 and 3 rows of cells (lines 2, 3, 4); **b** relationship between the relative effective shear modulus of a massif with cells and the mass fraction that is not occupied by cells. Bottom axis: the number of rows of cells for each variant of calculation

the ratio for earthquakes is $L \approx 0.3 E_s^{1/3}$. Basing on this relation, the size of the simulated massif was selected so that it could accumulate elastic energy corresponding to an earthquake M 3–3.5. The task has been solved in 2D (Fig. 3) and was considered in detail in Kocharyan et al. [10]. The size of the cells that simulate chambers in a mine, as well as distances between the cells (rows of cells) corresponded to actual dimensions of chambers adopted in one of the mines of the Kursk Magnetic Anomaly region. The obtained "shear stress—shear strain" dependences (Fig. 3a) for a monolithic block and for a block with 1, 2 and 3 cells, demonstrated that the effective shear modulus Geff is the smaller, the more destructed the rock massif is.

For one horizon of cells, the value of G_{eff} decreases by about 20%, for two— about 1.5 times. For three horizons the effective modulus of the rock massif almost halves; which may turn to be critical from the point of view of the possibility of triggering a dynamic motion along the fault. If the cells are filled with crushed rock with the modulus of elasticity of E = 5 GPa and Poisson's ratio of $v = 0.32$, the decrease of the effective modulus of rock massif is noticeably less. It lowers only by 34% even when 3 horizons of cells are involved (Fig. 3b). Such a simple measure reduces the possibility of an instability to occur if compared to a massif containing empty cells.

3 Conclusions

The main reasons for triggering dynamic fault slips by mining operations are:

– a quasi-static alteration of the stress pattern as a result of excavation and removal of rock;
– a change of the effective stiffness of the enclosing rock massif as a result of tunnelling;
– a change of hydro-geological regime of the fault zones;
– accumulation of small deformations localizing at discontinuities in stressed fault zones.

The following geomechanical criteria should be satisfied for a dynamic fault slip to occur: (i) shear stresses at a local fault segment should reach a level close to the current shear strength (it is true for active faults in most cases); (ii) the condition of velocity weakening when sliding along a fault must be realized; (iii) a certain ratio of the rock stiffness to the fault stiffness should be satisfied.

Our results show that for triggering an earthquake of a certain magnitude it is necessary to change the stress level or the material properties of the fault segment at least several times bigger in size than the area of nucleation zone of the future earthquake. If as a result of mining the stress-strain conditions change at a relatively big area, then a positive variation of the Coulomb's function by a value of some tenth of MPa may turn to be enough for triggering an earthquake.

The underground development of mineral deposits can change the effective elastic properties of the enclosing rock massif in the vicinity of an active fault. So, a rather powerful earthquake can take place even in a previously aseismic region.

Open pit mining in most cases has no effect neither on the mechanical properties of the massif at the hypocenter depth, nor on fault stiffness. Excavation and removal of rock in open mining in aseismic or weakly seismic regions cannot be the reason for large tectonic earthquakes to occur. In seismically active regions development of large quarries can essentially bring closer the moment of the future earthquake occurrence.

The anthropogenic effect in principle can both trigger seismic events and lower the level of seismic hazard. The magnitudes of events sensitive to human activities are limited and, according to expert judgment can hardly exceed the magnitudes of $M \sim 6$–6.5.

References

1. Das, S., Scholz, C.H.: Off-fault aftershock clusters caused by shear stress increase. Bull. Seismol. Soc. Am. **71**, 1669–1675 (1983)
2. Dieterich, J.H.: Modeling of rock friction: experimental results and constitutive equations. J. Geophys. Res. **84**, 2161–2168 (1979). https://doi.org/10.1029/JB084iB05p02161
3. Djadkov, P.G.: Induced seismicity at the Lake Baikal: principal role of load rate. In: The 29th General Assembly of the International Association of Seismology and Physics of the Earth's Interior, August 18–28, Thessaloniki, Greece, Abstracts, p. 359 (1997)
4. Domański, B., Gibowicz, S.: Comparison of source parameters estimated in the frequency and time domains for seismic events at the Rudna copper mine. Poland. Acta Geophys. **56**, 324–343 (2008)
5. Durrheim, R.J.: Mitigating the risk of rockbursts in the deep hard rock mines of South Africa: 100 years of research. In: Brune, J. (ed.) Extracting the Science: A Century of Mining Research, pp. 156–171. Society for Mining, Metallurgy, and Exploration, Inc. (2010). ISBN 978-0-87335-322-9
6. Florin, V.A.: Fundamentals of Soil Mechanics, vol. 1. Stroiizdat, Leningrad (1959). (in Russian)
7. Foulger, G.R., Wilson, M.P., Gluyas, J.G., Julian, B.R., Davies, R.J.: Global review of human-induced earthquakes. Earth-Sci. Rev. **178**, 438–514 (2018). https://doi.org/10.1016/j.earscirev.2017.07.008
8. Heesakkers, V., Murphy, S., Lockner, D.A., Reches, Z.: Earthquake rupture at focal depth, Part II: mechanics of the 2004 M2. 2 earthquake along the pretorius fault, TauTona Mine, South Africa. Pure Appl. Geophys. **168**, 2427–2449 (2011). http://dx.doi.org/10.1007/s00024-011-0355-6
9. King, G.C.P., Stein, R.S., Lin, J.: Static stress changes and the triggering of earthquakes. Bull. Seismol. Soc. Am. **84**, 935–953 (1994)
10. Kocharyan, G.G., Budkov, A.M., Kishkina, S.B.: Initiation of tectonic earthquakes during underground mining. Physical and Technical Problems of Development of Useful Minerals, № 4, pp. 34–43 (2018)

11. Kocharyan, G.G., Kishkina, S.B.: Initiation of tectonic earthquakes by surface mining. Physical and Technical Problems of Development of Useful Minerals, N5, pp. 45–53 (2018). https://doi.org/10.15372/ftprpi201805055

12. Kocharyan, G.G.: Geomechanics of faults. GEOS, Moscow (2016). (in Russian)

13. Kocharyan, G.G., Novikov, V.A., Ostapchuk, A.A., Pavlov, D.V.: A study of different fault slip modes governed by the gouge material composition in laboratory experiments. Geophys. Int. J. **208**, 521–528 (2017). https://doi.org/10.1093/gji/ggw409

14. Lizurek, G., Rudzinski, L., Plesiewicz, B.: Mining induced seismic event on an inactive fault. Acta Geophys. **63**(1) (2015)

15. Love, A.E.H.: A Treatise on the Mathematical Theory of Elasticity, 4th edn. Cambridge University Press, Cambridge (2013)

16. Melnikova, N.N. (ed.): A Seismicity During Mining. Publishing House of the KSC RAS, Apatity (2002). (in Russian)

17. Peng, Z., Gomberg, J.: An integrated perspective of the continuum between earthquakes and slow-slip phenomena. Nat. Geosci. **3**, 599–607 (2010). https://doi.org/10.1038/ngeo940

18. Scholz, C.H.: Earthquakes and friction laws. Nature **391**, 37–42 (1998). https://doi.org/10.1038/34097

Dynamics of Rock Mass Seismicity During Mining Near the Saamsky Fault in the Kirovsky Mine, Apatit JSC

Anatoly Kozyrev ⓘ, Svetlana Zhukova ⓘ and Olga Zhuravleva ⓘ

Abstract

The approach of the mining operations to the Saamsky fault (the Khibiny rock massif) has resulted in changes in the stress-strain state of the rock mass and the seismic regime, which is seen in an increase of a number of seismic events and their energy. In the last decade, the large seismic events (energy more than 10 MJ) began to occur near the Saamsky fault area, which indicates the activation of this fault. Each large seismic event is accompanied by a number of smaller events—foreshocks and aftershocks. This study presents the results of a retrospective analysis of microseismic monitoring data in the area of the Saamsky Fault, which is one of the largest radial subvertical faults of the Khibiny massif. The impact of the mining operations with approaching the fault and the dynamics of seismicity has been analyzed. The causes of the activation of seismicity and its migration have been defined. It is shown that the further approaching of mining operations to the fault (such as extraction of the ore body and driving of workings across the strike of the fault) can complicate the geodynamic situation and requires further monitoring.

A. Kozyrev · S. Zhukova (✉) · O. Zhuravleva
Mining Institute Kola Science Centre RAS, 184209 Apatity, Russia
e-mail: svetlana.zhukowa@yandex.ru

1 Introduction

The Khibiny apatite-nepheline deposits have been developed since 1929 by open mining and since 1933—by underground mining. The mining operations started in the Saamsky open pit (Kirovsky mine), which is a section between the Kukisvumchorr and Yuksporsky deposits developed by underground mining. Currently, the open pit has been watered and the open mining completed.

The Kirovsky mine field is divided into blocks formed by the Kukisvumchorr (Vortkeuaivsky) fault of the second rank and faults of the third rank: the Saamsky, Yukspor and Hakman faults complicated by faults of the fourth rank [1]. The Saamsky open pit is crossed by the same-named radial fault, which runs along the Saamsky valley and across the ore body of the Kukisvumchorr deposit. It can be traced to a 30 km depth. Its length is about 10 km. The fault is referred to strike-slip type. It is a heterogeneous zone of crushing, cataclase and milonitization with a thickness within the open pit from several meters to 136 m, inside of which there are numerous blocks, lenses and coarse-grained pieces of oxidized host rocks. By the fall, the fault was traced in the open pit and in the underground workings of the Kirovsky mine for more than 200 m [2]. On mark +90 m the fault is completed with a loose mass of oxidized rocks width for more than 10 m.

During the underground mining of mineral deposits, the problem of the dynamic destruction of the rock mass particularly arises. Large-scale mining operations significantly impact on the geodynamic regime of the geological environment of the deposits. This statement is confirmed by the fact that the number of seismic events in the mines and the rock mass deformation rate increase. The deepening of underground levels sharply complicates the mining conditions of the deposit due to the rock pressure growth and changes in the physic mechanical properties and structural features of the rock mass.

In the last decade the large seismic events (energy more than 10 MJ) in the area began to occur, which indicates the activation of the Saamsky fault.

The study of the seismic activity in the Saamsky fault area is important now because such powerful tectonic faults cause a dominant impact on the stress-strain state of the rock mass and can be activated by the mining operations.

2 Research Methods

The continuous seismic monitoring has been performed at the Kirovsky mine, Apatit JSC, since 1987 [3].

The monitoring of seismic activity near the Saamsky fault with accuracy sufficient for detailed research began in mid-2007.

The seismic activity of the fault is influenced by both the distance to the mining operations and their depth. This paper shows the impact of the mining operations as they approach the Saamsky open pit along the strike of the ore body, as well as the development of the mining operations to depth and their approach to the lower level

of an open pit excavation (the bottom of the Saamsky open pit is located at +170 m level).

The open pit excavation has a significant impact to the redistribution of stresses. The fault body is exposed to a lesser vertical load, and, therefore, the tectonic stresses in the fault area exceed the vertical component than in more significantly Kukisvumchorr and the Yukspor deposits. The work [4] contains an assessment of the results of a multivariate numerical simulation of the rock mass stress-strain state when modelling the successive excavation of the ore body at level +10 m of the Kirovsky mine. The danger of approaching of the extraction front to the Saamsky fault is shown. The paper has analyzed the seismic data for a 10-year monitoring period in the area of the Saamsky Fault. The study area was chosen taking into account the fault impact zone and open pit boundaries (600 m × 2000 m).

The graphs (Fig. 1) show the seismic regime analysis results in the Saamsky fault area. It can be noted that the background seismicity values changed slightly until 2014 and amounted to ≈1000 J; after 2015 the background seismicity level became higher than 10 kJ. Most of these seismic events occurred due to the combined impact of geological and mining factors and due to the intensive mining operations, during which the stress-strain state of the rock mass constantly varies.

Characteristic peaks on the graphs are observed in those years when tremors were recorded in the area of the Saamsky fault and were felt on the territory of the industrial site of the Kirovsky mine.

Figure 2 shows a histogram of the seismic events distribution by energy classes registered in the research area.

A tendency of growth in the number of events both with a low energy and with a high one is observed.

The location of the events' hypocentres allows noting that in recent years the overwhelming majority of events is confined to deep horizons +172 m, +90 m and below as well as to the north-eastern part of the Saamsky open pit, passing into the
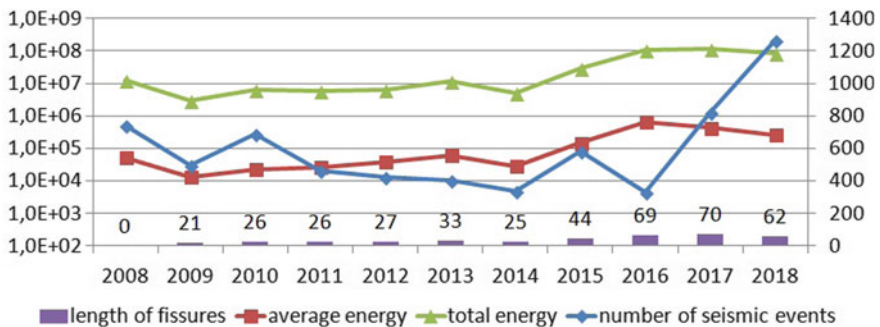
Fig. 1 Parameters of the seismic regime of the researched area of the Saamsky fault (on the main vertical axis the values of average and total seismic energy of events are shown; on the auxiliary axis there are data of the number of seismic events and the estimated total length of fractures (m))

Fig. 2 Distribution of the seismic events by energy classes recorded in the Saamsky fault area for a 10-year monitoring period

zone of fissuring and failure of the overlying rocks of the Yukspor edge of the Kirovsky mine.

With the development of mining at marks above +300 m, the redistribution of stresses apparently has little effect on the change in seismicity in the considered part of the rock mass. Whereas, in the transition of the mining operations to the lower levels, the rock mass is disturbed already at the level of marks comparable to the depth of the open pit.

3 Research Results

Further, the dynamics of the seismic activity depending on the rate of the mining operations and their approach to the Saamsky fault is considered in detail. For studying of the seismic activity, the levels from +236 m and below were selected. The seismic activity and its features vary on different levels. Figure 3 shows the
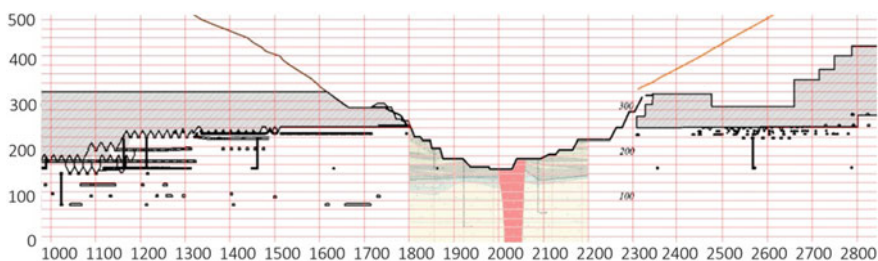
Fig. 3 The actual extraction of ore body and driving of workings at the end of 2018 (where ⌐⌐ —the open pit's contours; ▨—extracted ore body; ▲ ⬭ ⟞—excavated workings; ▬—the Saamsky fault)
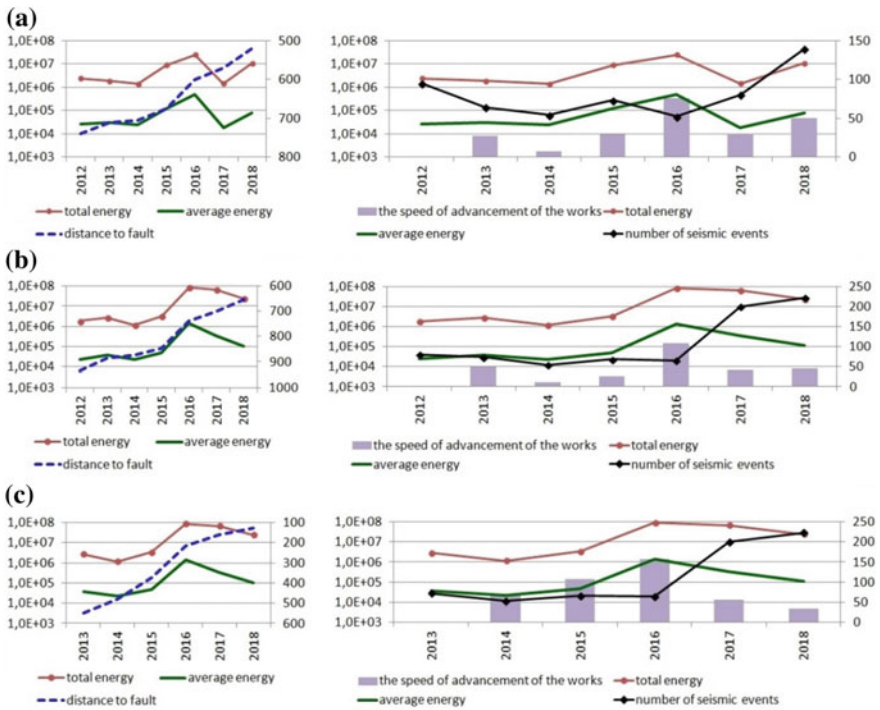
Fig. 4 The dynamics of seismicity depending on the rate of mining operations and their approaching to the Saamsky fault (**a**—extraction of the ore body, level +236 m, **b**—extraction of the ore body, level +183 m, **c**—driving of workings, level +183 m)

combined section along +450 m line of the Kukisvumchorr side (left) and along the −100 m line of the Yukspor side (right) with a longitudinal geological section in the Saamsky fault. It can be seen, what was a distance between the fault at different levels and the mining operations and driving workings by the end of 2018 on both sides of the mine (for the corresponding lines).

Further, the development of the mining operations on the Kukisvumchorr side at levels of +236 m and +183 m in the direction of the Saamsky fault is considered (Fig. 4).

An intensification of the extraction of the ore body is observed which is seen in the seismic response of the rock mass. The seismic energy of events increased with a decreasing in the distance to the Saamsky fault and an increasing in the rate of the mining operations. The total number of the seismic events in 2016 was less than in

other years, but their seismic energy became higher. This may indicate the rock mass unloading with impact of several factors such as high tectonic stress, the stress concentration in the zone of influence of the reference pressure and the impact of the overlying rocks.

By the end of 2018 in the Kukisvumchorr side the stoping operations at level +236 m approached the Saamsky fault at a distance of about 500 m (on average for three years—52 m per year) and at level +183 m—about 650 m (an average of three years—64 m per year).

The driving of workings (Fig. 4c) on the Kukisvumchorr side proceeds towards the Saamsky fault and on the Yukspor side proceeds from it. By the end of 2018 on the Kukisvumchorr side the haulage drifts at level + 172 m approached directly into the impact zone of the Saamsky fault. At the level + 90 m the backlog was about 380 m compared to the level +172 m. On the Yukspor side the driving of workings near the Saamsky fault at level +172 m started from 2013. In addition the number of excavated workings in 2016–2018 increased significantly, which also impacted the increasing of the seismic activity.

The detailed analysis of the seismic activity by different levels showed the following.

On the level +236 m, the annual number of the seismic events did not exceed 100 before 2018. During 2018, 139 seismic events occurred (about 40% more than the maximum annual number of seismic events in 2008–2017). The significant changes in the total and average seismic energy were observed in 2015, 2016 and 2018 (Fig. 5). At the same time, the average seismic energy in 2018 was less than in 2015 and 2016, because the number of small seismic events increased (energy class 3–5). The largest seismic event (energy class 7) occurred at this level in 2016.

On level +172 m, the annual number of the seismic events until 2017 did not exceed 100 (with the exception of 2008). In 2017, 200 seismic events were recorded, and in 2018—223 seismic events (which is almost twice greater than the annual number of events in 2008–2016) (Fig. 5). Significant changes in the total and average seismic energy were observed starting from 2016. In 2017 and 2018 the number of small seismic events also increased, which is seen in a decrease of the average seismic energy.

On level +90 m, the annual number of the seismic events in 2008–2014 did not exceed 100 (on average, 64 seismic events). The first peak was observed in 2015 (160 seismic events). Then, in 2017–2018, an extreme increase in the seismic activity was observed (342 and 377 seismic events per year, respectively). The maximum values of energy characteristics were also observed in 2017–2018 (Fig. 5). The seismic activity was possibly moving up to the next scale level.

It was found that areas with increased seismic activity, where the largest seismic events occur, are located on the side of the Kukisvumchorr deposit in the footwall of the ore deposit and are concentrated in the vicinity of the extraction space,
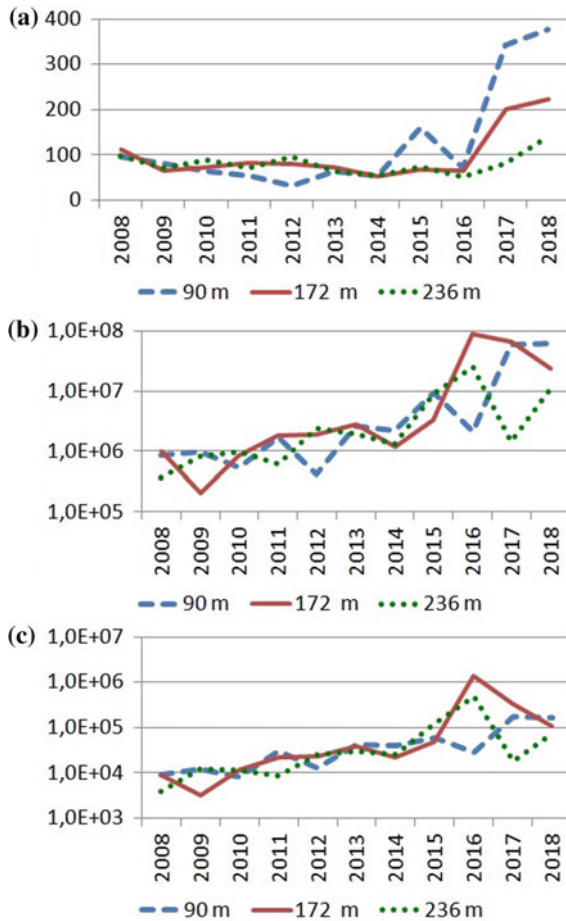
Fig. 5 Changing of seismic activity at several levels of the mine field (**a**—the number of seismic events; **b**—the total seismic energy of events; **c**—is the average seismic energy)

geological disturbances and in the area of the mining operations (Figs. 6 and 7). The first series of the large seismic events occurred near the Saamsky fault (the projection of the coordinates of some seismic events coincides with the projection of the fault structure). Later, an area of the rock mass, located at some distance away from the fault, was activated but apparently in the zone of its influence. It should be noted that on the Yukspor side there is also an increase in seismicity on the level +90 m and below. A single cloud of the seismic events can be seen in this area, including the seismic events from the Kukisvumchorr side.
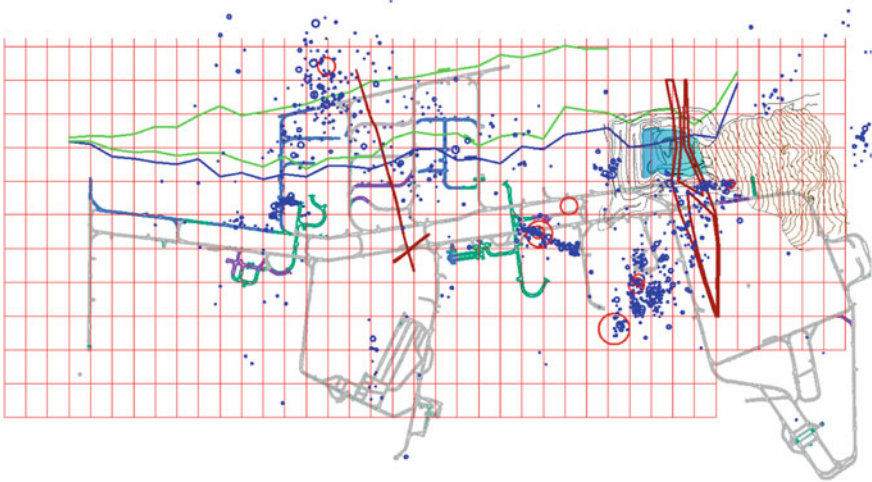
Fig. 6 The map of the seismic events, 2018 (projection on level +90 m, the seismic events occurred from 40 to 140 m levels)
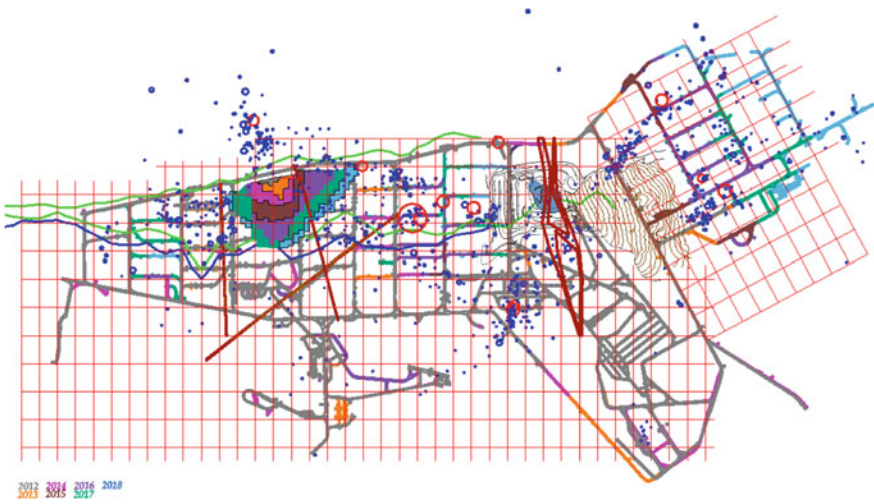
Fig. 7 The map of the seismic events, 2018 (projection on level +172 m, the seismic events occurred from 122 to 222 m levels)

On the level +172 m (Fig. 7), on the Kukisvumchorr deposit, the seismic activity is lower than on the lower level. On the Yukspor side, there are areas of increased seismic activity associated with both the driving of workings and the processes of fracturing in the console of the overlying rocks of the hanging wall of the deposit and partial failure of the rocks into the Saamsky open pit.

4 Conclusions

As the mining operations associated with both the ore extraction and driving of workings approach the Saamsky fault, the stress-strain state of the rock mass and seismic regime change, which is manifested as an increase of the number of the seismic events and their energy. The activation of seismicity is observed to a greater extent in the lower levels. The seismicity of the area near the Saamsky fault is significantly impacted by the intensity of the mining operations. The most seismically active area of the rock mass is located on the Kukisvumchorr side in the footwall of the ore deposit.

Thus, according to the results of the analysis, the main causes of the activation of the Saamsky fault have been defined. It is shown that the further development of the ore body's extraction works and the driving of the workings across the strike of the fault can lead to complication of the geodynamic situation and further monitoring of this area is required.

References

1. Zak, S.I., Kamenev, E.A.: New data on the geology of the Khibiny alkaline massif. Sov. Geol. (7), 42–51 (1964) (in Russian)
2. Kozyrev, A.A., Kasparyan, E.V., Zhirov, D.V., Smagina, Y.G.: The Khibiny Saamsky fault: an abormal character of modern deformations. Vestnik of MSTU **12**(4), 30–46 (2009) (in Russian)
3. Korchak, P.A., Zhukova, S.A.: Method of receiving basic data for the seismic monitoring at underground mines of Apatit JSC. Min. Inf. Anal. Bull. (10), 15–20 (2014) (in Russian)
4. Semenova, I.E., Avetisian, I.M., Zemtsovskiy, A.V.: Geomechanical modeling of deep-level mining under difficult geological and geodynamic conditions. Min. Inf. Anal. Bull. (12), 65–73 (2018). https://doi.org/10.25018/0236-1493-2018-12-0-65-73 (in Russian)

An Integrated Approach for Prediction of Hazardous Dynamic Events (Case Study of Retrospective Data in the Area of a Tectonic Rockburst in the Rasvumchorr Mine on January 9, 2018)

Anatoly Kozyrev, Olga Zhuravleva and Inna Semenova

Abstract

The study discusses the results of multifactor analysis of a large 3.3 magnitude seismic event which occurred on January 9, 2018 (6:00 AM MSK) in the Rasvumchorr mine (the Apatitovy Tsirk deposit). The event's hypocenter was in the footwall of the ore body outside the mining zone. The event was accompanied by a strong noise, underground and surface shaking and severe damage to mine excavations, and was felt both by mine personnel and residents of Kirovsk and Apatity towns. Destructions in mine excavations were detected within the elevations up to 100 m. Events of such rank occur at the Khibiny rockburst hazardous deposits at intervals of 5–10 and more years. This large dynamic event could be triggered by a technologic blast on January 8, 2018, when the rock mass went into an extremely unstable state. Here, an integrated approach for prediction of hazardous dynamic events is invoked for retrospective data. The proposed approach is based on combining probabilistic assessments for seismically dangerous zones and 3D numerical modeling of the rock mass stress-strain state. It also takes into account main geological, geomechanical and mining-engineering factors at several large-scale levels. It is shown that the combined use of various indicators of seismic hazard and parameters of the stress-strain state of a particular site during development of mining operations makes it possible to increase reliability of seismic predictions in hazardous zones.

A. Kozyrev · O. Zhuravleva (✉) · I. Semenova
Mining Institute Kola Science Centre RAS, 24 Fersman str., Apatity,
Murmank Region 184209, Russia
e-mail: zhuravlevaog@goi.kolasc.net.ru

339

1   Introduction

Large-scale mining significantly changes the stress state of rock massifs, which can lead to an increase in seismic activity and to occurrence of rockbursts and mining-induced earthquakes. This problem is still relevant for many mines in the world [1–3], including the rockburst-hazardous deposits of the Khibiny rock massif, where mining is accompanied by occurrence of a dynamic rock pressure [4, 5].

In this regard, assessing and forecasting the level of seismic hazard at the developed rockburst hazardous deposits of the Khibiny rock massif is of immediate interest and an important component of the geodynamic risk assessment through a comprehensive analysis of geological, geophysical and mining factors. A detailed study of seismic activity and identification of increased seismic hazard areas make it possible to assess sensitivity of rock mass areas to mining operations and to identify geodynamically active structures, etc.

2   Study Object

On January 9, 2018, large seismic event (with magnitude 3.3) occurred at the Rasvumchorr mine. The event was qualified by the Commission for mining rockburst of Apatit JSC as a tectonic rockburst. The event was accompanied by a strong sound, shaking of the rock mass and the Earth's surface, and was felt by both the mine workers and residents of Kirovsk and Apatity towns [5].

Work [5] presents actual data on the mining openings survey on January 9, 2018 immediately after the event, a general analysis of seismic data of the Automated Monitoring System of the Rasvumchorr mine rock mass state, and considers geological, geomechanical and mining factors that affect the geodynamic regime of this site. Based on the received information, the authors proposed a hypothesis about the origin of the event and its classification.

This work presents an integrated approach to prediction of dangerous dynamic events on the base of retrospective data. The proposed approach is based on combining probabilistic assessments for occurrence of powerful seismic events of energy class 6–8 with 3D data of numerical simulations of the rock mass stress-strain state in potentially hazardous areas. It takes into account main geological, geomechanical and mining factors at several large-scale levels. It is shown that the combined use of various indicators of seismic hazard and parameters of the stress-strain state of a particular site during development of mining operations makes it possible to increase reliability of seismic forecasts in hazardous zones.

3 Study Methods

3.1 Assessment of Level of Seismic Danger at Developed Deposits

Assessing and forecasting the level of seismic hazard at the developed deposits of Khibiny rock massif is an important component of the geodynamic risk assessment, which is carried out through a comprehensive analysis of geological, geophysical and mining engineering factors. For example, a detailed study of seismic activity is necessary when identifying geodynamically active structures, assessing sensitivity of rock mass site to mining operations, etc.

Seismic hazard assessment is carried out on the basis of three methods:

–   probabilistic forecast of large seismic events;
–   study of dynamics of seismically active zones on the basis of a comprehensive assessment of individual precursors;
–   combined use of energy index and cumulative apparent volume criteria.

The probabilistic forecast of large seismic events and study of dynamics of seismically active zones are carried out on the basis of integrated assessment of several precursors that are different in physical meaning and complement to each other: fractal criterion, b-value and concentration criterion [6].

For the joint use of the criteria reflecting various parameters of seismic emission stream, the values of complex indicator K_j are calculated in each space-time cell j:

$$K_j = \frac{1}{N} \sum_{j=1}^{N} k_{ij}. \tag{1}$$

where N—number of individual precursors, k_{ij}—value of a precursor i in a space-time cell j.

Changes in number, configuration and location of allocated seismically active zones reflect the nature of redistribution of the existing stresses in the rock mass depending on the intensity of large-scale mining operations. According to degree of seismic activity, three types of zones are determined: stable, pulsatile and growing (the most dangerous).

The probabilistic approach of the prediction of large seismic events for the conditions of the Khibiny apatite mines is based on an algorithm for calculating the retrospective statistical characteristics of dynamic precursors [7]. In each spatial cell, if there is a precursor (the value of the complex criterion exceeds the critical level defined for each deposit), an alarm is set, i.e., an anomaly is found, which either ends with occurrence of large seismic event, or with its absence (a false alarm/anomaly).

For an existing anomaly, probability of occurrence of a large seismic event can be determined via a complex of precursors as:

$$P(K|D1) = \frac{N_{al} - N_{al}^*}{N_{total}}. \tag{2}$$

where $P(K \mid D1)$—probability of a large event in the presence of a precursor (probability of detection), N_{al}—number of space cells in which the alarm was set (total number of anomalies), N_{al}^*—number of anomalies for which the time of expectation of a large event exceeded an average time of expectation of large seismic events (taking into account the mean-square error of its definition), N_{total}—total number of large seismic events occurred during observation period at a certain observation area [7].

The main seismically active zones in the deposits are considered independently of each other, since they can be influenced by various mining and geological factors [6]. This approach allows zoning of rock mass sections by types of seismicity, i.e., according to the probability values of a large seismic event in the presence of an anomaly predicted by a complex of precursors.

One of the possible problems that reduce the effectiveness of the proposed approach under dynamically changing mining-geological conditions is the presence of gaps in the target, i.e., a large seismic event may occur at a rock mass site with zero probability values, i.e., in those areas where no events of such energy class were previously observed. In this regard, to improve the reliability of the forecast, it is necessary to take into account the whole complex of geological, geomechanical and mining-technical factors that influence the geodynamic regime of the rock mass sections.

The third method for assessing seismic hazard level is the study of applicability of other criteria: the energy index and the cumulative apparent volume in the Khibiny apatite mines that have been used in the practice of seismological monitoring in mines [8, 9].

The event energy index (EI) is the ratio of the observed released seismic energy of this event E to the average energy E_{av} released by events having the same seismic moment M_0 [8], and characterizes heterogeneity of the existing stresses in the rock mass:

$$EI = \frac{E}{E_{av}(M_0)}. \tag{3}$$

Cumulative Apparent Volume (CAV) is a measure of rock mass deformation [9]. It is calculated as a sum of the apparent volumes of V_A for seismic events' sources located in a specific area of the rock mass:

$$V_A = \frac{M_0^2}{2\mu E}. \tag{4}$$

where M_0—seismic moment, E—seismic energy, μ—modulus of rigidity.

An unstable state of the rock mass occurs when *EI* (a measure of the relative stress) decreases, which means a drop in stresses. At the same time, the deformation (quantified by *CAV*) starts to increase significantly.

3.2 Rock Mass Stress-Strain State Modelling with Consideration of Mining-Engineering and Geological Factors

For the purposes of numerical simulation we choose the finite-element method (in the elastic formulation) implemented in the original Sigma GT software. It allows geomechanical calculations on several scale levels with automatic compression of the network of finite elements and interpolation of boundary conditions [10]. Due to high levels of the bottom of Rasvumchorr valley and vast plateau surrounding the Rasvumchorr mine from three sides, the levels of +530 and +470 m can be attributed to the deep ones. The parameters of the initial stress field are fairly stable over the surfaces/levels and with depth. The initial direction of the vectors of the maximum component of the principal stress is close to the strike of the ore body. However, development of an underground stoping excavation and an open pit largely transforms the stress field in its vicinity; the orientation of stresses and their absolute values change. Both stress concentration areas (for example, in the support zone of underworked rocks) and tensile stress areas (for example, when hole-through underground stoping works with an open pit) are formed.

A finite-element model of the Rasvumchorr mine was developed; it allows predicting the stress-strain state for different scenarios of development of underground mining at levels +450, +470 and +530 m. At that, development of reserves by the sublevel caving mining, both with drift and ort preparation, was simulated at the elevations of the sublevel workings up to the level of +310 m, and in less detail in vertical direction to the level of +230 m.

Figure 1 shows a small-scale model.

As factors affecting the stress-strain state, the model takes into account the current tectonic stresses, relief, geometry of the ore bodies, differences in the elastic characteristics of the ore bodies and host rocks, the parameters of the clearing recesses and the largest fault structures.

Thus, the chosen research methods allow taking into account various factors affecting the rock mass and reflecting its behaviour during mining. The stress-strain state modeling allows identification of potentially dangerous parts of the rock mass. The seismic data study makes it possible to determine the critical changes in the rock mass and define the level of danger in the rock mass site. Comparison of these results allows identifying the most dangerous parts of the rock mass.
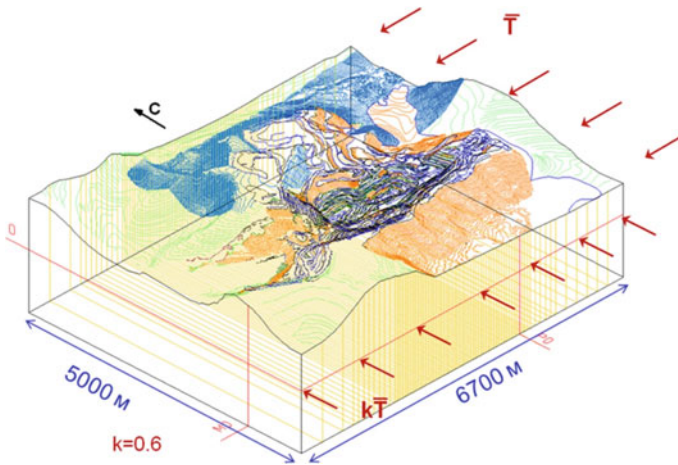
Fig. 1 3D small-scale model of the Khibiny apatite arc part, including the Rasvumchorr mine reserves and the boundary conditions setting scheme

4 Study Results

Calculations of the stress-strain state of the Rasvumchorr mine rock mass before the tectonic rockburst were carried out taking into account the actual development of mining operations. The analysis of current tangential stresses shows that their values are close to critical, and one of the areas of action of τ_{max} coincides with direction of the fault zone, along which with (high probability) the displacement occurred. Earlier, rockbursts had already occurred near this fault zone.

Figure 2 presents the calculation results (1 January 2018) in the form of a distribution map of the maximum component of the principal stresses at mark +450 m together with actual seismic events (January 2018).

Let us consider application of three methods for assessment of seismic hazard.

Figure 3 presents the map of probabilities of a large seismic event in the presence of an anomaly set by a complex of precursors (calculations are made for 1 January 2018). Figure 3 also shows seismic events that occurred during the period 1–31 January 2018.

In the identified area of increased probabilities, growth in seismic activity is observed in January 2018, i.e., an anomaly was identified by a set of precursors (Fig. 4). The seismically active zone in the section of the rock mass, where the tectonic rockburst subsequently occurred (around 6:00), emerged on 1 September 2018 at 0:00. Later on, it gradually increased and an hour before the implementation of the tectonic rockburst covered a large area. An hour after the tectonic rockburst, the seismically active zone increased significantly, which reflected the behaviour of the rock mass after a powerful dynamic event.
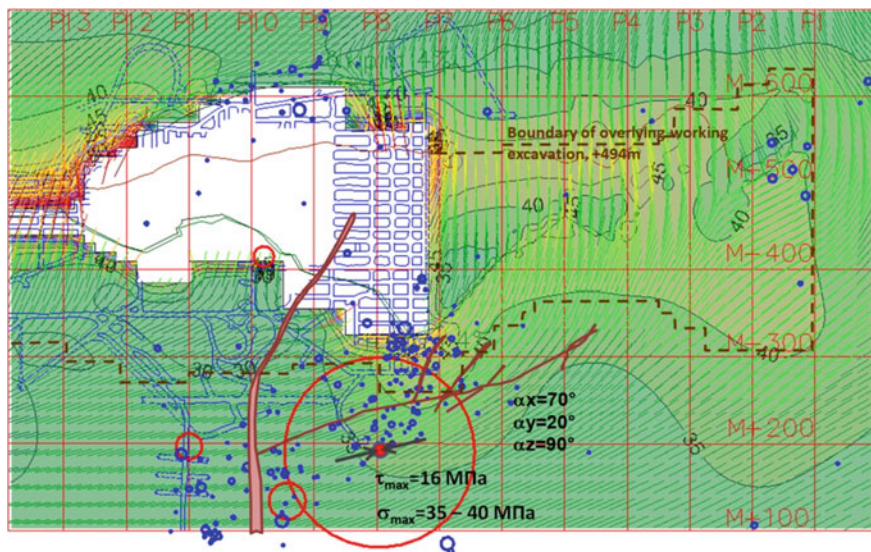
Fig. 2 Distribution map of the maximum component of the principal stresses at mark +450 m together with actual seismic events (January 2018)
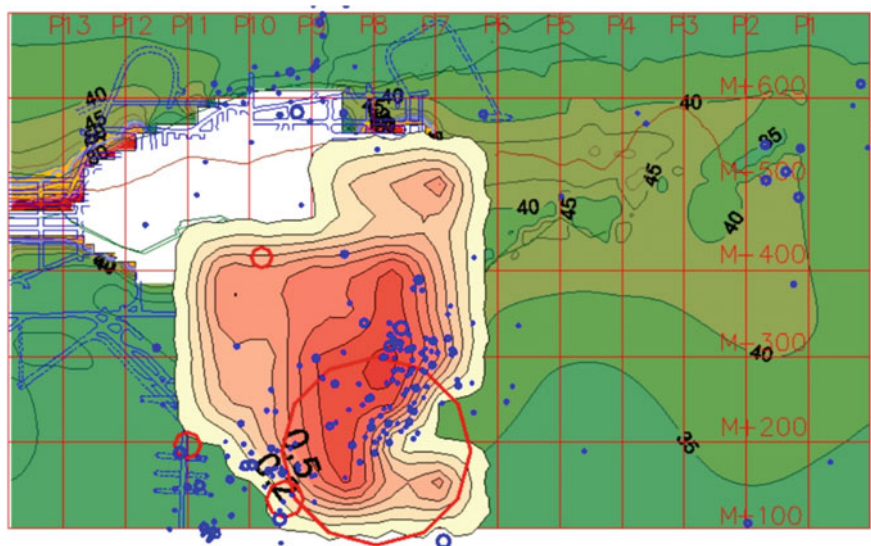
Fig. 3 Map of probability of a large seismic event in the presence of an anomaly set by several precursors (1 January 2018)
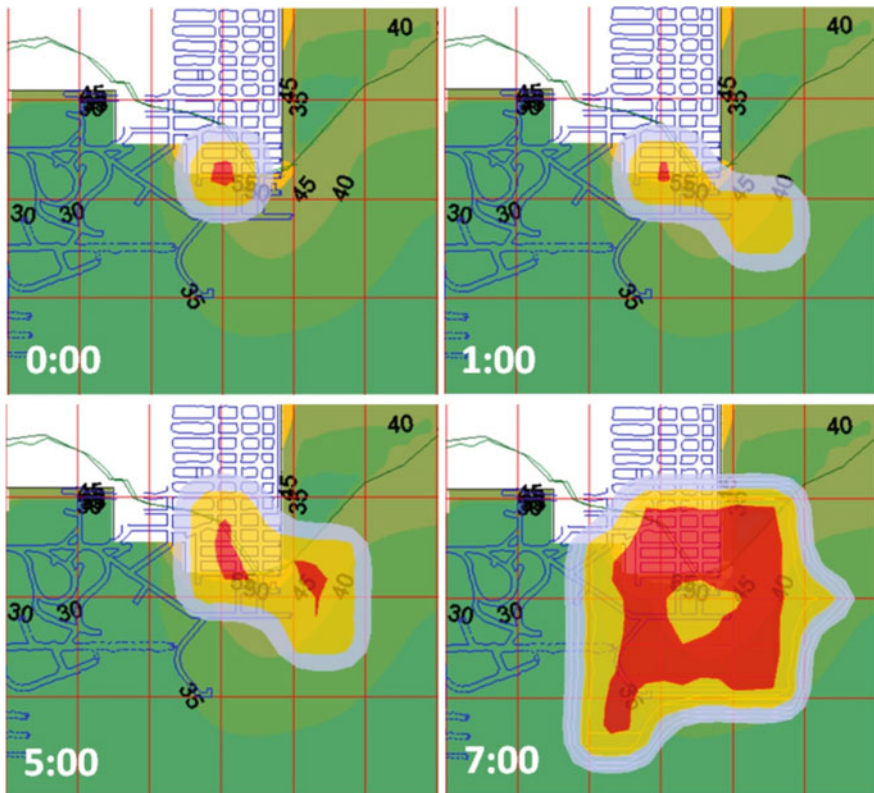
Fig. 4 Maps of increased seismic activity zones (9 January 2018)

Figure 5 shows the graphs of changes in *EI* and *CAV* parameters in the rock mass section where the tectonic rockburst occurred. From the graphs it can be seen that in about 1.5 months possible precursor is observed—*EI* value has decreased significantly and *CAV* value has increased. After that, *CAV* values changed slightly, and *EI* values gradually increased.

A few hours before the tectonic rockburst, an end-face blast was carried out (8 January 2018 at 22:48). Immediately after it at 22:50, the maximum *EI* value is observed, which slightly decreased before the time of the rockburst implementation (the horizontal arrow on the graph). At the same time, the increase in *CAV* accelerated first, and then slowed down. After the tectonic rockburst, there is a decline in *EI* and a significant increase in *CAV*, which slowed then.
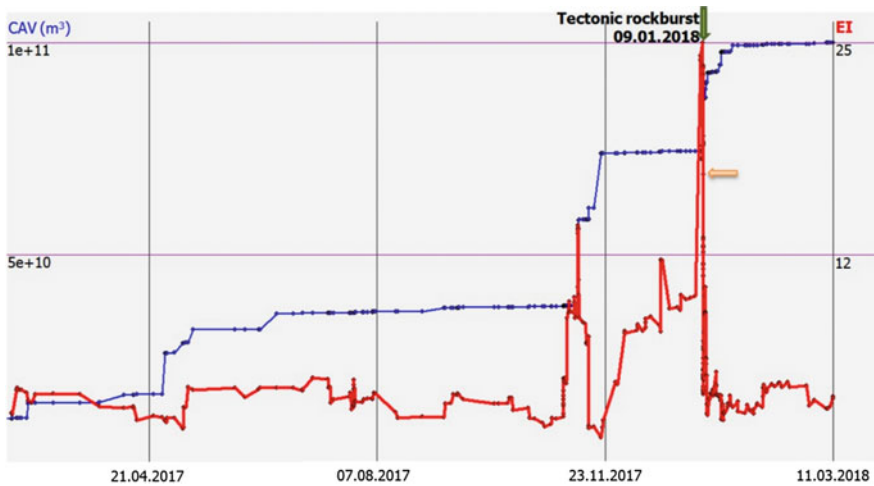
Fig. 5 Change in *EI* and *CAV* parameters for the tectonic rockburst area

5 Conclusions

Analysis of retrospective data on the tectonic rockburst that occurred at the Rasvumchorr mine shows capabilities of an integrated approach to predicting dangerous dynamic events.

For the purposes of identification of potentially hazardous events, on monthly basis there can be built the forecast maps of probabilities of a large seismic event under the condition of presence of an anomaly set by a suite of precursors. Daily localization of seismically active zones allows identification of anomalies by means of evaluating a set of precursors. The use of additional indicators of the rock mass state such as the energy index and cumulative apparent volume can reveal changes in its state.

The parameters of the stress-strain state of a rock mass section indicate potentially dangerous parts with consideration of various geological, mining and technological factors. Redistribution of stresses during mining operations can be estimated by seismic emission parameters. It should be borne in mind that seismic event (as well as technological blast) can lead to rock mass unloading, and vice versa—a stronger event can start forming.

Retrospective analysis of data on the seismicity of the rock massif, stress field with consideration of mining, technical and geological factors in the tectonic rockburst area at the Rasvumchorr mine showed perspectives of using an integrated approach to predicting dangerous dynamic events in rockburst-prone deposits. It should be borne in mind that the use of various indicators allows, in the first place, identifying potentially dangerous sections of the rock massif, and there can be

several such sections in the mine. At the same time, it is impossible to make an unequivocal conclusion that a large seismic event will occur at a certain section and, all the more so, to predict its exact time.

References

1. Hudyma, M., Brown, L., Cortolezzis, D.: Seismic risk in Canadian mines. In: CIM MEMO Conference, Sudbury, p. 14 (2016)
2. Lasocki, S., Orlecka-Sikora, B., Mutke, G., Pytel, W., Rudzinski, L., Markowski, P., Piasecki, P.: A catastrophic event in Rudna copper-ore mine in Poland on 29 November, 2016: what, how and why. In: Vallejos J.A. (ed.) Rock Mass Response to Mining and Underground Construction, Proceedings of the 9th International Symposium on Rockburst and Seismicity in Mines, 15–17 November 2017, Santiago, Chile, pp. 316–324. Editec S.A., Santiago, Chile (2017)
3. Van Aswegen, G.: Seismic sources and rock burst damage in South Africa and Chile. In: Vallejos J.A. (ed.) Rock Mass Response to Mining and Underground Construction, Proceedings of the 9th International Symposium on Rockburst and Seismicity in Mines, 15–17 November 2017, Santiago, Chile, pp. 72–86. Editec S.A., Santiago, Chile (2017)
4. Kozyrev, A.A., Panin, V.I., Savchenko, S.N., et al.: Seismicity During Mining. KSC RAS Publishing House, Apatity (2002) (in Russian)
5. Kozyrev, A.A., Semenova, I.E., Zhuravleva, O.G., Panteleev, A.V.: Hypothesis of strong seismic event origin in Rasvumchorr Mine on January 9, 2018. Min. Inf. Anal. Bull. (12), 74–83 (2018). https://doi.org/10.25018/0236-1493-2018-12-0-74-83 (in Russian)
6. Kozyrev, A.A., Fedotova, I.V., Zhuravleva, O.G.: Some results on mining-induced seismicity prediction in the Khibiny apatite mines. In: Rockbursts and Seismicity in Mines. Proceeding of the 8th International Symposium, pp. 313–317. Inter-YES Ltd., Perm, Russia (2013)
7. Zavyalov, A.D.: Medium-term earthquake forecast: basis, methods, implementation. The Schmidt Institute of Physics of the Earth. Nauka, Moscow (2006) (in Russian)
8. Van Aswegen, G., Butler, A.: Applications of quantitative seismology in South African gold mines. In: Proceedings 3rd International Symposium in Rockbursts and Seismicity in Mines, pp. 261–266. Balkema, Rotterdam (1993)
9. Mendecki, A.J.: Seismic Monitoring in Mines. Chapman and Hall, London (1997)
10. Kozyrev, A.A., Semenova, I.E., Shestov, A.A.: Numerical modelling of the stress-strain state of the rock mass as the basis for the rockburst hazard prediction at different stages of deposit development. In: Proceedings of All-Russian Scientific Conference with International Participation "Computer Technologies in the Design and Planning of Mining", pp. 251–256. Renome, St. Petersburg (2009) (in Russian)

Regularities of Increase and Decrease of the Triggered Seismicity in the Rock Mass During the Lovozero Rare-Metal Deposit Development

Aleksandr Lovchikov[ID]

Abstract

The article describes regularities of changes in mining-induced seismicity during development of the Lovozero rare metal deposit. The seismicity at the deposit is shown to arise as a result of rare-metal extraction. The increase in seismicity, including the occurrence of strong events in the rock mass ($M > 1$), is associated with the joint mining of adjacent gently dipping ore deposits. The location of the Lovozero deposit on the Kola Peninsula map until the 1990s was considered as an aseismic territory, since no earthquakes had been recorded there. The earthquakes with magnitudes $M_L > 1$ began to occur at the deposit after a new Umbozero mine had been put into exploitation in 1984. Seismic events at this mine occurred after the simultaneous mining of two contiguous gently dipping ore deposits (the distance between the deposits is 40–60 m vertically) at a depth of 200–400 m from the surface. The development of seismicity at the Umbozero mine led to the strongest mining-induced earthquake in the entire history of the Russian mines (magnitude $M_L = 5.0$, energy class k = 11.8), which occurred in the mine on August 17, 1999. The mine openings were destroyed within an area of 650 thousand m^2. Shortly after this event, the Umbozero mine was closed (in 2004). The mining-induced seismicity occurred in 2002 at the nearby Karnasurt mine (10 km from the Umbozero mine). The seismological observations have revealed that up to 13 strong seismic events occur in the Karnasurt mine (magnitude $M_L > 1$) per year. The mine simultaneously produced two gently dipping (incidence angle with horizon of about 10–15°) thin (1.2 m each) ore deposits at a depth of 50–600 m below the surface. The distance between the orebodies is 100 m. It has been established that the cause of seismic events at the Lovozero deposit is simultaneous mining of the adjacent ore bodies in the area of large gravitational-tectonic stresses in the rock massif. The measurements have

A. Lovchikov (✉)
Mining Institute KSC RAS, 184209 Apatity, Russia
e-mail: vocson@goi.kolasc.net.ru

revealed the horizontal tectonic stresses with a magnitude of 40–60 MPa at the reached depths in the Umbozero and Karnasurt mines. The concentration of gravitational-tectonic stresses in the zone of contiguous mining of ore bodies causes seismic events in the mines' rock mass.

1   Introduction

Until the 90s of the last century, the area of location of Lovozero deposit on the seismic map of the Kola Peninsula (where seismological observations have been carried out since February 1956) was considered as a "dead zone" since not a single seismic event was recorded there. And only from the beginning of 90s, when a new Umbozero mine began operating at the deposit (in 1984), and two adjacent ore bodies began to be mined at the same time, the mining-induced seismicity at the Lovozero rock massif started its violent development [1]. Hence, it is obvious that seismicity of Lovozero deposit is induced by mining operations. If the Lovozero rare-metal deposit had not been developed, this region would still have remained a "dead zone" in terms of seismicity.

The increase in mining-induced seismicity at the deposit led to the strongest mining-induced earthquake (a tectonic rockburst) for all the history of the Russian mines. The event took place on August 17, 1999 at the Umbozero mine and resulted in damage to the mine openings on an area of 650 thousand m^2. According to the Kola Regional Seismological Centre (KRSC) GS RAS, its magnitude M_L was 5.0 and energy class k was 11.8 [2]. One of the consequences was the closure of the mine in 2004 and its subsequent flooding in 2009. Naturally, the conservation and the subsequent flooding of the mine resulted in the almost total decay of the seismicity in the rock mass.

Currently, the Lovozero deposit is being developed only by the Karnasurt mine, which works two flat-dipping (10–15° with horizon) tabular ore bodies each 1.2 m thick, separated by a rock seam 90–110 m thick. The Karnasurt mine has been in operation since 1951 [3] and before 2002 there had not been seismic events. Since 2002, after seismic events at the Umbozero mine, the triggered seismicity emerged and began to increase at the Karnasurt mine.

2   Methods and Results

The seismic events at the mine are recorded by two seismic stations located underground in the mine openings at a depth of 200–300 m from the surface. One of the seismic stations, the Lovozero seismic station, is a part of the unified seismological network of the Geophysical Survey RAS. The other station, the Apatity

seismic station, belongs to the seismological service GS RAS, located 50 km from the mine.

The specialists regularly carry out mutual verification of the strong seismic events registered by the Lovozero and Apatity seismic stations. Figure 1 shows a schematic mining plan for the lower and most developed ore body of the Karnasurt mine and the location of seismic stations in its mine field. Currently, the length of the mined part of the deposit is 7 km along the strike, with a maximum width of 1.3 km and a mining depth up to 50–600 m. A distinctive feature of the stress state of the Lovozero rock massif as a whole, as well as of the rock mass at the Umbozero and Karnasurt mines in particular, is its high tectonic tension [1].

The experimental in situ measurements in the Karnasurt mine estimate modern horizontal tectonic stresses as 40–60 MPa at the developed depths, directed in azimuths (50°–90°) ± 180°, which exceeds the maximum stress from the weight of the overlying strata by a factor of 4–6. The direction of maximum tectonic stresses in the horizontal plane is shown in Fig. 1 in the form of stress ellipses.

The high tectonic intensity of the rock massif is, in our opinion, the main cause of the mining-induced seismicity during the mining operations and dynamic rock pressure in mining openings. In particular, the high level of gravitational-tectonic stresses in the rock mass explains the origin of a tectonic rockburst of August 17, 1999 at the Umbozero mine (M_L = 5.0 k = 11.8). The work of [4] showed that the rockburst occurred as a result of superposition of the gravitational-tectonic stress field concentration with simultaneous removal of two closely spaced ore bodies at the mine. Superposition of stress fields from each of the ore bodies resulted in excess of the tensile strength of the rocks by stresses in an interlayer and in formation of an inclined crack about 500 m long in the rock mass. The crack passed from the interlayer of the ore bodies to the surface at an angle of 40° to the horizon, through the zone of maximum tensile stresses in the rock mass. As a result of the tectonic rockburst, the mining openings were destroyed on an area of 650 thousand m^2.
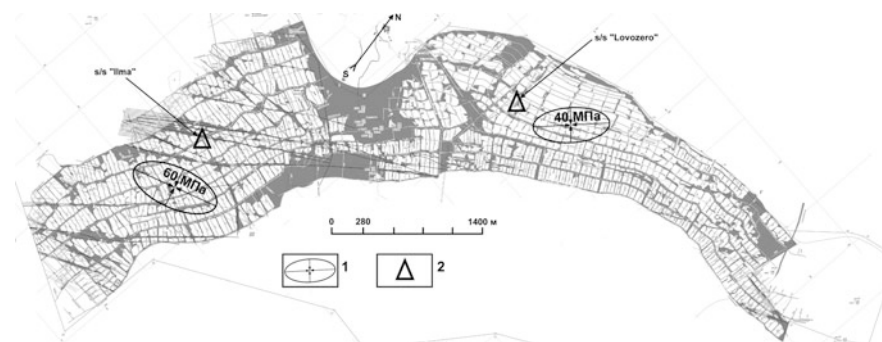
Fig. 1 A schematic plan of mining operations at the Karnasurt mine on II-4 ore body (1—ellipses of horizontal tectonic stresses; 2—seismic stations)

The Federal Service for Environmental, Technological, and Nuclear Supervision of the Russian Federation refers the Lovozero deposit to rockburst-prone and rockburst-hazardous deposits. The mine openings of the Karnasurt mine are rockburst-dangerous from a depth of 400 m from the surface. Due to high level of horizontal tectonic stresses in the rock mass and vertical stresses in pillars, which support the subsurface strata, the mine seismic stations annually register from 1 to 15 strong seismic events with a magnitude $M_L > 1$ and from 100 to 900 events of a smaller level (10^3–10^4 J). Figure 2 shows the histograms of the distribution by year of the strong ($M_L > 1.0$) and weak seismic events in the rock mass.

As is seen from Fig. 2, until 2004 the Lovozero deposit was exposed to seismicity in the Umbozero rock mass while it was functioning. After 2004, the Karnasurt mine began to determine the mining-induced seismicity of the deposit, in the rock mass of which up to 10–13 strong seismic events occur annually (Fig. 2b). The seismicity peak (Fig. 2a) (19 events) in 2009 was caused by the flooding of the Umbozero mine [5], whereas this event did not affect the seismicity of the Karnasurt mine rock mass (Fig. 2b).
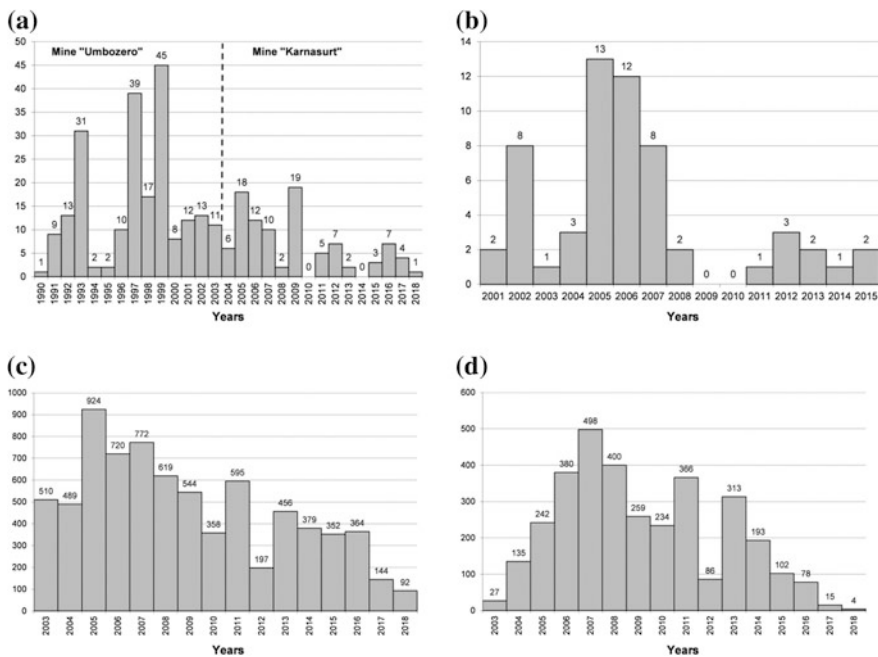
Fig. 2 Histograms of the distribution by years of seismic events in the rock mass of the Lovozero deposit: **a** strong events ($M_L > 1$) for the entire observation period; **b** strong events ($M_L > 1$) in the Karnasurt mine rock mass; **c** weak events (10^3–10^4 J) in the Karnasurt mine rock mass; **d** weak events (10^3–10^4 J) on the upper ore body I-4

Figure 2c illustrates distribution of weak seismic events by year. They naturally follow the distribution of strong seismic events in the rock mass of the mine (Fig. 2b). As can be seen from Fig. 2, the seismic activity in the rock mass of the Lovozero deposit during mining operations has been significantly reduced in recent years.

3   Discussion of Results

However, during the maximum rise of seismicity at the Umbozero mine (in 1991–1999) and at the Karnasurt mine (in 2005–2007) there was a common pattern associated with mining at the contiguous ore deposits. The first seismic occurrences at the Umbozero mine appeared immediately after mining another ore body in 1990–1991 just over the mined part of the ore body III-10 (the distance between the ore bodies is 40–60 m). As the working area of the overlying ore body increased over the mined part of the underlying one, the seismicity of the rock mass increased (Fig. 1) until it ended with a tectonic rockburst on August 17, 1999 [6]. It is significant that in the previous 7 years of the mine's operation (since 1984), when only one underlying ore body III-10 was in production, there were no seismic events in the ore mass. Similarly, at the Karnasurt mine, the seismicity of the rock mass sharply increased after resuming of stope operations to extract the overlying ore body I-4 (urtite) above the mined part of the underlying ore body II-4 (malinite) in 2004–2005. The vertical distance between the deposits is about 100 m.

The overlying urtite ore body (I-4) at the Karnasurt mine has been developed since 1978. The underlying malinite deposit (II-4) has been produced since 1951. The urtite ore body began to be mined from the lower horizons (+430 m) in the direction of the ore body strike in a band ∼300 m wide, above the mined part of the lower ore body and upwards in the direction of the ore body uprising to its surface outcrops. The development of this "band" (3 km length) took place during 1978–1990 without any noticeable occurrences of rock pressure in the mine openings.

The second part of the overlying urtite ore body from level +513 m to the outcrops (level +580 m) has been mined since 2000 up to the present. Figure 3 shows a schematic mining development plan for the urtite ore body with a time indication. The urtite ore bodies were excavated 100 m higher above the worked-out part of the malinite ore body (II-4). Immediately after starting the second stage of the urtite ore body development in the 2000s, the number of seismic pulses in the inter-area rock mass sharply increased (Fig. 2d). The strong seismic events during the urtite ore body mining were few but they (13 events) mainly occurred in 2006 during the undermining of a radial tectonic fault—the Glavny uplift that intersected both ore bodies [7].

Figure 3 demonstrates a combined schematic plan of the joint mining of the underlying ore body II-4 (malinite) and the overlying ore body I-4 (urtite), with the development of the urtite ore body by years. It should be noted that the underlying
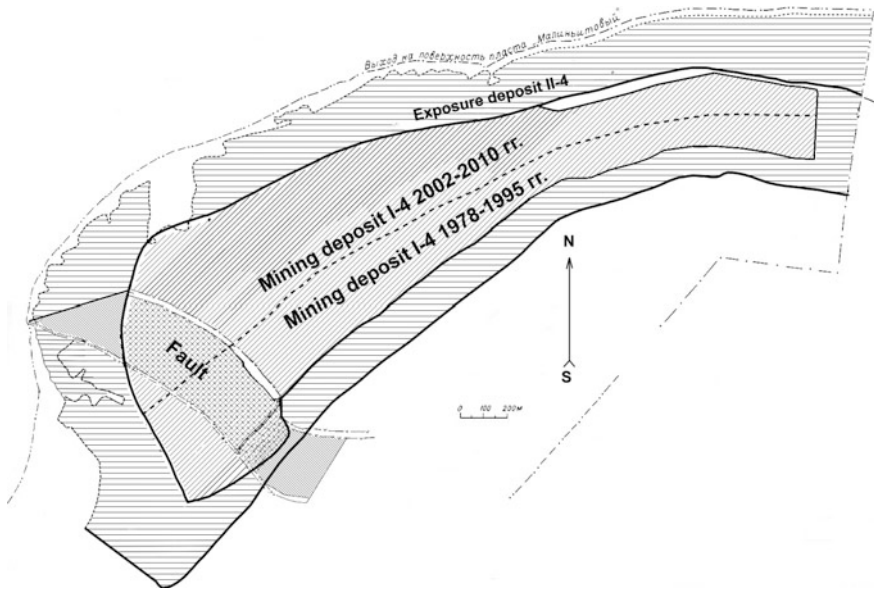
Fig. 3 A spatial scheme of the overlying ore body I-4 development above the mined part of the ore body II-4

malinite ore body under this section was developed more than three decades ago. During development of the urtite ore body over this area in the interlayer of the deposits, movements began in the structural-block environment of the rock mass and caused the seismicity increase in the interlayer (Fig. 2d).

Thus, the highly tectonically intense rock mass of the Lovozero deposit is very sensitive to changes in its state when developing the adjacent flat dipping low and average thick ore bodies.

The Umbozero mine developed two contiguous gently dipping ore bodies. The dip of angle of both deposits was 17° to the horizon; thickness −2.5 m (lower) and 5.5 m (upper); a distance between ore bodies was 40–60 m. The simultaneous mining of the two ore bodies had caused a powerful seismic event with magnitude $M_L = 5.0$ which resulted in great damage to mine openings at the lower ore body, penetration of 500 m long crack from the interlayer of the ore bodies to the surface. At the Karnasurt mine two gently dipping (angle with horizpn of about 10–12°) adjacent ore bodies have less thickness (1.2 m each) and the distance of about 90–110 m. The development of one ore body caused a series of microseismic events in the interlayer.

However, it did not result in strong geodynamic events in the mine's rock mass or damage to mine openings. It should be added that the value of horizontal tectonic stresses in the Umbozero mine mass is 50–60 MPa, which is higher than in the Karnasurt mine mass (40–50 MPa) [1]. All these circumstances contributed to

significantly lower seismic effects at the Karnasurt mine than at the Umbozero mine. Consequently, the triggered seismicity of the rock mass when developing the contiguous deposits depends on the following factors:

1. the tectonic intensity of the rock mass;
2. the thickness of an interlayer;
3. the thickness of the ore bodies themselves.

As to decrease in seismic activity of the rock mass during current development of the Karnasurt mine (Fig. 2a), I think it is caused by decrease in the area of overworking and, in practice, the cessation of this overworking these days. When overworking of the upper ore body above the mined part of the lower ore body is resumed at the mine's western side (the Kedykhvyrpakhk sector), the seismicity of the rock mass will apparently increase again.

4   Conclusion

It was established that mining-induced seismicity at the Lovozero deposit is purely triggered and due to loparite ore production operations. The seismicity occurs during simultaneous development of contiguous deposits in case concentrations of gravitational-tectonic stresses from each of the developed ore bodies overlap each other. The level of seismicity and occurrences of rock pressure on the adjacent deposits depend mainly on the following factors:

1. the magnitude of maximum gravitational-tectonic stresses in the rock mass;
2. the distance between the adjacent ore bodies and the area of mining for each of them;
3. the extraction capacity of each ore body.

References

1. Lovchikov, A.V., Asming, V.E.: Changes in the geodynamic regime of the Lovozero rock massif (Kola Peninsula) under the influence of mining. Mining in the Arctic. In: Proceedings of the 8th International Symposium Mining in the Arctic, pp. 48–55. Ivan Fedorov Printing House, St. Petersburg (2005)
2. Seismicity in Mining/Group of Authors. Apatity, Kola Science Centre RAS (in Russian)
3. Matytsyn, A.V., Borisov, Y.M.: 60 years of Lovozersky mining and concentrating plant. Gorny Zhurnal (10), 5–8 (2011)
4. Savchenko, S.N., Lovchikov, A.V., Kozyrev, A.A. (2004) Retrospective analysis of the mining-induced earthquake source at the Umbozero mine of August 17, 1999. Mining-induced seismicity in mining: source models, forecast, prevention. In: Proceedings of the International Meeting, Part 1, pp. 170–179. KSC RAS, Apatity (in Russian)

5. Lovchikov, A.V.: Investigation of seismicity caused by approved flooding of the mine. Gorny Zhurnal (9), 47–50 (2010)
6. Kozyrev, A.A., Lovchikov, A.V., Kuzmin, I.A.: The strongest mining-induced earthquake in Russian mines on August 17, 1999, the Umbozero mine (Kola Peninsula). Min. Inf. Anal. Bull. (6), 169–173 (2000) (in Russian)
7. Lovchikov, A.V.: Seismicity near the Glavny fault during stope operations at the Karnasurt mine. Problems and trends of efficient and safe development of geo-resources. In: Proceedings of Scientific Conference Dedicated to the 50th Anniversary of MI KSC RAS, St. Petersburg, pp 391–396 (2011) (in Russian)

A Study of the Trigger Effect in a Rock Burst-Hazard Rock Massif by Laser Interferometry

Vladimir Lugovoy ⓘ, Grigoriy Dolgikh ⓘ, Denis Tsoy ⓘ,
Andrey Gladyr ⓘ and Maksim Rasskazov ⓘ

Abstract

The article presents a comprehensive multi-level monitoring system including a laser deformograph and a nanobarograph installed in the mine workings at a depth of 300 m. The results of experimental studies of the laser deformograph at recording deformation disturbances in a rock massif are presented. The research results prove that this equipment can register both oscillations of the rock mass, caused by explosive works and reciprocating movement of tectonic blocks. We have researched the performance of slow deformation waves and present the brief overview of the research results in this article. The results of the registration of earthquakes in the Baikal rift zone are given. Experimental studies were carried out by using the laser deformograph, the laser nanobarograph and an automated multichannel geoacoustic system "PROGNOZ ADS" for monitoring the rock pressure. The main research tasks were to assess the impact of earthquakes on the state of the mountain massif in the area of mining operations in the uranium deposits of Streltsovsky ore field, to work out methods for registering earthquakes and earthquake precursors. The relationship between remote earthquakes and indicators of the rock mass acoustic activity in the form of a significantly increased number of acoustic events and their energy growth after the registration of a seismic wave is established. To monitor the pre- and post-history of seismic events, two-day recordings of the deformograph and nanobarograph have been analyzed before and after the earthquake. In this context, we see a high degree of correlation of the obtained results, which can be

V. Lugovoy (✉) · D. Tsoy · A. Gladyr · M. Rasskazov
Institute of Mining, Far East Branch, Russian Academy of Sciences, Turgenev st., 51, 680000 Khabarovsk, Russia
e-mail: lugovoy@dst.khv.ru; adm@igd.khv.ru

G. Dolgikh
V.I. Ilichev Pacific Oceanological Institute, Far East Branch, Russian Academy of Sciences, Baltic st., 43, 690043 Vladivostok, Russia

explained by interference of the mechanical vibrations and the refraction factor modifications occurring in the air-filled optic path of the deformograph.

1 Introduction

The high intensity of mining operations in the mines of "Priargunsky Industrial Mining and Chemical Union", OJSC has caused the geosphere technogenic disturbance within a large area. This was one of the reasons for the intensification of geodynamic processes in the rock massif containing the developed fields [1].

For the comprehensive research of geodynamic and seismic conditions a multi-level system of complex geodynamic monitoring was installed at the fields of "Priargunsky Industrial Mining and Chemical Union", OJSC. This system combines seismic, geoacoustic and deformation methods as well as measurement systems into a single measuring network [2–4].

As a part of the multi-level comprehensive geodynamic monitoring system located at "Streltsovskoe" ore field area in 2012, a 50 m laser deformograph was installed (Fig. 1) [5]. The interferometer is capable of recording crustal movements with the accuracy of up to 0.1 nm within the frequency width of 0–1000 Hz [5–7].
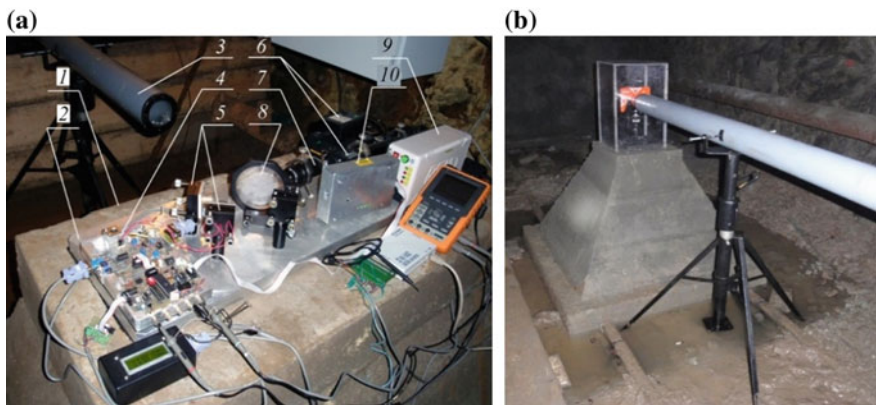
Fig. 1 Laser deformograph installed at geodynamic testing area in the vicinity of "Streltsovskoe" ore field: **a**—interferential unit; **b**—angle reflector and a fragment of air-filled beam mode guide: 1—concrete bed; 2—optical bench; 3—beam mode guide; 4—monitoring system; 5—piezoceramic units; 6—laser with a power unit; 7—collimator; 8—separating plate; 9—monitoring system power unit; 10—resonance amplifier

The laser nanobarograph is located in the hardware section to record changes of the atmospheric pressure. This is an original device developed at the V.I. Il'ichev Pacific Oceanological Institute (Vladivostok) with the measurement accuracy or resolution of 50 µPa.

2 Summary of a Laser Deformograph Test Results

The installation works of the laser deformograph included test and commissioning works. The results of the data obtained at the test and commissioning works were processed. They contain the detected characteristic spectrum of the Earth's natural oscillations range from main spheroidal tone $_0S_2$ to another main spheroidal tone $_0S$, which confirms the high quality of the deformograph's technical characteristics. In the higher frequency range (from 1 min to the period of the main spheroidal tone), the natural oscillation periods of the earth may coincide with the natural oscillation periods of the Earth's crust geoblocks; this must be taken into account at mining, as resonant and near-resonance effects are possible.

The 14-day record contains daily and semi-daily fluctuations, with the magnitude thereof 23 h 18 min and 11 h 53 min, respectively, at the background of long-period fluctuations. Confident registration of daily and semi-daily fluctuations indicates the stabilization of the base on which the optical bench and the corner reflector of the deformograph are installed, and the possibility to record long-period displacements of the rock mass.

It has been established that the deformograph reliably records oscillations of the rock mass caused by explosive works in the mines. To estimate the parameters of explosion impacts on the deformation field in the area of the laser deformograph placing, a series of test blasts were carried out. Based on the results of the test blasts, the radiation pattern and its impact on the sensitivity of the laser deformograph and the signal attenuation degree in the rock massif were studied.

It has been established that oscillations of various amplitudes with a period of about 2 min occur practically in all parts of the deformation records, which may be due to the natural frequencies of one of the geoblocks in the area of the deformograph installation. External influences lead to tectonic block oscillations (the deformograph has recorded their reciprocating motion with a period of 2 and 3 min), which, in its turn, can lead to resonant phenomena that can initiate deformation waves causing dynamic destruction of high-stressed sections of the rock mass.

3 A Review of the Slow Deformation Waves Research Results

The most important task of making the deformographic measurements is the detection of precursors of earthquakes and rock bursts, which can act as a trigger for high-energy seismic events in a shock-hazardous rock massif.

In the papers [8, 9], the initiation of deformation processes in the crust by weak perturbations is discussed in detail. The articles consider the possibility of deformation of the block-structured environment due to the accumulation of the impacts of "insignificant" force fields. They occur due to the nonlinearity of the deformation characteristics of the interblock fault zones in the areas of small deformations [10]. It is shown that the uniqueness of the stress-displacement relations, known for continual environment, does not always fulfill in the block-structured environment [11]. Both integrated weak impacts and short-term dynamic impacts on the metastable block environment can initiate a slow deformation process. The contribution of this deformation process to the entire assemblage of deformations can be quite significant.

The hierarchical block model describes fast seismic waves and slow deformation waves. The fast seismic waves are generated by the destruction of solid rock, while the slow deformation waves accompany the process of the propagation of elastic deformation energy through the interaction of individual blocks having their own vibrational degrees of freedom. The positive result in the search for such waves would allow us to develop new methods for predicting dangerous geodynamic events.

The articles [12, 13] describe that deformation-wave processes in the Earth's crust are the trigger mechanism of various high-energy seismic events: earthquakes, rock bursts, etc. At the same time, they may be harbingers of these events. The task of their detection and registration becomes relevant. The results of the conducted studies show that the required measurement facilities for recording the deformation-wave processes and methodological developments for the extraction of slow deformation waves make it possible to control the dynamic-kinematic characteristics of these waves on the regional and global scale.

Many papers contain experimental material proving the existence of a deformation buildup with oscillation periods in the 0.5–2 h band for 1.5–2 days before seismic events. The calculated velocity range of deformation pendulum waves is $0.5 \div 2$ m/s. We assume that identification and analysis of the rock bursts records made for "Streltsovskoe" ore field at a relatively small distances from the seismic event, for instance, several kilometers, make it possible to register the deformation waves, determine the time of their entry and the amplitude-time characteristics of the deformation train. This will significantly improve the accuracy of the forecast of geodynamic events and their energy parameters in shock-hazardous rock massifs, thus preventing catastrophic events at the field development.

4 The Influence of Faraway Earthquakes on the "Streltsovskoe" Ore Field Rock Massif State

To assess the impact of earthquakes on the state of the rock mass in the mining area, test the method of recording earthquakes and earthquake precursors, experimental research was made. The research was conducted on the uranium deposits of "Streltsovskoe" ore field using a laser deformograph, a laser nanobarograph and the "PROGNOZ-ADS" automated multichannel geoacoustic monitoring system, which allows recording and determining parameters of seismic-acoustic events in the frequency range 0.5–12 kHz [14].

The research was made during 2015–2017.

As an example, below are the results of the registration of earthquakes near Lake Baikal on November 22, 2016 with a magnitude of M = 4.6, at a distance of 736 km from the observation area (Fig. 2). We used the laser deformograph, the laser nanobarograph, and the geoacoustic system for the registration of the earthquakes.

Figure 3a, b show the recording of the earthquake made on the laser deformograph and nanobarograph in the Baikal zone.

Figures 4 and 5 present the results of the Baikal zone earthquake influence on the geodynamic activity of "Streltsovskoe" ore field, obtained from the "PROGNOZ-ADS" automated multichannel geoacoustic monitoring system.

In Fig. 4 the vertical indicates the earthquake time. The figure shows the significantly increased number of events and the average energy of events.

Fig. 2 Earthquake in the Baikal zone
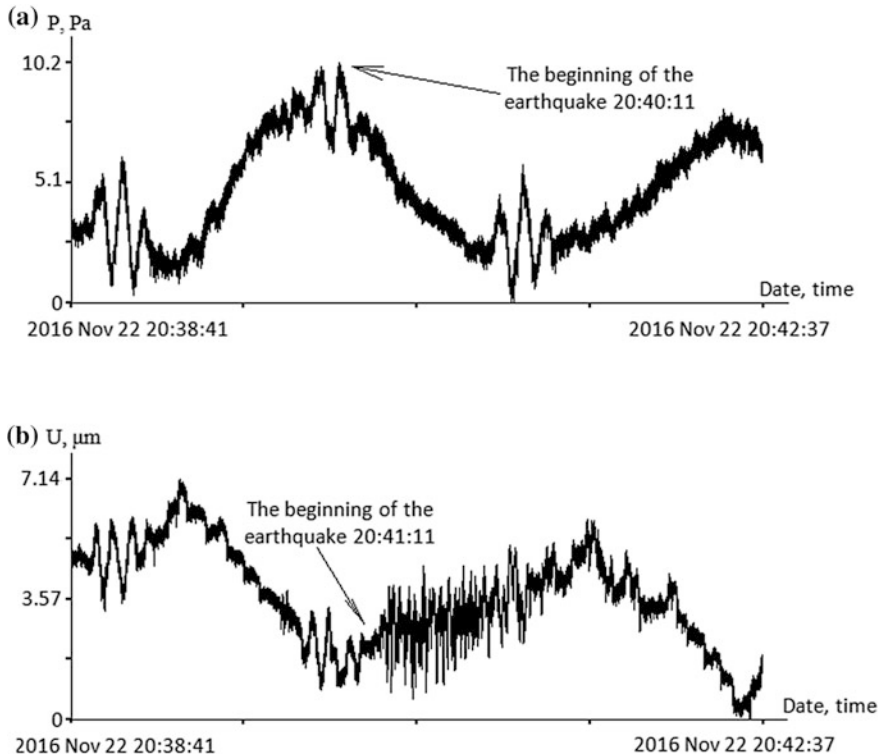
Fig. 3 The signal from the nanobarograph (**a**) and deformograph (**b**)

At the same time, a significantly increased number of events was recorded in the same mine block in which they had been observed before the earthquake. In Fig. 5, the recorded geoacoustic events before and after the earthquake are plotted on the mine plan of the «Glubokiy» mine of OJSC «PIMCU» in the projection onto vertical plane.

It should be noted that this situation was not always the same. There were other cases when the increased geodynamic activity after earthquakes was established in neighboring blocks, i.e. spread over the mine workings. The authors believe that this largely depends on the direction of arrival of the seismic wave. To establish the pre- and post-history of the seismic event, 48 h and daily records before and after the earthquake were analyzed. Figure 6 shows the 48 h records of the deformograph (a) and nanobarograph (b). Here, in contrast to the records of the earthquake moment, the high degree of correlation of the results (correlation coefficient is −0.9986) obtained from the deformograph and nanobarograph stands out. The signals are bipolar because the operating points of the interferometers of the nanobarograph and deformograph are on different/opposite slopes.
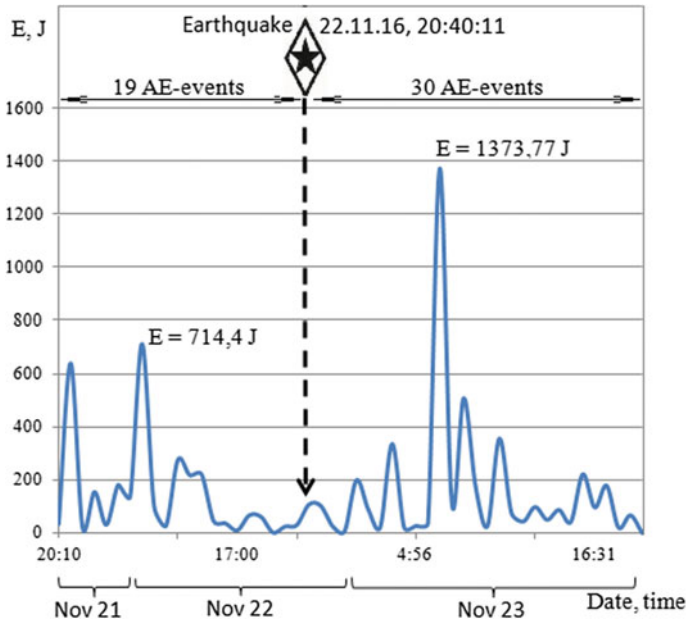
Fig. 4 Geoacoustic activity chart before and after the earthquake
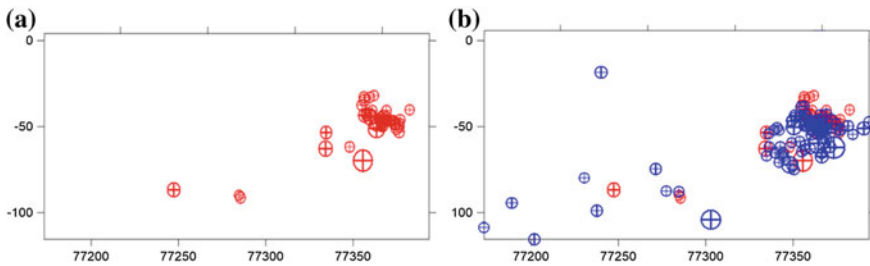
Fig. 5 Geoacoustic activity chart, **a** before the earthquake; **b** after the earthquake

The high degree of correlation is explained by the fact that the deformograph has the built-it air-filled fiber, so the variations of the refractive index are superimposed on the mechanical vibrations.

Another feature of the results obtained is that all records of various earthquakes include the bay-shaped signals of considerable amplitude (circled areas in Fig. 6).

This may be the response of the rock mass to industrial explosions. This reasoning relies on the accompanying oscillations with a frequency of 95 Hz, clearly seen on the explosion records. The figures show that the deformation returns almost

(a) U, μm

The beginning of the
earthquake
22.11.16, 20:40:11

80.8

40.4

0
2016 Nov 21 21:32:43   Date, time   2016 Nov 23 21:32:43

(b) P, Pa

The beginning of the
earthquake
22.11.16, 20:40:11

912.4

456.2

0
2016 Nov 21 21:32:43   Date, time   2016 Nov 23 21:32:43
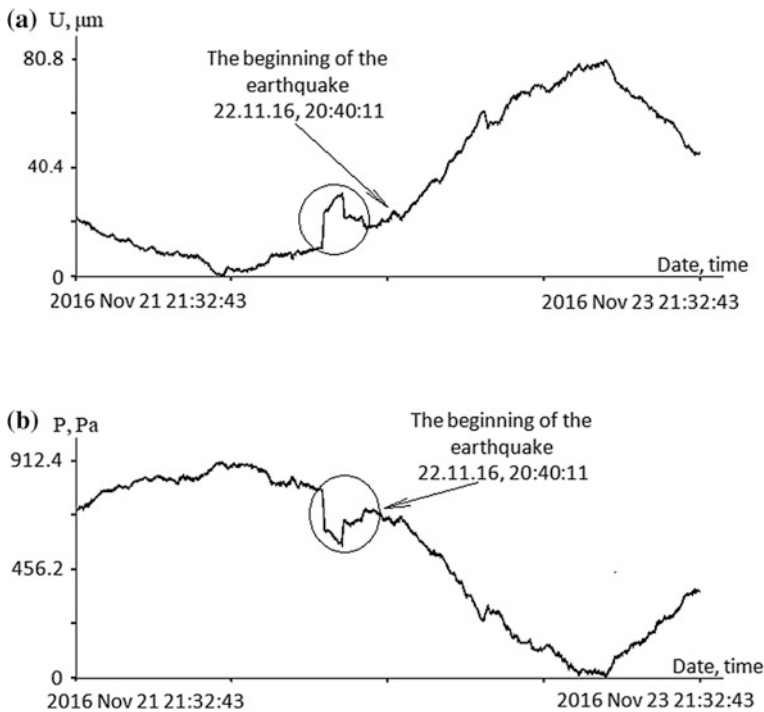
Fig. 6 The signal from the deformograph (**a**) and nanobarograph (**b**)

to the starting point. Otherwise, it should be assumed that the deformation is increasing at some other area which can lead to the destruction and collapse of the rock mass.

5 Conclusion

Currently, trigger effects are widely discussed in papers relating to the study and analysis of seismic processes. The observations show that the environment responds more or less to various natural or man-made nature impacts. Understanding of the triggering feature of processes requires application of complex research methodology including seismic, geoacoustic, deformation methods with the use of automated measurement and recording systems.

In 2015–2017, the comprehensive research was carried out at the mines of OJSC «PIMCU» to study the geodynamic and seismic conditions. Within this research, the impact of distant earthquakes on the geoacoustic activity of the massif in the area of mining operations was studied. The research relied on using the following measuring and recording equipment: the laser deformograph,

the nanobarograph, and the automated geoacoustic system for rock pressure monitoring "PROGNOZ ADS".

According to the research results, a high correlation was established between the readings of the laser deformograph and nanobarograph.

It has been proved that the distant earthquakes influence on the geodynamic activity of Streltsovsky ore field. The impact manifests itself in the form of a significant increase in the number of acoustic events and their average energy. As practice shows, such increase of these parameters often leads to activation of geodynamic processes in the rock massif, which can cause various dynamic manifestations.

Thus, seismic waves from distant earthquakes can be classified as additional factors that initiate deformation processes in the rock mass. Timely registration of such waves and their correct interpretation will significantly improve the accuracy of forecast of geodynamic events and their power s in shock-hazardous rock masses for prevention of catastrophic events at the development of deposits.

References

1. Adushkin, V.V., Turuntaev, S.B.: Technogenic Seismicity—Induced and Trigger. IGD RAS, Moscow (2015) (in Russian)
2. Rasskazov, I.Y., Petrov, V.A., Gladyr, A.V., Tyurin. D.V.: Geodynamic polygon of the "Streltsovskoe" ore field: practice and prospects. Min. J. **7**, 17–21 (2018) (in Russian)
3. Rasskazov, I.Y., Tereshkin, A.A., Gladyr, A.V., Tsirel, S.V., Rozanov, A.O.: Application of acoustic measurement data to characterize initiation and development of disintegration focus in a rock mass. J. Min. Sci. **2**(53), 224–231 (2017) (in Russian)
4. Rasskazov, I.Y., Gladyr, A.V., Anikin, P.A., Svyatsetsky, V.S., Prosekin, B.A.: Development and modernization of the monitoring system of dynamic manifestations of rock pressure in the mines of JSC PIMCU. Min. J. **8**–2, 9–14 (2013) (in Russian)
5. Dolgikh, G.I., Rasskazov, I.Y., Lugovoy, V.A., Anikin, P.A., Tsoi, D.I., Shvets, V.A., Yakovenko, S.V.: Krasnokamensky laser deformograph. In: Instruments and Technique of Experiment, vol. 5, pp. 138–139 (2013) (in Russian)
6. Dolgikh, G.I., Privalov, V.E.: Lasers systems. Dalnauka, Vladivostok (2009)
7. Rasskazov, IYu., Dolgikh, G.I., Petrov, V.A., Lugovoy, V.A., Dolgikh, S.G., Saksin, B.G., Tsoi, D.I.: Use of a laser deformograph in a complex system geodynamic monitoring in the area of "Streltsovskoe" ore field. J. Min. Sci. **6**, 29–37 (2016) (in Russian)
8. Kocharyan, G.G., Kostyuchenko, V.N., Pavlov, D.V.: Initiation of deformation processes in the earth's crust by weak disturbances. Phys. Mezomech. **1**(7), 5–22 (2004) (in Russian)
9. Kocharyan, G.G., Fedorov, A.E.: About the features of the seismic process mechanics in the block geophysical environment. Reports of the Academy of Sciences of the USSR, vol. 6, no. 315, pp. 1345–1349 (1990) (in Russian)
10. Kocharyan, G.G., Kostyuchenko, V.N., Pavlov, D.V.: Initiation of deformation processes in the earth's crust by weak perturbations. Phys. Mezomech. **1**(7), 5–22 (2004) (in Russian)
11. Kocharyan, G.G., Spivak, A.A.: Dynamics of Deformation of Block Massifs of Rocks. Academic Book, Moscow (2003) (in Russian)
12. Oparin, V.N., and Others: Methods and Systems for Seismic Deformation Monitoring of Techno Gene Earthquakes and Rock Bursts, vols. 1, 2. Publishing House of the Siberian Branch of the Russian Academy of Sciences, Novosibirsk (2009) (in Russian)

13. Larionov, I.A., Shevtsov, B.M.: Geoacoustic emission and deformation of sedimentary rocks. In: Problems of Complex Geophysical Monitoring of the Russian Far East, Petropavlovsk-Kamchatsky (2009) (in Russian)
14. Lugovoy, V.A., Rasskazov, I. Y., Tsoy, D.I, Rasskazov, M.I., Sidliar, A.V.: The research of remote earthquakes impact on the intensity of geomechanical processes in bump hazardous rock massif. In: VII International Scientific Conference "Problems of Complex Development of Georesources" (PCDG 2018), vol. 56. E3S Web of Conferences, Khabarovsk, Russia (2018)

Stress-Strain State Monitoring of a Man-Induced Landslide Based on the Lithospheric Component Parameters of the Earth's Pulsed Electromagnetic Field

Sergey Malyshkov⬤, Vasiliy Gordeev⬤, Vitaliy Polivach⬤ and Sergey Shtalin⬤

Abstract

The work summarizes the results of estimating dynamic changes in the state of a man-induced landslide using the Earth's natural pulsed electromagnetic field (ENPEMF) recording methods and its geomorphological analysis. Research was carried out in the North Caucasus orogenic region with active geodynamics. When choosing a profile research object using the ENPEMF method, 20 dangerous landslide areas were revealed on the Russian section of the Dzaurikau-Tskhinvali gas pipeline (North Ossetia) in 2010. The landslides were ranked by the level of danger to the operation of industrial facilities. Currently, a periodic inspection of rock mass strain-stress state change dynamics using the EMPEMF method is carried out on the most active of those landslides. The probability of activation of dangerous geological processes in this area is especially high, due to the fact that a steep slope was cut at the intersection of two fractures during pipeline construction. Tectonic faults were detected through satellite image interpretation. Over the 9-year period, a significant change in the terrain and an increase in the landslide body has taken place. The abnormal stress-strain state persists. Places of new block detachments and ground subsidence are well predicted. Instrumental survey data is coherent with geomorphological analysis results. The paper provides recommendations on ENPEMF recorder settings, spatial anomaly detection and their interpretation for rock mass stress-strain state estimation.

S. Malyshkov (✉) · V. Gordeev · V. Polivach
Institute of Monitoring of Climatic and Ecological of the Systems, Siberian Branch of the Russian Academy of Sciences, 634055 Tomsk, Russia
e-mail: msergey@imces.ru

S. Shtalin
Tomsk State University of Control Systems and Radioelectronics, 634050 Tomsk, Russia

367

1 Introduction

There is a great number of works on forecasting geodynamic events based on changes in the VLF electromagnetic signal propagation conditions. There are works that describe research using a transmitter and receiver [1]. Other researchers detect variations in the parameters of received electromagnetic signals of thunderstorm sources (atmospherics) [2]. The number of publications on small-scale geodynamic event research based on electromagnetic signals of lithospheric origin in this frequency range is insignificant. It was first proposed to apply the Earth's natural pulsed electromagnetic field (ENPEMF) recording methods to solving engineering geology problems, in particular, those of estimating landslide processes, in 1983 [3]. However, those methods were rarely used until recently due to a large number of interference pulses in the ENPEMF structure. Electromagnetic pulses contain information on the Earth's core structure. They emerge in the rock mass due to the natural ever-present geodynamic movement of the Earth's core. That movement causes dynamoelectric energy conversion leading to the ENPEMF pulse flow. The intensity and amplitude-frequency structure of that field is defined by the structural and lithological composition of rock-bedding and its stress-strain state [4]. Nevertheless, interpretation of results tends to be complicated, as only a fraction of the total number of recorded pulses contains information about the stress-strain state (SSS) of the research subject. The vast majority of recorded pulses is generated by distant sources of lithospheric and atmospheric origin and by artificial noise that is irrelevant to the subject in question.

The ENPEMF structure includes pulses from different sources:

1. Pulses of the thunderstorm atmospheric origin, both from local thunderstorm processes in summer and from powerful tropical storm discharges.
2. The lithospheric component pulse flow caused by long-period deformation waves from the lower mantle, related to the eccentric rotation of the Earth's core and mantle.
3. Pulses related to regional tectonic processes, preparation, progress, and relaxation of tectonic stress in the earthquake focus.
4. Local tectonic processes associated with changes in the soil tectonic activity, activation of landslide processes, and ground movements.

When using data on the Earth's pulsed electromagnetic field, it is necessary to take the following into account:

1. Noise specifics of the registered signal and its high instability in time. The number of recorded pulses increases exponentially with a decrease in the equipment discriminating threshold.
2. The presence of an evident diurnal variation. In addition to that, the diurnal variation is not uniform, its shape changes radically during a year.
3. A large number of split bands in time series spectrum characteristics.

4. The presence of atmospherics, pulses of the lithospheric origin, and powerful pulses from distant sources in the recorded flow. The presence of artificial noise.

It might seem that such a number of influences makes it rather difficult to obtain quality geophysical information. At least, this conclusion is confirmed by the insignificant number of published works on the use of ENPEMF methods in geophysical survey.

2   Methods and Equipment

Work [5] for the first time demonstrated the ENPEMF modulation pattern by the Earth's lower mantle deformation waves and suggested techniques for setting up the recording equipment to increase the share of lithosphere-originated pulses in the total recorded pulse flow. To solve geophysical problems, work [6] suggested using reference field recorders to distinguish the temporal variation component in the ENPEMF. Practical implementation of that idea was made possible thanks to the creation of a new class of recording equipment [7], which enabled fine tuning of software for amplification paths and linking of results to the internal clock. Currently, VLF pulsed electromagnetic fields for geophysical survey are increasingly used in engineering geology. In particular, to choose the location of construction sites for hazardous facilities in the nuclear and oil industries and to monitor the stress-strain state of rocks.

The results presented in this work were obtained using the multichannel geophysical recorder "MGR-01", developed in the Institute of Monitoring of Climatic and Ecological Systems SB RAS (IMCES SB RAS). "MGR-01" recorders are certified, registered in the state registry of measurement devices under No. 31892-06, and approved for use in the Russian Federation. These recorders allow measuring magnetic fields with the intensity range from 2×10^{-7} A/m to 400 A/m or magnetic flux density from 2.5×10^{-4} nT to 5×10^{-4} T. The average field intensity near the Earth surface is about 40 A/m. The experience in recording data throughout different regions of the Northern hemisphere shows that there is no necessity to carry out measurements with a very high sensitivity of the equipment to obtain robust and reproducible results.

A recorded pulse flow is determined by spatiotemporal variations. In case of geophysical survey, a recorded signal should be filtered from temporal field variations and all pulses from distant sources to retain only spatial variations of "local" pulses. Filtering of temporal field variations and separation of pulses into distant and local ones can be performed using a network of several simultaneously running recorders. Some recorders are static (reference) and measure only temporal variations of electromagnetic fields. Other recorders, called route recorders, measure both temporal and spatial ENPEMF variations along the profiles covering the territory surveyed.

Local and distant signal sources can be distinguished by the signal incoming time and amplitude difference on spatially distributed recorders. Distant source pulses, such as atmospherics, will propagate in the Earth-ionosphere waveguide and reach the recorders located at a small distance from each other nearly simultaneously and with equal amplitudes. Signals from powerful distant lithospheric sources, once surfaced, will then propagate by the ground wave with a speed close to the speed of light and a weak attenuation. Hence, those pulses will also be recorded by all the network devices nearly simultaneously and their amplitude values will be close.

The picture is different for pulses of the local lithospheric origin at a relatively close distance from the recording equipment. Their path trace to the field recorder will mostly run through the rock mass. Strong attenuation of electromagnetic waves in the Earth's crust will lead to a considerable difference in signal amplitudes over the source and in more distant points even in case of slight differences in trace lengths. Using devices with a threshold recording system, cutting off low amplitude pulses will result in a situation when a more distant recorder will log less pulses over a certain period as compared to the recorder located directly above the emitting geophysical anomaly. If particular pulses from a local source have amplitudes that are high enough to be logged by all the spatially distributed recorders, then the amplitudes of those pulses will still vary greatly depending on the distance of the specific recorder from the source. Such distinguishing allows obtaining good reproducible results of ENPEMF profile variations suitable for geophysical survey of structural and lithological inconsistencies in the Earth's crust and rock mass stress-strain state analysis. The more devices used, the higher the accuracy of anomaly detection. Those differences in the manifestation of distant and local field sources is used as a basis for the special-purpose equipment and measuring techniques we have developed.

The quality of obtained geophysical information depends largely on the accuracy of equipment settings. As our long-term research experience shows, temporal variations in the Earth's radio-wave field are determined by diurnal and yearly Earth's crust movement cycles and have diurnal variations depending on the calendar date, geographical location coordinates, and geophysical features. If the equipment sensitivity is too high, interference pulse and atmospheric noises dominate in the recorded pulse flow. If the sensitivity is too low, only the pulses of the most powerful thunderstorm discharges are recorded, while the pulses from local lithospheric sources are missing. Therefore, before starting the work, the recorders' sensitivity is set to some optimal values around 10 nT, with a frequency of 14–17 kHz.

3   Experiment

This work describes the results of estimating the stress-strain state of a landslide slope cut by the ramp of the Dzaurikau-Tskhinvali gas pipeline. The research period is 2010–2016. In 2010, the authors of this paper and experts from OOO

"GEOTEK" participated in the mapping of active landslides along the pipeline and ranking them by danger for the operation of industrial facilities. This was done for the first time since the gas pipeline construction. The surveyed route (25–82 km) passed the northern slope of the main ridge of the Greater Caucasus in the Alagir region of the Republic of Northern Ossetia–Alania. The geomorphological feature of that region is the alternation of dividing ridges and intermountain valleys of the general Caucasian direction (280°–295°), intersected by narrower valleys of sub meridional strike.

The terrain of the surveyed pipeline route has three basic levels: the low-mountain, mid-mountain and high-mountain topography with steep-sided slopes, rugged terrain, gullies and ravines. The complex zone topography also causes altitude-aerial climatic heterogeneity. High energy of the terrain (steepness of the slopes) and a considerable amount of precipitation (with a maximum in May–June) result in the slope instability and development of hazardous processes, such as sloughing, slumping, and landslides. A significant part of the pipeline route is located in the area of dangerous geological processes (DGP) and slope processes, which is natural for orogenic areas with active geodynamics, seismicity, geomorphological heterogeneity, and a very rugged terrain. Most common DGPs are isolation, rain wash, talus sliding, erosion, mudflow, gravity slope (sloughing and avalanching) processes. Karst-suffusion processes are less significant.

According to Construction Standards and Regulations 2.01.15-90, this territory is defined as highly hazardous due to the development of exogenous geological processes and geological risks. This calls for protective engineering and geological measures for gas transportation facilities, especially in the areas of combined influence of different processes. For example, a combination of erosion processes, slope rain-wash, and sharply and rapidly changing climatic factors usually leads to slope activation and landslide formation, not to mention a seismic impact and active tectonic faults.

Landslide bodies along the gas pipeline route are a sort of usual hillside waste, differing from it by larger fractional composition, higher natural humidity, lower density and stability. The landslide power may exceed several dozens of meters. Landslides mostly have a seismic nature, localized in the strong tectonic fracture zones. The landslide water source is atmospheric precipitation and bedding rock fracture water. The sources' yield reaches 1 l/s, their mineralization is 0.2–0.5 g/l, and water temperature is 5–8 °C. The landslide process is the most dangerous one for the gas pipeline.

While performing the work, the radio-frequency equipment was set up within the research area, near the pipeline crossing of the Ardon River, at the 30.6 km waypoint mark. At that location, the pipeline ramp is neither prone to landslide processes nor within large tectonic fault zones. To fine-tune the devices for optimal sensitivity, we used special calibration dependencies obtained over the many years of research. Amplification paths and discrimination threshold values were set up using the software. The setup process was aimed at making recorded temporal variations close in shape to the diurnal variation typical of the respective season. Once the optimal sensitivity was set, the next step was to set up all the devices to

receive identical pulses. Such tuning is extremely important and should be done scrupulously, as the quality of geophysical information primarily depends on the identity of reference and route devices. The lack of identity will result in different recording of the same pulse on different devices. This could lead to recognition errors in distant and local source pulses and hence to the degradation of the method accuracy. When setting up the identity, all the antennas of all the devices were placed in close proximity. The recorders' identity by sensitivity parameters was checked both by the number of pulses registered in a certain time unit and by comparing the incoming time of specific pulses.

While interpreting the field survey results, we subtract the reference station ENPEMF intensity from each waypoint intensity recorded at the same time. Points with values close to 0 are treated as undisturbed field. High values indicate the presence of fracture zones or tension strains on that waypoint; negative values indicate compression strain zones.

Over the course of fieldwork and geomorphological research in 2010, a total of 20 landslide areas, dangerous to the gas pipeline operation, were revealed. All the landslides developed along the track can be classified into two groups by their shift type, viscoplastic and shear slides, with the latter prevailing. The most dangerous landslide was found at the 53.5 km mark of the pipeline. Although, in November 2010, there weren't any large flakes yet (Fig. 1), but only emerging cutter breaks about 10 m long and with a 2–10 cm opening. This location features very high values of electromagnetic fields, interpreted as a tension zone, and a rapid change to a large negative anomaly, indicating a compression strain zone. Such a mosaic field structure shows landslide activity at this part of the pipeline. A steep sign change indicates a high probability of landsliding. Based on the above, we made a conclusion of an imminent landslide danger to the pipeline, which requires immediate management decisions.

In six months after that survey, follow-up work was done in the same area to estimate the SSS of the rock mass and to carry out geomorphological analysis. Within that period, serious changes in the terrain occurred due to landslide activation. As a result, the landslide occupied the pipeline ramp over a distance of 80 m. Its width reached 1.5–2 m. The thrust wall was vertical, scalloped, and 1.7 m high. It ran within 1.5–2 m of the pipeline route. The disturbance mechanism was quite complex: slanted surface slip with the evidence of ground flow. The landslide body consisted of three blocks of different configuration. The ramp surface slope reached 17° with a hill slope angle of 35–40°.

The landslide body at the surface consisted of sandstone eluvium (chunks, debris, slack, clay, and silt fractions). A deeper section is unknown as there are no excavations in that area. At the time of research, there wasn't any data on the depth of the solid rock. Its position in the section determined the power of a landslide, with the distribution in the lateral continuity and the power of soft sediments being the main parameters for forecasting new landslide splits. The landsliding basis was a ramp located lower by the slope, so one split block would lead to another.
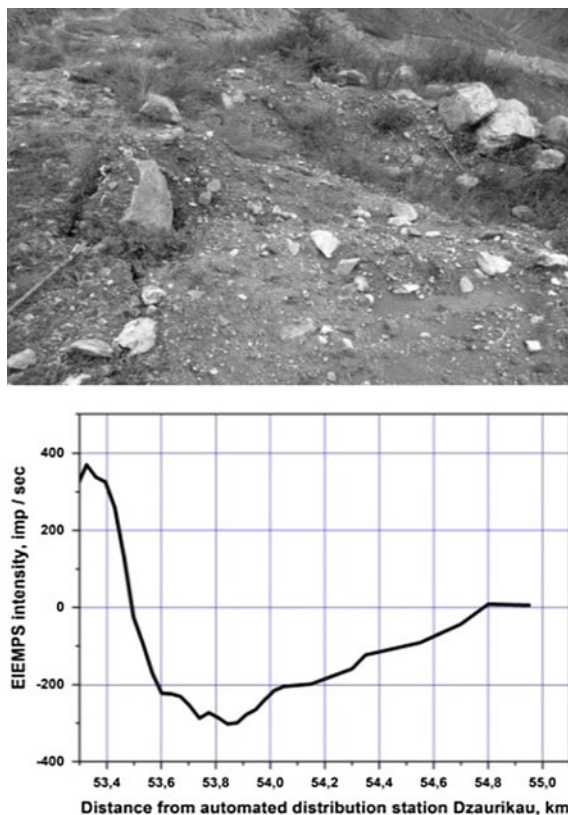
Fig. 1 Landslide, survey stake 53.5 km. November 2010

See the picture of the survey stake 53.5 km in Fig. 2a. The ENPEMF spatial variations at that stake compared with the first measurement session are shown in Fig. 2b. In the period from November 2010 to April 2011, the vertical settlement of landslide deposits was 1.5–1.7 m. Comparative analysis of measurement results showed that the terrain change led to a change in the SSS of the rocks in that area. Due to the steepness of the slope at that location, the pipeline was built in a twisting manner. While retaining the tension zone at the survey stakes 53–53.8 km, the compression zone moved lower by the axis of the pipeline. The landslide started to threaten the facility section located on the ramp lower than the survey stake 53.5 km. Finally, in 2012, due to ground subsidence of the major thrust, the gas pipe was uncovered from the survey stake 53.46 km to the survey stake 53.55 km.

In 2013, we repeated geomorphological analysis and SSS estimation of the landslide slope using the ENPEMF method. The estimation results are shown in Fig. 4a as compared with the results of 2011. During that period, at the survey stake 54 km, where in 2010–2011 the rock mass was in a compression state, a tension
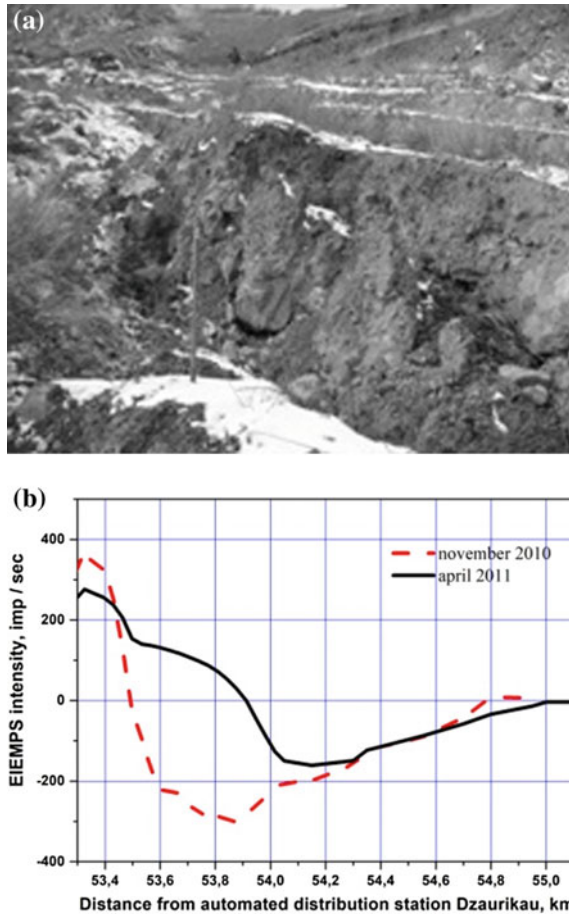
Fig. 2 Landslide, survey stake 53.5 km. April 2011

zone emerged due to dynamic changes in the ground condition. Active landslide parameters as of 2013 were the following: length by the shift axis was 350 m, the average width was 120 m, and the total area was $\sim 40,000$ m^2 (4 ha). Above the head part of the landslide, in the upper slope of the pipeline terrace (survey stake 53.28 km), narrow tension cracks (up to 3 cm) and a soft ground slump 25–30 m wide were registered. The head part of the landslide was represented by a series of lowered tension cracks in the form of scarps with the total height of up to 3.5–4 m in a lower slope of the pipeline terrace. Landslide edges featured open sloughing shear and compression cracks (up to 20–30 cm) with pressed out ramparts along them with a height of 0.5–1 m in the upper parts and up to 2.5 m in the lower parts. The left edge of the landslide was coherent to the submeridional fracture zone
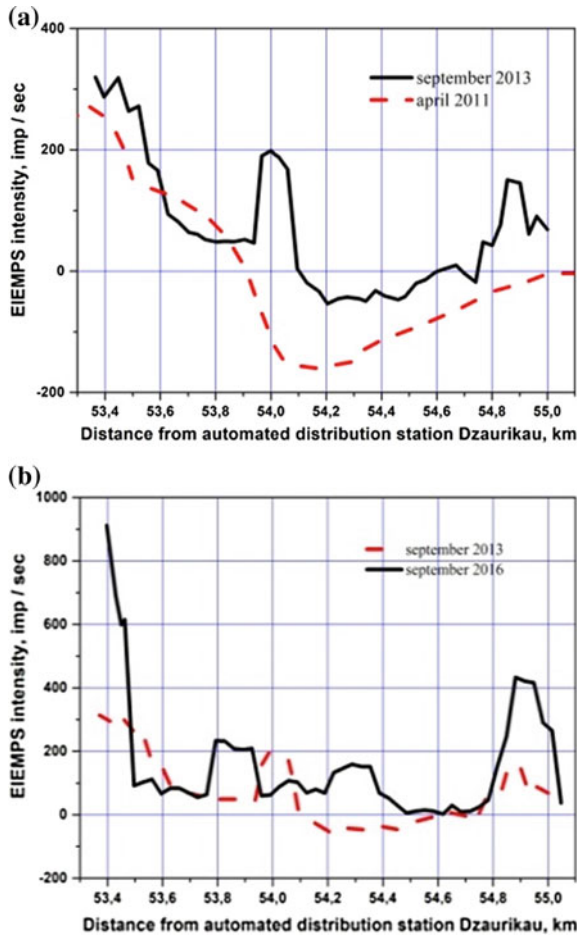
Fig. 3 Landslide at survey stake 53.5 km. In September 2013 (**a**) and in September 2016 (**b**)

(340°), detected by satellite image interpretation and confirmed by profile survey of emanation of radioactive gases (radon and thoron).

The landslide body, within general lowering (hollow) of the research area, constituted a positive landform (ridge), i.e., a pressured out rampart bound by cut-off stripping of the landslide. Notably, the thickness of landslide deposits was around 8–10 m in the lower part and over 10–12 m in the upper part. This indicates the slope deposit mass imbalance and is a prerequisite for landslide development.

The landslide's rollover rampart, 8 m in height, unloads to the pipeline route from the survey stake 54.11 km to the survey stake 54.17 km and threatens to disrupt it on a section 60 m long. Profile geophysical survey and SSS monitoring using the ENPEMF method indicate a compression zone in the tongue part of the landslide.
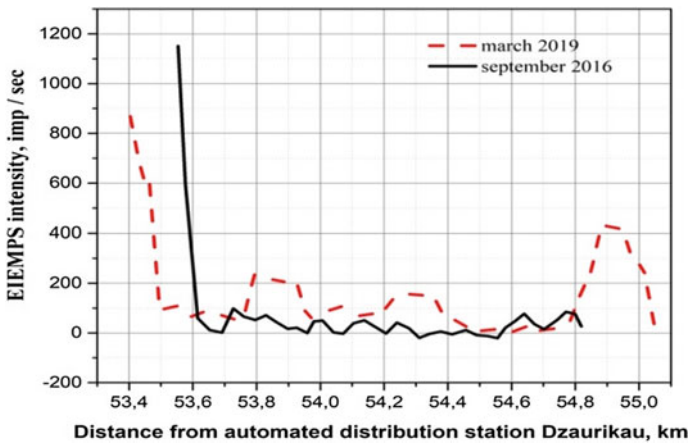
Fig. 4 Landslide, survey stake 53.5 km. March 2019

In general, the landslide is perched on a steep (30° and over) slope. The rollover rampart doesn't have any retaining buttress and hasn't reached the unloading base, so the landslide will stay active, especially in spring when the wetness is maximum during snow melting. In the pipeline section from the survey stake 54.84 km to the survey stake 54.91 km, there is a moderate devolution (~ 250 m^2) of bedrock crumbled granites, composing an upper slope of the pipeline terrace. The granites are splintered by two types of tectonic fractures: submeridional direction (340°), with vertical displacement surfaces, and sub latitudinal direction ($\sim 80°$), with a surface in a plane of fault displacement and slickenside at a 50°–60° angle a-dipping by the Ardon River shoreface.

Satellite image interpretation revealed an intersection zone of fractures of those directions in that location.

Another instrumental survey of the rock mass SSS in this area took place in September 2016. Its results, in comparison with the results of 2013, are shown in Fig. 3b. Heightened ENPEMF values recorded along the entire profile running over the pipeline ramp indicated that the rock mass was in a tension state through the full length. Over the period of 2013–2016, the landslide developed within the parameters discovered earlier. The survey stakes 53.28–54.17 km featured a horizontal shift of landslide deposits by ~ 1.5–2.0 m per year. The vertical subsidence was equal to ~ 1.2–1.5 m.

4 Summary

As of today, the latest field instrumental survey to estimate that area's SSS was carried out in March 2019. In the current year, the slope doesn't feature any fresh landslide deformations. However the danger of further landslide development

persists. The ENPEMF method based SSS estimation data confirms the abnormal ground state in the lower part of the landslide (Fig. 4). Over the 9-year period, dramatic changes in the terrain and an increase in the landslide body have taken place. The anomalous stress-strain state persists. Places of new block detachments and ground subsidence are well predicted. The instrumental survey data is coherent with the geomorphological analysis results.

References

1. Popova, I., Rozhnoi, A., Solovieva, M., Levin, B., Chebrov, V.: Neural network technique for identifying prognostic anomalies from low-frequency electromagnetic signals in the Kuril-Kamchatka region. Izvestiya—Phys. Solid Earth **52**, 305–317 (2016)
2. Mullayarov, V., Abzaletdinova, L., Argunov, V., Korsakov, A.: Variations of parameters of threshold electromagnetic signals on the roads passing over earthquake areas. Geomag. Aeron. **51**, 1–11 (2011)
3. Mastov, S., Salomatin, V., Yavorovich, L.: Identification of the degree of deformation of landslide areas by the method of registration of electromagnetic field pulses. Eng. Geol. **2**, 98–101 (1983)
4. Malyshkov, Y., Malyshkov, S., Gordeev, V., Shtalin, S., Polivach, V., Krutikov, V., Zaderigolova, M.: Electromagnetic Fields: Principles, Engineering Applications and Biophysical Effects. Earth's Natural Electromagnetic Noises in a Very-Low Frequency Band. Nova Science Publishers, New York (2013)
5. Malyshkov, Yu., Malyshkov, S.: Periodicity of geophysical fields and seismicity: possible links with core motion. Russ. Geol. Geophys. **50**, 115–130 (2009)
6. Malyshkov, Yu., Malyshkov, S., Gordeev, V., Shtalin, S., Polivach, V., Krutikov, V., Zaderigolova, M.: Earth's natural electromagnetic noises: Their deep-seated origin, effect on people, recording and application in geophysics. Horiz. World Phys. **283**, 43–128 (2015)
7. Shtalin, S., Malyshkov, S., Gordeev, V., Polivach, V., Malyshkov, Y.: Recorder of pulsed electromagnetic fields for monitoring geodynamic processes and geophysical prospecting. Sens. Syst. **4**, 32–37 (2012)

The Analysis of Conditions of Geodynamic Process Activation and Manifestation of Technogenic Seismicity on Underground Mines of the Far East Region

Igor Rasskazov, Vladimir Lugovoy, Denis Tsoy and Alexander Sidlyar

Abstract

Research results of the problems concerning rock burst and technogenic seismicity on a number of mineral deposits of the Far East region of Russia are presented in the paper. The specificities and consequences of hazardous geodynamic phenomena on the underground mines, caused by activation of geomechanical processes in the course of large-scale mining operations, are considered in this article. The geomechanical processes are reflected in the form of reorganization and self-organization of block-structured rock massifs on the burst hazard Nikolayevsk and Antey mineral deposits. Comprehensive geomechanical monitoring systems are set up for studying multi-scale natural and technogenic processes. These systems consist of deformation and microseismic measuring devices and an acoustic emission recorder and other devices as well, ensuring an effective registration and in-depth analysis of a wide range of parameters of geophysical wave fields, which are variable in respect to space and time. New experimental data concerning the impact of seismic waves from technological explosions and remote earthquakes on the deformation field of the Earth's crust site is obtained by applying a system of geomechanical methods. These seismic waves have played a role of triggering devices for a number of destructive geodynamic phenomena in the conditions of the extremely stressed and complex-structural rock massifs. Seismic waves have caused a steep increase of number and energy of seismic-acoustic events by 3–4 times on the Antey mineral deposit. It demonstrates the initiation of potentially burst hazard process of restructuring of the rock massif.

I. Rasskazov (✉) · V. Lugovoy · D. Tsoy · A. Sidlyar
Mining Institute, Far East Branch, Russian Academy of Sciences, Turgenev st., 51, 680000 Khabarovsk, Russia
e-mail: rasskazov@igd.khv.ru

1 Introduction

An intensive development of mineral deposits, the increase of depth, volumes and rates of extraction of mineral resources lead to activation of geodynamic processes in large-scale mining operation areas [1–5]. Such activation is followed by technogenic (mine) seismicity and often other destructive geodynamic phenomena on underground mines of Dalnegorsk and Streltsovsk ore districts of the Far East of Russia. Antey and Nikolaevsk polymetallic uranium ore deposits are characterized as having the most complex geomechanical and bump hazardous conditions in the region [6, 7]. Mining operations in these areas have reached depths of 700–800 m and more and the total volume of mined-out areas exceeds several millions of cubic meters. The specificity of both mineral deposits is their complex geological and tectonic structure.

The main structural elements that have a direct impact on the geodynamic parameters of a rock massif zone in Nikolaevsk deposit are a large limestone plate (olistolith) with dimensions of $1800 \times 700 \times 300$ m and a number of high-angle faults and first of all, a complex-structured submeridional tectonic zone TN-3 (Fig. 1). The deposits are localized on the contact point of olistolith with liparite and andesite tuffs that overlap them and where ore bodies of complex morphology, lenses and veins have formed.

The geological and structural features of Antey mineral deposit are determined by the presence of a complex system of steeply dipping tectonic faults of various orientations in the area. The assemblage of these faults along with a series of minor disturbances and fractured zones forms the main ore-controlling structure. The increased rock-burst hazard of the mineral deposit is observed in the length of approach (at a distance of up to 12 m) of two faults with a head dipping. Inclusions (lenses) of leucocratic granites of increased strength and fragility are located within the limits of the length of approach.

According to the results of geomechanical studies, it was established that uneven-component stress fields exist in the massifs of burst hazard mineral deposits in the region. Horizontal (due to the action of tectonic forces) compressive stresses are 2–2.5 or more times higher than vertical (gravitational) stresses. The process depends largely on the geodynamic position of the mineral deposits within the limits of the tectonically active Amur Plate, which is characterized by high structural heterogeneity, tectonic fragmentation and the presence of areas of enhanced stress [8]. The whole spectrum of dynamic occurrences of rock pressure is recorded to the extent of strong with severe consequences of rock and mountain-tectonic impacts in Amur Plate, and technogenic seismicity events have been recorded there in recent years [6, 7].
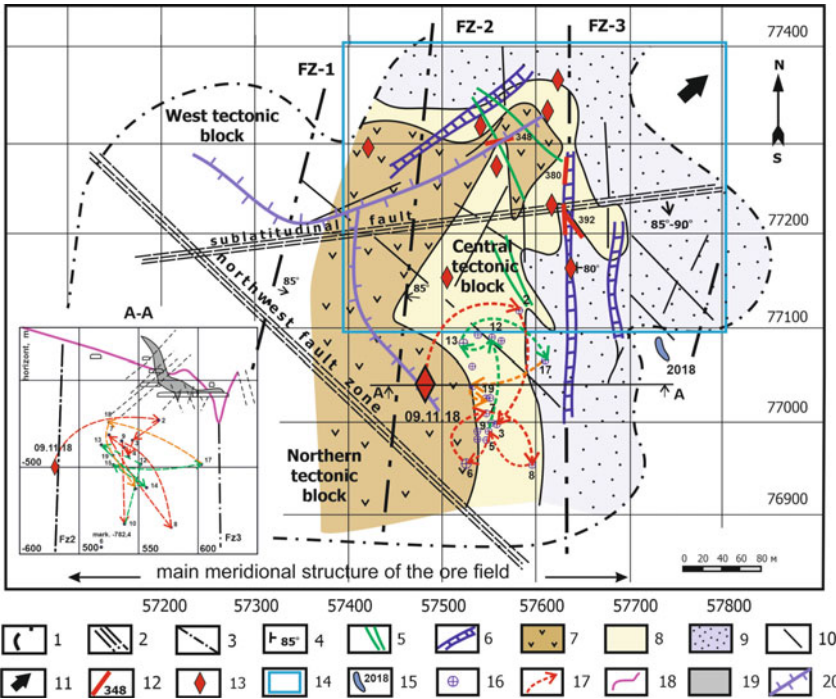
Fig. 1 Tectonic structure of Nikolaevsk mineral deposit and process dynamics of stress relief as a result of technogenic seismicity occurrence in November 2018. 1—projection of the olistolite contour onto a horizontal plane; 2–6—data of geological exploration work; 2—block-forming faults and their names; 3—other tectonic disturbances and their numbers; 4—established elements of occurrence; 5—dikes of medium and basic composition; 6—gorges in the body of limestone, filled with metasomatites; 7–10—geodynamic regions formed by morphological features of olistolith and the modern stress field: 7—a relatively geodynamically stable (elevated or near-mountain range) region; 8—slightly flat slope area with intermediate geodynamic activity; 9—steep-sided geodynamically active peripheral area; 10—lineaments of olistolith roof relief; 11—the direction of contemporary horizontal movement of the ore-hosting geoblock and the maximum main stress; 12—location of open cracks associated with dynamic occurrences on March 23, 2016; 13—the position of major dynamic occurrences of rock pressure in the period 2016–2017; 14—general outline of geoacoustic monitoring studies; 15—new steeply dipping zone of anomalous acoustic activity (in 2018) at the eastern edge of olistolith (horizons −340 … −400 m); 16—after-bump events accompanying the technogenic seismicity occurrence dated November 9, 2018; 17—the direction of movement of event epicenters in the horizontal plane; 18—the position of the olistolith roof; 19—contour of the ore body; 20—linear watershed of the buried olistolith roof (the red dotted line indicates the direction of movement of event epicentres in the vertical plane dated November 9, 2018, green dotted line—dated November 10, 2018 and orange dotted line—dated November 11, 2018)

In this context, it has become obvious that in-depth comprehensive studies are required in order to obtain some fundamentally new information on the properties and stress-strain state of the geological environment. Determining the precise occurrence time of a hazardous event is the most difficult task for a solution to the problem of rock bursts and technogenic seismicity, since a hazardous event depends

on many factors and in many respects has a probabilistic nature. In such case, an important role is played by the so-called "trigger effect" i.e. when a destructive geodynamic phenomenon (rock burst or induced earthquake) can be triggered by an accidental mild impact from a technological explosion or other source of seismic waves [9–12]. Applying a set of measuring tools, including wave processes that record parameters in a wide frequency range, is necessary for studying this effect and to substantiate reliable precursors of destructive geodynamic phenomena.

2 Methods and Technical Facilities

Comprehensive geomechanical monitoring systems have been set up for studying multi-scale natural and technogenic processes in the mineral deposits of Dalnegorsk and Streltsovo ore districts. They include deformation and microseismic monitoring stations, as well as facilities for recording acoustic emission and other devices having a different measurement base and ensuring efficient recording and in-depth analysis of a wide range of parameters of geophysical wave fields, which are variable in respect to space and time [13–15].

26 to 35 receiving transducers (accelerometers) of Prognoz ADS geoacoustic rock pressure monitoring system are installed in Antey and Nikolaevsk mineral deposits, allowing to record and determine parameters of AE-events with energy ranging from 10 to 104 J in the frequency range of 0.5–12 kHz. The Prognoz S microseismic system, installed in Streltsovsky ore field and controlling a section of the rock mass of more than 12 km^3, currently has 12 seismic pavilions in underground mine work on horizons from V to XIV. The system allows to record seismic events with energy up to 107 J in the frequency range from 10 to 1000 Hz. The sensitivity of three-component electrodynamic seismic detectors of GMT-12.5 type is 30 V/m · s^{-1} and the operating frequency range is from 10 to 500 Hz. A laser-based deformograph is installed in the horizontal underground mine at a depth of more than 300 m from the surface. Its optical part is assembled on the basis of a modified Michelson interferometer of unequal-arm type with an operating arm length of 50 m and a MellesGriott frequency-stabilized laser. The laser-based deformograph ensures measurements of variations in the level of deformations of the Earth crust in the frequency range from 0 to 1000 Hz with the following characteristics: noise value, measured in units of displacement which is approximately 59 picometres; sensitivity threshold i.e. deformation at the 50 m base of the deformograph is $1.2 \cdot 10^{-12}$; dynamic range is 120 dB.

The technical facilities of the comprehensive geomechanical monitoring system are integrated into a single observation network, which ensures the following: information exchange with a transmission rate of up to 15.2 Mbit/s; maintaining a coordinated time in all systems with an accuracy of at least 15 ms; maintaining a single database [13].

A combined analysis of measurement results of deformation parameters and seismic acoustic events was carried out. The measurements were recorded by Prognoz ADS geoacoustic rock pressure monitoring system and Prognoz S

microseismic system. The data of geoacoustic monitoring of the marginal rock massif by means of Prognoz L and visual observations of the occurrences of rock pressure were used [15].

3   Research Results

A significant influence of seismic waves from technological explosions and remote earthquakes on the deformation field of a rock massif disturbed by mining operations has been established as a result of comprehensive studies under the conditions of deep-lying Antey and Nikolaevsk mineral deposits.

A number of destructive dynamic phenomena in Nikolaevsk mineral deposit caused an earthquake of magnitude 4, with the epicentre of 30 km south–east of the deposit, which occurred on March 25, 2016. The geodynamic phenomena caused numerous damage to mine operations on the 4 levels of the underground mine, formed open breaks and cracks of tens of meters in length with shifts of 10–12 cm in the rock massif [7]. Seismoacoustic activity exceeded 3 times higher than the average level within 3 days after the geodynamic event. Particularly, high seismoacoustic activity was recorded along the boundaries of the osteolith and in TN3 fault zone in the area of intensive mining operations. The origins of seismic acoustic wave sources were recorded not only in the areas of destruction of mining, but also in the depth of the massif at a distance of more than 100 m from the mining area.

The series of seismic events was recorded in Nikolaevsk mineral deposit in the period from 9 to 11 November 2018. These seismic events were provoked by explosive operations during excavation of underground mines. The largest seismic event of 194,144 J was recorded at a depth of more than 900 m (horizon −501 m) below the mining sites (Fig. 1). This event is confined to the inner part of osteolith and the intersection area of the north–western blocking zone with TN-2 fault. The event caused destruction of mines on the horizon −433 m and was accompanied by numerous aftershock tremors of the massif which occurred during the two days following the event. The migration of the epicentre of aftershock events reflects their distribution around a certain centre, where the formation of a source of a larger geodynamic phenomenon is possible. This is also indicated by a picture of stress discharge that covered relatively shallow depths.

Analysis of the reviewed and a number of other occurrences of technogenic seismicity in Nikolaevsk mineral deposit indicates their strong interrelation with tectonic structure of the rock massif, which is in an extremely stressful state. A process of structural adjustment and self-organization of the block-structured rock massif, accompanied by an increased seismoacoustic and deformation activity is being observed under these conditions.

Antey mineral deposit area, confined to Tulukuyevsk volcano-tectonic structure, is characterized by contemporary increased seismic activity of geological structures and heterogeneity of the stress-strain state of rock massifs [6, 13]. According to the research results, a distinct influence of remote seismic events on the geodynamic
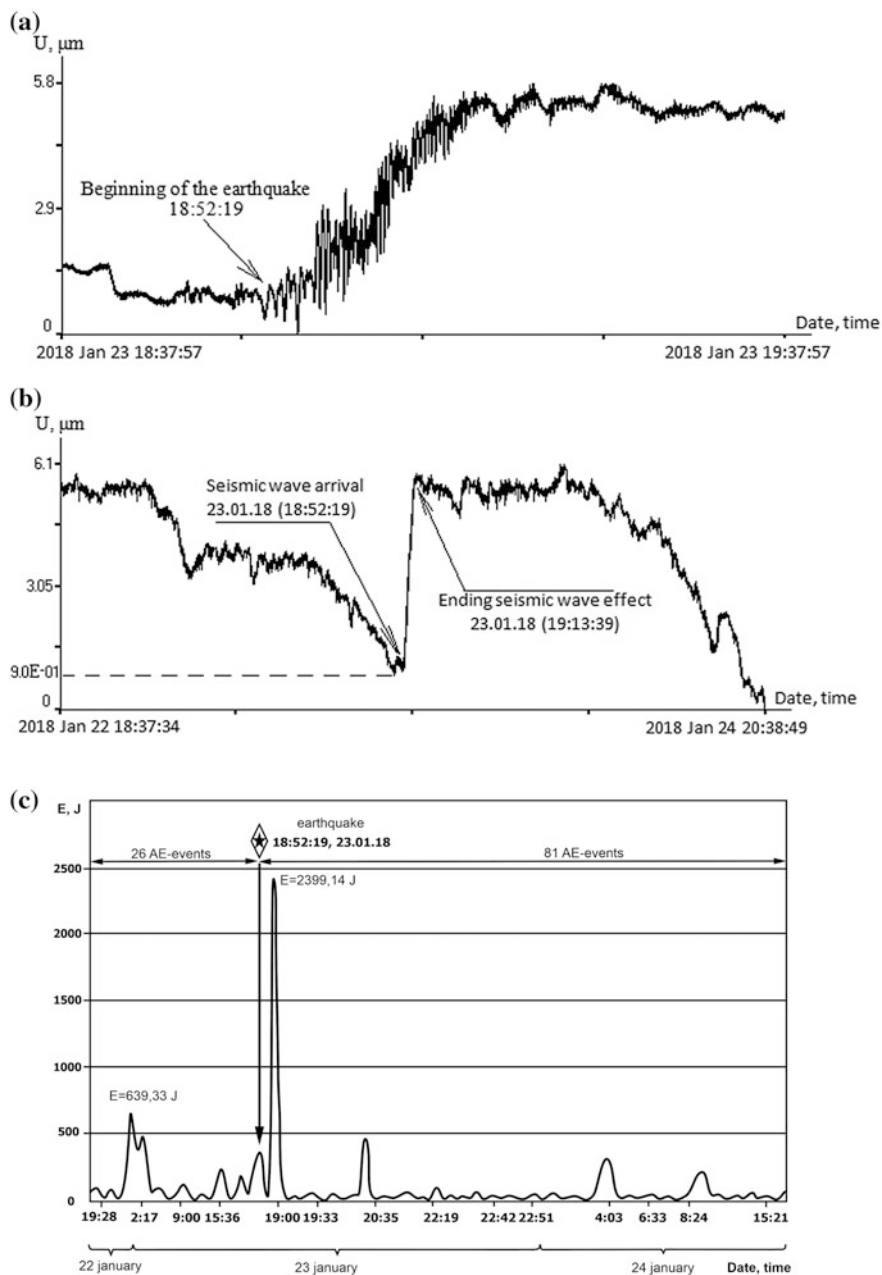
Fig. 2 The assessment results of the impact of seismic waves from the earthquake in the Gulf of Alaska on January 23, 2018 on the change in the number and energy of the seismic-acoustic events in Antey deposit array: **a** is the recording area of the seismic wave entry moment; **b** deformograph recording a day before and after the earthquake; **c** change in seismic activity in the stopes 1102 and 1302

activity of a shock-hazardous rock massif has been established. It has been established that seismic waves from remote earthquakes cause an increase in seismoacoustic activity by 2.5–3 times or more in the stopes in the vicinity of the ore-controlling faults 160 and 13, at the seams of which vertical displacements of up to 80–120 mm were recorded previously [6].

As an example, let us consider the impact on the geomechanical state of Antey mineral deposit massif of a large remote earthquake of magnitude 7.8 that occurred in the Gulf of Alaska on January 23, 2018 at 18:31:39 local time. The deformation oscillations of the mountain range due to the earthquake, recorded by a laser-based deformograph, are shown in Fig. 2a (the arrow indicates the time of the earthquake). The logging time of these fluctuations was 18:52:19. In this case, the calculated "apparent" velocity of the deformation wave is equal to 4637 m/s (according to the Planeta Cale website, the distance from the earthquake source to the deformograph is 5750 km).

As a result of the earthquake, there was a sharp increase in shifts from 0.9 to 6.1 μm (within 21 min from the starting point of the seismic wave arrival to the end of its impact on the mountain massif), which is clearly visible in the two-day recording of the laser-based deformograph (Fig. 2b). After the earthquake, the number of seismoacoustic events recorded in the area of stopes 1102 and 1302 increased more than 3 times and their total energy increased from 639 to 2399 J (Fig. 2c). At the same time, migration of seismic-acoustic event foci was observed.

Thus, seismic waves from remote earthquakes have a significant impact on the geomechanical state of extremely stressed rock mass and can act as a triggering device for large destructive geodynamic phenomena.

4   Conclusions

The intensive underground mining operations of Dalnegorsk and Streltsovsky ore districts of the Far East of Russia is accompanied by dynamic occurrences of rock pressure, mine bumps and technogenic seismicity and lead to activation of geodynamic processes. These processes have been taking place in recent years in the busrt-hazardous deep-seated Nikolaevsk and Antey mineral deposits in form of restructuring and self-organization of block-structured rock mass and are accompanied by shifts and movements along tectonic disturbances of various scale levels, and release of considerable elastic strain energy.

According to the results of comprehensive geomechanical studies under the conditions of Nikolaevsk and Antey mineral deposits, a noticeable impact of seismic waves from technological explosions and distant earthquakes on the stress-strain state of the rock mass was established. The rock mass acted as a triggering device for a number of destructive dynamic phenomena. The seismic waves caused a sharp increase in the number and energy of seismic—acoustic events by 3–4 times, which indicates the initiation of a potentially hazardous structural adjustment process in the areas of extremely stressed rock mass.

References

1. Technogenic seismicity during mining: foci models, prognosis, prevention. In: Melnikov, N. N. (ed.) Proceedings of conference. RAS Center Researches Team, Apatity (2004)
2. Adushkin, V.V., Turuntaev, S.B.: Technogenic Seismicity—Induced and Trigger. IDG RAS, Moscow (2015)
3. Oparin, V.N., Adushkin, V.V., Bariah, A.A.: Geomechanical fields and processes: experimental-and-analytical research into initiation and growth of source zones of disastrous events in geotechnical and natural systems. Siberian Branch of RAS, Novosibirsk (2018)
4. Marcak, H., Mutke, G.: Seismic activation of tectonic stresses by mining. J. Seismol. **17**(4), 1139–1148 (2013)
5. Snelling, P.E., Godin, L., McKinnon, S.D.: The role of geologic structure and stress in triggering remote seismicity in Creighton Mine, Sudbury, Canada. Int. J. Rock Mech. Min. Sci. **58**, 166–179 (2013)
6. Rasskazov, I.I., Saksin, B.G., Petrov, V.A., Prosekin B.A.: Geomechanical conditions and features of the dynamic manifestations of rock pressure at the Antey deposit. In: Physical and Technical Problems of the Development of Mineral Resources, no. 3, pp. 3–13 (2012)
7. Rasskazov, I., Saksin, B.G., Usikov, V.I., Potapchuk, M.I.: A geodynamic condition of the ore massif of Nikolaev polymetallic field and peculiarities of burst-hazard phenomenon in the process of its development. Min. J. **12**, 13–19 (2016)
8. Rasskazov, I.I., Saksin, B.G., Petrov, V.A., Shevchenko, B.F., Usikov, V.I., Gil'manova, G. Z.: Present day stress strain state in the upper crust of the Amurian Lithosphere Plate. Izv., Phys. Solid Earth **50**(3), 444–452 (2014)
9. Oparin, V.N.: The destruction of the earth's crust and the processes of self-organization in areas of strong anthropogenic impact. Publishing House of the Siberian Branch of the Russian Academy of Sciences, Novosibirsk (2012)
10. Adushkin, V.V., Kishkina, S.B., Kocharian, G.G.: New approach to monitoring of technogenic-tectonic earthquakes. Phys. Technical Probl. Dev. Miner. Resour. **1**, 3–14 (2017)
11. Shtirts, V.A., Eremenko, A.A., Konurin, A.I., Klishin, I.V.: Experience of forecasting geodynamic phenomena during mass explosions. Min. Inf. Anal. Bull. **7**, 196–206 (2015)
12. Verkholantsev, F.G., Belevskaia, M.A.: Trigger seismicity at the Verkhnekamskoye Potassium salt deposit from 2008 to 2010. In: Proceedings of X International Seismological Workshop "Modern Methods of Processing and Interpretation of Seismological Data", pp. 52–55. GS RAS, Obninsk (2011)
13. Rasskazov, I., Petrov, V.A., Gladyr, A.V., Tyurin, D.V.: Geodynamic polygon of the "Streltsovskoe" ore field: practice and prospects. Min. J. **7**, 17–21 (2018)
14. Rasskazov, I., Dolgikh, G.I., Petrov, V.A.: Application of a laser deformograph in the system of complex geodynamic monitoring near the Streltsovsky ore field. J. Min. Sci. **6**, 29–37 (2016)
15. Rasskazov, I., Migunov, D.S., Anikin, P.A., Gladyr', A.V., Tereshkin, A.A., Zhelnin, D.O.: New-generation portable geoacoustic instrument for rockburst hazard assessment. J. Min. Sci. **51**(3), 614–623 (2015)

Determination of Critical Deformation and Destruction Parameters of the Zhelezny Open Pit Rock Mass (JSC Kovdorsky GOK) Based on IBIS FM Ground Radar Data

Ivan Rozanov and Aleksander Zavialov

Abstract

It is impossible to predict the state of rock mass without determining the ultimate values of deformation parameters. A widespread method for their determination is to identify empirical patterns obtained by analyzing the in situ observation results. One of the most effective tools of the slope and pit wall stability monitoring today is the use of ground-based interferometric radars. In Russia, radars have come into use relatively recently, about 5 years ago, and today this monitoring method is gaining popularity despite quite expensive equipment. This is due to its apparent advantages over other methods: the capability to produce a large amount of information on the rock mass movement in a short period, 24×7 monitoring of the rock mass conditions in all weathers, highly accurate observations, etc. The paper presents the data on registered rock falls in the open pit of the Zhelezny mine recorded by the IBIS FM radar (IDS, Italy) and the results of determination of critical parameters.

I. Rozanov (✉)
Mining Institute Kola Science Centre RAS, 184209 Apatity, Russia
e-mail: ivan-rozanov@yandex.ru

A. Zavialov (✉)
JSC Kovdorsky GOK, 184141 Kovdor, Russia
e-mail: aleksander.zavyalov@eurochem.ru

1 Introduction

An increase in the planned size and depth of open pits makes slope stability monitoring increasingly relevant.

Slope stability monitoring is the process of performing various in situ measurements to collect information on the current state of the rock mass and to forecast its future state, including the moment of transition to the limit state.

It is impossible to predict the state of the rock mass without determining the ultimate values of deformation parameters, the excess of which leads to the destruction of the rocks composing a pit wall.

A widespread method for determining the critical deformation parameters is to identify empirical patterns obtained by analyzing the in situ observation results. Techniques for identifying these patterns are described in [1–3]. However, all those techniques are based on data from field observations of the landslide process development that occurs in soil, semi-rock and rock massifs with a tensile strength for uniaxial compression not exceeding 50 MPa. In particular, source [1] presents data on the values of the observed displacements with a decrease in the stability factor. For example, with the reduction of the stability factor to 1.15–1.3 in the area adjacent to the pit wall, displacements recorded by surveying measurements reached 50–70 mm, while with the stability factor ranging from 1.05 to 1.15, displacements reached dangerous values of 0.5–2 m.

These limit values are not always applicable to deposits that are mined under high-strength rock mass conditions, where the uniaxial compressive strength of certain rocks is 100–120 MPa. Most of the Kola Peninsula deposits, including the Kovdor one, can be attributed to such deposits.

2 Pit Wall Stability Monitoring in the Zhelezny Open Pit Mine, JSC Kovdorsky GOK

Geomechanical monitoring was first applied by mining companies in the 1920–30s. Back then, specialists started instrumental observations of rock mass deformations and failures and systematic studies of their deformation and strength properties. They accumulated and summarized the observations of the types and nature of slope and pit wall instability. The observation methods and tools were mainly taken from mine surveying and geological exploration practices.

In 1971, the All-Russian Research Institute of Mining Geomechanics and Survey published the "Instruction for monitoring of pit walls, slopes and dumps deformations and developing measures to ensure their stability" [3]. The main monitoring methods of that period were the 4th grade geometric leveling and trigonometric leveling with the use of a theodolite with the accuracy along a vertical circle of no more than 30 s. The distance between the reference points was measured with a steel tape measure or a tape at least 30 m long. This instruction is still used in open pit mining.

More than 45 years have passed since its publication. New monitoring methods and related instruments and equipment have appeared.

Today, GPS measurements, various total stations, optical distance meters, levels, and laser scanners are widely used for monitoring purposes. However, one of the most effective tools for slope and pit wall stability monitoring today is ground-based interferometric radars. Despite the fact that these tools have been employed by foreign enterprises for more than 15 years, the first radar appeared in Russia only in 2014 and was installed on the wall of the Zhelezny open pit mine, Kovdorsky GOK [4].

The IBIS FM container-mounted radar has the following characteristics:

- Range of action: from 10 to 4000 m.
- Pixel size: 4.4 m by 0.75 m (at a distance of 1000 m) and 8.8 m by 0.75 m (at a distance of 2000 m).
- Operating ambient temperature range: from −50 to +55 °C.
- Time of one full scan: 2 min.
- Measurement accuracy: 0.1 mm (according to the equipment manufacturer).

The radar installation site was chosen based on the mining, geological and technical conditions in the open pit. It was installed on its western side and directed towards the eastern side of the wall, most problematic in terms of slope stability (Fig. 1).

The main objective at that time was to get acquainted with the radar operating principle and to determine the correspondence between its real and declared accuracy. The analysis of the instrument data and test measurement results (depending on the measurement conditions and location of the observed area) established the accuracy of the fixed displacements at $\pm(0.1 \div 0.3)$ mm.

Based on the established accuracy of the fixed displacements, data on failures that occurred in the pit in 2014–2015 was analyzed. During this period, one major 100,000 m^3 failure was recorded by the radar. It occurred on August 24, 2015, in the eastern part of the wall (level +70 m; −35 m).

The value of the ultimate displacement of the area after which the failure occurred was 70 mm. By the magnitudes of the displacements preceding the failures, the velocity and acceleration values were calculated and the corresponding graphs were plotted. It was established that, at a certain moment during the deformation process development, nearly a threefold increase in the values of acceleration and velocity was observed. The acceleration increased from 0.13 to 2 mm/h^2 and the velocity—from 1 to 3 mm/h. After that, the rate of process development continued to increase until the moment of failure, which occurred within four hours [4]. Therefore, it can be assumed that, at this moment, the rock mass goes into the limit state after which a failure is inevitable and 3 mm/h is presumably the limiting deformation velocity.
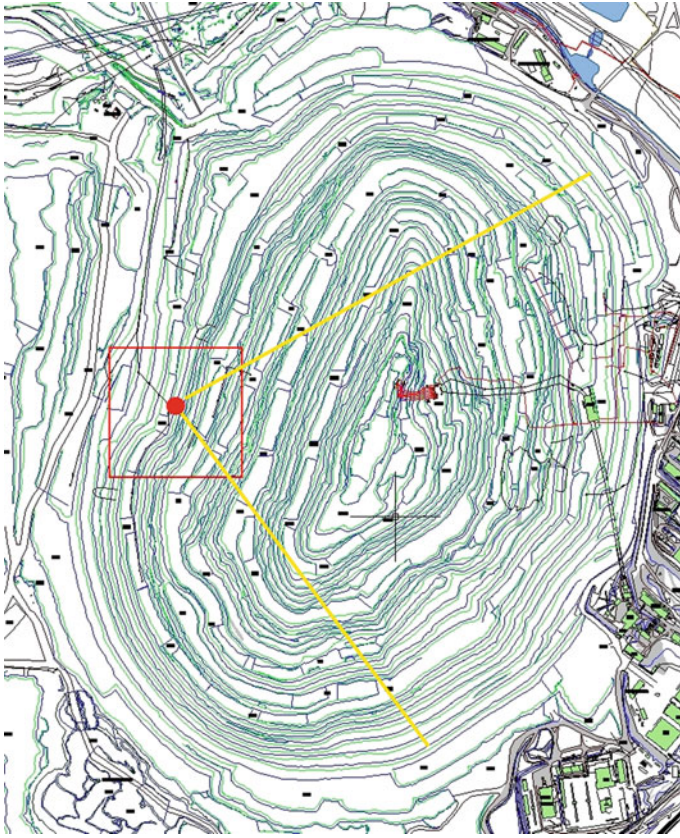
Fig. 1 IBIS FM radar location site

3 Verification of the Identified Limiting Deformation Velocity

Once the limiting deformation velocity was determined, it was necessary to check its reliability in other failures that occurred in the Kovdor deposit.

In 2018, a series of minor failures of about 100 m^3 were recorded. For the test, data on three failures, also recorded by the IBIS FM radar, was selected and analyzed. It should be noted that all these failures occurred in October during heavy rains.

The first failure occurred on October 8. The process of deformation from the beginning to the moment of failure lasted about 21 h. The maximum fixed displacement of the area was 20 mm. Figure 2 shows a graph of the rate of deformation process development over time with marked velocity limits.
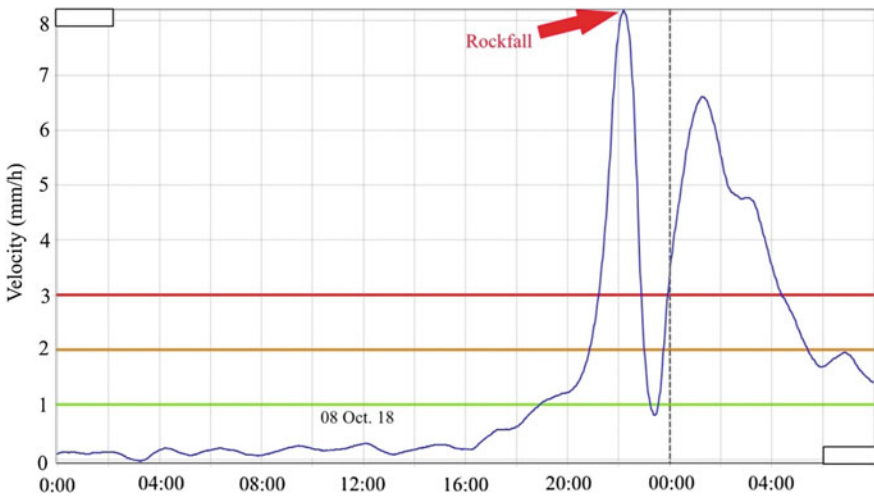
Fig. 2 Graph of the rock mass displacement velocity with exposed limit values (08.10.2018)

The experience of using the radar showed that, for more effective detection and further observations of the deformable section, it is reasonable to set three threshold values for the displacement velocity (1, 2, and 3 mm/h). The failure occurred approximately 1 h after the velocity limit was exceeded.

The second failure occurred on October 16. The deformation process until the failure took about 30 h. The fixed limiting displacement of the area was 42 mm. Figure 3 shows a graph of the rate of deformation process development over time
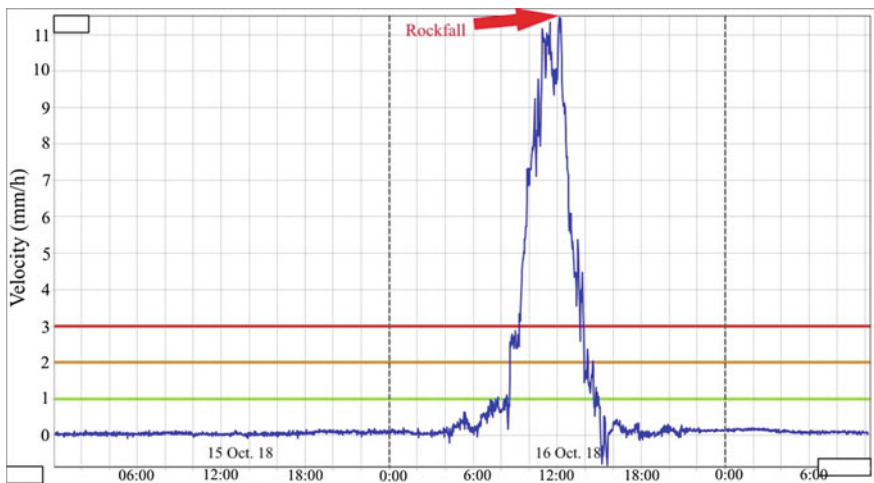
Fig. 3 Graph of the rock mass displacement velocity with exposed limit values (16.10.2018)

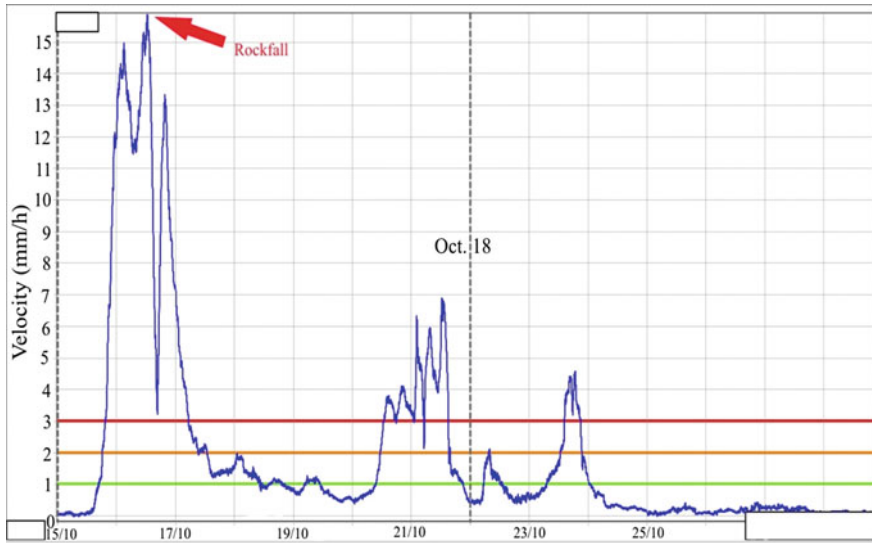**Fig. 4** Graph of the rock mass displacement velocity with exposed limit values (17.10.2018)

with marked velocity limits. A warning was triggered around 9 am, that is, 3 h before the failure that occurred at 12 o'clock.

The third failure occurred on October 17 (Fig. 4). The deformation process developed in poor and disintegrated rock mass. As a result, a landslide was observed and the maximum displacement was 350 mm. The deformation process until the main failure took about 24 h.

It took about 20 h from the excess of the limited velocity to the moment of the main failure. The graph also shows that the deformation process lasted another 10 days after the failure, and minor rock slides were observed at this site.

4   Conclusions

1. The IBIS FM radar data on the failures showed that, in high-strength rock mass, the displacements observed directly before the failure were insignificant and most likely depended on the volume of the collapsed rock. The displacement during the failure of June 24, 2015, was 70 mm with a volume of 100,000 m^3, while, for example, the displacement during the failure of August 10, 2018, was 20 mm with a volume of less than 100 m^3.
2. The velocity limit established during the analysis of data on the failure of August 24, 2015, was reliable and applicable to identify and further monitor the deformation of the rock mass under the Kovdor deposit conditions.

3. In the future, it is necessary to investigate the dependence of the change in the critical parameters of the rock mass deformation (displacement, velocity, and acceleration) on the volumes of a shifting area, the physical and mechanical properties of rocks, and a variety of external factors.
4. All the established parameters and the experience with the radar were used in the development of the "Temporary instructions for monitoring the deformations of the walls and slopes of the open pit using the IBIS FM radar".

References

1. Turintsev, YuI: Geomechanical basis for predicting the open pit slope stability. Izvestiavuzov. Min. J. **9**, 84–87 (1992). (in Russia)
2. Mochalov, A.M.: Estimation of open pit slope stability by observed deformations. In: Proceedings of VNIMI, pp. 42–52 (1985) (in Russia)
3. Fisenko, G.L.: Instruction for monitoring of pit walls, slopes and dumps deformations and developing measures to ensure their stability. L.: VNIMI (1971) (in Russia)
4. Rozanov, IYu., Zavyalov, A.A.: The use of the IBIS FM radar for monitoring the state of the Zhelezny open pit mine (JSC Kovdorsky GOK). GIAB **7**, 40–46 (2018). (in Russia)

Causal Factors of Mudflows (a Study of the Tyrnyauz Tungsten-Molybdenum Plant in Tyrnyauz City Kabardino-Balkarian Republic)

Zalim Terekulov

Abstract

The article studies the matters related to formation of natural-technogenic geosystems, hazardous natural processes, disturbed (technogenic) landscapes, mudflow hazards and uprush of pools in the area of mining enterprises (in the case of the Tyrnyauz Tungsten-Molybdenum Plant). The main objects were specified as factors in destabilization of slope processes and ecological situations. Data on avalanche-mudflow, landslide and landslide-scree hazards are examined, refined and supplemented. Characteristics of the zones with disturbed landscapes are presented. Active development of mountain areas inevitably leads to an increased slope erosion and activation of mudflow processes. The impact of human activities affects the course of mudflow processes. In this case, due to storage of dumps of mining enterprises, construction of reservoirs with substandard dams, roads and other construction works, using explosives that disturb the sheath of covering sediments on the slopes. As a general rule, formation of technogenic mudflows on dumps differs by high periodicity. The maximum volumes of mudflow runoffs are classified as large runoffs, despite the predominance of small-size mudflow water catchment areas. In general, technogenic mudflows formed on dumps, are characterized by local distribution, increased and diverse amount of mudflow runoffs. Such mud streams are neoformations with a modified mudflow state. Significant impacts on the environment change the conditions of mud formation qualitatively. This leads to the change in nature of the distribution of mudflows as well as in the activity level of the mudflow process and in the regime of mudflows.

Keywords

Mudflows · Technogenic landscapes · Intense rainfall · Dumps of mining enterprises · Ecological situations

Z. Terekulov (✉)
High-Mountain Geophysical Institute, 360030 Nalchik, Russia
e-mail: kabbalkeko@rambler.ru

1   Introduction

Natural and technogenic geosystems are most often formed in the area of mining enterprises, for example, in the area of the Tyrnyauz Tungsten-Molybdenum Plant of Kabardino-Balkarian Republic. A number of settlements with a population of at least 50 thousand people and a large number of important national economic entities are located in the region of adverse effect of the Tyrnyauz Tungsten-Molybdenum Plant.

The main factors of destabilization of technogenic nature and formation of hazardous natural processes in the tungsten-molybdenum mining region are the following:

1. The zone for dumps is above Tyrnyauz city (i.e., the Maliy and Bolshoi Mukulan valleys);
2. Mudflow basin of the Kamyksu River is within the city limits;
3. Tailing dump with a system of treatment pools is below Tyrnyauz city (i.e., estuary of the Gizhgit River).

The main factors of occurrence of mud streams on watercourses are the following:

1. Technogenic sediments of waste rock of the Tyrnyauz Ore Mining and Processing Enterprise on slopes;
2. Precipitation amount and air temperature conditions, causing the intensity of weathering and flushing, as well as the consumption of watercourses, at which washing-out of the channel sediments is ensured;
3. Landslide processes as a result of heavy rainfall and wide-spread rain and stability disturbance of the slopes, which contribute to the occurrence of technogenic mudflows, reaching the Baksan river course [7].

Basins of the Maliy and Bolshoi Mukulan watercourses have been characterized by significant activities in recent years, where occurrence of mudflows, is related with technogenic sediments and is directly dependent on the amount of precipitation [10].

A series of large-scale mudflows took place along the Bolshoi Mukulan River on the 24 and 25 of June, 1984. The parameters of the largest among them, determined by measurement tools, were as follows: maximum flow rate—100 m^3/s; depth of the flow—3.5 m; average width—10 m; run off volume $\sim$150 thousand m^3 [5].

A reduction in the frequency and the strength of mud streams along the Bolshoi and Maliy Mukulan is not expected in the years ahead. The incidents concerning the Baksan River repeated closures by mud-rock mass of technogenic dumps are known. However, the river storage ponds did not exist for a long time, from 10 till 40 min, and more than 40 min in March, 2004 when the mud stream descent along the Bolshoi and Maliy Mukulan rivers took place simultaneously [6].

Uprush of a storage pond is destructive due to formation of a flood rampart, which is extremely destructive for Tyrnyauz city. A bursting wave rushing downstream leads to a rise in level of the Baksan River since the river water is high in suspended and pebbled material content and reaches the city limits [1] (Fig. 1). On the other hand, deposited mudflow materials leads to a rise in level of the river course bed and a decrease in the clearance height of the retaining wall along the bank respectively. The volume of technogenic materials of the Bolshoi Mukulan River, thrown into the Baksan River, reaches 150–200 thousand m^3 during the mudflow period.
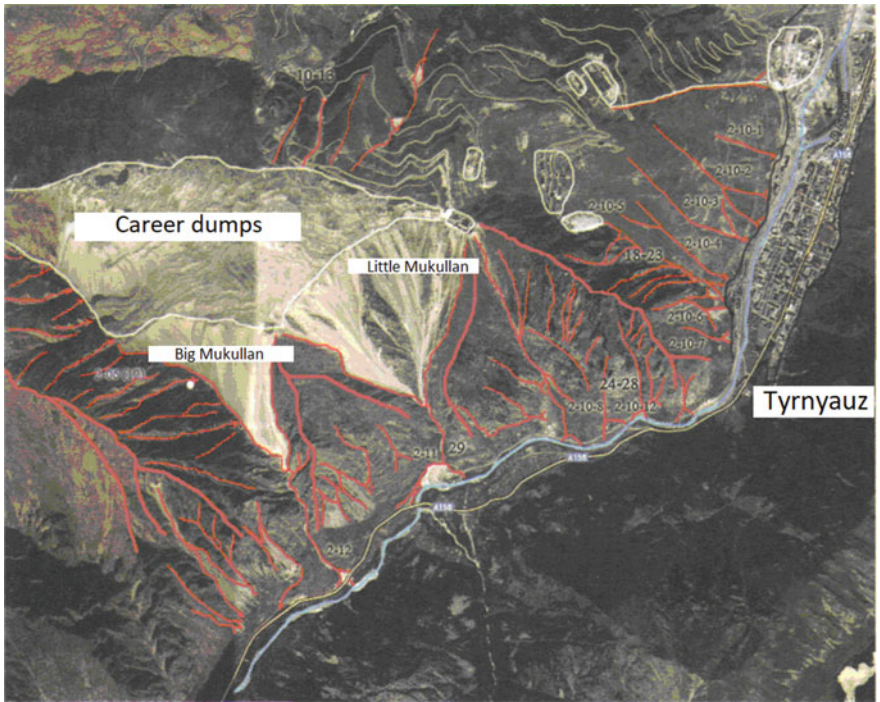
Fig. 1 Technogenic sediments on the slopes of the Bolshoi and Maliy Mukulan rivers
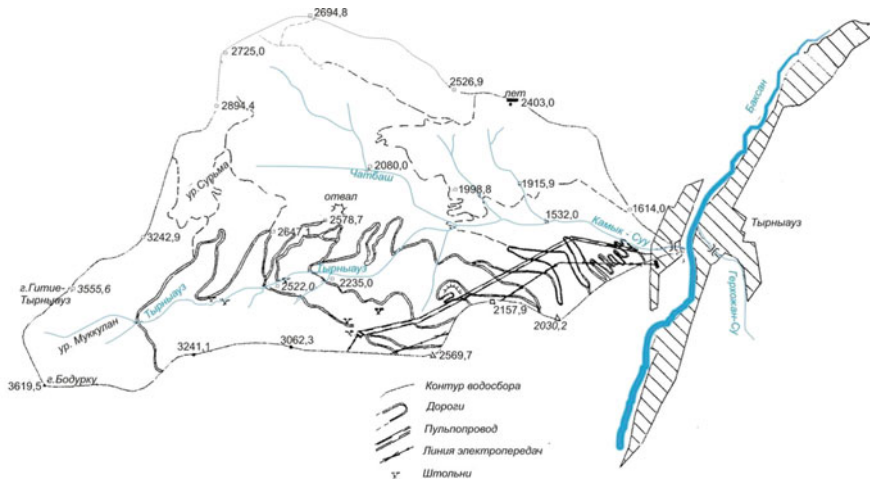
Fig. 2 The Kamyksu river basin

2 Mud Stream Estimation Method

Calculation of the mud stream probability of 1% sufficiency in the study of the Bolshoi Mukulan River can be carried out on the basis of the existing method [9]:

$$Q_{C1\%} = a \cdot Q_{B1\%}, \tag{1}$$

where a is the correction coefficient for the solid component, determined by the formula:

$$a = \frac{P}{\gamma_H(100 - P)} + 1 = \frac{55.45}{1.4(100 - 55.45)} + 1 = 1.89, \tag{2}$$

where γ_H is volume weight of sediment and is equal to 1.4 t/m^3; P is the percentage (%) of the weight content of sediment, determined by the formula:

$$P = 80 \cdot i^{0.4} = 55.45, \tag{3}$$

where i—the slope of the Bolshoi Mukulan river bed and $i = 0.4$ [8], $Q_{B1\%}$—water discharge flow rate of 1% probability at a known value; $Q_{B1\%} = 83.24 \, \text{m}^3/\text{s}$ the mudflow rate of 1% probability is determined:

$$Q_{C1\%} = 1.89 \cdot 83.24 = 157 \, \text{m}^3/\text{s}.$$

3 The Kamyksu River

The Kamyksu River is a left-bank tributary of the Baksan River, flowing into the central part territory of the city. The residential area of the city and the industrial buildings of the Tyrnyauz Ore Mining and Processing Enterprise are located on its debris cone. The origins of the Kamyksu River are located on the slopes of Front Range of the Greater Caucasus mountain range and its spurs. The left-bank tributary of the Kamyksu River is called Chatbash and is formed at the confluence of sources of the Left and Right Chatbash. The maximum height of the basin is 3642 m and the average slope from the source to the estuary is 11.50° (Fig. 1). The river is fed in a mixed pattern, i.e., thawing water predominate in spring, rain water is available in summer and spring-fed pattern is available throughout a year.

The diversion canal of the Baksan Hydroelectric Power Station (HPS) may suffer from major flooding on the Baksan River downstream. Major flooding may occur as a result of blockage of the Baksan river course by mudflow mass, followed by failure of the dike-dam. Such phenomenon was observed in 1937, when the river was impounded with mudflows that descended along the Kamyksu and Gerkhozhansu rivers and which led to an accident at the hydroelectric power plant. A mudslide took place at the estuary of the Kamyksu River in 1972. The mud stream blocked the Baksan River with a debris flow of approximately 35 thousand m³. The flow rate was 190.0 m³/s, established by hydrologists at that time and the mudflow rate with probability of P−1%, calculated by the existing method, was the amount of precipitations that caused descends of mudflows along Terskol settlement and which reached 80–90 mm per day. Hydrological calculations are made in the case of mudslide hazardous Kamyksu River [6]. At descent of mudflows along the Kamyksu River, the mass transport of mudflows can block the Baksan river course with subsequent flooding territory of Tyrnyauz city. Therefore, the existing methods have been set out in this section for calculating the maximum flow rate of rainfall-specific mudflow discharge in the case of the Kamyksu River (i.e., left-bank tributary of the Baksan River) near the area of Tyrnyauz city.

The great uncertainty of the forecasted characteristics of expected mudflows and the available field data are preconditioned by the data insufficiency for rigorous definition of the design parameters, which compels to recommend for applying the range of their values at this stage, i.e., 100–200 m³/s of mudflow rate at the estuary [3].

The hydromorphological data of the Kamyksu River was defined for calculation based on the physical map of the Kabardino-Balkarian Republic of 1:100,000 scale. Where $F = 24.3$ km², is the basin area; $i = 0.2$ is the slope of the river; $H = 2390$ m, is the average height of the water-catchment area, (m) (BC); $L = 3.8$ km, is the length of the river course; $i_{CB} = 0.45$ is the average slope of the water-catchment area.

Calculation of the mudflow rate of 1% probability in the case of the Kamyksu River, is carried out according to the following formula [9]:

$$Q_{C\max 1\%} = C \cdot J \cdot K \cdot F^{0.75}, \tag{4}$$

where C is a coefficient, defining the discharge intensity or the porosity coefficient for mountainous terrain and ($C = 12$); J is the permeability coefficient ($J = 0.5$); K is the climatic coefficient for the Caucasus, defined according to the following function:

$$K = \frac{h}{33} = \frac{89.9}{33} = 2.72,$$ (5)

where h is the maximum daily precipitation in a year, in the area of Tyrnyauz city, during 1.5 h; F is the water-catchment area of the Kamyksu River.

If we substitute all the values in the formula (4), we get

$$Q_{C\max1\%} = 12 \cdot 0.5 \cdot 2.72 \cdot 24.3^{0.75} = 178.6 \, \text{m}^3/\text{s}$$

The results of forecasted calculations of the mud stream rate of P = 1% probability for the Kamyksu River correspond to the recommended range of values of up to 200 m³/s and which is used in the design at this stage.

4   Ecological State Assessment of the Gizhgit River

Now let us consider the ecological condition of the Gizhgit River and tailing dumps of Tyrnyauz Ore Mining and Processing Plant in terms of man-made impact on the environment. The Gizhgit River, i.e., Dzhuargen, Tash-Orun is the left-bank tributary of the Baksan River. The estuary of the river is located on the area in 15 km downstream from the ore-processing plant. The river is fed in a mixed pattern, i.e., by spring water and snow-and-rain water. The Gizhgit River is enclosed in a tunnel in downstream, which diverts the river from the tailing dump and is designed to pass 64 m³/s. The tailing dump of the Tyrnyauz Ore Mining and Processing Plant is located in the estuary part of the Gizhgit river valley and the dump is on the territory of the Elbrus District on the left bank of the Baksan River, 1.5 km from Bylym settlement. It is a natural canyon of the Gizhgit River, closed from the estuary side with a dam (Fig. 3) [3].

The area of land allotment is 176 ha. 119.47 10⁶ m³ of waste from processing works has been accumulated over the entire period of operation at production of tungsten and molybdenum concentrates. The total area of the hydraulic engineering installation is 98 ha, including 33 ha of dry beachfront, which was reclaimed in 2003 (Fig. 4).

The tailing dump is classified as hazard class 1 (Fig. 5). Floods on the Gizhgit River can progress in a mudflow pattern. The flood flowrate of mudflow pattern reached to a maximum of 110–130 m³/s in front of the tunnel entrance portal in summer 2002.

The tunnel could not let the flood pass through at that time and the water began to fill the residual capacity in the reservoir area, which threatened with erosion of containment ramparts. Flood of varying patterns, i.e., from a saturated water stream
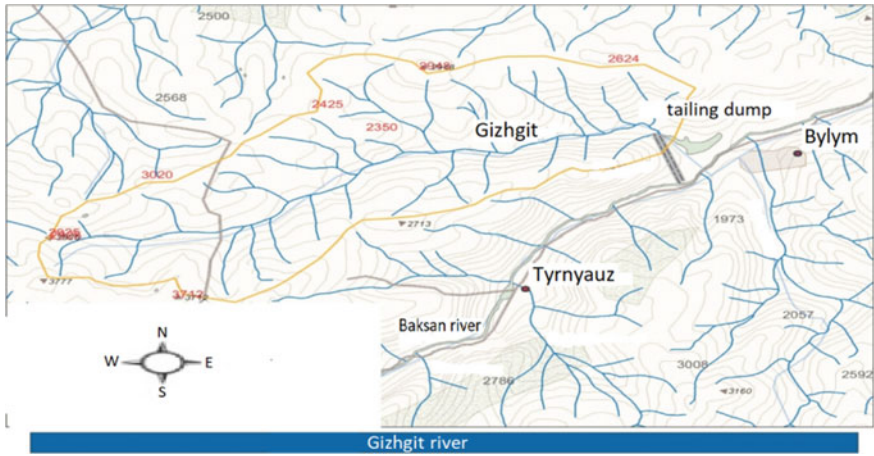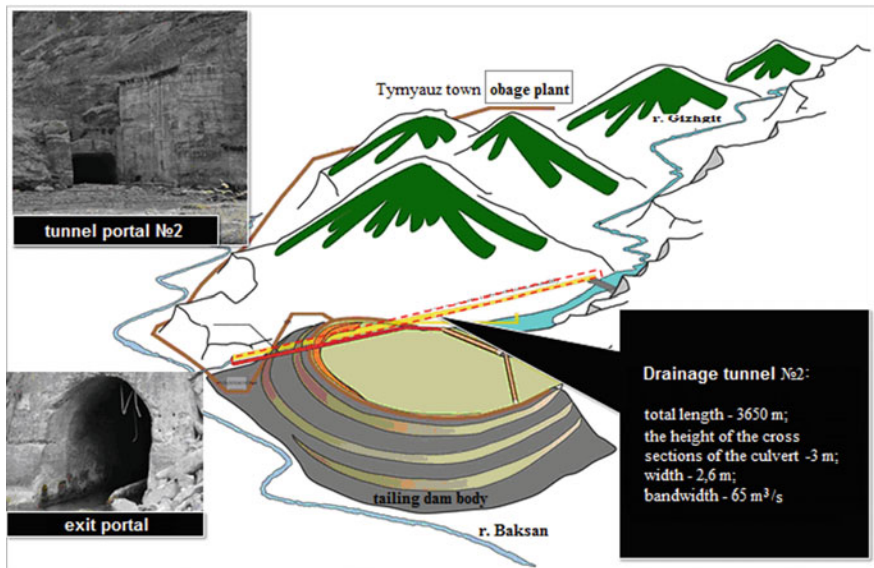
Fig. 3 The Gizhgit river basin

Fig. 4 Drainage facility of the tailing dump

to a water-and-rock debris flow with a maximum discharge of 63.2 m³/s, took place along the Gizhgit River in upstream side of the tunnel on May 21, 2014.

Atmospheric precipitation and surface runoff, which formed flood and caused landslide processes on the slopes, covered a part of the basin. Precipitation in summer months may capture the entire basin and which may lead to a more large-scale floods and mudflows of substantial volume and to dike failure as well (Fig. 6).

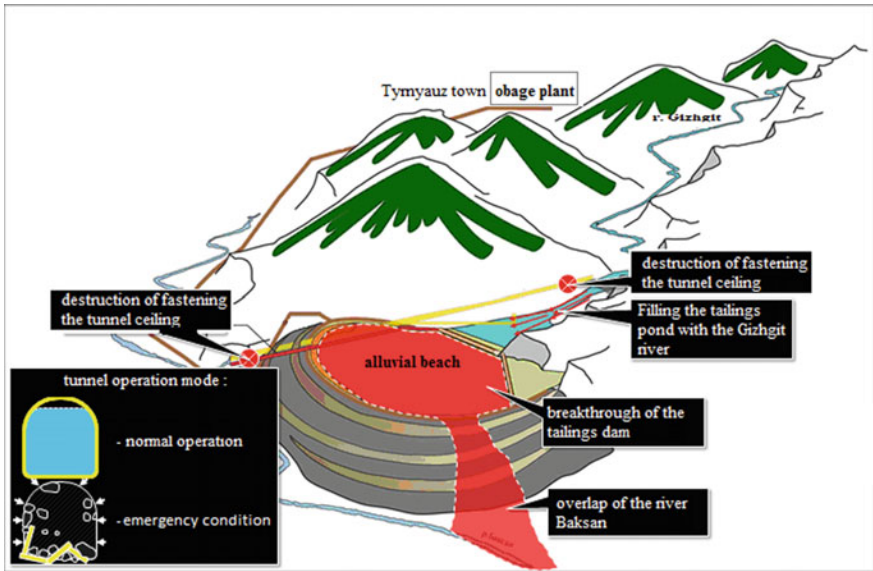**Fig. 5** Tailing dump of Tyrnyauz mining and processing plant

Fig. 6 Development of accident scenario

Reoccurrence of such floods can lead to closure of the Baksan river course with subsequent formation of flood wave and flooding of habitable territories, located downstream subsequently causing unpredictable consequences for the tailing dump, which contains water-saturated finely dispersed mass of toxic products of enrichment, and for the Baksan River as well (Fig. 7).
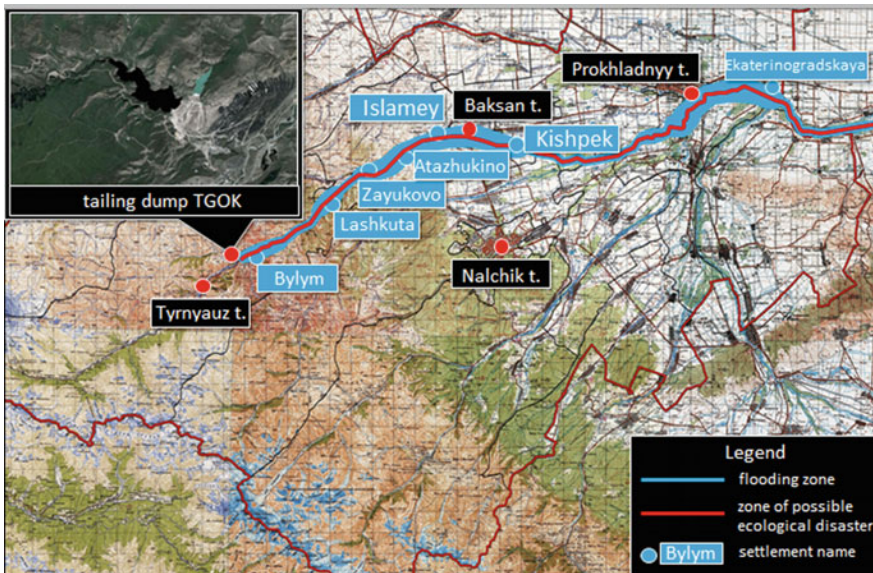

Fig. 7 Map of the Kabardino-Balkarian Republic (the Baksan river basin)

5 Conclusion

The most important factors, influencing the formation of maximum rainwater runoff, are as follows: intensity of rain; rain duration and the area, covered by rain; water infiltration into the soil; rainwater reaching the channel network of the basin [3]. Against the backdrop of climate change, i.e., global warming, there is an increased activation of hazardous natural processes. The main triggering effect of the processes in the geosystem is the increase in precipitation intensity of up to 90 mm per day and as a result of which, excess water saturation of landslide masses. The landslide masses are production dumps, formed in the course of Tyrnyauz Tungsten-Molybdenum Plant activities and they are involved as a solid component in formation of mud stream flows.

Practically in all the studied basins, the technogenic landscapes which were formed at the operation sites of the Tyrnyauz Tungsten-Molybdenum Plant, are the causes for activating hazardous natural processes, taking into consideration of their instability and mobility as artificial-anthropogenic neofromations of natural environment [7]. In addition to the outspread of slope-specific hazardous natural processes, i.e., avalanches, mudflows, landslides, earth fall and screes, these landscapes can cause environmental pollution, such as a threat of uprush of treatment pools in the floodplain of the Baksan and Gizhgit rivers and pollution of the aqueous basin, spread of dust-like mass from the dumps and the threat of air pollution, e.g., alluvial and diluvia processes.

Production dumps and tailings management facility of the Tyrnyauz Tungsten-Molybdenum Plant are threats to ecosystem of the region and the presented issue requires further comprehensive research and forming a development programme on improving the ecological situation for the territory.

References

1. Boyarskij, I.N., Semivol, G.L.: Quantitative indicators of the dynamics of mudslides with a flashy-landslide genesis (on the example of Small Mukulan) (Kolichestvennye pokazateli dinamiki selej oplyvno-opolznevogo(na primere reki Malyj Mukulan)). Seli v gornyh rajonah SSSR.—MGU, pp. 12–24 (1979)
2. Bryuhanov, V.A.: On some aspects of the anthropogenic impact on river channel processes (O nekotoryh aspektah antropogennogo vozdejstviya na ruslovye processy rek (na primere Altaya)). Meteorologiya i gidrologiya, №12 (1990)
3. Gegiev, K.A., Sherhov, A.H., Anaev, M.T., Gergokova, Z.Z.H., Terekulov Z. M. Field surveys of mudflow basins in the area of Tyrnyauz (Naturnye obsledovaniya seleopasnyh bassejnov v rajone goroda Tyrnyauz). VGI Bulletin, vol. 100 (2017)
4. Ozrokova, L.G., Gegiev, K.A., Sherhov, A.H., Anaev, M.T., Gergokova, Z.Z.H., Anahaev, K.N.: Analysis of existing methods for calculating rain and mudflows. (Analiz sushchestvuyushchih metodov rascheta dozhdevyh i selevyh potokov). Izvestiya KBGAU **1**(15), 73–80 (2017)

5. Zaporozhchenko, E.V.: Engineering solutions of mudflow problems in the built up mouth of the left tributary of the Baksan-Kamyk River (Inzhenernye resheniya selevyh problem zastroennogo ust'ya levogo pritoka r. Baksan-r. Kamyk). Trudy Vserossijskoj konferencii po selyam (26–28.10.2005). M., pp. 289–301 (2007)

6. Zaporozhchenko Eh.V. Mudflow processes of a rainfall origin on the anthropogenic and natural background (Selevye processy livnevogo genezisa na antropogenno-prirodnom fone). Sb. OAO « Sevkavgiprovodhoz » . Vyp. 16. Pyatigorsk, pp. 36–47 (2003)

7. Kuhl, E.V., Borisova, N.A.: Activation of hazardous processes in natural and man-made geosystems (by example of TVMP, KBR, Russia) (Aktivizatsiya opasnych processov v prirodno-technogennych geosystemach (na primere Tyrnyauzskogo volframo-molibdenovogo kombinata, KBR, Rossiya)). Basseyn reki Terek: problem regulirovaniya, vosstanovleniya I rehabilitatsii vodnykh objectov—Materials of the all-Russian conference, Makhachkala-Pyatigorsk, pp. 201–205 (2015)

8. Kondrat'eva, N.V.: Cadastre of mudflow danger in the south of the European part of Russia (Kadastr selevoj opasnosti yuga evropejskoj chasti Rossii. M., Nal'chik, p. 84 (2015)

9. Sokolovskij, D.L.: Mudflows and their hydrological features and calculation method (Selevye pavodki i ih gidrologicheskie osobennosti i metodika rascheta). Metrologiya i gidrologiya. M. **5**, 65–75 (1947)

10. Flejshman, S.M. Mudflow phenomena in the Elbrus region (yavleniya v Priel'brus'e). MGU, pp. 58–64 (1979)

On Deformation Stability of Rock Massif

Vitaly Trofimov

Abstract

The article deals with the description of the deformation regularities and the conditions for the transition of stable, quasi-static destruction of specific areas of the rock massif under its loading into the unstable one and catastrophic. The decisive role at this process is played by the array loading mode: "soft" or "hard" determined by the spatial distribution of the deformation parameters in the rock massif. Such a change in the nature of the destruction is possible only if the massifs contain areas with deformation characteristics having a falling branch of stress-strain deformation curve. An example of building such solution for loading of a separation pillar under the development of a reservoir is given. An analytical solution was written out and the parameters of such a transition were determined. An important role is played by the dimensions ratio of the pillar and the span of the exposed roof. The latter, as mining works develops, gradually increases, which provides additional loading on the pillar. When the loading threshold value is reached, the solution of the corresponding geomechanical problem ceases to exist. This can be interpreted as a transition of the quasistatic process of destruction into the dynamic phase.

V. Trofimov (✉)
Institute of Comprehensive Exploitation of Mineral Resources Russian Academy of Sciences, 111020 Moscow, Russia
e-mail: asas_2001@mail.ru

1 Introduction

Large-scale catastrophic destruction in the rock massif when developing solid minerals are quite rare natural phenomena. These include rock bursts of various nature, sudden collapses of roof rocks in mine workings, sudden subsidence of the Earth's surface, sudden emission of coal and gas, etc. A characteristic feature of these phenomena is a sudden, abrupt change in the state as a result of the destruction of one or another mining structure within the framework of the operating system used.

There is no doubt that all the above-listed natural phenomena associated with development of solid minerals, i.e. with creation of open spaces in the rock massif, in other words workings, are catastrophic. At that, as the mining operations develop, a system of voids is gradually formed, sometimes filled with a bookmark or collapsed rocks, which for the most part of its lifetime is stable and subjected to insignificant local destruction only. During this period, the parameters describing its state change continuously, without significant jumps. It is in this mode, taking into account the specific mining and geological conditions of the field, that any operating system should function.

Nevertheless, sometimes there are situations in which the continuous nature of changes in the system parameters is broken down, which leads to stability loss and catastrophic damage, both in underground workings and on the Earth's surface. In this case, as usual, the loss of stability implies that under certain conditions a small change in the loading parameter leads to a significant change in the parameters describing the system.

Let us note the necessary conditions for the occurrence of such phenomenon.

First, in rock massif one can always identify structural elements that play the role of a "loading system" (hereinafter "system") and the "loading element" itself ("element"), which mainly perceives the load from a "system". For example, a pillar and host rocks. Alternatively, a joint in rock, in which the filler and the irregularities of the crack surfaces constitute an "element" and the medium near the crack is a "system".

Secondly, the considered catastrophic damage is always associated with the initial destruction of the "element" and the subsequent movements of the rock mass. In this case, the kinetic energy of moving rocks ("loading system") is a destructive factor. Displacements can be insignificant, about several centimeters, but the energy is high due to involvement of large masses of rock in the movement. It can be realized in the form of destruction in the workings at a considerable distance from the "element".

Thirdly, the force interaction of the "system" and the "element" should occur in the mode of "soft" loading. In general, this means that in some sense the deformation characteristics of the "system" and "element" should provide a higher pliability for the "system" than for the "element". "System" and "element" are deformed together, i.e. the principle of compatibility of deformations, which is expressed in the continuity of displacements at their common boundary, must be
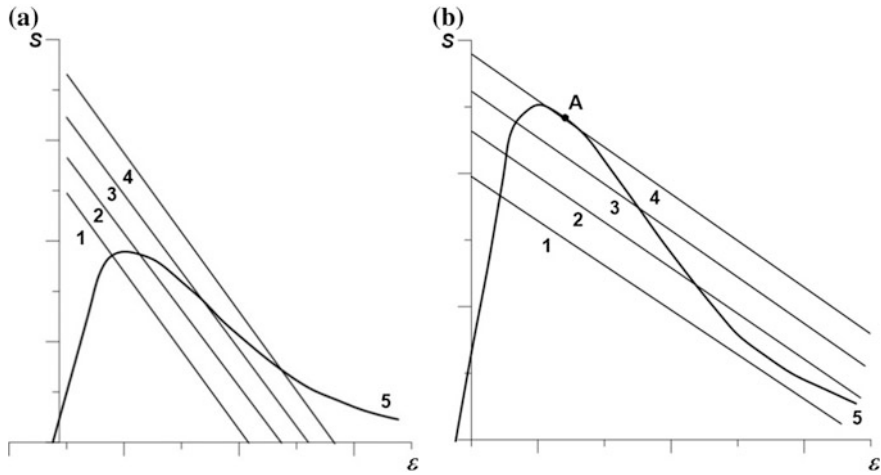
Fig. 1 Schematic representation of "hard" (**a**) and "soft" (**b**) loading

fulfilled. In the case of "soft" loading, these displacements are determined mainly by the deformation properties of the "element", whereas with "hard" loading, the properties of the "system". Figure 1 shows the conditional schemes for these two types of loading—(a) hard, (b) soft.

Usually, during the preparation of a catastrophic phenomenon and its course, the rock massif is deformed in such a way that the "system" is unloaded, i.e. its deformations increase, and the force factors (say, stresses) decrease. Families of lines (1–4) show the relationship between them in Fig. 1, where some loading parameter is used as a family parameter. In this capacity, the length of the mined space, changing in time or the distance from the front of development, approaching the fracture, to this discontinuity in the rock massif, etc. depending on the mining conditions can be used.

In this case, as the loading parameter increases, the corresponding curves from the mentioned families gradually shift upwards. Note that the shape of these curves depends on the specific loading conditions, however, it can be stated that the rigid the "system" is, the greater curves slopes (1–4) in Fig. 1.

At the same time, for the "element" there is a loading, which described by the corresponding deformation diagram, in the general case with a post failure branch (curve 5). Note that catastrophic destruction will occur at point A in Fig. 1b. It is characterized by the fact that in addition to the equality in it of the force and deformation factors for the "system" and "element", it observes the equality of the slopes for the corresponding curves. Thus, their contact takes place, that is, the equality of derivatives. In addition, their curvature should be strictly positive. Note that in Fig. 1a. there are no such points.

In underground mining of mineral deposits, it is often necessary to maintain an exposed roof by pillars and thereby control the rock pressure in mining area. These pillars are counting on high rock pressure and long-term sustainability. However, as the mining practice shows, in this case dangerous by rock bumps situations often arise that can be associated with many technological and geological factors. Therefore, there is always a need to know under what rule the load on the pillar changes during the development of mining operations and how it depends on the mining and geological parameters, which reflect the deformation properties of the pillar and host rocks, when it begins and how the stage of quasi-static destruction of the pillar develops, under what conditions there is a dynamic manifestation of rock pressure, i.e. rock bump. It is obvious that the answer to these questions can be quite complete and substantiated if the dependencies of the main indicators of rock pressure manifestation on the geological and mining parameters are established. However, to establish these dependencies in the general case complicated by a variety of secondary factors, is very problematic. Therefore, when formulating and solving the corresponding problem of rock mechanics, within the framework of which the considered problem of rock pressure is described, it is advisable to proceed from a certain schematization of particular stages of mining development and idealization of a rock massif, including the ore body.

2 Pillar Destruction

Farther, as an example illustrating the above, specific relations are given. They describe the deformation of pillar when mining a horizontal tabular deposit and the conditions for the onset of rock bump in it.

A pattern of this pillar and surrounding mining areas of tabular deposit with an exposed roof is shown in Fig. 2. The main parameters in this scheme are development depth H, formation thickness 2h, initial rock pressure q_H^0, deformation parameters of rock massifs E, ν, pillar width 2l, spread of the developed areas of the formation L-l.
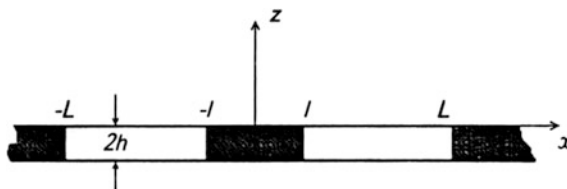
Fig. 2 Schematic representation of the seam under development and separation pillar between the host rocks

In accordance with the scheme in Fig. 2, we denote by $\sigma_\text{ц}$ the intensity of its response to compression by host rocks averaged over the entire area of the pillar, and by $2\Delta h_\text{ц}$ the deformation of the pillar caused by the seam mining.

These two variables are related. Under the condition of equilibrium and continuity of rocks around the workings, this relationship is determined from the solution of the corresponding geomechanical problem, the mathematical formulation of which and its general solution are given in [1–3]. In this case, the ratio is derived from the solution, which relates the intensity of the pillar reaction and the convergence of the roof and the soil in the pillar area. In the accepted notation, this equation has the form

$$\frac{\sigma_\text{ц}}{\gamma H} = A\left(\frac{L}{l}\right) - MB\left(\frac{L}{l}\right)\frac{\Delta h_\text{ц}}{h}, \tag{1}$$

where

$$M = \frac{1}{\gamma H\left(\frac{1-\nu_\text{п}^2}{E_\text{п}}+\frac{1-\nu_\text{к}^2}{E_\text{к}}\right)}\frac{h}{l}, \tag{2}$$

$A\left(\frac{L}{l}\right), B\left(\frac{L}{l}\right)$—known functions. They are relatively simply written through the complete elliptic integrals $K(k), E(k)$ in the form

$$A\left(\frac{L}{l}\right) = \left[E(k) - K(k) + \frac{K(k)}{K(k')}E(k')\right]\frac{1}{k}, B\left(\frac{L}{l}\right) = \frac{K(k)}{K(k')}, \tag{3}$$

where

$$k = \frac{l}{L}, k' = \sqrt{1 - \left(\frac{l}{L}\right)^2} \tag{4}$$

In Eq. (1) there are three variables: $\frac{\sigma_\text{ц}}{\gamma H}, \frac{\Delta h_\text{ц}}{h}, \frac{L}{l}$. Of these, $\frac{L}{l}$—is an independent quantity, which is completely determined by the technology of mining operations and cannot decrease.

Pay attention to the coefficient M in Eq. (1). It combines the initial parameters of the rock massif and the relative pillar size, but do not depend on its deformation characteristics. Usually, the values of the parameter M and its variations in situ are determined in advance based on the geological conditions of the seam development.

The whole process of pillar loading is associated with Eq. (1). In particular, it follows that the response of the pillar $\frac{\sigma_\text{ц}}{\gamma H}$ and the convergence of the roof and the soil $\frac{\Delta h_\text{ц}}{h}$ are connected linearly. At that, the larger $\frac{\Delta h_\text{ц}}{h}$, the smaller $\frac{\sigma_\text{ц}}{\gamma H}$ and vice versa, the larger $\frac{\sigma_\text{ц}}{\gamma H}$, the smaller $\frac{\Delta h_\text{ц}}{h}$. Its features are clearly visible in the geometric image in Fig. 3, where Cartesian coordinates are represented by variables—$\frac{\sigma_\text{ц}}{\gamma H}, \frac{\Delta h_\text{ц}}{h}, \frac{L}{l}$. In these coordinates at a constant value of M, Eq. (1) describes the surface of the

continuity of interaction between the host rocks and the pillar at all stages of it is deforming until complete destruction. In other words, compression deformation of the pillar, regardless of its deformation properties, both at the loading stage and at the post failure deformation stage will correspond to the convergence of lateral rocks $\frac{\Delta h}{h}$, linearly related to $\frac{\sigma_y}{\gamma H}$ by Eq. (1).

In Fig. 3, such a surface is shown for an M equals to 20.

At constant values of $\frac{L}{l}$, the section of the continuity surface will be straight lines, which are described in the coordinate plane $-\frac{\sigma_y}{\gamma H}, \frac{\Delta h}{h}$ by the same Eq. (1). These straight lines will be called generating lines of the continuity surface, each of which corresponds to a certain value of $\frac{L}{l}$.

Each pillar, as well as its constituent rocks, has its own stress-strain-deformation diagram with a post failure descending branch. The characteristic view of this diagram is shown in Fig. 4. The stress-strain diagram equation is written as

$$\sigma_{\text{сж}} = \gamma H F\left(\frac{\Delta h}{h}\right), \ F(0) = 1. \tag{5}$$

Note that this diagram refers to the quasi-static loading of the pillar, including the descending branch of the deformation. Equation (1) also refers to the quasi-static convergence of host rocks depending on $\frac{L}{l}$. Therefore, as long as the process of compression of the pillar by the host rocks remains quasistatic, the reaction of the pillar σ_{u} and the average compressive stresses $\sigma_{cж}$ must not only be equal for the same values $\frac{\Delta h}{h}$, but also simultaneously satisfy Eqs. (1) and (5).

The joint solution of these equations gives the dependence of the load on the pillar and it's deformation on $\frac{L}{l}$. On the surface of continuity, this solution gives the corresponding spatial curve, the projection of which on the coordinate plane $-\frac{\sigma_y}{\gamma H}, \frac{\Delta h}{h}$ will coincide with the deformation pattern of the pillar in the area of the
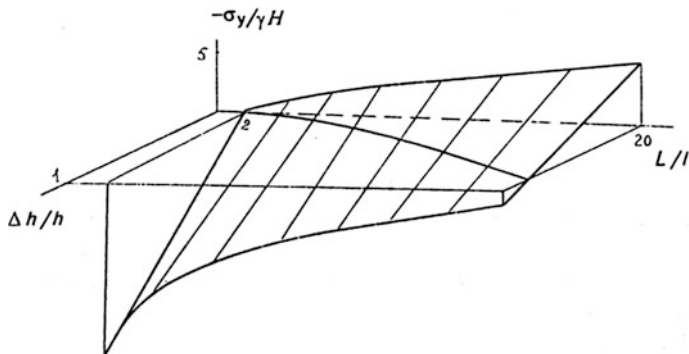

Fig. 3 The surface of the continuous interaction between the host rocks and the separation pillar for the value of the similarity parameter M = 20
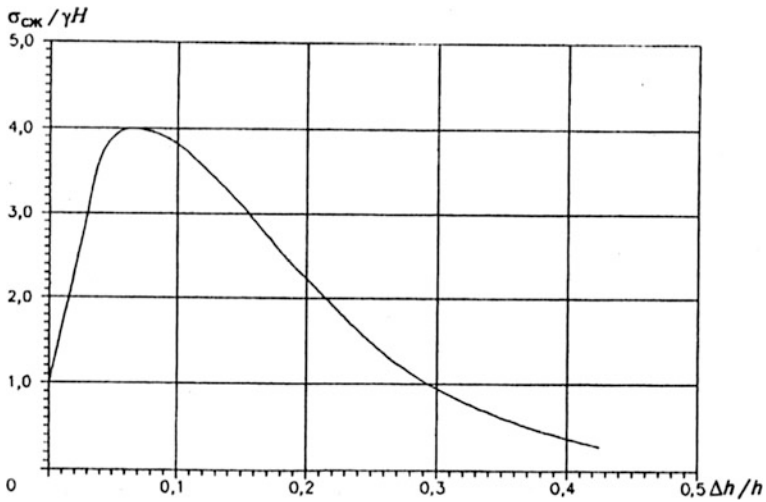
Fig. 4 The characteristic form of the dimensionless stress-strain diagram for the pillar

joint solution of Eqs. (1) and (5). Figure 5 shows the complete stress-strain diagram for pillar and the family of straight lines, which are projections of the generating lines of the continuity surface. In other words, these straight lines are solutions of the linear Eq. (1) for different values of $\frac{L}{l}$.
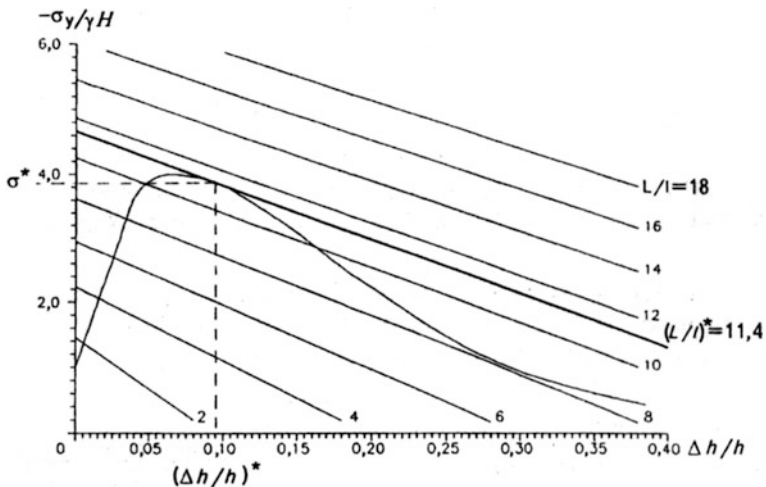
Fig. 5 The projections of surface of continuity sections for M = 20 with $\frac{L}{l} = 2, 4, 6, 8, 10, 12, 14,$ 16, 18 on the coordinate plane $-\frac{\sigma_y}{\gamma H}, \frac{\Delta h}{h}$ and the loading curve for the pillar, which coincides with the stress-strain diagram

The points of intersection of these lines with the stress-strain diagram correspond to joint solutions of Eqs. (1) and (5). From these intersection points, it is easy to see how the load on the pillar changes with increasing $\frac{L}{l}$ and how it deforms. It is obvious that the lines of the family that do not intersect the stress-strain diagram of the pillar correspond to the values of $\frac{L}{l}$, for which there are no joint solutions of Eqs. (1) and (5). These $\frac{L}{l}$ values cannot physically be realized.

In Fig. 5, as term of straight lines family, given as an example for the parameter M = 20, there is one that is in contact with to stress-strain diagram on the falling branch. It corresponds to a certain value $\frac{L}{l}$, which we denote as $\left(\frac{L}{l}\right)^*$. Note, the smaller the M value, the more gently sloping the straight lines of the family become, and the tangency point is located closer to the maximum on the diagram, remaining on the falling branch.

Moving from Eqs. (1) and (5) to its solution in the form of intersection of the pillar diagram by a family of corresponding straight lines (see Fig. 5), we see that the load on the pillar increases to the maximum value as $\frac{L}{l}$ increases. When the load on the pillar reaches a maximum value equal to the extreme bearing capacity, it remains in a steady state and provide sufficient resistance to the quasistatic convergence of the host rocks. With further increase in the relative span $\frac{L}{l}$, but as long as it remains less $\left(\frac{L}{l}\right)^*$, the convergence of host rocks will also occur in quasi-static way. At the same time, the load on the pillar and the corresponding reaction of the pillar will fall along the falling branch of deformation diagram. Here, the static equilibrium is maintained due to the fact that at fixed values of $\frac{L}{l}$, the stresses σ_u holding the roof and the soil in equilibrium, with increasing $\frac{\Delta h}{h}$, fall linearly more abruptly than the carrying capacity of the pillar $\sigma_{cж}$ along the falling branch of its diagram.

The relative span of the $\frac{L}{l}$ for development area in the seam will be critical if it reaches the value $\left(\frac{L}{l}\right)^*$. In this case, the equilibrium of the host rocks becomes unstable, and it spontaneously transforms into dynamic compression of the pillar. Indeed, with the critical value $\frac{L}{l}$ equal to $\left(\frac{L}{l}\right)^*$ and the corresponding value $\left(\frac{\Delta h}{h}\right)^*$, the further spontaneous convergence of the surrounding rocks becomes impossible, since with increasing $\frac{\Delta h}{h}$, the stress σ_u, corresponding to the static reaction of the pillar, turns out to be greater than the carrying capacity of the pillar itself.

3   Conclusions

The article discusses the mechanism of deformation stability loss for the pillar and the host rock mass as mining develops. At that, the deformation of the rock mass is smooth and continuous until the front of mining operations reaches a certain position $\left(\frac{L}{l}\right)^*$, depending on the deformation properties of the pillar and host rocks. After this, a dynamic destruction of the system occurs, accompanied by significant

displacements of the rocks massif. This is a typical example of the trigger effect, which actually takes place in the mining practice.

Note that a similar effect can also occur in the case when the pillar is worked out with fixed edge areas of the formation. In this case, the value of l decreases, and $\frac{L}{l}$ grows and when the critical value $\left(\frac{L}{l}\right)^*$ is reached, destruction will occur [4, 5].

Similarly, the trigger effect is manifested in case of a continuous change in deformation properties of the pillar or the host rocks, or manifestation of their rheological properties. All this is fully reflected by the relations (1), (2), or similar.

Moreover, within the framework of the developed formalism, the problem of a shear trigger effect can be solved when an intermeshing occurs at a certain section of the discontinuity, and the system is loaded with shear loads along the discontinuity. In this case, the deformation curves of the contact on the intermeshing section must have a falling branch, so that the possibility of dynamic deformation would arise. In this case, there are also two loading modes: soft and hard. In the first case, the transition from continuous shift to dynamic slippage is possible.

References

1. Kuznetsov, S.V.: General laws and characteristic features of stress redistribution in rock masses during the development of a worked space. Fiz.-Tekh. Probl. Razrab. Polezn. Iskop. **6**, 18–31 (1988)
2. Kuznetsov, S.V.: Certain laws and relationships defining face caving. Fiz.-Tekh. Probl. Razrab. Polezn. Iskop. **5**, 3–19 (1965)
3. Trubetskoi, K.N., Bronnikov, D.M., Kuznetsov, S.V., Trofimov, V.A.: Mine-shock mechanism and loads on dividing columns for workings in plate strata. J. Min. Sci. **31**(5), 321–332 (1995)
4. Trubetskoi, K.N., Bronnikov, D.M., Kuznetsov, S.V., Trofimov, V.A.: Stability of rock masses based on the criterion of the dynamic manifestation of mine pressure during the depletion of a separation pillar. J. Min. Sci. **33**(2), 103–112 (1997)
5. Trubetskoi, K.N., Bronnikov, D.M., Kuznetsov, S.V., Trofimov, V.A.: Stress state of rock and pressure on interchamber pillars. J. Min. Sci. **33**(5), 389–398 (1997)

About Interaction of Blasting and Geomechanical Processes in Mining

Sergey Viktorov , Vladimir Zakalinsky , Ivan Shipovskii
and Rafael Mingazov

Abstract

The interrelationship between the blast processes and geomechanics is studied as part of the synergetic interaction and interpreted as a research and technology concept with the trigger-effect features, with a view to prevent the undesired consequences inevitably accompanying the integrated industrial mining of the ore minerals. A synergistic effect is the result of two or more processes interacting together to produce an effect that is greater than the cumulative effect that those processes produce when used individually. The concept relies on the integrated approach based on geomechanical simulation of the safe ore minerals mining ensured by the reduced blasting impact, which is the most important factor of dynamic anthropogenic influence. The purpose of this study is to develop the methodology and algorithm for calculating changes of the stress-strain state of rock mass at the development of ore, coal and other mineral deposits, taking into account the trigger effect. A trigger problem is formulated for industrial operations in the geosphere. Solutions and approaches to solve the trigger-associated problem are shown. It was established that the selected computational approach is applicable for obtaining the adequate assessment of the seismic impact of explosion of charges of various designs, and the blast consequence forecasts. Optimization of the charge design for given

S. Viktorov · V. Zakalinsky (✉) · I. Shipovskii · R. Mingazov
Institute of Comprehensive Exploitation of Mineral Resources, Russian Academy of Sciences, 111020 Moscow, Russia
e-mail: vmzakal@mail.ru

S. Viktorov
e-mail: victorov_s@mail.ru

I. Shipovskii
e-mail: iv_ev@mail.ru

R. Mingazov
e-mail: ghost1064@yandex.ru

mining conditions provides for significant improvement of the seismic performance indicators in the area of drilling and blasting. Explosive impact of the investigated charge designs on the stress-strain state of the rock body is identified and described. This supports the informed choice of the blasting parameters for reduction of the negative impact of blasts on the geo-environment. The concept has been tested in the context of large-scale mining operations, and its efficiency is assessed. The concept and proposed computational approach open up prospects for the future research and development in this knowledge domain.

1 Introduction

For a long time, the Russian mining industry has focused on extracting of higher volumes of mineral resources and growing rates at the mining operations, which was due to the post-war situation in the national economy. Modern mining technology has made it possible to achieve maximum production rates. At the same time, on the one hand, mining operations involve excavation work and the use of intrusive mining systems, such as combined shrinkage and caving or block caving, when an underground rock mass 60 m high and weighing several hundred thousand tons is caved simultaneously. On the other hand, a significant and often the primary contribution here comes from rock blasting as the principal method of breaking up a rock mass at mining operations. Besides, until recently, blasting and crushing have been considered as the main research interests in the field of explosive mining, while other directions of research—as secondary and local. Meanwhile, seismic vibrations of the rock mass at the blasting operations are a real problem, since hundred or thousand tons of explosives is consumed at mass blasting. Thus, the trigger effect upsetting the rock mass balance and resulting in rock deformation and shifts in the operation of ore, coal, and other mineral deposits is a highly relevant research object. Experience demonstrates that this form of anthropogenic environmental impact, in addition to the increased extraction rates achieved by the rapidly developing mining technology, is accompanied by the increased number of emergencies, including those caused by uncontrolled developments in rock body geomechanics. The unsatisfactory safety level directly affects process and economic performance. A lot of attention has been paid to solving this problem, and at this stage, the potential approach based on the integrated geomechanical design method is considered [1]. The underlying idea of the proposed method is to develop the concept of geomechanical design ensuring the safe mining operations by reduction

of the effect of the most important anthropogenic impact factor, i.e. the intensity of blasting operations. The conceptual approach is based on a multidisciplinary research in geomechanics and rock failure, which allows the use of theoretical and experimental analogs, and the relevant tools of one of the research disciplines for the techniques and methods of another.

2 Methods

It is known that there are no rigorous theoretical solutions satisfying the diverse and heterogeneous needs of development of geodynamically hazardous deposits. Besides, from the point of geomechanics, multiple displacement and rock breaking mechanisms caused by the impacts of blasting at mining operations have yet to be explained [2].

The methodology is based on the hypothesis of applicability of a well-known interdisciplinary approach, benefiting from advances in related research areas, to mining engineering. Its essence lies in applying methods and procedures, similar in terms of the nature of research, of one discipline to another and the synthesis of the results obtained in different research disciplines. This, when combined, help solve the existing research and technology problems in mining engineering. This attitude has led to a paradigm change in the relationship between the two mining disciplines and justifies a fundamentally new concept of the synergy of explosive rock breaking and geomechanics in the challenging context of mining operations.

Structurally, the concept is based on the following postulates:

– an integrated problem solving approach is used,
– the integrated approach is based, in addition to its mining engineering content, on the hypothesis about the possibility of using in mining engineering the results obtained through an interdisciplinary approach in related research,
– the study of the nature and origin of the factors and their interactions involves establishing functional relationships between the factors,
– the legitimacy is examined of applying interdisciplinary theoretical, modeling, and experimental tools in the various solutions to the problem,
– on the basis of the analysis of dynamic phenomena of various nature, including explosive effects, and of the environmental reaction, a new methodological concept is formulated,
– the study of the instrumental aspect of controlling the stress-strain state under dynamic loads.

In the context of the challenges faced by specific mining operations and associated with typical manifestations of anthropogenic impacts in difficult mining conditions typical of the combined open-pit and underground coal mining

operations, as well as underground mining at hazardous mines and coal operations, the key algorithms of the interaction processes between the research objects were examined.

3   Calculation and Result

We used numerical simulation to solve the task of the blast wave passing through a barrier represented by various structural materials, that simulate a new design of wellbore charge in a rock. The first case describes an experimental massive explosion at Zarechny open-pit mine underlain by the underground coal mine Taldinskaya-Zapadnaya 2. According to the model experiment, the explosive wave was formed by the explosion of a cylindrical charge weighing 200 g with a diameter of 40 mm and a height of 100 mm. The charge was placed inside a cylindrical woven mesh container with an inner diameter of 108 mm and an outer diameter of 118 mm. The main parameters of the transmitted and reflected shock waves in various media and the description of the calculation scheme were analyzed by comparing numerical solutions on the processing system STAR−CCM + [3].

The diverse structure of the rock materials significantly reduces the load in terms of both the amplitude and the impulse magnitude of the transmitted shock wave. The numerical simulation has allowed us to quantify the damping properties of the barrier.

This result proves that the layer of loose rock formed at the experimental blasting efficiently dampens the propagation of the high-frequency energy of the main charge into the rock body [1, 4]. It is shown that the negative destructive impact of the blast wave caused by the overlying borehole charges on the rock body state is minimized and ensures the improved stability of underground mining sites.

The second case involves underground mining of instable ore deposits [5]. As part of the concept of reducing the blasting intensity, being a risk factor in mining operations, we have conducted studies to find an effective method of ensuring geomechanical safety when the blasting method is used. It is well known that mining of such ore minerals, in particular at the mining operations in Western Siberia, is associated with dynamic phenomena of varying intensity caused by massive blasting of up to several hundred tons of explosives. Embedding such large quantities of explosives in a rock body requires dedicated mine workings or large-diameter boreholes. The idea behind the approach is based on changing the prevailing paradigm involving drilling of boreholes and excavating a circular cavity to place the explosive charge. The mining science and practice has long been interested in developing rock disintegration methods with an asymmetric distribution of the explosion energy, allowing the energy to focus in certain directions. In this regard, experimental studies were conducted to address the conceptual aspects of the new priority area of research [6].
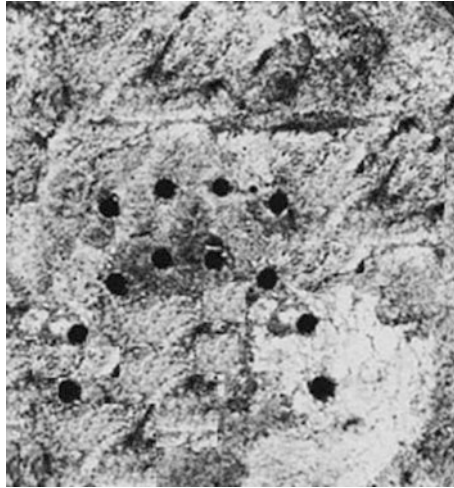
Fig. 1 Cumulative arrangement of contiguous explosive charges to form a single unit with a directed explosion wave

A direct consequence of the blasting method in this example was the possibility of spreading the mass of the explosives from a single large-diameter cavity to several smaller cavities. With this arrangement of close charges (Fig. 1), it is possible to control the direction of the beam explosion energy and obtain the expected cumulative effect [6, 7]. This can be used to achieve selective intensity of the explosion in the interests of geomechanical provisioning at the field development.

In the third case, the behavior of a rock mass during the blasting of a mine working adjacent to a coal seam with a high outburst hazard was studied by using computer simulation and the smoothed particle method (SPH) [8, 9]. We estimated the following main parameters: stress distribution under loading, formation of failure areas, and outburst evolution risk. The theoretical part of the study includes the built model of the studied processes and the formulated boundary-value problem. The proposed new computer simulation approach provides researchers with a tool allowing them to make informed decisions when choosing a safe method of excavation. Based on the calculation results, for a chosen excavation layout, the moment and origination point of the outburst can be identified and the consequences of filling the excavation with the ejected coal debris and rock particles can be assessed. The study contains the assessment of the state of the coal body adjacent to the hazardous seam, used to refine the safe excavation layout parameters through applying the new methodological approaches. Tracking the history of parameter changes in characteristic places in the vicinity of the most likely place or "plug" of breakthrough near an outburst hazardous coal seam allows us to predict the outburst start moment for the considered development scheme carried out by drilling and blasting method. Thus, Fig. 2 shows the change in time of the vertical mass velocity
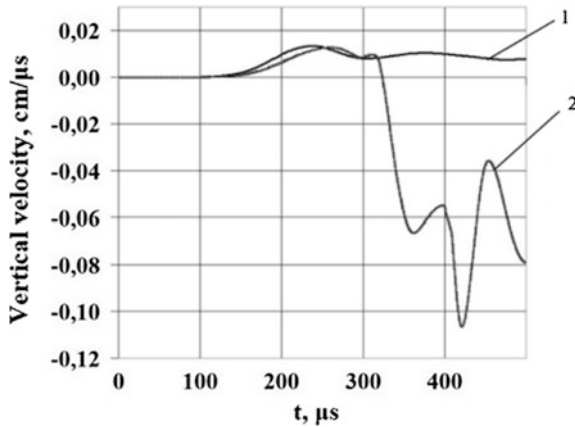
Fig. 2 The history of the velocity change at the place of the most probable breakthrough of the plug. After 300 μs, a cork breakthrough begins—the irreversible movement of the rock mass down. 1—non-outburst coal seam; 2—outburst coal seam

near the working of coal seam. It can be seen that, unlike the case of working near an unbroken coal seam, after 300 μs, irreversible movement of the material downward is observed, which is a clear sign of the beginning of a plug breakthrough.

Figure 3 shows a calculation fragment of the detonation wave progression along the charge axis with a time increment of 0.6 ms during the blasting process. The calculation is done with use of the smoothed particle method (SPH).
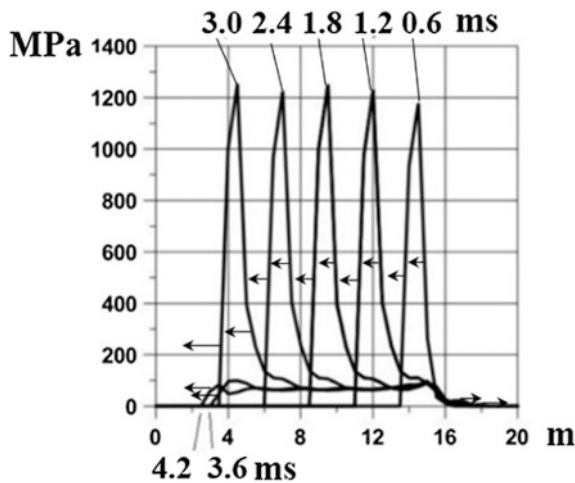
Fig. 3 Detonation wave progression along the charge axis. Time increment 0.6 ms

The pressure in the detonation products drops sharply after the entire charge explosion. The proposed method allows us to obtain the calculation results required to build adequate engineering models describing the conditions, under which an outburst situation can arise, and tracing the outburst situation origin and development.

4 Discussion

The original concept presented in this paper is of undoubted importance as it is aimed at reduction of the blasting impact on the geoenvironment, being a trigger effect and the main factor of dynamic anthropogenic influence. Based on a large empirical material, the paradigm of the relationships between the different mining disciplines is examined.

The experimental results in principle support the idea underlying the concept of synergistic interaction between explosive rock breaking processes and geomechanics. Conducting research with combination of simultaneity, compatibility and interaction of various mining processes is a new concept of synergistic interaction between the processes of explosive destruction and geomechanics. The essence of this interaction is that the results of the addition of the action of two heterogeneous processes, owing to the properties and manifestation of additional effects, is greater than the result of a simple arithmetic sum thereof. The scientific apparatus of synergetics is very convenient and flexible for describing many problems, characterized by unusual approaches and models that reveal the principles and regularities of the processes of nonlinear and self-organizing growth. The integrated approach applied to several cases demonstrates that, by reducing the effect of blasting as the most important factor of dynamic anthropogenic impacts, a process characterized by trigger effects is initiated. The scientific novelty lies in the paradigm change in the relationship between the different mining disciplines, justifying a fundamentally new concept of a synergy between explosive destruction and geomechanics in the challenging context of mining operations [5, 6]. The practical relevance lies in the scientific evidence for the application algorithm of the trigger effect in mining operations, which is expected to significantly improve the safety of mining operations in the development of mineral resources [7, 8].

Examining as a research problem the synergies between explosive destruction and geomechanics in the challenging conditions of mining operations will contribute to improving the safety of mining operations in the development of mineral resources. The individual sections of this paper are logically interrelated and supported by references to existing literature and research.

5 Conclusion

1. Industrial activity triggering various natural phenomena, including those fraught with undesired consequences, can and should be monitored within the scope of the existing research and technology capabilities of the respective industries.
2. To address environmental and safety challenges inevitably arising at the integrated mining of ore minerals, we propose the research and technology concept of synergistic interaction between the blast processes and geomechanics, having the character of trigger effect at mining the ore minerals.
3. The direct consequence of synergistic interactions are the results of experimental studies in the above three examples of blasting operations in various development systems. Their results, within the scope of the article, exceed the standard achievements known in these cases due to synergistic interaction, including due to the trigger effect of provoking a rock bump or coal outburst by the impact of an explosion.
4. The concept is based on the integrated approach aimed at geomechanical provisioning of the safe mining of the ore minerals, ensured by reduction of the blasting impact as the most dangerous factor of dynamic anthropogenic influence.
5. The efficiency of the proposed concept usage is considered in the context of several mining operations.
6. For the first time ever in the mining science and practice, the trigger problem was formulated, the possibilities and ways of solving the problem at mining the ore minerals are shown, which testifies to the novelty and practical relevance of the research results.

References

1. Viktorov, S.D., Zakharov, V.N., Zakalinsky, V.M.: Reducing the seismic impact of large-scale blasting in an open-pit mine on the stability of the rock mass and underground structures in the combined mining coal minerals. J. Min. **12**, 59–64 (2016)
2. Viktorov, S.D., Zakalinsky, V.M., Osokin, A.A.: Effective blasting preparation in the mining bedded ore minerals. Bull. Russ. Acad. Sci. **85**(2), 138–145 (2015)
3. Meltsas, V.Y., Portnyagina, G.F., Soloviev, V.P.: Numerical simulation of the passage of shock waves through the screening grids. VANT (3), 26–31 (1993)
4. Paramonov, G.P., Mysin, A.V., Kovalevskiy, V.N.: Predicting the shotpile of blasted rock massat a granite deposit. Int. J. Mech. Eng. Tech. **11**(9), 1926–1935 (2018)
5. Viktorov, S.D., Eremenko, A.A., Zakalinsky, V.M., Mashukov, I.V.: Large-scale blasting at the hazardous ore minerals in Siberia, p. 212. Nauka, Novosibirsk (2005)
6. Viktorov, S.D., Galchenko, Yu.P., Zakalinsky, V.M., Rubtsov, S.K.: Rock breakage by contiguous charges. In: Trubetskoy, K.N., (eds.) Acad., p. 276. Nauchtekhlitizdat, Moscow (2006)
7. Eremenko, A.A.: Improvements to the drilling and blasting technology at the iron ore deposits in Western Siberia, p. 192. Nauka, Novosibirsk (2013)

8. Shipovskii, I.E.: Brittle rock fracture calculations using the meshless method. Bull. Natl. Min. Univ. Dnepropetrovsk **145**(1), 76–82 (2015)
9. Sastry, V.R., Chandra, G.R., Adithya, N., Saiprasad, S.A.: Application of high-speed videography in assessing the performance of blasts. Int. J. Geol. Geotech. Eng. **1**(2), 19–33 (2015)

Methane Generation During Coal Failure

Valery Zakharov and Olga Malinnikova

Abstract

The phenomenon of increased gas release in coal and gas outbursts has been known for a long time, while no common opinions on the causes of this phenomenon exists yet. An abrupt change in the stress state of coal with high gas content during face advance launches a chain of processes which can result in avalanche failure of coal in the form of an outburst. At lateral stress drops, rock mass becomes over-saturated with elastic compression energy, due to decreased coal strength, and with energy of expanding gas, quantity of which increases at the expense of methane desorption in opening cracks and micropores. The experimental research demonstrates that interatomic bonds break at extensive fragmentation of coal down to fine fractions. Coal loses many aliphatic CH_3 groups. The detached radicals i.e. CH_3 groups are chemically active and can together with never less active atomic hydrogen also detached from coal molecule fringes generate methane. Methane generation in plastic failure of coal takes place under rather high stresses, when the minor principal stress is not less than 5 MPa and major principal stress is at least three times higher. The quantity of methane generation is governed by the conditions of coal failure.

Keywords

Coal seam · Sudden outburst · Generation of methane · Energy content of coal failure

V. Zakharov · O. Malinnikova (✉)
Institute of Comprehensive Exploitation of Mineral Resources, Russian Academy of Sciences, Kryukovsky tup., 4, 111020 Moscow, Russia
e-mail: olga_malinnikova@mail.ru

1   Introduction

The scope of methane generation in process of an outburst was spotlighted by Myuller R.L. for the first time ever [1]. According to his estimates, it is possible to obtain a quite substantial amount of methane emission of up to 58 m^3/t, which is generated from detached radicals and hydrogen atoms from coal fringes i.e. the aliphatic portion of coal structure at approximately 30 kcal/mole of energy activation. The author emphasizes that coal with branched subjacent fringes is the most outburst-hazardous since the denser fringe is less stable. Gaseous molecular methane is generated at fringe discharge. This process is thermodynamically proven and occurs more intensively in coal with thicker fringes.

Discussions on energy generation, methane and coal bonding as well as increased gas releases during outbursts have been arising on several occasions. Several researchers have gradually inclined towards assuming the mechanochemical nature of increased gas releases under sudden outbursts [2, 3] and even tend to believe that "abrupt and regular methane releases in the course of coal mining possess a uniform mechanochemical nature and are not the consequence of emission of "ready-made" methane that is accumulated in adsorption volume of inorganic coal mass throughout geological history of coal seams" [4].

Research on increased gas release during outbursts has been done less often in recent years [5] and, probably, due to closure of a number of outburst-hazardous coal mines. However, the problems remain relevant in Ukraine [6, 7]. Furthermore, China publishes more and more studies on sudden outbursts and involvement of methane in these outburst [8–10].

2   Experimental Research

We have established the phenomenon of methane generation in physical simulation of coal failure conditions in a stress concentration zone of near-wellbore area of coal seam.

The physical simulation machine allowed triaxial compression of coal samples at varied ratios of principal stresses $\sigma_1 > \sigma_2 = \sigma_3$ and gas pressure P up to 5 MPa, which was maintained in the course of the experiment [11]. The experiment involved automatic recording of axial stress–axial strain curve ($\sigma_1-\varepsilon_1$), lateral stress $\sigma_2 = \sigma_3$, gas pressure P and coal sample temperature variation ΔT (Fig. 1). The lateral stress was constant while the axial stress σ_1 increased till failure of the sample in the course of the experiment.

At the increase of axial stress σ_1, the temperature in the coal sample starts rising noticeably at values $\sigma_1 = 0.7-0.8$ of the ultimate stress limit σ_{1max}, which approximately conforms with the transition from elastic deformation to elastoplastic deformation and initiation of partial crack formation. The temperature continues to increase also in the post-limiting deformation domain in combination with loss of supporting capacity of the sample.
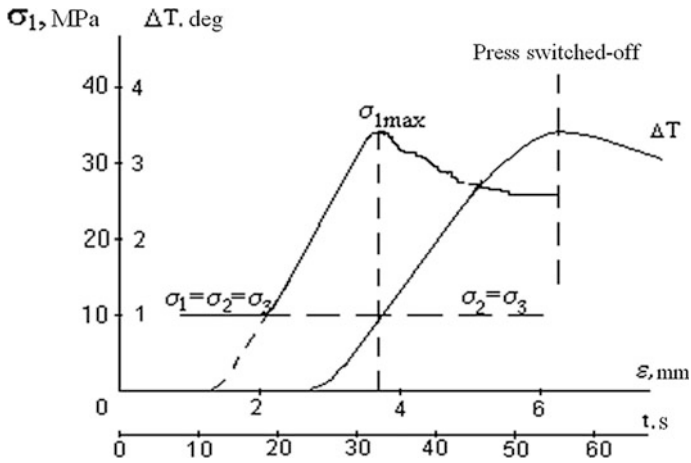
Fig. 1 Dependency diagram of the experiment (stress–strain–temperature diagram in triaxial compression)

In terms of the area bounded by the stress compression variation curve σ_1 in the range of ε_1–ε_2, it is possible to estimate the mechanical energy taken from the press by the sample. The calculations demonstrate that the heat content Q sometimes exceeds the mechanical energy W by 2–3 times, taken from the press by the sample in the majority of the conducted experiments (Fig. 2).

Gus saturation: ○ - methane, ■ – helium
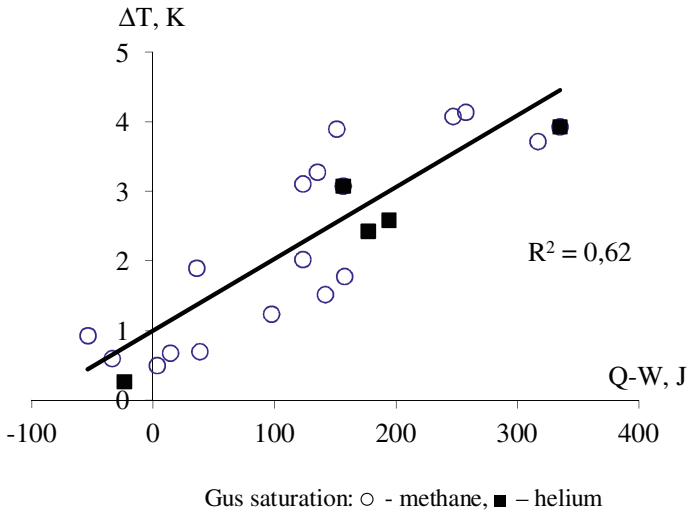
Fig. 2 Variation in temperature as a function of difference of energy spent for heating the sample and taken from the press
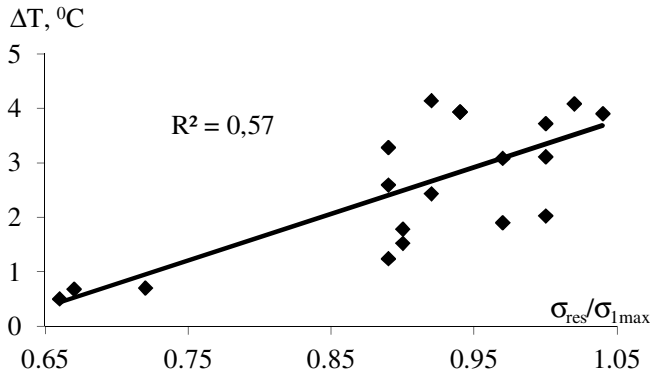
Fig. 3 Variation in temperature as a function of failure brittleness

In brittle coal failure, which is often observed at low values of lateral compression, the sample temperature rise is insignificant and the value of the heat Q approaches the values of the mechanical energy W obtained by the sample from the press. The higher the ratio of the residual strength of the sample in the post-limiting deformation domain to its strength $\sigma_{res}/\sigma_{1max}$, the more ductile coal failure process. The temperature rises strongly and the heat Q exceeds the value of mechanical energy W by a large number (Fig. 3).

The process of coal failure becomes ductile when $\sigma_3 > 5-7$. The failure is brittle at lower values of the lateral stress, $\sigma_{res}/\sigma_{1max} < 0.75$ and $Q \leq W$.

Anomalous heating of coal samples in the experiments can only be explained by assuming that additional sorption of methane takes place in coal from the beginning of crack formation process ($0.7-0.8\ \sigma_{1max}$) since neither of any possible processes in coal under such conditions can lead to such a substantial change in coal temperature except for sorption.

The series of tests on coal samples, saturated with helium under the same experimental conditions, demonstrate the same temperature variation (Fig. 2). Inasmuch as helium is not adsorbed by coal and has no ability to influence the change in coal temperature, it is evident that desorption of methane takes place, which is generated in the course of coal failure. According to our assessment, the anomalous rise in temperature of coal in the experiments is explained by the fact that up to 1.28 cm^3/g of methane is generated and adsorbed in coal failure [12].

3 Gas Release During Outbursts

Specific gas release during outbursts i.e. volume of released gas in gas outburst, taken relative to ton of extruded coal in Kuzbass mines ranges between 30 and 550 m^3/t and in average 89.7 m^3/t i.e. multiple times exceeds the gas content of

coal seams. Specific gas release during outburst is even higher in Vorkuta mines. For example, 49 outbursts released 124.3 m^3/t of gas in Dvoinoi coal seam of Mine no. 1 Kapitalnaya, whereas 99 outbursts released 100.2 m^3/t of gas in Troinoi coal seam of Mine no. 5, which exceeds the gas content of the seams by several times.

Several researchers stated that increased gas release during outbursts was conditioned by degassing of coal seams enclosing an underground opening. Thus, we collected the data on extruded coal volumes and released methane during outbursts in mines of such coal basins as Donbass, Kuzbass, Pechora and Karaganda [13]. The data were processed on the hypothesis that if gas release takes place mostly from extruded coal, then the released gas volume Q should be proportional to the extruded coal volume S i.e. $Q = a \cdot S + b$; where a and b are coefficients. If gas release takes place mostly from rock mass surrounding the outburst cavity, the released gas should be proportional to the surface area of the cavity i.e. the extruded coal volume in the power of 2/3 or $Q = c \cdot S^{(2/3)} + d$; where c and d are coefficients.

The regression analysis demonstrates that the equation $Q = c \cdot S^{(2/3)} + d$ has no physical significance since the coefficient d is negative and high-modulus in all samplings. Similarly, taking into account both processes at the same time, the equation of multiple linear regression $Q = f \cdot S + g \cdot S^{2/3} + k$, where f, g and k are numerical coefficients, is contradictory to physical sense as well since g is negative i.e. it has been established that gas release takes place from broken and extruded coal during outburst.

4 Physicochemical Research

The research implemented by the high-resolution C^{13} nuclear magnetic resonance method demonstrates that the ratio of carbon atoms in sp^2 (aromatic) and sp^3 (aliphatic) hybridization as well as the number of CH_2 and CH_3 groups is different for coal from outburst-non-hazardous, outburst-hazardous zones and in extruded coal [14]. For instance, the content of CH_3 groups in coal samples of outburst-hazardous zones is considerably higher than the content of CH_3 groups of outburst-non-hazardous zones in the same coal seams. This means that coal in outburst-hazardous zones possesses more extensive fringes as was supposed by Myuller [1]. A decrease in the number of CH_3 groups in extruded coal samples takes place down to a level characterizing the outburst-non-hazardous zone and even below the level.

The petrographic analysis of coal samples also demonstrates that coal from outburst-hazardous zone initially contains much more aliphatic components than coal from outburst-non-hazardous seam zone. During outburst, weaker bonds rupture, mostly in aliphatic components, and coal fines, which are more disintegrated coal, become higher metamorphosed [14].

The infrared spectra analysis of coal allowed to obtain quantitative characteristics of structural fragments in coal organic mass, to estimate the volume of methane generation at sudden outbursts and prove the fact that the number of CH_3

groups lessens. The carbon amount in aromatic CH_{ar} and methyl CH_3 groups was determined by means of IR spectra, and it was established that CH_{ar}/CH_3 ratio was much higher for coal from outburst-hazardous seams and geological disturbance zones than in coal from outburst-non-hazardous seams. The ratio increases noticeably in extruded coal samples from outburst.

Supposing that aromatic rings are not ruptured and methyl groups can get detached under outburst, it is possible to estimate the quantity of ruptured bonds. Methane volume Q could be generated if each methyl group detached from coal would join with atomic hydrogen and join methane molecule with the atomic hydrogen. The results of such assessment and estimation of the methane volume Q demonstrate that 51 m^3 of methane per 1 ton of coal can be formed additionally during an outburst in Mazur coal seam of Yunkom mine. On the other hand, 36.7 m3 of methane per 1 ton of coal can be formed during an outburst in Aleksandrovsky coal seam of Kondratevka mine. The carbon content in structure groups decreased from 3 to 0.1% for methyl groups and increased from 11.2 to 14.1% for aromatic groups during outburst in the first case. The carbon content dropped from 2 to 0.1% in methyl groups and from 11.6 to 5.3% in aromatic groups under outburst in the second case.

5 Assessment of Energy Consumption in Methane Generation

According to the research, microstructural bonds rupture in the molecules of coal during outburst and a considerable part of aliphatic CH_3 groups is lost [15] whereas the strongly bonded methyl groups remain (0.1% in terms of carbon from C^{daf}). The detached structural fragments are chemically active radicals, i.e. CH_3 groups and atomic hydrogen, and can generate methane. This assumption is based on the fact that a large amount of atomic hydrogen should be generated during detachment of fragments from coal molecule since there is a lot of hydrogen as any change in coal fringes ends up with hydrogen and hydrogen has the weakest bond with coal molecule at the bonding energy from 8 to 40 kJ/mole. The bonding energy in methyl groups depends on the pattern of groups in coal and can range both as 240 −320 kJ/mole [16] or 280 kJ/mole on average and as 297−385 kJ/mole in case of much closer bonding with coal [17, 18]. Thus, the detachment of basic components for methane generation consumes from 248−362 to 425 kJ/mole of energy.

Ionization energy of methane is 426 kJ/mole, and the same amount of energy is released in methane generation from methyl groups and hydrogen. Let us assume that each methyl group, which is detached from coal, joins with hydrogen atom and forms methane molecule. Then, the methyl groups, which are more weakly bonded to coal, require 637.5 MJ/t of energy to detach the methyl groups and hydrogen from coal and to form 51 m^3 of methane. This energy figure is smaller than the energy released when methyl groups join with methane molecule. Thus, the process of methane generation is energetically favourable and even can produce extra

energy (heat). It is apparent that this assumption is unrealistic since some methyl groups can form heavier hydrocarbons or enter into other compounds. However, it is energetically favourable for free methyl groups to take the weakest-bonded hydrogen from coal to generate methane.

Apparently, the process of methane generation can take place at minimum energy consumption as long as sufficient energy is available in the coal failure zone to detach methyl groups from coal.

According to Myuller's estimates, detachment of methyl groups from coal and subsequent methane generation requires about 30 kJ/mole of energy, which is equivalent to 1.3 MJ/m$^3_{gas}$ [1]. The comparison of this value with activation energy of different bonding types between methane molecule and coal from publication [19] demonstrates that the value is barely 1.5 times higher than the desorption activation energy of 17–21 kJ/mole and significantly lower than the energy of 170–200 kJ/mole, which is required to liberate methane from dissolved state, and the energy of 300–400 kJ/mole, particularly required to liberate from gaseous crystalline state.

Since methane generation process in coal failure requires activation energy, the process becomes particularly evident under coal and gas outbursts i.e. when rock mass releases large amount of accumulated energy.

Figure 4 illustrates the relationship between energy content of coal failure A, determined from the experimental $\sigma_1 - \varepsilon_1$ curves for Livensky coal seam in Donetsk–Makeevka region in Donbass, and the effective minor principal stress σ_3', taking into account the methane pressure of saturate coal, σ_3' $= \sigma_3$—P, where P is the pressure of methane.
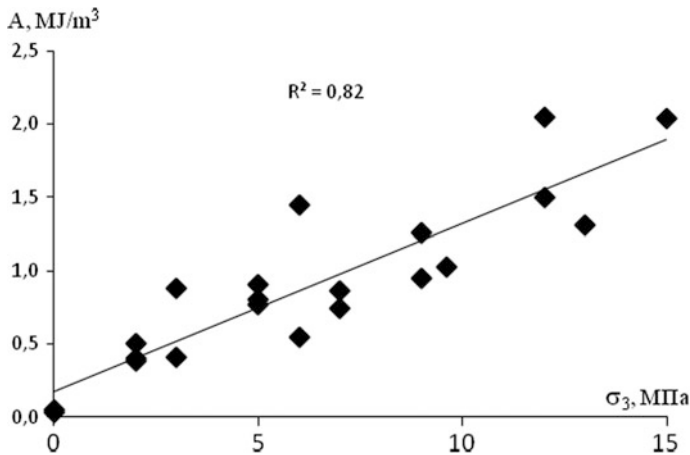
Fig. 4 Energy content of coal failure as a function of effective lateral stress

At a considerably high value of lateral compression $\sigma_3 \geq 10$ MPa, plastic failure of high strength coal takes place and the energy intensity ranges as 1.5 -2 MJ/m^3. However, at decrease in the lateral compression, a sharp decrease in strength and energy content of failure is observed depending on the changes.

A similar process of decrease in energy content of coal failure in the near-wellbore zone of coal seam takes place at the moment of the face advance and decrease in the minor principal stress σ_3, which acts from the face side in mines. At sharp decrease in lateral stress e.g. in drilling-and-blasting, the change in minor principal stress while propagating in rock mass at a sound speed, decreases in a certain volume of the face area. Simultaneously, the energy content of coal failure slumps, for instance, from 2.04 MJ/m^3 at $\sigma_3 = 15$ MPa to 0.38 MJ/m^3 at $\sigma_3 = 3$ MPa (Fig. 4), and coal becomes over-saturated with elastic compression energy, which is 1.66 MJ/m$^3_{coa}$ At rapid change in stress, the "extra" energy fails to be dissipated by rock mass and an intensive fragmentation takes place in rock mass down to fine fractions along with interatomic rupture of bonds in coal. In such situation, the surplus of elastic energy is commensurable with energy generation of approximately 1.2 m^3 of methane from 1 m^3 of coal, on the hypothesis that activation requires 300 kJ/mole i.e. for methyl groups having stronger bonds with coal and which is quite sufficient for launching methane generation process.

6   Conclusions

During plastic failure of coal i.e. in shear failure, mechanochemical processes of methane generation take place under the conditions of high stresses at minor principal stress $\sigma_3 > 5-7$ MPa. The volume of generated methane is governed by coal failure conditions. Methane generation is most intensive during sudden coal and gas outbursts.

Bonds in aliphatic portion of coal structure rupture under sudden outburst and even a large quantity of weakly bonded methyl groups detach and they can generate methane by joining with hydrogen.

The energy content of methane generation process from detached methyl groups and hydrogen is very small. Moreover, the more branched aliphatic structure coal possesses, the less energy is required to activate methane generation and more methane can be generated.

At sharp drop in minor principal stress, the strength of coal i.e. energy content of failure drops. Rock mass in the near-wellbore area of coal seam becomes over-saturated with elastic compression energy and an instant fragmentation takes place in rock mass down to fine fractions along with rupture of bonds in the aliphatic part of coal molecules and induces methane generation.

The research into conditions of methane generation is expected to be applied in forecasting gas-dynamic phenomena and can be an instrument in developing mechanochemical methods of methane production during coal failure.

References

1. Myuller, R.L.: Conceivable part of chemical processes in coal and gas outbursts in mines. In: Theory of Coal and Gas Outbursts: Proceedings of All-Union Seminar, 156–172. IGD, Moscow (1959). (in Russian)
2. Muchnik, S.V.: The role of chemisorption of methane on fossil coal. J. Min. Sci. **11**(5), 599–600 (1975)
3. Frolkov, G.D., Malova, G.V., Frantsuzov, S.A., Frolkov, A.G.: Mechanochemical concept of outburst hazard in coal seams. Ugol'. **7**, 60–64 (1998). (in Russian)
4. Frolkov, G.D., Frolkov, A.G.: Mechanochemical concept of outburst hazard in coal seams. Ugol' **2**, 18–22 (2005). (in Russian)
5. Menzhulin, M.G., Montikov, A.V., Vasil'ev, S.V.: Physical processes of methane generation in disintegration of coal. Zapiski Gornogo instituta **207**, 222–225 (2014). (in Russian)
6. Skipochka, S.I., Palamarchuk, T.A., Omel'chenko, S.A., Khmelenko, O.V.: Methane generation and metamorphism of coal. Geotekhnichna mekhanika **115**, 15–22 (2014). (in Russian)
7. Bulat, A.F., Skipochka, S.I., Palamarchuk, T.A., Antsiferov, V.A.: Methane Generation in Coal Seams. Lira LTD, Dneptopetrovsk (2010). (in Russian)
8. Gao, B., Wang, Z., Li, H., Su, C.: Experimental study on the effect of outburst-proneness of coal by gas pressure. J. China Coal Soc. **43**(1), 140–148 (2018)
9. Zhang, G., Ouyang, Z., Qi, Q., Li, H., Deng, Z., Jiang, J.: Experimental research on the influence of gas on coal burst tendency. J. China Coal Soc. **42**(12), 3159–3165 (2017)
10. Song, Z.-L., Han, P.-B., Li, W.-P., Yin, G.-Z., Li, M.-H., Kang, X.-T.: Impact of energy dissipation of coal samples with rockburst tendency from gas in its failure process. J. China Coal Soc. **40**(4), 843–849 (2015)
11. Feit, G.N.: Limiting states and failure of outburst-hazardous coalprediction and prevention of outbursts in development heading in outburst-hazardous seams. Skochinsky Inst. Min. Trans. **252**, 104–113 (1986). (in Russian)
12. Malinnikova, O.N.: Estimation of extra methane quantity generated in initiation of outburst source in coal. Methane: Special Issue. GIAB, **4**, 138–145 (2008). (in Russian)
13. Malinnikova, O.N.: "Extra" methane generation in coal seam under anthropogenic effect. In: Fundamental Problems of Geoenvironment Formation under Industrial Impact: Proceedings of All-Russian Conference with Foreign Participation, vol. II, Geotechnology, 185–190. IGD SO RAN, Novosibirsk (2010). (in Russian)
14. Malinnikova, O.N., Ulyanova, E.V., Dolgova, M.O., Zverev, I.V.: Transformation of fossil coal microstructure under coal and gas outbursts. Gornyi Zhurnal **5**, 27–32 (2017). (in Russian)
15. Yanovskaya, M.F., Bryzgalova, N.I., Khrenkova, T.M., Khrustalev, YuA, Kirda, V.S.: Chemical structural of coal in outburst-hazardous and nonhazardous seams. Khimiya Tverdogo Topliva **1**, 20–22 (1986). (in Russian)
16. Tager, A.A.: Physicochemistry of Polymers. Khimia, Moscow (1986). (in Russian)

17. Bobin, V.A.: Sorption Processes in Natural Coal. IPKON RAN, Moscow (1987). (in Russian)
18. New Handbook for Chemist and Process Engineer: Basic Properties of Inorganic, Organic and Element-Organic Compounds. Mir Semya, Saint-Petersburg (2002). (in Russian)
19. Vasyuchkov, Yu.F.: Procedure to determine parameters of hydraulic fracturing for gas drainage of coal seam. In: Special Issue: Methane. GIAB. Collection of Scientific Papers of Miner's Week-2006 Symposium, pp. 257–267. MGGU, Moscow (2006). (in Russian)

About Order of Comprehensive Solving the Seismic and Pre-splitting Issues for Drill-and-Blastin Open-Pits

Sergey Zharikov and Vyacheslav Kutuev

Abstract

At present, the scientific and technical literature does not cover enough the issues relating to the drill-and-blast works in the border zone of open-pit mines and directly to the pre-splitting works. Although, there is a relentless demand of operating mining enterprises for the solution of related tasks. Basing on the competence of implementing the special technology of the drill-and-blast works at various mining enterprises, we have stated the basic provisions to characterize the concept of implementation of technological solutions at pre-splitting. The paper describes the sequence of fulfillment and control of the drill-and-blast works in the border zone, i.e. study of the blast impact on the aquifer rock mass; establishment of the patterns of wave processes in the rock mass; description of the interaction of the contour ribbon charges, depending on the strength characteristics of the rock mass; pilot tests of the pre-splitting; description of the phasing approach of technological blasts in the protected area; as well as development of the criteria for evaluation of the drill-and-blast works efficiency. The paper has proposed the theme for discussion on standardization of the pre-splitting works.

S. Zharikov (✉) · V. Kutuev (✉)
Institute of Mining, Ural Branch of RAS, Mamina-Sibiryaka str. 58, 620075 Yekaterinburg, Russia
e-mail: 333vista@mail.ru

V. Kutuev
e-mail: Slavikl988@mail.ru

1   Introduction

An increase in the angle of the open-pit side slope leads to the reduction in the amount of cutback and the improvement in the economic mining efficiency. However, this increases the risk of collapse of sloping structures in the open-pit mine as a result of geodynamic movements associated with the rock pressure and the impact of short-term impulse loads caused by blast works. An estimate of the steady state of sloping structure at a certain angle is based on measurements of the rock mass movement in one or another direction within sufficiently long observation periods [1–4], while short-period deformations leading to local interblock movements in validating the stable angles are not taken into account. In this regard, insufficiently smooth drill-and-blast works in the vicinity of sloping structures can cause a violation of their stability and lead to catastrophic landslide developments.

# 2   Materials and Methods of Research

Recently, mining enterprises have shown a special interest in the pre-splitting works at approaching the drill-and-blast works to the limit contour of the open-pit mine. Firstly, it is obvious that even an increase in the D&B costs in the border zone with an increase in the quality of execution and the corresponding control leads to a better safety of mining operations, the preservation of stable state of slopes, and, consequently, the increased economical efficiency of the mining as a whole. For example, liquidation of the landslide consequences requires partial or full stop of the mining operations, removal of the damage caused and in some cases is associated with death of people. That is why improvement of the security at a hazardous production facility is not just the issue of costs, but a significant contribution to the development of a business, which directly influences the economic mining efficiency in future operation periods.

Currently, two opposite views on the issue of regulating the drill-and-blast works, concerning the setting of the benches in the limit position exist. Both of them have their supporters stating serious arguments, but we will not go into unnecessary details within the framework of this paper. Instead, it is worth to focus on what is actually happening in the mining industry. In commercial sphere everything is solved lightning-fast. If a business owner has the possibility to reduce its costs by reduction of the amount of cutback, he will use it immediately. Given the successful implementation of similar solutions at other market participants, he will accelerate the solution implementation at his business without paying attention to mining, geological and technical conditions of the resource development and the personnel qualification. The results of rapid changes in the mining parameters without organizational and cultural modification of the production departments will be catastrophic landslide phenomena that occur suddenly and, as a rule, unexpectedly even for the surveying service. Economic benefit in this case begins to depend very significantly on whether the open-pit side falls or not. Someone will

think that it will fall, and someone else will think that it will not, but when it comes to safety and the lives of miners, it is always necessary to consider the adverse outcome. An engineer should not be guided by the hope that it will not fall, but must provide for the safe working conditions, in other words, the miners will be safe even if the open-pit side falls. From this point, the regulation of pre-splitting works appears to be the right way to improve the safety of mining operations. In this regard, the world practice points out [5]. A detailed review of this work is published in [6]. The review is generally positive. The paper prepared by the Australian researchers are a technical guide for training and development of engineers, allowing them to have a coherent picture for the preparation and decision-making at solving geomecanical tasks at the deep open-pit mining. The said papers are worth taking into account at the design of national open-pit sides, even for the reason that we yet to have our own papers in this knowledge domain. However, major developments for solving this problem, such as work out of federal rules and regulations to ensure the stability of the open-pit sides and open cuts, will fill up this blank space. At the same time, it should be noted that geomechanical observations and predictive calculations in accordance with modern progressive measurement methods and the analysis thereof, which is often promptly introduced at many businesses, will not detect in most cases the development of geodynamic movements as a consequence of the impact on the rock mass of short-period impulse loads caused by blast works, until the cutter break formation becomes obvious. In this regard, the solution of geomechanical problems in the design of the mine sides should be closely connected with the drill-and-blast works, not only in the formation of the slope contour, but also in the approach of technological blasts to this contour. Taking into account that these areas of knowledge use different methods, and deformation processes are considered in different periods, the organizational combination of geomechanical and blasting engineers in the framework of regulating the pre-splitting works is quite a difficult task, which in principle cannot be solved as a result of their parallel work. Such works can only be organized sequentially. In the beginning, the geomechanical evaluation of the rock mass state with the determination of stable angles is carried out, then the blast dynamics is studied, and then the special technology for drill-and-blast works on the limit contour of the open-pit mine is developed and implemented. The procedure for the organization of the drill-and-blast works during the pre-splitting works is described below. The specified sequence has been tested during the research at the mining enterprises of Russia and Kazakhstan.

The initial data for the final stage of the non-working bench, as indicated above, are the results of the analysis of the geomechanical situation, or the expert opinion on the state of the sloping structures.

The introduction of the technology for the pre-splitting is carried out in two stages. The first stage includes study of the seismic state of the rock mass during the blast works. Researchers do the calculations and compare the calculated results and the actual measurements obtained at seismic of blasts, which should be at least 10. Figure 1 shows an example of comparison of the measured vibration velocity with the acceptable seismic resistance at an open pit. The difference of the values of
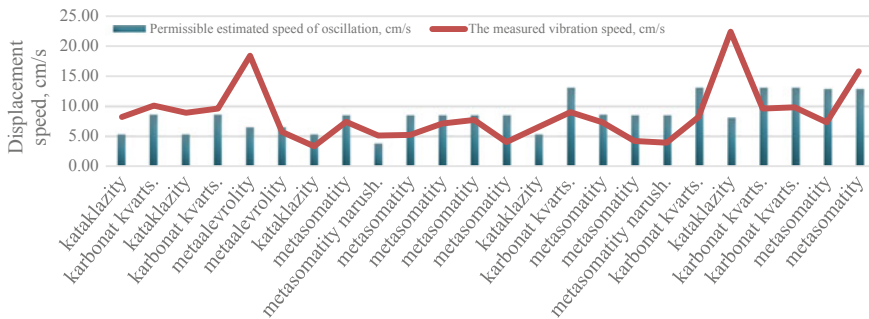
Fig. 1 Comparison of the measured velocity fluctuations with acceptable seismic resistance at one of the quarries

permissible velocities for quartz carbonate rocks is due to their different grit and the corresponding strength in different parts of the pit.

The methods of complex research of seismic stability of the rock mass are presented in the publications [7–23]. The shielding parameters are determined by the rock complexes depending on the applied parameters of the charges and the diameters of the boreholes of the contour ribbons (Figs. 2 and 3 and expressions (1)–(4)).

$$P = \frac{r^2_{\text{charge}}}{2\,r^2_{\text{hole}}}\,P_{\text{d}}, \text{ MPa}, \tag{1}$$

where P—pressure on the borehole wall, MPa; r_{charge}—charge radius, m;
  r_{hole}—borehole radius, m; P_{d}—detonation wave pressure, MPa.
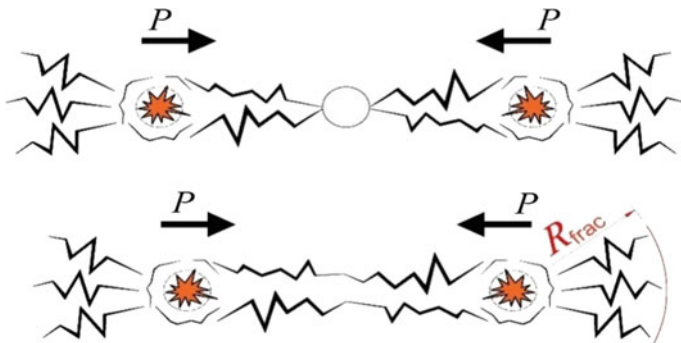
Fig. 2 Comparative analysis of pressures in determining the rational parameters of trim blasting: P—pressure on the borehole wall, MPa; Rfrac—fracture radius, m

Rock	Tensile strength in array, MPa	Dynamic limit strength, MPa	Radius of crack formation, m			
			Ammonite 6GW			
			D_{hole}/d_{charge}			
			215/60	246/60	215/90	246/90
Cataclysms carbon	0,36	0,47	2,3	2,2	4,0	3,8
Carbon carbonate quartz rocks	0,56	0,73	1,7	1,7	3,0	2,8
Carbon metasiltstones	0,42	0,54	2,1	2,0	3,6	3,5
Metasomatites	0,53	0,69	1,8	1,7	3,1	3,0
Metasomatites intensely disturbed	0,24	0,31	3,1	2,9	5,3	5,0

	Distance from charge, m	215/60	246/60	215/90	246/90
	1	1,66	1,56	3,75	3,50
	2	0,59	0,55	1,32	1,24
	3	0,32	0,30	0,72	0,67
The pressure from the blast contour of the charge at a distance, MPa	4	0,21	0,19	0,47	0,44
	5	0,15	0,14	0,33	0,31
	6	0,11	0,11	0,25	0,24
	7	0,09	0,08	0,20	0,19
	8	0,07	0,07	0,17	0,15

Fig. 3 Fragment of the scheme for determining the distances between the boreholes of the pre-split blast row according to the table of values obtained in accordance with the expressions presented in (1)–(4)

$$P_d = \frac{\rho_{exp} D^2}{1+n}, \text{ MPa}, \tag{2}$$

where P_d—pressure of detonation wave, MPa; ρ_{exp}—density of explosives, kg/m³; D—speed of detonation, m/s; n—indicator of expansion of blast products.

$$R_{frac} = r_{hole} \sqrt[3]{(P/\sigma_{dyn})^2}, \text{ m}, \tag{3}$$

where R_{frac}—radius of fracture, m; r_{hole}—radius of borehole, m; P—pressure on the borehole wall, MPa; σ_{dyn}—permissible dynamic strength of rocks, MPa.

$$P_R = P \left(\frac{r_{hole}}{R}\right)^{1,5}, \text{ MPa}, \tag{4}$$

where P_R—pressure in the rock mass from blast of cylindrical charge at a distance, MPa; P—pressure on the borehole wall, MPa; r_{hole}—radius of the borehole, m; R—distance from the charge blast, m.

Based on the results of seismic stability studies of rocks, the special technology is developed for the drill-and-blast works on the limit contour of the open-pit outline. The completion of the first stage is the development of a program of pilot testing methods of drill-and-blast works on the limit contour of the open-pit mine.

At the second stage, the program is implemented and, according to the results obtained, the most suitable solutions are selected. The program includes: stages of implementation, list of necessary resources, procedure of control. After the implementation of the program and pilot tests, the results are analyzed and an internal normative document of the enterprise is drawn up for the drill-and-blast works on the limit contour of the open-pit mine (technological regulations). The completion of the second stage of the work is the approval of the technological regulations for the drill-and-blast works on the limit contour of the open-pit mine.

The main competitive advantage of this development is that it is especially efficient at increased intensity of mining operations. Industrial safety is also improved owing to the regulation of the works at the limit contours of the open-pit mine. The application area includes the open-pit mines with cyclical mining technology for mining the steep deposits of mineral resources.

Within the framework of such research and development, seismic actions of blasts are being investigated to establish, on the one hand, the correspondence between the actual vibrations and the calculated permissible vibrations determined for the investigated soils on the basis of geological documentation. On the other hand, according to the deformation phenomena from technological blasts, the properties of soils are approximately established and the approximate zones are determined for development of: cracks [24, 25], interblock movements and residual deformations [26]. The specified information serves as a criterion for the selection of various parameters for the drill-and-blast works included in the program of pilot tests. Also, depending on the properties of the soils and the properties of the used explosives, the parameters of the charges of the pre-splits of slot raises are determined during the shielding [27]. This research allows you to have the most complete picture of the propagation of wave processes [28, 29] in specific rocks and, accordingly, to manage them rationally. First of all, this concerns the drill-and-blast works at the pre-splitting works, as well as at the subsequent technological blasts.

As shown above, a scientifically based approach to the drill-and-blast works is no less, if not more complicated, than solving the geomechanical problems because the blasts complete the formation of non-working benches and, hence, are the most responsible step for maintaining the rock mass stability.

As the bottom line we can distinguish the main provisions of the introduction of the technology of pre-splitting with the use of drill-and-blast works:

Geomechanical studies in the open-pit mine should precede the study of the dynamics of the impact of blasts on the rock mass;

Control of quality performance of the drill-and-blast works should be ensured and the work of the services of the enterprise in the border zone is possible by regulation of works (in case of an accident it will be possible to quickly determine who made the mistake);

Technological regulations for pre-splitting works are recommended to implement as early as possible, at the initial stages of mining (this will allow to correct the mistakes in time and prepare the blast personnel for responsible work on the lower horizons).

3 Conclusion

Experience shows that neglecting the control of the seismic impact of technological explosions usually leads to exceeding the maximum permissible fluctuations on the criterion of seismic resistance. Even under the condition of high-quality shielding of the explosion, excessive seismics can have a significant destructive impact on the massif and, accordingly, on the stability of the slope structures.

While carrying out the drilling and blasting operations in the surrounding zone of the open pit, the following tasks should be solved jointly. To determinate the parameters of contour charges, the distance between the wells and the order of formation of contour tapes in order to create screens in the form of cut-off slots. To establish the value of the marginal zone, in which the dimensions of the excavation units of drilling and blasting parameters, providing the minimum seismic effect, are to define separately. To limit the parameters of the technological explosions when approaching the marginal zone (mostly by choosing schemes of charge initiation).

Experience shows that careful management of drill-and-blast works, which do not disturb the stable state of the array, is possible when regulation in the framework of joint solving the seismic questions and the pre-splitting tasks are being held on. The presented approach is being implemented at a number of mining enterprises in the form of an internal complex instruction (technological regulations for drilling and blasting operations on the limit contour zone of the open pit).

References

1. Sashurin, A., Balek, A., Panzhin, A., Usanov, S.: Innovative technology for the diagnostics of geodynamic activity of the geological environment and assessment of safety of objects of subsurface use. Min. J. **12**, 16–20 (2017)
2. Panzhin, A., Panzhina, N.: Satellite geodesy-aided geodynamic monitoring in mineral mining in the Urals. J. Min. Sci. **48**(6), 982–989 (2012)
3. Panzhin, A.: Space-time geodynamic monitoring at the objects of subsoil use. Min. J. **1**, 39–43 (2012)
4. Sashurin, A., Bermukhambetov, V., Panzhin, A., Usanov, S., Bolikov, V.: The impact of modern geodynamic movements on the stability of open-pit mine sides. Subsoil Use Probl. **3**, 38–43 (2017)

5. Read, J., Stacey, P.: Guidelines for Open Pit Slope Design. CRC Press/Balkema, China (2009)
6. Evaluation of the Possibility of Using the "Guidelines for the Design of Open-Pit Sides" in the Design of Open Mining of Ore Deposits in Modern Russia, https://mining-media.ru/ru/article/ogr/. Accessed 25 Jan 2018
7. Bersenev, G., Senin, L., Menshikov, P.: Blasting in confined spaces. Explos. Technol. **97**(54), 56–66 (2007)
8. Menshikov, P.: Impact of the shock wave on buildings and structures on the earth's surface. Explos. Technol. **97**(54), 77–82 (2007)
9. Bogatsky, V., Pergament, V.: Seismic Safety During Blasting Operations. Nedra Publishing, Moscow (1978)
10. Bogatsky, V., Friedman, A.: Protection of Engineering Structures and the Environment from the Harmful Effects of Industrial Explosions. Nedra Publishing, Moscow (1982)
11. Fadeev, A.: Crushing and Seismic Effects of the Explosion in the Open-Pit Mines. Nedra Publishing, Moscow (1972)
12. A method of providing seismic safety technology of blasting. IM MFM USSR, Sverdlovsk (1984)
13. Zharikov, S., Shemenev, V.: On the impact of blasting operations on the stability of open-pit mine boards. News of the Higher Institutions. Min. J. (2), 80–83 (2013)
14. Zharikov, S., Shemenev, V.: On the impact of blasting on the stress state of the rock mass and geodynamic phenomena. News of the Higher Institutions. Min. J. (3) 90–97 (2013)
15. Bondarenko, I., Zharikov, S., Zyryanov, I., Shemenev, V.: Blasting in Kimberlite Open Pits of Yakutia. IM UB RAS, Ekaterinburg (2017)
16. Shemenev, V., Zharikov, S.: On the state of scientific research in the field of rock destruction at the IM UB RAS. Subsoil use Probl. **4**, 30–40 (2016)
17. Zharikov, S., Shemenev, V., Kutuev, V.: Methods for clarifying the properties of rocks in the production of drilling and blasting. Sustain. Dev. Mt. T. **9**(1), 74–80 (2017)
18. Zharikov, S., Kutuev, V.: The study of the seismic effect of the explosion in the open-pit mine for the introduction of a special technology of work on the formulation of the boards in the limit position. In: Martyshko, P., Khachay, Yu. (eds.) Deep Structure, Geodynamics, Thermal Field of the Earth, Interpretation of Geophysical Fields: Conference Materials 2017, pp. 179–183. Institute of Geophysics, Urals branch of RAS, Ekaterinburg (2017)
19. Zharikov, S., Timofeev, I., Gulenkov, E., Bushkov, V.: Improvement of drilling and blasting operations on the ultimate contour of the open-pit mine. News of the Higher Institutions. Min. J. (1), 48–55 (2018)
20. Kahriman, A.: Analysis of parameters of ground vibration produced from bench blasting at a limestone quarry. Soil Dyn. Earthq. Eng. **24**(11), 887–892 (2004)
21. Ak, H., Konuk, A.: The effect of discontinuity frequency on ground vibrations produced from bench blasting: a case study. Soil Dyn. Earthq. Eng. **28**(9), 686–694 (2008)
22. Ak, H., Iphar, M., Yavuz, M., Konuk, A.: Evaluation of ground vibration effect of blasting operations in a magnesite mine. Soil Dyn. Earthq. Eng. **29**(4), 669–676 (2009)
23. Kumar, R., Choudhury, D., Bhargava, K.: Determination of blast-induced ground vibration equations for rocks using mechanical and geological properties. J. Rock Mech. Geotech. Eng. **8**(3), 341–349 (2016)
24. Chen, S., Zhao, J.: A study of UDEC modelling for blast wave transmission in jointed rock masses. Int. J. Rock Mech. Min. Sci. **35**(1), 93–99 (1998)
25. Brady, B., Hsiung, S., Chowdhury, A., Philip, J.: Verification studies on the UDEC computational model of jointed rock. In: Mechanics of Jointed and Faulted Rock, pp. 551–558. Balkema, Rotterdam (1990)
26. Knyazev, D., Zharikov, S.: The study of the seismic effect of explosions in underground mines. Explos. Technol. **112**(69), 251–261 (2014)
27. Zharikov, S., Kutuev, V.: Charge initiation schemes to ensure high-performance operation of the cycle link of the cycle-flow technology. News Ural State Min. Univ. **3**, 76–79 (2017)

28. Gui, Y., Zhao, Z., Jayasinghe, L., Zhou, H., Goh, A., Tao, M.: Blast wave induced spatial variation of ground vibration considering field geological conditions. Int. J. Rock Mech. Min. Sci. **101**, 63–68 (2018)
29. Snelling, P., Godin, L., McKinnon, S.: The role of geologic structure and stress in triggering remote seismicity in Creighton Mine, Sudbury, Canada. Int. J. Rock Mech. Min. Sci. **58**, 166–179 (2013)

Part IV
Dynamic Effects in Upper Geospheres

Analysis of the Probability Fields of Ionospheric Parameters Used for the Probabilistic Plasma-Chemical Modeling of the Lower Ionosphere

Bekker Susanna

Abstract Concentration of electrons and ions depends on spatial, seasonal and temporal variations of atmospheric parameters, such as the neutral component temperature and concentrations. Experimental data is the most reliable source of knowledge of ionospheric parameters behavior. This paper features the results of processing and analysis of the long-term atmospheric data from the AURA satellite. The probability density functions (PDFs) of temperature T and concentrations of $[N_2]$, $[O_2]$, $[H_2O]$ and $[O_3]$ were plotted and analyzed at heights in the range of 50–90 km. Dependences of probability density functions' values on latitude, season and time of day are studied. The 5-component and 8-component systems of differential equations of ionization-recombination cycle were solved, by using the input parameters obtained under different heliogeophysical conditions. The cosmic rays' ionization, NO ionization by the $L\alpha$ line, UV and X-ray ionization are taken into account to calculate the ionization rate of the ionospheric D-region. The paper features the comparison of two plasma-chemical models' results containing the electron concentrations under the calm conditions and the solar flare.

B. Susanna (✉)
Sadovsky Institute of Geospheres Dynamics RAS,
Leninskiy pr., 38b1, 119334 Moscow, Russia
e-mail: susanna.bekker@gmail.com

1 Introduction

Nowadays there are many theoretical estimates and experimental data on the processes occurring in the ionospheric plasma and on the spatial distribution of components' concentrations. However, the accuracy of predicting the ionospheric parameters' dynamics is still low under certain heliogeophysical conditions.

Long-term monitoring of radio physical characteristics of the VLF signals shows the significant amplitude and phase variations even under the calm heliogeophysical conditions. Such variations are related to a continuous change of ionospheric parameters.

The probabilistic plasma-chemical model of the lower ionosphere is based on a system of differential equations of the ionization-recombination cycle of the ionospheric D-region [1, 2]. Input parameters of the system are varied. In this paper 5- and 8-component systems are used. They include ionization rate q, temperature T, concentrations of $[O_2]$, $[N_2]$, $[H_2O]$, $[O_3]$, $[O]$ and $[CO_2]$ as input parameters. The evaluation of PDFs of T, $[O_2]$, $[N_2]$, $[H_2O]$, $[O_3]$, $[O]$ and $[CO_2]$ can be more accurate with use of the sufficient volume of experimental data.

In order to evaluate the electron concentration reaction to variations of a particular parameter, the sensitivity analysis of solutions of the ionization-recombination cycle equations was carried out. It is detected that electron concentration Ne primarily depends on the temperature of neutrals T, concentration $[O_2]$ and the ionization rate q, while the influence of small neutral components' concentrations is extremely lower [3]. Therefore, the main objective of this work is a more accurate evaluation of the temperature and the total concentration of neutrals M, based on the long-term experimental satellite data.

# 2 Spatial and Temporal Dependences of Atmosphere Parameters

The experimental AURA databases on T, $[O_2]$ and $[N_2]$ have been accumulated for 15 years. All the data was statistically processed to determine the PDFs of parameters for different combinations of heliogeophysical conditions at $h = 50$–90 km.

Figure 1 shows the month and solar zenith angle distribution of data, and Fig. 2—spatial distribution of the measurements. It can be seen from Fig. 2, that the majority of values was measured at the equatorial and polar latitudes.

As the AURA satellite has a sun-synchronous orbit, its data does not contain the necessary combinations of the all possible zenith angle, season and latitude. Therefore, to determine the heliogeophysical conditions having the strongest influence on T and M behavior, the latitudinal, longitudinal, daily, and seasonal dependences are studied separately for each parameter under different levels of solar activity.
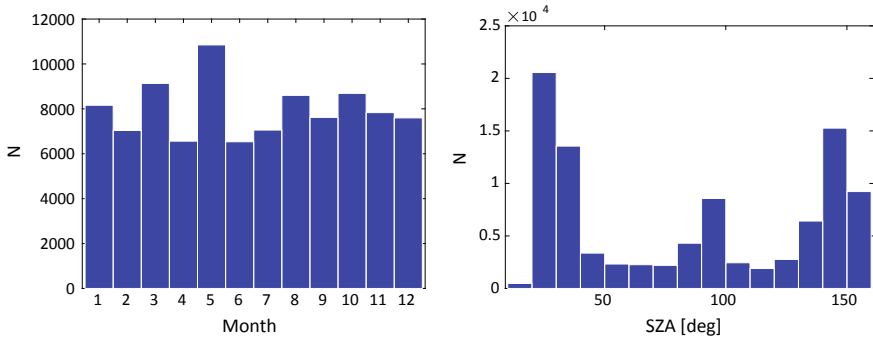
Fig. 1 Number of the satellite measurements for different months and solar zenith angles
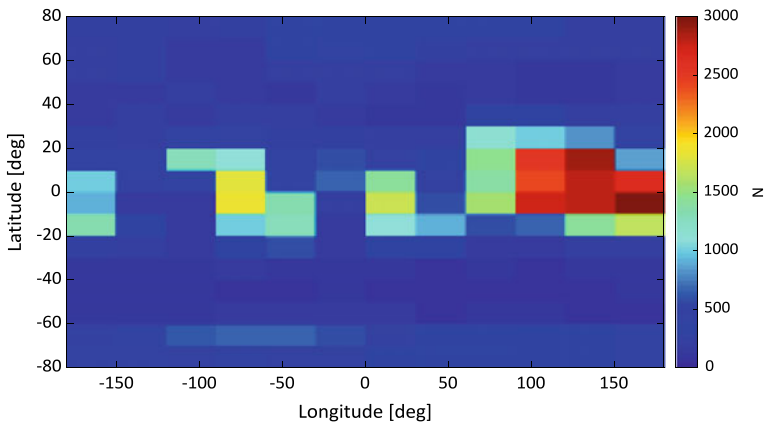
Fig. 2 Spatial distribution of the satellite measurements

Figure 3 shows the latitudinal distribution of T at the height of $h = 90$ km for the one–day period in August (left figure) and for the values accumulated for all Augusts since 2004 (right figure). Colours on the right graph indicate the values of the probability density functions $P(T)$ normalized to their maximums. These two graphs have similar profiles, and the greatest difference is observed at latitudes of $|\varphi| < 20°$, however, the diurnal values differ only by $3 - 5\%$ from the most probable values obtained from PDFs. Anyway, T has the clear-cut latitudinal dependence, consequently, the increment of latitude $\Delta\varphi$ should be small enough so that the difference ΔT were not significant. For example, if we select $\Delta\varphi = 10°$ under the considered conditions, the difference between the T values does not exceed 3.5%.
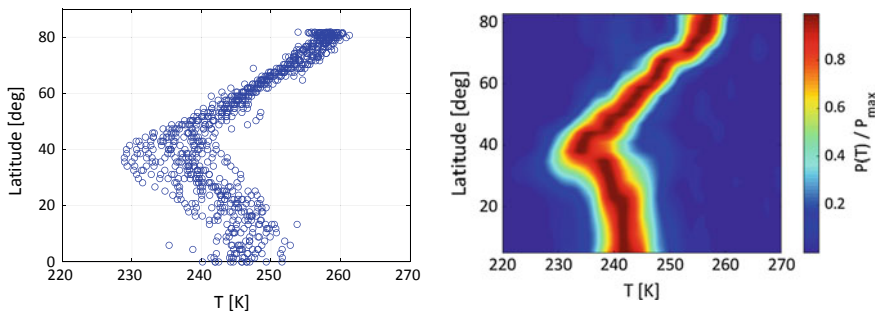
Fig. 3 Latitudinal dependence of T for 11/08/2004 (left) and latitudinal dependence of $P(T)/P_{max}$ obtained from all-August data (right) ($h = 90$ km)

It is detected that behaviour of $P(T)$ functions can differ even during the months of the same season. It can be seen from the right picture in Figs. 3 and 4, on which the latitudinal dependence of $P(T)/P_{max}$ is shown for the June and August data at $h = 90$ km.

The concentration of neutrals M practically does not depend on latitude. At the same time, it should be noted that dispersion of values is higher at small latitudes ($\varphi < 20°$), and the probability density function $P(M)$ is heavy-tailed.

As expected, the neutral component temperature T has a strong seasonal dependence at any height and during any solar activity. The seasonal variations of the neutral component concentration M can be observed only at altitudes of $h \leq 80$ km. Moreover, Fig. 5 shows, how the curve can change depending on latitudes: at $\varphi > 40°$ concentration varies from $0.7 \cdot 10^{15}$ sm^{-3} to $2.3 \cdot 10^{15}$ sm^{-3}, and at $0° < \varphi < 40°$ fluctuations are completely insignificant.

The diurnal variation of the discussed parameters in the altitude range of 50 km $\leq h \leq$ 90 km are not detected. The solar activity also does not influence the medians and the most probable values of temperature and concentration.
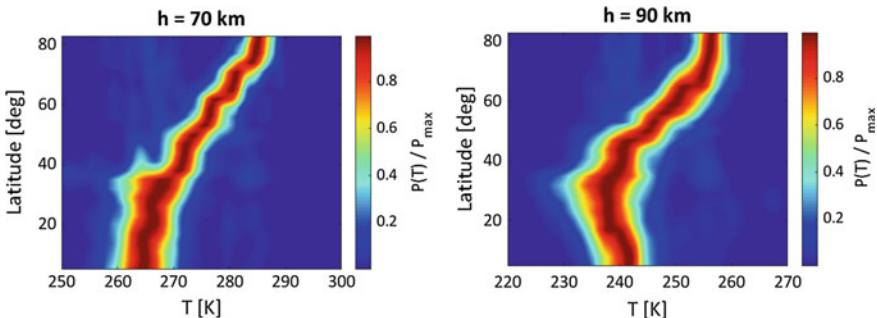
Fig. 4 Latitudinal dependence of $P(T)/P_{max}$ obtained from all-June data at $h = 70$ km (left) and at $h = 90$ km (right)
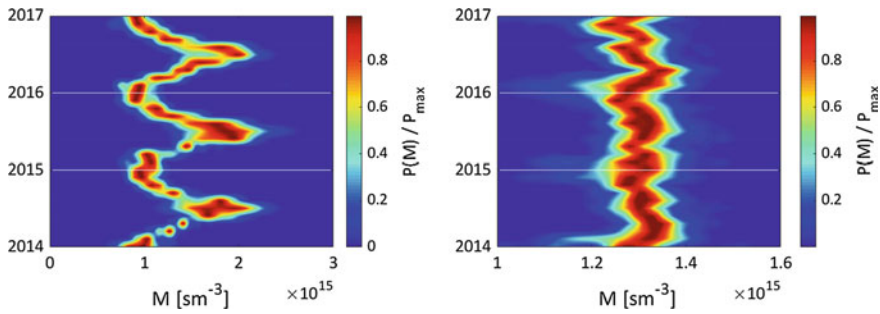
Fig. 5 Seasonal dependence of $P(M)/P_{max}$ at $h = 70$ km for $\varphi > 40°$ (left) and $0° < \varphi < 40°$ (right)

However, $F10.7$ index increase leads to the high dispersion of T and M values under all heliogeophysical conditions.

3 Ionization Rate and Electron Concentration Calculation

As mentioned above, the calculation of Ne of the ionospheric D-region was carried out by using the 5- and 8-component models [4, 5], which include T, q, $[O_2]$, $[N_2]$, $[H_2O]$, $[CO_2]$, $[O_3]$ and $[O]$ as input parameters. Considering the statistical analysis presented above, the appropriate ranges of heliogeophysical conditions were selected, the maximum points of the probability density functions of the input parameters were determined and used to solve the systems of equations of the ionization-recombination cycle. Ionization rate was calculated by using the main sources of D-region ionization including the cosmic rays' ionization, NO ionization by the Lα line, UV and X-ray ionization. The results of Ne calculation at two heights during the solar flare on March 9, 2012 are shown in Fig. 6. The power of
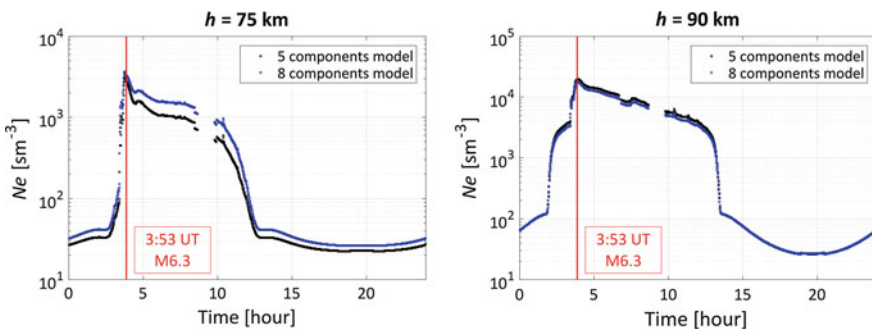
Fig. 6 Electron concentration at $h = 75$ km and $h = 90$ km (09/03/2012; $\varphi = 55°$, $\lambda = 70°$)

the flare was M6.3. The necessary radiation fluxes were taken from the GOES and SDO satellites.

4 Conclusion

The probabilistic-statistical analysis of the experimental data from the AURA satellite has minimized the data inaccuracy for the temperature and concentrations of neutral components. Therefore, the calculation accuracy for the charged components now depends primarily on the profile of the ionization rate and the selected ionization-recombination cycle. The difference between the results of the 5- and 8-component models was insignificant both under the calm conditions and during the solar flare, especially at altitudes $h > 75$ km. The question of the correctness of the used ionization rate profile and selecting one or another plasma-chemical model can be solved by verification with use of experimental radio physical data of the VLF-LF propagation.

References

1. Bekker, S.Z.: Analysis of electron density calculations using deterministic-probabilistic model of the ionospheric D-region. Solar-Terr. Phys. **4**(3), 67–75 (2018)
2. Kozlov, S.I., Lyakhov, A.N., Bekker, S.Z.: Key principles of constructing probabilistic statistical ionosphere models for the radiowave propagation problems. Geomagn. Aeron. **54**(6), 767–779 (2014)
3. Bekker, S.Z., Kozlov, S.I., Lyakhov, A.N.: On some methods of increasing the accuracy of statistical models of the ionospheric D-region. In: Proceedings of the IV All-Russian scientific conference "Problems of military-applied geophysics and control of the state of the environment", pp. 62–66. Saint-Petersburg (2016)
4. Egoshin, A.A., Ermak, V.M., Zetzer, YuI, Kozlov, S.I., Kudryavtsev, V.P., Lyakhov, A.N., Poklad, YuV, Yakimenko, E.N.: Influence of meteorological and wave processes on the lower ionosphere during solar minimum conditions according to the data on midlatitude VLF–LF propagation. Phys. Solid Earth **48**(3), 275–286 (2012)
5. Kudryavtsev, V.P., Romanyukha, NYu.: Modelling of ionization-recombination processes in the middle atmosphere. Math. Model. **7**(3), 3–18 (1995)

A Mathematical Model of the Ionospheric Electric Field Which Closes the Global Electric Circuit

Valery Denisenko, Michael Rycroft and R. Giles Harrison

Abstract

A model for the distribution of the ionospheric electric potential which drives the currents which close the global electric circuit is constructed. Only the internal electric fields and currents generated by thunderstorms are studied. The atmospheric conductivity profiles with altitude are empirically determined, and the topography of the Earth's surface is taken into account. A two-dimensional approximation of the ionospheric conductor is based on large conductivities along the geomagnetic field; the Pedersen and Hall conductivity distributions are calculated using the empirical models IRI, MSIS and IGRF. The maximum calculated voltage difference in the ionosphere under typical conditions for July, under low solar activity, at 19:00 UT, is about 85 V. In our model the potential has identical values at ionospheric conjugate points. With our more realistic

V. Denisenko (✉)
Institute of Computational Modelling, Russian Academy of Sciences,
Siberian Branch, 660036 Krasnoyarsk, Russia
e-mail: denisen@icm.krasn.ru

Siberian Federal University, 660041 Krasnoyarsk, Russia

M. Rycroft
CAESAR Consultancy, Cambridge CB3 9HW, UK

Centre for Space, Atmospheric and Oceanic Science, Department of Electronic and Electrical Engineering, University of Bath, Bath BA2 7AY, UK

R. G. Harrison
Department of Meteorology, University of Reading, Earley Gate, Reading RG6 6BB, UK

Department of Electronic and Electrical Engineering, University of Bath, Bath BA2 7AY, UK

ionospheric model, the electric fields are found to be an order of magnitude smaller than those of the well-known model of Hays and Roble [9].

1 Introduction

There are several mechanisms of ionospheric electric field generation. First of all, there are magnetohydrodynamic processes in the magnetosphere, associated with the interaction of the solar wind with the Earth's magnetic dipole. The second most important mechanism is associated with winds in the upper atmosphere, which cause movement of the ionospheric medium. There are also ionospheric electric fields due to the currents from the atmosphere. These are the currents of the global electric circuit (GEC), which are generated by thunderstorms and other electrified clouds. Although numerous articles analyze the GEC, its ionospheric part is still insufficiently studied.

The objective of the paper is to create a model of electric fields and currents, which constitute the ionospheric part of the GEC. The first results of our modelling efforts are presented in [5], with a published correction to the paper [6]. Here we briefly describe the model and present new results for the periods with low solar activity.

2 The Electric Conductivity Equation

The basic equations for the steady state electric field $\mathbf{E}$ and current density $\mathbf{j}$ are Faraday's law, the charge conservation law, and Ohm's law,

$$\operatorname{curl}\mathbf{E} = \mathbf{0}, \quad \operatorname{div}\mathbf{j} = Q, \quad \mathbf{j} = \hat{\sigma}\mathbf{E}, \tag{1}$$

where $\hat{\sigma}$ is the conductivity tensor. The given function Q differs from zero if an external electric current exists. Then the total current density is equal to $\mathbf{j} + \mathbf{j_{ext}}$ and the second equation (1) with $Q = -\operatorname{div}\mathbf{j_{ext}}$ is the charge conservation law for the total current.

Because of the first equation (1) the electric potential V can be introduced so that

$$\mathbf{E} = -\operatorname{grad}V. \tag{2}$$

Then the system of the Eqs. (1) is reduced to the electric conductivity equation

$$-\mathrm{div}(\hat{\sigma}\,\mathrm{grad}\,V) = Q. \tag{3}$$

We use mainly spherical geomagnetic coordinates r, θ_m, φ_m, geomagnetic latitude $\lambda_m = \pi/2 - \theta_m$ and height above mean sea level h.

3 Separation of Ionospheric and Atmospheric Conductors

The lower boundary of the atmosphere is the Earth's surface. Our model of the topography is presented in detail in [7].

The air near the ground is much less conductive than the ground and the ocean water. So the Earth's ground is usually regarded as an ideal conductor, that means a constant value of the electric potential at the Earth's surface

$$V|_{h=h_g(\theta,\varphi)} = -V_0, \tag{4}$$

where V_0 is a constant whose value will be defined later.

After separating the ground with the help of the boundary condition (4) the remaining conductor consists of the atmosphere, ionosphere and magnetosphere. There are no clear boundaries separating the ionosphere, but we define its conditional boundaries at the altitudes of $h_I = 90$ km and $h_M = 500$ km to divide the regions with substantially different conductivities. Ionospheric currents flow across the magnetic field mainly at heights of 80–500 km [8]. In the separated ionosphere, the conductivity in the direction of the magnetic field **B** exceeds by several orders of magnitude the conductivity in the perpendicular directions, which makes it possible to use the 2-D model. To simulate the magnetosphere, defined as a region above 500 km, we regard the conductivity in directions perpendicular to **B** as zero.

Since the ionospheric conductivity is many orders of magnitude larger than the atmospheric conductivity, the ionosphere can be approximately simulated as an ideal conductor when the atmosphere is simulated using

$$V|_{h=h_I} = 0. \tag{5}$$

This boundary condition completes the Dirichlet boundary value problem (3-5) for the atmosphere that is simulated as a conductor between two ideal conductors. Such a problem has a unique solution when the constant V_0 is given. Because of the large horizontal scale of the simulated processes we use the flat 1-D model instead of the 3-D equation (3) with boundary conditions (4, 5)

$$-\frac{d}{dh}\left(\sigma(h)\frac{d}{dh}V(h)\right) = 0, \quad V|_{h=h_0} = 0, \quad V|_{h=h_g(\theta,\varphi)} = -V_0. \tag{6}$$
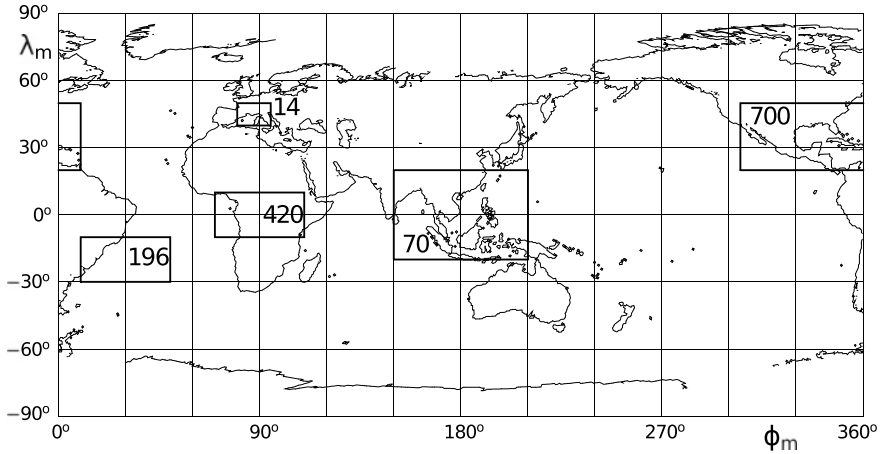
Fig. 1 The rectangles show the regions with electric current to the ionosphere from thunderstorm clouds [9]. Numbers show actual model values of the total currents (in Amperes) in the five different regions

The obtained solution gives the fair weather electric field near the ground. The value V_0 is taken to balance the total fair weather current and thunderstorm currents between the ground and the ionosphere.

We use the height distributions of the conductivity $\sigma(h)$ similar to that proposed for fair weather above ground by the empirical model [11] and satisfies two conditions: a vertical current density $j_0 = -2\,\mathrm{pA/m^2}$ when the vertical electric field strength equals $E_0 = -130\,\mathrm{V/m}$; the potential difference between the ground and the ionosphere is $V_0 = 250\,\mathrm{kV}$ for the same E_0. The given values of E_0, j_0, V_0 are considered to be typical for the GEC [10].

We use the model [9] of the global distribution of thunderstorm activity which separates five main thunderstorm regions as typical ones for a northern hemisphere summer at 19:00 UT. These regions are shown in Fig. 1. The total current flowing through the atmosphere I is driven by the potential difference between ground and the ionosphere. The total resistance of the atmosphere for the conductivity model used is found above as $R = 180\,\Omega$. To fulfill the charge conservation law when $I_{ext} = -I = V_0/R = 1.4\,\mathrm{kA}$ we reduce the density of external currents [9] by 1.43 times.

4 Conductivity in the Earth's Ionosphere

We use parallel and normal to the direction of magnetic induction **B** components of vectors which are marked with symbols $\parallel$ and $\perp$. Then Ohm's law (1) in a gyrotropic medium takes the form

$$j_\parallel = \sigma_\parallel E_\parallel, \qquad \mathbf{j}_\perp = \sigma_P \mathbf{E}_\perp - \sigma_H [\mathbf{E}_\perp \times \mathbf{B}]/B, \tag{7}$$

with Hall (σ_H), Pedersen (σ_P) and field-aligned ($\sigma_\parallel$) conductivities.

We have created the model [4] to calculate the components σ_P, σ_H, $\sigma_\parallel$ of the conductivity tensor $\hat{\sigma}$, that is based on the empirical models IRI, MSISE, IGRF.

It is shown in [8] how to reduce a 3-D model to a 2-D one when the conductivity in the direction of the magnetic field $\sigma_\parallel$ is a few orders of magnitude larger than σ_P, σ_H. Our version of this type of model is presented in [2]. In such a model, a magnetic field line has its own value of the electric potential V. It can obtain or lose charge by currents $\mathbf{j}_\perp$ and it does not matter for its total charge at what point along the magnetic field line $\mathbf{j}_\perp$ exists, because charges can go freely along the line according to infinite $\sigma_\parallel$. Then $\mathbf{E}_\perp$ is constant in this integration and so

$$\mathbf{J}_\perp = \begin{pmatrix} \Sigma_P & -\Sigma_H \\ \Sigma_H & \Sigma_P \end{pmatrix} \mathbf{E}_\perp, \tag{8}$$

where Pedersen and Hall conductances Σ_P, Σ_H are obtained by integration along a magnetic field line. The integral conductance Σ_P or Σ_H at each half of a magnetic field line can be shown at the surface $h = 120$ km in the dot where the line crosses the surface. The obtained global distributions of Σ_P, Σ_H are presented in Fig. 2; a logarithmic scale is used since the values vary by almost four orders of magnitude.

5 Boundary Value Problems

The charge conservation law (3) for the 2-D model is satisfied as integrated along a magnetic field line. It is useful to construct some plane with Cartesian coordinates x, y that presents all magnetic field lines of interest and to write this equation as

$$-\frac{\partial}{\partial x}\left(\Sigma_{xx}\frac{\partial V}{\partial x} + \Sigma_{xy}\frac{\partial V}{\partial y}\right) - \frac{\partial}{\partial y}\left(\Sigma_{yx}\frac{\partial V}{\partial x} + \Sigma_{yy}\frac{\partial V}{\partial y}\right) = Q_{ext}, \tag{9}$$

where Q_{ext} is the density of current from the atmosphere, transformed to the new coordinates x, y. The coefficients Σ_{xx}, Σ_{xy}, Σ_{yx}, Σ_{yy} differ from Σ_P, Σ_H only by geometrical factors defined by the chosen plane.

If only the dipolar part of the geomagnetic field is taken into account there exists a conformal transformation. Then $\Sigma_{xx} = \Sigma_{yy} = \Sigma_P$, $-\Sigma_{xy} = \Sigma_{yx} = \Sigma_H$ [3]. The partial differential equation (9) is an equation of elliptical type which means that one can use boundary conditions similar to those for Poisson's equation.

The auroral zones are equivalent to almost ideal conductors because they are connected in parallel with good magnetospheric conductors. We approximately regard them as ideal ones and put $V = 0$ in the auroral zones. This condition cuts the ionosphere into three parts which are the Northern and Southern polar caps and
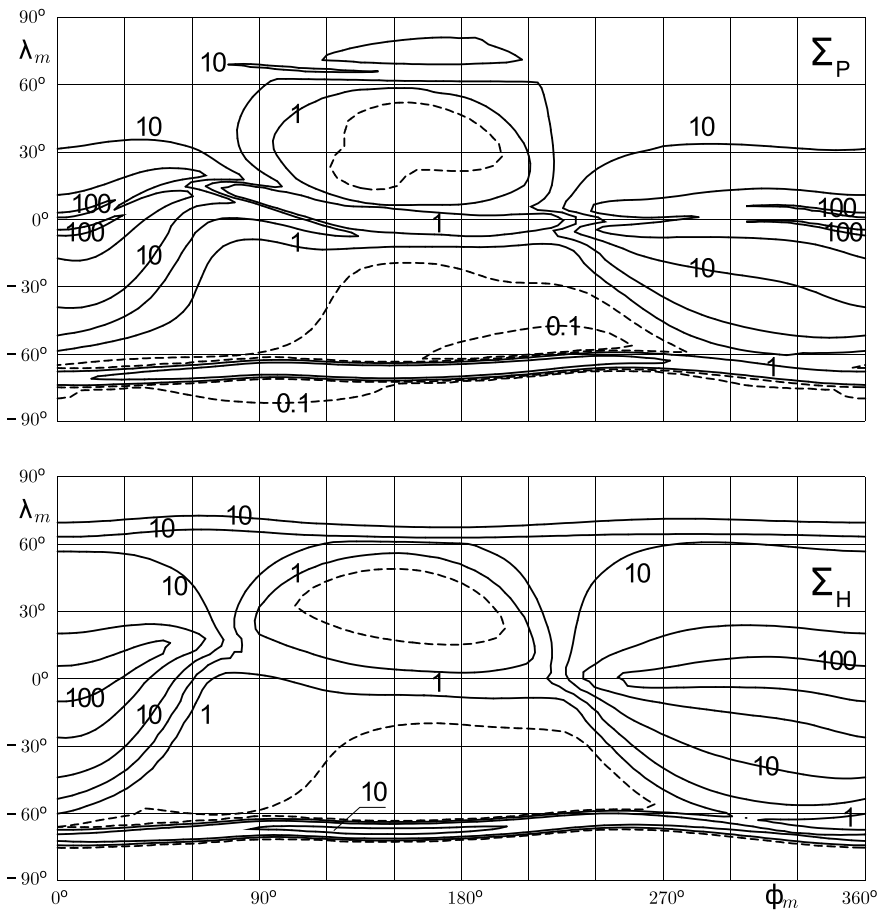
Fig. 2 Distribution of the integral Pedersen conductance Σ_P (top panel) and Hall conductance Σ_H (bottom panel) in units of S. The points with λ_m, φ_m geomagnetic coordinates at 120 km height in the ionosphere identify halves of magnetic field lines. Maps are calculated under typical conditions for July under low solar activity at the considered point in time, 19:00 UT

the main part that contains middle- and low latitudes. These parts of the ionospheric conductor in many aspects can be analyzed independently since the potential at their boundaries is already defined as zero:

$$V|_{\Gamma_N} = 0, \quad V|_{\Gamma_S} = 0, \tag{10}$$

$$V|_{\Gamma_{aur}} = 0, \tag{11}$$

where we denote the boundaries of the Northern and Southern polar caps as Γ_N and Γ_S. In this paper we have concentrated on the main part of the ionosphere that corresponds to the domain Ω. Its auroral boundary is Γ_{aur}. Its second boundary Γ_{eq} corresponds to the last magnetic field lines which are regarded as ionospheric ones. The boundary condition as a consequence of the charge conservation law defines the current component normal to the boundary

$$J_v|_{\Gamma_{eq}} = -J_{eq}^0. \tag{12}$$

In view of (8, 2) it defines the value of the derivative of V.

Our numerical method for the boundary value problem (9, 11, 12) in the domain Ω is described in detail in [1].

6 The Results of the Calculations

The solution for the boundary value problem (9, 11, 12) in the main part of the ionosphere is presented in Fig. 3. The distribution of the electric potential $V(\theta_m, \varphi_m)$ at height $h = 120$ km in the ionosphere is shown by the positions of the equipotentials, which are plotted with a contour interval equal to 5 V. Maximum potential difference is about 86 V.
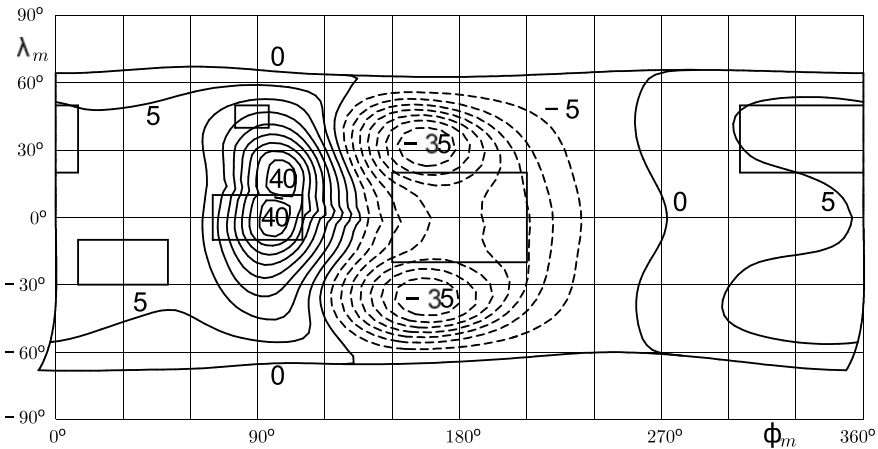
Fig. 3 Distribution of the electric potential at 120 km height in the ionosphere. Equipotentials are plotted with contour interval 5 V. Dashed lines correspond to negative values of potential. The rectangles show the thunderstorm regions. The Northern and Southern auroral zones in which the electric potential equals zero and the polar caps are not shown. The map is calculated under typical conditions for July under low solar activity at the considered point in time, 19:00 UT

In the well known model [9] the ionospheric integral conductances were principally simplified as $\Sigma_H \equiv 0$ and $\Sigma_P \equiv 0.05\,\text{S}$ in comparison with rather realistic distributions of the ionospheric conductance in actual model shown in Fig. 2. The maximum potential difference within the ionosphere equals 1575 V in the model [9] that is about 20 times larger than the 86 V in this model. The positions of the maximum values of the ionospheric potential in the model [9] are close to ours because they correspond to large thunderstorm generators in the center of Africa and in Central America which are dominating as is seen in Fig. 1. The second thunderstorm region produces much less voltage because of the large day-time ionospheric conductance in comparison with the small conductance under the night-time conditions above Africa at the considered point in time, 19:00 UT.

Due to the smaller length of the atmospheric column between the ground and the ionosphere above the Himalayas the column conductance is large and the fair-weather current density has a maximum there. This means that there is a large negative divergence of the ionospheric electric current Q_{ext} in Eq. (9). So the minimum of the ionospheric electric potential is found just there.

In our model the potential has identical values at the ionospheric conjugate points. So the minimum above the Himalayas is repeated in the Southern hemisphere. The Asian thunderstorm region increases the potential in the ionosphere between these regions. The domains with positive values of the ionospheric potential above the thunderstorm regions are also repeated in the conjugate hemisphere. The largest of them is the maximum of about 40 V above Central Africa and its equivalent in the Northern hemisphere.

The model potentials in the ionosphere would be different from those presented in Fig. 3 at other times and under different solar activity conditions. Anyway the potential difference between ionospheric regions above thunderstorm areas and above fair-weather areas is always less than 200 V [5].

The key parameters in our model of the GEC are the following: voltage between the ground and the ionosphere $V_0 = 250\,\text{kV}$, fair weather electric field near ground $E_0 = -130\,\text{V/m}$ with corresponding current density $j_0 = -2\,\text{pA/m}^2$, the total current flowing upwards from thundery areas to the ionosphere is $I_{ext} = 1.4\,\text{kA}$. These values are considered to be typical for the GEC, but in view of the linearity of the model they could be multiplied by any common constant.

The obtained horizontal electric field strength in the ionosphere is also an order of magnitude less than that in the model [9]. The main reason for the different orders of magnitudes is a better approach for the simulation of the ionospheric conductivity in our model. That is our principal improvement to the model [9].

References

1. Denisenko, V.V.: Multigrid method for a global Hall conductor in the Earth's ionosphere. In: Virtual Proceedings of the 10-th Anniversary International GAMM-Workshop on Multigrid Methods (1998). http://www.mgnet.org/mgnet-parmgm98.html

2. Denisenko, V.V.: 2-D model of the global ionospheric conductor connected with the magnetospheric conductors (2018). http://arxiv.org/abs/1802.07955

3. Denisenko, V.V., Zamay, S.S.: Electric field in the equatorial ionosphere. Planet. Space Sci. **40**(7), 941–952 (1992). https://doi.org/10.1016/0032-0633(92)90134-A

4. Denisenko, V.V., Biernat, H.K., Mezentsev, A.V., Shaidurov, V.A., Zamay, S.S.: Modification of conductivity due to acceleration of the ionospheric medium. Ann. Geophys. **26**, 2111–2130 (2008). https://doi.org/10.5194/angeo-26-2111-2008

5. Denisenko, V.V., Rycroft, M.J., Harrison, R.G.: Mathematical simulation of the ionospheric electric field as a part of the global electric circuit. Surv. Geophys. **40**(1), 1–35 (2019). https://doi.org/10.1007/s10712-018-9499-6

6. Denisenko, V.V., Rycroft, M.J., Harrison, R.G.: Correction to: mathematical simulation of the ionospheric electric field as a part of the global electric circuit. Surv. Geophys. **40**(1), 37 (2019). https://doi.org/10.1007/s10712-018-9505-z

7. Denisenko, V.V., Yakubailik, O.E.: The contribution of topography to the resistance of the global atmospheric conductor. Solar-Terr. Ph. **1**(1), 104–108 (2015). (in Russian). https://doi.org/10.12737/6044

8. Hargreaves, J.K.: The Upper Atmosphere and Solar-Terrestrial Relations. Van Nostrand Reinhold Co Ltd., NY (1979)

9. Hays, P.B., Roble, R.G.: A quasi-static model of global atmospheric electricity. 1. The lower atmosphere. J. Geophys. Res. **84**(A7), 3291–3305 (1979). https://doi.org/10.1029/JA084iA07p03291

10. Rycroft, M.J., Harrison, R.G., Nicoll, K.A., Mareev, E.A.: An overview of Earth's global electric circuit and atmospheric conductivity. Space Sci. Rev. **137**, 83–105 (2008). https://doi.org/10.1007/s11214-008-9368-6

11. Rycroft, M.J., Odzimek, A.: Effects of lightning and sprites on the ionospheric potential, and threshold effects on sprite initiation, obtained using an analog model of the global atmospheric electric circuit. J. Geophys. Res. **115**, A00E37 (2010). https://doi.org/10.1029/2009JA014758

Experimental Study of Mid-latitude Ionosphere Disturbances Caused by Auroral Phenomena and Heating Experiments

Boris Gavrilov, Julius Zetzer, Yuriy Poklad, Iliya Ryakhovskiy, Andrey Lyakhov, Vladimir Rybakov, Dmitriy Egorov and Vladimir Ermak

Abstract

The main objective of our research is to study the phenomena in the lithosphere, atmosphere and ionosphere and their interaction to understand the physical mechanisms responsible for the state and dynamics of the Geosphere system as a whole. The important element of these studies are experimental data. In addition to using global geophysical data the data of their local or regional manifestations are needed, especially in mid-latitude Russia. To solve this problem at the "Mikhnevo" Observatory near Moscow has created a unique measuring system that allows you to obtain comprehensive information on geophysical process. The complex includes magnetometers, sensors of an electric field and a atmosphere current, LFM ionosonde, a complex of multisystem GNSS receivers, broadband radio receivers, acoustic sensors and other equipment which together with a complex of seismic observations allows to solve many geophysical problems. In the article the tasks and results of investigations in the observatory are shown on the example of several scientific directions, which the "Mikhnevo" observatory is engaged in.

B. Gavrilov (✉) · J. Zetzer · Y. Poklad · I. Ryakhovskiy · A. Lyakhov · V. Rybakov · D. Egorov · V. Ermak
Sadovsky Institute of Geospheres Dynamics RAS, 119334 Moscow, Russia
e-mail: boris.gavrilov34@gmail.com

1   Introduction

The investigation of the mechanisms of interrelated disturbances in the internal and external geospheres requires comprehensive studies of variations of different geophysical fields. For that, the multifunctional measurement complex was created on the territory of the geophysical observatory "Mikhnevo" of the Institute of Geosphere Dynamics of the Russian Academy of Sciences. The observatory is located 80 km south of Moscow (54.57'26" N, 37.45'23" E).

The complex includes three-component fluxgate magnetometer, a complex of broadband magnetometers, the complex of spatially separated multi-system GNSS receivers, wideband HF receivers, a super sensitive VLF receivers, probes of the electric field and surface current of the atmosphere, acoustic sensors and other equipment. The observatory is constantly studying the effects of solar eclipses [1], powerful solar flares [2], remote earthquakes, other natural and anthropogenic events in the lithosphere, atmosphere and ionosphere of the Earth. The article describes several examples of the use of complex equipment to solve some of them.

2   Experimental Study of the Mechanisms of Transfer of High-Latitude Geophysical Disturbances to the Middle Latitudes

It is known that the mid-latitude variations of geophysical fields and the ionosphere are largely due to geomagnetic disturbances in the polar regions. At the same time, the real mechanisms and channels of energy supply from high to middle latitudes have not been sufficiently studied. The study of these processes is carried out in the Mikhnevo observatory. The method is based on the determination of the reaction time of mid-latitude geophysical parameters to high-latitude disturbances.

Three main mechanisms of transmission of disturbances from the high-latitude to the mid-latitude ionosphere are considered. The first one is the thermospheric wind. Its speed reaches 50 m/s during the day, up to $\sim$100–200 m/s at night and up to 300–700 m/s during strong geomagnetic storms. The second agents are acoustic-gravitational waves (AGV) that observed against the background of regular daily oscillations in the form of moving ionospheric perturbations. AGV are divided into medium-scale waves (wavelengths of several hundred kilometers, periods of 15–60 min and speeds of 100–250 m/s) and large-scale waves (wavelengths of more than 1000 km, periods of 30–180 min and horizontal velocities of 400–1000 m/s). In mid-latitudes the large-scale waves are the main mechanism of ionospheric disturbances. It is also known that mid-latitude and low-latitude geomagnetic and ionospheric perturbations may coincide with magnetic storms and substorms. Their occurrence is associated with the entry into the ionosphere of a horizontal electric field from the magnetosphere.
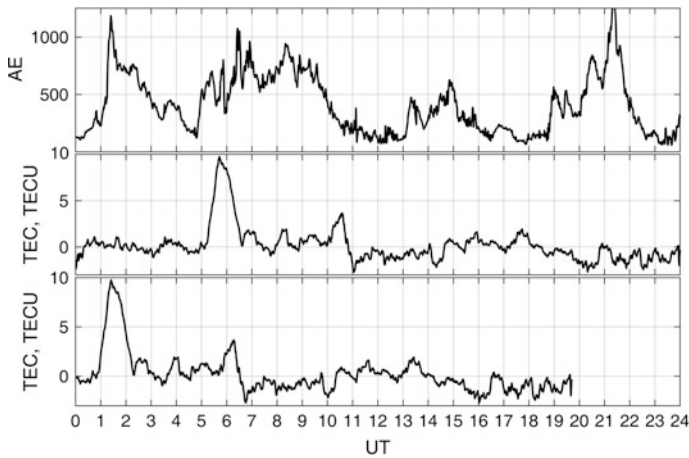
Fig. 1 The upper panel is AE index on 9 April 2006, the middle panel is TEC variations, the lower panel is TEC curve shifted back to the best match to AE index and TEC burst

The AE-index is used as a marker of magnetic disturbances in the auroral zone, and the reaction of the mid-latitude ionosphere is determined by the change of the total electron content (TEC) of the ionosphere according to the data of GPS receivers. Figures 1, 2 and 3 illustrate this approach by the example of three days with different perturbations of the mid-latitude ionosphere.

Substorm on 9 April 2006 at 1:30 UT shown by a burst of the AE index (Fig. 1, top panel). It is not accompanied by noticeable variations of TEC. However, at 6:30 UT there is a surge of TEC, the shape of which and the following TEC variations are close to the variations of the AE index. At the bottom panel, the TEC curve is shifted so that the bursts of the AE index and the TEC coincide. The offset time that corresponds to the delay of the reaction of the mid-latitude ionosphere to substorm is about 5 h. The distance from the Aurora oval to the observatory is taken to be 2000 km. Then the average velocity of the perturbation propagation is ~ 100 m/s. This velocity is typical for the thermospheric wind.

In the Fig. 2 the data for 14 April 2006 are shown. The delay of the ionosphere response to the magnetic substorm is 1.5 h, which corresponds to the propagation velocity of the perturbation ~ 400 m/s. In this case, the most likely perturbation agent of the mid-latitude ionosphere is acoustic-gravitational wave.

In the example shown in Fig. 3, the delay of the ionosphere reaction from the AE index is not more than 30 min, which corresponds to the propagation velocity of the perturbation of more than 4000 km/s. Such a rapid propagation of the perturbation can be connected to the prompt penetration of the magnetospheric electric field.
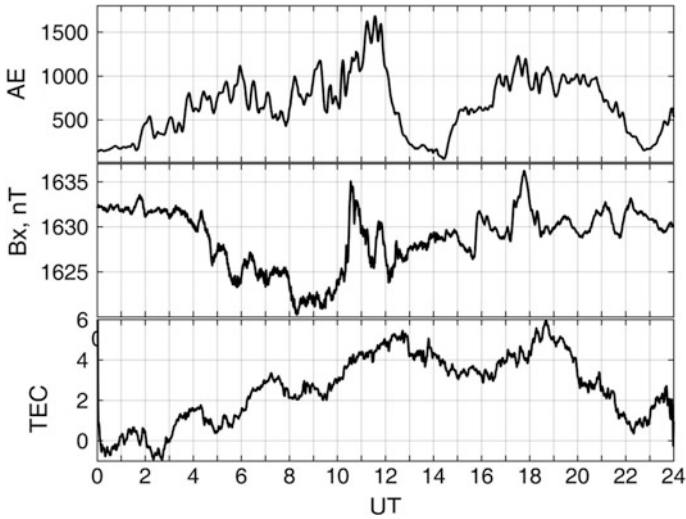
Fig. 2 AE-index, variations of the horizontal component of the magnetic field in the Mikhnevo observatory and TEC variation on 14 April 2006

Fig. 3 AE index and TEC variation on 15 April 2006
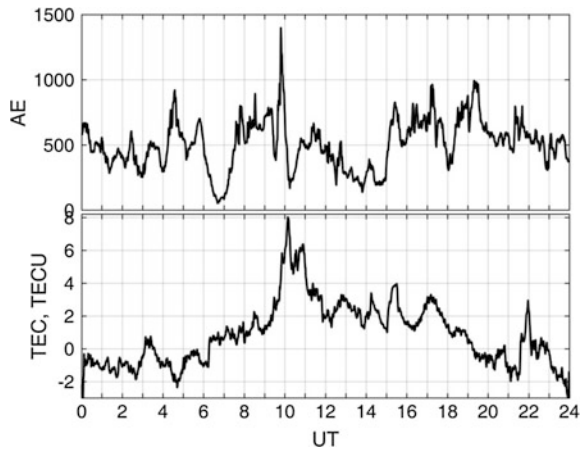
Thus, measurements of variations in the geomagnetic field and local ionospheric parameters, together with data on high-latitude geomagnetic disturbances allowed to determine the dominant mechanisms of energy supply from high to mid-latitudes.

3 Investigation of the Mechanisms of the Relationship of Disturbances in the Upper and Lower Ionosphere

Studies of the relationship of disturbances in the upper and lower ionospheres were performed for a powerful geomagnetic storm St. Patrick Day 17 March 2015 [3].

TEC data from the two-frequency Javad Sigma receiver and the data of the world network of navigation receivers SOPAC were used for the research of the F layer of the ionosphere. Data on the lower ionosphere were obtained by registering the amplitude and phase of signals of VLF transmitters. In waveguide propagation, the main influence on the amplitude-phase characteristics of VLF signals is exerted by the walls of the waveguide, mainly the D-layer of the ionosphere. The transmitting stations were selected in such a way that the radio signal routes passed under different azimuths over the territory of Europe from its northern to southern regions (Fig. 4).

Data on changes in the phases of VLF signals and TEC variations allow us to make a qualitative representation of the movement of ionospheric inhomogeneities.

Figures 5 and 6 show the phase changes on the VLF transmitters—Mikhnevo routes and the vertical TEC change for European stations located near the same VLF routes. All figures for comparison show data (bold curves) for a calm day on 14 March 2015.
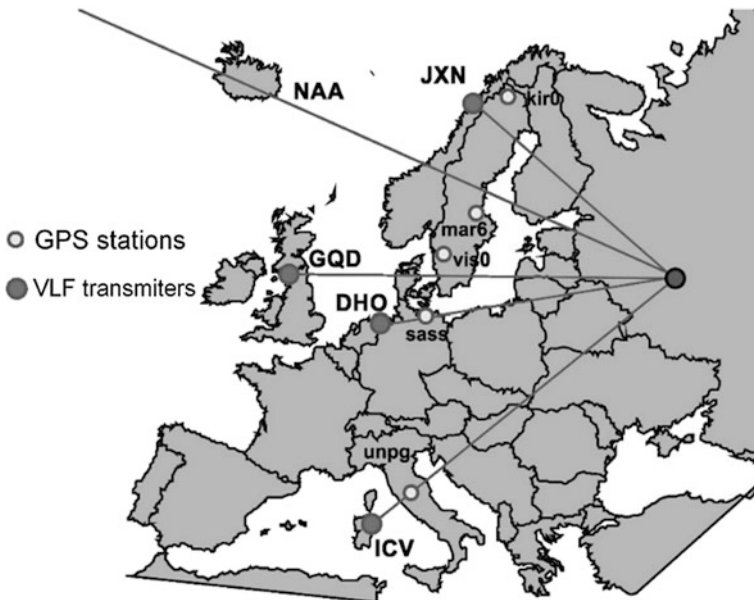
Fig. 4 Location of VLF transmitters and stations of the SOPAC network, the data of which were used during the experiment
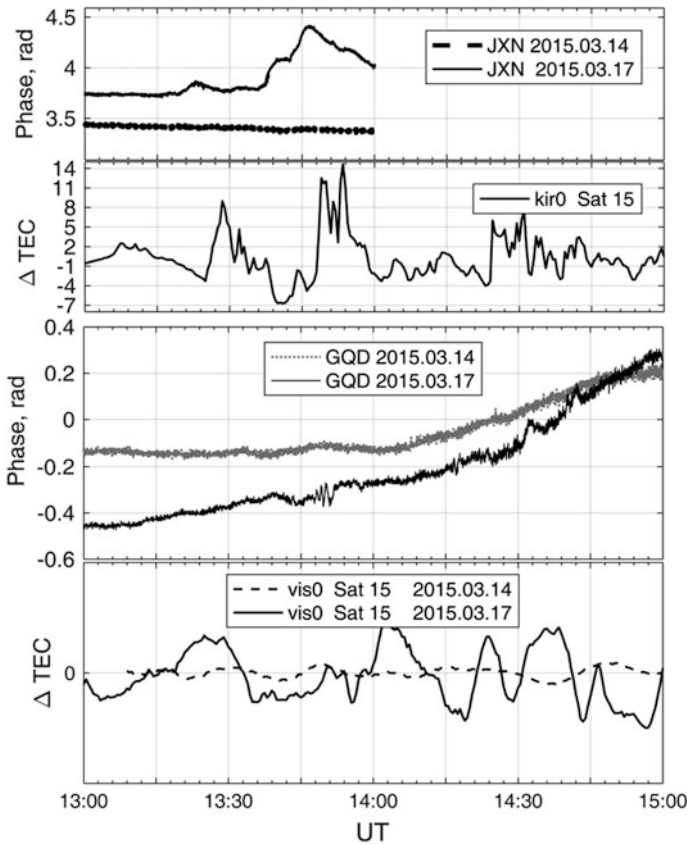
Fig. 5 Perturbations of the phase of VLF signals on the route Mikhnevo—JXN and TEC for *kir0* station (upper panel) and on the route Mikhnevo—GOD and TEC for *vis0* station (lower panel) from 13 to 15 UT on 17 March 2015

The upper panel of Fig. 5 shows the perturbation of the VLF signal phase of the signal on the route Mikhnevo-transmitter JXN and TEC in the *kir0* station from 13:30 to 14:00 UT. The lower panel shows the phase change of the VLF signal on the Mikhnevo—GOD transmitter route and the TEC for the *vis0* station. Since the upper panel refers to the latitude of about 69° and the lower to the latitude of 57°, it can be assumed that the boundary of the disturbance at this time was between these latitudes.

In the upper panel of Fig. 6 the perturbation of the VLF phase of the signal on the route Mikhnevo—GOD and TEC in *vis0* station at time 15:45 UT is shown.
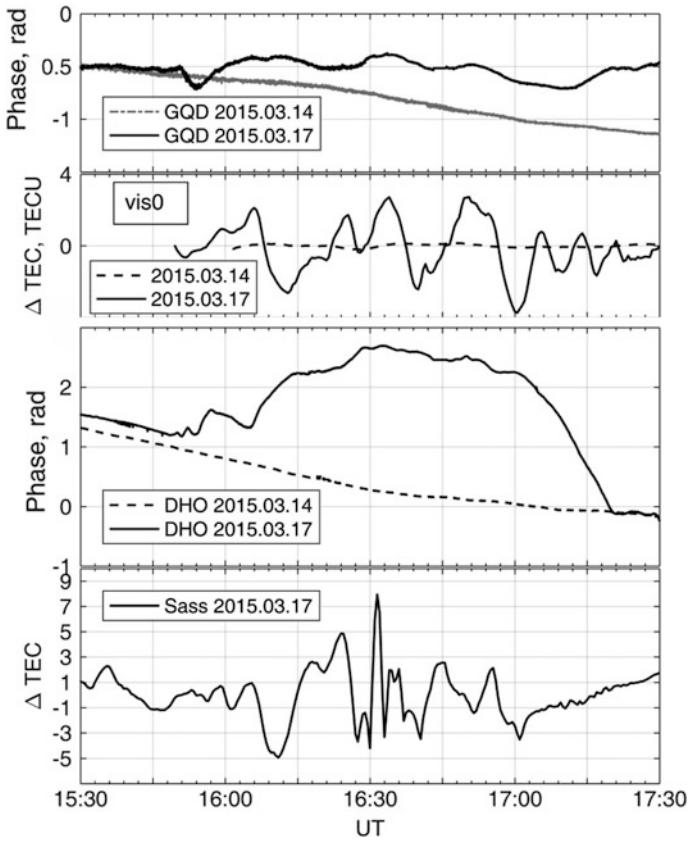
Fig. 6 Perturbations of the phase of VLF signals on the track Mikhnevo—GOD and TEC for *vis0* stations (upper panel) and on the route Mikhnevo—DHO and TEC for *sass* station (lower panel) from 15:30 to 17:30 UT on 17 March 2015

The bottom panel shows the same data for the DHO transmitter and the *sass* station. Perturbation of the ionosphere is observed on all charts. The upper panel refers to the latitude of about 57°, and the lower to the latitude of 53–54°. It is obvious that the ionospheric disturbance captured both areas.

Correlated changes in TEC and VLF signals indicate that the perturbation region covers the heights from D to F ionosphere layers.

4 Remote Study of Ionospheric Effects Caused by Heating Experiments

In experiments at the EISCAT facility in February and October 2012 [4] the propagation of electromagnetic radiation over long distances and the effect of heliogeophysical conditions on the propagation of HF and VLF radio waves was investigated.

One of the tasks of the experiment was introduced the tasks associated with the study of the generation and propagation of the VLF/ELF signals, caused by the impact on the ionosphere powerful HF radiation modulated at frequencies of 0.5, 2.01, 3.01, and 6.02 kHz.

Figure 7 shows the layout of the measuring points. The same type of receiving equipment was installed in Mikhnevo, the "Gorkovskaya" observatory of the AARI and "Verkhnetulomskiy" of PGI KSC RAS. The analysis of the measurement results revealed significant differences in the amplitude-phase characteristics of the signals due to changes in the heliogeophysical conditions in the heating area and on the signal propagation path.

Figure 8 shows the results of signal registration at the modulation frequency of 2017 Hz. EISCAT worked in the mode of 5 min heating, 5 min pause. The use of new recording equipment allowed to register signals with an amplitude of 0.5–5 fT at distances up to 2000 km from the source. The amplitudes of the signals recorded
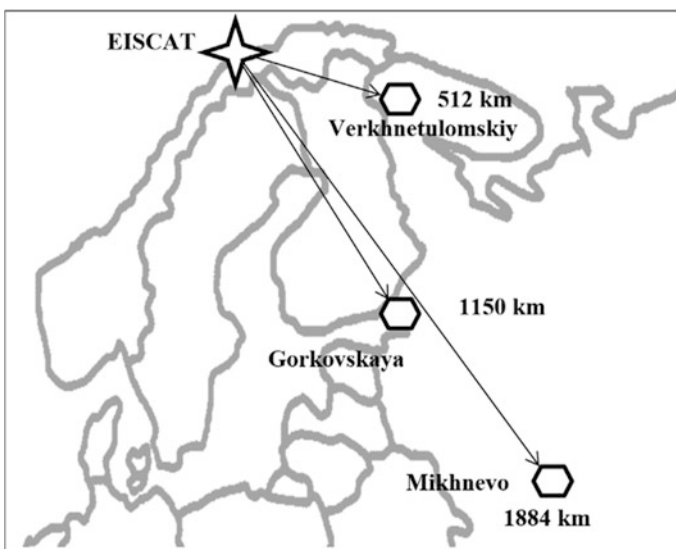
Fig. 7 Layout of the EISCAT stand and measuring points during the 2012 experiments. The heating periods are shown by strokes
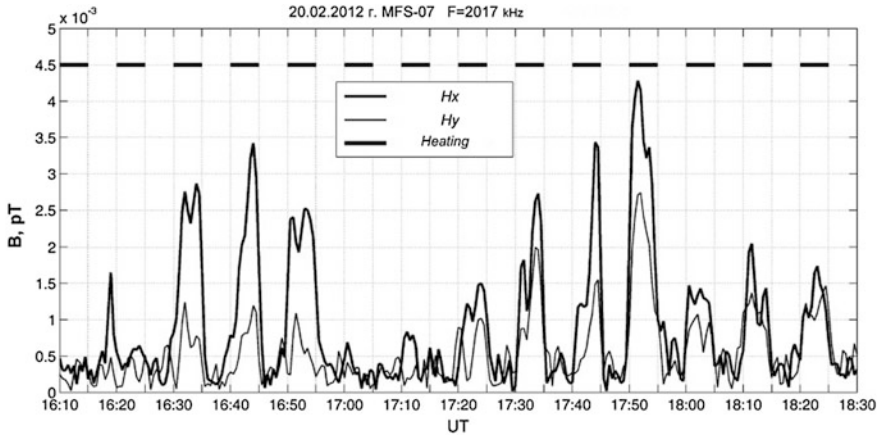
Fig. 8 Signal amplitudes at the frequency of 2017 Hz recorded on the channel Hx (thick curve) and channel Hy (thin curve) in the period from 16:00 to 19:00 UT on 20 February 2012

on the Hx channel ranged from 1 to 4 FTL and on average 2–3 times higher than the amplitudes of the signals recorded on the Hy channel.

Registration of all modulation frequencies during the February experiment made it possible to investigate the influence of the signal propagation path and helio-geophysical conditions on the polarization of the received signals [5].

Analysis of the synchronous measurements carried out at the distances from 500 to 2000 km from the source revealed significant differences in the amplitude-phase characteristics of the signals due to different heliogeophysical conditions. Experimental confirmation of the relationship between the intensity of LF generation with the intensity of the electrojet was obtained.

5 Conclusion

The complex of the Geophysical Observatory "Mikhnevo" let to solve many geophysical tasks. The measurements of variations in the mid-latitude geomagnetic field and local ionospheric parameters together with data on high-latitude disturbances allowed to determine the dominant mechanisms of energy supply from high latitudes to mid-latitudes.

Simultaneous measurements of the amplitudes and phases of the VLF signals and variations of the TEC allows to study the relationship between perturbations of the upper and lower ionosphere. It is possible to trace the dynamics of ionospheric disturbances in both vertical and horizontal directions. Another important result of these studies is the possibility to estimate the contribution of the lower ionosphere to the total electron content of the ionosphere, determined by the GNSS receivers.

References

1. Adushkin, V.V., Gavrilov, B.G., Gorelyi, K.I., Rybnov, Y.S., Kharlamov, V.A.: Geophysical effects of the March 29, 2006. Dokl. Earth Sci. **417**(2), 1393–1397 (2007)
2. Gavrilov, B.G., Lyakhov, A.N., Poklad, Y.V., Rybakov, V.A., Ryakhovsky, I.A., Loseva, T. V.: Geophysical effects of solar flare on 6 September 2017. In: Proceedings of the SPIE 10833, 24th International Symposium on Atmosphere ic and Ocean Optics: Atmospheric Physics, vol. 1083397 (2018). https://doi.org/10.1117/12.2502477
3. Astafyeva, E., Zakharenkova, I., Forster, M.: Ionospheric respons to the 2015 St. Patrick's Day storm: a global multi-instrumental overview. J. Geophys. Res. Space Phys. **120**(10), 9023–9037 (2015). https://doi.org/10.1002/2015ja021629
4. Blagoveshchenskaya, N.F., Borisova, T.D., Yeoman, T.K., Rietveld, M.T., Ivanova, I.M., Baddeley, L.J.: Artificial small scale field aligned irregularities in the high latitude F region of the ionosphere induced by an X-mode HF heater wave. Geophys. Res. Lett. **38**(8) (2011). https://doi.org/10.1029/2011gl046724
5. Gavrilov, B.G., Zetser, YuI, Ryakhovskii, I.A., Poklad, YuV, Ermak, V.M.: Remote sensing of ELF/VLF radiation induced in experiments on artificial modification of the ionosphere. Geomag. Aeron. **55**(4), 450–456 (2015)

Scaling Relations for Shock Wave Effects from the Impacts of Cosmic Objects with Diameters from a Few Meters to 3 Km

Dmitry Glazachev , Elena Podobnaya , Olga Popova ,
Vladimir Svetsov , Valery Shuvalov and Natalia Artemieva

Abstract

Asteroids risk models require understanding how an asteroid (or a comet) entering into the atmosphere can harm people and infrastructure. A shock wave is one of the main dangerous effects of the cosmic object impact. Serial numerical simulations of high-velocity impacts of cosmic objects from 10 m to 3 km in diameter are used to build scaling relations of shock wave properties (overpressure and wind speed) near the surface. Obtained scaling relations, which are dependent only on parameters of impactor, are used for the Tunguska and Chelyabinsk events and show satisfactory agreement with observations and numerical models. A separate class of scaling laws presents crater-forming impacts and shows much better correlation with models than previously used estimates. All scaling relations described in this paper are implemented into the web-based Calculator for fast assessment of hazardous consequences from the impact of cosmic objects on the Earth. The Calculator is available at the link: http://AsteroidHazard.pro.

1 Introduction

Asteroid risk assessment models require understanding how an asteroid (or a comet) entering into the atmosphere harm people and infrastructure [11, 12]. One of the main dangerous effects of the cosmic object impact is a shock wave. The destructive

D. Glazachev (✉) · E. Podobnaya · O. Popova · V. Svetsov · V. Shuvalov · N. Artemieva
Sadovsky Institute of Geospheres Dynamics RAS, 119334 Moscow, Russia
e-mail: glazachevd@gmail.com

effects of a shock wave are usually associated with the value of maximum over-pressure and wind speed behind it, which can result in various degree of damage (from broken windows to total destruction of buildings). For example, window glasses are typically broken at the loading 500 Pa [5]; the results of nuclear tests [6] show that a collapse of ∼30 cm brick wall begins at an overpressure of 20 kPa. Overpressure can be fatal for people causing concussion, lung and/or eardrum damage, and shock. Strong winds also cause infrastructure damage which, in turn, may be dangerous for people (collapsing glass, trees, and other flying objects). In addition, strong winds may disperse hazardous chemical materials over wide area [6].

Impact consequences cannot be fully studied in laboratory experiments, whereas comprehensive numerical models even of one impact are time-consuming and require high computer power. Therefore, most of quick assessments of impact hazard use various scaling relations which are mainly based on the results of nuclear tests [3, 4].

Complex numerical model was elaborated to study impacts of cosmic objects of different sizes and their consequences (e.g., [16]. At the first step (2D simulations) the impactor passage through the atmosphere is simulated taking into account its deformation, deceleration, fragmentation, and evaporation. The obtained distributions of gas-dynamic and thermodynamic parameters in the atmosphere are used in 3D simulations to calculate the overpressure and gas velocity behind the shock wave (wind speed) as it propagated along the surface [16].

Systematic numerical simulations have been performed for 82 possible impact scenarios; comet and asteroid diameters vary from 20 m to 3 km; velocities are in the range of 15–70 km/s; and impact angles are from 15° to 90° [1].

These numerical simulations are treated as the basis for scaling relations allowing quick calculations of overpressure/wind on the surface using properties of the impactor as entry values.

2 Scaling Relations for Airbursts

Until recently, an impact of 10–20 m asteroid was considered as harmless. However, the Chelyabinsk event (2013) demonstrated that the deceleration and fragmentation of such object and the transfer of its kinetic energy to the atmosphere, even at high altitude, is able to create an atmospheric shock wave reaching the Earth's surface and causing significant damage. The Chelyabinsk asteroid, which released the bulk of its energy at an altitude of about 30 km, broke window glasses at about 24,000 km^2 and injured more than 1600 people [13].

The atmospheric entry of a high-velocity cosmic body may be classified as an "airburst" if the main part of the body's mass does not reach the surface (or reaches it with a velocity much lower than the entry velocity) and shock waves in the air generated during the entry are strong enough to reach the surface and to cause at least some damage [14]. It is usually assumed that airbursts are typical for a vertical

entry of asteroids smaller than 100 m and comets smaller than 150 m. Impacts from projectiles more than 300 m are usually crater-forming. Only 0.3 km diameter comets at impact angles <30° lose most of their energy in atmosphere producing powerful airbursts, and are unable to form a crater. Intermediate cases, where a part of energy releases at the atmosphere, but crater is formed, are also possible. In some cases an airburst is accompanied by a cratering event (in 2007, the relatively small (0.06–0.32 kt TNT) Carancas meteoroid impact resulted in the formation of a 14 m diameter crater in Peru, 3800 m above sea level [2, 10].

Scaling relations are suggested for the relative pressure distribution p/p0 (x, y), i.e. the ratio of maximum shock pressure value p at the point with coordinates (x, y) to the atmospheric pressure at zero altitude level p0. The impactor parameters include its diameter D (m), velocity V (km/s), an entry angle α to horizon (degrees), and density ρ (kg/m^3). Approximations are based on numerical results for comets and asteroids, therefore, for other impactor densities the linear interpolation on density between cometary and asteroidal bodies has to be used.

For an airburst case we suggested to search description as the following:

$$p/p0 = 1 + a * \left(\frac{E_{kt}^{2/3}}{H_{eff}^2 + (x - x_0)^2 + el * y^2} \right)^b \tag{1}$$

where x and y (in km) are spatial coordinates (the coordinate origin is at the intersection of the impactor trajectory without deceleration with the Earth's surface, the trajectory is along the x-axis from positive direction to negative one), x_0 is distance between maximum pressure point and the coordinate origin (for airbursts the point where trajectory crosses the Earth surface is not equal to the point of maximal energy release), a and b are the constants of the model, E_{kt} is the kinetic energy of the impactor in kiloton of TNT. Heff is an effective height (in km) of an equivalent point source (see Eq. 2 below), i.e. height of an explosion, which creates a shock wave as from a cosmic body with given parameters; this height roughly corresponds to an altitude, where the impactor loses most of its energy and slows down [15].

$$H_{eff} = (-1.3 * H * Ln(D * (\sin \alpha / H) * (\rho/\rho0)^{2/3}) + H)/1000 \tag{2}$$

where H = 7500 m is the atmospheric scale height and $\rho0 = 1.29$ kg/m^3 is the atmosphere density at the sea level.

The asymmetry of the pressure field is taken into account using the ellipticity parameter el.

All parameters in the scaling relation (Eq. 1) should depend only on impactor characteristics.

We used the following procedure for search these relations. The values of parameters (a, x_0, el, b) were determined for each variant of numerical simulations set (i.e. for every impact scenario) by minimizing the losses function over whole

considered spatial area. Different losses functions were applied (standard deviation, relative standard deviation, with and without weight-function). Finally, the weighted relative standard deviation was used.

The combination of impactor properties in different powers was assumed as probable dependence for each required parameter. Entry angle was included through trigonometric function. In some cases the logarithmic function of kinetic energy was used. The coefficients and power exponents for these combinations were estimated by minimizing uncertainty function for all considered impact scenarios. The final choice between dependencies was done taking into account the fit error (minimal value of uncertainty function) and simplicity.

The general matrix was constructed, which includes all spatial points from all impact scenarios. The final scaling relations were found as minimal error solution for this matrix.

Distance along the x-axis between maximal pressure point and point of origin varies with the projectile density and grows with effective height increase and an entry angle decrease:

$$x_0 = \begin{cases} 0.57 * H_{eff}^{1.3} * (\cot \alpha)^{0.71}, \rho = 1000 \text{ kg/m}^3 \\ 0.69 * H_{eff}^{1.3} * (\cot \alpha)^{0.71}, \rho = 3320 \text{ kg/m}^3 \end{cases} \tag{3}$$

The difference between the approximation (Eq. 3) and the results of numerical simulations usually does not exceed 5 km except for the case of highly oblique entry angles. The mean error is about 2 km.

Approximations for coefficients a, b and el (Eq. 1) do not directly depend on the density of impactor and are the same for cometary and asteroidal bodies. The a-coefficient depends on the kinetic energy and the effective height (Eq. 4). The ellipticity coefficient depends on the effective height, entry angle, and the kinetic energy (Eq. 5). Finally, the b exponent (model coefficient) is constant and is equal to 0.66.

$$a = 0.2 * \frac{E_{kt}^{0.035}}{H_{eff}^{0.22}} \tag{4}$$

$$el = 1 - 0.002 * H_{eff}^{1.16} * (\cos \alpha)^{2.7} \ln E_{kt}. \tag{5}$$

Figure 1 shows a distribution of relative pressure after a 50 m comet entry with velocity of 70 km/s at the 30° to horizon. Both, numerical simulations and the scaling relations, describe the relative pressure levels from 1.05 up to the 1.3 (the lowest threshold of building collapse). Areas of lower pressures are not enough accurate. Corresponding Relative errors (the ratio of the approximated value to the value from numerical simulations) are usually smaller than 2 times except for small areas near the projectile trajectory projection on the surface.

In addition, a scaling relation for the maximal value of overpressure (over all x-y coordinates) is obtained. It depends on the effective height and increases with kinetic energy of impactor. Relative error for this approximation is more than 60% only for one large cometary object (diameter 150 m, entering angle 45° and velocity 20 km/s), but in most cases relative error less than 50%.

Earlier, another scaling relations based on the results of nuclear explosions and semi-analytical models of meteoroid`s entry with fragmentation were suggested by [3]. This model was recently revised in Collins et al. [4] as the previous version underestimated airbusts overpressures. The updated model may be written as follows:

$$p(r) = 3.14 \times 10^{11} * \left(r^2 + z_b^2\right)^{-\frac{2.6}{2}} + \left(r^2 + z_b^2\right)^{-\frac{1.13}{2}} \tag{6}$$

$$r^2 = x^2 + y^2$$

here p is overpressure (Pa), r means radius on the surface in meters and z_b is an effective height in meters (the height above the surface, at which the fragmented impactor, which is described in the frame of the pancake model, increases its diameter by a factor of $\sim$ 7, all the impact energy is assumed to be deposited at this altitude), both normalized on $E_{kt}^{1/3}$.

Pressure distribution according to the Eq. 6 is shown in Fig. 2 for the same cometary impact; relative error also does not exceed the value of 4.
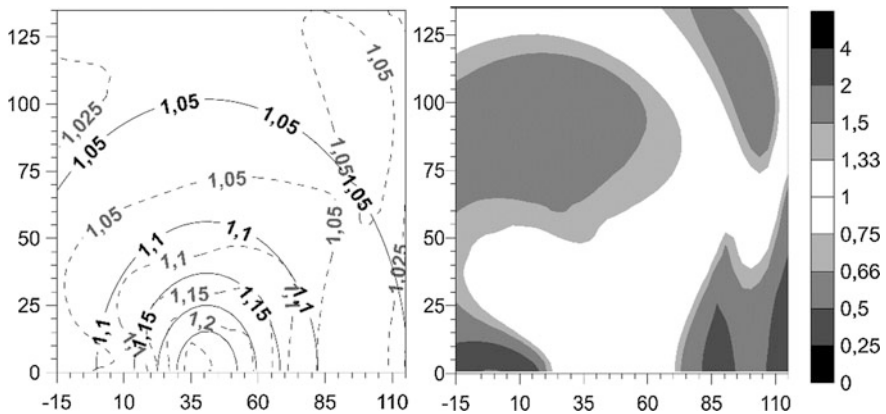
Fig. 1 The pressure p/p0 distribution for a 50-m-diameter cometary body with a velocity of 70 km/s, entry angle 30°. The trajectory coincides with the x-axis and the comet moves from right to left. **Left**: Labels correspond to relative pressure (p/p0) values. Curves drawn by dashed lines with grey labels correspond to the results of numerical simulations; solid curves with bold labels denote a distribution of relative pressure from Eq. (1). **Right**: Relative error distribution (results calculated with Eq. 1 divided by the results of numerical simulations)
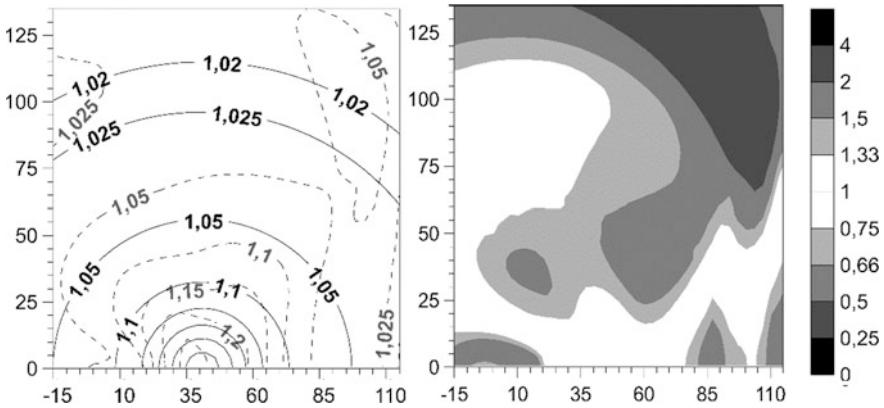
Fig. 2 The relative pressure p/p0 distribution for a 50-m-diameter cometary body entering with a velocity of 70 km/s at 30°. The trajectory is along the X-axis from right to left. **Left**: Curves drawn by dashed lines with grey labels refer to results of numerical simulations; solid curves with bold labels denote a distribution of relative pressure from model (Eq. 6). **Right**: Relative error distributions between numerical simulations and by Collins et al. [4] approximations

The comparison of scaling relations (Eqs. 1–5) and (Eq. 6) for the whole considered set of impact scenarios demonstrates that both relations satisfactory describe pressure distributions. About third part of impact scenarios are described with the same mean relative error. The areas, where relative error values are about 0.7–1.3, are almost equal for both scaling relations (Eqs. 1–5 and Eq. 6). The other ones are described better with scaling relations suggested in this paper (Eqs. 1–5). In addition, scaling relations by Collins et al. [3, 4] (Eq. 6) describes relative pressure distribution noticeably worse for larger (100–150 m) diameters of cosmic bodies. Moreover, Collins et al. model is inherently axisymmetric and, hence, errors for highly oblique impacts are substantial.

We apply suggested above scaling relations to two most famous events, i.e. the Chelyabinsk entry in 2013 and the Tunguska event of 1908(Fig. 3). Maximal overpressure is about 2.5 kPa for Chelyabinsk and 30 kPa for Tunguska.

The comparison of scaling relation results for the Chelyabinsk meteoroid with data on damages and inquires shows a good agreement [9]. The comparison of numerical simulation results [17] with scaling relations estimates is given in Fig. 3 and demonstrates a satisfactory agreement. It should be noted that modelled areas obtained by the scaling relation (Eqs. 1–5) are wider in the direction perpendicular to the trajectory and narrower along the trajectory than obtained by numerical simulation. This is an indicator that the parameter "el" is underestimated for shallow angle entries of relatively small bodies. The possible reason may include the fact that the relative overpressure values in this case are low (at the lower boundary of considering relative pressure values) and their precision is lower than in other cases.
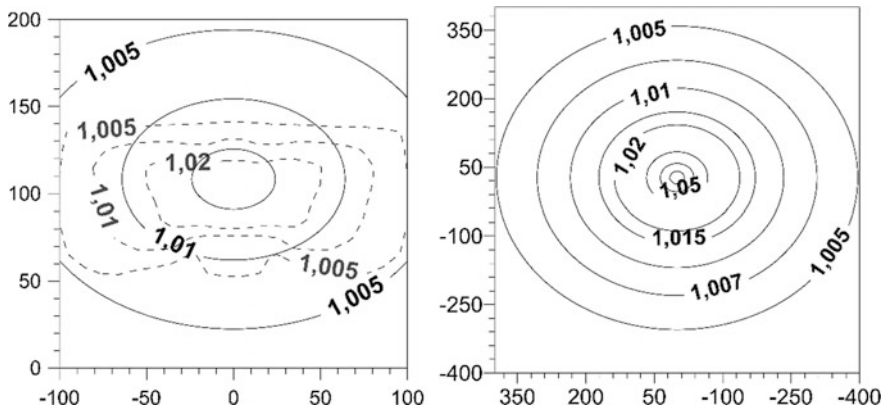
Fig. 3 Scaling relations results for relative pressure (p/p0). **Left**: The Chelyabinsk body with density of 3320 kg/m³, entry angle 18°, diameter 19 m, velocity 19 km/s, and the kinetic energy of 514 kt TNT. Dashed lines are numerical simulations; solid lines are scaling relations results. **Right**: Tunguska body with density of 1000 kg/m³, entry angle 30°, diameter 84 m, velocity 20 km/s, and kinetic energy of 15 Mt TNT; solid lines are scaling relations results

In the case of the Tunguska cosmic body many different variants of projectile parameters have been suggested (i.e. kinetic energy from 10 to 15 Mt TNT; meteoroid density of 1000 and 3320 kg/m³; the entry angle in the range of 20–45°, and the velocity range of 15–40 km/s). One possible solution for the Tunguska meteoroid is shown in Fig. 3. The comparison of scaling results (Eqs. 1–5) with eyewitness testimonies demonstrates satisfactory agreement: the predicted overpressures at 300–400 km distances are in the same range as recently found data on glass window damage [8].

The level of overpressure and the wind speed behind the shock front are connected through Hugoniot equations. Therefore, the wind velocity distribution could be obtained from the overpressure distribution. For all considered scenarios and wind velocities larger than 20 m/s relative errors are less than 4.

Wind distributions for the model (Eqs. 1–5) was considered and compared with numerical simulations. Considerable values of wind speed were from 20 m/s (dry branches start falling from the trees). On the other hand, "telegraph forest" zone, where almost all dead trees remain standing upright with their crowns torn off, cannot be described in the frame of our approximation as in this zone standard one-dimensional Hugoniot equations are not applicable. Thus, at the considered area an average relative error of the model (Eqs. 1–5) results is about 2.

3 Crater-Forming Events

In the case of crater-forming events (cosmic bodies are from 300 m to 3 km in diameter) the pressure distributions are searched with the spatial heterogeneity as an two semi-ellipses in polar coordinates. The distribution is described as following:

$$\frac{p}{p0} = 1 + \frac{10^6 * el * f * E_k^{pe/3}}{d^{pe}} \tag{7}$$

$$d^2 = (x^2 + y^2) \times 10^6$$

In the suggested equations (Eq. 7) x and y are spatial coordinates (in km), the point of origin is the center of the crater. The numerical coefficient f is a scaling multiplier depending on the kinetic energy of the cosmic body. The power coefficient pe is equal to 1.4 whereas the larger value of 2 (the point source assumption) results in much more worse distributions. The ellipticity parameter (Eq. 8) allows to take into account spatial heterogeneity. An ellipse in polar coordinates (φ—polar angle) with three controlled parameters a (controls x-axis width), b (controls positive half of y-axis) and c (controls negative half of y-axis) is calculated (Eq. 8).

$$el = \frac{a * \text{If}[0 < \phi < \pi, b, c]}{\sqrt{a^2 \text{Sin}[\phi]^2 + \text{If}[0 < \phi < \pi, b, c]^2 \text{Cos}[\phi]^2}} \tag{8}$$

The coefficients (Eq. 7) are calculated to minimize errors in comparison with numerical simulations. The same procedure (described in Sect. 2) was used to find the coefficients. The model coefficient f decreases with an increase of impactor energy (Eq. 9). All coefficients from ellipticity relation (Eq. 8) depend only on the entry angle and the impactor density (Eqs. 10–12).

$$f = 0.0046 - 0.0004 * \log_{10} E_k \tag{9}$$

$$a = \begin{cases} 1.1 * (\sin \alpha)^{-0.34}, \rho = 1000 \text{ kg/m}^3 \\ 0.56 * (\sin \alpha)^{-0.27}, \rho = 3320 \text{ kg/m}^3 \end{cases} \tag{10}$$

$$b = \begin{cases} 1.7 * (\sin \alpha)^{-0.54}, \rho = 1000 \text{ kg/m}^3 \\ 0.84 * (\sin \alpha)^{-1.2}, \rho = 3320 \text{ kg/m}^3 \end{cases} \tag{11}$$

$$c = \begin{cases} 0.65 + 0.064 * (\sin \alpha)^{-2.8}, \rho = 1000 \text{ kg/m}^3 \\ 0.44 + 0.0083 * (\sin \alpha)^{-3.8}, \rho = 3320 \text{ kg/m}^3 \end{cases} \tag{12}$$

The results are shown in Fig. 4. Only the small area in the center demonstrates relative error larger than 4.
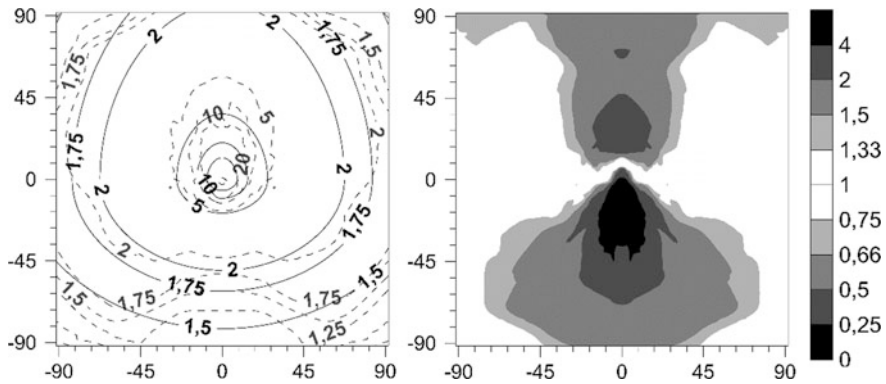
Fig. 4 A distribution of relative pressure p/p0 for a 1-km-diameter cometary body, entry angle of 45° and impact velocity of 20 km/s. The Trajectory of the cosmic object is from top to bottom. **Left**: Curves drawn by dashed lines with grey labels refer to results of numerical simulations; solid curves with black labels denote a distribution of relative pressure from the model (Eq. 7). **Right**: Relative error distributions between numerical simulation and the approximation (Eq. 7)

Results of approximation (Eqs. 7–12) were also compared with the model by Collins et al. [3, 4] (Eq. 6). Collins et al. [4] model plotted in Fig. 5 for the same cometary scenario (parameters are shown in the Fig. 5) demonstrates that a negative y-axis area is described noticeably better than with our approximation (Eqs. 7–12;
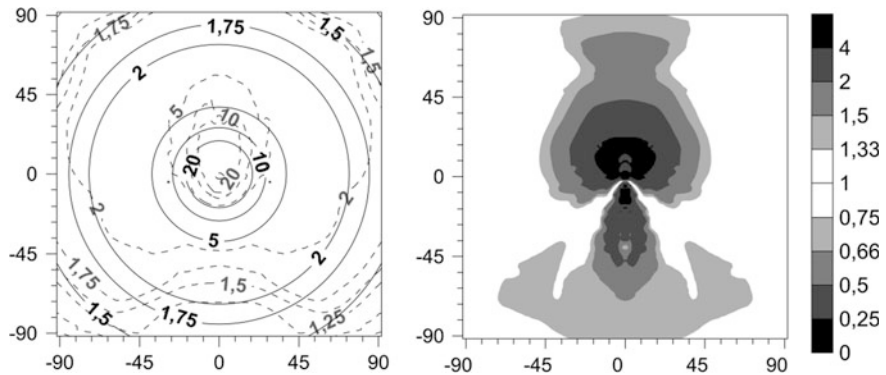
Fig. 5 The pressure p/p0 distribution for cometary body with diameter 1 km, entry angle 45° and velocity of entering to atmosphere 20 km/s according model by Collins et al. [4]. The trajectory is from top to bottom. **Left**: A distribution of relative pressure (ratio of pressure at the point to atmospheric one). Curves drawn by dashed lines with grey labels refer to results of numerical simulations; solid curves with bold labels denote a distribution of relative pressure from model (Eq. 6). **Right**: Relative error distributions between numerical simulation and model (Eq. 6) results

Fig. 4). On the other hand, a positive y-axis area is describes better by the scaling relation (Eq. 7).

In general, within the whole set of impact scenarios the scaling relations (Eqs. 7–12) demonstrate better results for relative error distributions, i.e. an area with relative error values 0.7–1.3 are bigger for almost all cosmic bodies from the set and mean relative error is closer to 1 for them, whereas the model by Collins et al. [4] demonstrates worse description. The model by Collins et al. [4] results in relative error exceeding 4 within the entire area under consideration for about a quarter of considered cosmic bodies.

Wind distributions for the model (Eqs. 7–12) are considered and compared with numerical simulations. Considered values of wind speed vary from 20 m/s (dry branches start falling from the trees) to 200 m/s (extremely powerful tornado). In this area an average relative error of our model (Eqs. 7–12) results is about 4.

To calculate hazardous effects produced by a cosmic object with another density a linear interpolation between cometary and asteroidal values is used. Pressures for scenarios, in which an airburst is accompanied by a cratering event, are calculated via linear interpolation by kinetic energy of the impactor between scenarios of a 150 m and 300 m diameter projectiles keeping all other parameters constant.

4   Web-Based Calculator of Impact Consequences

There are several web-based calculators on the Internet. The most popular is ImpactEarth (https://impact.ese.ic.ac.uk/ImpactEarth/), which is described in detail in Collins et al. [3]. This calculator is based on the simplified models and on nuclear explosion data. Estimates for some of the effects are usable; others show significant errors [15]; some effects are not calculated at all. For example, this calculator does not estimate the radiation arising during the passage and destruction of a cosmic body in the atmosphere. Other calculators available on the Internet (http://www.killerasteroids.org/impact.php; http://simulator.down2earth.eu; https://www.purdue.edu/impactearth) rely on the same approaches as outlined in [3].

Our online calculator is available on http://AsteroidHazard.pro and implements the presented scaling relations, which are based on massive numeric simulations of the atmospheric passage of a cosmic body. Besides shock wave effects the calculator also give an assessment of radiation effects, crater formation and ejecta parameters, seismic effects, and atmospheric disturbances in the upper atmosphere. Appropriate equations will be presented in our next paper.

5 Conclusion

Numerical simulations of impacts for a wide range of impactor properties [1] are used to create relatively simple approximations allowing quick calculations of damage on the surface.

Scaling relations were suggested for the pressure and wind speed distributions for both, airbursts and crater-forming impacts. The results are compared with numerical simulations and with available observations. In general, the precision for the overpressure and wind speed predictions differ from numerical simulations less than a factor of 2. Application of scaling relation results to the Tunguska Event and the Chelyabink meteoroid shows satisfactorily agreement with observations of these events [7–9, 17]. An accuracy for crater-forming impacts is lower but still not larger than a factor of 4.

All scaling relations described in this paper are implemented in the web-based Calculator which can be used for fast assessment of hazardous consequences of impacts.

References

1. Artemieva, N., Shuvalov, V.: Atmospheric shock waves after impacts of cosmic bodies up to 1000 m in diameter. Meteorit. Planet. Sci. **54**(3), 592–608 (2019)
2. Brown, P., et al.: Analysis of a crater-forming meteorite impact in Peru. J. Geophys. Res. **113** (E9) (2008)
3. Collins, G.S., Melosh, H.J., Marcus, R.A.: Earth impact effects program: a web-based computer program for calculating the regional environmental consequences of a meteoroid impact on Earth. Meteorit. Planet. Sci. **40**(6), 817–840 (2005)
4. Collins, G.S., Lynch, E., McAdam, R., Davison, T.M.: A numerical assessment of simple airblast models of impact airbursts. Meteorit. Planet. Sci. **52**(8), 1542–1560 (2017)
5. Gi, N., Brown, P., Aftosmis, M.: The frequency of window damage caused by bolide airbursts: a quarter century case study. Meteorit. Planet. Sci. **53**(7), 1413–1431 (2018)
6. Glasstone, S., Dolan, P.J.: The Effects of Nuclear Weapons, 3rd edn. United States Department of Defense and Department of Energy, Washington (1977)
7. Glazachev, D.O., Podobnaya, E.D., Popova, O.P., Artemieva, N.A., Shuvalov, V.V.: Scaling relations for shock wave effects from large meteoroids decelerated in the Earth's atmosphere. In: 81st Annual Meeting of the Meteoritical Society, LPI Contributions, 2067 (2018)
8. Jenniskens, P., Popova, O.P., Glazachev, D.O., Podobnaya, E.D., Kartashova, A.P.: Tunguska eyewitness accounts, injuries, and casualties. Icarus **327**, 4–18 (2019)
9. Kartashova, A.P., Popova, O.P., Glazachev, D.O., Jenniskens, P., Emel'yanenko, V.V., Podobnaya, E.D., Skripnik, A.Y.: Study of injuries from the Chelyabinsk airburst event. Planet. Space Sci. **160**, 107–114 (2018)
10. Kenkmann, T., Artemieva, N.A., Wünnemann, K., Poelchau, M.H., Elbeshausen, D., Prado, H.N.D.: The Carancas meteorite impact crater, Peru: Geologic surveying and modeling of crater formation and atmospheric passage. Meteorit. Planet. Sci. **44**(7), 985–1000 (2009)
11. Mathias, D., Wheeler, L., Dotson, J.L.: A probabilistic asteroid impact risk model: assessment of sub-300 m impacts. Icarus **289**, 106–119 (2017)
12. Nemtchinov, I., Svetsov, V., Shuvalov, V.: Main factors of hazards due to comets and asteroids. In: Adushkin, V.V., Nemtchinov, I.V. (eds.) Catastrophic events Caused by Cosmic Objects, pp. 1–89. Springer, Moscow, Russia (2008)

13. Popova, O.P., et al.: Chelyabinsk airburst, damage assessment, meteorite recovery, and characterization. Science **342**(6162), 1069–1073 (2013)
14. Shuvalov, V.V., Svettsov, V.V., Trubetskaya, I.A.: An estimate for the size of the area of damage on the Earth's surface after impacts of 10–300-m asteroids. Sol. Syst. Res. **47**, 260–267 (2013)
15. Shuvalov, V.V., Popova, O.P., Svettsov, V.V., Trubetskaya, I.A., Glazachev, D.O.: Determination of the height of the "meteoric explosion". Sol. Syst. Res. **50**, 1–12 (2016)
16. Shuvalov, V.V., Svettsov, V.V., Artemieva, N.A., Trubetskaya, I.A., Popova, O.P., Glazachev, D.O.: Asteroid Apophis: evaluating the impact hazards of such bodies. Sol. Syst. Res. **51**, 44–58 (2017)
17. Shuvalov, V.V., Svetsov, V.V., Popova, O.P., Glazachev, D.O.: Numerical model of the Chelyabinsk meteoroid as a strengthless object. Planet. Space Sci. **147**, 38–47 (2017)

Effects of the Impact of Jet Engines of Progress Spaceships on the Ionosphere According to GPS Receivers of the Japanese Network GEONET

Artem Ishin ⓘ, Sergey Voeykov ⓘ and Vitaly Khakhinov ⓘ

Abstract

The present study focuses on the determination of the parameters of disturbance occurring in the ionosphere as a result of the impact of the jet engines of the spaceship "Progress" on the example of an active experiment May 4, 2006. The disturbance parameters were determined using total electron content data from the GPS station IRKT, as well as from the dense Japanese network GEONET. Analysis of the TEC series shows that a negative disturbance occurs in the affected area. The amplitude of the disturbance was about 0.03–0.04 TECU. According to the simulation data, the corresponding amplitude in electron density was estimated. It was about 3.5×10^5 el/cm^3. The disturbance transverse size was about 120–140 km. The duration of the disturbance did not exceed 8 min. It is shown that the use of dense networks of stations of global navigation satellite systems can be effective for studying the dynamics of local electron density perturbations.

Keywords

GPS · GNSS · Active experiments in the ionosphere · ISS

A. Ishin (✉)
Irkutsk National Research Technical University, 664074 Irkutsk, Russia
e-mail: ishin@iszf.irk.ru

S. Voeykov · V. Khakhinov
Institute of Solar-Terrestrial Physics SB RAS, 664033 Irkutsk, Russia
e-mail: serg3108@iszf.irk.ru

V. Khakhinov
e-mail: khakhin@iszf.irk.ru

1 Introduction

For several years, using the tools of the Institute of Solar-Terrestrial Physics (ISTP) SB RAS, the Radar-Progress experiments were carried out to register and determine the parameters of ionospheric responses to the impact of the jet engines of the Progress transport and cargo spaceships. The engines of the Progress spacecraft produced a local effect on the ionosphere both during correction of the ISS orbit and after undocking. The SibNet [1] network of permanent dual-frequency GPS/GLONASS receivers, owned by the ISTP SB RAS, was one of the tools. As a result of the experiments, a number of interesting results were obtained according to the data of various tools [2–7]. In particular, according to the SibNet data, it was found that in the area affected by the spacecraft engines, negative disturbances were observed in the total electron content (TEC) [7]. The mechanism of the formation of such negative disturbances is described in [6]. These results were obtained by analyzing the ionospheric effects of the Progress engines in the Baikal region. Unfortunately, the density of the SibNet network is insufficient for analyzing the scale and dynamics of the observed disturbances.

For a more detailed analysis, it would be interesting to use data from dense networks of stations, such as GEONET in Japan and New Zealand. Repeated scanning through the area of influence could allow one to establish possible spatial features of the arising disturbances and the perspective dependencies of their observations.

The peculiarity of the experiment on May 4, 2006 was that the section of the ISS trajectory with the active engines was very long: almost from Irkutsk to Japan. This made it possible to determine the parameters of the ionospheric response to the operation of the engines according to the data of both the Japanese GEONET network and the data of the Irkutsk station IRKT (in 2006, the SibNet network did not exist).

2 The Experiment Description

The basis of the experiment on May 4, 2006 was a single-pulse correction of the orbit of the ISS. The correction was made using 8 docking and orientation engines of the Progress spacecraft. The section of the ISS trajectory with active "Progress" engines ran from northern Mongolia almost to Hokkaido Island (Fig. 1). During the operation of the engines, the orbit altitude increased from 337 to 347 km. At the time of the experiment, the GEONET network included more than 1,200 stations, of which about 160 were located in Hokkaido. The engines were turned off at a distance of 180 km to the north-west of Hokkaido Island. At such a distance, the impact area of the engines could be seen through by several lines of sight (LOS) between navigational satellites and GEONET stations.
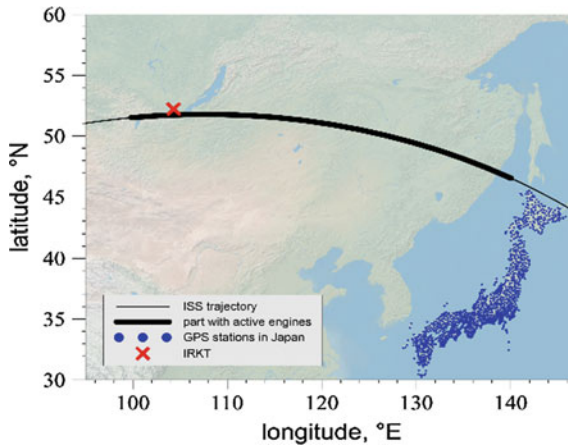
Fig. 1 The experiment geometry

On the day of the experiment, a moderate magnetic storm was observed. The Kp index reached the value of 5-, the Dst index dropped to −40 nT, the maximum value of Ae was 881 nT (Fig. 2a). The "Progress" engines were turned on near the beginning of the specified geomagnetic disturbance (Fig. 2b).

3 The Results of the Experiment According to the Irkutsk Station

We used the TEC obtained by the GPS receiver IRKT as initial data to search for a possible response to the operation of the Progress spacecraft engines. To remove slow variations, the TEC series were filtered in the range of periods of 0.5–5 min.

When analyzing the trajectories of ionospheric points (i.e., satellite-receiver intersection points with the main ionospheric maximum), it was found that the area of impact for the next few minutes after the engines were crossed by the LOSs of two GPS satellites: PRN14 and PRN25 (Fig. 3a). An analysis of the time series of TEC data obtained on the LOS "PRN14-IRKT" showed that 2–3 min after the operation of the engines, when the LOS crossed the area of influence, a negative disturbance was observed (Fig. 3b). The amplitude of the TEC disturbance was about –0.025 TECU. At the same time, according to the TEC, obtained on the LOS "PRN25-IRKT", which crossed the affected area 12 min later, such a disturbance is not observed (Fig. 3c).

To determine the spatial scale of the observed negative perturbation, we simulated the TEC response when the LOS "PRN14-IRKT" crossed the electron density perturbation caused by the operation of "Progress" engines (Fig. 4). The disturbance was simulated with the following assumptions:
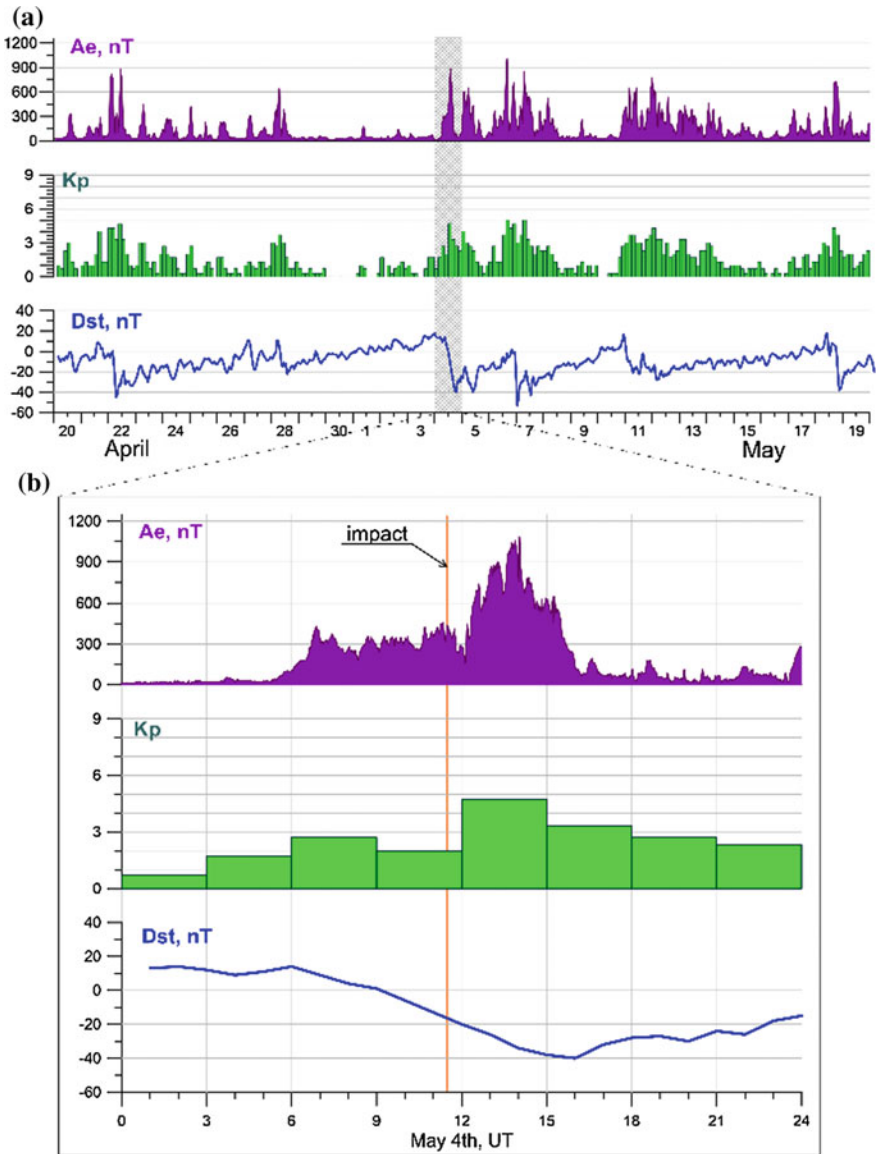
Fig. 2 Geomagnetic indices. Vertical line indicates the time of impact

1. disturbance does not change with time;
2. disturbance does not move;
3. disturbance is symmetric about the axis directed along the ISS trajectory;
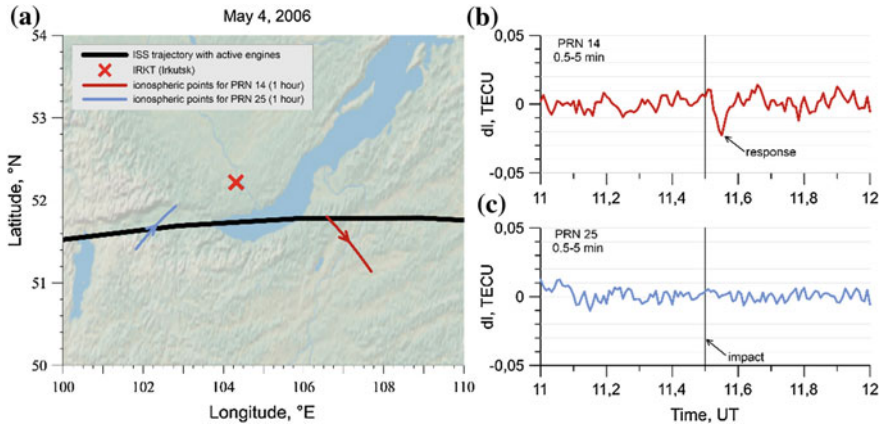
Fig. 3 The experiment map (panel a) shows the sections of the trajectories of the ionospheric points crossing the affected area. Marked areas correspond to the time interval from 11.5 to 12 UT. The series of TEC variations for the corresponding satellites are given in panels b and c. The vertical line indicates the moment of exposure

4. in the cross section, the electron density perturbation has a maximum on the axis of symmetry and decreases with distance from it according to the Gauss law.

As a result of the simulation, it was found that the transverse size of the disturbance is about 10 km. The decrease in electron density at the maximum of the disturbance is about 3.5×10^5 el/cm^3.
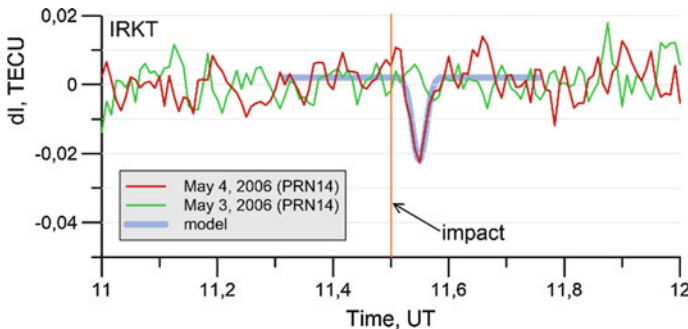
Fig. 4 Series of TEC variations obtained on the day of exposure (May 4) and on the previous day (May 3). The vertical line indicates the moment of exposure. The result of the simulation is represented by a thick line

The simulation results were obtained under the assumption that the disturbance was static. However, it can be seen that after a few minutes the disturbance amplitude becomes lower than the level of background variations (Fig. 3c). It is clear that under such conditions the assumption of the invariance of the observed disturbance can be taken with great reservations. The dynamics of such disturbances can be considered in more detail using data from a dense network of observation stations.

4 The Results of the Experiment According to the Japanese Network GEONET

For each 30-second interval, maps of TEC variations were constructed, where the color of the ionospheric point indicated the current value of TEC variations. These maps made it possible to visually present the spatial dynamics of the disturbance development (Figs. 5 and 6).

Figure 5 shows the position of all ionospheric points for all LOSs of the GEONET network at the moment near the time of ISS flight. It can be seen that the section of the ISS trajectory with the active engines passes along the edge of the region scanned by the LOSs. On the other hand, it is noticeable that in the area of
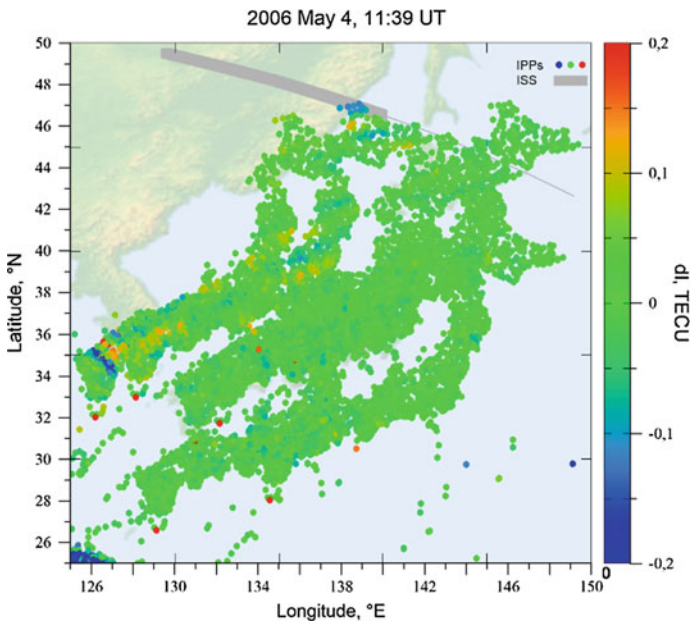
Fig. 5 The location of the ISS trajectory (gray line) and ionospheric points (colored dots) 3 min after exposure. The active part of the trajectory is indicated by a thick gray line. The dot color indicates the current value of TEC variations
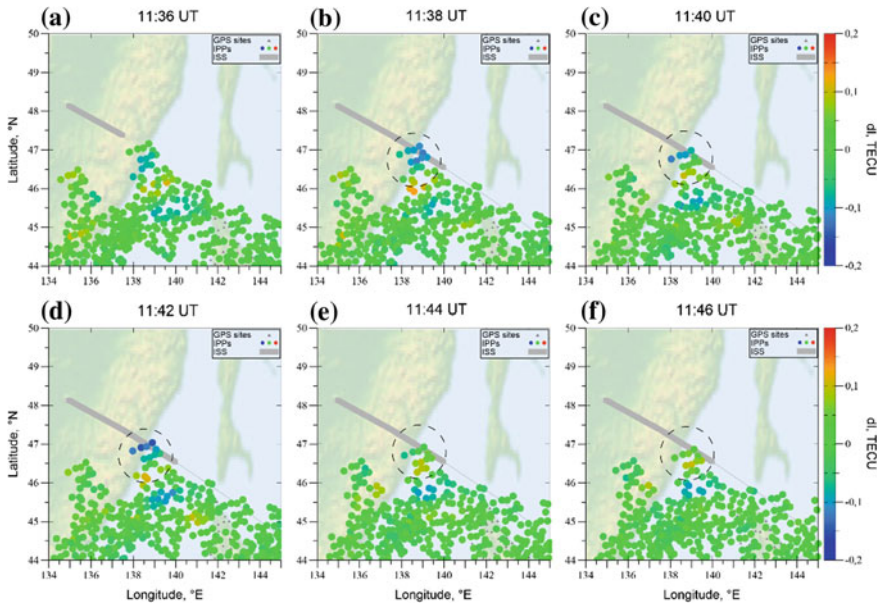
Fig. 6 The designation is the same as in Fig. 5. The triangles mark the position of the GEONET ground stations

influence there is a negative disturbance in the TEC series. Some disturbances not related to the operation of the engines are observed at a significant distance from the active part of the ISS trajectory (100 km or more).

As can be seen (Fig. 6), a negative perturbation in the TEC is observed in the area of impact (marked with a dashed line). The specified disturbance is recorded within 6 min (panels b, c, d, e). The maximum distance from the trajectory at which the disturbance is recorded is about 70 km.

The TEC series for the ionospheric points located closest to the impact area were analyzed in more detail (Fig. 7a).

A short-term drop in the TEC is observed on all data series of the nearby LOSs (Fig. 7b). Unfortunately, the registration of ionospheric parameters with a step of 30 s does not allow for a detailed analysis of the dynamics of the disturbance development. However, even from these data, it is clearly seen that after exposure, a negative perturbation is observed on all TEC rows with an amplitude of up to 0.03–0.04 TECU. Also, the resulting disturbance is well manifested in the data of the derivative of the TEC series (Fig. 7c). The magnitude of the negative impulse of the TEC derivative is about 0.2 TECU/min, which is significantly ($\sim$ 5 times) greater than the average neighboring values. Therefore, it can be concluded with certainty that the observed effects are related to the impact of "Progress" engines.

It should be noted that the series of variations and the derivative of TEC have oscillations with a period of 18–20 min, starting before the impact and continuing after. The same oscillations were observed on the LOSs, more than 100 km away
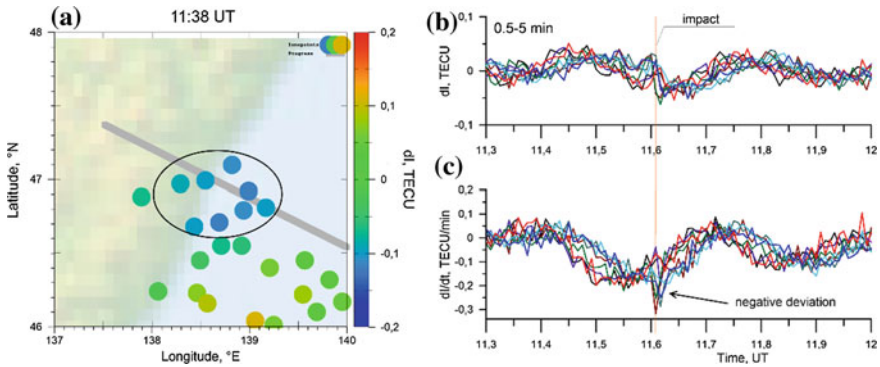
Fig. 7 Ionospheric points for the closest LOSs "satellite-receiver" (highlighted with an oval on panel a), and the corresponding filtered TEC variations (panel b) and the TEC derivative (panel c)

from the impact area. However, no similar sharp decrease in the TEC variations was observed on those LOSs, nor a negative impulse in the TEC derivatives series.

5 Conclusions

An analysis of the TEC series obtained at the receivers of the dense Japanese network GEONET showed that a negative disturbance occurred in the area of impact of the Progress jet engines. The amplitude of the disturbance, for given geometry of the relative position of the receivers and GPS satellites, is estimated at 0.03–0.04 TECU. According to the simulation data, the corresponding amplitude in electron density was estimated. It was about 3.5×10^5 el/cm^3.

The main reason for the change in the state of the ionospheric plasma during the operation of spacecraft engines is the creation of recombination centers that create a zone of low concentration of atomic oxygen [6].

The high density of the GEONET network allowed us to estimate the spatial transverse scales of the disturbance. The amplitude of the disturbance decreases with distance from the area of influence, and at a distance of 60–70 km becomes less than the amplitude of the background oscillations. Accordingly, the transverse size of the disturbance, observed using GEONET, is about 120–140 km. The duration of the observed disturbance does not exceed 8 min.

The obtained data are consistent with the results of determining the disturbance parameters according to the Irkutsk station data. So on the LOS passing through the area of influence after 11–12 min, no disturbance is recorded, which stands out from the background variations. However, a negative disturbance is observed on the closest LOS 1.5–2 min after exposure. The transverse disturbance scale observed according to the data of the Irkutsk station was about 10 km.

The discrepancy in the estimation of the scales obtained from the Irkutsk and Japanese data may be caused by the elongation of the disturbance along the Earth's magnetic field. Then the angle dependence of the observed transverse size of the disturbance on the relative position of LOSs and the magnetic field at the height of the impact will naturally occur.

To resolve this uncertainty, it is necessary to simultaneously register the disturbance according to several LOSs that intersect the area of influence with different angle conditions.

Our results may be useful for developing new and correcting existing ionospheric models.

The results obtained are consistent with the experimental results obtained earlier on the SibNet network.

References

1. Potekhin, A.P., Khakhinov, V.V., Medvedev, A.V., Kushnarev, D.S., Lebedev, V.P., Shpynev, B.G.: Active space experiments with the use of the transport spacecraft "Progress" and Irkutsk IS Radar. In: Proceedings of PIERS 2009, pp. 223–227. The Electromagnetics Academy, Moscow (2009)
2. Ishin, A.B., Perevalova, N.P., Voeykov, S.V., Khakhinov, V.V.: First results of registering the ionospheric disturbances according to SibNet network of GNSS receivers in active space experiments. Sol.-Terr. Phys. **3**(4), 74–82 (2017). https://doi.org/10.12737/stp-34201708
3. Khakhinov, V.V., Shpynev, B.G., Lebedev, V.P., Kushnarev, D.S., Alsatkin, S.S., Khabituev, D.S.: Radiosounding of ionospheric disturbances generated by exhaust streams of the transport spacecraft "Progress" engines. In: Proceedings of PIERS 2012, pp. 1168–1171. The Electromagnetics Academy, Moscow (2012)
4. Mikhalev, A.V., Khakhinov, V.V., Beletskii, A.B., Lebedev, V.P.: Optical effects of the operation of the onboard engine of the Progress M-17M spacecraft at thermospheric heights. Cosm. Res. **54**(2), 105–110 (2016). https://doi.org/10.1134/S0010952516020039
5. Lipko, Y.V., Pashinin, A.Y., Rakhmatulin, R.A., Khakhinov, V.V.: Geomagnetic effects caused by rocket exhaust jets. Sol.-Terr. Phys. **2**(3), 43–55 (2016). https://doi.org/10.12737/22284
6. Shpynev, B.G., Alsatkin, S.S., Khakhinov, V.V., Lebedev, V.P.: Investigating the ionosphere response to exhaust products of Progress cargo spacecraft engines on the basis of Irkutsk incoherent scatter radar data. Sol.-Terr. Phys. **3**(1), 114–127 (2017). https://doi.org/10.12737/article_58f9722a233f33.55738104
7. Ishin, A.B., Perevalova, N.P., Voeykov, S.V., Khakhinov, V.V.: Complex analysis of the ionospheric response to operation of "Progress" cargo spacecrafts according to the data of GNSS receivers in Baikal region. Sol.-Terr. Phys. **3**(4), 83–92 (2017). https://doi.org/10.12737/stp-34201709

Acoustic Fluidization During Impact Crater's Formation

Boris Ivanov

Abstract

The explanation of impact crater morphology and, possibly, rock avalanche's long runout demands a temporary dry friction reduction. We review main assumptions for one of main models proposed to explain this phenomenon, namely the acoustic fluidization (AF) model. The governing model parameter is the decay time for internal oscillations assumed to be generated in fragmented rock bodies under high strain rates, typical for growing impact craters and moving rock avalanches. Using numerous published results for impact crater on various planetary bodies with different gravity acceleration, we try to improve our understanding of some critical AF model issues.

1 Introduction

The analysis of various geophysical problems (like fault's propagation, landslide's motion, etc.) allows us to assume the dry friction decrease for interaction of adjacent rock blocks at high strain rates. Many models are proposed to explain dry friction reduction for shear strain between rock surfaces [1] or in granulated media [2]. The prominent natural event is the impact crater formation, observed on all planets and satellites with solid (icy or rocky) surface in our Solar System. Small impact craters are simple bowl-shaped depressions easily simulated at laboratory

B. Ivanov (✉)

Institute for Dynamics of Geospheres, RAS, Leninsky prospect 38-1, 119334 Moscow, Russia
e-mail: baivanov@idg.chph.ras.ru

497

impacts or surface HE bursts. Complex impact craters have uplifted central mounds formed of rocks, initially buried at depths of $D/10$, where D is the crater diameter. About 30 years ago researches realized that the formation of complex craters in the observed diameter range cannot be explained without an assumption of the temporary dry friction decrease in rocks around a forming impact crater [3, 4]. The acoustic fluidization (AF) model has been proposed [5] to explain the temporary friction loss with oscillation of rock blocks. The AF model has been incorporated in hydrocodes [6].

The AF model assumes that internal block oscillations in the crater-forming rock flow periodically increase and diminish the local pressure, p, at the value $p_{vib}(t)$, estimated as $p_{vib} = \rho \times c_{snd} \times v_{vib} \times \sin(2\pi t/T_{vib})$, where ρ is the material density, c_{snd} is the bulk sound speed, v_{vib} and T_{vib} are amplitude and period of internal oscillations. When two fictional blocks with friction f between them are loaded with the local shear stress $\tau > f \times [p - p_{vib}(t)]$, one block slides over the other block. The AF model recalculates the difference $p - \rho \times c_{snd} \times v_{vib}$ into an effective quasi-viscosity, expressing the start-stop motion of blocks due to periodic sliding [6]. The key parameter of the AF model is the decay time, T_{dec}, expressing how quick the assumed internal block oscillations decay, restoring normal static friction between blocks: $v_{vib} \sim \exp(t/T_{dec})$.

Multiple numerical modeling revealed that the decay time, T_{dec}, is the main parameter, controlling the final collapsed crater shape. The aim of presented work is the analysis of best fit T_{dec} values for numerical models of impact cratering on planetary bodies with various values of a surface gravity.

2 Models with Fitted AF Parameters

2.1 The Earth

In the last two decades a set of terrestrial impact craters have been analyzed with the help of the numerical modeling. To start the modeling, parameters of the AF model have been estimated with the simple scaling technique, described above. However, in most cases the first guess has been verified and improved with a parametric model runs to find the best similarity between available geological and geophysical data (including the deep drilling study) and the assumed initial crater profile. Due to the active terrestrial geologic environment, erosion and sedimentation often shadowed the crater geometry in contrast with extraterrestrial impact craters.

The best available data about complex crater initial geometries are available for young craters (like Bosumtwi, Ghana, $D \approx 10$ km, $T_{dec} \approx 8$ s [7]) or for craters buried with younger sediments (e.g. Steinheim, Germany, $D \approx 3.4$ km, $T_{dec} \approx 6$ s [8] and Puchezh-Katunki, Russia, $D \approx 40$ km, $T_{dec} \approx 45$ s [9]). In [7–9] the critical AF decay parameter, T_{dec}, has been fitted by trials and errors to reach the best reproduction of the available crater profiles and shock pressure levels, recorded in drill core samples. Three mid-size craters (Ries, Germany, $D \approx 24$ km; Haughton,

Canada, $D \approx 23$ km; and El'gygytgyn, Russia, $D \approx 18$ km) have been modeled in [10] using the same value of $T_{dec} = 30$ s. The West Clearwater crater (Canada) is modeled in [11] (D from 35 to 40 km, T_{dec} around 60 s). Four largest craters (Popigai, Russia, $D \approx 90$ km, $T_{dec} = 90$ s, and so called Big Three: Vredeford, South Africa, Sudbury, Canada, and Chicxulub, Mexico, all three with $D \approx 180$ km and T_{dec} from 120 to 180 s) has been modeled in [12] with the model parameter fit to available surface geological data. The Chicxulub crater is a permanent target for the numerical modeling, as the youngest (65 Ma) and largest ($D \sim 180$ km) well preserved impact crater [13].

To illustrate the process of the AF model parameter fitting Fig. 1 compares model crater profiles, computed to simulate the Puchezh-Katunki crater formation. A set of model runs has been done for a double-layer target (2 km of sediments over granite basement). The spherical rock (granite) projectile impacts vertically with the velocity of 16 km s^{-1}. Target materials are described with Tillotson's equation of state [14]. The brittle rock behavior is simulated with the model [15]. In all model runs shown in Fig. 1 all parameters are the same except the assumed AF oscillation's decay time.

Figure 1 illustrates that without the AF model we get a simple crater. In this case we observe considerable landslides from crater walls, filling the initial transient cavity ~ 8 km in depth. However, rocks, forming the floor of the transient cavity stay at this depth, being buried under the wall collapsed material. The AF model implementation results in the transient cavity floor uplift into position shown in Fig. 1. The best fit to observed crater structure allows us to choose $T_{dec} \sim 45$ s [16].
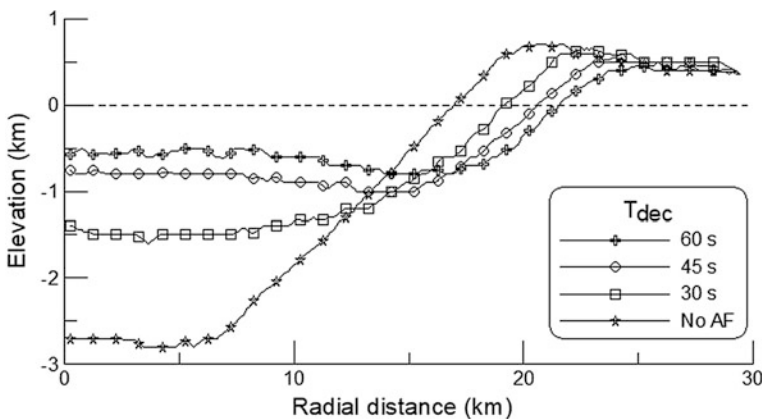
Fig. 1 Modeled crater profiles for the Puchezh-Katunki impact crater formation. The projectile of 3.2 km in diameter impacts vertically the two-layer target, creating a transient cavity of about 9 km depth and 12 km radius. Without the AF usage the final crater is formed mostly by the crater wall collapse, resulted in a simple crater of about 3 km depth and 17 km radius. The nominal AF model produces the final crater with less than 1 km depth and the radius on the pre-impact level of about 21 km (42 km in diameter). The real crater is about 40 km in diameter. The variation of the T_{dec} parameter from 30 to 60 s significantly change the model crater profile

2.2 The Moon and Mars

The systematic modeling of lunar craters with diameters near the simple-to-complex crater transition is published in [17]. Here authors present a wide variation of the AF model parameters. Most of modeling for lunar craters has been done for large impact basins, where the AF model usage is not as critical as the thermal state of the Moon during the late heavy bombardment period [18, 19].

An impact craters on Mars has been modeled to estimate the sedimentary infilling of the Gusev crater with diameter $D \sim 170$ km [20].

2.3 Asteroid Vesta

The largest impact structure named Rheasilvia near South Pole of the asteroid Vesta has been studied during the DAWN space mission [21]. The small size of the asteroid (diameter of 520 km) results in the low gravity acceleration of about 0.25 m s^{-2} (~ 0.025G). The simple-to-complex impact crater morphology is estimated in the crater diameter range of 30–40 km [22], the central peak is clearly visible in craters with diameters more than ~ 60 km [23].

Figure 2 demonstrates a couple of model runs to fit AF parameters to reproduce the measured crater cross-section. The transient crater (depth ~ 70 km, diameter ~ 120 km) collapses to the final crater ~ 19 km in depth, widening to 220–230 km in radius (final rim crater diameter of 440–460 km). The AF decay tine T_{dec} is assumed to be equal 900 s. Using tabulated modeling data from [24] we illustrate the model crater parameter variations in a wide range of T_{dec}.

3 Generalization of Impact Crater Modeling Results

The numerical modeling runs for various planetary bodies allow us to generalize the best fit values of the AF model decay time, T_{dec}, in a wide range of gravity accelerations at surfaces of these bodies. The plot of T_{dec} versus the final complex crater diameter is shown in Fig. 3. It is interesting to note, that all available data tend to be aligned along a single line which may be written as

$$T_{dec}(s) \approx 1.2D \text{ (km)} \tag{1}$$

We should note that model results shown in Fig. 3 differ not only in values of a surface gravity accelerations, but in the assumed impact velocity corresponding to planetary body's orbital parameters. The average impact velocity on selected planetary bodies vary from ~ 20 km s^{-1} on Earth and the Moon to ~ 10 km s^{-1} on Mars, and to ~ 4.5 km s^{-1} on the Vesta asteroid.
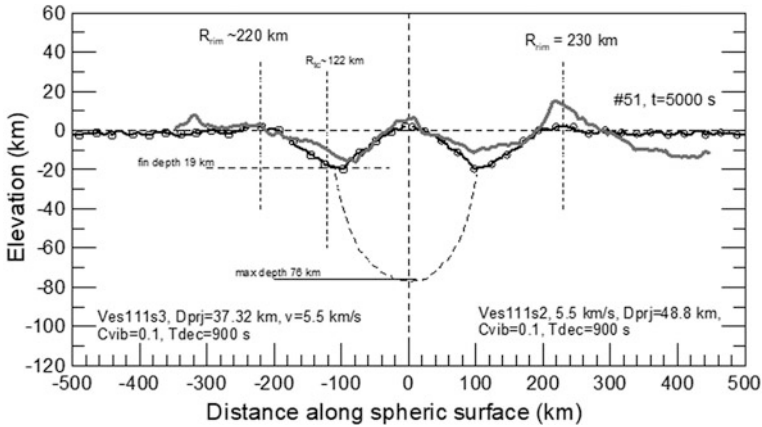
Fig. 2 The observed cross-section of the Rheasilvia impact crater on Vesta [21], thick gray curve in the comparison with two model results from [24] (black curves with signs). The left part (negative distances) is for projectile diameter D_{prj} = 37 km, the right part (positive distances) is for D_{prj} = 49 km. Impact velocity is 5.5 km s^{-1}, the decay time T_{dec} = 900 s for both variants. Details of the modeling are published in [24]
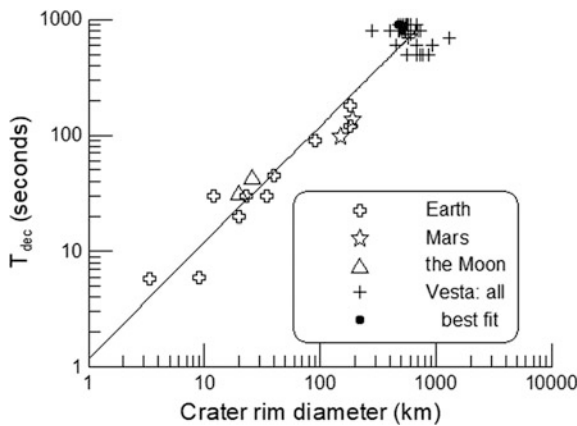
Fig. 3 Best fit values of the AF model T_{dec} parameter as a function of the modeled rim crater diameter for planetary bodies with various surface gravity acceleration, g (measured in m s^{-2}): earth (g = 9.81), mars (g = 3.72), the moon (g = 1.62), asteroid vesta (g = 0.22)

4   Discussion and Conclusion

The data presented in Fig. 3 were unexpected. While the surface gravity in our data collection varies a factor of 50, and the impact velocity varies a factor of 4, the best T_{dec} depends mostly of the final crater size. The difference in the impact velocity

results in the difference in the crater size to the impactor size ratio. It means that the projectile size does not seem to be a good scaling factor for AF parameters to begin trial model runs.

Previously authors [25] have recommended to use the projectile size to scale AF parameters from one crater to another. This recommendation was based on the original Melosh's note [26], page 96, that the AF internal oscillation period is defined as the impact velocity divided by the projectile size. While for the relatively narrow range of assumed impact velocities on Earth (typically 15–18 km s^{-1} in early modeling), the exact recipe to choose the AF parameters was not as critical, the modeling for low-gravity bodies (such as the Moon, Mars, and large asteroids) the proper starting AF parameters is important.

The alternative approach [27] proposes to scale the AF model block size linearly with the transient cavity size. All other parameters in [27] are derived from standard assumptions of similarity and constancy of the quality factor, controlled the decay rate of AF internal oscillations.

According to [27] the key parameter of the AF model is the characteristic block size, h_b. The internal oscillation period T_{osc} is proportional to h_b, and the decay time is proportional to the quality factor Q: $T_{dec} \sim QT_{osc}$. Hence, the model [27] allows us to assume that $T_{dec} \sim h_b$. If the block size h_b is proportional to the transient cavity diameter, D_{tc}, we need to check how the final rim diameter of the collapsed complex crater, D, depends on D_{tc}.

Basing on geology of terrestrial craters Croft [28] proposed the relation between D and D_{tc} for crater diameters above the simple-to-complex crater transitional diameter, D_{sc}:

$$D_{tc} = D_{sc}^{0.15} D^{0.85} \tag{2}$$

equivalent to the inverse relation

$$D = D_{tc}^{-0.18} D_{tc}^{1.18}. \tag{3}$$

In the time of the paper [28] publication, the clear definitions for D and D_{tc} were unclear yet. For example, for most terrestrial craters the rim diameter value is unknown due to relatively fast rim erosion. One could assume that in most cases the measured with geological maps crater diameters are closer to so called "apparent" diameters D_a, i.e. diameters measured at the pre-impact level. This study should be extended in a future. Here we only refer the model experience accumulated for studied terrestrial impact craters.

Following a short-generalized summary in [29], Fig. 3 on page 336, we note that numerical models for terrestrial craters with rim diameters D from $\sim$3 to $\sim$200 km result in an approximately linear $D(D_{tc})$ dependence: $D \approx 1.45 \times D_{tc}^{1.07}$, where diameters are measured in km. A similar relation for apparent model crater diameters has a little bit larger exponent: $D_a \approx 1.12 \times D_{tc}^{1.1}$, what is close to the Eq. 3 cited above.

A weak deviation from the direct proportionality indicates, that one should expect slightly non-linear relation between T_{dec} and D. In addition, the value of D_{sc} in Eqs. 2 and 3 is a function of gravity. The widely used Pike's relation $D_{sc} \sim g^{-1}$ [30] after new observations [22, 23] seems to need more attention, first of all one should compare how various authors define simple to complex crater transition.

Concluding the presented short communication, we should outline the main result—the key AF model parameter, namely the decay time of internal rock block oscillations T_{dec} in successful model runs is roughly proportional to the final model crater rim diameter. This fact seems to support the published earlier assumption that the model block size should be scaled with the transient cavity size, not only with the projectile size.

However, the accurate description of the AF influence at the simple/complex transition, started in [6, 25], is still under consideration, as well as possible AF effects for large simple impact crater formation.

References

1. Rice, J.R.: Heating and weakening of faults during earthquake slip. J. Geophys. Res. **111**(B5), B05311: 1–29 (2006)
2. Jop, P., Forterre, Y., Pouliquen, O: A constitutive law for dense granular flows. Nature **441** (7094), 727–730 (2006)
3. Melosh, H.J.: Crater modification by gravity—a mechanical analysis of slumping. In: Pepin, R.O., Merrill, R.B., Roddy, D.J. (eds.) Impact and Explosion Cratering: Planetary and Terrestrial Implications, pp. 1245–1260. Pergamon Press, NY (1977)
4. McKinnon, W.B.: An investigation into the role of plastic failure in crater modification. In: Lunar and Planetary Science Conference 9th (Geochimica et Cosmochimica Acta, Supplement 10), pp. 3965–3973 (1978)
5. Melosh, H.J.: Acoustic fluidization—a new geologic process. J. Geophys. Res. **84**(B13), 7513–7520 (1979)
6. Melosh, H.J., Ivanov, B.A.: Impact crater collapse. Annual Rev. Earth Plant. Sci. **27**, 385–415 (1999)
7. Ferriere, L., Koeberl, C., Ivanov, B.A., Reimold, W.U.: Shock metamorphism of Bosumtwi impact crater rocks, shock attenuation, and uplift formation. Science **322**(5908), 1678–1681 (2008)
8. Ivanov, B.A., Stöffler, D.: The Steinheim impact crater, Germany: modeling of a complex crater with central Uplift. In: 36th Annual Lunar and Planetary Science Conference. Abs. #1443. LPI, Houston, TX (2005)
9. Ivanov, B.A.: Deep drilling results and numerical modeling: Puchezh-Katunki impact crater, Russia. In: Proceedings of Lunar and Planetary Science Conference, Abs. #1286. Lunar and Planetary Institute, Houston, TX (2002)
10. Collins, G.S., Kenkmann, T., Osinski, G.R., Wunnemann, K.: Mid-sized complex crater formation in mixed crystalline-sedimentary targets: Insight from modeling and observation. Meteorit. Planet. Sci. **43**(12), 1955–1977 (2008)

11. Rae, A.S.P., Collins, G.S., Grieve, R.A.F., Osinski, G.R., Morgan, J.V.: Complex crater formation: insights from combining observations of shock pressure distribution with numerical models at the West Clearwater Lake impact structure. Meteorit. Planet. Sci. **52** (7), 1330–1350 (2017)

12. Ivanov, B.A.: Numerical modeling of the largest terrestrial meteorite craters. Sol. Syst. Res. **39**(5), 381–409 (2005)

13. Morgan, J.V., Gulick, S.P.S., Bralower, T., Chenot, E., Christeson, G., Claeys, P., Cockell, C., Collins, G.S., Coolen, M.J.L., Ferrière, L., Gebhardt, C., Goto, K., Jones, H., Kring, D.A., Le Ber, E., Lofi, J., Long, X., Lowery, C., Mellett, C., Ocampo-Torres, R., Osinski, G.R., Perez-Cruz, L., Pickersgill, A., Poelchau, M., Rae, A., Rasmussen, C., Rebolledo-Vieyra, M., Riller, U., Sato, H., Schmitt, D.R., Smit, J., Tikoo, S., Tomioka, N., Urrutia-Fucugauchi, J., Whalen, M., Wittmann, A., Yamaguchi, K.E., Zylberman, W.: The formation of peak rings in large impact craters. Science **354**(6314), 878–882 (2016)

14. Melosh, H.J: Impact Cratering—A Geologic Process, 245 pp. Oxford, New York (1989)

15. Collins, G.S., Melosh, H.J., Ivanov, B.A.: Modeling damage and deformation in impact simulations. Meteorit. Planet. Sci. **39**(2), 217–231 (2004)

16. Ivanov, B.: Geologic Effects of Large Terrestrial Impact Crater Formation. In: Adushkin, V. V., Nemchinov, I.V. (eds.) Catastrophic Events Caused by Cosmic Objects, pp. 163–205. Springer, Berlin (2008)

17. Silber, E.A., Osinski, G.R., Johnson, B.C., Grieve, R.A.F.: Effect of impact velocity and acoustic fluidization on the simple-to-complex transition of lunar craters. J. Geophys. Res. Planets **122**(5), 800–821 (2017)

18. Ivanov, B.A., Melosh, H.J., Pierazzo, E.: Basin-forming impacts: Reconnaissance modeling. In: Gibson, R.L., Reimold, W.U. (eds.) GSA Special Papers 465, pp. 29–49. Geological Society of America, Boulder, Colorado, USA (2010)

19. Kring, D.A., Kramer, G.Y., Collins, G.S., Potter, R.W.K., Chandnani, M.: Peak-ring structure and kinematics from a multi-disciplinary study of the Schrödinger impact basin. Nat. Commun. **7** (Article #13161), 1–10 (2016)

20. Parker, M.V.K., Zegers, T., Kneissl, T., Ivanov, B., Foing, B., Neukum, G.: 3D structure of the Gusev crater region. Earth Plan. Sci. Lett. **294**(3–4), 411–423 (2010)

21. Schenk, P., et al.: The geologically recent giant impact basins at Vesta's south pole. Science **336**, 694–697 (2012)

22. Hiesinger, H., Marchi, S., Schmedemann, N., Schenk, P., Pasckert, J. H., Neesemann, A., O'Brien, D. P., Kneissl, T., Ermakov, A.I., Fu, R.R., Bland, M.T., Nathues, A., Platz, T., Williams, D.A., Jaumann, R., Castillo-Rogez, J.C., Ruesch, O., Schmidt, B., Park, R.S., Preusker, F., Buczkowski, D.L., Russell, C.T., Raymond, C.A.: Cratering on ceres: implications for its crust and evolution. Science **353**(6303), aaf4759, 1–8 (2016)

23. Kramer, G.Y., Schenk, P.: Morphologies of Fresh Craters, Lunar Analogs, and the Simple-Complex Transition on Vesta, in 46th Lunar and Planetary Science Conference, Abs. #2571. LPI, Woodland, TX (2015)

24. Ivanov, B.A., Melosh, H.J.: Two-dimensional numerical modeling of the Rheasilvia impact formation. J. Geophys. Res. Planets **118**(7), 1545–1557 (2013)

25. Wünnemann, K., Ivanov, B.A.: Numerical modelling of the impact crater depth–diameter dependence in an acoustically fluidized target. Planet. Space Sci. **51**(13), 831–845 (2003)

26. Melosh, H.J.: The physics of very large landslides. Acta Mech. **64**(1), 89–99 (1986)

27. Ivanov, B.A., Artemieva, N.A.: Numerical modeling of the formation of large impact craters. In: Koeberl C., MacLeod K. (eds.) Catastrophic Events and Mass Extinctions: Impact and Beyond, Geological Society of America Special Papers 356, pp. 619–630, GSA, Boulder, Colorado (2002)

28. Croft, S.K.: The scaling of complex craters. J. Geophys. Res. **90**, C828–C842 (1985)

29. Werner, S.C., Ivanov, B.A.: Exogenic dynamics, cratering, and surface ages (Chapter 10.10). In: Schubert, G. (ed.) Treatise on Geophysics, 2nd edn, pp. 327–365. Elsevier, Oxford (2015)
30. Pike, R. J.: Control of crater morphology by gravity and target type—mars, earth, moon. In: Proceedings of the Lunar and Planetary Science Conference 11th, pp. 2159–2189. Pergamon Press, New York (1980)

Dust Particle Dynamics in Convective Vortices Near the Surface of the Earth: Comparison with Mars

Yulia Izvekova 🄳, Sergey Popel 🄳 and Oleg Izvekov 🄳

Abstract

We study dynamics of dust particles in convective vortices near the surface of Earth and Mars. Dust vortices called dust devils appear over the hot surface as a result of convective instability and are frequent phenomena for both planets. We use similarity theory to find similar scales and velocities for vortices on both planets. Collisions and friction between dust particles in a vortex lead to charging of dust particles due to triboelectric effect. As a result small particles acquire negative charges and large particles become positively charged. This leads to spatial charge separation in an upward flux and electric field generation. Electric fields in terrestrial dust vortices have been repeatedly measured. We show the model of electric field generation in a vortex and study the dynamics of dust with taking into account the electric field. We discuss the conditions under which the breakdown values of the electric field in the Martian atmosphere can be achieved. Probability of lightning phenomena in dust events on Mars and consequences of that are discussed.

Y. Izvekova (✉) · S. Popel
Space Research Institute, Russian Academy of Sciences, ul. Profsoyuznaya 84/32, 117997 Moscow, Russia
e-mail: besedina_yn@mail.ru

S. Popel
National Research University Higher School of Economics, 20 Myasnitskaya Ulitsa, 101000 Moscow, Russia

O. Izvekov
LLC "Oil &Gas Center MIPT", Institutsky Pereulok 9, 141700 Dolgoprudny, Russia

507

1   Introduction

Dust vortices called dust devils are well-formed vortex formations with characteristic horizontal dimensions from half a meter to one hundred meters and from several meters to hundreds of meters in height in the Earth's atmosphere. Large eddies are much less common than small ones. Such vortices are clearly visible, as they capture and carry sand and dust from the surface. The main parameters of dust vortices on the Earth, such as dimensions, vertical and horizontal velocities, electric and magnetic fields are measured in experiments on the territory of deserts, where these eddies often arise. Thus, in terrestrial vortices, electric fields of 4.35 kV/m were measured for a vortex with a diameter of 7 m [1], 20 kV/m for a vortex with a diameter of 30 m [2]. The values of electric fields for terrestrial vortices can reach 150 kV/m, without reaching breakdown values. In rarefied atmosphere of Mars breakdown values of electric fields are lower—near 25 kV/m [3] and the question of values of possible electric fields generated in dust events remains relevant. On the other side, no direct measurements of electric fields on the surface of the Red planet have been provided yet.

Dust plays a very sufficient role in a heat balance in the rarefied and arid Martian atmosphere. Dust devils, which are regularly observed on the surface of Mars along with dust storms, raise dust particles to the Martian atmosphere. Martian dust devils are large than terrestrial with horizontal dimensions reaching some kilometers and vertical dimensions up to ten kilometers. Strong electrification in these vortices suggests that in some cases breakdowns may occur [4, 5]. According to [6], upon reaching the breakdown values of the electric field, when $pd < 200$ (where p is the pressure in Torr, d is the distance between the electrodes in cm), a glow discharge occurs. For values $pd > 10^3$ the discharge occurs according to the streamer-leader mechanism (spark discharge). For the Martian atmosphere $pd \sim 10^5$ (with a discharge length of about 1 km), so the second situation takes place.

Here we discuss similarity between the terrestrial and Martian vortices, electrification in the dust devils, dust dynamics and possible results of achieving high values of electric fields in the Martian atmosphere.

2   Similarity of Dust Vortices on the Earth and Mars

In the Earth atmosphere people have many abilities to study dust devils experimentally. Despite the fact that Martian dust devils are being observed and discussed for some tens of years there are no measurements of vertical velocities and inner structure of the vortices. Knowledge of similarity criteria can help in studying Martian vortices. The similarity theory for Martian and terrestrial dust devils has been built in [7], here we show some consequences.

The main role in the formation of dust vortices on Mars and the Earth plays thermal convection. Let us estimate the parameters (characteristic scale and velocity of gas flow) of a vortex on Mars, which is similar to a typical vortex on Earth. Let

l and τ be the characteristic length and time scales, ΔT and P are the maximum temperature difference and pressure, $\nu,$ $\chi,$ and β are kinematic viscosity, thermal conductivity and thermal expansion coefficient of the atmosphere, respectively, g is gravity. Under free thermal convection conditions the Peclet number vl/χ or the Reynolds number vl/v can be the form of the dimensionless velocity v, and the similarity criterion is the combination of Grashof Gr and Prandtl Pr criteria [8]. The Grashof criterion (number) $\mathrm{Gr} = gl^3\beta\Delta T/v^2$ is a measure of the ratio of the Archimedean force caused by the nonuniform distribution of the gas density in a nonuniform temperature field and the viscosity forces. Prandtl criterion $\mathrm{Pr} = v/\chi$ characterizes the ratio between the intensities of molecular momentum transfer and heat transfer by thermal conductivity, it is almost independent of temperature for gases, about 0.72 for diatomic gases, and 0.75–1 for polyatomic gases. Since the developed dust vortex can be attributed to the situation when the inertial force has a large relative value compared to the viscosity effects, we take the dimensionless velocity in the form $\tilde{\mathbf{v}} = \mathbf{v}l/\chi$, and as the similarity criterion we use the value $\mathrm{Gr}\cdot\mathrm{Pr}^2$, rather than Gr and Pr separately. In our case dimensionless velocity looks like:

$$\mathbf{v} = \frac{\chi}{l}f\left(\frac{\mathbf{x}}{l},\ \mathrm{Gr}\cdot\overset{2}{\mathrm{Pr}}\right).$$

We use the following parameter ratios (subscripts E and M denote the Earth and Mars respectively):

$$\frac{g_E}{g_M} = 2.65,\quad \frac{\beta_E}{\beta_M} \approx 1,\quad \frac{T_M^3}{T_E^3} \approx \left(\frac{200}{300}\right)^3 \approx 0.3,\quad \frac{P_E^2}{P_M^2} \approx 10^4.$$

Let us take $\Delta T_E/\Delta T_M \approx 1$, taking into account that the maximum temperature change in Martian vortices is about 5–6 °C [9], as well as in terrestrial vortices.

Assuming for similar vortices that $\left(\mathrm{Gr}\cdot\mathrm{Pr}^2\right)_E = \left(\mathrm{Gr}\cdot\mathrm{Pr}^2\right)_M$, we obtain the ratio between the characteristic scales $l_M \approx 17l_E$. Further, from the equality of dimensionless velocities for the Earth and Mars we obtain the ratio of the characteristic speeds $v_M \approx 2.6v_E$. The values obtained do not contradict the available data. Thus, the vertical speeds in the earth vortices have values of the order of 10 m/s, and the speeds in the Martian vortices according to estimates made on the basis of measurements of the landing gears Viking 1 and Viking 2 [10] are several times larger.

3 Charging of Dust Particles and Electric Fields in Dust Devils

Collisions and friction between dust particles in a vortex lead to charging of dust particles due to triboelectric effect. As a result small particles acquire negative charges and large particles become positively charged [3, 11]. This leads to spatial charge separation in an upward flux and electric field generation.

We study the following simplified model of the vortex. Let the upper half of the vortex be negatively charged, and the lower positive, with the absolute value of the charge $|Q^+| = |Q^-| = Q$ growing in time. The absolute value of the average charge density is $\rho_q = Q/V_{1/2}$, with $V_{1/2}$ being the volume of the half of the vortex. The value of the rate of change of the average density $\partial \rho_q/\partial t$ may vary depending on the efficiency of tribocharging and the rate of charge separation. Assuming electroneutrality of the vortex, i.e. $n_L \Delta q_L = n_S \Delta q_S$, where n_L, n_S, Δq_L, Δq_S are densities and average charges of large and small particles, respectively, we estimate $\partial \rho_q/\partial t$ as follows:

$$\frac{\partial \rho_q}{\partial t} = \frac{2 n_L \Delta q_L \Delta u}{h},$$

where Δu is the difference of the vertical component of the velocities of large and small particles and h is the height of the vortex column. For $\Delta u = 1$ m/s [12], $n_L = 5 \cdot 10^6$ m^{-3} [3], $\Delta q_L = 5 \cdot 10^{-14}$ C (for particle of the radius of 50 μm) [3, 12], $h = 10^4$ m we get $\partial \rho_q/\partial t = 5 \cdot 10^{-11}$ C m^{-3} s^{-1}. Note that the obtained estimate for the value $\partial \rho_q/\partial t$ can vary significantly up or down.

Spatial charge separation in an upward flow leads to the appearance of an electric field. For building a model of electric field **E** distribution taking into account atmospheric conductivity σ we solve Poisson's equation for potential φ and the charge continuity equation for dust particles density ρ_q:

$$\Delta \varphi = -\frac{\rho_q}{\varepsilon_0}$$

$$\frac{\partial \rho_q}{\partial t} + (\nabla \sigma) \cdot \mathbf{E} + \frac{\sigma \rho_q}{\varepsilon_0} = 0$$

Here $\varepsilon_0 = 8.85 \cdot 10^{-12}$ F/m. The vortex is represented in the form of a cylinder, within which the spatial separation of the charge occurs, at the initial moment of time the charge is zero. Accounting for the conductivity of the atmosphere limits the maximum charge and electric field. The charge in the vortex is given by two cylinders, in which the charge density value decreases from the center of the cylinder along a Gaussian curve with a smooth transition according to a linear law

from a positive charge to a negative vertical. At each time step Δt the average charge density $\bar{\rho}_q$ increases at the bottom of the vortex and decreases at the top by an amount $(\partial \bar{\rho}_q / \partial t)\Delta t$. Then the electric field and charge relaxation are calculated.

Figure 1a presents the results of the calculation of the electric field values for an intense Martian vortex with an average charge separation rate $\partial \bar{\rho}_q / \partial t = 5.5 \cdot 10^{-11}$ C/(m^3 s), a core radius of 1.5 km and a height of 10 km in the saturation state, i.e., 10 s after the start of the charge separation process. Atmospheric conductivity is accepted $\sigma = 5 \cdot 10^{-12}$ S/m . It should be noted that the conductivity is inversely proportional to the maximum field.

Figure 1b shows the evolution of the maximum value of the electric field in the process of charge separation. The maximum charge accumulated in the half of the vortex, corresponding to $\partial \bar{\rho}_q / \partial t = 7.4 \cdot 10^{-11}$ C/(m^3 s), is equal to 5.37 C, and corresponding to $\partial \bar{\rho}_q / \partial t = 5.5 \cdot 10^{-11}$ C/(m^3 s), is equal to 4.02 C. It can be seen that for large values of $\partial \bar{\rho}_q / \partial t$ breakdown values of the electric field (about 25 kV/m) can be achieved, and at lower rates of charge separation, the maximum field is set below breakdown values. In the case when the field in the vortex reaches breakdown values, one can speak about the possibility of lightning discharges in Martian dust devils.

To study dust dynamics in dust devils we use model [13, 14], where dust particle is moving under the action of the gravity force, the electrostatic force and the hydrodynamic force acting from the vortex structure. Particles are efficiently uplifted by both the terrestrial and Martian vortices. The trajectory for particle of 1 μm carrying the charge of $-1.6 \cdot 10^{-17}$ C in the typical terrestrial dust devil with
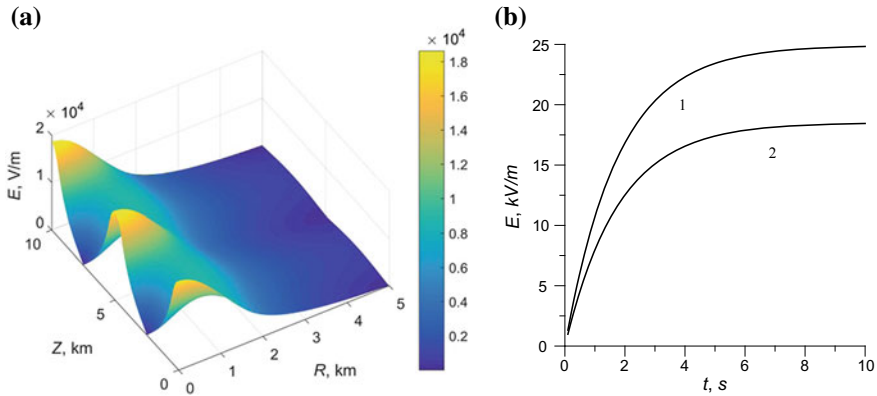
Fig. 1 a Electric field in the Martian dust devil with core radius of 1.5 km and a height of 10 km in the saturation state (average charge separation rate $\partial \bar{\rho}_q / \partial t = 5.5 \cdot 10^{-11}$ C m^{-3} s^{-1}). **b** Evolution of the maximum value of the electric field in the process of charge separation. (1) $\partial \bar{\rho}_q / \partial t = 7.4 \cdot 10^{-11}$ C m^{-3} s^{-1}, (2) $\partial \bar{\rho}_q / \partial t = 5.5 \cdot 10^{-11}$ C m^{-3} s^{-1}
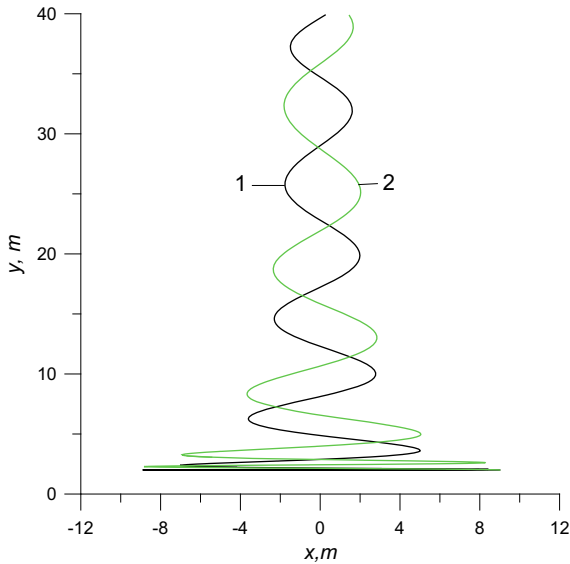
Fig. 2 Trajectories of the 1 μm particle carrying charge of $-1.6 \cdot 10^{-17}$ C in terrestrial dust devil (radius 10 m). (1) Without electric field, (2) with electric field generated by the vortex

the radius of 10 m is shown in the Fig. 2. It should be mentioned that for the conditions in the Earth's atmosphere the process of charge stabilization takes about 10 min with maximum values of electric field being equal to about 100 kV/m.

4 Results and Discussion

We have shown hydrodynamic similarity for terrestrial and Martian dust devils and found characteristic scales and velocities of gas flow in the Martian vortices similar to terrestrial ones. We have studied electrification in dust devils and calculated electric field pattern for different conditions. The electric field modelled has been used for dust dynamics calculations. At high rate of charge separation in big Martian vortices breakdown values of electric fields can be reached. This can result in lightning activity. Lightning can excite oscillation in Schumann cavity on Mars. There is no experimental evidence on lightning on Mars nowadays [15]. Nevertheless in 2009 [16] with the help of radiotelescope during the Martian dust storm the emission spectrum peaks in the vicinity of the predicted values of the first three modes of Schumann oscillations on Mars were observed. Aspects of the influence of dust particles in the Earth's atmosphere on Schumann oscillations were discussed in [17]. Here we can estimate the number of suitable dust devils that must

simultaneously be on the surface of Mars for the amplitude of Schumann resonances on Mars to be comparable with that on the Earth.

Let's estimate the energy released during the discharge of lightning as

$$W = \frac{1}{8\pi\varepsilon_0} \frac{Q^2}{l},$$

where Q is the charge carrying by the discharge, l is the length of the discharge. For average terrestrial lightning $W_E \approx 2 \cdot 10^9$ J [18]. According to the calculations given in the previous paragraph for a dust vortex on Mars $Q \approx 5$ C, $l \approx 5$ km, an estimate of the energy of a possible single discharge gives $W_M \approx W_E/20$. According to [18], only 0.01–0.1% of the total discharge energy goes directly to the pumping of the resonator. Possible discharge frequency can be estimated on the speed of reaching the electric field breakdown values due to charge separation. Let us estimate the required number of dust vortices, in which the electric field reaches breakdown values, so that the amplitude of Schumann resonances on Mars is comparable to that on the Earth. We take into account that the square of the amplitude of the electric field in the resonator is proportional to the radiated energy and we set $\left(v_M W_M^{(1)} \middle/ v_E W_E^{(1)}\right)^{1/2} (V_E/V_M)^{1/2} = 1$, where $v_M(v_E)$, $W_M^{(1)}$, $(W_M^{(1)})$ are the frequency of discharges and the energy of single discharges on Mars (on the Earth), $V_E(V_M)$ is the volume of the Earth (Martian) resonator. Thus $v_M \approx 5.7\, v_E$, from where we get the estimate for the number of dust vortices $N \approx 5.7\, v_E \Delta t_M$. For the characteristic frequency of discharges on Earth $v_E = 100$ s^{-1} [18], and the time of charge separation in the Martian vortex $\Delta t_M \approx 10$ s, the number of suitable dust vortices that must simultaneously be on the surface of Mars is $N \approx 5.7 \cdot 10^3$.

References

1. Farrell, W.M., Smith, P.H., Delory, G.T., Hillard, G.B., Marshall, J.R., Catling, D., Tratt, D. M., Renno, N., Desch, M.D., Cummer, S.A., Houser, J.G., Johnson B.: Electric and magnetic signatures of dust devils from the 2000–2001 MATADOR desert tests. J. Geophys. Res. **109** (E03004) (2004)
2. Delory, G.T., Farrell, W.M., Atreya, S.K., Renno, N.O., Wong, A.-S., Cummer, S.A., Sentman, D.D., Marshall, J.R., Rafkin, S.C.R., Catling, D.C.: Oxidant enhancement in Martian dust devils and storms: storm electric fields and electron dissociative attachment. Astrobiology **6**(3), 451–462 (2006)
3. Melnik, O., Parrot, M.: Electrostatic discharge in Martian dust storms. J. Geophys. Res. **103** (A12), 29107–29117 (1998)
4. Zhai, Y., Cummer, S.A., Farrell, W.M.: Quasi-electrostatic field analysis and simulation of Martian and terrestrial dust devils. J. Geophys. Res. Planets **111**(E06016), 1–8 (2006)

5. Renno, N.O., Wong, A.S., Atreya, S.K., de Pater, I., Roos-Serote, M.: Electrical discharges and broadband radio emission by Martian dust devils and dust storms. Geophys. Res. Lett. **30** (22), 1–4 (2003)
6. Bazelyan, E.M., Raizer, YuP: Lightning Physics and Lightning Protection. IOP, Bristol (2000)
7. Izvekova, Y.N., Popel, S.I., Izvekov O.Y.: On calculation of vortex parameters in near-surface atmosphere of mars. Solar Syst. Res. **53**(5) (2019) [in press]
8. Guhman, A.A.: Introduction to similarity theory. Vysshaya Shkola, Moscow (1973) [in Russian]
9. Balme, M., Greeley, R.: Dust devils on earth and mars. Rev. Geophys. **44**(RG3003), 1–22 (2006)
10. Ryan, J.A., Lucich, R.D.: Possible dust devils, vortices on Mars. J. Geophys. Res. Ocean. **88** (C15), 11005–11011 (1983)
11. Lacks, D.J., Levandovsky, A.: Effect of particle size distribution on the polarity of triboelectric charging in granular insulator systems. J. Electrostat. **65**(2), 107–112 (2007)
12. Farrell, W.M., Delory, G.T., Cummer, S.A., Marshall, J.R.: A simple electrodynamic model of a dust devil. Geophys. Res. Lett. **30**(20) (2003)
13. Izvekova, Y.N., Popel, S.I.: Plasma effects in dust devils near the Martian surface. Plasma Phys. Rep. **43**(12), 1172–1178 (2017)
14. Izvekova, Y.N., Popel, S.I.: Nonlinear wave structures and plasma—dust effects in the earth's atmosphere. Plasma Phys. Rep. **44**(9), 835–839 (2018)
15. Gurnett, D.A., Huff, R.L., Morgan, D.D., Persoon, A.M., Averkamp, T.F., Kirchner, D.L., Duru, F., Akalina, F., Kopf, A.J., Nielsen, E., Safaeinili, A., Plaut, J.J., Picardi, G.: An overview of radar soundings of the Martian ionosphere from the Mars express spacecraft. Adv. Space Res. **41**(9), 1335–1346 (2008)
16. Ruf, C., Renno, N.O., Kok, J.F., Bandelier, E., Sander, M.J., Gross, S., Skjerve, L., Cantor, B.: Emission of non-thermal microwave radiation by a Martian dust storm. Geophys. Res. Lett. **36**(L13202), 1–6 (2009)
17. Besedina, Y.N., Popel, S.I.: Nano-and microscale particles and global electromagnetic resonances in the Earth-ionosphere cavity. Plasma Phys. Rep. **33**(2), 138–145 (2007)
18. Bliokh, P.V., Nikolaenko, A.P., Filippov, YuF: Global electromagnetic resonances in the earth-ionosphere cavity. Naukova Dumka, Kiev (1977) (in Russian)

The Lower Atmosphere Response to Seismic Events Using Satellite Data

Valentine Kashkin, Roman Odintsov, Tatyana Rubleva, Alexey Romanov and Konstantin Simonov

Abstract

Modern space technologies allow finding vertical profiles of temperature, pressure and humidity in the troposphere and stratosphere for the entire globe. Together with the use of signals from the GLONASS and GPS space systems, the data on the vertical profiles can detect the atmosphere effect of internal gravity waves excited during seismic events. The temperature time series of the atmosphere temperature at the isobaric levels of 450 and 200 hPa were studied in the period from February 1 to April 14, 2011 near the epicentral area of the earthquake in Japan, 2011. It was found that along with temperature fluctuations in the troposphere and in the stratosphere a mirror wave is observed, there are oscillations similar to those of the troposphere oscillations, but which are in opposite phase with them. The mechanism of the origin of the mirror wave is presented as well as the process of its simulation. It is shown that the troposphere and the stratosphere can be used as an antenna receiving infrasonic waves during seismic events, and space technologies as a means of recording these waves.

V. Kashkin (✉) · R. Odintsov · T. Rubleva (✉) · A. Romanov
Siberian Federal University, Svobodny str. 79, 660041 Krasnoyarsk, Russian Federation
e-mail: rtcvbk@rambler.ru

T. Rubleva
e-mail: tvrubleva@mail.ru

K. Simonov
Institute of Computational Modeling of the Siberian Branch of the Russian Academy of Sciences, Akademgorodok 50/44, 660036 Krasnoyarsk, Russian Federation
e-mail: simonovkv50@gmail.com

Modern space technologies allow us to explore the Earth's atmosphere, to obtain vertical profiles of temperature, pressure and humidity in the troposphere and stratosphere for the entire globe [1–4]. NOAA spacecrafts, as well as Suomi NPP and Metop with ATOVS, ATMS and CrIS instruments are used for evaluating the vertical profiles of the atmosphere [5–7]. We used information from the Air Recourse Laboratory NOAA website on a $1° \times 1°$ grid in latitude and longitude, set at intervals of 3 h [8].

The vertical profiles data are applied in meteorology and aviation, these data allow us to estimate the tropospheric delay of signals of satellite navigation systems GLONASS and GPS [9]. Finally, these data allow us to observe interesting geophysical phenomena.

Slow oscillations of the earth's surface occur during seismic activity in the epicentral region of the earthquake, and acoustic (infrasonic) vibrations with a period of several days are emitted. Direct registration of such oscillations is extremely difficult. However, they can be detected by indirect signs—by the excitation of internal gravitational waves (IGW) in the atmosphere [9]. Internal gravitational waves [10] provoke a change in the electron content in the ionosphere, the phenomenon can be revealed with the GLONASS/GPS receiving equipment [9, 11]. The IGW can affect the troposphere and the stratosphere.

A catastrophic earthquake of magnitude $M = 9$ [12–16] occurred off the coast of Japan on March 11, 2011. It was accompanied by a tsunami and caused numerous victims among the population, as well as the destruction of the Fukushima nuclear power plant. The epicentral area of the earthquake was located in the Pacific Ocean, the epicenter coordinates are 38º N, 142º E. Figure 1 shows the of time series graphs of temperature changes in atmosphere at the isobaric levels of 450 and 200 hPa from February 1 to April 14, 2011 near the epicentral area of the earthquake. The arrows show the time of the main shock with a magnitude of $M = 9$ and the strongest aftershock with $M = 7$.
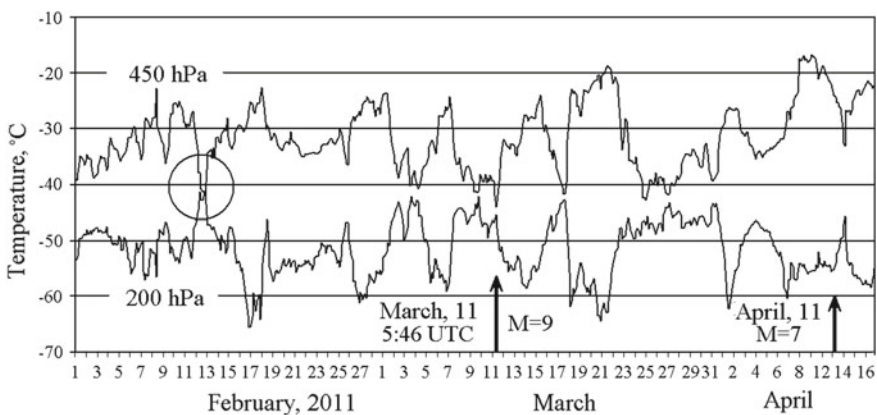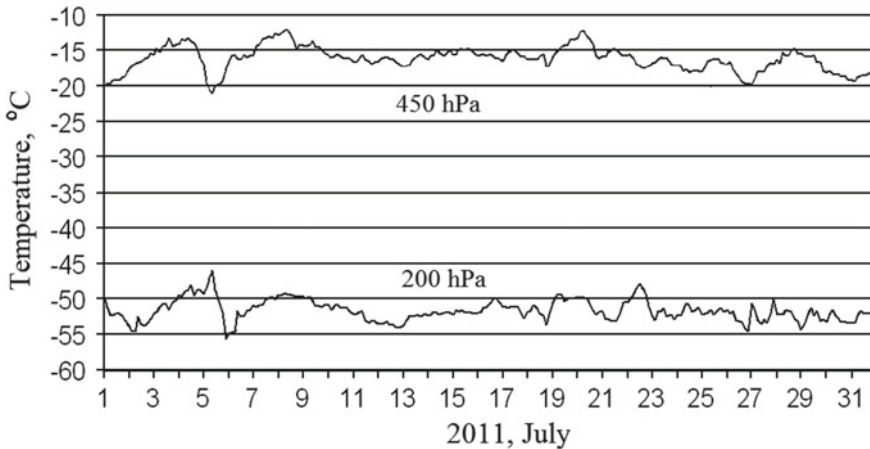

Fig. 1 Temperature change at isobaric levels of 450 and 200 hPa at a point with coordinates 38° N, 142° E in the Pacific in the epicentral area of the earthquake in Japan 2011

The isobaric level of 450 hPa corresponds to a height above sea level of about 6300 m, which is the troposphere. Let us call the graph at the level of 200 hPa a mirror wave (MW). The level of 200 hPa corresponds to height of about 12,000 m and is located at the low level of the stratosphere. We take into account that the epicentral area of the earthquake is in the Pacific, there is no land there and, therefore, no orographic phenomena. It is known [9] that sea waves (except for tsunami waves) cannot excite waves in the atmosphere. Thus, it can be argued that temperature fluctuations in Fig. 1 are caused precisely by the internal gravity waves generated by seismic processes. The rare sampling step did not allow detecting the moments of seismic shocks, but infrasonic temperature fluctuations in the atmosphere (frequency is less 10^{-5} Hz after the earthquake and in front of it are clearly visible.

The time series shown in the graphs contain significant wave oscillations. The standard deviation of temperature is $\sigma = 4.7$ K for the time series at the isobaric level of 200 hPa and $\sigma = 4.5$ K for the time series at the level of 450 hPa. The correlation coefficient between the temperature series at the levels of 450 and 200 hPa is $R = -0.76$ for the period from February 1 to April 14. The largest negative correlation coefficient falls on the period from February 27 to March 28 and is equal to $R = -0.86$. Further, the correlation coefficient began to increase and in June became positive. Variations in the electron content in the ionosphere during the period of seismic activity associated with the earthquake are considered in [9].

Figure 2 shows the "background" graph of temperature fluctuations for the same point with the coordinates of 38º N, 142º E in July 2011, when seismic events have almost stopped. The temperature time series in Fig. 2 are similar to each other. The

Fig. 2 Temperature variations at isobaric levels of 200 and 450 hPa in the Pacific Ocean, point with coordinates of 38° N, 142° E

paired correlation coefficients for the time series in July–August at the levels are positive and are in the range R = 0.26–0.75. The time series have a standard deviation of $\sigma = 1.6$ K for a level of 200 hPa and $\sigma = 1.8$ K for a level of 450 hPa.

In the troposphere the temperature decreases with height, for the standard troposphere, a constant vertical temperature gradient $\alpha = 0.65$ K/100 m is adopted, the temperature dependence on the height z above sea level has the form $T = T_0 - \alpha z$, $T_0 = 288.15$ K [11]. In this case, the dependence of pressure p on height is described by the barometric formula for a polytropic atmosphere [17, 18]:

$$p = p_0 \left(\frac{T_0 - \alpha z}{T_0} \right)^{\frac{g}{R_c \alpha}}. \tag{1}$$

In (1) $p_0 = 1013.25$ hPa, g is the acceleration of free fall, $R_c = 287$ m^2/(s^2 K) is the specific gas constant of dry air. The dependence of temperature on pressure is nonlinear:

$$T = T_0 \left(\frac{p}{p_0} \right)^{\frac{R_c \alpha}{g}}. \tag{2}$$

The origin of the mirror wave is easy to understand, given that the temperature in the stratosphere increases with height, starting from the upper tropopause boundary z_1: $T = T_1 + \beta(z - z_1)$, where $\beta < 0$. Instead of (2) we have

$$T = T_1 \left(\frac{p}{p_1} \right)^{\frac{-R_c |\beta|}{g}} = T_1 \left(\frac{p_1}{p} \right)^{\frac{R_c |\beta|}{g}}, \tag{3}$$

where T_1 and p_1 are the temperature and pressure at the height z_1.

Let's consider a possible model for the excitation of waves in the troposphere [6, 7]. Let the pressure at the ground level change according to the law: $p_0' = p_0 + P \cos(\omega t)$, for example, due to the influence of meteorological factors or due to the movements of the earth's crust. It is assumed that the infrasonic waves excited by a change in pressure move with the speed of sound and during the passage of the wave the state of the air medium does not have time to change (adiabatic approximation), this allows using the equations of atmospheric static, which include (1), (2) and (3).

In Fig. 3 on the left is a model of the atmosphere. The dependence of temperature on height is depicted as two straight lines: AB, where the temperature decreases linearly with height and the BC, where it linearly increases. Thus, we have two sections of a polytropic atmosphere.

We assume that for these sections the temperature T_1 and the pressure p_1 coincided at the break point B. The temperature at the isobaric level p is defined by (1). In the upper right part of Fig. 3 there is a graph of the time dependence of a model infrasound wave at a level of $p = 450$ hPa, representing in some approximation an internal gravitational wave. Here T_0, p_0 and α are defined the same as for
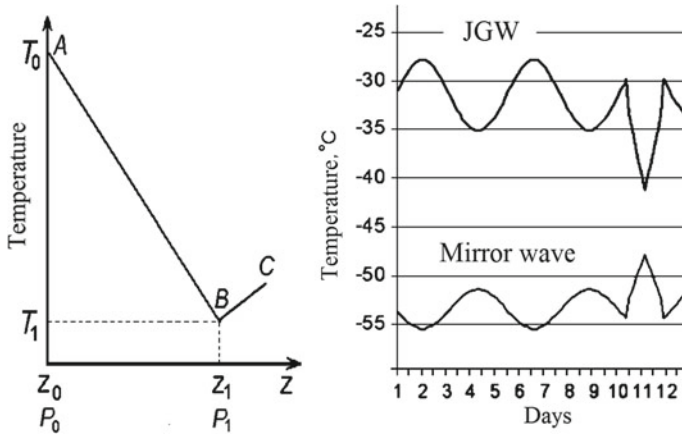
Fig. 3 Simulation of an internal gravity and a mirror waves

the standard atmosphere, with $P = 80$ hPa. This graph also shows the "surge" of temperature that simulates a seismic event.

Let the temperature T_1 be set at point B, then the pressure at that point can be represented as

$$p_1 = p_0' \left(\frac{T_1}{T_0}\right)^{\frac{g}{R_c\alpha}}. \tag{4}$$

In the interval BC the temperature can be estimated according to this formula

$$T = T_1 \left(\frac{p}{p_1}\right)^{\frac{-R_c|\beta|}{g}} = T_1 \left(\frac{p_1}{p}\right)^{\frac{R_c|\beta|}{g}} = T_1 \left(\frac{p_0'}{p}\right)^{\frac{R_c|\beta|}{g}} \left(\frac{T_1}{T_0}\right)^{\frac{|\beta|}{\alpha}}. \tag{5}$$

Using (5) for $T_1 = 213.15$ K, $p = 200$ hPa, $\beta = -4$, a mirror wave was constructed, shown in Fig. 3, bottom right.

When IGW is excited changes in surface temperature are not taken into account. In addition, it is not taken into account that the mirror waves depend not only on IGW, but also on the state of water vapor in the troposphere. Nevertheless, the graphs in Fig. 3, from a qualitative point of view, reflects the observed phenomena in a correct way.

The waves in the atmosphere depicted in Figs. 1 and 3 are analogous to waves in a stratified ocean, which were discussed by Shuleikin [19]. At the water–air interface, there are surface waves excited by the wind. Particles of water in them move along elliptical paths. In the ocean the average density of water increases downwards; there is a boundary between waters of different densities. When a surface wave moves up and down, either a rarefaction or an overpressure occurs at

the boundary. Due to the condition of maintaining hydrostatic equilibrium (continuity condition), water particles move upward under the base wave sole and down under its crest at the boundary. In oceanology, the newly formed wave is called the internal (gravitational) wave [19]. Surface and internal waves move in opposite phase. In the troposphere IGW is the surface analog and the MW in the stratosphere is the analog of the internal wave.

It is believed that the infrasonic oscillations of the earth's crust are one of the forerunners of the earthquake, but there are significant difficulties in detecting such oscillations. The results presented above show that the troposphere and stratosphere can serve as an antenna that receives these oscillations and space technologies as a means of recording. However, at the present level of development neither these techniques nor other methods of seismic control show reliability in making short-term earthquake predictions.

Nevertheless, using data on the vertical profiles of the atmosphere, it is possible to outline area and some features of the location of seismic phenomena. In Fig. 1 it can be seen that on February 12, 2011, a month before the main seismic event, for a short time (3–6 h) two differently directed temperature "surge" appeared at the levels of 450 and 200 hPa (they are shown in a circle). This might be a result of the movement of tectonic plates, a precursor of the main shock, as well as of the multidirectional fluctuations in temperature on March 2, 7 and 10.

References

1. Salby, M.L.: Fundamentals of Atmospheric Physics. International Geophysics Series 61. Academic Press, New York, London (1996)
2. Scherllin-Pirscher, B., Steiner, A.K., Kirchengast, G., Schwärz, M., Leroy, S.S.: The power of vertical geolocation of atmospheric profiles from GNSS radio occultation. J. Geophys. Res. Atmos. **122**(3), 1595–1616 (2017). https://doi.org/10.1002/2016jd025902
3. Blunden, J., Arndt, D.S., Hartfield, G.: State of the climate in 2017. Bull. Amer. Meteor. Soc. **99**(8), 332 pp. (2018). https://doi.org/10.1175/2018bamsstateoftheclimate.1
4. Zuev, V.E., Komarov, V.S.: Statistical models of temperature and gas components of the atmosphere. Modern problems of atmospheric optics. 1, Gidrometeoizdat, Leningrad (1986) (in Russian)
5. Courcoux, N., Schröder, M.: The CM SAF ATOVS data record: overview of methodology and evaluation of total column water and profiles of tropospheric humidity. Earth Syst. Sci. Data **7**(2), 397–414 (2015). https://doi.org/10.5194/essd-7-397-2015
6. Xue, T., Xu, J., Guan, Z., Chen, H.-C., Chiu, L.S., Shao, M.: An assessment of the impact of ATMS and CrIS data assimilation on precipitation prediction over the Tibetan Plateau. Atmos. Meas. Tech. **10**, 2517–2531 (2017). https://doi.org/10.5194/amt-10-2517-2017
7. Zhou, L., Divakarla, M., Liu X., Layns, A., Goldberg, M.: An overview of the science performances and calibration. Validation of joint polar satellite system operational products. Remote Sens **2**(11), 698 pp. (2019). https://doi.org/10.3390/rs11060698
8. National Oceanic and Atmospheric Administration. http://www.arl.noaa.gov/ready/cmet.html. Last accessed 16 Apr 2019
9. Kashkin, V.B., Vladimirov, V.M., Klykov, A.O.: Zenith tropospheric delay of GLONASS/GPS signals on the basis of ATOVS satellite data. Atmos. Ocean. Opt. **28**(1), 68–73 (2015)
10. Afraimovich, E.L., Astafieva, E.I., Gokhberg, M.B., Lapshin, V.M., Permyakova, V.E., Steblov, G.M., Shalimov, S.L.: Variations of the total electron content in the ionosphere from

GPS data recorded during the Hector Mine earthquake of October 16, 1999. California. Russ. J. Earth Sci. **6**(5), 339–354 (2004)

11. Andrews, D.G.: An Introduction to Atmospheric Physics, 2nd edn. Cambridge University Press, New York (2010)
12. Oyama, K.-I., Devi, M., Ryu, K., Chen, C.H., Liu, J.Y., Liu1, H., Bankov, L., Kodama, T.: Modifications of the ionosphere prior to large earthquakes: report from the Ionosphere Precursor Study Group. Geosci. Lett. **3**(6), 2–10 (2016)
13. Nature. http://www.nature.com/nature. Last accessed 6 Mar 2019
14. Dunbar, P., McCullough, H., Mungov, G., Varner, J., Stroker, K.: 2011 Tohoku earthquake and tsunami data available from the national oceanic and atmospheric administration. Geomat. Nat. Hazards Risk **2**(4), 305–323 (2011). https://doi.org/10.1080/19475705.2011.632443
15. United States Geological Survey. https://earthquake.usgs.gov/earthquakes/. Last accessed 21 Mar 2019
16. Incorporated Research Institutions for Seismology. https://www.iris.edu/hq/. Last accessed 20 Feb 2019
17. Golitzin, G.S., Romanova, N.N., Chunchuzov, E.P.: The triggering of atmospheric internal waves with sea disturbance. Izvestiya Academii Nauk SSSR. Fizika Atmosfery i Okeana. **12**(6), 669–673 (1976) (in Russian)
18. Fleagle, R.G., Businger, J.A.: An Introduction to Atmospheric Physics. Academic Press, New York, London, Toronto, Sydney, San Francisco (1980)
19. Shuleikin, V.V.: Sea Phys. Nauka, Moscow (1968) (in Russian)

Chicxulub Impact as a Trigger of One of Deccan Volcanism Phases: Threshold of Seismic Energy Density

Valery Khazins and Valery Shuvalov

Abstract

One of the hypotheses of mass extinction at the Cretaceous–Paleogene boundary is associated with a sharp increase in the volcanic activity of the Large Igneous Province of Deccan due to the impact of a ten-kilometre asteroid near the Gulf of Mexico [1, 2]. A sudden increase in mantle effective permeability (MEP) initiated by seismic disturbances of the impact was considered in [2] as a cause of the increase in the flow rate of magma. We used an empirical method to estimate the density of seismic energy dissipated in the ground at various distances. The threshold of energy density for increasing the MEP and the energy density released in the province of Deccan after the Chicxulub impact have been revised using this method. It is shown that the threshold values of the energy density can be an order of magnitude higher. At the same time, the use of refined data on seismic efficiency and energy of the Chicxulub impact allows us to increase the density of dissipated energy in the province of Dean also by an order of magnitude. Thus, our analysis supports the idea that the Deccan volcanism could be accelerated by the Chicxulub impact occurred at a distance of about 13,000 km.

V. Khazins (✉) · V. Shuvalov
Sadovsky Institute of Geospheres Dynamics RAS, Leninskiy Prospekt 38-1, Moscow 119334, Russia
e-mail: khazins@idg.chph.ras.ru

1 Introduction

Investigations using the high-precision radioisotope method (^{40}Ar/^{39}Ar) [1] led to the conclusion that up to 70% of lava in the province of Deccan was erupted at the final stage of formation of Deccan traps. The beginning of the period of acceleration of volcanism and the impact of a large asteroid near the Gulf of Mexico (Chicxulub impact) at the Cretaceous–Paleogene boundary fall into the time span of 50,000 years. The proximity of these events suggested that the Chicxulub impact had a significant influence on the acceleration of the Deccan volcanism [1, 2]. This hypothesis seems to be quite original, because 66 million years ago the magmatic Deccan province was distant from the point of the impact by about 130°, and seismic disturbances at such long distances should have been significantly weakened. The strongest seismic disturbances can be expected either near the impact point [3] or in the antipodal region [4]. However, a number of volcanoes, the triggering mechanism of which is associated with remote earthquakes [5], require relatively small amounts of energy to initiate an eruption. A speculative model of magma release from magmatic chamber is given for this case in [6]. In short, the main suggestions in [6] are as follows. Approximately 10% of magma entering a magma chamber solidifies, significantly changing a pressure in melt. The effect of seismic waves with some energy partially or completely destroys pore partitions and leads to fast vertical redistribution of pressure due to diffusion of liquid or gas phases. As a result, part of the magma reaches a critical state and an eruption occurs. The effect of increasing the effective permeability of magma under the action of seismic disturbances is not sufficiently justified even for relatively shallow magmatic systems. For the case of magma chamber located below the lithosphere/asthenosphere, as suggested in the case of the Deccan volcanism, the question about physical reasons for the acceleration of volcanism has not been studied. However, under the assumption of instantaneous increase in effective permeability as a result of the Chicxulub impact, it is shown [2] that the accelerated mode of formation of Deccan traps could last $\sim 100,000$ years. This assessment is consistent with the results of studies of Deccan traps, which serves as an indirect confirmation of the validity of the assumption about a role of effective permeability. The use of observational data and some empirical relationships allowed [2] to estimate threshold values of energy for eruptions, initiated by an increase in MEP, and to demonstrate an accordance of threshold values with the seismic energy released in the province of Deccan as a result of the Chicxulub impact (based on the results of numerical modeling [4]).

This paper presents empirical estimates of the energy density released in the ground during the propagation of seismic waves that are different from those used in [2]. Threshold values of energy density required for volcanic eruptions due to increased permeability are estimated, and obtained results are compared with the conclusions of [2].

2 Method to Estimate Seismic Energy Density at Different Distances from the Epicenter

The volume density of seismic energy in the first approximation is proportional to the square of the maximum velocity of particles (peak ground velocity, PGV):

$$e = \rho \times PGV^2/2 \tag{1}$$

To estimate seismic energy at large distances r (in km) from the event with magnitude M, we use the effective magnitude $M_{eff}(r)$ [7]:

$$M_{eff}(r) = \begin{cases} M - 0.0238r & r < 60\,km \\ M - 0.0048r - 1.1644 & 60 \le r < 700\,km \\ M - 1.66\log_{10}r - 0.084 & r \ge 700\,km \end{cases} \tag{2}$$

Here, the local effective magnitude $M_{eff}(r)$ in the point located at a distance r from the event with magnitude M is equal to the magnitude of a hypothetical source located at this point and generating at this point the same ground motion as the event with magnitude M. To link the effective magnitude $M_{eff}(r)$ with the intensity of the earthquake I, we use the empirical dependence [8]:

$$M_{eff} = 1 + \frac{2}{3}I, \tag{3}$$

which is justified by a sufficiently large amount of data for $I > 5$. In turn, the intensity I is related to instrumental characteristics of a seismic disturbance. In particular, the intensity, defined according to the modified scale of Mercalli, and the maximum velocity of ground motion are related by [9]:

$$\log_{10}PGV = 0.29I - 0.68I \ge 5, \tag{4}$$

$$\log_{10}PGV = 0.48I - 1.62I < 5. \tag{5}$$

Here PGV is in cm/s.

Figure 1a illustrates a series of calculations of the maximum velocity of ground particles at different distances for different magnitudes of seismic disturbances based on relations (2)–(5). In the near zone ($r < 60$ km) and at regional distances ($60 \le r < 700$ km), the reflection of seismic waves from the Mohorovich boundary and the lower and upper mantle affects the results, and the dependence behaves in a rather complex way. At teleseismic distances ($r > 700$ km) the velocity decreases with the distance according to the power law

$$PGV \sim r^{-1.2}. \tag{6}$$
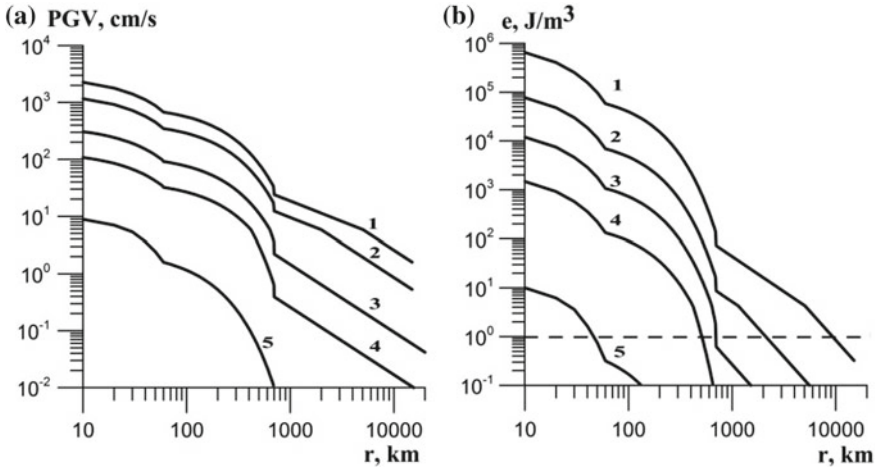
Fig. 1 Dependence of the maximum velocity of ground particles (**a**) and the volume energy density (**b**) on the distance to the source of seismic disturbances. Curves 1–5 are obtained for source magnitudes of 10.6, 9.5, 8.6, 7.5 and 5 respectively

The kink of the curve 1 at distances of about 5000 km is associated with a decrease in the values of I to 5 (see relations (4)–(5)).

Figure 1b shows a distribution of volumetric density of energy calculated using the relations (1)–(5). A soil density in the ratio (1) was $\rho = 2600$ kg/m^3. From Fig. 1b it follows that for a seismic disturbance with a magnitude of 10.6 at distances of the order of 10,000 to 20,000 km the energy values fall into the range

$$0.1 < e < 1 \text{ J/m}^3. \tag{7}$$

According to the estimate [2], the threshold value of the energy density at which a transition to the MEP increase mode is possible lies in the same range, i.e., a volcanic eruption may be initiated in this case.

To use the relations (1)–(5) for the problems of large impacts, it is necessary to determine the fraction of impactor kinetic energy converted into the energy of seismic waves. The seismic efficiency k, i.e. the ratio of seismic to kinetic energy, varies widely [10], from 10^{-6} to 10^{-2}. The seismic efficiency of 10^{-4} is a commonly adopted value. However, modern theoretical [11] and laboratory [12] studies have shown that the average value of k is an order of magnitude higher. In theoretical studies [11] it was assumed that if a crater-forming impact and an underground explosion generate identical shock waves at distances significantly exceeding the size of the region of energy release and the depth of a charge, then, most likely, seismic waves from these sources should be also close in amplitude. Numerical analysis [11] has shown that impacts and explosions in quartz target produce identical shock waves if the impact energy is 3–5 times greater than the initial

energy of the underground explosion. Hence, the values of seismic efficiency obtained from the underground explosion tests and reduced by 3–5 times can be used to estimate the seismic effect of crater-forming impacts. The seismic efficiency of underground explosions is weakly dependent on the power of explosions and is rather well known. For underground explosions in granite, seismic efficiency is $(1 \div 3) \times 10^{-2}$. Granite density is only slightly different from quartz density. Therefore, the seismic efficiency of crater-forming impacts should be $(2 \div 6) \times 10^{-3}$ in quartz. This value is close to the value obtained in laboratory experiments for a quartz target [12]. The study of seismic efficiency in laboratory experiments [12] and underground explosions (see, for example, [11]) showed that an increase in the porosity and humidity of the environment leads to a decrease in seismic efficiency up to an order of magnitude compared to quartz (granite).Taking into account the variability of Earth soil composition, we used some average value, $k = 10^{-3}$ in contrast to $k = 10^{-4}$ assumed in [2].

Taking into account the relationship between seismic energy and magnitude determined by the Gutenberg-Richter formula [13]

$$M = \frac{2}{3}(\log_{10} E_{seism} - 4.8) \tag{8}$$

and the above-mentioned coefficient of seismic efficiency k, we can assume that $M = 10.6$, 8.6 and 7.5 correspond to the impactor sizes of 10, 1 and 0.3 km accordingly. It is assumed that the asteroid consists of chondritic material (density of about 3300 kg/m^3), and has a speed of 20 km/s. Consequently, the impact of the asteroid, which created the Chicxulub crater, could initiate the Deccan volcanism.

Thus, the application of estimates (1)–(5) led us to the same conclusions about energy dissipated in the province of Deccan, as in [2]. We do not take into account the possible deviation of the velocity of soil particles from the law (6) and the effect of the accumulation of seismic waves in the antipodal hemisphere. Therefore, we consider these results as the first approximation. At the same time, such estimates are useful for comparative analysis of seismic effects of different sources.

Let us consider one more example of application of these estimates. In [2], a possible influence of seismic waves produced by an earthquake with magnitude $M = 9.5$ on the magmatic province Deccan was considered. The nearest subduction zone was located at a distance of 4–5 thousand kilometers from the province of Deccan 66 million years ago [14]. Due to such remoteness, it was assumed in [2] that such an earthquake was not able to initiate an increase in MEP. However, from Fig. 2b it follows that at distances of 2,000–5,000 km an earthquake with a magnitude of 9.5 can produce the same energy release as the impact of a ten-kilometer asteroid at distances of 10,000–20,000 km. A seismic energy density generated in the province of Deccan, calculated by this method, does not contradict estimates obtained by the authors of the hypothesis in a different way. Therefore, an extreme earthquake in the subduction zone could be an alternative reason for the increase in Deccan volcanism.
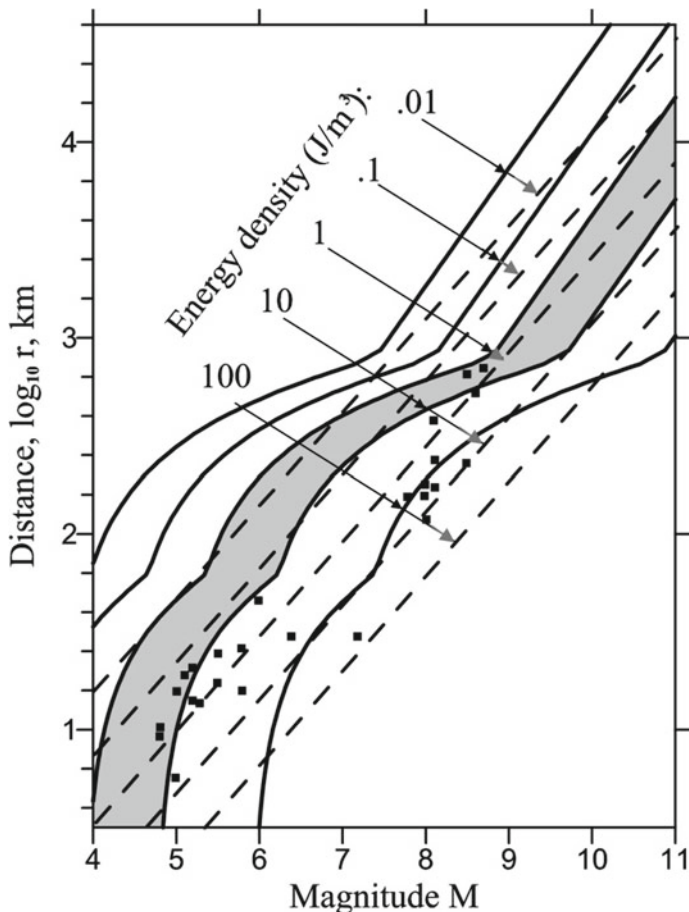
Fig. 2 Magmatic volcanoes triggered by earthquakes as a function of magnitude and epicentral distance. The squares are magmatic volcanoes. The dashed lines are isolines from (9). The solid lines are isolines from (1)–(5)

3 A Comparison of Estimates of Threshold Seismic Energy Density with Observations

Seismic energy densities necessary for increase in MEP resulting in volcano eruption was estimated in [2] from an empirical formula

$$\log_{10} r = 0.48M - 0.33 \log_{10} e - 1.4 \tag{9}$$

where e is the volumetric seismic energy density in J/m³, M is the magnitude of an earthquake. When obtaining the ratio (9), the simplest approximation of PGV attenuation with distance was used:

$$PGV \sim r^{-1.5} \tag{10}$$

The absolute value of the exponent is 1.5. This is higher than an analogous value in the dependence (6) of our model, which significantly affects the PGV at long distances of about 10,000 km.

For simplicity, we limited ourselves to magmatic eruptions triggered by earthquakes and used in the analysis [2]. As noted in [2] and as follows from Fig. 2, the threshold values of the energy density in the case of the use of the relation (9) lie in the range $0.1 < e* < 1$ J/m3.

The solid curves in Fig. 2 show the isolines of energy density, resulted from the relations (1)–(5). At distances up to 1000 km, these curves can be approximated with sufficiently good accuracy by straight lines with a slope corresponding to the isolines resulted from the relation (9). Most likely, this is due to the use of the simplified relation (10). Within the framework of estimates (1)–(5), the threshold energy density e*, necessary for an increase in MEP, should lie in the range $1 < e* < 10$ J/m³ (the area colored in gray). The estimate [2] of energy released in the province Deccan after Chicxulub impact is less than the minimum limit of this range.

4 Conclusions and Discussion

Comparison of our estimates with observational data show that the threshold energy density necessary for initiating volcanism due to an increase in MEP should be an order of magnitude higher than that used in [2] to justify the acceleration of Deccan volcanism. However, in estimates of the threshold energy density we used the ratios obtained as a result of processing of seismic data, the spread of which reaches an order of magnitude. A similar remark applies to the relations (9)–(10) used in [2]. Under these conditions, obtaining alternative estimates seems to be useful from the point of view of variations of threshold energy density. At the same time, seismic energy released in the province Deccan by the impact should also be much higher than estimated in [2], since the seismic conversion efficiency of 10^{-3} seems to be more reasonable than 10^{-4} adopted in [2]. In addition, scaling relations for crater dimensions [7] show that a crater 180 km in diameter (approximately equal to the Chicxulub crater) is created by the impact of an asteroid with a diameter 15 km, rather than 10 km, with the same impact velocity of 20 km/s. Consequently, the seismic energy released as a result of the Chicxulub impact can be 30–40 times higher than the values used in [2] to estimate the specific energy dissipated in the province of Deccan. With an increase in seismic energy, the density of dissipated energy also increases. According to [4], an increase in the seismic efficiency coefficient by a factor of 40 with the same energy of Chicxulub impact leads to an increase in the energy density

near the antipodal surface by about an order of magnitude. Therefore, within the framework of the estimation errors, we can assume that the energy density dissipated in the province of Deccan can fit into the range of threshold values. Thus, our analysis supports the idea that the Deccan volcanism could be accelerated by the Chicxulub impact occurred at a distance of about 13,000 km.

References

1. Renne, P., Sprain, C., Richards, M., Self, S., Vanderkluysen, L., Pande, K.: State shift in Deccan volcanism at the Cretaceous-Paleogene boundary, possibly induced by impact. Science **350**(6256), 76–78 (2015)
2. Richards, M., Renne, P., Alvarez, W., DePalma, R., Smit, J., Manga, M., Karlstrom, L., Vanderkluysen, L., Fainstein, R., Gibson, S.: Triggering of the largest Deccan eruptions by the Chicxulub impact. Geol. Soc. Am. Bull. **127**, 1507–1520 (2015)
3. Ivanov, B., Melosh, H.: Impacts do not initiate volcanic eruptions: eruptions near the crater. Geology **31**(10), 869–872 (2003)
4. Meschede, M., Myhrvold, C., Tromp, J.: Antipodal focusing of seismic waves due to large meteorite impacts on earth. Geophys. J. Int. **187**, 529–537 (2011)
5. Manga, M., Brodsky, E.: Seismic triggering of eruptions in the far field: volcanoes and geysers. Annu. Rev. Earth Planet. Sci. **34**, 263–291 (2006)
6. Wang, C.-Y., Manga, M.: Hydrologic responses to earthquakes and a general metric. Geofluids **10**, 206–216 (2010)
7. Collins, G., Melosh, H., Marcus, R.: Earth impact effects program: a web-based computer program for calculating the regional environmental consequences of a meteoroid impact on earth. Meteorit. Planet. Sci. **40**(6), 817–840 (2005)
8. Gutenberg, B., Richter, C.: Earthquake magnitude, intensity, energy, and acceleration: (Second paper). Bull. Seismol. Soc. Am. **46**, 105–145 (1956)
9. Wald, D., Quitoriano, V., Heaton, T., Kanamori, H.: Relationships between peak ground acceleration, peak ground velocity, and modified Mercalli intensity in California. Earthq. Spectra **15**(3), 557–564 (1999)
10. Schultz, P., Gault, D.: Seismic effects from major basin formations on the Moon and Mercury. Earth Moon Planet. **12**(2), 159–177 (1975)
11. Khazins, V., Shuvalov, V., Svettsov, V.: The seismic efficiency of space body impacts. Sol. Syst. Res. **52**(6), 547–556 (2018)
12. Güldemeister, N., Wünnemann, K.: Quantitative analysis of impact-induced seismic signals by numerical modeling. Icarus **296**, 15–27 (2017)
13. Gutenberg, B., Richter, C.: Magnitude and energy of earthquakes. Ann. Geophys. **9**(1), 1–15 (1956)
14. Chatterjee, S., Goswami, A., Scotese, C.: The longest voyage: tectonic, magmatic, and paleoclimatic evolution of the Indian plate during its northward flight from Gondwana to Asia. Gondwana Res. **23**, 238–267 (2013)

Studies of the Disturbances of the Geomagnetic Field in the 0.001–0.03 Hz Range Under Influence on the Ionosphere by Powerful Radio Emission of the SURA Facility

D. S. Kotik [ORCID], A. V. Ryabov, V. I. Ivanov, V. P. Esin and D. V. Myazdrikov

Abstract

This paper presents the results of an experiment on the possible reaction of the geomagnetic field to the modification of the ionosphere by powerful radio emission from the SURA facility. The measurements were carried out at two remote points tens of kilometers to the north and south of the SURA. Pulsations in the Pc 3–5 range were detected during the SURA facility operation at both points, and their waveform and spectra were close to identity. An interpretation of the observed phenomenon on the basis of the ionospheric RF heating mechanism for the excitation of the so-called ionospheric feedback instability is given.

Keywords

SURA facility · Ionosphere modification · ULF pulsations · Geomagnetic field · Magnetospheric resonator

1 Introduction

This paper presents the results of an experiment to study the effect of the SURA facility (with the parameter of the magnetic shell L = 2.6) on the Alfven magnetospheric resonator in the ultralow frequency range (0.001–0.03 Hz). The purpose

D. S. Kotik (✉) · A. V. Ryabov
Radio Physical Research Institute University Nizhnij Novgorod, 603950 Nizhnij Novgorod, Russia
e-mail: dmitry.kotik@nirfi.unn.ru

V. I. Ivanov · V. P. Esin · D. V. Myazdrikov
Scientific - Production Association "Typhoon", Pobedy 4 str., 249038 Obninsk, Russia

of the experiment was to try to detect the trigger effect in the excitation of a magnetic flux tube that foot prints on the area of influence.

The first experiment demonstrated the possibility of the ionosphere modification effect on the magnetosphere was conducted in October 1996 at the EISCAT heater in Tromsø using the INTERBALL-2 satellite (AURORAL PROBE), according to the author's opinion [1, 2]. A perturbation of the geomagnetic field was observed in the Ps 4–5 pulsation range during the facility operation for two and a half hours. Then a substorm followed when about an hour after the heater was turned off.

Similar experiments were carried out in 2012 at the HAARP facility [3, 4]. The experiment was carried out before the sub-storms on February 22, 2012. A long-period disturbances before the substorms were also observed during the operation of the HAARP in the AM mode with a frequency of 5 MHz (200 s). In total, four successful experiments were conducted at the HAARP, in which the excitation of ULF pulsations preceded the substorm. No subsequent substorm was observed as well in several experiments in which HAARP induced ULF waves [4].

An attempt to detect this kind of effect in mid-latitudes was made at the SURA facility in July 2015. A description of the conditions and results of this experiment are given below.

2 Conditions and Technique of the Experiment

In experiments in July 2015, the SURA operated with a power of 500 kW, the antenna array beam was directed to 16° south (magnetic zenith). The experiment time was chosen from 21:30 to 23:30 Moscow time. The modulation frequency (on/off period) and radiation polarization varied by day, the SURA carrier frequency was chosen 0.5–1 MHz below the critical frequency of the F-layer (see Table 1). The geomagnetic conditions were rather calm (see Table 1).

Magnetometric measurements were carried out at two points spaced 56 km apart. The first point was located in the area of Yurino 24 km from the stand (hereafter—point "North"), the second point in the village of Ilyina Gora, 36 km from the SURA (hereafter—point "South", see Fig. 1). For measuring the variations of the geomagnetic field induction (GMF), the special stations for magnetic field monitoring CMM—09 (range: 0.001–1000 Hz, sensitivity—1.5×10^{-3} nT/Hz ^ 1/2 at 1 Hz frequency) were used at each point.

Table 1 Technical data of the SURA radiation and the geomagnetic activity index Kp

| Date	Frequency (kHz) mode	Period (s)	Modulation frq. (Hz)	Kp
05.07	4785, « O»	15	0.06(6)	**2**
09.07	5828, « O»	200	0.005	2
21.07	6500, « X»	520	0.002	1
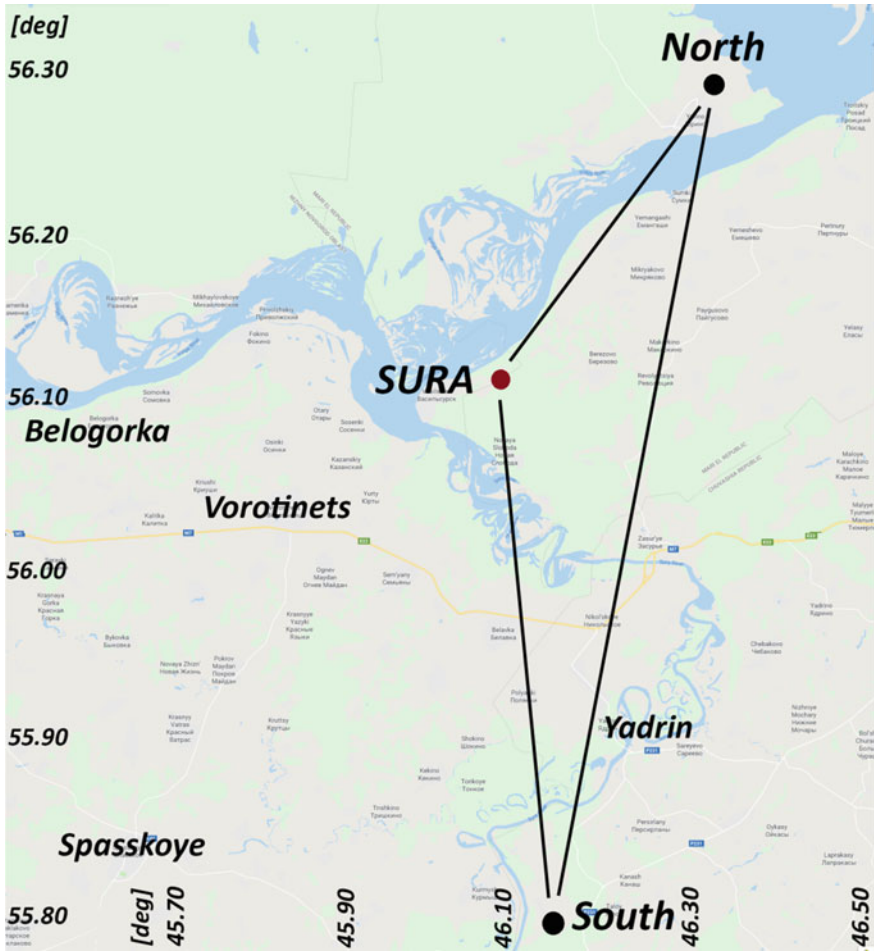
**Fig. 1** Location of measuring points "North" and "South" relative to the SURA facility

3 Results of Experiment

The results of recording the variations of the geomagnetic field in the frequency range under study and their spectral analysis are presented in Figs. 2, 3, and 4. The main feature is almost complete identity of both the wave forms of the geomagnetic field variations and their spectra in both points.

The pulsations appeared at the end of the first session on July 5, 2015 with a modulation period of 15 s and lasted about another 25 min after the end of it (see Fig. 2). The frequency of the maximum in the spectrum was 16 MHz (T = 62.5 s).
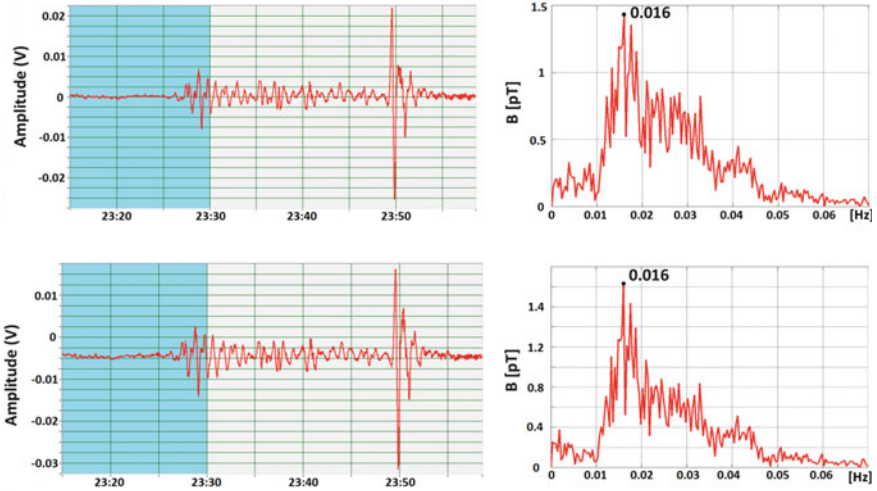
Fig. 2 Variations of the geomagnetic field 05.07.15 in the range of 0.001–0.03 and their amplitude spectra in the "North" point (upper panel) and in the "South" point (lower panel). The blue sectors are the operating time of the SURA with modulation frequency of 0.07 Hz
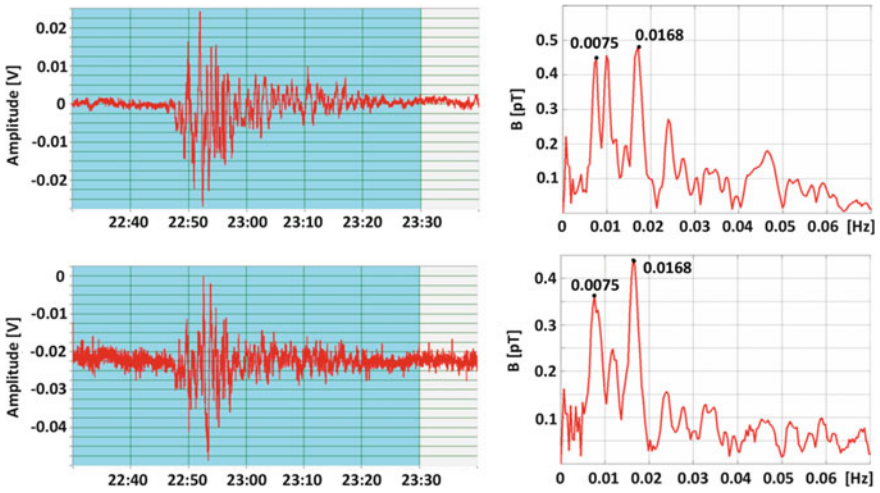
Fig. 3 Same as in Fig. 2 for 07.09.15. The blue sectors are the operating time of the SURA with modulation frequency of 0.005 Hz
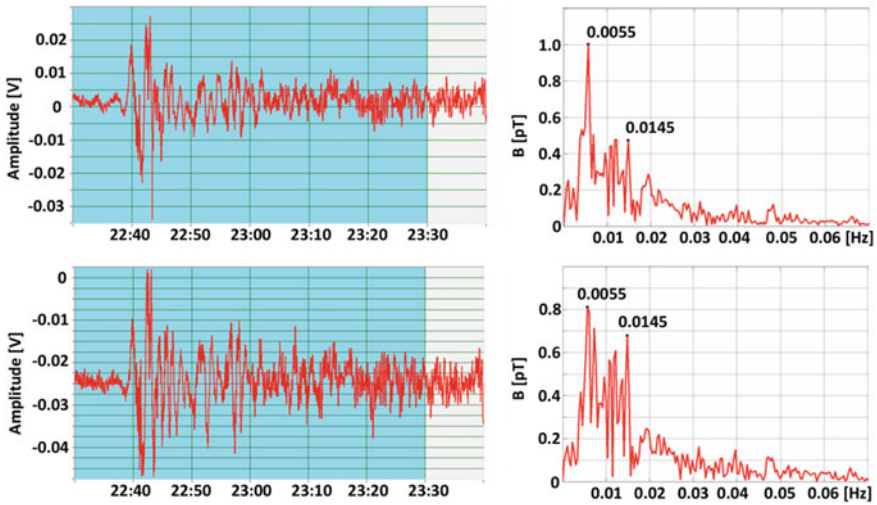
Fig. 4 Same as in Fig. 2 for 07.21.15. The blue sectors are the operating time of the SURA with modulation of 0.002 Hz

In the second session of July 9, 2015 with a modulation frequency of 5 MHz (T = 200 s) pulsations appeared during the session approximately 75 min after its start and lasted until the end of the session (see Fig. 3). Two frequency maxima in the spectrum at 7.5 and 1.6 MHz were observed (T = 133 and 62.5 s).

In the third session on July 21, 2015 with a modulation frequency of 2 MHz (T = 520 s) the pulsations appeared during the session approximately also 75 min after its start and lasted until the end of the session (see Fig. 4). There were also two frequency maxima in the spectrum at 5.5 and 1.45 MHz (periods T = 181 and 69 s).

4 Discussion

The generation of ULF long period magnetic pulsations using ionospheric RF heating was investigated in [5, 6]. The physical mechanism of such events is based on so-called ionospheric feedback instability (IFI) which was previously proposed to explain ionospheric–magnetospheric processes in the region of polar aurora arcs [7]. The main idea of this instability is that the current pulse flowing along the magnetic field line in the form of an Alfven wave increases with increasing density and conductivity of the ionosphere by precipitating electrons into the E-layer. The increased conductivity then returns to the structure and amplitude of the incident wave. The amplitude of ULF waves can be significantly enhanced if these waves form a standing structure inside the global magnetospheric resonator. The results of

numerical simulation presented in [5] showed that even relatively weak (at the 10% level) modification of the ionospheric conductivity using HF heating can initiate IFI and enhance its development.

Perhaps, this mechanism was realized in our experiments. In July 2015, another 5 sessions were held in the evening, in which no effects similar to those presented above were observed. However, in these sessions, the periods of manipulation of the SURA operation differed greatly from the modes of operation in the sessions in which the perturbations of the GMF were detected. Note that the powerful HF wave acting on the ionosphere must be modulated by the frequency of the most unstable ULF mode of the magnetospheric resonator. Most likely, in successful sessions such a coincidence happened fortuitously.

5 Conclusion

For a final understanding of the effects found in our experiment, it is necessary to simulate ionospheric feedback instability for mid-latitudes following the method described in [5] and repeat the experiment with preliminarily selected SYRA operating modes. In addition, it is necessary more carefully process the data already available.

References

1. Zelenov, L.N., Petrukovich, A.A., Lutsen, V.N., Mogiltvsky, M.M.: Interboll mission generates results on magnetospheric dynamics and magnetosphere–ionosphere interaction. EOS **85**(17), 169–176 (2004)
2. Mogilevsky, M.: Resonant interaction in the magnetosphere. In: Proceedings of RF Ionospheric Interaction Conference, pp. 340–354, Santa Fe, NM (2002)
3. Streltsov, A.V.: Resonant ULF Waves in the Magnetosphere: RF Ionospheric Interactions Workshop. Santa Fe, NM, April (2012)
4. Chang, C.-L.: BRIOCHE Program: Recent Results: RF Ionospheric Interactions Workshop, Santa Fe, NM, April (2012).
5. Streltsov, A., Lotko, W., Milikh, G.: Simulations of ULF field aligned currents generated by HF heating of the ionosphere. J. Geophys. Res. **110**(A4), 1–11 (2005)
6. Streltsov, A.V., Pedersen, T.R., Mishin, E.V., Snyder, A.L.: Ionospheric feedback instability and substorm development. J. Geophys. Res. **115**(A7), 1–11 (2010)
7. Atkinson, G.: Auroral arcs: Result of the interaction of a dynamic magnetosphere with the ionosphere. J. Geophys. Res. **7**(25), 4746–4755 (1970)

Simulation of Aluminum Jet Expansion in Active Geophysical Experiments Taking into Account Deviation of Ionization State from Thermodynamic Equilibrium

Marina Kuzmicheva🄳

Abstract

The results of the simulation of non-equilibrium ionization state of a rapidly expanding aluminum plasma jet of an explosive generator are presented. The jet is injected into ionosphere in active geophysical rocket experiments to produce a calibrated disturbance. A state of plasma with rapidly changing parameters deviates from equilibrium state, so numerical simulations of its behavior were performed by solving gas dynamics equations jointly with equations for ionization kinetics. "Freezing" of ionization degree in rapidly expanding plasma jet is demonstrated. Typical rates of ionization–recombination processes for electron temperatures and concentrations obtained in simulations are presented. Influence of ionization–recombination processes under consideration on values of gas dynamic parameters is shown. The applicability of the obtained results for various injection scenarios is demonstrated.

Keywords

Active geophysical experiment · Ionization · Calibrated disturbance

1 Introduction

One of the possible methods for studying the physical processes in the ionosphere and magnetosphere are active geophysical rocket experiments (AGRE), during which some calibrated disturbance source is impacted on the medium. To interpret

M. Kuzmicheva (✉)
Sadovsky Institute of Geospheres Dynamics RAS,
Leninsky prospect 38, b. 1, 119334 Moscow, Russia
e-mail: kuzm@idg.chph.ras.ru; mukuzmgm@gmail.com

the recorded phenomena, it is necessary to evaluate properly the parameters of the source used, its evolution and interaction with the background environment.

At the first stage of AGRE, plasma was injected at an altitude of 150 km, the mass of aluminum plasma was 15 g, and the energy was 3 MJ. In further experiments it was supposed to increase the mass and energy of the produced plasma. In the experiment, an aluminum plasma with an initial size of several centimeters and a speed of 30–40 km/s is scattered for several kilometers, while its relative density δ varies in tens of milliseconds from values from 10^3 to 10^{-10} ($\delta = \rho/\rho_0$, where ρ is the density of the jet, ρ_0 is equal 1.2 10^{-3} g/cm^3) [1, 2].

Traditional plasma state models (local thermodynamic equilibrium approximation (LTE), coronal equilibrium), describing a stationary plasma, are unsuitable for modeling a plasma with rapidly changing parameters. In this case, when considering the gas-dynamic motion, it is necessary to take into account the deviation of ion concentrations in both ground and excited states from stationary values.

2   Investigation Procedure

The simulation of the plasma jet expansion was carried out with help of the the solution of the system of one-dimensional gas-dynamic equations (1) written in lagrangian coordinates for the spherical symmetry. Comparison of the results of two-dimensional calculations with one-dimensional showed that for the axial part of the jet in a 1D calculation, the values of the parameters were obtained, which are similar to that obtained in a 2D calculation. Since the problem is solved taking into account the deviation of the plasma state from the LTE, the energy equations are written for the energies of ions and free electrons. The system of equations takes into account the difference between the electron and ion temperatures, the energy exchange of electrons and ions in elastic collisions, the electron thermal conductivity, the change in the energy of free electrons in inelastic electron-ion interactions (following [3]).

$$\frac{\partial u}{\partial t} = -\frac{r^{v-1}\partial p}{\partial m}$$

$$\frac{\partial(1/\rho)}{\partial t} = \frac{\partial(u \cdot r^{v-1})}{\partial m}$$

$$\frac{\partial r}{\partial t} = u \tag{1}$$

$$\frac{\partial e_i}{\partial t} + p_i\frac{\partial(u \cdot r^{v-1})}{\partial m} = \frac{Q_\Delta}{\rho}$$

$$\frac{\partial e_e}{\partial t} + p_e \frac{\partial (u \cdot r^{\nu-1})}{\partial m} + \frac{\partial (q \cdot r^{\nu-1})}{\partial m} = -\frac{Q_\Delta}{\rho} + \frac{Q_{nc}}{\rho}$$

$$q = -\rho \cdot \varkappa_e \cdot r^{\nu-1} \cdot \frac{\partial (T_e)}{\partial m}$$

$$p = p_i + p_e; \ N_i = \rho / m_{ion}; p_i = N_i \cdot T_i; \ e_i = 1.5 \cdot \frac{p_i}{\rho};$$

$$p_e = N_e \cdot T_e = \bar{z} \cdot \frac{\rho \cdot T_e}{m_{ion}}; \ e_e = 1.5 \cdot \frac{N_e \cdot T_e}{\rho}; \nu = 3;$$

$$p_i(t, r_{end}) = p_e(t, r_{end}) = 0; \ u(t, r_{init}) = const;$$

$$q(t, r_{init}) = q(t, r_{end}) = 0;$$

$$u(0, m) = u_0(m) \ ; \ T_e(0, m) = T_{e0}(m);$$

$$T_i(0, m) = T_{i0}(m); \ \rho(0, m) = \rho_0(m); \bar{z}(0, m) = z_0(m)$$

Here m is a lagrangian coordinate, t, u, r, ρ, p_e, p_i, T_e, T_i are time, velocity, an eulerian coordinate, density, electron and ion pressures and temperatures, respectively, e_e and e_i—energies of free electrons and ions per mass unit, N_e and N_i—electron and ion concentrations, $\bar{z}$—the mean ion charge, m_{ion}—ion mass, $\varkappa_e$—electronic thermal conductivity, q—heat, transferred by electron flow, r_{init}, r_{end} are the left and the right radii of the spherical segment, simulating the plasma jet, $u_0(m)$, $T_{e0}(m)$, $T_{i0}(m)$, $\rho_0(m)$, $z_0(m)$—initial distributions of variables. The right sides of the equations for electron and ion energies include various sources of energy release: Q_Δ—energy change in elastic electron-ion collisions and Q_{nc}—energy change due to non-elastic electron-ion collisions. The change of energy in elastic electron-ion exchange is written in the form (2) [3]:

$$Q_\Delta = \frac{3m_e N_e}{m_{ion} \tau_{ei}} (T_e - T_i) \tag{2}$$

where τ_{ei} is a typical time of electron-ion collisions [3], m_e—the electron mass. As inelastic processes leading to a change in the energy of free electrons, triple recombination, photo recombination, dielectron recombination, and ionization by electron impact were taken into account, rates of the processes were determined, according to [4]. In this approach [3], it is required to solve the system of ordinary differential equations (3) for the relative populations of the ground ion states simultaneously with the gas dynamic equations (1):

$$\frac{\partial \alpha^z}{\partial t} = \begin{cases} \text{Wrec}^{z+1} - \text{Wion}^z, z = 1 \\ \text{Wrec}^{z+1} - \text{Wion}^z - \text{Wrec}^z + \text{Wion}^{z-1}, 1 < z < z_{\text{nuc}} \\ -\text{Wrec}^z + \text{Wion}^{z-1}, z = z_{\text{nuc}} = 3 \end{cases} \quad (3)$$

$$\sum_z \alpha^z = 1; \ \text{Wion}^z = k_i^z \cdot N_e \cdot \alpha^z; \ \text{Wrec}^z = k_{\text{rec}}^z \cdot N_e \cdot N_e \cdot \alpha^{z+1};$$

$$\bar{z} = \sum_z (z - 1) \cdot \alpha^z; N_e = \bar{z} \cdot N_i;$$

Here α^z is a concentration of ions with a spectroscopic symbol z and multiplicity $z - 1$, related to total ion concentration N_i, Wrec^z and Wion^z—recombination and ionization flows, k_i^z—radiation–collision ionization coefficient, k_{rec}^z—radiation–collision recombination coefficient.

3 Simulation Results

3.1 Results of the Early Stage of the Expansion in Approximation of the LTE

The choice of initial conditions for the non-equilibrium task was based on the earlier calculation of the expansion of a high-temperature plasma jet with the speed distribution, obtained for the VGPS-5 generator, density 0.2 g/cm^3 and temperature of 2 eV in an assumption of the LTE. In time of $2 \cdot 10^{-4}$ s this aluminum plasma jet expands up to 8 m, it sets the temperature of 0.2–0.55 eV and a sharply falling density profile. The ionization degree in the jet is set at the level of 0.03–0.5.

3.2 Simulation of the Expansion Taking into Account Deviations from the LTE

In the non-equilibrium expansion simulations an aluminum jet with a mass of 1000 g/sr was considered. The jet speed grew almost linearly from 0 to 42 km/s, density was from 10^{-4} g/cm^3 down to 10^{-8} g/cm^3. Initially the electron and ion temperatures were equal to each other (1 eV—the case A, 0.5 eV—the case B), the initial degree of ionization was set equal to 0.5.

In Fig. 1a speed distributions over mass at time moments 0 ms и 10 ms are given, in Fig. 1b mass density distributions at times moments 0, 0.2, 1, 10 ms are shown. The change in speed and density over time is almost independent on the initial electron temperatures, because of the jet energy is dominated by kinetic energy.
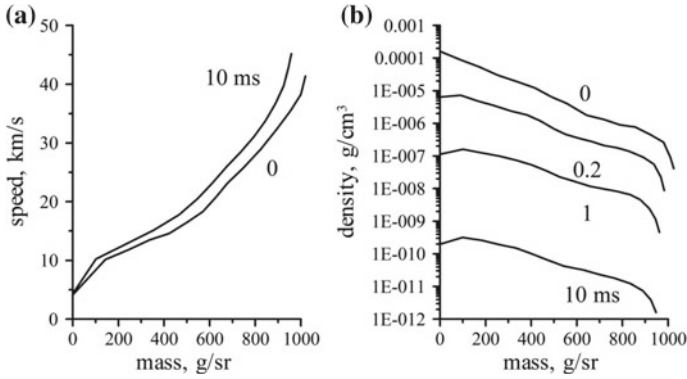
Fig. 1 Distributions of speed over mass coordinate at time 0 and 10 ms (**a**). Density distributions over mass coordinate at time points 0, 0.2, 1, 10 ms (**b**)

For the time of 10 ms the jet speed increased slightly and density decreased down to 10^{-12}–10^{-10} g/cm^3. The distributions of the electron temperature and the mean ion charge are shown in Fig. 2a,b for the two cases of initial temperatures A and B. The distributions of the electron temperature and the mean ion charge, which have been formed to the time point 0.2 ms, remain almost unchanged up to 10 ms. The plasma of the jet partially recombined, the initial state retained at the right edge in terms of the mean ion charge (designated by az) and electron temperature. "Freezing" of the degree of ionization is observed: a jet in the mass range from 600 to 1000 g/sr retains the mean ion charge of more than 0.1.
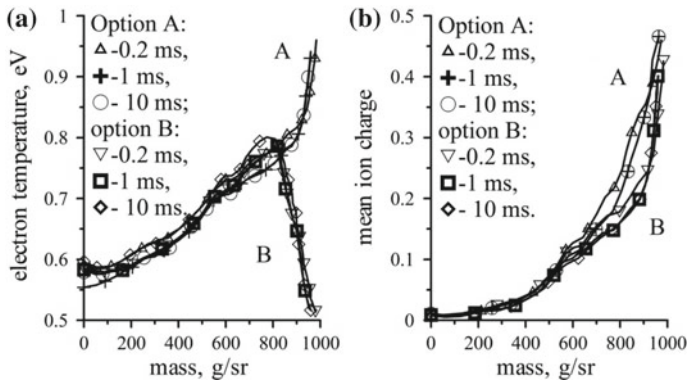
Fig. 2 Electron temperatures over mass for options A and B at different time points (**a**). Mean ion charge distributions over mass for options A and B at different time points (**b**)
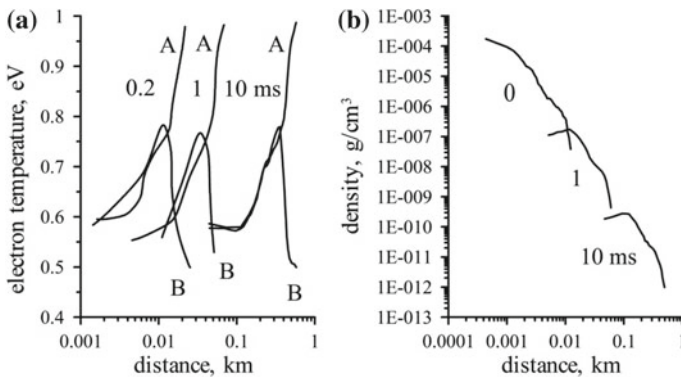
Fig. 3 Distributions of T_e along the jet axis for options A and B at time points 0.2, 1, 10 ms (**a**). Density distributions along the jet axis at time points 0, 1, 10 ms (**b**)

At different initial values of the electron temperature, the final distributions in the range of the jet mass from 0 to 600 g/sr are close. T_e lies in the range of 0.6–0.8 eV, az—in the range of 0.01–0.15.

In Fig. 3a,b, 4 the distributions of electron temperature, density, electron density, depending on the distance along the jet axis at different points in time are given. By the time of 10 ms, the right edge of the jet reaches a distance of approximately 550 meters, the speed retains the linear distribution. The average ion charge exceeding 0.1 is observed on distances from 250 to 550 m, electron temperatures in this area make up 0.7–1 eV (the case A) и 0.7–0.5 eV (the case B). The area where the electron concentration exceeds 10^{10} 1/cm³, extends from 50 to 450 m. The average charge retains values higher than 0.15 at the jet density of 10^{-6} g/cm³ and less (corresponds to a mass value of 600 g/sr). We can conclude that at the leading edge of the jet (the jet mass range from 600 to 1000 g/sr) the "freezing" of the ionization state is observed. The region of non-equilibrium ionization is several hundred meters. The value of the "frozen" degree of ionization depends on values of the jet parameters at a transition point from the LTE to the non-equilibrium stage.

4   Discussion of the Results

In general, the rate of relaxation of ionic composition is determined by the concentration and temperature of electrons and the initial composition. For a better understanding of the results consider the values of rates of ionization-recombination and the exchange of electrons and ions. Other processes: charge exchange of excited states of ions, for example, have smaller values of cross sections in comparison with these ones [4]. Temperature dependencies appear as [4]:

(a) for an electron impact ionization coefficient ci:

$$ci \sim \sqrt{bet} \cdot \frac{\exp(-bet)}{bet + hi}, \quad bet = \frac{ei}{T}; \tag{4}$$

(T is temperature, hi is a constant, ei—ionization energy);

(b) for a photo-recombination coefficient ph:

$$ph \sim bet \cdot \sqrt{bet}; \tag{5}$$

(c) for a three-particle recombination coefficient t:

$$t \sim ci \cdot \exp(bet)/T^{3/2} \tag{6}$$

Values of the coefficients for various temperatures are presented in Table 1.

At the beginning of the expansion the electron density lies in the range from 10^{18} to 10^{14} cm^{-3} (Fig. 4). Typical times of change of ions concentrations due to ionization-recombination are defined by the expressions $(ci \cdot N_e)^{-1}$, $(ph \cdot N_e)^{-1}$, $(t \cdot N_e^2)^{-1}$. At temperatures below 0.5 eV and electron concentration of 10^{15} cm^{-3} photo-recombination becomes the main process determining the ionic composition. The relaxation time due to photo-recombination is comparable with the expansion time, and the ionic composition "quenched" at an early stage of expansion. By the time of 10 ms the electron concentration falls down to 10^{11} cm^{-3}, the ionic composition is "frozen".

Elastic collisions of electrons and ions influence the temperature of electrons, thus influencing the ionic composition of the jet. Typical times τ for the electron-ion energy exchange are given in Table 2.

When the electron concentration drops down to 10^{11} cm^{-3}, electron-ion exchange slows down.

If plasma is quasi-adiabatic, its temperature decreases following to a well-known law (7):

Table 1 Kinetic coefficients

T_e, eV	Ci	Ph	T	Diel
2.0	6.41e−11	2.31e−13	2.1e−30	2.31e−11
1.5	2.83e−11	2.55e−13	2.37e−30	1.68e−11
1.0	9.35e−13	3.53e−13	3.56e−30	3.74e−12
0.5	4.3e−17	6.16e−13	7.18e−30	1.94e−14
0.3	8.8e−23	9.27e−13	1.29e−30	9.42e−18
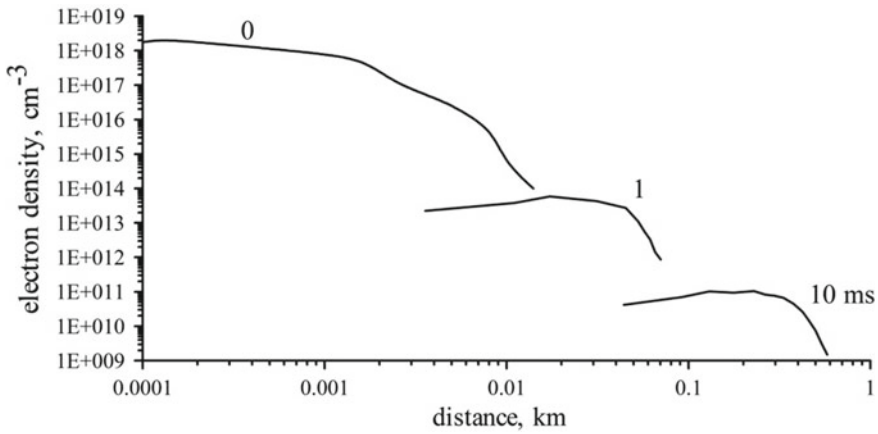
Fig. 4 Distributions of electron density along the jet axis at time points 0, 1, 10 ms

Table 2 Times of electron-ion energy exchange

N_e, cm^{-3}	T_e, eV	τ, s
1.0e+15	1.0	1.38e−06
1.0e+13	1.0	1.0e−04
1.0e+11	1.0	7.9e−03
1.0e+15	0.5	5.9e−07
1.0e+13	0.5	4.05e−05
1.0e+11	0.5	3.09e−03
1.0e+15	0.3	3.19e−07
1.0e+13	0.3	2.05e−05
1.0e+11	0.3	1.55e−03

$$T_2 = T_1 \cdot \left(\frac{V_1}{V_2}\right)^{\gamma-1} \tag{7}$$

where V_1, V_2 are the specific volumes (inverse densities) at different times, γ is the effective adiabatic exponent. Table 3 shows the estimate of ion temperature for the densities obtained in the simulation of expansion (Fig. 1b). The curves are counted from the top to the bottom, the initial temperature corresponds to the case A, γ is chosen to be 1.2.

Table 3 Ion temperatures

Density	1	2	3	4
T_i, eV	1.0	5.43e−01	3.66e−02	4.64e−04

The electron temperature, obtained in these simulations at the time point of 10 ms (Fig. 2a) is noticeably greater than the estimated ion temperature (Table 3). This result is possible to be explained by the fact that the electron temperature is determined by contributions of various processes. It falls during adiabatic expansion, decreases by ionization, by photo-recombination radiation, by exchange with ions, and increases by three-particle recombination. Upon further expansion under the conditions of "quenching" of the ionic composition, there is no recombination heating, the electron temperature should fall, but the degree of ionization does not decrease in that case.

4.1 Another Jet Injection Scenario

The results of the non-equilibrium simulations are possible to use for study other injection scenarios to predict when "quenching" of ionic composition can occur. An injection of a jet of the VGPS-1 generator into highly rarefied air was considered [5]. The simulation was performed in the framework of 2D cylindrical geometry under the LTE conditions. In Fig. 5a,b temperature and electron density distributions along the jet axis at the time of 10 μs are shown, soon after the end of the injection. In accordance with the numbers in Table 1 and the electron concentrations, the assumption that the plasma jet is in the LTE is correct.

In Fig. 6a,b the same distributions are shown for the moment of time of 23 μs. The temperature and electron concentration fell. According to the values of the ionization-recombination rates (Table 1) the jet plasma, displaced at 10 cm from the injection site is not in the LTE. While the jet mass exceeds the air mass, involved in the interaction, inertial expansion will take place, the electron concentration will decrease proportionally to the density with a constant ionization degree.
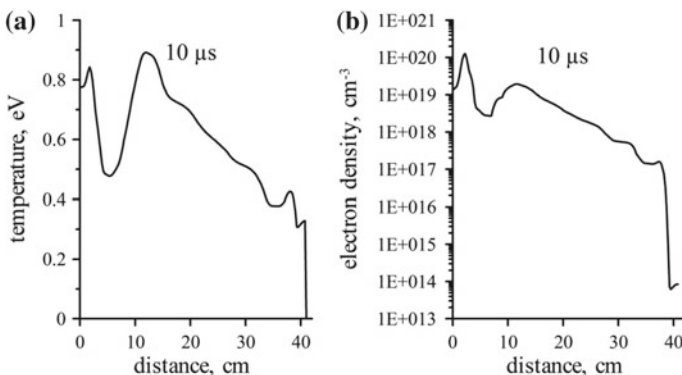
Fig. 5 Temperature distribution along the jet axis at the time moment of 10 μs (**a**). Electron density distribution along the jet axis at the time moment of 10 μs (**b**)
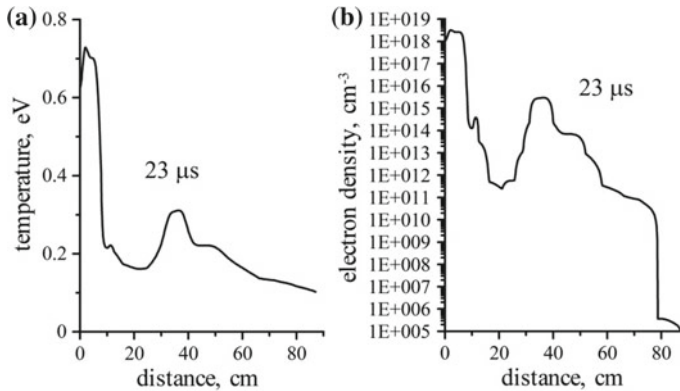
Fig. 6 Temperature distribution along the jet axis at the time moment of 23 μs (**a**). Electron density distribution along the jet axis at the time moment of 23 μs (**b**)

5 Conclusions

"Quenching" of ionic composition of the expanding jet was demonstrated by simulations. Influence of ionization–recombination processes on values of electron temperatures was shown. Results of the simulations are possible to be applied to various scenarios of injection of aluminum jets in order to estimate plasma ionization state and electron concentrations. A comparison with measurements made during the AGRE will be made in the future.

References

1. Adushkin, V., Zetser, Yu., et al.: Aktivnie geofizicheskie raketnie experimenti s injectiey plasmennoy strui v ionosphere (Active geophysical rocket experiments with injection of plasma jet into ionosphere). DAN (Doklady Earth Sciences) 331, 486–489 (1993) (in Russian)
2. Gavrilov, B., Erlandson, R., et al.: Dynamics of a high energy plasma jet in space: in situ experiment and laboratory simulation. Adv. Space Res. **21**(5), 773–776 (1998)
3. Gudzenko, L., Yakovlenko, C.: Plasmennie laseri. (Plasma Lasers) Atomizdat, Moscow (1978) (in Russian)
4. Sobelman, I., Vainshtein, L., Yukov, E.: Exitaion of Atoms and Broadening of Spectral Lines, 2nd edn. Springer, Berlin Heidelberg, New York (1995)
5. Loseva, T., Golub, A. et al.: Nachalnaya stadiya razvitiya plasmennoy strui v AGRE. (Initial stage of plasma jet evolution). Dinamicheskie processi v geosferah (Dynamical Processes in Geospheres), pp. 102–110. GEOS, Moscow (2017) (in Russian)

VLF Emission Excited by Electric Generator Mounted on Satellite INTERCOSMOS-24

Yuriy Mikhailov

Abstract

The paper presents the results of the VLF emission stimulated by electric generator mounted on the satellite INTERCOSMOS-24. Electric generator excited each second the 250 ms impulses at frequencies within the range from 1.5 to 19.5 kHz with increment of 1 kHz. The impulse amplitude within a cycle was constant and c hanged only from cycle to cycle by 50 V from 50 to 200 V. The corresponding antenna current changed from 0.75 to 2 mA. A three-component VLF receiver mounted on the same satellite operated in the frequency band from 20 Hz to 20 kHz. The paper features the analysis of the specific discrete and noise effects observed at the generator operation. We have detected the ELF and LHR noises, discrete signals with falling frequency, and "echo", as well as the prolonged impulse generator and its spectrum broadening. Some of these effects are similar to natural processes occurring at operation of terrestrial transmitters. At first, for interpreting these effects, we consider theoretical statements used for explanation of the natural signals. In particular, it is assumed that the generator impulse broadening can be explained by the nonlinear addition of the impulse itself and natural noise signal.

Y. Mikhailov (✉)
Institute of Terrestrial Magnetism, Ionosphere and Radio Wave Propagation (IZMIRAN), 108840 Troitsk, Moscow, Russia
e-mail: yumikh@izmiran.ru

1 Introduction

In his papers [2, 3] Helliwell proves that many wave effects have a complicated time structure and cannot be explained by the linear theory. For example, he has detected an interesting phenomenon occurring at registration of the SIPLE transmitter located in Antarctica at a frequency of 5 kHz at the Riverball station (Canada) in the Northern hemisphere. The pulse modulation of a signal with a changing impulse duration helped detect that the impulse back front induced emission. The induced emission range can be broad enough and the emission form depends on duration of the pulse modulation. Further investigation was carried out both as the terrestrial observation of the SIPLE transmitter at the conjugate point and as the observation of the terrestrial long-wave signals received on the satellites: ISIS, DE-1 [1]. The articles mentioned above contain the main judgments for interpretation of the observed phenomena.

At the eighties of the previous century, the idea to mount both the emission source and the receivers on the same satellite was proposed. Electrical and magnetic antennas, as well as the relating generators and a VLF receiver for recording the emission were mounted on the satellite INTERCOSMOS-24. It should be noted that the article written by Molchanov [7] has the results of the magnetic antenna (3 on Fig. 1) operation, while the papers written by Mikhailov and Gdalevich with other authors [6, 8] feature the analysis of the electrical antenna work. In the latter papers, it has been shown that the effects occurring at artificial influence on plasma by electric field are very similar to those observed in nature. We relied on this fact in our theoretical explanation of the effects under consideration. The monograph written by Trachtengerts and Ratclif [11], featuring the classified description of the nonlinear effects, greatly influenced at our explanation. At the same time, the artificial influence at plasma onboard the satellite raised questions discussed in this paper. Besides, new experimental capabilities have opened and they can be advantageous for further investigation in space.

2 Experiment

The satellite INTERCOSMOS-24 was launched September 28, 1989 on the orbit with parameters: apogee—2500 km, perigee—500 km, inclination—82.5, orbit period—116 min [8]. Figure 1 features the picture of the satellite. Satellite had the three-axis orientation: with its Z-axis directed to the Earth center, X coinciding with the satellite velocity direction and Y perpendicularly of velocity direction. A plasma excitation source (PES) was one of the main research tools and contained a generator of electrical impulses with a duration of 250 ms with the frequency modulated by 1 kHz within the frequency range from 0.5 to 19.5 kHz and the pulse/pause ratio equal to 1/3. The generator at its operation repeated four cycles with the different amplitudes: 50, 100, 150 and 200 V, while the antenna current was equal to 1.5 mA at the voltage of 100 V. The oscillating magnetic field of 1.8
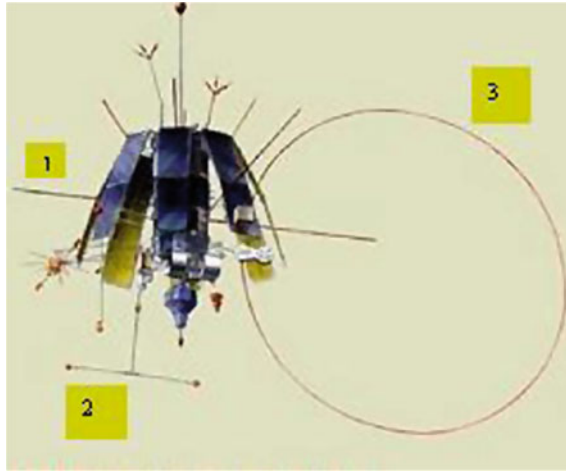
Fig. 1 The picture of the satellite INTERCOSMOS-24

nT was at a distance of 1 m from the antenna. Such magnetic field in the close zone of emission corresponds to the electric-field intensity of $E \sim 2.0$ mV/m.

A linear antenna of PES (1 on Fig. 1) with the X-axis directed beam of 7.5 m served as the impulse emitter. The electric (2 on Fig. 1) and the magnetic antennas (missing on figure) of the received device ANCH– 2ME also mounted on the satellite. The device electrical probes were in line with X-axis at a distance of 2.5 m from each other and 7 m from the antenna in the direction perpendicular to it's axis (1 on Fig. 1).

The paper presents the copies of photographic films of the dynamic spectra of primary analog signal records emitted from the satellite and received by using analog spectrum analyzer. Below we consider four cases on the nonlinear processes induced in plasma by the PES impulses.

In first case (Fig. 2) the excited VLF emission was been registered on orbit 954 13.12.1990 at 20:21:00 Moscow time ($L = 2$, $h = 503$ km) [5]. Noise signals containing frequencies below the PES impulse frequency were detected within the impulse duration. In some cases, a frequency gap between the impulse emitted and the induced noise band was detected in the spectrogram.

Figure 2b presents amplitude spectra of the broadband channel recorded on the device ANCH-2ME. Spectra were formed each 25 ms. Emission having the noise character at the frequency range 1–2 and 5–7 kHz was detected at the generator operation at 11 and 14.5 kHz and it could be considered electrostatic noise. The spectrum intensity is estimated within the interval 5–35 dB relating to $E = 5 \text{mkV/m/Hz}^{1/2}$ in the X-axis direction at the scale 30 dB/cm.

In the second case, a set of noise emissions at the frequency range 0.5–2 kHz (Fig. 3), induced in plasma was detected. Another induced signal with frequency falling down to $f \sim 1$ kHz (16–19) occurred at the time of the back front of the
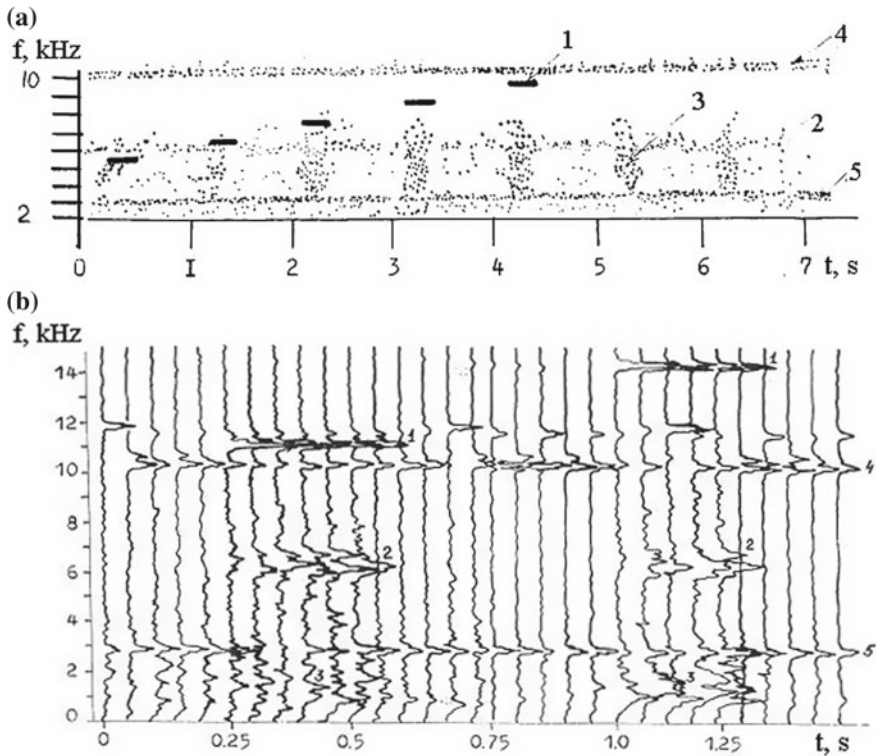
Fig. 2 a Spectrogram of the broadband VLF record (the band of 2–10 kHz); 1—generator impulses with the amplitude of 50 V at frequencies from 5.5 to 9.5 kHz, 2—LHR-noises, 3—induced signals, 4 and 5—the satellite signals. **b** Amplitude spectra at the scale 30 dB/cm: 1—generator signals, 2—LHR noises, 3—ELF noise, 4 and 5—the satellite signals

generator impulse. The signal had the discrete structure of its time and frequency. At the frequencies 5.5 and 8.5 kHz the generator impulse time increased by 3–4 times.

Figure 4a features the continuation of the cycle started on Fig. 3. The generator impulses with frequencies higher than 10 kHz that are not seen on the figure trigger signals with falling frequency (20–23…) at the range below LHR. We also paid attention to the LHR emissions, marked as 5, occurring simultaneously with the generator operation at the frequency range from ∼4.5 to ∼7.5 kHz. See three peeks at the frequency band f ∼ 1 kHz. Figure 4b features the example of the signal processing of the signal with falling frequency, marked 21 on Fig. 4a, with use of the Tarcsai program [10]. The crisscrosses on the dashed curve show the values measured on spectrogram, and the continuous curve is obtained by using the least square method inbuilt in the program for calculation of the signal characteristics and parameters of the ionosphere.
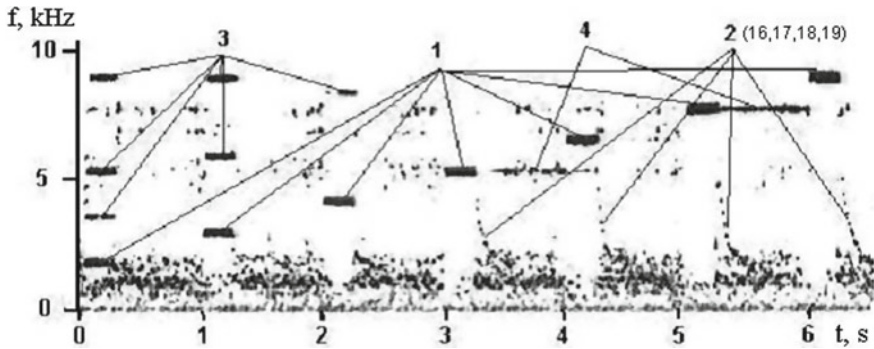
Fig. 3 Spectrogram of the VLF emission within the range 0–10 kHz at the generator operation amplitude 50 V at orbit 1238. The cycle stated at 17:02:20: MSK. The satellite orbit data: $h = 873$ km, $\varphi = 42°$, $\lambda = 38°$, $L = 1.8$. Legend: 1—signals of the generator; 2 and 4—induced signals, 3—generator signal harmonics

Figure 5 features the example of a cycle starting at 17:04:20: MSK and the amplitude of the generator signal 100 V. We observe the prolonged generator impulse almost at all frequencies. Besides, the interrupted signals with the falling frequency occur at the time of the impulse back front or after the prolonged impulse. These signals are characterized by low intensity.

Figure 6 features the case of the echo signals. A sequence of the PES impulses superposes with another sequence of impulses in the reverse mode. It is possible if such this sequence is the echo signals coming after main signals with a delay of 20 s or more due to the propagation among higher L shells. It should be noted that the echo signals with a significant delay for separate impulses have also been detected in the paper [7].

3 Discussions

Now we consider the following groups of signals.

(a) Low frequency noise (Fig. 2a). We assume that the noises under consideration are electrostatic noises transformed under the influence of a strong external signal with a higher frequency. By using principle of phase synchronization, we write the waves property equation (external ω1) and ELF wave (ω2):

$$\omega_1 \pm \omega_2 = \omega; \; k_1 \pm k_2 = k, \tag{1}$$

where $\omega_1 > \omega > \omega_2$ and $k_1 > k > k_2$. This method was applied for solving the problem of broadening spectrum of the low-frequency signals in the ionosphere plasma [9]. We also assumed that external signal propagates in the "whistler" mode and angle between $\mathbf{k}_1$ and $\mathbf{B}_0$ is significant at $\omega_p/\omega_{Be} >> 1$ (ω_p, ω_{Be}—plasma and gyro
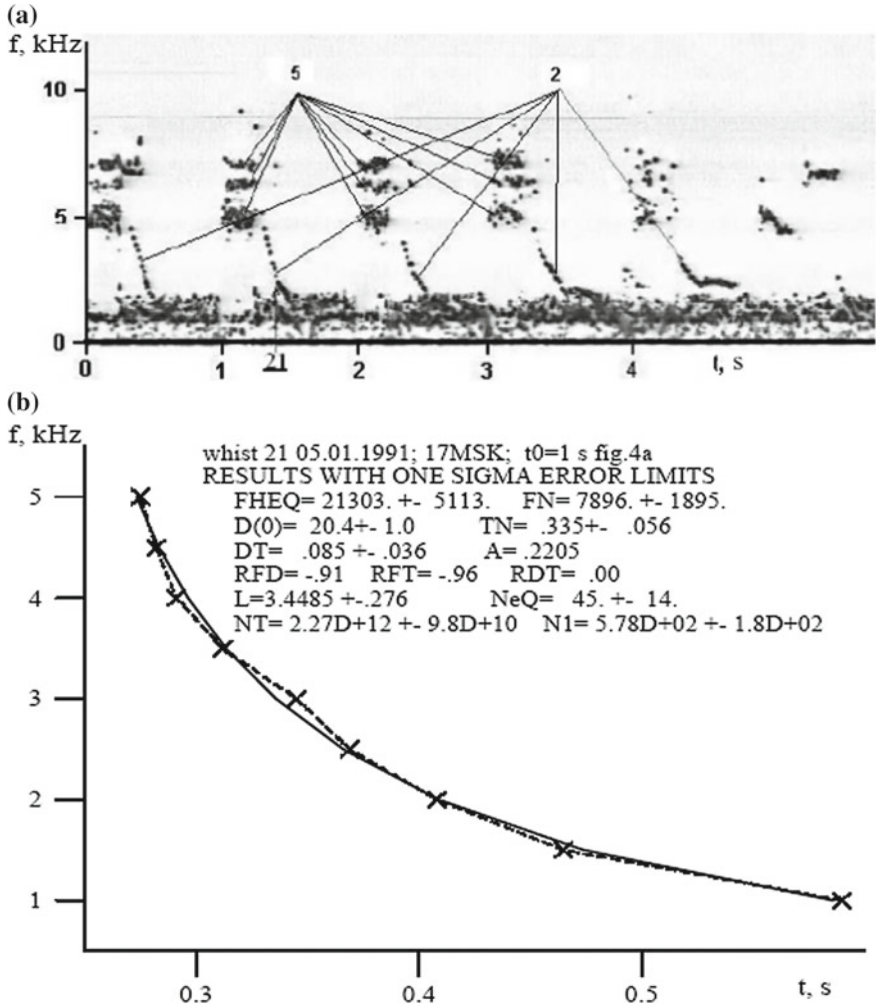
Fig. 4 **a** Spectrogram of VLF signal at the band 0–10 kHz, continuation of the cycle with the amplitude of 50 V at the frequency range from 11.5 to 19.5 kHz. The figure features only the lower part of the spectrum. 2—induced signals with falling spectrum; **b** Example of a phase of the digital processing of the signal marked as 21

frequencies), $k_1 = 20$ km^{-1}. To establish the relation between ω_1 and k_1 we use the equation

$$\omega_1 = \omega_{Be}k_{1Z}/k_1\left(1 + \omega_p^2/k_1c^2\right)^{-1} \tag{2}$$
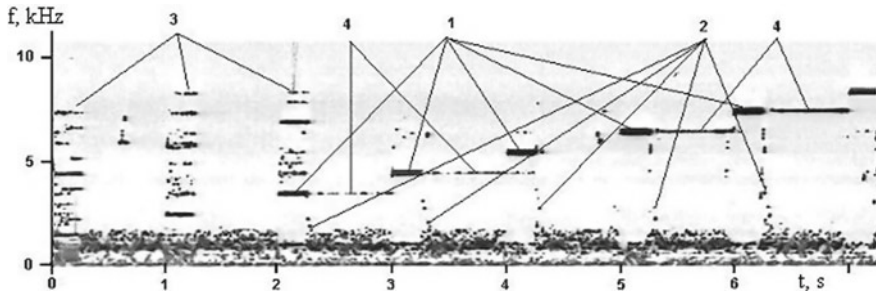
Fig. 5 Spectrogram of the VLF signals at the frequency range 0–10 kHz, marked the same as on Fig. 3. At this time, the satellite was at a height of 920 km and the L shell equal to 2.3

17:03:00
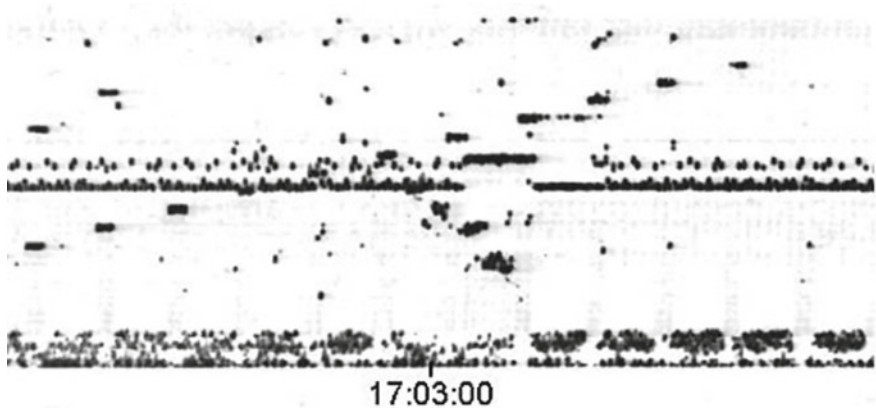
Fig. 6 Echo signals of the generator impulse in the reverse mode

For ELF-waves, we assumed $f_2 = 2$ kHz as the characteristic frequency, $k_2 = 3$ km^{-1}, angle $\theta_2 \leq \pi/2$ and the relation between $\mathbf{k}_2$ and ω_2 had the following form

$$\omega_2 = \omega_B \mathbf{k}_{2Z}/\mathbf{k}_2 \left(\mathbf{k}_2 c^2/\omega_p^2 \right), \tag{3}$$

where ω_B—the proton gyrofrequency.

Then, by using nonlinear relation between the constant ε and amplitudes of waves E_1 and E_2, we defined non-linear current occurring between the waves. Under these conditions it was significant that the angles θ_1 and $\theta_2 \leq \pi/2$, thus the relation of the amplitudes of the newly created wave E and the external wave was equal to E/E_1. The final result is: at $f_{Be} = 850$ kHz, $f_p = 6 \cdot 10^{3 \text{ kHz}}$, $B = 3 \cdot 10^{-5}$ T, $\lambda = 100$ m, volume $E/E_1 = 0.05$. Now return to our experiment. In this case, the Eq. (1) is written as $\omega = \omega_1 - \omega_2$, $\mathbf{k} = \mathbf{k}_1 - \mathbf{k}_2$. So, this problem should be considered

separately. At this phase we just compare the results of primary processing of our experimental data with the theoretical calculations presented in the paper [9] may be considered as analogy we applied quality comparison of our results with the same by authors of [9].

For a PES signal with a frequency 11 kHz (Fig. 2a) at a height of 500 km we have at $f_{Be} = 7000$ kHz, $f_p = 60000$ kHz, $B = 3 \cdot 10^{-4}$ T, $k_1 = 6$ km^{-1}, $k_2 = 2.1$ km^{-1}, $E_1 = 3.5$ mV/m, $E/E_1 \sim 0.12$.

Thus, our results correspond qualitatively to the model adopted in the above mentioned paper. It means that the mechanism proposed in this paper can be applied for explanation of the effects occurring at the PES operation.

(b) Interrupted signals. At processing the interrupted "whistles" [4] it have been established that if two frequency-modulated signals with fast changing frequencies act on filter, they can be separated, if $(\delta t)^2 > \delta t_{opt}/\Delta F_{opt}$, where δt—the interval between signals, ΔF_{opt}—optimal band of filter, δt_{opt}—response of filter. Band of filter and velocity of changing of frequency are connected by the equation, if $\delta t > \delta t_{opt}/\Delta F_{opt}$, where δt—the interval between signals, ΔF_{opt}—optimal band of filter, δt_{opt}—response of filter. Band of filter and velocity of changing of frequency connected by equation

$$\Delta F_{opt} = \beta/(\pi \cdot f_{ins}), \tag{4}$$

where $\beta = df/dt$—velocity of the frequency change, f_{ins}—instant frequency. The applied filter analysis band of 100 Hz complies (4) for the nonlinear signal with the normal frequency change velocities $\beta \sim 10^3$ Hz/s [8]. However at the sharp frequency drop at the PSE operation mode, i.e., the impulse back front = 1 ms, β can reach 106 *Hz*/s, which leads to violation of this condition. Using a filter with a lower analysis band inevitably results in a longer analysis time and makes the separation of such signals impossible.

(c) LHR-noises. The signals shown on Fig. 3 consist of two branches. The first branch spreads from the impulse back front frequency to the low hybrid resonance frequency, and the second one is characterized by the drastic decrease from the LHR frequency to the ULF range of about 10 Hz. Note that the second branch has a very high dispersion and a wide spread of data across the L shells. Apparently, these signals propagate by some other way different from the "whistler" mode. On the other part, Fig. 6 show a contrary situation in which the low-frequency signals are close to the "whistler" mode and at the same time the signal dispersion is about 10–15 s^{-1}. The signal delay relating to the impulse back front of about 1 s can be explained at least double way of the signal along the magnetic field line. We link the induction of these signals with the cyclotron resonance and nonlinear triggering of the signal. The delay of approximately one second may be caused by the fact the signals have covered the double way from the force line top to ionosphere and backward to the generator location area.

(d) Prolonged impulses. Figures 3, 4 and 5 show, that some impulses have a longer length. We have called this phenomenon as the prolonged length or the length prolongation. It can reach several seconds. Helliwell had already observed

this effect on earth [3] and on the satellite ISIS. Later Smith and Nunn [8] did the computer simulation after the operation in plasma, for which they used the relation:

$$\frac{\partial f}{\partial t} \sim V^2 g \frac{dk}{dz}, \tag{5}$$

where V_g—group velocity. This relation, obtained earlier by Nunn, results in:

$$\frac{dk}{dz} \sim \frac{1}{V^2 g} \frac{\partial f}{\partial t}, \tag{6}$$

Now, by placing the origin point in the impulse end and transferring to the integrated form we obtain

$$k_{1Z} - k_{2Z} = \frac{1}{V_g^2} \frac{\partial f}{\partial t} \Delta z \tag{7}$$

Then we assume $\kappa_{2z} = 0$, which results in the relation

$$\Delta z = k_{1z} V_g^2 \frac{\partial t}{\partial f}, \tag{8}$$

By using the equation for the group velocity of whistles

$$V_g = 2c \frac{\sqrt{ff_B} \cos \theta}{f_p} \tag{9}$$

and taking in (9) $f_B = 5.7 \cdot 10^6$ Hz, $f_p = 2 \cdot 10^7$ Hz, with consideration of Fig. 5, we obtain $V_g = 4.7 \cdot 10^3$ km/s. Then we substitute V_g^2 in (8) by its value equal to $22 \cdot 10^6$ km^2/s^2. For the purpose of assessment we set the impulse back front duration 1 ms, which corresponds to $4 \cdot 10^{-3}$ of the impulse duration of 250 ms. Considering the front duration and the basic frequency $8 \cdot 10^3$ Hz we obtain $dt/df = 0.127 \cdot 10^{-6}$ c^2. For $f = 8 \cdot 10^3$ Hz we obtain $k = 2.3$ km^{-1}. As a result (8) is written as:

$$\Delta z = 2,3 \cdot 22 \cdot 10^6 \cdot 0.129 \cdot 10^{-6} = 7 \text{ km}.$$

The impulse delays vary within the range from 0.5 to 1.5 s. The satellite can cover approximately 3.5–14 km for this time. As satellite trajectory may be other than the z direction we selected, we consider that the values show the good correspondence with each other.

(e) Trajectory of signals excited by generators and the signal dispersion. Earlier in this paper, we studied the modification of the signal spectra. In this part, we consider trajectory of excited signal with the purpose to establish how these signals propagate. We tried to process by using the Tarcsai program designed for

processing the whistle signals [10]. When doing that we were not certain that the program was applicable for the signals created by PES.

Below are the signal processing results. Figure 3 features the signals marked by 16, 17, 18 and 19. The subsequent signals of this cycle (20, 21, 22, 23), corresponding to the excitation frequency from 11.5 to 19.5 kHz are shown on Fig. 4. Tarcsai have stated that the iteration procedure inbuilt in the program converges rapidly if the characteristics of studied signals correspond to the theoretical provisions of the whistle signals propagation. Application of the program for processing the signals marked 16–22 shows that the best processing result is achieved for signal 21. Figure 4b features the processing result: curve 1 shows the drape effect obtained by using the least square method for curve 2. This curve is drawn basing on the data of the narrow photo film containing the result of spectrum analysis of tape record.

As a result, the parameters of both "virtual whistler" and plasma in the field tube were obtain. Besides that, we have correctly identified the L shape at the excitation area as equal to 2.3. We also defined the following parameters: $N_T = 3 \cdot 10^{12}$—the number of electrons in the field tube, $n_e = 3 \cdot 10^3$ 1/cm^3—density of electrons at the height of 1000 km, $n_B = 337$ 1/cm^3—density of electrons at the top point of the field tube. The signal dispersion $D_0 = 20$ 1/s makes us assume that the signal propagates by the whistler mode.

The obtained plasma parameters are in good correlation with the known parameters of the night conditions at wintertime. Thus, it have been established that the PES signal trajectories coincide with the whistle trajectories at least for separate cases. Figure 6 features a fragment of a PES signal that is superposed with a fragment of a similar signal however having the reverse sequence of the frequencies. It may be the echo signal, however in this case its delay should be approximately 20 s, which corresponds to the time of one cycle. Such phenomena confirm the fact that the PES signal packets move in the magnetic field tubes with quite considerable L values.

4   Conclusions

This paper features a set of signals excited in plasma by electric generator. These signals are a wide range of linear and nonlinear signals. During the investigation performed, we have worked out three possible explanations concerning these signals:

- a nonlinear current caused by the nonlinear interaction of waves with the different intensity and frequency values;
- the signal fragmentation caused by beating of two signals with close values of frequencies;
- the signal prolongation as a result of impact of interaction of processes of rapidly changing signal frequencies in plasma.

It should be noted, that we detected the coincidence of the PES signals trajectories with the whistle trajectories, so the signal propagating through these channels can be considered the trigger whistles. By processing these signals with use of the Tarcsai program, we have assessed the plasma parameters both for a height of 1,000 km and for the top point of the magnetic field lines of the L shell locating the satellite. The issue concerning propagation of the artificially excited whistlers to the Earth is advantageous for the further investigation. It is known that the most of ducted whistles were detected on the earth. The intensity of the excited whistles is comparable with that of natural whistles. This gives the grounds to believe that these whistles can be observed on the Earth too.

References

1. Bell, T.F., Helliwell, R.A., Hudson, M.K.: Lower hybrid waves excited through linear coupling and the heating of ions in the auroral and subauroral magnetosphere. J. Geophys. Res. **2**(96), NA7, 11.379–11.388 (1991)
2. Helliwell, R.A.: VLF wave-injection experiments from SIPLE station. Antarct. A-db. Space Res. **8**(1), 279–289 (1988)
3. Helliwell R.A. Whistlers and Related Ionospheric Phenomena, p. 350. Stanford University Press, Palo Alto California (1965)
4. Mikhailova, G.A., Kapustina, O.V.: Some results of analyze of quasi period structure at active experiments. Cosmic Investig. (in Russian), **XIII**(3), pp. 458–460 (1976)
5. Mikhalov, YuM, Kapustina, O.V., Ershova, V.A., Roste, O.Z., Shulchishin, YuM, Kochnev, V.A., Smilauer, J.: Definition of the low hibrid frequency by activ wave method on Intercosmos 24 satellite and comparison these data with mass-spectrometer experiments. Adv. Space Res. **15**(12), 147 (1995)
6. Mikhalov, Yu.M., Klos, Z.: Injection. Scientific cooperation between Russian Academia of the Sciences and Polish Academia of the Sciences. Results of the Cooperative Investigations. Moskva IKI (in Russian), pp. 149–158 (2016)
7. Molchanov, O.A., Mogilevski, M.M., Afonin, V.V., Klos, Z., Hayakawa, M., Shima, N.: Nonlinear ELF-VLF-effects observed on Active satellite. Asian J. Geophysics. **1**(1), 1–12 (1997)
8. Smith, A.S., Nunn, D.: Numerical simulation of VLF risers, fallersand hooks, observed in Antarctica. J. Geophys. Res. **103**(4), 6771–6784 (1998)
9. Sotnikov V.I., Fiala, V., Lefevre, F., Lagoutie, D.: Excitation sideband due to nonlinear coupling between VLF transmitter signal and a natural ELF Emission. JGR. **96**(17), 11363–11369 (1991)
10. Tarcsai, G.: Routine whistler analysis by means of accurate curve fitting. J. Atmos. Terr. Phys. **37**, 1947–1957 (1975)
11. Trakhtengerts, V.Y., Ryscroft, M.J.: Whistler and alfen mode cyclotron masers in space, p. 344. Cambridge university Press (2011)

The Influence of the Magnetic Field Inclination on the Quasistationary Electric Field Penetration from the Ground to the Ionosphere

Semen Nesterov , Valery Denisenko ,
Mohammed Yahia Boudjada and Helmut Lammer

Abstract

A quantitative model of the penetration of a quasistationary electric field from the Earth's surface into the ionosphere with an inclined magnetic field is developed. A two-dimensional model is constructed and applied when the earthquake preparation zone is extended along a magnetic meridian. In the main part of the atmosphere up to a height of 50 km, we use an empirical conductivity model. Above 90 km we use the model, which is based on the empirical models IRI, MSISE and IGRF. In the rest layer the values of the components of the conductivity tensor are interpolated. The conjugate ionosphere is included to the model since the field-aligned conductivity in the magnetosphere is regarded as an infinite one. We solve the electric conductivity problem using Fourier transform at each height and numerically solve the systems of ordinary differential equations for the Fourier coefficients. The space distributions of the electric field strength and the current density are calculated. The current lines in both hemispheres are plotted. The electric field strength in the ionosphere is in the microvolt per meter range when it is about 100 mV/m in the air near ground. The known approximate estimates of the decrease of the electric field penetrating into the ionosphere with the decrease of the magnetic latitude are confirmed and

S. Nesterov (✉) · V. Denisenko
Siberian Federal University, 79 Svobodny Prospect, 660041 Krasnoyarsk, Russia
e-mail: Twist3r0k@yandex.ru

V. Denisenko
Institute of Computational Modelling, Russian Academy of Sciences, Siberian Branch, 660036 Krasnoyarsk, Russia

M. Y. Boudjada · H. Lammer
Space Research Institute, Austrian Academy of Sciences, Schmiedlstrasse 6, 8042 Graz, Austria

detailed. The penetration of the electric field and current from the ground to the ionosphere through the atmospheric conductor cannot be a physical process which creates observed ionospheric precursors of earthquakes.

Keywords

Atmosphere · Ionosphere · Earthquake · Mathematical model

1 Introduction

Interest in lithosphere-ionosphere relationship is mainly caused by the need to forecast earthquakes, since several satellite observations show ionospheric electric field perturbations above seismic regions. Nowadays, the most popular models consider the lithosphere as a generator of an electric current or an electric field in the atmosphere. These models take into account the atmosphere and the ionosphere as a united conductor and are based on a stationary model of electrical conductivity. In other words, the penetration of a quasistationary electric field from the Earth's surface into the ionosphere is the basic physical process in such models. Such models are associated to numerous observations of disturbance in the vertical component of the atmospheric electric field before and after earthquakes. At the present time, three- and two-dimensional models of a conductor that includes the atmosphere and the ionosphere are known [1, 2]. However, such models are created for a vertical magnetic field, and therefore they are applicable only at high latitudes. An exception is the work [3], but it contains incorrect simplifications which significantly distort the results, as shown in the article [1]. Some new models are analyzed in article [4]. The article [5] considered the role of the magnetic field slope for the preparation zones of earthquakes elongated in magnetic longitude.

The purpose of this work is to build a quantitative model of the penetration of a quasistationary electric field from the Earth's surface into the ionosphere with an inclined magnetic field. A two-dimensional model is constructed, which is applicable when the earthquake preparation zone is extended along the magnetic meridian. For such a case, estimates are done in [6].

2 Basic Equations

In general, the physical model used by us is formulated in the monograph [7]. It is adequate to use a steady state model for a conductor with the conductivity tensor $\hat{\sigma}$ if the typical time of the process is much larger than the charge relaxation time $\tau = \varepsilon_0/\sigma$. Minimal value near ground is $\sigma > 10^{-14}$ S/m. The charge relaxation time in the Earth's atmosphere does not exceed a quarter of an hour.

The basic equations for the steady state electric field $\vec{E}$ and current density $\vec{j}$ are Faraday's law, the charge conservation law, and Ohm's law,

$$\text{curl } \vec{E} = 0, \tag{1}$$

$$\text{div } \vec{j} = 0, \tag{2}$$

$$\vec{j} = \hat{\sigma}\vec{E}, \tag{3}$$

Because of Eq. (1) the electric potential V can be introduced so that

$$\vec{E} = -\text{grad } V. \tag{4}$$

Then the system of Eqs. (1)–(3) is reduced to the electric conductivity equation

$$-\text{div}(\hat{\sigma}\text{grad } V) = 0. \tag{5}$$
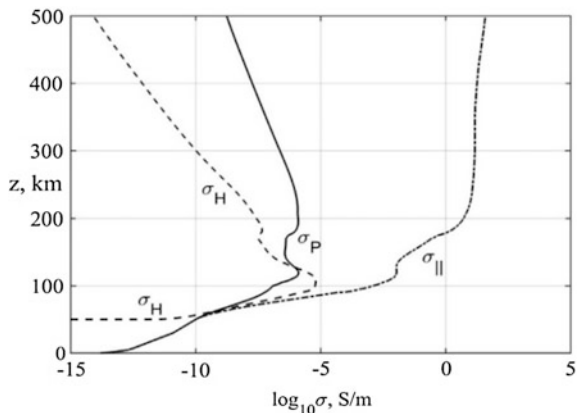
3 Conductivity

Here we study a two-dimensional model, which is approximately valid for fracture regions stretched in one direction, i.e. along the magnetic meridian. Therefore, we assume that all parameters have no dependency on coordinate x. The origin of coordinates is located in the epicenter, the x axis is directed along the tectonic fault, the y axis is horizontal and normal to x, and the z axis is directed from the ground to the ionosphere. The distribution of the electric field in such a model depends only on the coordinates y, z, and along the tectonic fault the electric field remains unchanged.

In the main part of the atmosphere up to a height of 50 km, we use the empirical conductivity model by Rycroft and Odzimek [5]. Above 50 km, the air becomes sufficiently rarefied so that the influence of the magnetic field is manifested, and the conductivity becomes a gyrotropic tensor. Since we are considering local phenomena, we neglect the curvature of the Earth's surface.

The magnetic induction vector $\vec{B}$ is located in the x, z plane. The magnetic inclination I is the angle between the direction to the magnetic north pole and the magnetic induction vector $\vec{B}$, such that at the north and south magnetic poles I = 90° and −90°, respectively. Ohm's law (3) in detailed form can be written as

$$\begin{pmatrix} j_x \\ j_y \\ j_z \end{pmatrix} = \hat{T}^* \begin{pmatrix} \sigma_P(z) & -\sigma_H(z) & 0 \\ \sigma_H(z) & \sigma_P(z) & 0 \\ 0 & 0 & \sigma_{\parallel}(z) \end{pmatrix} \hat{T} \begin{pmatrix} E_x \\ E_y \\ E_z \end{pmatrix}, \tag{6}$$

Fig. 1 Profiles of the components of the electric conductivity tensor for a mid-latitude night-time ionosphere and low solar activity

where $\sigma_P, \sigma_H, \sigma_\parallel$ are the Pedersen, Hall and field-aligned conductivities and the matrix $\hat{T}$ defines rotation of coordinate system:

$$\hat{T} = \begin{pmatrix} -\sin I & 0 & -\cos I \\ 0 & 1 & 0 \\ \cos I & 0 & -\sin I \end{pmatrix}, \tag{7}$$

here conjugate matrix $\hat{T}^*$ means opposite rotation.

Above 90 km we use the model [8], which is based on the empirical models IRI, MSISE and IGRF. Since we consider local phenomena, conductivity is regarded as dependent only on the vertical coordinate z. In the layer $50 < z < 90$ km the values for σ_P and $\sigma_\parallel$ are interpolated by cubic functions, and we use the formula $\sigma_H = \left[\sigma_P (\sigma_\parallel - \sigma_P) \right]^{1/2}$, which is typical for plasma with one predominated kind of charged particles [9]. At altitudes of 90–100 km, this ratio is valid, and considered below 90 km. An example of the obtained profiles of the components of the electric conductivity tensor is presented in Fig. 1.

Thus, the electric conductivity Eq. (5) takes shape:

$$-\frac{\partial}{\partial y} \left[\sigma_{yy}(z) \frac{\partial V(y,z)}{\partial y} + \sigma_{yz}(z) \frac{\partial V(y,z)}{\partial z} \right] - \frac{\partial}{\partial z} \left[\sigma_{zy}(z) \frac{\partial V(y,z)}{\partial y} + \sigma_{zz}(z) \frac{\partial V(y,z)}{\partial z} \right]$$
$$= 0. \tag{8}$$

According to (7) $\sigma_{yy} = \sigma_P, \sigma_{yz} = -\sigma_H \cos I, \ \sigma_{zy} = \sigma_H \cos I, \ \sigma_{zz} = \sigma_P \cos^2 I + \sigma_\parallel \sin^2 I$.

4 Boundary Value Problem

On the surface of the Earth, like many other authors, for example, [2, 3, 10], we assume a given distribution of the vertical component of the perturbation of the electric field strength. This corresponds to the boundary condition of the form

$$E_z|_{z=0} = E_0\gamma(1 + \cos(\pi y/y_0))\sin(\pi y/y_0), \tag{9}$$

where a simple horizontal distribution is considered due to the lack of electric field observations. Here $y_0 = 300$ km—typical width of the source area, $E_0 = 100$ V/m, which is typical for moderate earthquakes, $\gamma \approx 0.77$ is normalization factor.

The ionosphere as a conductor is not bounded from above since there is the magnetosphere, which is a rather complicated object. In this work, we do not take into consideration the polar caps and the auroral zones. So there the conjugate ionosphere is present in our model. The values of the potential at the conjugate points at the upper boundary of the ionosphere, $z = z_\infty$, are assumed to be equal due to the high conductivity along magnetic field lines in the magnetosphere.

In the conjugate ionosphere, the same Eq. (8) is valid with the boundary condition

$$E_y(\tilde{y}, \tilde{z})|_{\tilde{z}=0} = 0, \tag{10}$$

which corresponds to the highest conductivity of ground and sea water.

The vertical electric field near the Earth's surface exists only in certain area $|y| < y_0$. It is necessary to take into account the condition for the reduction of the electric field far from this main region of perturbation. We substitute it with the periodicity condition with the large period $2L$

$$V(-L, z) = V(L, z). \tag{11}$$

It means the periodical analytic continuation of $V(y, z)$ and $E_z^0(y)$ describing the generator at ground (see Eq. (9)) over the whole y-axis with a period of $2L$. To ascertain that the results of calculations are not disturbed in the domain of interest, i.e. $|y| < 2y_0$, by such substitution, the length of the period is chosen such that $L \gg y_0$. We take $L = 10y_0$.

The solution for the boundary value problem (8–11) exists and it is unique. We numerically solve this problem using Fourier transform in the manner similar to one used in [8].

5 The Main Results

Figures 2 and 3 show the projections in the YZ plane of the current lines (solid lines) when the magnetic field inclination equals $I = 60°$. A current of 0.28 pA/m flows between adjacent lines. The dashed lines indicate the contour lines of the X

component of the current density with a contour interval equal to 1 pA/m^2 in the northern and southern hemispheres, respectively.

In this model, the electric field strength vector lies in the YZ plane. Therefore, the X component of the current density is due only to the Hall conductivity. The figure shows that the main part j_x is concentrated at altitudes of about 100 km, as a result of which the current lines in this area are elongated in the direction of the X axis.

Figure 4 displays similar features like in Fig. 2 but in the XZ plane. The current line passing through the region of the highest concentration of the X-component of the current density is much more elongated along the X axis than the other current lines. The following are the altitude distributions of the electric field.

The altitude distributions of the electric field are shown in Fig. 5 with maximum values estimated at each height for the three components, i.e. the field-aligned and the two normal, in the XZ- and YZ-planes. Figure 6 shows the dependence of the ionospherical $E_\perp^y$ on the magnetic inclination I. We do not consider other components ($E_\perp^z$ and $E_\parallel$) as they are three orders of magnitude smaller than $E_\perp^y$ (Fig. 5). In our model $E_\perp^y = E_y$ because the magnetic field is in XZ plane, and $E_x \equiv 0$ and $E_\perp^z = -E_\parallel \mathrm{ctg} I$ due to no dependency of V potential on x.

According to (6), (7) $\sigma_{yy} = \sigma_P$, so σ_{yy} does not depend on $\overrightarrow{B}$. Therefore the electric field component E_y, required for the closure of currents coming from the atmosphere to the ionosphere weakly depends on the magnetic inclination. This can
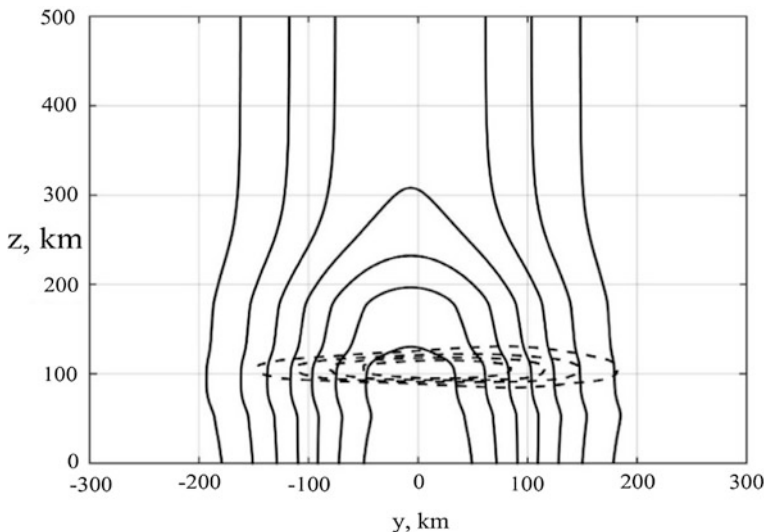
Fig. 2 Projections in the YZ plane of the current lines (solid lines) and contour lines of j_x (dashed lines) in the northern hemisphere above earthquakes preparation zone
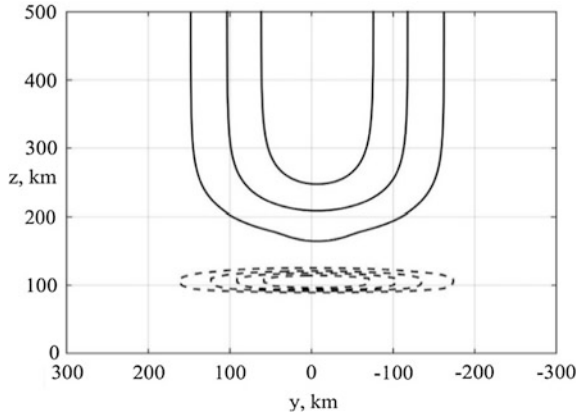
Fig. 3 Projections in the YZ plane of the current lines (solid lines) and contour lines of j_x (dashed lines) in the southern hemisphere
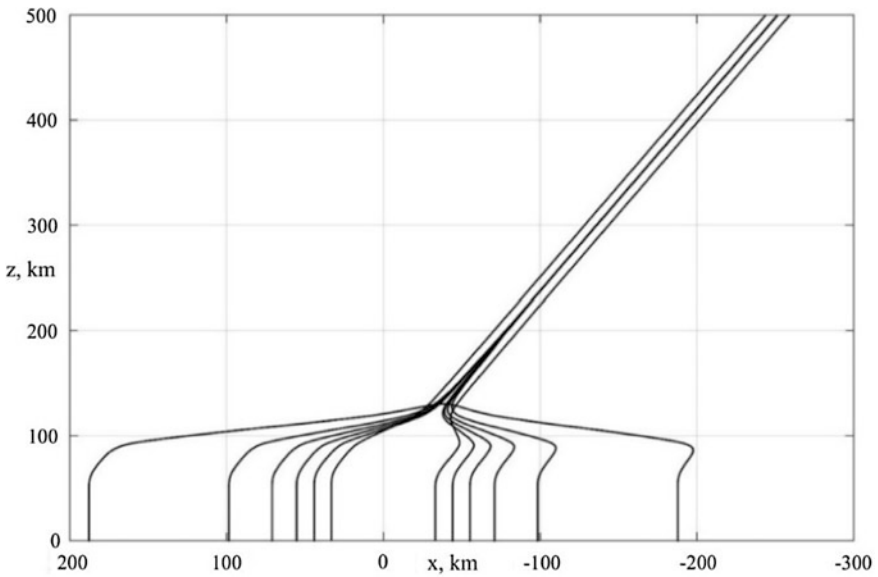
**Fig. 4** Projections in the XZ plane of the current lines in the northern hemisphere

be seen in Fig. 6 where one notes a small variation of about 7%. This supports the investigations in [6] which found not dependent on I. However for faults in the normal direction, a strong dependence on the magnetic inclination was obtained in [5], the field in the ionosphere varies proportionally to *sin I*.
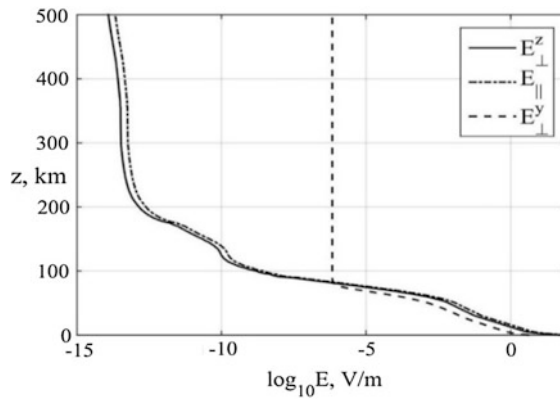
Fig. 5 Components of the electric field strength: field-aligned component $E_\parallel$ (dash-dotted line), and two components normal to the magnetic field, namely $E_\perp^x$ in XZ plane (solid line) and $E_\perp^y$ in YZ plane (dashed line) when the magnetic inclination $I = 60°$
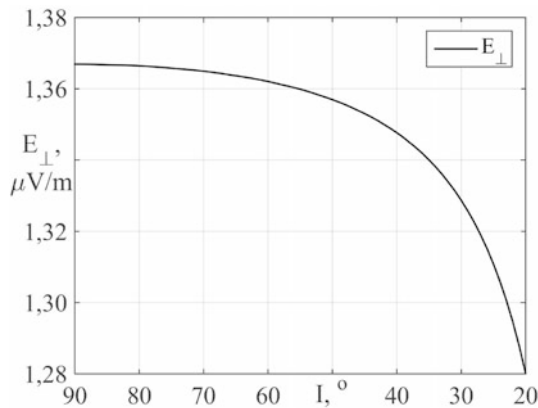
Fig. 6 Dependence of the ionospheric electric field $E_\perp^y$ on the magnetic inclination I.

We find in our study the increase in the strength of the electric field, penetrating into the ionosphere, with the increase of the magnetic field inclination. This is in agreement with previous investigations. In the constructed model, the obtained electric field is three orders of magnitude smaller than the field variations observed in the ionosphere before strong earthquakes. Therefore, the model confirms the conclusion about the need to explore other physical mechanism of lithosphere-atmosphere-ionosphere coupling.

References

1. Denisenko, V.V., Ampferer, M., Pomozov, E.V., Kitaev, A.V., Hausleitner, W., Stangl, G., Biernat, H.K.: On electric field penetration from ground into the ionosphere. J. Atmos. Solar-Terr. Phys. **102**, 341–353 (2013). https://doi.org/10.1016/j.jastp.2013.05.019
2. Hegai, V.V., Kim, V.P., Liu, J.Y.: On a possible seismomagnetic effect in the topside ionosphere. Adv. Space Res. **56**, 1707–1713 (2015)
3. Grimalsky, V.V., Hayakawa, M., Ivchenko, V.N., Rapoport, Yu.G., Zadorozhnii, V.I.: Penetration of an electrostatic field from the lithosphere into the ionosphere and its effects on the D-region before earthquakes. J. Atmos. Sol.-Terr. Phys. **65**, 391–407 (2003)
4. Denisenko, V.V., Boudjada, M.Y., Lammer, H.: Propagation of seismogenic electric currents through the Earth's atmosphere. J. Geophys. Res. Space Phys. **123**(5), 4290–4297 (2018). https://doi.org/10.1029/2018ja025228
5. Denisenko, V.V., Nesterov, S.A., Boudjada, M.Y., Lammer, H.: A mathematical model of quasistationary electric field penetration from ground to the ionosphere with inclined magnetic field. J. Atmos. Solar Terr. Phys. **179**, 527–537 (2018). https://doi.org/10.1016/j.jastp.2018.09.002
6. Denisenko, V.V., Boudjada, M.Y., Horn, M., Pomozov, E.V., Biernat, H.K., Schwingenschuh, K., Lammer, H., Prattes, G., Cristea, E.: Ionospheric conductivity effects on electrostatic field penetration into the ionosphere. Nat. Hazards Earth Syst. Sci. **8**, 1009–1017 (2008). https://doi.org/10.5194/nhess-8-1009-2008
7. Molchanov, O., Hayakawa, M.: Seismo-Electromagnetics and Related Phenomena: History and Latest Results. Terrapub, Tokyo (2008)
8. Denisenko, V.V., Biernat, H.K., Mezentsev, A.V., Shaidurov, V.A., Zamay, S.S.: Modification of conductivity due to acceleration of the ionospheric medium. Ann. Geophys. **26**, 2111–2130 (2008). https://doi.org/10.5194/angeo-26-2111-2008
9. Hargreaves, J.K.: The upper atmosphere and Solar-terrestrial relations. Van Nostrand Reinold Co Ltd, NY (1979)
10. Depuev, V.Kh., Hegai, V.V., Kim, V.P., Pulinets S.A.: Unusual longitude modification of the night time midlatitude F2 region ionosphere in July 1980 over the array of tectonic faults in the Andes area: observations and interpretation. Geophys. Res. Lett. **25**(22), 4133–4136 (1998)

Scaling Relations for Radiation Effects Due to Impacts of Large Cosmic Objects

Elena Podobnaya , Dmitry Glazachev , Olga Popova ,
Vladimir Svetsov and Valery Shuvalov

Abstract

Asteroids risk models require understanding how an asteroid (or a comet) entering into the atmosphere can harm people and infrastructure. Radiation produced due to the flight of a cosmic object in the atmosphere and due to an emission of a plume is one of the main dangerous consequences of a crater-forming impact. This thermal radiation can be strong enough to be dangerous to people, to ignite fires and even to melt rocks. The effects of the radiation may be estimated based on the data on nuclear explosions or based on the especially elaborated model. Numerical simulation of the impacts of large cosmic objects provides a basis for construction of scaling relations, which allow estimating easily the thermal exposure distribution on the surface and some other important parameters. These scaling relations are useful tool for rapid assessments of hazardous effects of thermal radiation. All scaling relations described in this article are implemented in the developed web-based Calculator for fast assessment of dangerous consequences from the impact of cosmic objects on the Earth.

Keywords

Radiation · Impact · Plume · Asteroid · Comet · Impact consequences · Scaling relations

E. Podobnaya (✉) · D. Glazachev · O. Popova · V. Svetsov · V. Shuvalov
Sadovsky Institute of Geospheres Dynamics RAS,
Leninsky prospekt 38(1), 119334 Moscow, Russia
e-mail: epodobnaya@gmail.com

1 Introduction

Radiation produced due to the deceleration of a cosmic object in the atmosphere and due to an emission of a plume generated by crater-forming impacts is one of the main dangerous consequences of these impacts. The thermal radiation can be strong enough to be dangerous to people, to ignite fires and even to melt rocks.

It may be recalled that the Chixculub crater-forming impact of an asteroid 10–15 km in size generated global wildfires [1]. The famous 1908 Tunguska event, caused by the entry of an object about 50 m in diameter, generated a forest fire within a radius of 10–15 km [2].

The effects of the thermal radiation could be evaluated based both on the data on nuclear explosions [3] and on the especially elaborated model [4, 5]. Our approach uses results of the serial numerical simulations [5], which are shortly described below.

Numerical simulations of the cosmic object flight were conducted in the frame of quasi-liquid model [4, 5]. Assuming that the body moves at altitudes where aerodynamic load considerably exceeds its strength and, therefore, can be considered as a liquid, the hydrodynamic equations to model deformation, deceleration, and fragmentation of a cosmic object during its flight through the atmosphere were used. After the impact on the ground, formation of craters and plumes was simulated. The temperature and density distributions obtained in these simulations were used to calculate radiation fluxes on the Earth's surface by integrating the equation of radiative transfer along rays passing through a luminous region. The tables of the equation of state of dunite and quartz (for stony impactors and a target) and air, as well as tables of absorption coefficients of air, vapor of ordinary chondrite and vapor of cometary material were used [5]. The opacity of the undisturbed atmosphere is approximately taken into account by addition of the extinction coefficient to the coefficient of absorption. It was assumed that atmospheric visibility at sea level is 30 km and varies proportionally to the air density [5].

This especially elaborated model was used to conduct 3D numerical simulations of the impacts of stony and icy bodies of different sizes (300 m, 1 km, and 3 km) with various impact angles (15–75°) and velocities (15–50 km/s) [5]. Both the stage of the flight through the atmosphere and the impact on the ground were considered. The emphasis was placed on the assessment of thermal effects [5].

These modeling results provide the basis to derive scaling relations for the most important parameters of the radiation field. The scaling relations allow to get fast assessment of hazardous effects based only on assumed properties of impacting cosmic object without complicated and time-consuming numerical modeling.

2   Model of Thermal Field and Scaling Relations

Thermal radiation on the ground may cause various effects: injuries, fires, and melting of soil. Whether the impact event leads to a fire depends both on the radiation flux density, on the irradiated object, and on the length of the radiation period, i.e., the energy per unit area (radiant or thermal exposure). The radiation in the whole spectral range was considered. After the impact of 300 m asteroid with speed 20 km/s, entering the atmosphere at an angle 45°, a fire can occur at a distance of 250 km. Moreover, if the asteroid is 3 km in diameter, the distance can grow up to 2000 km [5].

Preliminary analysis of the numerical simulation results for the crater-forming impacts (0.3–3 km) showed that in the first order approximation the thermal exposure distribution on the surface may be described as a point source radiation (Eq. 1), where point source is located at some effective altitude Hrad (in km).

$$Q = \frac{A * Ekt * \eta}{(Hrad^2 + r^2)} \tag{1}$$

where $A \approx 1/3$ is a dimensionless coefficient.

Here Q (J/cm^2) is density of a thermal energy on the ground, Ekt is the kinetic energy (in kt TNT) of the impactor with diameter D (in m) and density ρ (kg/m^3), which entries in the atmosphere with velocity V (km/s) and entry angle α (degrees), η is an integral luminous efficiency (%). Radius r is calculated by the standard relation $r = \sqrt{x^2 + y^2}$, where x and y are spatial coordinates (km) (point of origin is at the center of a crater). Here and below, the most attention is paid to the thermal exposure values in the range 10–500 J/cm^2 (approximate boundary for the burns is about 10 J/cm^2 [6] and thermal exposure of 500 J/cm^2 exceeds the melting of the surface [4]).

The special procedure to find the best fit for simulation results was developed, which allows to find a number of scaling relations and to choose the scaling relation with minimal deviation from numerical simulation results. All values, which are incorporated into the relation (Eq. 1) and all other characteristics of the thermal field should have been expressed through the properties of the impactor (density, diameter, entry angle and velocity) and point coordinates (x, y).

Comparison of the pure point source approximation (Eq. 1) with modeling data demonstrates that the simulated thermal field decreases faster at large distances from the source (Fig. 1). Therefore, an additional term was included into the relation for thermal exposure Q (Eq. 2).

$$Q = \frac{A * Ekt * \eta}{(Hrad^2 + r^2)} * C_{fix}, \ C_{fix} = \begin{cases} \cos\left(\frac{\pi * r}{2 * CosScale}\right). & \alpha \le 75° \\ 1 & \alpha > 75° \end{cases} \tag{2}$$
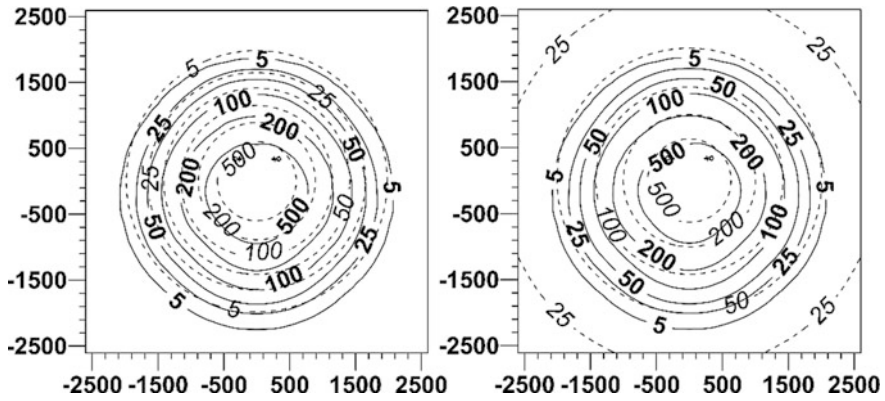
Fig. 1 Thermal exposure distributions (J/cm^2) for a 1 km asteroid entering the atmosphere at an angle 45° and with velocity 25 km/s obtained in the numerical simulations (solid contours with bold labels). Axis show distances in km. Left: Dashed contours with italic labels refer to approximation (2) with the limiter CosScale. Right: Dashed contours with italic labels refer to approximation (1) without spatial limiter

The limiter of the thermal field CosScale allows reaching better description of the radiation field at the outer boundary of the affected area (Fig. 1). Its values increase with a kinetic energy of cosmic body kinetic energy or as the angle approaches 90° (Eq. 3). At distances $r \approx CosScale$ the limiter is decreasing $C_{fix} \rightarrow$ 0, and the radiant exposure became negligible $Q \rightarrow 0$. The parameter CosScale describes the boundary of the thermal effect. The Eq. 2 is applicable only for distances r less than CosScale. Therefore, the limiter C_{fix} is not trully periodic function.

$$CosScale = 190 * Ekt^{0.11} * V^{0.11} * \sin(\alpha/2)^{0.43}. \qquad (3)$$

Effective altitude Hrad greatly varies for asteroidal and cometary impactors:

$$Hrad = \begin{cases} \frac{2700 * Ekt^{0.84}}{V^{7.5} * \sin(\alpha)^{3.8}}, \rho = 1000 \; \frac{\text{kg}}{\text{m}^3} \\ \frac{0.8 * Ekt^{0.48}}{V^{1.5} * \sin(\alpha)^{1.5}}, \rho = 3320 \; \frac{\text{kg}}{\text{m}^3} \end{cases}. \qquad (4)$$

The effective radiative altitude depends on size, density and velocity of the impactor (Eq. 4). It decreases with impact angle growth. Estimates for the radiative effective height for some cosmic objects larger than 1.5 km in diameter result in unreliable values up to 1000 km. Numerical simulations [5] demonstrated that impact plumes effectively radiate up to altitudes of about 50–200 km mainly. So, we restricted the value Hrad by an upper boundary of 100–200 km for large cosmic objects (D > 1.5 km). The precise value of Hrad for these large impactors is not very essential, as its value affects mainly the central zone near the origin of

coordinates, and the fluxes there are substantially larger than the considered range of 10–500 J/cm^2.

An important quantity in the scaling relation (Eqs. 1 and 2) is the integral luminous efficiency, i.e. the fraction of the impactor kinetic energy, which is converted into the radiation. Scaling relation for luminous efficiency is given below (Eq. 5). Suggested luminous efficiency grows with the impact velocity (approximately as a square root) and decreases with the density of the cosmic object. Numerical simulations [5] demonstrated that luminous efficiency has a complicated dependence on the entry angle. Here it should be noted that in the paper [5] the values η/2 are discussed. For example, for 45° impact at 20 km/s luminous efficiency η/2 grows from about 4 to 5.5% for 300 m and 1 km asteroids, and decreases down to 3% for 3 km impactor. The dependence on size is different for oblique impact of the same objects. Therefore, the dependence of radiation efficiency on entry angles and impactor sizes turns out to be quite complicated and is not monotonic. As a whole, all calculated luminous efficiencies η/2 are in the range 0.5–8% (Fig. 2a).

The effectiveness of radiation is quite complicated. It depends on several factors: on vaporized mass (vapor is the main source of radiation), on mixing of vapor with cold air and ejecta from a crater, on the optical thickness (the radiation is most effective at optical thicknesses of the order of unity), the velocity of expansion of a
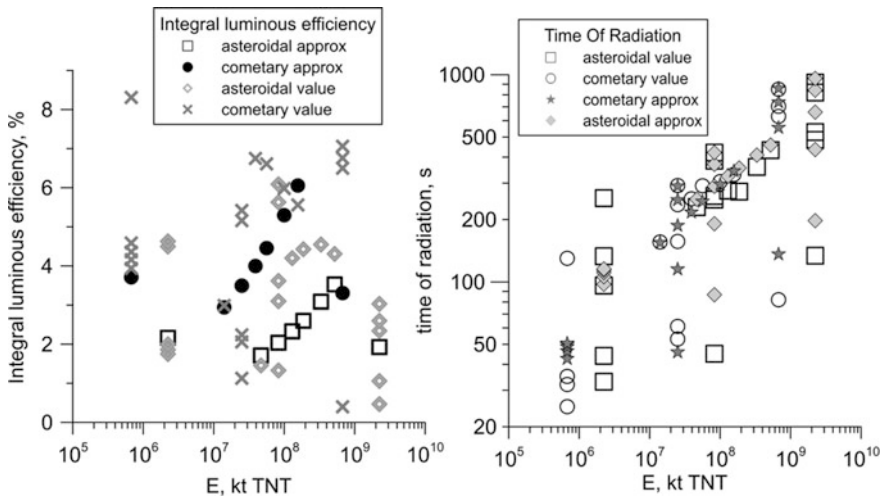
Fig. 2 Comparison of suggested scaling relations with results of numerical simulations. **Left**: The integral luminous efficiency η/2 for asteroidal and cometary bodies in dependence on the impactor kinetic energy. Gray markers refer to modelling results and black ones refer to its scaling relation. **Right**: The characteristic time of radiation (80% of total thermal exposure is irradiated during this period) in dependence on impactor kinetic energy. Empty symbols correspond to the numerical simulation results; filled symbols demonstrate the suggested approximations

plume (which leads to its adiabatic cooling), and on the influence of a trail left by the body in the atmosphere (for details—see [5]).

So, as it is needed to suggest scaling relation over large number of possible impact cases the entry angle dependence was not included:

$$\eta = \frac{0.021 * D^{1.3} * V^{1.5}}{Ekt^{0.45}} \tag{5}$$

For the same list of impactors (considered by [5]) the scaling relation (Eq. 5) results in the 1.7–6% values for $\eta/2$ (Fig. 2a). Comparison of the luminous efficiency $\eta/2$ found by suggested scaling relations with results of numerical simulations demonstrates that in general the difference does not exceed two times.

The luminous efficiency of nuclear explosions in the atmosphere is above 35% and can reach ∼60% for high-altitude air bursts [6, 7]. The value of luminous efficiency only slightly (on few percent) varies with explosion energy [6]. For the crater-forming impacts the radiation efficiency is much lower and demonstrates complicated dependence on impactor parameters (see Eq. 5).

For better estimation of suggested distributions quality, relative error was calculated. In most cases an uncertainty in estimates based on suggested scaling relation do not exceed 4 times in the considered range of thermal exposure. However, cases of large projectiles (3 km in diameter) and oblique impacts are described worse. Figure 3 shows an accuracy of thermal exposure approximations for two cosmic bodies with different density. Cometary body is described with 2
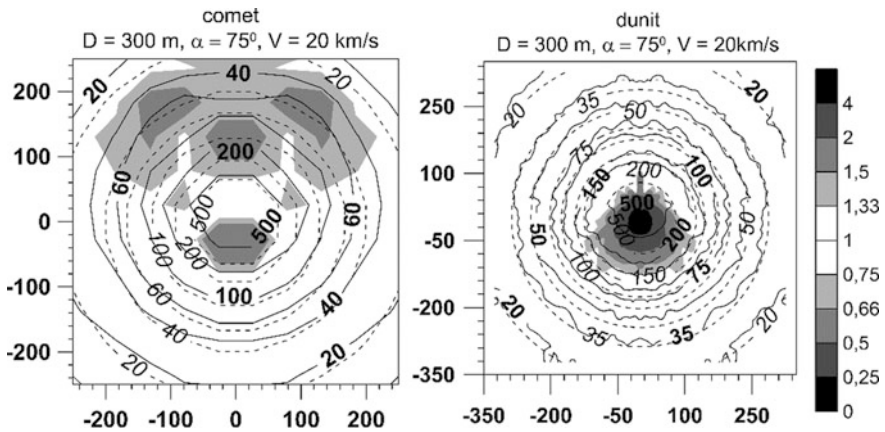
Fig. 3 Thermal exposure distributions (J/cm²) for impacts of cometary and asteroidal bodies (parameters are shown on panels) obtained in the numerical simulations (solid contours with bold black labels) and based on the suggested scaling relation (1) (dashed contours with italic labels). Axis correspond to distance in km, point of origin is under the point of maximal thermal effect, and impactor trajectory is top-bottom. Grayscale corresponds to the relative error and shows an accuracy of the approximation

times accuracy throughout all area of interest whereas asteroidal body is described with 4 times accuracy at levels close to the maximum of considering area.

Suggested scaling relations in general follow all main dependences on impactor parameters found in the numerical simulations, and they permit to predict areas of important effects. Thermal exposure distributions for impacts of cometary bodies, which differ only in the impact velocity obtained in the numerical simulations and by scaling relations are shown on Fig. 4.

Area of ignition of all materials (i.e. >500 J/cm^2) essentially increases with impact velocity as expected both in numerical modeling and in results of suggested scaling relations (Fig. 4). The same is valid for other effects, for example for the
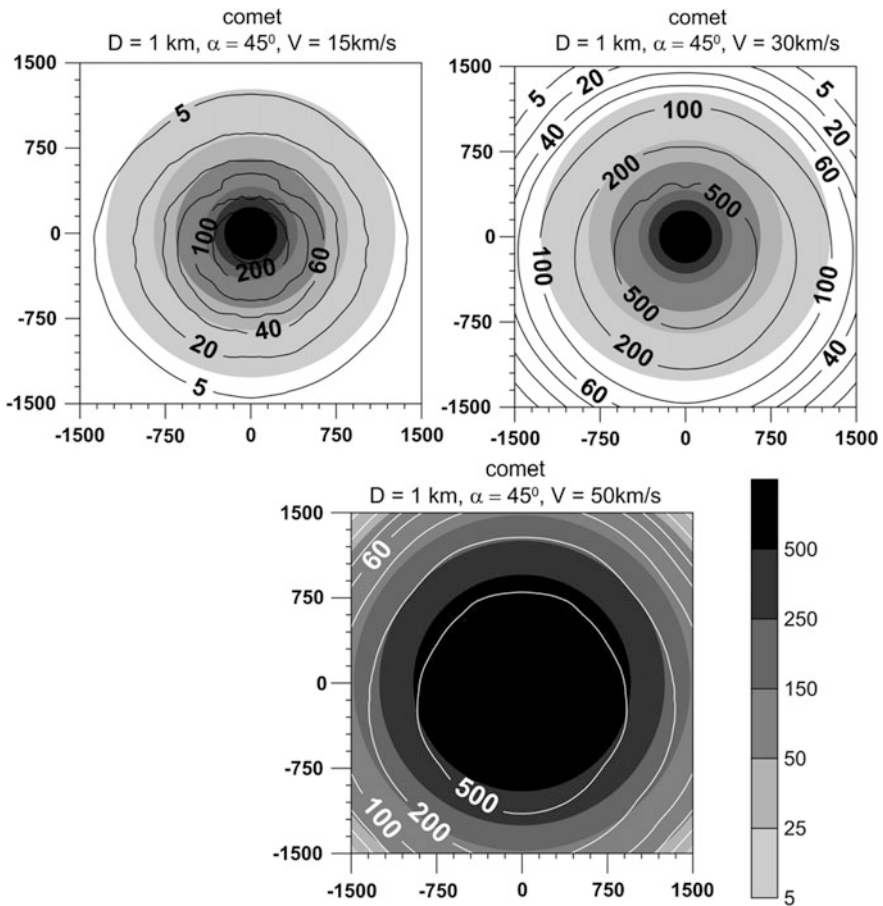
Fig. 4 Thermal exposure distributions for impacts of cometary bodies, which differ only in the impact velocity (parameters are shown on panels) obtained in the numerical simulations (solid contours with bold labels (J/cm^2)). Scaling relation results of thermal exposure are shown by grey color. (Color scale is given on the right). Axis correspond to distance in km, point of origin is in the point of maximal thermal effect, comet trajectory is top-bottom

areas of ignition of a newspaper (50 J/cm^2) and ignition of cotton (88 J/cm^2). The area, where the thermal exposure may cause serious injuries (42 J/cm^2 correspond to third degree burn [5]) grows accordingly.

The time of radiation (80% of total thermal energy is irradiated during this period) and maximal thermal exposure occurred to be dependent mainly on the impactor kinetic energy and the entry angle. As expected, both time of radiation and maximal thermal exposure grow with kinetic energy, but the first one grows with the entry angle and the second one decrease. Figure 2b shows a dependency of thermal radiation duration on the kinetic energy for results of numerical simulations and approximation (Eq. 6). Comets 300 m in diameter give the smallest radiation duration (20–40 s) and 3 km asteroids give maximum (1000 s). An accuracy of the approximation for thermal radiation duration (Eq. 6) is 2–3 times.

$$trad = \begin{cases} \frac{93000 * Ekt^{0.69} * \sin(\alpha)^{0.13}}{V^{5.6}}, D = 300\,\text{m} \\ 1.1 * Ekt^{0.33} * \sin(\alpha)^{1.4}, D > 300\,\text{m}\ and\ \rho = 1000\,\frac{\text{kg}}{\text{m}^3} \\ 4.6 * Ekt^{0.25} * \sin(\alpha)^{1.2}, D > 300\,\text{m}\ and\ \rho = 3320\,\frac{\text{kg}}{\text{m}^3} \end{cases} \qquad (6)$$

3   Summary

Analyzes of numerical simulation results permit to suggest simplified approximations, which allow to estimate the thermal exposure on the surface and some other important parameters. Suggested scaling relations are useful tool for rapid assessments of hazardous effects of thermal radiation. An uncertainty in estimates of thermal exposure does not exceed 4 times in the range 10–500 J/cm^2 in most cases. All quantities in scaling relations are dependent only on parameters of impactor; corresponding approximations for them were found. Some of them have disadvantages which will be corrected in the nearest future.

All suggested approximation relations are used for the description of thermal radiation parameters in the Impact effect Calculator. This web-based Calculator is available at the link: http://AsteroidHazard.pro. Besides thermal effects, this calculator permits to estimate an air blast wave, seismic effect, crater, ejecta and atmospheric disturbances for given cosmic body.

References

1. Morgan, J., Artemieva, N., Goldin, T.: Revisiting wildfires at the K–Pg boundary. J. Geophys. Res. Biogeosci. **118**(4), 1508–1520 (2013)
2. Svetsov, V., Shuvalov, V.: Tunguska catastrophe of 30 June 1908. In: Adushkin, V.V., Nemchinov, I.V. (eds.) Catastrophic Events Caused by Cosmic Objects, pp. 227–266. Springer, Dordrecht (2008)

3. Collins, G., Melosh, H., Marcus, R.: Earth impact effects program: a web-based computer program for calculating the regional environmental consequences of a meteoroid impact on Earth. Meteorit. Planet. Sci. **40**(6), 817–840 (2010)
4. Shuvalov, V., Svettsov, V., Artem'eva, N., Trubetskaya, I., Popova, O., Glazachev, D.: Asteriod apophis: evaluating the impact hazards of such bodies. Sol. Syst. Res. **51**(1), 44–58 (2017)
5. Svetsov, V., Shuvalov, V.: Thermal radiation from impact plumes. Meteorit. Planet. Sci. **54**(1), 126–141 (2019)
6. Glasstone, S., Dolan, P.J.: The Effects of Nuclear Weapons, 3rd edn. U.S. Government Printing Office, Washington, DC
7. Svettsov, V.V.: Explosions in the lower and middle atmosphere: the spherically symmetrical stage. Combust. Explos. Shock. Waves **30**(5), 696–707 (1994)

Trigger Excitation of IPDP ULF Waves (Maltseva–Vinogradova Effect)

Alexander Potapov ⓘ, Boris Dovbnya ⓘ, Boris Klain
and Anatol Guglielmi ⓘ

Abstract

The Maltseva–Vinogradova effect was discovered by Soviet/Russian geomagnetologists in 1971. It consists in the fact that after pulsed injection of energetic protons from the magnetotail to the region of closed magnetic shells, frequency-modulated irregular pulsations of a diminishing period (IPDP, 0.1–5 Hz) are excited. Pulsations are generated in such a way that in the evening sector of the magnetosphere an azimuthal movement of the oscillation source at a given fixed frequency from east to west is observed. The present paper studies the effect of the westward drift of the IPDP frequency from the results of simultaneous observation of oscillations at the Mondy and Borok observatories separated in the geomagnetic longitude by 60°. Our interest is motivated, firstly, by the fact that IPDP belongs to the class of trigger events. Secondly, the interpretation of the frequency modulation of the IPDP and, in particular, the interpretation of the Maltseva–Vinogradova effect makes it possible to penetrate the essence of the whole complex of physical processes accompanying the origin and evolution of geomagnetic storms. We will demonstrate the analyzed effect on the new observational material, discuss the problems of excitation and propagation of IPDP, and point out ways of using IPDP to diagnose the

A. Potapov (✉)
Institute of Solar-Terrestrial Physics SB RAS, 664033, Irkutsk, Russia
e-mail: potapov@iszf.irk.ru

B. Dovbnya · B. Klain
Borok Geophysical Observatory of IPhE RAS, Yaroslavl, 152742 Borok, Russia
e-mail: dovbnya@inbox.ru

B. Klain
e-mail: klb314@mail.ru

A. Guglielmi
Schmidt Institute of Physics of the Earth RAS, 123242 Moscow, Russia
e-mail: guglielmi@mail.ru

magnetosphere and to predict space weather. In particular, we draw attention to the important fact that the observed properties of IPDP appear to contain useful information about the strength and possible duration of a geomagnetic storm.

1 Introduction

In 1969, Nadezhda Maltseva, an employee of the Institute of Physics of the Earth, USSR Academy of Sciences, and Valentina Vinogradova, an employee of the Siberian Institute of Terrestrial Magnetism, Ionosphere and Radio Wave Propagation of the USSR Academy of Sciences (now the of Solar-Terrestrial Physics of the Siberian Branch of the Russian Academy of Sciences) analyzed simultaneous observations of ultra low frequency (ULF) geomagnetic oscillations at two mid-latitude observatories. The synchronous recordings were conducted in 1961–1967 at Borok on the shore of the Rybinsk reservoir in the center of the European part of Russia and at Mondy on the border between Russia and Mongolia. These observatories are located at a distance of 60° in geomagnetic longitude. The result of the spectral-time analysis of irregular pulsations of a decreasing period (IPDP) showed that the instantaneous frequency of oscillations "moves" from east to west at a speed of about 2 deg/min [1]. The phenomenon Maltseva and Vinogradova had discovered turned out to be extremely important for the physics of the

Valeriya Troitskaya   Petr Vinogradov

Fig. 1 Founders of the study of ULF oscillations of the geomagnetic field

magnetosphere; it was called the westward drift of frequency (WDF) and under this title was included in monographs and reviews on ULF oscillations [2–5].

The discovery of the WDF effect was preceded by major events. The first network of observation stations for geomagnetic pulsations in the USSR was organized by Valeriya Troitskaya within the framework of the International Geophysical Year 1957–1958 and Petr Vinogradov, who in 1942 organized continuous measurements of telluric currents in the area of Lake Baikal (Fig. 1). According to the results of observations in 1959 V.A. Troitskaya together with her postgraduate student M.V. Melnikova have registered in the USSR State Register of Discoveries the discovery "The phenomenon of excitation of quasi-periodic oscillations of the Earth's magnetic field of increasing frequency" (Diploma No. 179).

The study of the phenomenon was continued by N.F. Maltseva (Institute of Physics of the Earth of the USSR Academy of Sciences, Moscow) and V.N. Vinogradova (SibIZMIR, now ISTP SB RAS, Irkutsk) based on data of simultaneous observations of pulsations at the SibISMIR observatory in Mondy and the Borok Geophysical Observatory of the IPhE. They discovered an important property of the IPDP oscillations. It consists in the fact that in the evening sector of the magnetosphere there is an azimuthal movement of the source of oscillations at a given fixed frequency from east to west—the so-called westward frequency drift. This effect is important in that it reflects key magnetospheric processes during geomagnetic disturbances, in particular, the formation of a ring current, and allows you to track the movement of charged particles in a remote magnetosphere using ground-based data.

IPDP fluctuations belong to the trigger family. The IPDP trigger is a reconnection of the geomagnetic field lines across the neutral layer of the geomagnetic tail, leading to an explosive release of magnetic energy accumulated in the tail. Part of the magnetic energy is transformed into the energy of charged particles, replenishing the ring current of a magnetic storm and exciting IPDP.

This article is dedicated to the 50th anniversary of the effect discovery. We processed and analyzed the data of synchronous IPDP registration at the Mondy (52° N, 101° E) and Borok (58° N, 38° E) observatories separated by 60° in geomagnetic longitude, and reliably confirmed the existence of the Maltseva–Vinogradova effect. The article considers a kinematic model, clearly illustrating the essence of the effect, and indicates the value of IPDP as an indicator of the formation of a partial ring current in the magnetosphere at the main phase of a geomagnetic storm.

2 Observation of the Effect of the Frequency Westward Drift

While the results of N.F. Maltseva and V.N. Vinogradova were based on the analysis of the terrestrial current records, in modern studies highly sensitive induction magnetometers are used (Fig. 2). In 1996, our institutes, with the

Fig. 2 Search-coil magnetometer INT-1 for recording geomagnetic pulsations

participation of the Tokyo University professor Kanji Hayashi installed two of such identical magnetometers in Borok and Mondy. They included a sensitive primary transducer in the form of an induction coil with a large number of turns of copper wire and a permalloy core. The electrical signal was fed through a long cable to the selection unit and amplifier, then it went to a digital converter and an storage device. The time reference was made using GPS. The data acquired in such a way were analyzed in stationary conditions, primarily through the construction of dynamic spectra of signals, as well as frequency filtering with subsequent analysis of the amplitude-time behavior of individual spectral bands.

In this work, we used synchronous measurements of geomagnetic pulsations at the two observatories from 1996 to 2001. We were interested in the twin IPDP events, that is, those observed at the same time in Borok and Mondy. In less than 5 years of simultaneous observations, about 15 such events were found, which is comparable with the results of [1] (30 events in 7 years).

We demonstrate the observations by the example of two events, each of which has its own characteristics. Figure 3 shows one of these cases. Two spectrograms are shown constructed according to obs. Mondy (top) and obs. Borok (below). Both depict the dynamic spectra of the X-component of the field (the north-south component). The duration of the entire event reaches about two hours, the frequency change interval is from 0.2 to 2 Hz. First of all, we see the apparent non-stationarity of the oscillation spectrum, which has the form of pulses, each of the subsequent ones reaches higher frequencies. This is especially noticeable in Borok. In Mondy, the impulse structure is less noticeable, but the impulses have a steep rise there.

The main issue here is the delay in the arrival of the signal at the western observatory compared with the eastern one. Due to the blurriness of the spectrum, it is difficult to determine the exact latency, but focusing on the position of the central part of the spectral body at a certain frequency, for example 1.0 Hz, it can be said that the delay is about 24 min. This corresponds to a drift velocity at this frequency equal to 2.5° of geomagnetic longitude per minute.
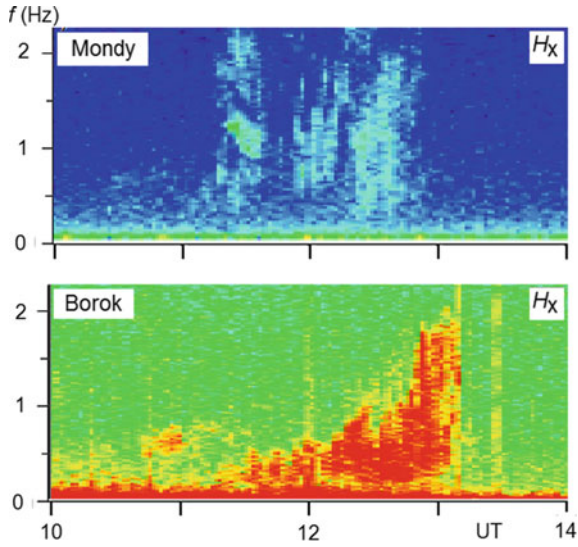
Fig. 3 IPDP oscillations observed at the two observatories on 22 November 1997

Another event is shown in Fig. 4. Here, the IPDP oscillations in Mondy last approximately from 14:30 to 16:00 UT, and in Borok from 15:40 to 17:00 UT. Thus, the delay is about an hour, which is significantly longer than in the first case. The speed of the azimuthal drift turns out to be correspondingly much less, about 1 deg/min. The upper frequency of oscillation is lower, up to 1.6 Hz. The impulse
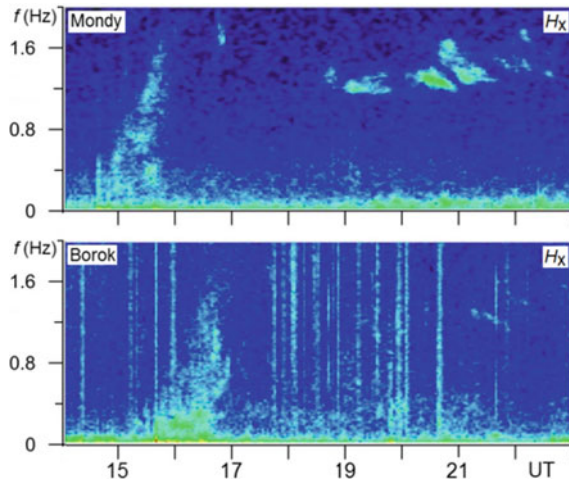
Fig. 4 IPDP oscillations observed with a delay at the two observatories on 29 May 1998

structure of the spectrum in this event is much less noticeable, especially in Mondy, where the signal has the form of a smooth slope, tapering upwards.

On this day, May 29, 1998, there was another interesting signal. In Mondy, from about 19 UT, a narrow-band emission was observed between 1.2 and 1.6 Hz. The low resolution of the recording does not allow us to resolve the fine structure of the signal, but these are clearly oscillations of the Pc1 type, it is unclear whether they are structured or not. An interesting fact is that in Borok there are traces of the two most intense fragments of this emission between 21:15 and 22:10 UT, approximately with the same delay regarding their observation in Mondy, as for the previously observed IPDP: about one hour. This may indicate the close nature of the IPDP and Pc1 fluctuations. But to test this assumption, additional and more convincing observational data are needed.

So, the speed of azimuthal frequency shift is, according to our data, from 1.0 to 2.5 deg/min. If we assume that the frequency drift is caused by the movement of the source, that is, charged particles drifting in a non-uniform dipole field (protons, judging by the direction of the drift), then we can try to estimate the particle energy. Neglecting the influence of a large-scale electric field and only considering particles with pitch angles equal to 90°, we have for the velocity of azimuthal proton drift [6]

$$\frac{d\varphi_p}{dt} = 3\frac{cR_E}{eM_E}E_pL,\tag{1}$$

where φ_p is the azimuth of the proton cloud; t is time; c is the speed of light; R_E is the radius of the Earth; e is the elementary electric charge; M_E is the magnetic moment of the Earth; E_p is the proton energy; L is the McIlwain parameter. From this it is not difficult to obtain that, for the measured values of the frequency drift velocity in azimuth (1.0–2.5 deg/min), the proton energy lies in the range from 120 to 300 keV/L. If we take the average value of the magnetic shell parameter between the Borok latitude ($L = 2.9$) and Mondy ($L = 2.2$), then we obtain the energy of the protons that cause the IPDP emission in the range of approximately 45–120 keV.

3 Interpretation of the Effect

The nonstationarity of the oscillation spectrum clearly reflects the nonstationarity of the magnetosphere during a magnetic storm. Recall that the main phase of the storm is characterized by a significant decrease in the geomagnetic field. The decrease is due to the amplification of the so-called ring current, which is formed by particles of the radiation belt drifting in azimuth around the Earth [7]. The amplification of the ring current can occur, firstly, as a result of pulsed injection of "fresh" particles into the magnetosphere and, secondly, as a result of increased magnetospheric convection and the associated movement of the ring current along the radius (closer to Earth).

Prior to the discovery of the WDF effect, it was widely believed in the literature that IPDP are excited as a result of ion-cyclotron instability during radial drift of resonant protons under the influence of a large-scale electric field of magnetospheric convection. The idea was proposed in [8], and the corresponding quantitative theory was developed in Zolotukhina [9] (see also [3]).

The injection of new particles into the ring current, as well as the ring current moving closer to the Earth as a result of the amplification of magnetospheric convection, leads to the formation of a nonequilibrium velocity distribution of energetic protons—nonmonotonic and, generally speaking, anisotropic. The non-equilibrium distribution may be unstable, with the oscillation frequency close to the so-called resonant frequency: $\omega \approx \omega_R$. If $c_A \ll V$, then the resonant frequency is approximately equal to

$$\omega_R \approx (c_A/v_p)\,\Omega_p. \tag{2}$$

Here $\Omega_p = eB/m_p c$ is the proton gyrofrequency, $c_A = B/\sqrt{4\pi\rho}$ is the Alfven velocity, v_p is the characteristic velocity of the ring current protons, m_p is the proton mass, ρ is the plasma density, B is the geomagnetic field at the equator of the magnetic shell with the $B \propto L^{-3}$. Estimated ω_R corresponds to the IPDP frequency range.

The discovery of the WDF effect stimulated the search for an alternative scenario. Let us imagine that at the moment t_0 in the vicinity of the midnight meridian there was a pulsed injection into the magnetosphere of energetic protons from the geomagnetic tail. We will count the longitude φ from midnight to the west. Let, for clarity, a compact proton cloud has at $\varphi = 0$ a steady velocity distribution of particles (the Maxwell equilibrium distribution). After injection ($t > t_0$), protons drift to the west, with the drift velocity of each particle being proportional to its energy. As a result, the cloud spreads in longitude, and the distribution function of particles becomes non-equilibrium (non-monotonic). In the evening sector ($\varphi \sim \pi/2$) at first, more energetic particles arrive and, accordingly, the oscillation increment has a peak at lower frequencies, and then less energetic particles arrive. As a result, the oscillation frequency monotonically increases. By the formula (2) we obtain the estimate:

$$\omega \propto \sqrt{t - t_0}. \tag{3}$$

The basic properties of IPDP, namely, self-excitation in the range of one hertz, localization mainly in the evening sector, the monotonous increase in frequency are naturally explained by this theory [3].

4   Discussion

Our interest in IPDP is motivated, firstly, by the fact that these fluctuations belong to the family of trigger events. Secondly, the interpretation of the frequency modulation of the IPDP and, in particular, the interpretation of the Maltseva–Vinogradova effect makes it possible to penetrate the essence of the whole complex of physical processes accompanying the origin and evolution of geomagnetic storms. We draw attention to the important fact that the observed properties of IPDP appear to contain useful information about the strength and possible duration of a geomagnetic storm.

IPDP occurs after the reconnection of the geomagnetic field lines in the magnetotail, leading to an explosive release of magnetic energy. The subsequent injection of charged particles in the midnight sector of the magnetosphere and the very fact of the appearance of the IPDP in the evening sector, coupled with a steady increase in the average frequency of oscillations, made it possible immediately after opening the IPDP to hypothesize the excitation of oscillations by a cloud of energetic protons drifting in azimuth on closed magnetic shells and replenishing the ring current of a geomagnetic storm. However, this did not happen, and the hypothesis of an increase in the oscillation frequency as a result of radial proton drift in the large-scale electric field of magnetospheric convection prevailed in the world literature. And only the discovery of the Maltseva–Vinogradova effect gave a strong experimental justification for the idea of IPDP generation as a result of the azimuthal drift of the cloud of injected protons.

As has often happened in the history of magnetospheric research, the seemingly rejected idea of an increase in the oscillation frequency as a result of radial drift turned out to be in demand. An employee of the ISTP SB RAS N.A. Zolotukhina made a thorough analysis and in her dissertation proved the existence of two types of IPDP, one of which arises as a result of azimuthal and the second as a result of radial drift [9]. She called the first type injection, and the second type convective types of IPDP.

Recently, the ISTP and IPhE employees discovered and documented a unique case of convective type IPDP excitation [10]. For more than half a century of regular observation of ULF oscillations of a downward period, oscillations of this type were recorded for the first time, unique in both the duration and the difference in carrier frequency (Fig. 5). The oscillations lasted continuously for 10 h, i.e. an order of magnitude longer than usual. The carrier frequency increases monotonically from the fractions of hertz to 3.5 Hz (usually the upper frequency does not exceed two hertz). Such an unusual natural phenomenon (or rather, the only one discovered so far) is of some concern. We are alarmed by the fact that, having already half a century of experience in ULF monitoring near-Earth space, we could not even conceive, and could not foresee that this is possible. In other words, this
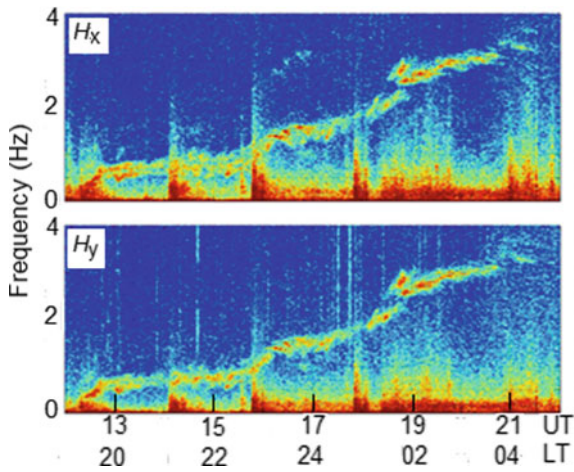
Fig. 5 Unusual event of oscillations of increasing frequency according to observations at the obs. Mondy on 17 March 2013 [10]

event is highly instructive. It teaches us that Cosmos is unpredictable, it is full of surprises and unexpected phenomena. The example given here testifies to the substantial incompleteness of our knowledge of near space.

5 Conclusions

The discovery of IPDP-type ULF oscillations in the second half of the last century and the finding of the effect of the westward frequency drift by Troitskaya, Melnikova, Maltseva and Vinogradova are among the outstanding achievements of Soviet cosmophysics. It is worth noting that this complex of productive research was carried out on the basis of many years of creative cooperation between two academic institutions, the ISTP SB RAS and the IPhE RAS.

In this paper, we confirmed the reality of the WDF effect, using data from modern magnetometric facilities, recalled the idea of interpreting the effect, briefly discussed the place of IPDP in the overall picture of physical processes playing out in near-earth space during a magnetic storm, and highlighted the potential of monitoring ULF oscillations at a pair of azimuthally spaced apart magnetic observatories to improve the quality of the space weather forecast.

References

1. Maltseva, N.F., Guglielmi, A.V., Vinogradova, V.N.: Effect of westward drift of frequency in the intervals of oscillations of diminishing period. Geomag. Aeron. **10**(5), 939–941 (1970)
2. Guglielmi, A.V., Troitskaya, V.A.: Geomagnitnye pulsatsii i diagnostika magnitosfery [Geomagnetic Pulsations and Diagnostics of the Magnetosphere]. Nauka Publishing, Moscow (1973)
3. Guglielmi, A.V., Pokhotelov, O.A.: Geoelectromagnetic Waves. IOP Publishing Ltd., Bristol and Philadelphia (1996)
4. Kangas, J., Guglielmi, A., Pokhotelov, O.: Morphology and physics of short-period magnetic pulsations (A review). Space Sci. Rev. **83**, 435–512 (1998)
5. Guglielmi, A.V., Potapov, A.S.: On the nonstationary processes in geophysical media. Geofizicheskiye Issledovaniya [Geophys. Res.] **19**(4), 5–15 (2018). https://doi.org/10.21455/gr2018.4-1
6. Lew, G.: Drift rate in a dipole field. J. Geophys. Res. **66**, 2681–2685 (1961)
7. Nishida, A.: Geomagnetic Diagnosis of the Magnetosphere. Springer, New York (1978)
8. Troitskaya, V.A., Shchepetnov, R.V., Guglielmi, A.V.: Evaluation of electric fields in the magnetosphere from the frequency drift of hydromagnetic emissions. Geomag. Aeron. **8**, 794–795 (1968)
9. Zolotukhina, N.A.: Vozbuzhdenie Geomagnitnyh Pulsatsii v Rezultate Inzhekcii i Nestatsionarnogo Drejfa Ehnergichnyh Chastic [Excitation of geomagnetic pulsations as a result of injection and non-stationary drift of energetic particles]. Abstract of Thesis of Candidate Dissertation. IPhE AS USSR, Moscow (1979)
10. Potapov, A.S., Dovbnya, B.V., Baishev, D.G., Polyushkina, T.N., Rakhmatulin, R.A.: Narrow-band emission with 0.5–3.5 Hz varying frequency in the background of the main phase of the 17 March 2013 magnetic storm. Sol.-Terr. Phys. **2**(4), 16–30 (2016). https://doi.org/10.12737/24271

Trigger Effect of an Asteroidal or Cometary Impact at the Permian–Triassic Boundary

Vladimir Svetsov and Valery Shuvalov

Abstract

The Araguainha impact crater in Brazil with a diameter of 40 km could be formed by the impact of an asteroid or a comet with a diameter of about 3 km. We conducted numerical simulations of the impacts of such objects with velocities 20 km/s (asteroid) and 50 km/s (comet) and calculated thermal fluxes on the surface of the Earth produced by direct thermal radiation from impact plumes. Estimates of the conditions of ignition of dry materials show that highly inflammable materials, such as dry grass and leaves, can catch fire in an area of 4000–4500 km in size. The impact also causes an earthquake of magnitude 9–10, which, according to some suggestions, could lead to release of methane from organic-rich sediments, including oil shale. The age of the Araguainha crater, within the limits of errors of its determination, is close to the time of the great mass extinction at the Permian–Triassic boundary, when the land was united into one supercontinent Pangea. Climatic conditions and the level of oxygen in the atmosphere at the end of the Permian period contributed to propagation of fires. It is likely that the Araguainha impact, in the conditions of stressed state of the biosphere at the end of the Permian, might lead to the extinction of plants and animals due to fires, an increase in carbon dioxide in the atmosphere, and a mechanical action of a shock wave propagating in the ground.

V. Svetsov (✉) · V. Shuvalov
Sadovsky Institute of Geospheres Dynamics RAS, 119334 Moscow, Russia
e-mail: svettsov07@rambler.ru

589

1   Introduction

The causes of all extinction events are not precisely clarified and remain the subject of controversy. Severe mass extinctions can occur when the biosphere under prolonged stress is subjected to strong short-term effects [1]. It is generally believed that the impact of an asteroid with a diameter of 10–20 km is the main cause of the Cretaceous–Paleogene mass extinction [2, 3]. Coincidence of ages of several of the largest craters (>70 km in diameter) with extinction events suggests that large impacts could trigger some other mass extinctions [4]. For the greatest Permian–Triassic mass extinction, the corresponding impact crater has been also found, the 40 km Araguainha crater in Brazil, which has been dated to 254.7 ± 2.5 million years ago, overlapping with estimates for the Permian–Triassic boundary [5]. The complex impact crater Araguainha with a diameter of 40 km has been formed by the gravitational collapse of a 20–25 km wide transient cavity [6]. The scaling laws [7–9] show that such a crater can be formed as a result of the impact of a stony asteroid with a diameter of 3 km at a speed of 20 km/s or an icy comet with a diameter of 3 km at a speed of 50 km/s, provided that a projectile enters the atmosphere at an angle of 45° (the most probable impact angle). At these energies, impact effects on environment are usually considered to be transitional between regional and global and insufficient for a direct cause of the global mass extinctions [10]. There are a dozen impact craters ranging in size from 40 to 70 km, which are not associated with the recognized extinction events. However, the Araguainha impact occurred in specific conditions and could trigger other destructive mechanisms.

The main hypotheses of the causes of the end-Permian extinction include massive volcanism—eruptions of Siberian Traps flood basalts, release of huge amounts of sulfur dioxide and greenhouse gases (CO_2, CH_4) into the air, heating the atmosphere, and acidification of the oceans [e.g., 11–13 and references therein]. The onset of Siberian Traps and intense arc volcanism in South China could significantly reduce the stability of the ecosystem to such an extent that one event could lead to its collapse [13].

The impact of an asteroid with a diameter of 3 km and a speed of 20 km/s causes an earthquake of magnitude 9–10 [14]. Studies of the Paraná Basin, a large cratonic sedimentary basin comprising the Araguainha crater, show the evidence of the impactogenic earthquake caused by the Araguainha impact [15]. Widespread occurrence of seismites is constrained to a stratigraphic horizon occupying the uppermost 10–100 m of the Passa Dois Group (Permian sedimentary rocks). And the lateral extent of soft-sediment deformations occurs within a radius of about 1000 km from the Araguainha impact site. The earthquake was probably accompanied by a large tsunami wave loaded with both washed off sediments and impact ejecta [15]. Much of the local rock was oil shale. It was suggested that the passage of this wave could cause rapid changes in lithostatic pressure for the oil shales (60–200 m below the paleosurface) contributing to release of trapped methane from the organic-rich rock [16]. The estimates [16] suggest that around 1600 Gt of methane

were released into the atmosphere at that time, which would have significant climatic consequences.

In this work, we estimate another trigger mechanism of the impact—fires initiated by radiation from the impact plume. Recently, we developed a code that allows us to simulate numerically the impacts, taking into account radiation, and to calculate thermal radiation fluxes on the Earth's surface [17]. We simulated the impacts of an asteroid and a comet with a diameter of 3 km and determined the areas of potential ignition of wood. The last section discusses specific conditions for the development of wildfires after the Araguainha impact at the end of the Permian.

2 Simulations of the Impacts

For simulations of the impacts, we used the hydrodynamic code SOVA [18]. The equation of radiative transfer, added to the equations of hydrodynamics, was numerically solved in the approximation of radiative heat conduction or in the volume-emission approximation. Temperature and density distributions obtained in the simulations were used for calculations of radiation fluxes on the Earth's surface by integrating the equation of radiative transfer along rays passing through a luminous region. We used tables of equations of state of quartz, dunite, and water for condensed material of a target, stony asteroid and cometary impactor, and tables of equations of state and absorption coefficients for vapor of ordinary chondrite, vapor of cometary material and air. The method is described in more detail in [17, 19].

Development of an impact plume after the impact of an asteroid with a diameter of 3 km at a speed of 20 km/s (close to the mean impact velocity of asteroids on the Earth) and an entry angle of 45° (the most probable angle) is shown in Fig. 1. 1.5 s after the asteroid contacts the Earth's surface, a trail consisting of vapor and air heated up to $\sim$25000 K remains in the atmosphere. Crater ejecta produces a plume of vapor and heated air, which develops in the direction of the impact and in 10 s reaches a height of about 100 km. The expanding plume creates a shock wave in the atmosphere, which accelerates upwards and reaches $\sim$700 km in 30 s and $\sim$1500 km in 50 s. Despite the high speed and high temperature behind the front of this wave, its radiation is insignificant due to very low densities at these heights. The main part of the radiation is emitted from a denser part of the plume with a temperature of 2000–3000 K, which reaches a height of 800 km in 50 s, and then falls under the action of gravity to heights of 100–200 km in 360 s, when its maximum temperature is still about 2000 K.

The radiating region extends along the surface for several hundred kilometers from the crater in the direction of the impact. The total radiation flux on the Earth is maximum in about 200 s, and then decreases with decreasing temperature and height of the radiating volume. The radiation impulse lasts about 600 s. The impact of the comet is similar to that of the asteroid, with the difference that the cometary
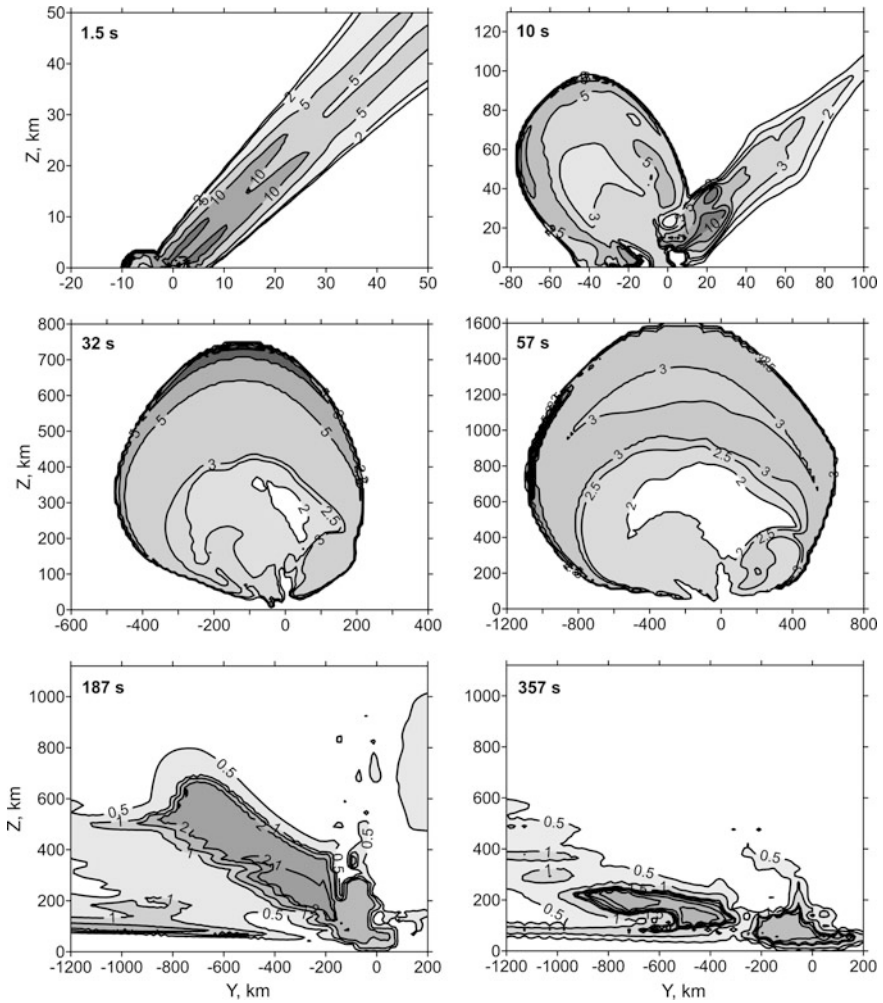
Fig. 1 Contours of temperature (in 1000 K) in the atmosphere after the impact of a 3-km-diameter asteroid that entered the atmosphere at an angle of 45° with a velocity of 20 km/s. Time, which is counted from the moment of a contact of the body with the surface, is indicated in the figures. Z is the height, and Y is the coordinate along the projection of the trajectory on the ground. $Y = 0$ corresponds to the intersection of the trajectory with the Earth's surface. The asteroid moved from the right to the left. Darker colors indicate higher temperatures

plume has higher temperatures and is somewhat larger due to the higher velocity and energy of the comet.

The effect of radiation on the ground depends on radiation flux density and specific radiation energy (radiant exposure), the isolines of which are shown in Fig. 2. Here we show the maximum radiative exposure relative to the orientation of
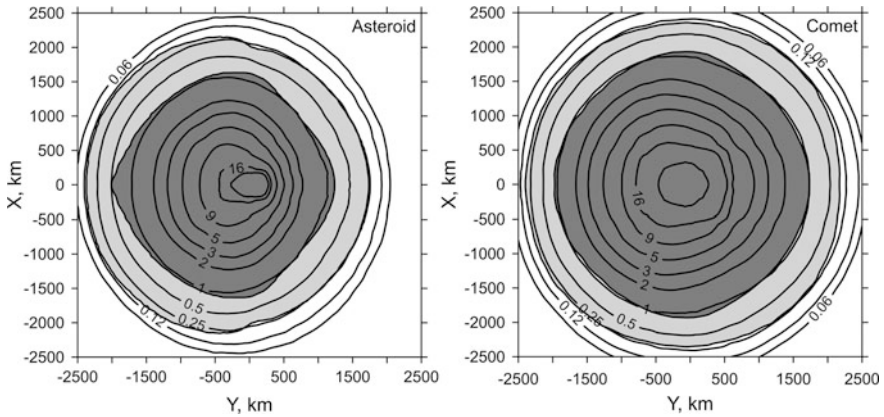
Fig. 2 Contour lines of radiant exposure on the ground in kJ/cm^2 for the asteroidal (the left panel) and cometary (the right panel) impacts. The area of potential fire initiation by ignition of dry grass is shown in gray, and ignition of wood is dark gray. The impact direction is from right to left

an irradiated object located at a certain point on the surface of the Earth. We calculated the radiation fluxes on the spherical surface of the Earth, but Fig. 2 shows the spherical surface transformed into a plane with a conservation of distances from a certain point on the spherical surface to the center of the crater at the origin.

A criterion for fire ignition, based on experimental data, was proposed in [17, 19] as

$$E > q_{cr}t + at^{0.45}, \tag{1}$$

where E is the radiant exposure in J/cm^2, q_{cr} in W/cm^2 is the critical irradiance below which the ignition does not occur, t is the time in seconds counted from a moment when the radiation flux density becomes greater than q_{cr}, and a is a constant. We used $q_{cr} = 2.5$ W/cm^2 and $a = 25.5$ for ignition of wood, and $q_{cr} = 0.85$ W/cm^2 and $a = 7.6$ for ignition of dry grass or leaves. The boundaries of areas where dry grass or leaves can catch fire are close to the isolines of specific radiation energy of about 0.25 kJ/cm^2, and the boundaries of wood ignition areas approximately correspond to values of specific energy about 1 kJ/cm^2.

In the case of the comet impact, the potential area of ignition is larger, because the comet's energy is approximately twice as large as that of the asteroid, and a somewhat larger fraction of the comet's kinetic energy (about 3.5%) is converted into thermal radiation energy that comes to the Earth. However, the asteroidal and cometary craters have the same size, since the comet, which has a lower density, transfers its energy to the ground less efficiently. The ignition of dry grass during the impact of the comet can occur at a distance along the Earth's surface about 2300 km from the crater center. This distance is limited mainly by direct visibility

of the impact plume. A shock wave propagating in the atmosphere above the surface of the Earth can fell trees at shorter distances from the crater—about 500 km. Our simulations for the case of the impact of a 10-km-diameter asteroid show that the size of a zone of initial ignition under the action of direct thermal radiation is doubled in comparison to the impact of a 3-km-diameter asteroid due to an increase in the energy and the height of the rise of the impact plume. The impact of an asteroid of this or greater size occurred at the Cretaceous–Paleogene boundary, which, in accordance with the generally accepted theory, triggered the extinction event.

3 Discussion and Conclusions

The impact Araguainha occurred on the supercontinent of Pangea that contained almost all of the Earth's land. In this case, the impact may be more dangerous than when the continents are far away from each other. The area of initial ignition covers the main part of modern South America and part of Africa. At the Permian–Triassic boundary, the climate was hot, arid at low latitudes, the temperatures were high, and the polar regions were free of ice [20]. The oxygen content in the atmosphere was higher than at present [21]. Under such conditions, a fire could spread far beyond the region of initial ignition and even cover most of the supercontinent. At the end of the Permian, there were frequent wildfires [21], but the fire generated by the impact burns a very large area. The burning of vegetation quickly increases the level of carbon dioxide in the atmosphere, but usually after some time it is balanced by the growth of plants that absorb this carbon dioxide. In the stressed state of the biosphere, the process of plant growth and stabilization of this balance can be considerably slowed down. Methane emissions [16] and its combustion can significantly worsen the situation.

At the Permian–Triassic boundary, a massive restructuring of ecosystems occurred, in which the number and distribution of plants changed greatly, all forests almost disappeared and many animal species became extinct. The lack of evidence of forest fires during the subsequent early Triassic could be due to the lack of forest trees necessary for such fires to occur. Probably, the extinction of land plants occurred several hundred thousand years before the most serious marine extinction [22]. In many places in the world, the devastation of forests of the latest Permian was followed by a short time when fungi became widespread, probably taking advantage of a large amount of dead and decaying biomass [23]. Note that among the numerous places containing evidence of the fungal event at the Permian–Triassic boundary, there are no such places in the fire zone initiated by the Araguainha impact [23]. This may be due to the climatic conditions and the lack of geological data, but also probably due to the complete burning of plants in the area.

The thermal effect of impacts is significantly less at low speeds close to the escape velocity, when the temperatures in the shock plume are not high enough. However, the impact parameters taken in our simulations are more probable, and,

therefore, it is likely that the impact might trigger the death of trees and animals on the supercontinent. Note that in addition to the Araguainha crater, several geological structures were considered as possible impact craters at the Permian–Triassic boundary, but so far these assumptions have not received sufficient evidence.

References

1. Arens, N.C., West, I.D.: Press-pulse: a general theory of mass extinction? Paleobiology **34**(4), 456–471 (2008)
2. Schulte, P., Alegret, L., Arenillas, I., et al.: The Chicxulub asteroid impact and mass extinction at the Cretaceous–Paleogene boundary. Science **327**(5970), 1214–1218 (2010)
3. Renne, P.R., Deino, A.L., Frederic, J., et al.: Time scales of critical events around the Cretaceous–Paleogene boundary. Science **339**(6120), 684–687 (2013)
4. Rampino, M.R., Caldeira, K.: Correlation of the largest craters, stratigraphic impact signatures, and extinction events over the past 250 Myr. Geosci. Front. **8**, 1241–1245 (2017)
5. Tohver, E., Lana, C., Cawood, P.A., et al.: Geochronological constrains on the age of a Permo–Triassic impact event: U–Pb and ^{40}Ar/^{39}Ar results for the 40 km Araguainha structure of central Brazil. Geochim. Cosmochim. Acta **86**, 214–227 (2012)
6. Lana, C., Souza Filho, C.R., Marangoni, Y.R., et al.: Structural evolution of the 40 km wide Araguainha impact structure, central Brazil. Meteorit. Planet. Sci. **43**(4), 701–716 (2008)
7. Gault, D.E.: Impact cratering. In: Greely, R., Schultz, P.H. (eds.) A Primer in Lunar Geology, pp. 137–175. NASA, Moffett Field, CA (1974)
8. Holsapple, K.A., Schmidt, R.M.: On the scaling of crater dimensions 2. Impact processes. J. Geophys. Res. **92**, 1849–1870 (1982)
9. Melosh, H.J.: Impact cratering: a geologic process. Oxford University Press, New York (1989)
10. Toon, O.B., Zahnle, K., Morrison, D.: Environmental perturbations caused by the impacts of asteroids and comets. Rev. Geophys. **35**(1), 41–78 (1997)
11. Burgess, S.D., Muirhead, J.D., Bowring, S.A.: Initial pulse of Siberian Traps sills as the trigger of the end-Permian mass extinction. Nat. Commun. **8**(164), 1–6 (2017)
12. Penn, J.L., Deutch, C., Payne, J.L., Sperling, E.A.: Temperature-dependent hypoxia explains biogeography and severity of end-Permian marine mass extinction. Science **363**(6419), eaat1327 (2018)
13. Shen, S.-Z., Ramezani, J., Chen, J., et al.: A sudden end-Permian mass extinction in South China. GSA Bulletin **131**(1/2), 205–223 (2019)
14. Khasins, V.M., Shuvalov, V.V., Svetsov, V.V.: The seismic efficiency of space body impacts. Sol. Syst. Res. **52**(6), 547–556 (2018)
15. Tohver, E., Schmieder, M., Lana, C., et al.: End-Permian impactogenic earthquake and tsunami deposits in the intracratonic Paraná Basin of Brazil. GSA Bulletin **130**(7–8), 1099–1120 (2018)
16. Tohver, E., Cawood, P.A., Riccomini, C., Lana, C., Trindade, R.I.F.: Shaking a methane fizz: seismicity from the Araguainha impact event and the Permian–Triassic global carbon isotope record. Palaeogeogr. Palaeoclimatol. Palaeoecol. **387**, 66–75 (2013)
17. Svetsov, V., Shuvalov, V.: Thermal radiation from impact plumes. Meteorit. Planet. Sci. **54**(1), 126–141 (2019)
18. Shuvalov, V.V.: Multi-dimensional hydrodynamic code SOVA for interfacial flows: application to the thermal layer effect. Shock Waves **9**(6), 381–390 (1999)

19. Svetsov, V.V., Shuvalov, V.V.: Thermal radiation and luminous efficiency of superbolides. Earth Planet. Sci. Lett. **503**, 10–16 (2018)
20. Benton, M.J., Newell, A.J.: Impacts of global warming on Permo–Triassic terrestrial ecosystems. Gondwana Res. **25**(4), 1308–1337 (2014)
21. Glasspool, I.J., Scott, A.C., Waltham, D., Pronina, N., Shao, L.: The impact of fire on the Late Paleozoic Earth system. Front. Plant Sci. **6** (2015). Article 756
22. Fielding, C.R., Frank, T.D., McLoughlin, S., Vajda, V., et al.: Age and pattern of the southern high-latitude continental end-Permian extinction constrained by multiproxy analysis. Nat. Commun. **10**, 385 (2019)
23. Rampino, M.R., Eshet, Y.: The fungal and acritarch events as time markers for the latest Permian mass extinction: an update. Geosci. Front. **9**(1), 147–154 (2018)

Seismo-acoustic Effects of the Lipetsk Bolide 21.06.2018

Alexander Varypaev [ORCID], Sergey Volosov, Natalia Konstantinovskaya, Margarita Nesterkina, Vladimir Kharlamov and Yuriy Rybnov

Abstract

The entry and destruction of large meteoroid occurred on 21.06.2018 in the Lipetsk region. This phenomenon caused infrasound and seismic vibrations recorded by a seismic-acoustic complex GFO «Mikhnevo». The results of a comprehensive analysis of seismic-acoustic registrations are presented. It is shown that infrasound wave excites ground motions directly at the seismometer installation points. Using modern array signal processing techniques at the seismic records there were found several time intervals where the presence of acoustic wave response was established. The estimation of the source azimuth and apparent velocity of the plane wavefront according to seismic observations was obtained. The source energy is estimated based on dominant frequency of the infrasound signal recorded by microbarometer. The bearing azimuth is in agreement with the coordinates of the source provided by U.S. Government optical satellites (UGS) data.

Keywords

Bolide · Meteoroid · Seismic array · Array data processing · Infrasound wave · Microbarometer · f-k analyses

A. Varypaev (✉) · S. Volosov · N. Konstantinovskaya · M. Nesterkina · V. Kharlamov · Y. Rybnov
Sadovsky Institute of Geospheres Dynamics RAS, 119334 Moscow, Russia
e-mail: avalex89@gmail.com

597

1   Introduction

Moving through atmosphere meteoroids produce low frequency acoustic waves (from 0.01 to 10 Hz) that can propagate on hundreds and even thousands kilometers. Some works report the registration of such infrasound waves by microbarometers [4]. One of the subjects of the study of such an astronomical phenomenon is the estimation of the bolide energy using acoustic data [5]. With the advent of U.S. satellite optical data it becomes possible to make a comparison of bolide energy estimates obtained from independent measurements.

Along with the analysis of acoustic data the analyses of seismic vibrations generated by the bolide is necessary to improve knowledge of the physics of acoustic-to-seismic energy coupling from sources above the Earth's surface [2]. Here it is required to use modern techniques of array data processing to detect weak seismic signals against strong background seismic noise.

On June 21, 2018, $\sim 01{:}15{:}00$ UTC the bright bolide was observed over the Lipetsk region, the radiation lasted few seconds and was observed from large distances up to 300–400 km. The motion and destruction of large meteoroids creates strong acoustic disturbances in the atmosphere that can cause seismic vibrations in the Earth's crust. Acoustic oscillations generated by this event and seismic motions caused by corresponding low frequency acoustic wave were recorded by seismic and acoustic instruments of GFO «Mikhnevo» of the Institute of geosphere dynamics. Analysis of complex field observations showed that seismic and acoustic vibrations are observed simultaneously and the registration time is about 01:30:46 UTC. It was established that seismic vibrations were excited by an infrasonic wave from a bolide that propagated in a stratospheric waveguide.

## 2   Seismic and Acoustic Measurements, Bolide Energy Estimation

Seismo-acoustic complex of the Mikhnevo Geophysical Observatory (GFO Mikhnevo) consists of a small aperture array and a three-point acoustic station. The layout of this equipment is shown at Fig. 1. It is known [14], that when cosmic bodies move in the Earth's atmosphere, there is a process of rapid release of a large amount of energy in a limited volume. This leads to the occurrence of a high-pressure region and the appearance of a shock wave in the atmosphere. With distance, the shock wave transforms into an infrasound wave, which can extend hundreds and even thousands of kilometers.

The waveform of the registered infrasound signal from the flight and destruction of the meteoroid in the atmosphere is shown in Fig. 2. Its spectrum is presented on Fig. 3. The maximum amplitude (peak) is approximately at 01:30:48 UTC.

To estimate the bolide energy, the characteristic frequency f_0 corresponding to the maximum spectral density of the infrasonic signal was used [1]:
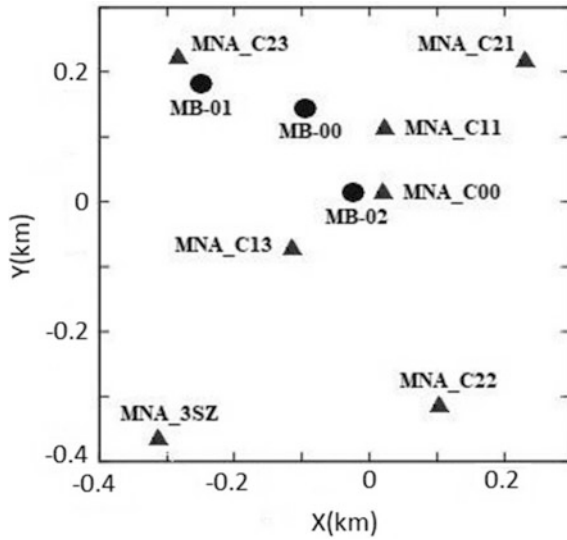
Fig. 1 Layout of registration equipment at Mikhnevo: Triangles—seismometers of seismic array; Circles—microbarometers
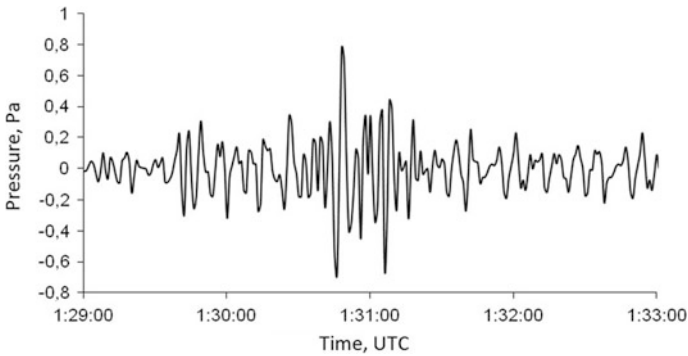
Fig. 2 Infrasonic signal recorded at the MB-00 acoustic sensor

$$E = \left(\frac{7182}{f_0}\right)^{2.7}. \tag{J}$$

Thus the estimated bolide energy is about 1.3×10^{13} J (≈ 3.1 kt) is in agreement with independent meteoroid initial kinetic energy estimate based on radiation ≈ 3 kt (US Governmental satellites (UGS)).
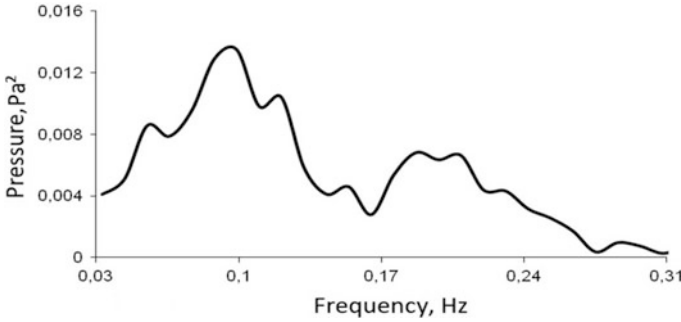
Fig. 3 Spectrum of the registered infrasound signal
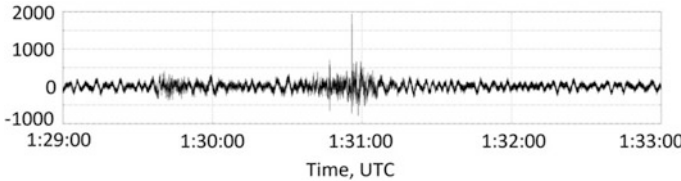

Fig. 4 Seismic record of the highest amplitude of seismic response caused by acoustic wave of Lipetsk bolide at the MNA_C22 seismic sensor

We used seismic observations, to establish the effect of the wave front on the seismic array, as well as the expected direction of arrival of the plane wave. The signal from the bolide was recorded by all sensors of the seismic array, and Fig. 4 shows the characteristic seismogram of one of the recorded signals.

3   Mathematical Model of Observations on the Mikhnevo Seismic Array and Multichannel Processing Algorithms

Propagation of infrasonic wave in the atmosphere and its seismic response can be described by a mathematical model of a multidimensional linear system with one input and several outputs [7, 12, 13]:

$$x_l(t) = \int\limits_{-\infty}^{\infty} h_l(z, \boldsymbol{\theta}) s(t - z) dz + \xi_l(t), \ \ l \in \overline{1, M}, t \in R, \tag{1}$$

where $x_l(t)$ is array sensor output (observations) with number l, $h_l(z, \boldsymbol{\theta})$ is a pulse transient characteristic of a multidimensional linear system that describes the

passage of an acoustic wave front through the layers of the atmosphere from the acoustic emission point to the sensor l, $s(t)$—source oscillation function, $\xi_l(t), l \in \overline{1,M}$ is an additive interference affecting the sensors of the seismic array, presented in the form of a random stationary process. The notation $\boldsymbol{\theta}$ is vector parameter of the linear system, which in the framework of the problem in question plays the role of a vector of apparent slowness. In practice, a continuous process $x_l(t)$ is observed as discrete values with a frequency f_s—$x_l(t) = x_l\left(t \cdot f_s^{-1}\right), t = \overline{1,N}$. The apparent slowness $\boldsymbol{\theta}$ is the vector parameter of the linear system which is required to be estimated in practice. To build «statistically effective» parameter estimation algorithms of $\boldsymbol{\theta}$ [9] it is necessary to consider frequency domain observation model, which is equivalent to the model (1):

$$X_l(f_j) = H_l(f_j, \boldsymbol{\theta})S(f_j) + \zeta_l(f_j) \tag{2}$$

where X, H, S are discrete finite Fourier transform (DFFT) of the corresponding time series $x_l(t)$, $s(t)$, $h_l(t, \boldsymbol{\theta})$, $\xi_l(t)t = \overline{1,N}$.

To detect intervals of seismic event signals, the concept of a «multidimensional coherence measure» is introduced, which is calculated as a measure of the degeneracy of the matrix power spectral density:

$$\begin{aligned}
\hat{\mathbf{F}}_x(f_j) &= \left(\hat{F}_{lm}(f_j)\right)_{l=1,m=1}^{M,M}, \\
\hat{F}_{lm}(f_j) &= \left\langle X_l^*(f_j)X_m(f_j)\right\rangle, f_j = j\frac{f_{Nyquist}}{N}j = \overline{1,N},
\end{aligned} \tag{3}$$

where $\hat{F}_{ln}(f_j)$—cross power spectral density estimate of $x_l(t), x_n(t)$, sign «*» denotes complex conjugation, brackets «$\langle \ \rangle$» mean averaging values $X_l^*(f_j)X_m(f_j)$ according to the common theory of spectral characteristics estimation of time series [11]. The value of a multidimensional measure of coherence can be given by the following function of matrix $\hat{\mathbf{F}}_x(f_j)$:

$$\Lambda_x(f_j) = \frac{\lambda_1^2}{\sum\limits_{m=1}^{M-1} \lambda_{m+1}^2}, \tag{4}$$

where $\{\lambda_l\}_{l=1}^M$—is the sequence of singular values of $\hat{\mathbf{F}}_x(f_j)$ ordered in descending order. In sense of principal component analyses [6] expression (4) shows the proximity of $\hat{\mathbf{F}}_x(f_j)$ rank to unity. Actually, according to [8] the rank $k<M$ of matrix $\hat{\mathbf{F}}_x(f_j)$ corresponds to k independent sources. Therefore, the practical use of expression (4) assumes the absence of superposition of signals generated by several sources in the considered time interval of the observations. The detection function [15] can be then considered as the frequency-averaged value of the expression (4)

$$\overline{\Lambda_x} = \sum_{j=j_1}^{j_2} \Lambda_x(f_j), j_1 < j_2, \tag{5}$$

where indexes j_1, j_2 correspond to the specified frequency band, $0 \leq f_{j_1} < f_{j_2} \leq f_{Nyquist}$.

The corresponding detected time intervals can be used to estimate slowness vector $\boldsymbol{\theta}$ in the model (2). Estimation of slowness vector $\boldsymbol{\theta}$ is carried out using the phase «beamforming» algorithm, which is effective in case of strong additive interferences of the model (2) in acoustics [3, 16], as well as in geophysical applications [10, 15].

$$\hat{\boldsymbol{\theta}} = \arg\max_{\boldsymbol{\theta}} \sum_{j=j_1}^{j_2} \left| \sum_{l=1}^{M} \frac{X_l(f_j) e^{2\pi i f_j \tau_l(\boldsymbol{\theta})}}{|X_l(f_j)|} \right|^2, 0 \leq f_{j_1} < f_{j_2} \leq f_{Nyquist}, \tag{6}$$

where $\tau_l(\boldsymbol{\theta})$ is the relative time of the wave propagation to the sensor with number l.

4 Results of Seismic Data Processing of «Mikhnevo» Array from 21.06.18

Calculation of multidimensional coherence measure using Eq. 5 in 10 s long sliding window with 1 s increments (Fig. 5) showed the presence of several time intervals corresponding to some potential events that may result of from infrasonic waves initiated by Lipetsk bolide on the seismic array (Fig. 1). Times of signal entries were estimated according to maximum values of coherence function (Table 1). For each 10 s time interval backazimuth and apparent velocity of plane wavefront were estimated in the frequency band from 2 to 10 Hz, these estimated values are presented in Table 1 and corresponding examples of f-k diagrams (beam energy value in space of slowness vector) are shown at the Fig. 6. For seismic record of the highest amplitude of seismic signal (Fig. 4) the estimated values of backazimuth and apparent velocity are equal to 174.54° and 339 m/s respectively. In the seismic records several time intervals were found where the wavefront of signal is estimated as plane one. Could this be due to several sources of infrasound emission, or is this due to the wave propagation of an acoustic wave in the atmosphere? It would be interesting to investigate out the physical explanation of this fact in the future work.

The time shift between the peak of the infrasound signal (see Fig. 2) and the peak of the seismic signal (see Fig. 4) is about 1.0 s. This is due to spatial separation of the seismometer and microbarometer.

The distance from the point of maximum energy release to the registration point was calculated from coordinates of the source presented by UGS and coordinates of the microbarometer. Then the speed of propagation of an infrasonic wave over a
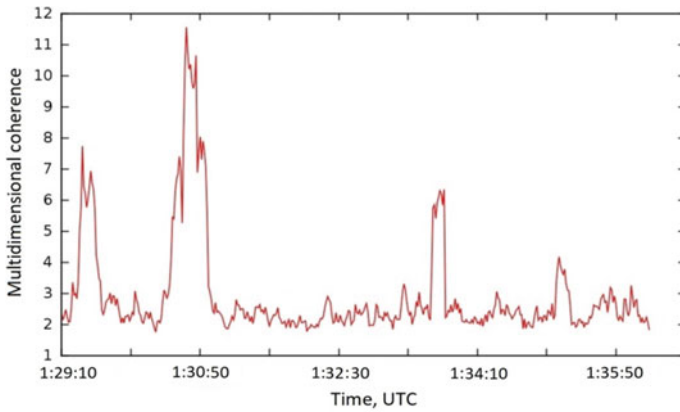
Fig. 5 Value of the frequency-averaged function of multidimensional coherence provided by expression (5), calculated in a sliding time window and in the frequency band (2–10 Hz). Initial time in UTC—01:29:10

Table 1 Times of entries of found intervals with seismic signals, caused by acoustic emission of Lipetsk bolide

Time, UTC	Back azimuth	Apparent velocity, km/s	Max. value of f-k function given by Eq. 6
2018-06-21 01:29:30	178.07	0.339	0.435000
2018-06-21 01:30:36.5	173.80	0.338	0.476475
2018-06-21 01:30:46.5	174.54	0.340	0.509978
2018-06-21 01:33:44	176.77	0.353	0.386682
2018-06-21 01:35:12	182.90	0.419	0.273890
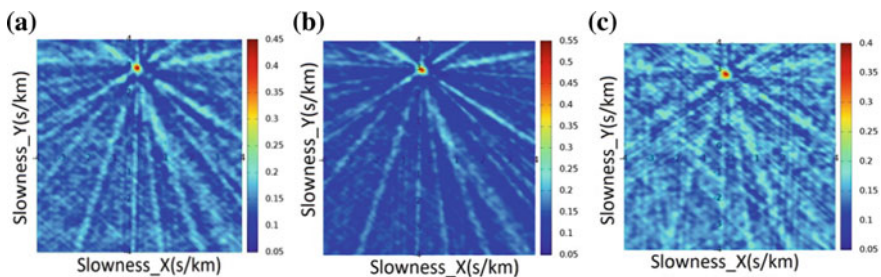
Fig. 6 Example of calculated f-k diagrams for detected time intervals of 10 s. using Eq. (6). Axis X and Y correspond to slowness vector coordinates (s/km). **a** (2018-06-21 01:29:30, 2018-06-21 01:29:40); **b** (2018-06-21 01:30:46.5, 2018-06-21 01:30:56.5); **c** (2018-06-21 01:33:44, 2018-06-21 01:33:54)

known propagation time can be estimated as $\approx$338 m/s, which coincides with results of processed seismic data given in Table 1.

The combination of these factors (time of entry, wave propagation velocity) allows us to conclude that the Lipetsk bolide was registered by the seismic and acoustic station of the Mikhnevo array.

5 Conclusions

1. Both acoustic and seismic vibrations caused by destruction of the Lipetsk bolide were recorded by the seismo-acoustic complex of IDG RAS (GFO "Mikhnevo").
2. Analysis of synchronous observations showed that seismic vibrations recorded by Mikhnevo seismic array were initiated by the wave front of the infrasonic wave from the bolide.
3. Using acoustic records, the estimated energy is $\approx 1.3 \times 10^{13}$ J ($\approx$3.1 kt TNT). UGS provided independent estimate based on bolide radiation ($\approx$3 kt TNT).
4. Several time intervals were found where the wavefront of signal recorded by the seismic array was defined as flat. According to estimated apparent velocities and absolute UTC times these intervals assigned to infrasound wave impact.
5. Estimated value of the source backazimuth from seismic data with the highest amplitude is equal to $\approx 174^{\circ}$, which is in agreement with coordinates of the event presented by UGS.

References

1. Adushkin, V., Rybnov, Y., Spivak, A., Kharlamov, V.: Estimation of the energy of sources of infrasonic signals based on spectral analysis. Izv. RAS. Phys. Earth **4** (2019) (in Print, in Russian)
2. Antolik, M., Ichinose, G., Creasey, J., Clauter, D.: Seismic and infrasonic analysis of the major bolide event of 15 February 2013. Seism. Res. Lett. **85**(2), 334–343 (2014). https://doi.org/10.1785/0220130061
3. Brandstein, M., Ward, D.: Microphone Arrays: Signal Processing Techniques and Applications. Springer, New York (2001)
4. Brown, P.G., Whitaker, R.W., ReVelle, D.O.: Multi-station infrasonic observations of two large bolides: signal interpretation and implications for monitoring of atmospheric explosions. Geophys. Res. Lett. **29**(13), 1–4 (2002)
5. Edwards, W.N., Brown, P.G., Revelle, D.O.: Bolide energy from infrasonic measurements. Earth Moon Planet **95**, 501–512 (2004). https://doi.org/10.1007/s11038-005-2244-4
6. Jollife, I.: Principal Component Analyses. Springer (1986)
7. Krim, H., Viberg, M., Institute of Technology, Laboratory for Information and Decision Systems, Massachusetts: Sensor array signal processing: two decades later (2019)

8. Kushnir, A.: Statistical and computational methods of seismic monitoring. URSS, Moscow (2012). (in Russian)
9. Kushnir, A., Rozhkov, N., Varypaev, A.: Statistically-based approach for monitoring of micro-seismic events. Int. J. Geomath. **4**(2), 201–225 (2013)
10. Kushnir, A., Varypaev, A.: Robustness of statistical algorithms for location of microseismic sources based on surface array data. Comput. Geosci. **21**(3), 459–477 (2017)
11. Marple, S.: Digital Spectral Analysis, Englewood Cliffs. Prentice-Hall, NJ (1985)
12. Singh, H., Jha R.M.: Trends in adaptive array processing. Int. J. Antennas Propag. (2012). https://doi.org/10.1155/2012/361768
13. Stoica, P., Moses, R.: Spectral Analysis. Prentice Hall, NJ (2005)
14. Tsikulin, M.: Shock Waves When Moving in the Atmosphere of Large Meteoritic Bodies. M.: Nauka (1969). (in Russian)
15. Varypaev, A., Sanina, I., Chulkov, A., Kushnir, A.: Application of robust phase algorithms for seismic emission detection in the area of blasting operations in mines. Seism. Instrum. **55**(2), 136–147 (2019)
16. Zhang, C., Florêncio, D.A., Ba, D.E., Zhang, Z.: Maximum likelihood sound source localization and beamforming for directional microphone arrays in distributed meetings. IEEE Trans. Multimed. **10**, 538–548 (2008)

Nightside Magnetic Impulsive Events: Statistics and Possible Mechanisms

Andrei Vorobev, Vyacheslav Pilipenko and Mark Engebretson

Abstract

At night, both against the background of substorms, and during magnetically quiet time, magnetic impulse events (MIEs) are often recorded at high-latitude stations. MIEs are pulses of large amplitude (of the order of tens to hundreds of nT in both horizontal and vertical components) with a characteristic duration of 5–10 min, localized in space with scales of about first hundred kilometers. Such rapid geomagnetic field changes can cause extreme values of geomagnetically induced currents that have a negative impact on infrastructure objects. The paper presents the results of analysis of statistical distributions for the values of amplitude and rate of change of geomagnetic variations at night, recorded during 2015–2017 in northeastern Canada (station Igloolik at geomagnetic latitude 77.6°). Both distributions are well approximated by the log-normal law, whereas tails of the distributions may be also approximated by the power-law function. According to the statistics obtained, the MIEs with dB/dt > 10 nT/s occur ~ 40 times per year. Possible generation mechanisms of nighttime isolated and multiple MIEs are associated with bursty bulk flows in the magnetotail.

A. Vorobev (✉)
Ufa State Aviation Technical University, 450008 Ufa, Russia
e-mail: geomagnet@list.ru

A. Vorobev · V. Pilipenko
Geophysical Center of the Russian Academy of Sciences, 119296 Moscow, Russia

V. Pilipenko
Institute of Physics of the Earth, 123242 Moscow, Russia

M. Engebretson
Augsburg University, Minneapolis, MN 55454, USA

1 Introduction

Space weather caused by the interaction of solar ejecta with the near-Earth environment activates global electromagnetic and plasma processes: intensification of the magnetosphere—ionosphere current systems, energization of ring current and radiation belt particles, bursts of accelerated electron precipitation into the auroral oval, etc. One of the most significant havoc of space weather for terrestrial technological systems is geomagnetically induced currents (GICs) related to abrupt changes of the geomagnetic field [1, 2]. Therefore, significant efforts and resources of the geophysical community are aimed at global modeling of storm/substorm activity augmented by the reconstruction of telluric electric field [3]. However, the highest risk of GIC may be related not directly to those processes with enormous energy yield, but to more localized and rapid processes [4]. Though the power of such processes is many orders of magnitude lower than the power of magnetospheric storms and substorms, the rapidly varying electromagnetic fields of these events can induce a significant GIC [5].

Diverse types of transient processes and perturbations of different spatial and temporal scales are permanently observed in the near-Earth space. At the dayside, impulsive perturbations include the storm sudden commencements (SCs) and traveling convection vortices (TCVs), which are a high-latitude response to an external impact on the magnetosphere. The terrestrial manifestation of a TCV is an isolated magnetic impulse event (MIE)—a sporadic perturbation of the geomagnetic field with a duration of ~ 5–10 min and amplitude of ~ 100 nT. Daytime MIEs were found to be associated with excitation of localized field-aligned currents by transient phenomena in the magnetosheath (plasma pressure disturbance, hot flow anomaly, plasma jets, IMF reconfiguration, etc.).

In addition to dayside TCVs, intense MIEs with similar time scale often appear in ground-based magnetometer records during nighttime. The nightside MIEs should not be confused with dayside MIEs, because their mechanisms are different. Examples of intense MIEs, augmented by observations from auroral imagers and high-altitude spacecraft in the nightside magnetosphere, were presented in [6]. The occurrence rate and statistical characteristics of nighttime MIEs in the high latitude regions that are the focus of this study are still relatively unknown. New characteristics of nighttime MIEs presented in this study may provide an additional clue to understand the mechanisms and drivers of this phenomenon.

2 Data Set and Event Identification Technique

Eastern Arctic Canada provides dense 2D ground magnetometer coverage at latitudes from the sub-auroral through auroral oval into the near-cusp and polar cap. We examine statistical characteristics of MIEs observed in this region from 2015 through 2017 using 0.5-s data from selected stations with best data coverage that are part of magnetometer arrays MACCS, AUTUMNX, and CARISMA. Magnetic field variations are in local geomagnetic coordinates X (North-South), Y (East-West), and vertical Z. We consider nighttime hours only, in the MLT sector 16-06 (2130-1130 UT).

MIEs included in this study were selected using the procedure, which combine visual identification of a pulse with automated capture of the extreme values of both the magnetic field disturbances ΔX, ΔY, ΔZ and their time derivatives dX/dt, dY/dt, dZ/dt [6]. In nearly all cases the X component perturbation was negative unipolar, but the Y and Z perturbations could be either unipolar or bipolar. The magnetic field disturbance is determined as $\Delta B = \sqrt{(\Delta X)^2 + (\Delta Y)^2 + (\Delta Z)^2}$, and the field variability is characterized by the magnitude of the time derivative $\frac{dB}{dt} = \sqrt{\left(\frac{dX}{dt}\right)^2 + \left(\frac{dY}{dt}\right)^2 + \left(\frac{dZ}{dt}\right)^2}$.

An example of typical nightside MIEs recorded on Oct. 10, 2015 at station Igloolik (IGL) at geomagnetic latitude 77.6° from MACCS array is given in Fig. 1. In these isolated pulses with duration ~ 10 min, magnetic disturbance (~ 400–500 nT) is mainly observed in X component. Often nightside MIEs are observed during the substorm expansion phase as a quasi-periodic series of impulses, named Ps6 pulsations. The Ps6 pulsations may be associated with specific auroral signatures—omega-bands, that is a localized distortion of auroral form resembling the inverted Greek letter Ω.
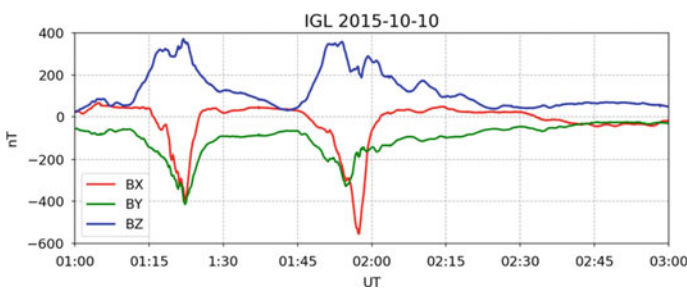
Fig. 1 Example of nightside MIEs recorded at station IGL on Oct. 10, 2015

3   Statistical Distributions of the MIE Amplitudes

During the analyzed period, peak perturbation amplitude ΔB reached 2120 nT, and peak derivative magnitudes dB/dt reached 47 nT/s. These maxima greatly exceed the commonly used threshold of 5 nT/s for potential damage to the electrical grid. For comparison, the Hydro Quebec collapse during the magnetic storm of 1986 was associated with a storm-related dB/dt value of ∼8 nT/s [7].

To obtain additional information about the physical mechanisms responsible for the MIE generation we examine the form of the probability distribution function (PDF) $F(A)$ of a set of perturbation amplitudes A. A non-gaussian distribution with a heavy tail indicates that the most intense fluctuations under study are not random, but are the result of the intermittency of the turbulence. The intermittency corresponds to turbulent processes where the rate of energy transfer is not constant, so periods of quiescence may change to bursts of activity. The PDF of amplitude detection in the interval A, $A+\Delta A$ is determined as the normalized number of events $N(A)$ with such amplitudes

$$n(A) = PDF(A) = \frac{N(A)}{N_t \Delta A}$$

Here N_t is the total number of events. The normalized histogram $n(A)$ provides the distribution of the probability to observe a given magnitude A in an interval ΔA during an analyzed period. The cumulative amplitude distribution $P(>A)$ (also known as the exceedance probability function or survival function) is determined as follows:

$$P(>A) = \int\limits_{A}^{\infty} n(A)dA$$

The exceedance probability function $P(>A)$ is the probability to observe a value exceeding A.

We examine the statistical distributions of impulse amplitude ΔB and field variability dB/dt at several high latitude stations from both 2015 and 2017. The results will be presented for station IGL only, because for other stations the results are qualitatively the same. Only the values above the threshold ΔB = 90 nT and dB/dt = 1 nT/s have been accounted for. The PDFs for data from all stations were found to be close to the log-normal or exponential Weibull distributions. The distribution function that fits best the measured PDF of both ΔB and dB/dt at IGL station according to the Kolmogorov–Smirnov test is the log-normal distribution (Fig. 2a, b).

$$F(x, \sigma) = \frac{1}{x\sqrt{2}} \exp\left(-\frac{\log^2(x)}{2^2}\right), \tag{1}$$
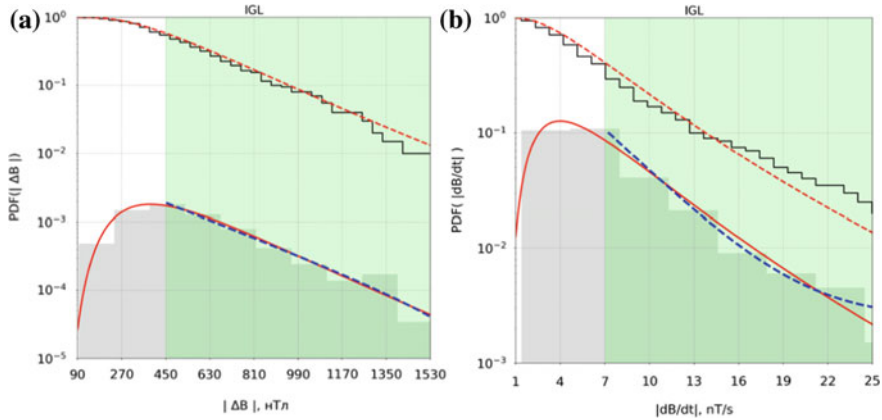
Fig. 2 a—Histograms of the probability distribution PDF(ΔB) (grey bars) and cumulative distribution (exceedance function) P(>B) (solid black lines) of data from IGL. The best fit log-normal approximations are denoted by solid red lines for ΔB and dashed red lines for P(>B); **b** —The same format, but for dB/dt. Blue dashed lines show the power-law approximation of the distribution tails (green-colored area)

where σ is a shape parameter. The plots in Figs. 2a, b (upper curves) also show the amplitude distribution $P(>A)$. These exceedance probability distributions are well approximated by log-normal functions, too.

To characterize quantitatively the deviation of the MIE statistics from the normal distribution of fluctuations, one may use the excess kurtosis K, which is determined via the statistical moments of the 2-nd order σ (standard deviation) and 4-th order μ_4 as follows: $K = \mu_4/\sigma^4 - 3$. For a normal Gaussian distribution $K = 0$. A distribution that is steeper and narrower than the normal one has $K < 0$, whereas a distribution with $K > 0$ has heavy tails relative to the normal distribution.

We also have estimated the skewness S that characterizes the asymmetry of the probability distribution, whether it is the same to the left and right parts of the center part (for normal distribution $S = 0$). The parameters of the PDF are summarized in Table 1.

High values of $K \gg 1$ for ΔB and dB/dt indicates that these distributions with long tail are the result of infrequent outliers.

Knowledge of the PDF makes it possible to estimate the probability of an extreme event, which during the observation period may not even be observed (assuming that it obeys the same law). The probabilities of impulses with dB/dt > 10 nT/s are 38% at IGL. Knowing the average number at IGL of events

Table 1 Parameters of the PDF

Parameter	|B|			|dB/dt|		
Station	σ	K	S	σ	K	S
IGL (Φ = 77.6°)	0.5	6.0	1.8	0.6	13.1	2.5
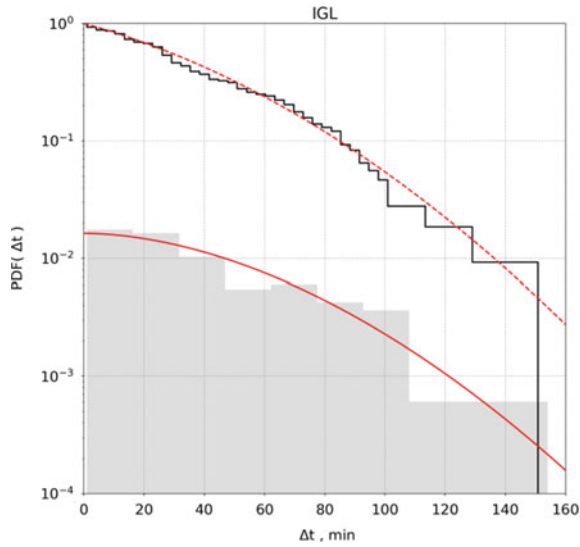
Fig. 3 The statistical distributions PDF(Δt) and P(>t) for the time delay Δt between the substorm intensification and MIE occurrence

(201) during two (2015, 2017) years one obtains that $(201 \cdot 0.38)/2 = 38$ events with dB/dt > 10 nT/s should occur per year. The probability of extreme impulse with dB/dt > 50 nT/s are 0.001%. Therefore, the expected annual rate of such extreme dB/dt is 0.1 events per year. The estimated probability of very high dB/dt gives us a possibility to evaluate a probability of extreme GIC in a given region.

Tails of PDFs in Fig. 2 may be reasonably well approximated by a power function $f(A) = A^{-a}$, where A is an impulse amplitude, and a is an exponent. The power-law approximation (with $a = 4.26$) applied to tails of PDF of nighttime MIEs is very close to the log-normal approximation in this domain (green-colored).

SuperMAG data portal (http://supermag.jhuapl.edu/mag) provides the list of time moments of substorm onsets and intensifications. This gives us a possibility to estimate a time delay Δt between these intensifications and the MIE occurrence. The statistics of Δt distribution is given in Fig. 3. The time delay may vary in a wide range from 0 to more than 2 h and can be approximated by the normal (Gaussian) distribution. Thus, the probability of the MIE occurrence decreases exponentially with time lapse after the substorm onset.

4 Discussion and Summary

Understanding the mechanism of nightside MIEs is important not from academic interest only, but it has an important practical application. The magnetic disturbances with large dB/dt, not accounted for by any geomagnetic indices, draw a

considerable interest as possible drivers of intense GIC bursts [8]. Comparison of fine impulsive structure of substorms with GIC recordings revealed that actual drivers of GIC are localized vortex-like ionospheric current structures, recorded on the ground as isolated or multiple pulses [4, 5]. Thus, nightside MIEs can be imagined as "cosmic tornados" during severe space weather events.

The mechanism of formation of a quasi-periodic series of MIEs, observed as Ps6 pulsations, has not been understood yet. Their periodicity 10–20 min is larger than typical Alfven eigenfrequency of field lines at auroral latitudes (3–10 min). Ps6 magnetic pulsations are often associated with the omega bands forms which typically occur at the poleward edge of the diffuse aurora. The substorm activations are typically associated with an activation of the most poleward arc system (called Poleward Boundary Intensifications—PBI) followed by the North-South aligned protrusions of auroral forms. A quasi-periodic sequence of these auroral forms is associated with Ps6 magnetic pulsations. Highly likely the PBI auroral events are the ionospheric manifestation of Bursty Bulk Flows (BBFs) in the magnetotail [9]. Therefore, nighttime MIEs during substorms can occur in association with magnetotail BBF, whereas multiple BBF could be a driver of Ps6 pulsations.

The statistical analyses presented may be of some help in efforts to determine the mechanisms responsible for the nighttime MIEs. Comparison of the statistical characteristics of different time series enables one to speculate about the similarity of their physical nature. Regularities of distributions of amplitudes of dayside MIEs have been investigated in [10] using observations from a number of high-latitude observatories. Tails of functions of impulse amplitude statistical distributions were reasonably well approximated by a power function. The majority of statistical distributions of dayside MIEs' amplitudes had the exponent $a > 2$ that is typical of chaotic regimes called strong intermittent turbulence. Comparison of the amplitude statistics for dayside MIEs and SCs showed that statistics for both types of impulses were well approximated by power-law function, whereas the correlation coefficient between the approximation curve and experimental data was 0.95–0.99 for MIEs and 0.90–0.97 for SSCs [11]. However, the power-law approximation was applied in [10, 11] to a rather narrow range of variables: the ratio between maximal and minimal values was ~ 3 only. Indeed, the power-law approximation applied to tails of PDF of nighttime MIEs (Fig. 2) visually coincides with the log-normal approximation. In a wider range of variables (maximum to minimum ratio is ~ 17) the power-law approximation is insufficient, and PDF is better modeled by the log-normal distribution.

The comparison of the statistical distributions of impulse amplitudes of both |Δ B| and |dB/dt| shows that PDFs at all stations fit best the log-normal distribution. The fact that amplitudes of nightside MIEs in the range of two magnitudes are described by the same law indicates that these impulsive disturbances are not accidental, but they are manifestation of some organized physical process. For example, the fact that the PDF appears to be log-normal may indicate that this distribution is formed as a result of a multiplicative stochastic effect. According to many observations, turbulence in the Earth magnetotail often has a log-normal form

[12]. Such a coincidence may indicate that the turbulence of the near-Earth plasma is largely responsible for the variability of the geomagnetic field on the time scale of these events.

References

1. Viljanen, A.: Relation of geomagnetically induced currents and local geomagnetic field variations. IEEE Trans. Power Deliv. **13**, 1285–1290 (1998)
2. Kappenman, J.G.: An overview of the impulsive geomagnetic field disturbances and power grid impacts associated with the violent Sun-Earth connection events of 29–31 October 2003 and a comparative evaluation with other contemporary storms. Space Weather **3**, S08C01 (2005). https://doi.org/10.1029/2004sw000128
3. Love, J.J., Lucas, G.M., Kelbert, A., Bedrosian, P.A.: Geoelectric hazard maps for the mid-Atlantic United States: 100 year extreme values and the 1989 magnetic storm. Geophys. Res. Lett. **44** (2018). https://doi.org/10.1002/2017gl076042
4. Belakhovsky, V., Pilipenko, V., Engebretson, M., Sakharov, Y., Selivanov, V.: Impulsive disturbances of the geomagnetic field as a cause of induced currents of electric power lines. J. Space Weather. Space Clim. **9**, A18 (2019). https://doi.org/10.1051/swsc/2019015
5. Pilipenko, V.A., Belakhovsky, V.B., Sakharov, Y.A., Selivanov, V.N.: Irregular geomagnetic disturbances embedded into substorms as a cause of induced currents in electric power lines, "Physics of Auroral Phenomena". In: Proceedings of the XLI Annual Seminar, Apatity, pp. 26–29 (2018)
6. Engebretson, M.J., Steinmetz, E.S., Posch, J.L., et al.: Multiple-instrument observations of nighttime magnetic impulse events (MIEs) at high latitudes. J. Geophys. Res. (2019, in Press)
7. Guillon, S., Toner, P., Gibson, L., et al.: Colorful blackout: the havoc caused by auroral electrojet generated magnetic field variations in 1989. IEEE Power Energy, 59–71 (2016)
8. Ngwira, C.M., Sibeck, D.G., Silveira, M.D.V., et al.: A study of intense local dB/dt variations during two geomagnetic storms. Space Weather **16**, 676–693 (2018)
9. Henderson, M.G., Kepko, L., Spence, et al.: The evolution of North-South aligned auroral forms into auroral torch structures: the generation of omega bands and Ps6 pulsations via flow bursts. In: Winglee, R.M. (ed.) Proceedings of the 6-th International Conference on Substorms. University of Washington, Seattle, USA (2002)
10. Klain, B.I., Kurazhkovskaya, N.A., Zotov, O.D.: Research into amplitude regularities of high-latitude magnetic impulses. Sol.-Terr. Phys. **10**, 81–88 (2007)
11. Kurazhkovskaya, N.A., Klain, B.I.: Magnetic impulsive events (MIEs) and storm sudden commencements (SSCs) in high-latitude magnetosphere. Geomag. Aeron. **56**, 33–45 (2016)
12. Kozak, L.V., Petrenko, B.A., Lui, A.T.Y., et al.: Turbulent processes in the Earth's magnetotail: spectral and statistical research. Ann. Geophys. **36**, 1303–1318 (2018)